~~CONFIDENTIAL~~

(Unclassified)

PRELIMINARY DESIGN AND EXPERIMENTAL INVESTIGATION

OF THE FDL-5A UNMANNED HIGH L/D SPACECRAFT
Part IV - Aerothermodynamics

*** Export controls have been removed ***

F. L. Guard

H. D. Schultz

This document is subject to special export controls and each transmittal to foreign governments or foreign nationals may be made only with prior approval of the Air Force Flight Dynamics Laboratory, Wright–Patterson Air Force Base, Ohio.

i

~~CONFIDENTIAL~~

TABLE OF CONTENTS

v

LIST OF ILLUSTRATIONS

vi

LIST OF ILLUSTRATIONS (Continued)

LIST OF ILLUSTRATIONS (Continued)

LIST OF ILLUSTRATIONS (Continued)

LIST OF ILLUSTRATIONS (Continued)

LIST OF ILLUSTRATIONS (Continued)

LIST OF ILLUSTRATIONS (Continued)

LIST OF ILLUSTRATIONS (Continued)

LIST OF ILLUSTRATIONS (Continued)

xiv

LIST OF ILLUSTRATIONS (Continued)

LIST OF ILLUSTRATIONS (Continued)

LIST OF ILLUSTRATIONS (Continued)

LIST OF ILLUSTRATIONS (Continued)

LIST OF ILLUSTRATIONS (Continued)

LIST OF ILLUSTRATIONS (Continued)

LIST OF ILLUSTRATIONS (Continued)

LIST OF TABLES

LIST OF SYMBOLS

a   major semi-axis of ellipse (ft)

b   minor semi-axis of ellipse (ft) or model skin thickness (ft)

C   specific heat (Btu/lb F)

C_{DLE} leading edge drag coefficient

C_{DN} nose drag coefficient

C_L lift coefficient

C_P pressure coefficient

D   drag (lb) or nose diameter (ft)

h   heat transfer coefficient (Btu/ft^2 sec $^{\circ}$R)

i   enthalpy (Btu/lb)

k   thermal conductivity (Btu/ft sec $^{\circ}$R)

L   lift (lb)
             or
     vehicle length (1.667 ft for wind tunnel model)

L_f length of fin leading edge (ft)

M   Mach number

P   pressure (lb/ft^2)

P_o' pitot pressure (lb/ft^2)

q   heating rate (Btu/ft^2 sec)

R   radius (ft)

Re   Reynolds number

S   reference planform area (ft^2)
             or
     surface distance measured from the model lower surface centerline (for lower surface data plots) or from the most outboard model position (for upper surface data plots) to the sensor location (ft)

$S_{\ell e}$	surface distance between the model lower surface centerline and the most outboard model position (ft)
S_{max}	surface distance between the most outboard model position and the upper surface centerline (ft)
St	Stanton number
T	temperature (^{O}R)
t	time (sec)
V	velocity (ft/sec)
W	vehicle weight (lb)
x_{eq}	surface distance between sensor location and assumed boundary layer origin (in.)
X	chordwise distance from model nose (ft)
X_f	distance along fin leading edge measured from base (ft)
$X_{\ell e}$	distance along body side panel measured normal to leading edge
Y	spanwise distance from model centerline (ft)
α	vehicle angle of attack (degrees)
α_{eff}	surface flow deflection angle (degrees)
β	yaw angle (degrees) or stagnation point velocity gradient (sec^{-1})
Γ	dihedral angle (degrees)
δ	surface flow expansion angle, relative to freestream (degrees)
δ_e	elevon deflection angle, positive when deflected into airstream (degrees)
ϵ	delta wing semi-apex angle (degrees) or surface emissivity
Λ	leading edge geometric sweepback angle (degrees)
Λ_{eff}	effective sweepback angle (degrees)
τ	fin toe-in angle (degrees)
ρ	density (lb/ft^3)
ϕ	bank angle (degrees) or fin roll-out angle (degrees)
ϕ_s	body side angle (degrees)

SUBSCRIPTS

c	circular or chord
e	boundary layer edge

xxiii

eff	effective
fr	forward ramp
lam	laminar
ℓ_e	leading edge
n	nose
o	reservoir
ref	reference
s	stagnation point
sl	stagnation line
tc	tangent conv
th	theoretical
turb	turbulent
w	wall
x	distance from boundary layer origin measured in flow direction
∞	freestream
ϑ	momentum thickness

SECTION 1

(U) INTRODUCTION AND SUMMARY

(U) The significant aerothermodynamic results obtained during the experimental portion of the study are presented in this volume. The principal objectives of the aerothermodynamic analyses were (1) to provide preliminary design information to determine the most feasible high L/D configuration concept, and (2) to conduct an extensive aerothermodynamic test program using the selected configuration to validate the design methods.

(U) Accomplishement of the first objective was initiated during the analytical portion of the study with the generation of parametric temperature data to illustrate the importance of design variables such as configuration geometry and attitude. During the experimental portion of the study, vehicle surface temperatures were predicted for the FDL-5 configuration.

(U) The second objective was accomplished by conducting a series of wind tunnel tests using scale models of the FDL-5 configuration. Heat transfer and pressure tests were run at nominal Mach numbers of 10 and 19 using facilities at the Arnold Engineering Development Center. Data were obtained for model angles of attack ranging from zero to 35 degrees, in 5-degree increments, and yaw angles of -2, 0, 2, 4, and 6 degrees. More than 17,000 data points were obtained during the program, providing a rich source of data from which selected correlations were made to accomplish the program objectives. A complete presentation of the reduced test data and the correlations are contained in this report. Correlation with theory was mainly directed at the FDL-5 design attitude, i.e., ten degrees angle of attack and zero yaw. Data obtained from these tests are compared with theoretical aerothermodynamic methods presented in Section 2 of this report, and the results incorporated in the FDL-5 preliminary design.

(C) Predicted FDL-5 surface temperatures, based on a high heating reference entry trajectory, are compatible with the proposed structural materials: tungsten-thoria for the nose cap, coated tantalum for the leading edges, coated columbium for the lower surface, and superalloys for the upper surface. From a heating standpoint, the lower surface is the most marginal. If a 6 percent design margin is added to the nominal temperature predictions, approximately 40 percent of the lower surface exceeds 2500°F, the assumed temperature limit for coated columbium. However, predicted maximum temperatures on essentially the entire lower surface result from turbulent flow, and the wind tunnel data indicate that the transition criterion employed in the heating predictions may be overly conservative.

1

(C) For angles of attack above 5 degrees, the AEDC lower surface pressure data generally agree with tangent cone theory within ± 10 percent. Satisfactory correlation of upper surface pressures was achieved using a prediction technique, based on blast wave theory, which resulted from analysis of leeward surface pressures on slab delta wings. Vehicle regions where satisfactory pressure data correlations were not achieved are the aft lower compression surface and dorsal fin. Forward ramp centerline heating rates are consistently higher than predicted by laminar swept cylinder theory by an average of about 20 percent. Aft lower surface centerline heating rates are overpredicted by laminar strip theory for angles of attack up to about 20 degrees and underpredicted at higher angles of attack. Near the leading edge however, aft lower surface heating rates are higher than strip theory at all angles of attack tested. Aft lower compression surface heating rates are generally underpredicted by laminar strip theory for angles up to about 10 degrees, and are overpredicted at higher angles of attack. Except for zero angle of attack, body side panel heating rates are lower than predicted by laminar strip theory, based on experimental pressures and surface flow directions. On the upper surface, the Tunnel C heating trends with angle of attack are frequently erratic, possibly as a result of boundary layer transition or vortices. For $10^\circ \leq \alpha \leq 20^\circ$, Tunnel C upper centerline heating rates are generally 20 to 50 percent lower than zero angle-of-attack turbulent strip theory, while corresponding Tunnel F data are 30 to 45 percent below zero angle-of-attack laminar strip theory.

(C) Radiation equilibrium isotherms based on the AEDC wind tunnel data generally agree with original predictions within ± 200°F on the lower surface, and within ± 100°F on the body side panels and aft lower compression surface. No material changes would be required as a result of the temperature revisions.

(U) The following section discusses the aerodynamic heating prediction methods used throughout this study. Section 3 presents surface temperature predictions for the FDL-5 configuration. A brief discussion is included on the effects of boundary layer transition and vehicle wing loading on peak temperature levels. Results of the heat transfer and pressure experimental tests are presented in Section 4. Revised FDL-5 temperature predictions, based on the wind tunnel results, are discussed in Section 5.

SECTION 2

(U) HEATING PREDICTION METHODS

(U) Accurate prediction of aerodynamic heating and resulting temperatures
is required for proper materials selection, structural design, sizing of
thermal insulation, and analysis of active cooling requirements. This
section reviews the theoretical/empirical methods employed to predict aero-
dynamic heating rates during this study. The methods discussed were used
to generate the aerothermodynamic parametric data presented in Part II,
to predict the FDL-5 surface temperatures shown in Section 3 of this report,
and for comparison with the wind tunnel data presented in Section 4 of this
report.

(U) Appendix I of this Part presents an analysis of delta wing heating and
pressure data from tests conducted by the Air Force Flight Dynamics Labora-
tory. This data analysis and correlation was performed to validate some
of the prediction methods initially selected for use during this study.

(U) Heating theories employed at various vehicle locations are summarized
below. In all cases, Hansen's equilibrium air properties (Ref. 1) and
1962 Standard Atmosphere Data were used in theory evaluation.

2.1 (U) NOSE AND LEADING EDGES

(U) Stagnation point heating rates were computed by the method of Fay and
Riddell (Ref. 2) with the velocity gradient based on the experimental data
of Boison and Curtiss (Ref. 3). These data and Newtonian theory are shown
in Figure 1 as non-dimensional velocity gradient (a β/V_∞) versus cross-
section aspect ratio (b/a). The data were obtained on ellipsoids at
Mach 4.75. Because the nondimensional velocity gradient is essentially
constant for Mach numbers above 5, the recommended curve of Figure 1 was
used for all hypersonic Mach numbers.

(U) The body and fin leading edge heating rates were computed by the swept
cylinder theory of Beckwith (Ref. 4). The sweep independence principle was
employed whereby it is assumed that the spanwise velocity component contri-
butes to the recovery enthalpy, but does not affect the heat transfer
coefficient. On highly swept configurations, the actual leading edge stag-
nation line is displaced from the geometric stagnation line by the angle ϕ_{sl}
which is related to the leading edge angle of attack and sweep angle by the
equation

$$\phi_{sl} = \tan^{-1}\left[\frac{\tan \alpha_{le}}{\cos \Lambda}\right] \tag{1}$$

3

(U) Consequently, at some vehicle attitudes the sonic line may be on the lower surface rather than the leading edge. The resulting flow interaction with the lower surface has been shown analytically and experimentally to reduce the stagnation line velocity gradient, and hence the heating rate, compared to the case of an isolated swept cylinder. Predicted leading edge stagnation line heating rates are therefore considered to be conservative at large vehicle angles of attack.

(C) Figure 2 shows a correlation of body leading edge heating data taken from Figures 14.1 and 14.3 of the X-20 (Dyna-Soar) leading edge heat transfer test summary report (Ref. 5). The data indicate that swept cylinder theory conservatively predicts leading edge heating rates for angles of attack up to 20 degrees. It should be noted, however, that the applicability of swept cylinder theory has not been demonstrated for sweep angles greater than about 75 degrees. Since the FDL-5 employs a leading edge sweep of 81 degrees (compared to 72.8 degrees for the X-20) experimental heating data on highly swept leading edges are most desirable.

2.2   (U) LOWER SURFACE

(C) Selection of the heating theory for the lower surface depends on the geometry under consideration, i.e., flat, curved, or dihedral. Theoretical methods for predicting heating rates on flat lower surfaces are discussed in detail in Reference 6. Briefly, the lower surface flow field is obtained from a real gas computer solution (Ref. 7) assuming the local conditions to be those behind a single oblique shock produced by a flow deflection equal to the local effective angle of attack. For small angles of attack, laminar and turbulent heat transfer coefficients were computed from strip theory using the methods of van Driest (Refs. 8 and 9). At larger angles, laminar strip theory heating rates were increased to account for spanwise flow. This was accomplished using the empirical data fairing of Neumann and Renfroe (Ref. 10) which were obtained from correlation of highly swept delta wing data from several impulse facilities. This result is shown in Figure 3, along with additional heating data on the centerline of five flat bottom delta wing models. The ratio of experimental to laminar strip heating rates is plotted as a function of the parameter $(\tan \alpha/\tan \epsilon)^{1/2}$ which is a correlation parameter for streamline divergence theory at hypersonic speeds (Ref. 10). At low angles of attack the experimental heating rates are a fraction of the strip theory values due to inflow caused by the high pressure region near the wing leading edges. The data indicate that no correction for outflow is required until the correlation parameter exceeds a value of about 1.0. At higher values of the correlation parameter reasonable agreement with streamline divergence theory is obtained, although the data scatter is excessive.

(C) Figure 4 shows a comparison of experimental and theoretical spanwise heating distributions on flat bottom delta wings. The data are compared with laminar strip theory evaluated using oblique shock flow properties with the characteristic dimension measured from the leading edge in a direction parallel to the model centerline. To avoid leading edge bluntness induced effects, all data were obtained from sharp leading edge models. Although the data scatter is considerable, strip theory provides a reasonable correlation to the data mean.

(C) Lower surface centerline heating rates on curved bottom configurations were based on Beckwith's swept cylinder theory (Ref. 4). The spanwise heating distribution from the stagnation line was based on Lees' laminar distribution (Ref. 11) or from available experimental distributions on similar configurations. Because swept cylinder theory may underpredict the heating rates at small angles of attack, the heating rates were compared with the strip theory, and the larger value used. If a curved lower surface experienced turbulent flow, centerline heating rates were based on turbulent swept cylinder or strip theory, whichever yielded the higher heating. Turbulent flow spanwise heating distributions were obtained from Figure 6-33 of Reference 12, and are based on streamline divergence theory for a sharp leading edge delta wing.

(U) Figure 5 shows a correlation of lower surface centerline heating data from the ASD Model W3 elliptic cone which approximates the high L/D configuration curved lower surface. The tests were performed in the Cornell Aeronautical Laboratory 48 inch Hypersonic Shock Tunnel at a freestream Mach number of 14.5 and Reynolds number per foot of 5.6×10^4 (Ref. 13). Data are compared with laminar swept cylinder theory based on local effective radius and with laminar strip theory neglecting outflow. The effective radius employed in the swept cylinder calculations was the local radius of an ellipse (a^2/b) multiplied by an empirical correction factor based on the stagnation point velocity gradient measurements of Boison and Curtiss (Fig. 1). For a 2:1 ellipse such as the W3 cone, the recommended correction factor to the radius is 1.18. The heating rate is thereby increased by 8.5 percent above the value predicted by using the Newtonian velocity gradient based on local stagnation line radius.

(C) In the angle of attack range of particular interest to the current study (10-20 degrees) the centerline heating data are in excellent agreement with swept cylinder theory. The zero angle of attack data are in good agreement with laminar strip theory. This is somewhat surprising since one might expect the zero angle of attack data to agree with cone theory. The correlation with strip theory suggests a thickening of the boundary layer along the centerline as a result of inflow from the leading edge region.

(C) Figure 6 shows spanwise hypersonic heating data from two elliptic cones with highly swept delta planforms. The Mach 14.5 data from the 0.5 aspect ratio ASW Model W3 were obtained at $\alpha = 10$ and 20 degrees (Ref. 13). Mach 7 data are also shown and were obtained on a 0.20 aspect ratio cone tested at $\alpha = 15$ and 30 degrees (Ref. 14). These data were used to predict the heating distributions on curved lower surface configurations because the spanwise heating distributions in the angle of attack range of interest are not amenable to analytical solution. It should be noted that the actual leading edge stagnation line heating rates were not measured on the elliptic cone models because the sensors at 100 percent span were located on the major axis, which is a true stagnation line only for $\alpha = 0$. Consequently, lower surface spanwise heating distributions were assumed to follow the trend of the elliptic cone data up to 90 percent span, and were then faired into the leading edge stagnation line heating rate.

(U) The method employed to calculate heating rates to a dihedraled lower surface and keel line depends on the dihedral angle, keel radius, and angle of attack. For effective angles of attack less than about 15 degrees, heating rates to the wing panels were predicted by laminar or turbulent strip theory, based on the methods of van Driest. The flow field was computed by oblique shock theory assuming a wedge angle equal to the wing panel effective angle of attack which is related to the configuration and attitude by

$$\alpha_{eff} = \sin^{-1} \frac{\tan \Gamma \tan \epsilon \cos \alpha + \sin \alpha}{\sqrt{1 + \left(\frac{\tan \Gamma}{\cos \epsilon}\right)^2}} \tag{2}$$

(U) The characteristic dimension is based on the wetted distance from the leading edge or keel stagnation line measured in a direction parallel to the projection of the freestream velocity vector into the plane of the dihedraled panel. Wing panel heating rates were faired into the keel line and leading edge heating rates, both of which were computed by swept cylinder theory and Lees' laminar distribution. At higher angles of attack, dihedraled panel heating rates were based on Lees' distribution computed in terms of the keel line heating rate.

(C) Figure 7 shows a correlation of lower surface heat transfer data obtained from two dihedraled delta wing configurations tested by Dunavant (Ref. 15). The pertinent geometric features and model attitudes are listed on the figure. The experimental heat transfer coefficients are ratioed to the laminar strip heat transfer coefficients and are plotted as a function of the ray angle from the vehicle centerline measured in the plane of the wing panel. Local flow properties were based on oblique shock theory with the effective angle of attack given by Eq. 2. The agreement between theory and data is good and a significant improvement results compared to the correlations of the same data presented by Dunavant (Figures 7C and 8C of Reference 15) where the characteristic dimension is based on the distance from the leading edge measured parallel to the model centerline.

2.3   (U) UPPER SURFACE

(U) The prediction of heating rates on leeward surfaces is subject to large unknowns due to the limited amount of theoretical and experimental work in this area. For the present study, upper surface centerline heating rates were based on hypersonic wind tunnel data from models of similar geometry; i.e., the AF-1 (Ref. 16), F-5A (Ref. 17) and ASSET (Ref. 18). Figure 8 shows these data and the curve used in heating predictions. The curve is conservative with respect to most of the data and is drawn through the point $q/q_S = 0.1$ at $S/R = 1.57$ because this is approximately the hypersonic heating rate at the shoulder of a hemisphere.

(U) For laminar flow, the experimental data were applied directly in calculating the upper surface heating. Transition to turbulent flow was accounted for by multiplying the experimental values of Figure 8 by the ratio of turbulent-to-laminar strip theory. The application of the laminar flow test data to turbulent heating predictions is an approximation which was used since no applicable hypersonic turbulent data on leeward surfaces were found.

6

(U) Two methods were used for computing heating rates on the upper body side panels. For the parametric studies, presented in Part II, Section 3, the heating at positive flow deflection angles was computed from laminar strip theory. For expansion angles greater than five degrees, the flow was assumed to be separated, and the heat transfer coefficient was taken as one-half the zero angle of attack strip flow value. This heating rate is indicated from Chapman's work on separated cavity flows (Ref. 19). A smooth curve was faired between the predicted heating rates at positive flow deflection angles and expansion angles above five degrees. Body side panel flow deflection angles were computed from the relation (Fig. 9),

$$\sin \alpha_{eff} = \frac{\tan \phi_S [\tan \beta + \tan \epsilon] - \tan \alpha - \tan \alpha_{fr}}{\sqrt{1 + \tan^2 \alpha + \tan^2 \beta} \ \sqrt{1 + \tan^2 \phi_S} (\tan \epsilon - \frac{\tan \alpha_{fr}}{\tan \phi_S})} \tag{3}$$

(C) To calculate temperature-time histories for the FDL-5 configuration, heating rates on the body side panels were computed by van Driest's strip theories, with the characteristic dimension assumed to be the wetted distance from the leading edge stagnation line measured in a plane inclined 30 degrees to the vehicle centerline. Pressures on the side panels were computed by the following semi-empirical relation which is shown in Appendix I to accurately predict leeward surface pressures on several slab delta wing and high L/D configurations:

$$\frac{P}{P_\infty} = 1 + (0.073 - 0.0033\delta) M_\infty^2 (C_{DN})^{\frac{1}{2}} / (X/R)^{\frac{2}{3}} \tag{4}$$

The nose drag coefficient was assumed to be 1.44, the Newtonian value for a 0.5 aspect ratio ellipsoid.

(C) This calculation procedure was adopted following the completion of a test program in the Lockheed-California Company Hypersonic Tunnel which measured Mach 10 heating distributions and surface streamline patterns on a representative high L/D configuration (Ref. 20). These tests indicated that the assumption made during the parametric analysis of separated flow over the body side panels for δ > 5 degrees, was erroneous. The length of the body side panel oil flow traces suggested a region of high shear, and it is doubtful if separation occurred until the flow reached the forebody side panel/top surface tangency line. As a result, the heating rates used for the parametric analysis (Part II) are somewhat low. This does not affect the conclusions of Part II, however.

2.4 (U) FINS

(U) Fin stagnation line heating rates were calculated from swept cylinder theory. The effective sweep angle was obtained by the geometric relation:

$$\sin \Lambda_{eff} = \frac{\sin \Lambda - \tan (\tau + \beta) \cos \Lambda \sin \phi + \tan \alpha \cos \Lambda \cos \phi}{\sqrt{1 + \tan^2 (\tau + \beta) + \tan^2 \alpha}} \qquad (5)$$

(C) Figure 10 shows a correlation of fin leading edge heating data from the X-20 model. These data were obtained from Figures 24.1, 24.3, and 24.7 of Reference 5 for vehicle angles of attack of 0, 10, and 15 degrees, respectively. The significant feature of Figure 10 is the high heating near the fin/wing junction where the flow upstream of the fin leading edge is influenced by the body. Heating rates approximately twice the swept cylinder theory prediction were measured on the X-20 model fins at low angles of attack. The heating rate increase can be attributed to the flow passing through a body generated shock wave before encountering the fin. For certain combinations of fin sweepback angles and body generated shock wave angles, the total pressure loss across the two shock waves will be considerably less than that across a single fin generated shock wave. Since the primary factors influencing heat transfer are pressure and total enthalpy, heating from the two shock flow field is higher than that for the single shock case. Although the increased heating can be readily explained, the magnitude of the increase cannot be accurately predicted because of the complex flow situation upstream of the fin. As indicated by Figure 10 the magnitude of the increased heating decreases as the angle of attack increases. At $\alpha = 20$ degrees, the heating rates along the fin leading edge are uniform and are in good agreement with swept cylinder theory.

(U) Heating on the fin side panels was computed from laminar strip theory corrected for pressure gradient using the method of Bertram and Feller (Ref. 21). The side panel effective angle of attack is given by:

$$\sin \alpha_{eff} = \cos \alpha \cos \beta \sin \tau \cos \phi + \cos \tau \cos \phi \sin \beta$$
$$+ \sin \phi \sin \alpha \cos \beta \qquad (6)$$

2.5 (U) TRANSITION CRITERION

(C) Boundary layer transition can strongly affect heating levels, and therefore was taken into consideration in the aerothermodynamic analysis. To establish a transition criterion, wind tunnel and inflight heating data obtained during the ASSET program were examined. ASSET flight data indicated that turbulent flow occurred on the vehicle lower surface when the ratio of momentum thickness Reynolds number to local Mach number exceeded a value of about 185. Figure 11 shows correlations of additional transition data from

several sharp delta wing models tested at Mach numbers ranging from 6 to 10. Data sources are noted on the figure. The transition criterion (Re_θ/M_e) is plotted versus local unit Reynolds number. Transition begins when $Re_\theta/M_e \approx 100$ to 130 and the flow is completely turbulent when $Re_\theta/M_e \approx 160$ to 200. A slight increase in transition Reynolds number with local unit Reynolds number is indicated.

(C) Based on the foregoing experimental data, the following criterion for boundary layer transition was employed during the study:

$$Re_\theta/M_e \geq 150 \qquad\qquad (7)$$

Although this is slightly unconservative with respect to the wind tunnel data plotted on Figure 11, nose and leading-edge bluntness are known to delay transition. For a typical high L/D entry, Eq. 7 results in a local Reynolds number at transition on the order of 2 to 8 million.

SECTION 3

(U) FDL-5 SURFACE TEMPERATURE PREDICTIONS

(U) Analytical/empirical techniques used for predicting aerodynamic heating are discussed in the preceding section. Based on these methods, surface temperature histories and vehicle isotherm locations were determined for the FDL-5 configuration. These predicted temperatures, including consideration of thermal margins, aided in the selection of vehicle structural materials and in the determination of thermal protection requirements.

(U) The basic vehicle structures under consideration employ a thin metal skin which is radiation cooled. These structures have little heat storage capacity, and at most vehicle locations, the structural design is such that the heat transfer rates from the surface to the vehicle interior are low compared with the surface convective heating rates. For these reasons, calculated surface temperatures are conservatively based on radiation equilibrium conditions: i.e., the convective heating rate to the vehicle surface is equal to the heat radiated to space. A surface emissivity equal to 0.7 was assumed for all temperature calculations. In addition, a $50^\circ R$ radiation sink temperature was used as per Reference 6.

(U) Geometric characteristics and dimensional details of the full-scale FDL-5 configuration are shown in Figure 12. The reference length of the vehicle, 33 feet, is taken from the nose cap (station 0) to the junction between the aft body leading edge and the vehicle base. The vehicle is basically a delta planform lifting body with a lift to drag ratio of approximately 3 at hypersonic speeds. A 2:1 ellipsoidal nose is employed with the axis rotated 11 degrees so that the geometric and flow stagnation point coincide at the vehicle design attitude. Body leading edge radii are 1.5 inches.

(U) The FDL-5 configuration employs compression surfaces on the upper and lower portions of the aft body area. The lower compression surfaces are rolled out 20 degrees from vertical and toed in 6 degrees. These "compression sharing" surfaces result in the elimination of any distinct fin geometry for hypersonic stability. A center fin, shielded by the body during hypersonic flight, is provided for low speed stability. A curved lower surface-forward ramp is employed to maximize internal volume. Upper forebody side panels are rolled in so as to be parallel with the free-stream flow at maximum L/D attitude. Additional description of the FDL-5 configuration is given in Part II, Section 5.

(U) The high heating reference entry trajectory used for temperature calculations is shown in Figure 13 as time histories of altitude and velocity.

Vehicle parameters and injection conditions are noted on the figure. A constant vehicle angle of attack (11 degrees) and bank angle (34 degrees) was assumed.

3.1 (U) TEMPERATURE HISTORIES

(U) Figure 14 shows predicted radiation equilibrium temperature histories at four locations on the FDL-5 vehicle. Maximum temperatures on the nose and leading edge are 4420°F and 2940°F, respectively. Both are within the capability of the proposed structural materials, tungsten-thoria and tantalum. At station 100, the peak lower surface centerline temperature based on laminar theory is 1930°F. Transition from laminar to turbulent flow (when $Re_\theta/M_e = 150$) occurs at 6250 seconds and is indicated by the discontinuity in the temperature curve. The peak temperature at station 100 during turbulent heating is 2450°F. At station 396, transition occurs at about 5730 seconds, and the resultant peak temperature is 2000°F.

(U) Shown in Figure 15 are both laminar and turbulent flow temperature histories on the FDL-5 lower surface for entry times between 4000 and 7000 seconds. Temperatures at eight locations are shown. Peak laminar temperatures occur at approximately 5200 seconds, which corresponds to a vehicle velocity of about 20,000 fps (Figure 13). Maximum turbulent temperatures occur at a velocity of approximately 18,000 fps.

(U) Assumed transition points are indicated by vertical lines connecting the corresponding laminar and turbulent flow temperature histories. Note that peak temperatures on essentially the entire lower surface result from turbulent heating. Peak temperatures from Figure 15 are plotted versus vehicle station in Figure 16. When a 6 percent margin is added to these temperatures, about 40 percent of the lower surface exceeds 2500°F, the assumed temperature limit for coated columbium. As a result, it is recommended that initial flights of a test vehicle be made with wings level to establish thermal design accuracy before proceeding with high heating banked flights.

3.2 (U) ISOTHERMS

(U) Figure 17 shows the predicted surface temperature distribution on the FDL-5 configuration at the design conditions of $V_\infty = 20,000$ fps, H = 200,000 ft, and $\alpha = 11$ degrees. This flight condition closely approximates the peak laminar heating point on the reference trajectory (Figure 13). Although the temperatures shown are generally not maximum values due to turbulent flow which predominates at lower velocities, these distributions are of particular interest since comparisons are possible between the values shown and predicted temperatures based on the results of the laminar flow wind tunnel tests.

(U) At the design condition, the predicted temperature on the 0.5 aspect ratio ellipsoidal nose is 4330°F. Leading-edge stagnation line temperatures are 2870°F forward of station 260, and 2790°F aft of this station, where the sweep angle increases from 81 to 84 degrees. Predicted stagnation line temperature on the 70-degree-sweep dorsal fin is 3200°F. Fin side panel temperatures range from about 1000 to 1500°F, which is within the capability of superalloys.

Excepting the aft lower compression surface, temperatures on the lower and upper surfaces are well within the capability of columbium and superalloys, respectively.

(U) Temperature variation on the FDL-5 aft lower compression surface with distance from the leading edge stagnation line is plotted in Figure 18. Predicted distributions at stations 300 and 380 are shown. At the design angle of attack, the inclination of this surface relative to freestream is 11 degrees. The locations of the tangency points connecting planar and cylindrical surface elements are indicated on the figure by the letters A through F.

(U) The predicted temperature at the side panel/body leading edge tangency point is about 2500°F. Minimum side panel temperatures at stations 300 and 380 are 1800°F and 1500°F, respectively. Considering that temperature margins must be added to these values and the effects of yaw are not included in the calculations, it appears that portions of the side panels must be fabricated from a refractory metal such as columbium, and the leading edge material (probably tantalum) must be extended approximately two inches beyond the side panel/leading edge tangency point.

(U) Predicted FDL-5 maximum surface temperatures for the reference trajectory (Figure 13) are shown as isotherms in Figure 19. The assumed vehicle attitude is 11 degrees angle of attack and zero yaw. As discussed previously, most of the peak temperatures result from turbulent heating at the assumed transition time. Consequently, the peak temperatures shown in Figure 19 do not occur simultaneously but represent a composite temperature map which includes the forward movement of the transition point during the entry period. For this reason the temperature gradients indicated by the isotherms are not necessarily the maximum experienced.

(U) By comparing the peak temperature isotherms with the laminar flow values of Figure 17, it may be observed that the major effect of boundary layer transition is to significantly increase the lower surface temperature levels (See also Figure 15). If the flow remained laminar throughout entry, these temperatures would range between about 1300 and 2000° F; whereas accounting for transition yields temperatures in excess of 2300°F over a major portion of this surface.

(U) Temperatures on the aft lower compression surface are also increased as a result of turbulent flow. The range of maximum temperatures on this surface is identical to that predicted for the lower surface. The maximum temperature occurs at the leading edge/side panel tangency line and is 2570°F.

(U) Stagnation point, body and fin leading edge temperatures are nominally the same in both isotherm figures as the flow is always laminar at these locations. Peak temperatures on the fin side panels are determined by turbulent heating for S/R > 40, which is just downstream of the 1200°F isotherm on Figure 19. The predicted maximum temperatures are between 1170 and 1500°F on approximately 90 percent of this surface.

(U) Peak upper body side panel temperatures are determined by turbulent heating when the wetted distance from the leading edge, measured in a plane 30 degrees to the horizontal, exceeds approximately three feet. Predicted temperatures are between 1300 and 1800°F on approximately 90 percent of the side panel surface. Maximum temperatures at each station occur at the leading edge/side panel tangency line. The estimated maximum temperature decreases from 2120°F at station 40 to 1850°F at station 260 as a result of the predicted pressure decrease along this surface.

(U) Upstream of station 40, peak upper surface centerline temperatures are nominally the same as at the design condition (Figure 17). Downstream of this location, maximum temperatures range from 870 to 1300°F; if the flow remained laminar throughout entry, these temperatures would be about 600 to 1200°F.

3.3 (U) TRANSITION AND WING LOADING EFFECTS

(U) Although peak lower surface temperatures generally result from turbulent flow, the boundary layer is assumed to be laminar at the point in the trajectory where peak turbulent heating would occur ($V_\infty \approx 18,000$ fps). Consequently, it is of interest to examine the effect of transition on peak temperatures. Figure 20 shows maximum lower surface centerline temperatures at stations 180 and 396 as a function of the transition criterion, Re_θ/M_e. Corresponding values of an alternate transition criterion, $Re_{e,x}$, are also shown. At the assumed transition point ($Re_\theta/M_e = 150$), the local Reynolds numbers, based on tangent wedge flow properties, are 2.0 and 3.6 million at stations 180 and 396, respectively. Boundary layer edge Mach numbers are on the order of 5 to 8 during transition.

(U) At station 396 the peak temperatures are between 1900°F and 2000°F for transition Reynolds numbers up to six million. Closer to the nose, peak temperatures are more sensitive to transition criterion. At station 180, for example, the peak temperatures decrease by about 70°F each time the transition Reynolds number is increased by one million.

(U) The FDL-5 reference trajectories are based on a wing loading of 35 psf. An approximate analysis was conducted to estimate the effect of wing loading on peak surface temperatures at specific vehicle locations. For an equilibrium glide the freestream density is given by

$$\rho_\infty = 2 \frac{W}{C_L S} \left[\frac{1}{V_\infty^2} - \frac{1}{V_c^2} \right]$$

Also

$$q_{lam} \sim \rho_\infty^{0.5}$$

and

$$q_{turb} \sim \rho_\infty^{0.8}$$

(U) Assuming the lift coefficient is independent of freestream density, the following relations apply for a given freestream velocity:

laminar flow
$$\frac{T_{w/s}}{T_{w/s\ =\ 35}} \approx \left[\frac{q_{w/s}}{q_{w/s\ =\ 35}}\right]^{0.25} \approx \left[\frac{W/S}{35}\right]^{0.125} \qquad (8a)$$

turbulent flow
$$\frac{T_{w/s}}{T_{w/s\ =\ 35}} \approx \left[\frac{q_{w/s}}{q_{w/s\ =\ 35}}\right]^{0.25} \approx \left[\frac{W/S}{35}\right]^{0.20} \qquad (8b)$$

(U) Peak temperatures presented in Figure 14 for a wing loading of 35 psf were modified according to the above relations, and are plotted as a function of wing loading in Figure 21. On the lower surface, which is most critical from a materials standpoint, the peak temperature exceeds 2500°F for wing loadings above 40 psf. At W/S = 35 psf the rate of change of temperature with wing loading is about 18°F/psf.

3.4 (U) TEMPERATURE MARGINS

(U) Computed surface temperatures presented in the preceding sections are nominal values and are felt to be the most probable. For preliminary design purposes temperature margins are added to the nominal temperature predictions for comparison with allowable structure temperatures. The temperature margins employed for the present study are those used on the ASSET program and are tabulated below as percent of temperature (°R) deviation at various vehicle locations.

Vehicle Location	Percent Deviation
Stagnation Point and Leading Edge	6
Windward Surfaces	6
Leeward Surfaces	10

(U) Additional discussion of these margins is contained in Reference 6. Design temperatures are plotted versus nominal temperatures in Figure 22 for margins of 6 and 10 percent.

SECTION 4

(U) EXPERIMENTAL PROGRAM

(U) Upon completion of the analytical predictions described in the preceding section, the FDL-5 configuration was tested in facilities at the Arnold Engineering Development Center, Tullahoma, Tennessee. Pressure and heat transfer tests were accomplished at nominal Mach numbers of 10 and 19 in Tunnels C and F of the von Karman Gas Dynamics Facility. Tunnel C is a continuous-flow wind tunnel with a 50-inch exit diameter contoured nozzle and uses air as the working gas. Tests were conducted in this facility at Reynolds numbers of 0.4 and 2.1 million per foot. Tunnel F is an arc-driven hypervelocity facility with a 100-inch exit diameter conical nozzle and uses nitrogen as the test gas. The useful run time, with the recently enlarged dump tank, is about 100 μsec. Testing in Tunnel F was accomplished at a nominal Reynolds number of 0.5×10^6 per foot. Detailed descriptions of both tunnels, including operating characteristics, are given in Reference 22. Aerodynamic force tests were conducted at various Mach numbers and additional pressure tests were run in Tunnel A. The results of the force and lower Mach number pressure tests are contained in Part III of this report.

4.1 (U) MODELS

(U) A total of three geometrically identical models were designed and fabricated for the pressure and heat transfer tests: (1) a stainless steel pressure model for Tunnel C, (2) a thin skin (0.050 inch nominal) heat transfer model for Tunnel C, and (3) a combined pressure and heat transfer aluminum model for Tunnel F. All models were 20 inches in length which resulted in a 0.0505 scale of the 33-foot FDL-5 configuration (Figure 12). A complete description of all the test models including design drawings and stress analyses, is contained in Reference 23.

(U) The Tunnel C pressure model was fabricated from Armco 17-4 PH stainless steel, heat treated to 1200°F. The model is hollow and consists of two halves (left and right) bolted together. A photograph of this model is shown in Figure 23.   Figure 24 shows the locations of the 99 pressure orifices (0.043 in. diameter) which are located on the righthand side of the model. The vertical fin is solid but was drilled for the installation of the nine pressure taps shown.

(U) The Tunnel C heat transfer model (Figure 25) consists of six formed sections of 0.050-inch 304 stainless steel welded together to form the body shell. Some deviations from true model contours were dictated by fabrication requirements. These included smaller radii where aft upper planar surfaces

intersect, and a reduced leading edge radius. Instrumentation consisted of 150 No. 30 Chromel-Alumel thermocouples welded to the inner skin surface. Sensor locations are shown in Figure 26. Skin thicknesses at each thermocouple location were measured prior to model assembly and were used in the AEDC data reduction program.

(U) The body of the Tunnel F heat transfer and pressure model was fabricated from 7075-T6 aluminum alloy and the vertical fin and elevons from 6061-T6 aluminum alloy. A photograph of this model is shown in Figure 27. The hollow model was fabricated in two pieces with a horizontal split plane. As shown in Figure 28, the model was instrumented at forty locations on the righthand side. Quarter-inch-diameter holes were bored through the model shell at each sensor location. During the pressure tests which were run first, each hole was fitted with a contoured slip-fit plug containing an 0.085-inch-diameter orifice. AEDC pressure transducers were connected to the origices with short lengths of flexible tubing. For the heat transfer tests, the plugs were removed, and contoured, 0.25-inch-diameter, AEDC heating transducers were installed.

4.2 (U) INSTRUMENTATION AND DATA REDUCTION

(U) All tests were accomplished using standard AEDC instrumentation and data reduction techniques. A detailed description of the Tunnel C test procedures, including instrumentation, calibration, and data reduction methods is presented in Reference 24. Tunnel C pressures were measured with Wiancko FM-types 1 and 15 psid transducers, referenced to a near vacuum. The transducers were automatically switched into and out of the recording system to allow measuring to the best precision. From repeat calibrations, the estimated pressure measurement precision was ±0.001 psia or ±0.5 percent, whichever was greater (Reference 24).

(U) The Tunnel C pressure data were recorded on multichannel oscillographs for monitoring during the tests and were also digitized on paper tape for final computing and data reduction at AEDC. For each run, final pressure data were listed on magnetic tape in the form

$$P(\text{psia}) \quad P/P_\infty, \quad P/P_o', \quad C_p$$

(U) Tunnel C heat transfer data were obtained as thermocouple output readings which were recorded on magnetic tape, at a rate of 20 times per second, from the start of the injection cycle until about 3 seconds after the model reached the tunnel centerline. Based on calibrations of the temperature recording system, the precision of the data is estimated at $\pm 0.2^\circ R/\text{sec}$ or ±2 percent, whichever is greater (Reference 24). Temperature data were reduced to standard coefficient form five times during each run, in 0.5-second intervals. At each thermocouple location, the wall temperature and the rate of change of wall temperature were computed using a least-squares parabola through 21 consecutive wall temperature points. The wall heating rate was then calculated

from the "thin skin" relation

$$q = \rho \, bC \, \frac{dT_W}{dt} \tag{9}$$

(U) The five reduced heating rates from each Tunnel C run generally varied less than 5 percent from the mean value. The second data reduction time was selected to achieve consistent and repeatable data minimally affected by either injection transients or conduction losses.

(U) An accurate knowledge of the model thermal properties in Eq (9) is required to insure maximum precision of the reduced data. To measure these properties, several samples of the 304 stainless steel sheet used for model fabrication were sent to Southern Research Institute (SRI). Specific heat was measured for the temperature range 400 to 1200°R and density at room temperature. The measured properties were incorporated in the AEDC data reduction program. The SRI final report documenting these measurements is presented as an appendix to this report.

(U) Heat transfer coefficient and Stanton number were computed from the Tunnel C data using the relations

$$h = \frac{q}{i_o - i_w} \tag{10}$$

and

$$St = \frac{h}{\rho_\infty V_\infty} \tag{11}$$

Along with model attitude and tunnel operating parameters, final heat transfer data were listed on magnetic tape as q and St/St_{th}, where St_{th} is the theoretical stagnation point Stanton number for the model nose based on the method of Fay and Riddell. The model nose radius used in evaluating St_{th} was 0.1515 inch. The computed Stanton number ratio is equivalent to the ratio of measured heating to stagnation point heating as a result of the method used in evaluating experimental heat transfer coefficients (Eq 10).

(U) Tabulations of the Tunnel C pressure and heat transfer data are contained in References 25 and 26, respectively. These data were automatically plotted using a CALCOMP plotter. Thirteen separate plot formats were written to accomplish the plotting.

(U) For pressure tests, the Tunnel F model was instrumented with 40 variable reluctance pressure transducers, which are described in detail in References 27 and 28. These transducers operate on the variable reluctance principle, i.e., the reluctance of a magnetic circuit is varied as the differential pressure across a diaphragm causes the diaphragm to deflect. The magnetic circuit is formed by the diaphragm, the sensor case, and an air gap between the diaphragm and case. Two air gaps are formed by the transducer configuration.

The change in reluctance is sensed by two coils, each encircling one of the magnetic circuits. The coils are arranged in a half-bridge and excited with 20-kc, 5-vrms power from the carrier amplifier system. Von Karman Facility (VKF) personnel estimate the uncertainties in the pressure measurements at ± 5 percent for $P \geq 0.005$ psia and ± 10 percent for $P < 0.005$ psia (Reference 29).

(U) The heat transfer gages used in Tunnel F are a refinement of the slug calorimeter. Details of their construction and calibration are given in References 27 and 28. A thin-film platinum resistor, deposited on the rear surface of an anodized aluminum calorimeter disc, is used as the sensing element to indicate the temperature rise of the caloric mass. The rate of change of resistance with respect to time is proportional to the heat input at the gage surface. The gages are calibrated by a flame torch before they are installed in a model. VKF personnel estimate the uncertainties in the measured heating rate at ± 10 percent for $q \geq 0.5$ Btu/ft^2 sec and ± 15 percent for $q < 0.5$ Btu/ft^2 sec (Reference 29). A total of 20 sensor replacements were required during the Tunnel F heat transfer tests (22 runs).

(U) The reduced Tunnel F pressure data were referenced to the pitot pressure measured on the tunnel probe. Heating data were reduced in the form of q/q_s where q_s is the stagnation point heating rate on the model nose (assumed to be a 0.1515-inch radius sphere). The latter was inferred from the measured stagnation point heating rate on a one-inch-radius hemispherical tunnel probe, i.e., $q_s = q_R = 1/\sqrt{0.1515}$.

4.3 (U) PRESSURE DATA AND CORRELATIONS

(U) Pressure tests were conducted in Tunnel C at a nominal Mach number of 10, and unit Reynolds numbers per foot of 2.1×10^6 for $\alpha \leq 20$ degrees and 0.4×10^6 for $\alpha > 20$ degrees. Tunnel F pressure tests were conducted at a nominal Mach number of 19 and Reynolds number per foot of 0.6×10^6. The range of test conditions is summarized below:

TUNNEL	α	β	δ_e	Re_∞/ft x 10^{-6}
C	0,5,10,15,20	-2,0,2,4,6	0	2.1
	25,30,35	-2,0,2,4,6	0	0.4
F	0,5,10,15,20,25,30	0	0	0.6
	10,15,20	-2,2,4,6	0	0.6

A single exception is that no Tunnel C pressure data were obtained at 15 degrees angle of attack and 2 degrees yaw, as $\beta = -2$ was inadvertently run twice at this angle of attack. Tables 1 and 2 list the Tunnel C and F test conditions according to run number. Including repeat runs, 49 tests were conducted in Tunnel C and 25 in Tunnel F.

(U) To minimize the run-to-run variation in tunnel operating conditions, the data from both test series are plotted as the ratio of measured surface pressure divided by the measured pitot pressure. Upper and lower surface

TABLE 1

(U) FLOW CONDITIONS FOR TUNNEL C PRESSURE TESTS

RUN	M_∞	Re_∞/ft (x 10^{-6})	T_O (°R)	P_O (psia)	α (degrees)	β (degrees)
399	10	2.1	1900	1740	0	0
400					5	0
401					10	0
402					15	0
403					20	0
404					0	-2
405*					0	0
406					0	2
407					0	4
408					0	6
409					5	-2
410*					5	0
411					5	2
412					5	4
413					5	6
414					10	-2
415*					10	0
416					10	2
417					10	4
418					10	6
419					15	-2
420*					15	0
421*					15	-2
422					15	4
423					15	6
424					20	2
425*					20	0
426					20	-2
427					20	4
428		2.1		1740	20	6
429		0.4		350	25	0
430					30	0
431					35	0
432					35	2
433*					25	0
434					25	2
435					25	4
436					25	6
437					30	-2
438*					30	0
439					30	2
440					30	4
441					30	6
442					35	-2
443*					35	0
444*					35	2
445					35	4
446					35	6
447	10	0.4	1900	350	25	-2

*Repeat Runs

TABLE 2

(U) FLOW CONDITIONS FOR TUNNEL F PRESSURE TESTS

RUN	α	β	M_∞	Re_∞/ft	i_o (Btu/lb)	T_o (°R)	P_o (lb/ft²)	P_∞ (lb/ft²)	V_∞ (ft/sec)	T_∞ (°R)	P'_o (lb/ft²)	$q_R = 1"$ (Btu/ft² sec)
2332	15	0	19.29	5.64 x 10⁵	1307	4450	212.8 x 10⁴	.485	8035	69.84	234.9	57.01
2333	15	-2	19.39	5.89	1348	4560	237.1	.518	8160	71.23	253.9	61.68
2334	15	2	19.13	5.75	1331	4520	219.0	.525	8107	72.25	249.8	60.19
2335	15	4	19.08	5.66	1319	4490	211.0	.516	8072	72.04	244.1	58.83
2336	15	6	18.90	6.14	1357	4595	233.3	.605	8186	75.46	281.2	65.52
2337	20	0	19.35	5.72	1311	4455	218.6	.488	8049	69.61	237.9	57.62
2338	20	-2	19.71	5.42	1379	4655	240.0	.463	8253	70.54	234.1	60.98
2339	20	2	19.52	5.85	1359	4590	243.5	.508	8194	70.90	252.1	62.13
2340	20	4	19.23	5.94	1348	4560	233.7	.541	8159	72.45	260.5	62.48
2341	20	6	19.64	5.63	1319	4475	226.1	.456	8073	68.00	229.1	56.96
2342	25	0	19.16	5.78	1249	4270	196.3	.476	7853	67.59	227.5	52.83
2243	30	0	19.37	5.77	1318	4475	222.7	.495	8068	69.84	241.3	58.40
2344*	30	0	19.51	6.10	1319	4475	238.6	.508	8073	68.90	251.6	59.71
2345	10	6	19.58	5.86	1346	4550	241.4	.496	8154	69.80	247.7	60.79
2346	10	4	19.49	5.81	1318	4470	227.8	.485	8069	69.00	240.0	58.25
2347	10	2	19.60	6.18	1346	4540	253.4	.521	8154	69.66	260.5	62.35
2348	10	-2	19.62	5.50	1318	4476	220.7	.448	8071	68.11	224.2	56.31
2349	10	0	19.47	5.33	1330	4520	214.1	.454	8104	69.75	223.8	56.89
2350	5	0	19.61	5.62	1364	4610	239.4	.482	8202	70.52	241.3	61.05
2351*	20	0	19.27	5.92	1341	4540	232.0	.531	8138	71.77	256.5	61.58
2352*	10	0	19.15	5.72	1308	4450	211.6	.506	8036	70.83	241.5	57.83
2353*	15	-2	19.47	5.61	1367	4620	235.6	.496	8216	71.64	244.9	61.67
2354*	15	6	19.54	6.24	1305	4420	239.5	.507	8029	67.91	252.3	58.94
2355	0	0	19.36	5.34	1285	4387	198.2	.441	7966	68.13	215.0	53.31
2356*	0	0	19.54	5.64	1311	4455	221.2	.463	8049	68.27	230.0	56.63

*Repeat Runs

centerline data are plotted versus nondimensional longitudinal distance. Spanwise distributions are plotted versus the nondimensional surface distances, S/S_{le} and S/S_{max}, which are defined by the sketch below:

BODY SIDE PANEL

AFT UPPER COMPRESSION SURFACE

S_{max}

S

S_{max}

S

LOWER SURFACE

S S_{le}

LOWER SURFACE

S S_{le}

AFT LOWER COMPRESSION SURFACE

X/L < 0.66

X/L ≥ 0.66
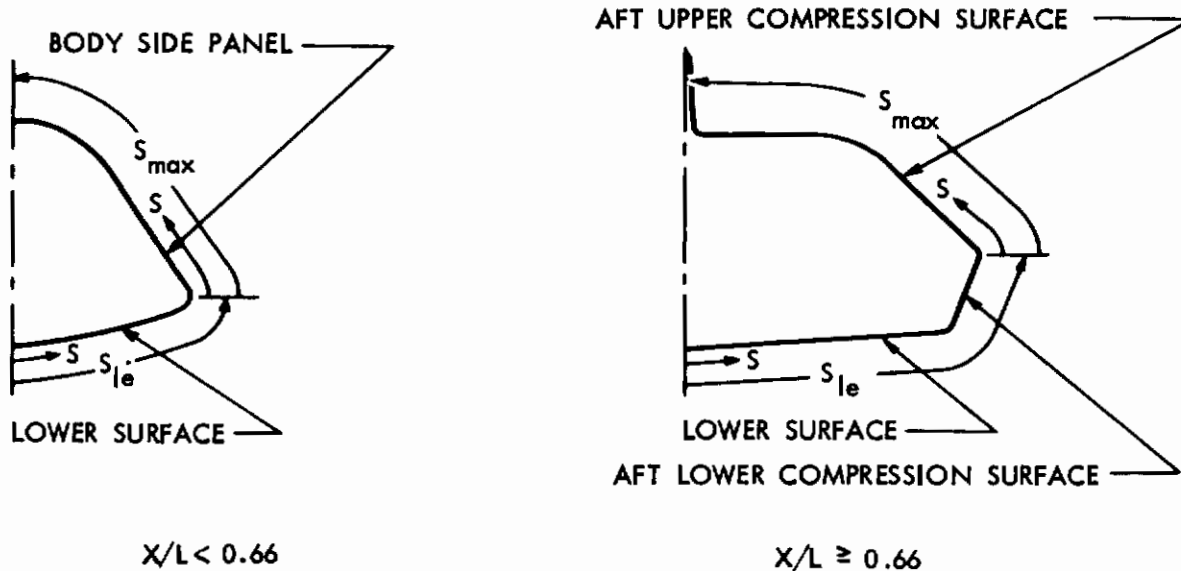
(U) The sketch also defines nomenclature used when referring to the various model surfaces. Data from Tunnel F sensors 4 and 5, sensor 15, and sensors 30 and 31, which could not be placed in the most desirable model locations due to sensor spacing limitations, are plotted with the spanwise distributions at 30, 50 and 95 percent chord, respectively (Figure 28).

(U) The Tunnel C and F pressure data, along with correlations with theory, are presented in the following sections according to model location.

4.3.1 (U) Lower Surface Pressure Distributions

(U) Machine plots of the Tunnel C lower surface centerline pressures versus nondimensional longitudinal distance are shown in Figures 29 through 33. Similar plots of the Tunnel F lower surface centerline data are shown in Figures 34 through 37. Tangent cone theory is shown on each figure and was obtained from the perfect gas tables of Sims (Reference 30). Also shown on the Tunnel F data plots are modified Newtonian and tangent wedge theories. Modified Newtonian pressures are based on the expression

$$\frac{C_p}{C_{p,\,max}} = \frac{P - P_\infty}{P_O' - P_\infty} = \sin^2 \alpha_{eff} \tag{12}$$

which, for $P_\infty \ll P_O'$, yields

$$\frac{P}{P_O'} = \frac{P_\infty}{P_O'} + \sin^2 \alpha_{eff} \tag{13}$$

21

(U) To evaluate real gas effects on the theoretical pressure levels, tangent wedge theory was calculated by solving the energy, momentum and continuity equations by an iterative procedure, using real gas equilbrium properties for air and nitrogen. For the Tunnel F test conditions this solution yielded results which agreed with perfect gas values (Reference 31) within 3 percent. For the Tunnel C test conditions the difference between the two calculation procedures was negligible.

(C) With the exception of the Tunnel F zero and five degree angle of attack data, the forward ramp centerline pressures shown in Figures 29 through 37 generally agree, within 7 percent, with tangent cone theory. The Tunnel F zero- and 5-degree angle-of-attack data are in better agreement with tangent wedge theory. Aft ramp centerline pressures generally agree within 10 percent with tangent cone theory with the exception of the zero- and 5-degree angle-of-attack data. The greatest discrepancy between theory and data occurs at zero angle of attack where the Tunnel F aft ramp pressures are about four times freestream pressure, although the flow deflection angle is zero.

(C) The zero-yaw forward ramp centerline pressures from both test facilities are ratioed to the tangent cone pressures and plotted versus the hypersonic similarity parameter $M_\infty \sin \alpha_{eff}$ in Figure 38. For $M_\infty \sin \alpha_{eff} \geq 2.5$ the data are consistently within ± 10 percent of the tangent cone prediction. A similar plot of the aft ramp centerline pressure data is shown in Figure 39. For $M_\infty \sin \alpha_{eff} \geq 2.5$ the pressure data agree with tangent cone theory within ± 12 percent.

(C) Plots of the Tunnel C lower surface spanwise pressure distributions at 30 percent chord are presented in Figures 40 through 44. Corresponding plots of the Tunnel F data at 30 percent chord are presented in Figures 45 through 49. With the exception of the zero- and five-degree angle-of-attack data, the measured pressures from both test facilities generally agree with tangent cone theory within six percent. Underprediction of the low angle-of-attack data is attributed primarily to bluntness and viscous induced pressures. Plots of the Tunnel C and F lower surface spanwise pressure distributions at 50 percent chord are presented in Figures 50 through 59. As with the data at 30 percent chord, the pressures generally agree within 6 percent with tangent cone theory for angles of attack greater than 5 degrees.

(C) The effect of yaw on the 10 and 15-degree angle-of-attack Tunnel F lower surface pressures shown in Figure 60 is based on data obtained from sensors 11, 12 and 14. These sensors are located at 50 percent chord at the spanwise locations noted on the figure. With the exception of the most outboard sensor (at $S/S_{le} = 0.86$), yaw has essentially no effect on the 15-degree angle-of-attack data. However, at 10 degrees angle of attack, the pressures increase with yaw at all three sensor locations. As the leading edge is approached the pressure increase with yaw becomes larger owing to the increase in local flow deflection angle which results from the surface curvature. (Figure 12.)

(C) Figures 61 through 65 and Figures 66 through 75 show lower surface spanwise pressure distributions at 75 and 96 percent chord, respectively.

As with the forward ramp data, spanwise pressures at these two aft ramp stations generally agree within 6 percent with tangent cone theory for angles of attack above 5 degrees. Pressures on the aft lower compression surface, however, are overpredicted at the higher angles of attack. Figure 76 shows the effect of yaw on the 10 and 15 degree angle of attack lower surface pressures at 96 percent chord. The data shown are from Tunnel F sensors 33 and 35, which are on the lower surface, and sensor 31, which is on the aft lower compression surface. Yaw tends to increase pressures on both surfaces, with the effect more significant as the angle of attack decreases and distance from the centerline increases.

(C) A comparison between tangent cone theory and the Tunnel C aft lower compression surface pressure data is shown in Figure 77 for zero and six degree yaw. A similar comparison for the Tunnel F data is presented in Figure 78. Although the zero angle of attack pressures agree within 15 percent with tangent cone theory, the remainder of the data are overpredicted. The discrepancy between data and theory increases with angle of attack and is apparently due to over-expansion of the lower surface crossflow component.

4.3.2 (U) Upper Surface Pressure Distributions

(U) Machine plots of upper surface pressure data are presented in Figures 79 through 125. An arrow on the ordinate of each plot indicates the freestream pressure ratio P_∞/P_o'.

(C) Plots of the Tunnel C upper surface centerline pressures versus non-dimensional longitudinal distance are shown in Figures 79 through 83. Similar plots of the Tunnel F upper centerline data are shown in Figures 84 through 88. For angles of attack greater than zero, the pressures tend to decrease with increasing chord station. Pressures also decrease with yaw angle. With increasing angle of attack the pressure levels decrease, reach a minimum at about 20 degrees angle of attack, and then increase with additional angle of attack. The reason for this variation with angle of attack is unknown; however, the results are consistent with upper centerline pressures on AFFDL high L/D configuration AF-1 (Reference 16) which has a similar upper forebody.

(C) Figures 89 through 125 show upper surface spanwise pressure distributions at 30, 50, 75 and 96 percent chord. Excepting the zero angle of attack data, the pressures decrease as the upper surface centerline is approached. For a given angle of attack, the side panel pressures, in general, increase with increasing yaw angle. At the upper surface centerline, however, the pressures tend to decrease with yaw angle. For a given yaw angle, spanwise pressure levels decrease with increasing angle of attack reaching a minimum at about 20 degrees, as with the centerline data. The pressure levels then tend to increase with increasing angle of attack. An exception to this trend is the Tunnel F data near the leading edge, where the pressures decrease monotonically with angle of attack up to 30 degrees.

(C) Appendix I presents the results of an investigation of pressure distributions on the leeward centerline of slab delta wings at small angles of attack. For $0 \leq \alpha \leq 10^\circ$, data from several hypersonic wind tunnel programs are correlated by the expression

$$\frac{P}{P_\infty} = 1 + (0.073 - 0.0033\ \delta)\ \frac{M_\infty^2 C_{DN}^{1/2}}{(X/R_n)^{2/3}} \tag{4}$$

(C) Equation (4) is also shown to agree with AEDC Tunnel F upper surface centerline pressures on AFFDL high L/D configuration AF-1 (Reference 16). Figure 126 shows the 10, 15 and 20 degree angle of attack upper centerline pressure data from AF-1 and FDL-5 plotted versus the blast wave parameter $M_\infty^2 C_{DN}^{1/2}/(X/R_n)^{2/3}$. Included are all of the zero-yaw FDL-5 Tunnel C and F pressure data forward of $X/L = 0.55$, where the upper centerline profile angle begins to change. At 10, 15 and 20 degrees angle of attack, the upper center-line flow expansion angles are 4, 9 and 14 degrees, respectively. The straight lines drawn through the data represent the expression

$$\frac{P}{P_\infty} = 0.7 + (0.073 - 0.0033\ \delta)\ \frac{M_\infty^2 C_{DN}^{1/2}}{(X/R_n)^{2/3}} \tag{14}$$

where the constant has been changed to achieve better agreement with the Mach 10 data.

(C) Figures 127 and 128 compare the Tunnel C and F zero-yaw upper centerline pressures with equation (14). At zero and five degrees angle of attack, this is a compression surface and the term 0.7 in equation (14) was replaced with the tangent cone pressure ratio, P_{tc}/P_∞. The data generally agree with Eq. (14) within 20 percent for angles of attack up to 20 degrees, where minimum pressures generally occur.

(C) As shown in Figures 89 through 108, most of the body side panel pressures are higher than freestream and decrease with distance from the leading edge. In performing data correlations it was assumed that these pressures are a result of local surface inclination, nose bluntness, and leading edge bluntness. Following the approach of Creager (Reference 32), the leading edge bluntness induced increment was added to the equilibrium pressure, which was assumed to be the pressure resulting from surface inclination and nose bluntness. The equilibrium pressure was based on the procedure used to correlate the upper centerline data. The resulting equations are

compression surface:

$$\frac{P}{P_\infty} = \frac{P_{tc}}{P_\infty} + 0.073\ \frac{M_\infty^2 C_{DN}^{1/2}}{(X/R_n)^{2/3}} + 0.112\ \frac{M_\infty^2 \cos^{2.67} \Lambda_{eff}\ C_{DLE}^{2/3}}{(X_{\ell e}/R_{\ell e})^{2/3}} \tag{15a}$$

24

expansion surface:

$$\frac{P}{P_\infty} = 0.7 + (0.073 - 0.0033\ \delta)\ \frac{M_\infty^2 C_{DN}^{1/2}}{(X/R_n)^{2/3}}$$

$$+ 0.112\ \frac{M_\infty^2 \cos^{2.67} \Lambda_{eff}\ C_{DLE}^{2/3}}{(X_{\ell e}/R_{\ell e})^{2/3}} \qquad (15b)$$

(C) Figures 129 and 130 compare Tunnel C upper surface pressure data at 30 and 50 percent chord with the distributions given by Eq. (15). Similar correlations for the Tunnel F data are shown in Figures 131 and 132. The Tunnel C data generally agree with Eq. (15) within 20 percent for angles of attack below 15 degrees. At higher angles of attack the pressures are lower than predicted, with the maximum discrepancy between data and prediction occurring at $\alpha = 20°$. The Tunnel F data generally agree with Eq. (15) within 25 percent for all three angles of attack investigated (10, 15 and 20 degrees). As predicted, the Tunnel F body side panel pressure gradient normal to the leading edge is larger than the Tunnel C gradient. The relatively poor agreement between the Tunnel C data and Eq. (15a) at $\alpha \approx 20$ degrees is a result of the 0.7 constant in Eq. (15b). This constant is the assumed equilibrium pressure in the absence of bluntness effects, and is probably dependent on Mach number and flow expansion angle.

4.3.3 (U) Fin Pressure Data

(C) The FDL-5 pressure model contains five pressure taps on the fin side panel and four taps on the fin stagnation line. Figure 133 shows the Tunnel C side panel pressure data for zero and six degrees yaw plotted versus angle of attack. A sketch showing the fin sensor locations and corresponding data symbols is included on the figure. For $\alpha \leq 20°$, the pressures decrease with both angle of attack and distance from the fin leading edge. An abrupt increase in pressure occurs between 20 and 25 degrees angle of attack. At zero and 5 degrees angle of attack, pressures increase with yaw angle as expected. However, at 10, 15 and 20 degrees angle of attack, pressures from the taps nearest the body decrease with yaw angle.

(C) Figure 134 compares the zero- and six-degree yaw fin stagnation line pressures with isolated swept cylinder theory. Data from only three of the four sensors along the fin leading edge are shown because the tap nearest the fin root was plugged during the entire test series. Consistent with theory, pressures nearest the fin root ($X_f/L_f = 0.37$) decrease monotonically with angle of attack up to 20 degrees. Similar to the fin side panel results, the leading edge pressures show a sudden rise between 20 and 25 degrees angle of attack. The reason for this pressure increase is unknown. Minimum pressures from the two taps nearest the fin tip occur at 5 degrees angle of attack.

As discussed in the flow visualization section (Part III, Section 3.3), the flow field in the fin region is extremely complex. As a result, fin pressure levels are probably affected by local flow separation and reattachment, vortex flow and shock wave-boundary layer interactions. These effects, in turn, are dependent on freestream flow conditions and model attitude. Considerable additional testing and analysis, which is beyond the scope of the present study is therefore required to achieve a complete understanding of the flow field.

(C) Summarizing the pressure correlations, the lower surface pressures from both test facilities generally agree with tangent cone theory within 10 percent for angles of attack above five degrees. Additional analysis of the low-angle-of-attack data is desirable to verify bluntness and viscous induced effects on the pressure levels. Good agreement between the lower surface data from Tunnels C and F is indicated by the consistent agreement with tangent cone theory. On the upper surface, where the flow deflection angles are small, Tunnel F pressures are generally higher, as predicted by blast wave theory. Satisfactory correlation of upper surface pressures was achieved (generally within $\pm 20\%$) using a prediction technique based on blast wave theory which resulted from analysis of leeward surface pressures on slab delta wings. Vehicle regions where satisfactory pressure correlations were not achieved are the aft lower compression surface and dorsal fin. The comparatively low pressure levels on the aft lower compression surface are believed to be due to over-expansion of the lower surface crossflow component. Additional flow visualization data, and possibly an analytical study of the inviscid flow field (method of characteristics solution) in this region, would be desirable.

4.4 (U) HEAT TRANSFER DATA AND CORRELATIONS

(U) Heat transfer tests were conducted in Tunnel C at a nominal Mach number of 10, and unit Reynolds numbers per foot of 0.4 and 2.1 million. Tunnel F heat transfer tests were conducted at a nominal Mach number of 19 and unit Reynolds number of 0.5 million. The range of test variables is summarized below:

Tunnel	α	β	δ_e	$Re_\infty/ft \times 10^{-6}$
C	0,5,10,15,20,25,30,35	-2,0,2,4,6	0	0.4
	0,5,10,15,20	0	0	2.1
	0,5,10,15	0	+10	0.4
F	0,5,10,15,20,25,30	0	0	0.5
	10,15,20	-2,2,4,6	0	0.5

(U) Tables 3 and 4 list the Tunnel C and F heat transfer test conditions according to run number. Including repeat runs, 74 tests were conducted in Tunnel C and 22 in Tunnel F.

(U) To minimize the run-to-run variation in tunnel operating conditions, the data from both test series are plotted as the ratio of measured heating rate to stagnation point heating rate on the model nose. The latter is assumed to be a 0.1515-inch radius sphere. Stagnation point heating rates for the Tunnel C

TABLE 3

(U) FLOW CONDITIONS FOR TUNNEL C HEAT TRANSFER TESTS

RUN	M_∞	Re_∞/ft $(x\ 10^{-6})$	T_o $(^\circ R)$	P_o (psia)	α (degrees)	β (degrees)	δ_e (degrees)
324	10.20	2.1	1910	1740	0	0	0
325					5	0	
326					10	0	
327					15	0	
328					20	0	
329					10	-2	
330						0	
331						2	
332						4	
333	10.20	2.1		1740	10	6	
334	10.05	0.4		360	0	0	
335					5	0	
336					10	0	
337					15	0	
338					20	0	
339					25	0	
340					0	-2	
341						0	
342						2	
343						4	
344					0	6	
345					5	-2	
346						0	
347						2	
348						4	
349					5	6	
350					10	-2	
351						0	
352						2	
353						4	
354					10	6	
355					15	-2	
356						0	
357						2	
358						4	
369					15	6	
360					20	-2	
361	10.05	0.4	1910	360	20	0	0

TABLE 3 (Cont)

(U) FLOW CONDITIONS FOR TUNNEL C HEAT TRANSFER TESTS (Continued)

RUN	M_∞	Re_∞/ft $(x\ 10^{-6})$	T_o $(^\circ R)$	P_o (psia)	α (degeees)	β (degrees)	δ_e (degrees)
362	10.05	0.4	1910	360	20	2	0
363					20	4	0
364					20	6	0
365					0	0	10
366					5	0	10
367					10	0	10
368					15	0	10
369					25	-2	0
370						0	
371						2	
372						4	
373					25	6	
374					30	-2	
375						0	
376						2	
377						4	
378					30	6	
379					35	-2	
380						0	
381						2	
382						4	
383	10.05	0.4		360	35	6	
384	10.20	2.1		1740	15	-2	
385						0	
386						2	
387						4	
388					15	6	
389					20	-2	
390						0	
391						2	
392						4	
393					20	6	
394					5	-2	
395						0	
396						2	
397						4	
398	10.20	2.1	1910	1740	5	6	0

TABLE 4

FLOW CONDITIONS FOR TUNNEL F HEAT TRANSFER TESTS

RUN	α	β	M_∞	Re_∞/ft	i_0 (Btu/lb)	T_0 (°R)	P_0 (lb/ft²)	P_∞ (lb/ft²)	V_∞ (ft/sec)	T_∞ (°R)	P_0' (lb/ft²)	$q_R = 1''$ (Btu/ft²sec)
2403	0	0	18.95	5.32×10^5	1598	5330	283×10^4	.663	8882	88.4	310.6	84.67
2404	5	0	19.32	5.30	1554	5189	280	.586	8761	82.8	285.2	78.36
2405	10	0	19.17	5.36	1430	4824	237	.540	8404	77.4	258.9	67.24
2406	15	0	19.22	5.09	1329	4531	199	.454	8102	71.5	218.5	56.21
2410	10	-2	18.84	5.80	1508	5051	269	.676	8627	84.3	313.2	79.07
2412	10	4	19.03	5.30	1573	5254	276	.633	8813	86.3	299.3	81.52
2413	10	6	19.24	5.34	1565	5224	283	.607	8793	84.1	293.1	80.18
2414	15	-2	19.06	5.54	1461	4914	251	.590	8494	79.9	279.5	71.80
2417	15	6	18.98	5.42	1505	5049	257	.612	8619	83.0	287.8	75.61
2418	20	-2	19.24	5.40	1373	4649	227	.491	8236	72.8	240.3	61.49
2419	20	2	19.46	5.33	1437	4838	248	.510	8426	75.5	251.8	66.72
2420	20	4	19.52	5.34	1408	4752	240	.488	8341	73.4	242.7	63.82
2421	20	6	19.56	5.35	1504	5035	274	.536	8621	78.2	267.8	72.90
2422	10	2	19.37	5.28	1416	4779	236	.502	8363	75.0	245.9	64.69
2423	25	0	19.29	5.12	1476	4964	246	.526	8538	78.8	255.7	69.55
2424	15	2	19.52	5.07	1409	4761	230	.464	8343	73.5	230.5	62.23
2425	30	0	19.35	5.37	1345	4567	217	.475	8151	71.4	231.8	58.78
2426	10	4	19.57	5.33	1397	4716	238	.477	8307	72.5	238.4	62.60
2427	0	0	19.33	5.18	1404	4747	227	.490	8327	74.6	238.8	63.06
2428	20	0	19.65	5.03	1411	4766	233	.449	8350	72.6	226.3	61.79
2429	15	4	19.45	5.26	1373	4653	224	.470	8237	72.2	232.1	60.44
2430	15	0	19.92	5.61	1340	4534	241	.439	8140	67.2	227.5	57.98

test conditions were computed by the method of Fay and Riddell. Tunnel F stagnation point heating rates were inferred from data on a one-inch radius hemispherical tunnel probe, i.e., $q_S = q_{R=1"}/\sqrt{0.1515}$.

(U) Upper and lower surface centerline heat transfer data are plotted versus nondimensional longitudinal distance. Spanwise distributions are plotted versus the nondimensional surface distances, $S/S_{\ell c}$ and S/S_{max}, which are defined in Section 4.3. The plots show Tunnel C low Reynolds number data for yaw angles of 0, -2, 2, 4 and 6 degrees, Tunnel C high Reynolds number data for zero yaw, and Tunnel F data for yaw angles of 0, -2, 2, 4 and 6 degrees. Angle of attack is a parameter on each plot. These data, along with correlations with theory, are presented below according to model locations.

4.4.1 (U) Lower Surface Heat Transfer Distributions

(C) Figures 135 through 145 show lower surface centerline heating distributions. In general, the data plot smoothly and appear to be of good quality. Data from the thermocouple nearest the nose on the Tunnel C model, however, does not appear valid. This thermocouple is attached to the machined nose cap and the temperatures are probably affected by conduction. The heating increase aft of 95 percent chord during the Tunnel C tests is believed to be due to imperfections in the model contours. The model lower surface is visibly warped in this region and forms a slight compression ramp with respect to the upstream flow. The fact that the location of the heating increase is relatively insensitive to Reynolds number and angle of attack makes it unlikely that boundary layer transition was the cause, although transitional flow had been expected on the aft ramp at the high Reynolds number test point. The transition criterion $Re_\theta/M_e > 150$ predicts turbulent flow aft of 36 percent chord for this test point.

(C) Lower surface spanwise heating distributions at 30-, 40- and 50-percent chord are shown in Figures 146 through 173. At small angles of attack the heating rates increase rapidly as the leading edge is approached. With increasing angle of attack, the magnitude of the increase becomes smaller as predicted by streamline divergence theory. At angles of attack above 20 degrees, the zero-yaw heating rates are nearly constant in the spanwise direction. Some of the Tunnel C low angle-of-attack, spanwise heating distributions do not plot smoothly, e.g., Figures 162 through 164 and 168. Corresponding Tunnel F distributions are uniform, and it is believed that the Tunnel C data are erroneous, possibly as a result of the low heating rates. AEDC personnel estimate that the accuracy of the VKF temperature recording system is ±0.2°F/sec or ±2 percent, whichever is greater (Ref. 24). During the Tunnel C low Reynolds number tests at zero yaw and zero angle of attack, forward ramp temperature derivatives ranged from 1.0 to 7.7°F/sec. Based on temperature derivative measurement error of ±0.2°F/sec, the corresponding heating rate errors range from 3 to 20 percent. For angles of attack above five degrees, heating rates from both test facilities plot smoothly and tend to decrease in the spanwise direction up to about 40 percent span. This effect is most evident at 30-percent chord (Figures 146 through 156) and is inconsistent with the results of vapor screen studies, presented in Part III, Section 3.3, which indicate a region of decreasing boundary

layer thickness up to roughly 30-percent span. However, vapor screen studies are a relatively new experimental technique, and the results may be subject to misinterpretation.

(C) Figures 174 through 190 show the lower surface spanwise heating distributions at 75 and 96 percent chord. The magnitude of the spanwise heating increase at these two aft lower surface locations is much greater than that on the forward ramp. This is attributed to (1) the relatively large increase in flow deflection angle as the leading edge is approached, and (2) a strong inboard flow over the leading edge at small angles of attack. An interesting feature of the distributions at 75-percent chord is the small effect of angle of attack on the aft lower compression surface heating rates. The pressure data are not consistent with the heating data in this respect. For example, at $S/S_{1e} = 0.97$, the Mach 10, 4-degree yaw pressure tests showed that $P_{\alpha=35}/P_{\alpha=0} \approx 2.2$ (Figure 64). Since the heating rate is roughly proportional to the square root of the pressure for laminar flow, the heating ratio $q_{\alpha=35}/q_{\alpha=0}$ should be about 1.5. However the experimental heating ratio from Figure 177 is less than 1.1. In contrast, for a fixed angle of attack, pressures and heating rates at this location approximately double as the yaw angle is increased from zero to six degrees.

(C) As noted on the Tunnel C run schedule (Table 3), four heat transfer tests were conducted with elevons deflected 10 degrees into the airstream. These tests were accomplished at a unit freestream Reynolds number per foot of 0.4 million, zero yaw, and 0, 5, 10 and 15 degrees angle of attack. The purpose of these tests was to investigate the effect of elevon deflection on lower surface heating and flow separation patterns. Figure 191 compares the lower surface longitudinal heating distributions upstream of the elevon for zero and ten degrees elevon deflection. The data are from a row of seven thermocouples located 1.75 inches off centerline, starting with T/C 101 at X/L = 0.910 and ending with T/C 144 at X/L = 0.997 (Figure 26). Heating data for 10 degrees elevon deflection and zero angle of attack appeared erroneous and are not shown. With this exception, the data for zero and ten degrees elevon deflection are in excellent agreement, and indicate that the flow did not separate. As discussed previously, the heating increase aft of X/L = 0.95 is probably due to imperfections in the model contour.

(U) Figures 192 and 193 compare the zero-yaw forward ramp centerline heating data with laminar swept cylinder, flat plate and tangent cone theories. Theoretical surface pressures were used for all theory evaluation. Swept cylinder heating rates were calculated by the method of Beckwith (Ref. 4), with the effective body radius based on experimental velocity gradient data of Boison and Curtiss (Ref. 3) as discussed in Section 2.1. Flat plate and tangent cone heating rates were computed by Eckert's reference enthalpy method (Ref. 33) with the model nose taken as the boundary layer origin. On Figures 192 and 193 the ordinate is $q\sqrt{X}/q_s$, which eliminates the dependence on sensor location for the wedge and cone theories. However, because the swept cylinder predictions do not vary with $X^{1/2}$, this theory must be shown as a band with the lower boundary applicable to the most rearward sensor (at X/L = 0.50) and the upper boundary applicable to the most forward sensor (at X/L = 0.15 for the Tunnel F model and at X/L = 0.10 for the Tunnel C model).

(C) The correlations shown on Figures 192 and 193 indicate that flat plate and cone theories are applicable over a very limited angle of attack range. Flat plate theory is in fair agreement with the zero angle of attack heating rates, but underpredicts the remainder of the data. Cone theory correlates the data in the 10-15 degree angle of attack range. Swept cylinder theory underpredicts the heating rates by an average of approximately 20 percent but the trends with angle of attack are accurately predicted. The fact that the deviation between theory and data is nearly constant at all positive angles of attack is interpreted as an indication that swept cylinder theory is applicable, but was improperly evaluated. To apply the theory requires a knowledge of boundary layer edge flow properties and the effective body radius used to calculate the spanwise velocity gradient. Beckwith's theory was evaluated using swept cylinder flow field properties which assumes that the shock wave is parallel to the body. The measured pressures, however, agree with tangent cone theory and are roughly 20 percent higher than predicted by swept cylinder theory. Since $q \sim P^{0.5}$, predicted heating rates using experimental pressures would be about 10 percent higher than those shown on Figures 192 and 193. The remainder of the discrepancy between theory and data is attributed primarily to the calculation of velocity gradient. Figure 194 compares the assumed effective body radius distribution used in the velocity gradient calculations with the radius distribution required to achieve perfect agreement between Beckwith's theory, evaluated using swept cylinder flow properties, and the Tunnel C heat transfer data for 10, 15 and 20 degrees angle of attack. For reference, the lower surface radius of curvature and the model semi-span are included on Figure 194. The latter represents the radius, which in the absence of test data, would be used to predict lower surface centerline swept cylinder heating rates if the FDL-5 lower surface were a half-cone. The semi-span is in surprisingly good agreement with the experimental effective body radius data. It is apparent from the correlations shown in Figures 192 and 193 that the experimental body radius distribution shown in Figure 194 can be employed in swept cylinder theory to predict the forward ramp centerline heating rates for all angles of attack greater than 5 degrees.

(C) Figure 195 compares the 10-degree angle-of-attack spanwise heating data on the forward ramp with the distribution assumed when predicting FDL-5 entry heating rates shown in Section 3. The predicted distribution was based on elliptic cone wind tunnel data. Although the data scatter on Figure 195 is considerable, the measured heating distributions up to 80 percent span generally agree with the predicted distribution within ±15 percent. An exception is the Tunnel C data at 50-percent chord, where heating rates near the leading edge are nearly 50 percent higher than predicted. In contrast, the Tunnel F data at 50 percent chord are within 10 percent of the predicted values.

(C) Figure 196 compares the zero-yaw Tunnel C lower surface spanwise heating rates at 75 percent chord with laminar strip theory. Similar comparisons for the Tunnel C and F lower surface heating data at 96 percent chord are presented in Figures 197 and 198. Heating rates were calculated by Eckert's reference enthalpy method, with the characteristic dimension based on the distance from the leading edge, measured parallel to the model centerline.

32

Local flow properties were computed by tangent wedge theory. Because the flow deflection angle increases in the spanwise direction, the heating rates increase more rapidly than given by $X^{-1/2}$. At 10 degrees angle of attack, the data at 75-percent chord generally agree with strip theory within ±5 percent. At lower angles of attack, heating rates near the centerline are overpredicted while those near the leading edge are underpredicted. Above ten degrees angle of attack, the data are consistently higher than strip theory. The discrepancy increases with angle of attack, and reaches a maximum of about 60 percent on the centerline at $\alpha = 35°$. However, good agreement with strip theory is not expected at the higher angles of attack, where considerable outflow occurs.

(C) The Tunnel C lower surface data at 96-percent chord do not have as uniform a trend as the data at 75 percent chord, and are in relatively poor agreement with strip theory. For angles of attack up to 20 degrees, strip theory over-predicts the Tunnel C centerline heating rates and underpredicts those near the leading edge. The discrepancy between data and theory is as high as 60 percent. The apparent boundary layer thickening near the centerline and thinning near the leading edge is consistent with the Tunnel C oil flow data presented in Part III, Section 3.3, which show inboard flow over the aft ramp for the 0 to 20-degree angle-of-attack range. For $20 \leq \alpha \leq 35$, the Tunnel C centerline heating rates agree within 15 percent with strip theory, but heating rates near the leading edge remain as much as 50 percent higher than predicted. Tunnel F aft lower surface heating ratios (q/q_s) at 96 percent chord are generally 20 to 80 percent higher than corresponding Tunnel C values. This discrepancy is possibly due to the Tunnel C model imperfections noted pre-viously, although at zero and five degrees angle of attack the exceptionally high Tunnel F aft lower surface pressures (Figure 34) undoubtedly contri-buted to the difference. At zero angle of attack the Tunnel F centerline heating rates are 20 percent lower than strip theory, although the measured pressures are about four times freestream pressure, which was used in theory evaluation. This indicates the magnitude of the boundary layer thickening due to inflow over the leading edges. Above 10 degrees angle of attack the Tunnel F aft lower surface heating rates at 96 percent chord are consistently higher than strip theory. As with the Tunnel C data, the discrepancy tends to increase in the spanwise direction.

(C) Figures 199 and 200 compare the zero-yaw aft lower compression surface heating data from both test facilities with laminar strip theory. The heating rates were evaluated using tangent wedge flow properties, with the character-istic dimension based on the wetted distance from the leading edge stagnation line, measured in the freestream flow direction. At zero angle of attack the data scatter is large, and the values are higher than predicted. This is probably due to the assumed flow direction. No oil flow data were obtained in this region but it is assumed that at $\alpha = 0$ the ridge formed by the intersection of the aft lower and aft upper compression surfaces will act as a flow parting line. Consequently the applicable characteristic dimen-sions will be smaller than the assumed values. For angles of attack around ten degrees, the data generally agree with the predicted values within ±30 percent. At higher angles of attack the heating rates are con-sistently lower than predicted, with the data mean at $\alpha = 30°$ approximately

half the strip theory value. This trend is consistent with the pressures, which are in fair agreement with tangent wedge theory at small angles of attack but are approximately half tangent wedge pressure at $\alpha = 30°$. The poor correlation of the aft lower compression surface pressure and heating data indicates a need for additonal analysis in this area.

4.4.2 (U) <u>Upper Surface Heat Transfer Distributions</u>

(C) Figures 201 through 211 show upper surface centerline heat transfer data plotted versus nondimensional longitudinal distance. Heating rates decrease in the chordwise direction, and decay rapidly aft of 55 percent chord where the profile angle changes. The heating trends with angle of attack are erratic, however, and are discussed below along with data correlations.

(C) Figures 212 through 239 show upper surface spanwise heating rates at 30, 40 and 50 percent chord. Body side panel heating rates decrease with distance from the leading edge, and in contrast to the upper centerline data, decrease monotonically with angle of attack up to 35 degrees. As expected, the side panel heating rates increase rapidly with yaw angle. At the higher angles of attack the side panel heating rates nearly triple as the yaw angle is increased from zero to six degrees.

(C) Figures 240 through 245 show Tunnel C upper surface spanwise heating distributions at 75 percent chord. Near the leading edge the heating rates decrease monotonically with angle of attack up to 35 degrees. However, as the distance from the leading edge increases, the trend with angle of attack becomes erratic. At zero yaw (Figure 240), the three highest heating rates at $S/S_{max} = 0.92$ occur at 0, 15 and 35 degrees angle of attack. The lowest heating rate occurs at $\alpha = 20$ degrees.

(C) Upper surface heating data at 96 percent chord are shown in Figures 246 through 256. On the aft upper compression surface ($0 \leq S/S_{max} \leq 0.3$), the heating rates decrease with distance from the leading edge, and decrease monotonically with angle of attack. On the surface adjacent to the fin, however, the data are highly irregular. Maximum heating rates occur at a variety of angles of attack, depending on the location and yaw angle. Impingement of the fin-generated shock wave on the upper surface is apparently responsible for the local heating increase observed around $S/S_{max} = 0.8$ during the Tunnel C low angle of attack tests.

(C) Figure 257 compares the Tunnel C and F upper centerline heating rates at 40 percent chord as a function of angle of attack. Only the Tunnel F data plot smoothly, and with the exception of the zero angle of attack tests, maximum Tunnel C heating rates occur in the angle-of-attack range which results in minimum Tunnel F heating, i.e., 10-20 degrees. At 15 degrees angle of attack, the Tunnel C high Reynolds number heating ratio, q/q_s, is 4.5 times the Tunnel F value. Although data from only one chord station are shown in Figure 257, the trends with angle of attack are representative of the heating data at all upper centerline stations.

(C) The exceptionally high heating rates on the upper centerline and aft upper surface may be due to boundary layer transition and vortices. Wind tunnel transition studies on cones have shown the leeward surface boundary layer to be considerably less stable than that on the windward side. Figure 258 shows the effect of angle of attack on the windward and leeward meridian transition locations on three cones tested by Stetson and Rushton (Ref. 34). Transition points were determined from the axial heating distributions during shock tunnel tests at a nominal Mach number of 5.5. At 8 degrees angle of attack the length of laminar flow on the windward meridian of the pointed cone is 4.5 times that on the leeward meridian. Consequently, it appears reasonable that the FDL-5 upper centerline transition location could be within a few inches of the nose and account for the irregular heating distributions shown on the upper surface heat transfer plots.

(C) Figure 259 compares the 10-, 15- and 20-degree angle of attack upper centerline heating distributions from Tunnels C and F with zero angle of attack flat plate theory. Heating rates were computed by Eckert's reference enthalpy method, evaluated using freestream flow properties, with the nose taken as the boundary layer origin. At all three angles of attack the Tunnel F heating rates are 30 to 45 percent lower than zero angle of attack laminar flat plate theory. However, at large chord stations, all of the Tunnel C high Reynolds number data and the 15-degree angle of attack low Reynolds number data exceed the laminar flat plate predictions. At $X/L = 0.60$, these heating rates are only 25 to 35 percent below zero angle of attack turbulent flat plate values. This comparison supports the assumption that a considerable portion of the upper centerline may have experienced turbulent flow during the Tunnel C tests.

(C) Figures 260, 261 and 262 compare Tunnel C body side panel heating distributions at 15-, 30- and 50-percent chord with laminar strip theory. Correlations of the Tunnel F body side panel heating data at 30- and 50-percent chord are shown in Figures 263 and 264. Heating predictions are based on Eckert's reference enthalpy method, with local flow properties based on an isentropic expansion of the leading edge stagnation line properties to the measured Tunnel C pressures. Two predictions are shown for each set of data. For the solid lines, the characteristic dimension is based on the wetted distance from the leading edge stagnation line, measured in the freestream flow direction. For the dashed lines, the characteristic dimension is based on the distance from the stagnation line, measured in the surface flow directions indicated by oil streak data obtained on the Lockheed/AFFDL F-4 high L/D configuration (Ref. 20). The upper forebody of the F-4 is almost identical to that of the FDL-5. The F-4 data were used because the FDL-5 side panel flow directions could not be determined from the Tunnel C oil flow photographs. The experimental body side panel flow directions are inclined 5, 21, 31, 38 and 43 degrees with respect to the angle of attack reference plane for $\alpha = 0, 5, 10, 15$ and 20 degrees, respectively. At zero angle of attack the side panel heating rates are consistently higher than predicted by either method. The predictions based on experimental surface flow directions are more accurate and generally correlate the data within 20 percent.

As the angle of attack increases, however, the data are in better agreement with the heating predictions which assume that the surface flow direction is parallel to freestream. With the exception of the 15-percent chord data at $S/S_{\ell e} = 0.12$, this method generally correlates the 10 and 15 degree angle of attack data within 15 percent. Body side panel pressure gradients are negligible at $\alpha = 0$ but are relatively large at the intermediate angles of attack (Figures 89 through 108). Consequently, including the effects of pressure gradients in the heating predictions would not significantly change the $\alpha = 0$ correlations, where the discrepancy between data and theory is largest, but would impair the correlations for larger angles of attack.

4.4.3 (U) Estimated Fin Stagnation Line Heating Rates

(U) Because the fins on the heat transfer models are uninstrumented, the only fin heat transfer information resulting from the AEDC tests is that which can be inferred from the Tunnel C pressure data. To do this, estimates of the flow properties upstream of the fin are required. These were computed by assuming that (1) the static pressure is equal to the surface pressure measured on the upper centerline at 75-percent chord, and (2) the flow is parallel to the upper surface adjacent to the fin, i.e., the fin leading edge is swept 62 degrees with respect to the upstream flow. The ratio of upstream static pressure to fin stagnation line pressure yields the Mach number normal to the fin leading edge. Then, with the assumed flow direction and conservation of total enthalpy, all other upstream flow properties can be computed.

(C) The estimated flow properties upstream of the fin were input to a computer program which calculates swept cylinder heating rates by the method of Beckwith (Ref. 4). Heating calculations were performed for all of the unyawed 0 to 20 degree angle-of-attack pressure data shown on Figure 134. The results are compared with isolated swept cylinder heating theory in Figure 265. Near the fin tip the inferred stagnation line heating rates exceed isolated cylinder values for angles of attack greater than six degrees. Fin stagnation line temperatures shown in Section 3 are based on isolated swept cylinder heating predictions for a vehicle angle of attack of zero degrees. As indicated in Section 3, the heating estimates were considered to be conservative, but no test data were available to substantiate lower estimates. From Figure 265, it is seen that $q_{data,\alpha=11}/q_{theory,\alpha=0} = 0.19/0.282 = 0.67$. If this ratio were applied to the low angle of attack ($\alpha = 11°$) reference trajectory heating predictions, the peak fin stagnation line temperature shown on Figure 19 would be reduced from 3270°F to 2900°F.

(C) In summary, the FDL-5 heat transfer data from both test facilities generally plot smoothly and appear to be of good quality. Some of the Tunnel C low angle of attack lower surface data appear questionable, possibly due to the low heating rates. Forward ramp centerline heating rates are higher than predicted by laminar swept cylinder theory by an average of about 20 percent. On the forward ramp, Tunnel F heating ratios (q/q_s) are 10 to 25 percent higher than the Tunnel C values, although swept cylinder theory predicts an increase of only 5 to 12 percent. Tunnel C lower surface heating rates at

36

75-percent chord generally agree with laminar strip theory within ±5 percent
at 10 degrees angle of attack. At lower angles of attack, centerline heating
rates are overpredicted, while those near the leading edge are underpredicted.
Above 10 degrees angle of attack the data are generally higher than strip
theory, with the maximum discrepancy occurring on the centerline. At 96-percent
chord lower surface centerline heating rates from Tunnel C generally agree
within ±15 percent with laminar strip theory for $20 \lesssim \alpha \leq 35$ degrees, but are
lower than predicted by strip theory at smaller angles of attack. Near the
leading edge, the heating rates are as much as 50 percent higher than pre-
dicted by strip theory. This discrepancy exists for angles of attack up to
35 degrees. Tunnel F lower surface heating ratios (q/q_s) at 96 percent chord
are generally 20 to 80 percent higher than corresponding Tunnel C values,
although laminar strip theory predicts nearly identical heating ratios for the
two facilities. Above 10 degrees angle of attack the Tunnel F heating rates
are consistently higher than strip theory. Aft lower compression surface
heating rates are higher than predicted by strip theory for $\alpha = 0$ but agree
within ±30 percent with strip theory at $\alpha = 10°$. At higher angles of attack
the heating rates are consistently lower than predicted with the data mean
at $\alpha = 30°$ approximately half the laminar strip value.

(C) On the upper surface, the Tunnel C heating trends with angle of attack are
frequently erratic, possibly as a result of boundary layer transition or
vortices. At 10 and 15 degrees angle of attack Tunnel C upper centerline
heating rates for $0.3 \leq X/L \leq 0.6$ are 25 to 35 percent lower than zero angle
of attack turbulent strip theory. Corresponding Tunnel F heating rates are
30 to 45 percent lower than zero angle of attack laminar strip theory. For
$\alpha > 0$, body side panel heating rates are generally lower than predicted by
laminar strip theory, based on experimental pressures and surface flow
directions. For 10 and 15 degrees angle of attack, the side panel data
generally agree within ±15 percent with strip theory predictions based on the
assumption that the surface flow direction is parallel to freestream.

SECTION 5

(U) REVISED FDL-5 TEMPERATURE PREDICTIONS

(U) Section 3 presents FDL-5 design point radiation equilibrium isotherms (for $V_\infty = 20,000$ fps, $H = 200,000$ ft, $\alpha = 11°$), and peak heating isotherms based on the low angle of attack reference trajectory. Due to the transition criterion employed during this study ($Re_\theta/M_e > 150$), the design point temperatures are based entirely on laminar flow. However, for the low-altitude reference trajectory, predicted maximum temperatures at most vehicle locations result from turbulent flow. Because no turbulent heating data were obtained from the AEDC test program, the results cannot be directly compared with heating predictions used to generate the peak heating isotherms. Section 4 compares the test data with analytical methods used to predict laminar flow heating rates. This section presents design point radiation equilibrium isotherms based on the AEDC test data, and compares the results with the isotherm predictions shown in Figure 17.

(U) Extrapolation of wind tunnel data to flight conditions requires the application of correction factors to account for differences between the tunnel and flight environments. Thomas, Perlbachs and Nagel (Ref. 12) present correction factors for extrapolating tunnel data to flight conditions based on the assumption that

$$\left(\frac{h}{h_{theory}}\right)_{flight} = \left(\frac{h_{experimental}}{h_{theory}}\right)_{wind\ tunnel} \tag{16}$$

Equation (16) is identical to

$$\left(\frac{q}{q_{theory}}\right)_{flight} = \left(\frac{q_{experimental}}{q_{theory}}\right)_{wind\ tunnel} \tag{17}$$

(U) Because the local-to-stagnation point heating ratio is relatively insensitive to flow conditions, it is convenient to normalize wind tunnel data with respect to stagnation point values. The resulting equation, which was used to extrapolate the AEDC data to the design point flight conditions, is

$$q_{flight} = q_{s,flight,theory}\left(\frac{(q/q_s)_{flight,theory}}{(q/q_s)_{wind\ tunnel,theory}}\right)\left(\frac{q_{experimental}}{q_{s,wind\ tunnel,theory}}\right) \tag{18}$$

Equation (18) is also identical to equations (16) and (17) since the stagnation point heating rates cancel. The ratio $(q/q_s)_{flight,theory}/(q/q_s)_{wind\ tunnel,theory}$ is a correction factor to be applied to the experimental value of q/q_s.

(U) To determine the correction factor applicable to the lower surface forward
ramp data, the ratio (q/q_S)flight, theory$/(q/q_S)$wind tunnel, theory was computed,
with the ramp centerline heating rates based on Beckwith's swept cylinder
theory (Ref. 4). Correction factors for the aft lower surface, aft lower
compression surface and upper surface were based on flat plate theory for $\alpha =$
11, 10 and 0 degrees, respectively. In all cases, stagnation point heating
rates were computed by Fay and Riddell theory. On the lower surface and body
side panels, the revised flight heating rates were based on data from the
more densely instrumented Tunnel C model. Tunnel F data were used for the
remainder of the upper surface, due to the irregular behavior of the Tunnel C
data in these areas. Lower surface spanwise heating rates $(q/q_{\mathcal{L}})$ were
assumed to be identical for flight and wind tunnel conditions. In all cases
the data were interpolated and faired to obtain smooth distributions appli-
cable to eleven degrees angle of attack.

(C) The revised radiation equilibrium temperatures are shown in the form of
isotherms on Figure 266. Aft of five percent chord the lower surface tem-
peratures range from 2300°F to 1100°F. Forward ramp centerline temperatures
are higher than the predicted values shown in Figure 17, with the dis-
crepancy as high as 200°F near the nose. Between 50 and 90 percent chord,
the predicted and experimental temperatures agree within ±100°F. Aft lower
compression surface temperatures generally range from 1700°F to 2000°F,
which is in good agreement with the predicted range of 1600°F to 2000°F.
Body side panel temperatures range from 1100°F to 1600°F, and consistently
agree within ±100°F with the predicted values. On the upper centerline the
temperatures aft of 30 percent chord range from 500°F to 780°F, and agree with
the predicted values within ±50°F. Upper centerline temperatures forward
of 30 percent chord are based on extrapolation of the heating data from the
most forward Tunnel F sensor according to $q \sim X^{-0.5}$.

(C) Figure 267 compares the predicted and revised temperature distributions
at 50 and 96 percent chord. At 50 percent chord, the revised lower surface
temperatures are higher than the predicted values, with the difference ranging
from 80°F on the centerline to 200°F near the leading edge. On the body side
panels, the predicted and revised temperatures agree within ±50°F. Near the
upper centerline the predicted temperatures are lower by as much as 100°F.
At 96 percent chord, the revised lower surface temperatures are approximately
200°F below the predicted values at the centerline, and 200°F higher near
the leading edge. On the aft lower compression surface the maximum tempera-
ture based on experimental heating rates is identical to the predicted
maximum (2000°F) but the heating rate decay with distance from the leading
edge is not as great as predicted. On the aft upper compression surface the
revised temperatures exceed the predicted values by as much as 250°F, which
is the largest discrepancy observed on any surface.

(C) In summary, the predicted and revised design point radiation equilibrium
isotherms generally agree within ±200°F on the lower surface, and within
±100°F on the body side panels and aft lower compression surface. The largest
difference between predicted and revised temperatures is about 250°F, and occurs
on the aft upper compression surface. No material changes would be required as
a result of the temperature revisions.

SECTION 6

(U) CONCLUSIONS

(U) Pertinent conclusions which may be drawn from results of the FDL-5 aerothermodynamic analyses are summarized below. In all cases these conclusions are based on a 34-degree bank angle, low-altitude reference trajectory which was selected as the critical thermal condition.

1. (U) For the low-altitude reference trajectory, predicted surface temperatures are compatible with the proposed structural materials: tungsten-thoria for the nose cap, coated tantalum for leading edges, coated columbium for the lower surface, and superalloys for the upper surface. The leading edge material must be extended approximately 4 inches beyond the leading edge/side panel tangency line, and portions of the forward upper surface must be fabricated from a material, such as coated columbium, which has a temperature capability exceeding that of superalloys.

2. (C) From a heating standpoint, the lower surface is the most marginal. Peak centerline temperatures on this surface range from about 2000°F at station 396 to 2450°F at station 120. If a 6 percent design margin is added to the nominal temperature predictions, approximately 40 percent of the lower surface exceeds 2500°F, the assumed temperature limit for coated columbium.

3. (C) For the low-altitude reference trajectory, predicted maximum temperatures on essentially the entire lower surface result from turbulent flow. For a practical range of transition Reynolds numbers, peak temperatues on the aft lower surface are not sensitive to transition criterion. Forward ramp peak temperatures, however, decrease significantly with increasing transition Reynolds number. Results of wind tunnel transition data on the FDL-5 and basic geometries indicate that heating rates based on the assumption of an instantaneous shift from laminar to turbulent flow at $Re_\theta/M_e = 150$ may be overly conservative.

4. (U) Increasing the vehicle wing loading from the assumed value of 35 psf results in an increase in lower surface temperature of approximately 18°F/psf.

(U) Pertinent conclusions which may be drawn from the AEDC pressure and heat transfer tests are:

1. (C) For angles of attack above five degrees, lower surface chordwise and spanwise pressures generally agree within ±10 percent with tangent cone theory. The degree of correlation with theory is nearly identical for the Tunnel C and F pressure data.

2. (C) Aft lower compression surface pressures generally agree within ±15 percent with tangent cone theory at zero angle of attack, but are lower than predicted for $\alpha > 0$. The discrepancy, which increases with angle of attack and Mach number, is attributed primarily to over-expansion of the lower surface crossflow component.

3. (C) Upper surface pressures generally reach a minimum at approximately 20 degrees angle of attack, although Tunnel F body side panel pressures near the leading edge decrease monotonically with angle of attack up to 30 degrees. For $\alpha \leq 20$ degrees, data from these regions were generally correlated within ±20 percent with a prediction technique, based on blast wave theory, which resulted from an analysis of leeward surface pressure data from slab delta wings.

4. (C) Forward ramp centerline heating rates are higher than predicted by laminar swept cylinder theory by an average of about 20 percent and maximum of 40 percent. The deviation is attributed to some extent to differences between the measured and assumed pressures but mainly to discrepancies in the assumed spanwise velocity gradient. On the forward ramp, Tunnel F heating ratios (q/q_s) are 10 to 25 percent higher than corresponding Tunnel C values, although swept cylinder theory predicts an increase of only 5 to 12 percent.

5. (C) Tunnel C lower surface heating rates at 75 percent chord generally agree with laminar strip theory within ±5 percent at 10 degrees angle of attack. At lower angles of attack centerline heating rates are overpredicted, while those near the leading edge are underpredicted. Above 10 degrees angle of attack the data are generally higher than strip theory, with the maximum discrepancy on the centerline. At 96 percent chord Tunnel C lower surface centerline heating rates generally agree within ±15 percent with laminar strip theory for $20 \leq \alpha \leq 35$ degrees, but are lower than predicted at smaller angles of attack. Near the leading edge, the heating rates are as much as 50 percent higher than predicted by strip theory. This discrepancy exists for angles of attack up to 35 degrees. Tunnel F aft lower surface heating ratios (q/q_s) are generally 20 to 80 percent higher than corresponding Tunnel C values, although laminar strip

theory predicts nearly identical heating ratios for $\alpha > 5$ degrees. Above ten degrees angle of attack Tunnel F aft lower surface heating rates are consistently higher than strip theory.

6. (U) The heating increase observed over approximately the last inch of the Tunnel C model lower surface is believed due to imperfections in the model contours, and not a result of boundary layer transition.

7. (C) Aft lower compression surface heating rates from both test facilities are higher than predicted by laminar strip theory at $\alpha = 0$, but agree within ±30 percent with strip theory at $\alpha = 10°$. At higher angles of attack, the heating rates are overpredicted, with the data mean at $\alpha = 30°$ approximately half the strip theory value.

8. (C) Body side panel heating rates are generally lower than predicted by laminar strip theory, based on experimental pressures and surface flow directions. For 10 and 15 degrees angle of attack, the side panel data generally agree within ±15 percent with strip theory predictions based on the assumption that the surface flow direction is parallel to freestream.

9. (C) For $10 \le \alpha \le 20$, Tunnel F upper centerline heating rates are 30 to 45 percent lower than zero angle of attack laminar strip theory. Tunnel C upper centerline heating distributions are erratic and are possibly affected by boundary layer transition or vortices. At 10 and 15 degrees angle of attack, Tunnel C upper centerline heating rates between 30 and 60 percent chord are 25 to 35 percent lower than zero angle of attack turbulent strip theory.

10. (C) At the design point flight conditions, radiation equilibrium temperatures based on the AEDC heat transfer data generally agree with analytically predicted temperatures within ±200°F on the lower surface, and within ±100°F on the body side panels and aft lower compression surface.

APPENDIX I

(U) DELTA WING HEATING AND PRESSURE DATA ANALYSIS

(U) Heating and pressure data obtained by the Air Force Flight Dynamics
Laboratory, AFFDL, were examined as part of the analytical effort on the
present study. These analyses were performed to supplement or modify
theoretical/empirical heating prediction methods used in evaluating the study
configurations. The data were obtained on an 80-degree sweep slab delta wing
model from tests in AEDC Tunnel F. Figure 268 shows a sketch of the 80-degree
delta wing model and the sensor layout. With the exception of one heating
rate sensor on the spherical nose cap, only the planar surface was instru-
mented. Tests were conducted at Mach 18.5 with angles of attack ranging
from -10 to +45 degrees. Model attitudes and tunnel flow conditions are
summarized in Table 5.

1   (U) PRESSURE DATA CORRELATIONS

(C) Figures 269 through 274 show the centerline pressure distribution on the
80-degree delta wing for angles of attack from zero to 25 degrees. Included
on each figure are pressure distributions predicted by Newtonian theory and
by two expressions based on blast wave theory. The expression proposed by
Creager (Ref. 32) is applicable to hypersonic flow over a blunted flat plate.
The expression given by Lukasiewicz (Ref. 35) is for hypersonic flow over a
blunted cylinder whose axis is aligned with the flow. Consequently, applica-
tion of these methods for a three-dimensional body is an approximation. The
expression proposed by Creager for estimating pressures on a slightly inclined,
blunted flat plate at hypersonic speeds is

$$\frac{P}{P'_o} = \frac{P_e}{P'_o} + 0.630 \; C_\gamma \; \frac{P_\infty}{P'_o} \frac{M_\infty^2 \; C_{DN}^{2/3}}{\left(\frac{X}{D}\right)^{2/3}} \tag{19}$$

where $C_\gamma = 0.112$ for $\gamma = 1.40$, and 0.169 for $\gamma = 1.67$. The term P_e/P'_o is the
inviscid pressure ratio for a sharp plate and was taken as the Newtonian
value, $\sin^2 \alpha$. The second term on the right side of equation 19 is the
bluntness induced pressure.

(U) The expression proposed by Lukasiewicz for flow over a blunted cylinder is

$$\frac{P}{P_\infty} = 0.44 + 0.067 \; \frac{M_\infty^2 \; C_{DN}^{1/2}}{\left(\frac{X}{D}\right)} \tag{20}$$

43

TABLE 5

(U) FLOW CONDITIONS FOR 80 DEGREE DELTA WING TESTS

Run No.	β	α	Re_∞/in.	T_o (°K)	T_∞ (°K)	P_∞ (PSIA)	P'_o (PSIA)	q_s	P'_o/P_o × 10^{-3}	M_∞
1893	0	5	22,400	2640	44.0	0.0020	0.908	37.2	0.119	18.6
1895	0	-5	22,500	2700	48.0	0.0023	1.07	47.2	0.120	18.2
1897	0	-10	25,300	2840	49.9	0.0028	1.21	58.4	0.129	18.2
1898	+5	10	27,400	2620	44.0	0.0025	1.11	49.9	0.122	18.5
1899	-5	10	22,500	2590	44.1	0.0021	0.901	43.9	0.127	18.3
1900	0	15	22,700	2750	41.7	0.0018	0.853	41.8	0.117	18.7
1901	0	20	23,500	2550	43.5	0.0021	0.920	43.5	0.129	18.3
1902	0	20	27,300	2350	39.2	0.0021	0.921	38.7	0.131	18.5
1904	+5	20	22,100	2660	47.1	0.0022	0.959	47.2	0.136	18.1
1905	-5	20	22,800	2660	46.1	0.0022	0.967	47.4	0.130	18.2
1906	0	10	24,500	2520	42.2	0.0021	0.924	42.8	0.126	18.5
1907	0	0	22,500	2530	42.0	0.0019	0.848	41.3	0.122	18.3
1908	0	25	23,000	2510	42.6	0.0019	0.873	41.3	0.129	18.7
1909	0	30	23,200	2490	40.6	0.0018	0.836	40.1	0.118	18.5
1910	0	30	24,300	2560	42.8	0.0021	0.939	44.4	0.122	18.5
1911	+5	30	22,500	2520	42.5	0.0019	0.855	41.2	0.127	18.3
1912	-5	30	22,500	2570	43.7	0.0020	0.887	43.1	0.128	18.6
1913	0	35	22,500	2590	43.1	0.0019	0.879	43.6	0.119	18.8
1914	0	40	22,900	2300	36.8	0.0015	0.715	32.9	0.119	18.7
1915	0	40	25,200	2450	40.1	0.0019	0.890	40.4	0.121	18.6
1916	0	45	22,700	2540	42.2	0.0019	0.863	41.9	0.121	18.7
1917	0	45	22,700	2560	42.1	0.0019	0.863	42.3	0.117	18.6
1918	0	10	25,300	2480	42.1	0.0021	0.943	42.2	0.132	18.3

Following Creager's approach, the bluntness induced pressure given by Eq. (20) was added to the equilibrium pressure, P_e/P_0, for comparison with angle-of-attack data. This implies that the shock shape does not change significantly with angle of attack. At all angles of attack Creager's two dimensional theory predicts higher induced pressures (Figures 269 through 274).

(C) Centerline pressure data for zero angle of attack are in fair agreement with the equation given by Lukasiewicz. As the angle of attack increases to 10 degrees, the data fall between this equation and Newtonian theory, indicating that the bluntness-induced pressure is overestimated. At the three higher angles of attack the flow over-expands near the shoulder and then approaches Newtonian pressure several nose radii downstream of the stagnation point. Data for five degrees yaw are included in Figures 271 and 273 and are in good agreement with the zero-yaw pressure data.

(C) Spanwise pressure distributions at station 12 are plotted in Figure 275. For zero yaw, the spanwise pressure variation is negligible for all angles of attack between zero and 20 degrees. At five degrees yaw, due to leading-edge effects, the pressures increase slightly in the spanwise direction on the side of the model which is positively yawed. Pressures on the opposite side are in good agreement with the zero-yaw data.

(U) Prediction of leeward surface-pressure distributions is difficult because of the complex flow in such regions. An attempt was made to correlate the delta wing leeward surface centerline pressure data in terms of the blast wave parameter $M_\infty^2\, C_{DN}^m/(X/R)^n$. As indicated by Eqs. (19) and (20), the exponents m and n are both 2/3 for two-dimensional flow and 1/2 and 1.0, respectively, for axisymmetric flow. The value used for m is comparatively insignificant because the nose drag coefficient is generally close to one, the Newtonian value for a hemisphere. To determine the appropriate value of n, delta wing leeward surface pressure data from various sources were plotted versus X/R. The slopes (on log-log paper) varied between 0.45 and 0.70, which are generally lower than predicted by blast wave theory for either axisymmetric or two-dimensional flow. No trends with Mach number or flow expansion angle could be established. For subsequent delta wing leeward surface pressure correlations, it was assumed that m = 1/2 and n = 2/3.

(C) Figure 276 shows leeward surface centerline pressure data from the 80-degree delta wing and from a NASA 70 degree slab delta wing tested at Mach 6.8 and 9.6 (Ref. 36) plotted as a function of $M_\infty^2\, C_{DN}^{1/2}/(X/R)^{2/3}$. The data were obtained at expansion angles of 0, 5, and 10 degrees. The expression

$$\frac{P}{P_\infty} = 1 + (0.073 - 0.0033\,\delta)\,\frac{M_\infty^2\, C_{DN}^{1/2}}{\left(\frac{X}{R}\right)^{2/3}} \tag{4}$$

45

correlates all of the data for $M_\infty^2 \, C_{DN}^{1/2}/(X/R)^{2/3} > 20$ within ± 15 percent. In evaluating equation (4) the flow expansion angle δ is in degrees and is a positive (or zero) quantity. The nose drag coefficient was assumed to be unity for both models.

(C) Figures 277 and 278 compare Eq. (4) with leeward surface pressure measurements on models of high L/D reentry configurations. The data shown in Figure 277 were obtained from four sensors on the upper surface centerline of a model tested in Tunnel F by the AFFDL. The data shown in Figure 278 were obtained from two sensors located on the upper forebody of a model of the F-5A Mod-1 configuration tested in the Lockheed-California Company Shock Tunnel. In all cases the pressures are within ± 25 percent of the pressures given by Eq. (4). Values of X/R on the 80 degree delta wing and the Air Force high L/D configuration ranged from 2 to 8 and from 13 to 53, respectively, indicating that Eq. (4) is applicable over a considerable distance downstream of the nose. The nose drag coefficient of the F-5A Mod-1 model was assumed to be 1.44, the Newtonian value for a 2:1 ellipse of revolution.

(C) According to Eq. (19), the bluntness-induced pressure on a blunted plate is 51 percent higher if the test gas is helium instead of air (through the term C_γ). Accordingly, Eq. (4) was written in the form

$$\frac{P}{P_\infty} = 1 + (0.110 - 0.0050\,\delta)\ \frac{M_\infty^2 \; C_{DN}^{2/3}}{\left(\frac{X}{R}\right)^{2/3}} \qquad (21)$$

and compared in Figure 279 with leeward surface pressure data from a NASA 70 degree slab delta wing tested at Mach 18 in helium (Ref. 36). The flow expansion angles were 0, 5, and 10 degrees. Agreement is satisfactory, with a maximum discrepancy of 22 percent.

(U) In Figures 280, 281 and 282, the zero angle of attack centerline pressure data from the 80-degree delta wing tested in Tunnel F and the 70 degree delta wing tested at NASA-Langley are compared with Lukasiewicz's solutions for pressure distributions on a blunted cylinder and on a blunted flat plate (Ref. 35). The expression for axisymmetric flow is Eq. (20). For two-dimensional flow, the expression is

$$\frac{P}{P_\infty} = 0.56 + 0.121\,\frac{M_\infty^2 \; C_{DN}^{2/3}}{\left(\frac{X}{D}\right)^{2/3}} \qquad (22)$$

(U) In Reference 35, these equations are shown to accurately predict experimental and analytical (method of characteristics) pressure distributions on

46

the geometries for which the equations were derived. However, neither expression is in good agreement with the delta wing centerline pressure data. The curves labeled $\Delta X/R = 2$ include a modification suggested by Lukasiewicz, whereby the origin of the X coordinate is taken as one nose diameter upstream of the stagnation point. This modification, however, does not result in better agreement with the data. Pressure distributions given by Eq. (4) are included in Figures 280, 281 and 282, and are consistently in better agreement with the data than are the axisymmetric or two-dimensional solutions.

(U) Leeward surface spanwise pressure distributions at stations 9 and 12 are plotted in Figure 283. The centerline pressures at these (uninstrumented) stations were determined by fairing a smooth curve through the centerline pressure data. The pressure consistently decreases in the spanwise direction; however, the overall decrease does not exceed 20 percent for any of the four distributions measured.

2 (U) HEAT TRANSFER DATA CORRELATIONS

(C) Centerline heating data from the 80 degree delta wing for angles of attack from zero to 25 degrees are plotted in Figure 284. An interesting feature of the heating distributions is the change in slope with model angle of attack. Only for $\alpha \approx 10$ to 15 degrees is the strip theory formula, $q \sim S^{-0.5}$, applicable. At lower angles of attack the heating rates decrease more rapidly with distance due to the combined effects of boundary layer growth and pressure decay. At higher angles of attack, the pressure is relatively uniform in the chordwise direction, but strip theory is no longer applicable. The less rapid decrease of heating rate with distance can be partly explained by cross flow theory, which is appropriate for predicting lower surface heating at high angles of attack. In applying this theory to a delta wing the stagnation line velocity gradient is usually obtained from a correlation of disc flow data (Ref. 15). Although the centerline heating rate varies according to $q \sim (du/dy)^{0.5}$, the velocity gradient, du/dy, is inversely proportional to chordwise distance only for a flat bottom delta wing with zero edge radius. On blunted wings the velocity gradient is a function of both the edge radius and the local span dimension. Consequently, the velocity gradient, and hence the heating rate, decrease more slowly with chordwise distance.

(C) The 80-degree delta wing centerline heating distributions for 10, 15, and 20 degrees angle of attack are compared with strip theory in Figure 285, 286, and 287. Local flow properties were based on an isentropic expansion of the stagnation point conditions to the Newtonian pressure. Heating rates were computed by Eckert's reference enthalpy method (Ref. 33) with the characteristic dimension based on the wetted distance from the nose stagnation point. The reference enthalpy method was selected in preference to the theory of van Driest because Eckert's theory has been shown to agree well with wind tunnel flat plate data whereas van Driest's method is generally low in comparison. All flow field and heating rates used in the correlations are based on thermodynamic and transport properties of Nitrogen. The heating data for $\alpha = 10$ and 15 degrees are in good agreement with strip theory. The data for

α = 20 degrees are apparently affected by the pressure oscillations shown in Figure 273, but are nevertheless in good agreement with the reference enthalpy prediction modified for outflow according to a semi-empirical correction factor proposed by Neumann and Refroe (Ref. 10).

(U) Figure 288 shows a correlation of centerline heating data from a NASA 70-degree sweep slab delta wing (Ref. 36) tested at angles of attack of 10.5 and 15.5 degrees. The methods used for flow field and heating rate prediction are identical to those described in the preceding paragraph. The data are in good agreement with theory for flow distances in excess of five nose radii. Using measured pressure distributions (Figure 26 of Ref. 36), the reference enthalpy heating rates were corrected for pressure gradient by the method of Bertram and Feller (Ref. 21). The correction, however, is less than 12 percent for all but the first data point shown in Figure 288 ($S/R \approx 1.4$). Because of the large heating rate gradients in this region of the model, conduction correction errors could be the major contributor to the discrepancy between data and theory.

(C) Spanwise heating distributions on the 80 degree delta wing at angles of attack from 5 to 20 degrees are plotted in Figure 289. At zero yaw, heating rates increase in the spanwise direction with the heating rates at the most outboard sensor ($Y/Y_{LE} \approx 0.74$) approximately 15 percent higher than the centerline values. Heating rates at $Y/Y_{LE} = 0.74$ increase by 25-30 percent when the vehicle is given a positive five degree yaw, and decrease by a like amount for a negative five degree yaw. Centerline heating rates increase by 10-20 percent when the vehicle is yawed five degrees.

(C) Leeward surface centerline heating data from the 80-degree slab delta wing tested at minus five and minus ten degrees are compared with laminar strip theory in Figures 290 and 291. Local flow properties are based on an isentropic expansion of the stagnation point properties to the measured pressure. Included on Figures 290 and 291 are curves representing the heating distribution when laminar strip theory is corrected for pressure gradient, and the heating distribution assuming local flow properties are freestream values. The latter was included only for reference purposes and it is coincidental that the data are best correlated by this solution. The experimental heating rates are also in fair agreement with strip theory corrected for pressure gradient.

(U) Leeward surface centerline heating data from a NASA 70 degree slab delta wing tested at Mach 9.6 at angles of attack of 5.2 and 10.5 (Ref. 36) are compared with strip theory in Figure 292. Methods for evaluating local flow properties and correcting for pressure gradients are identical to those described above. The data are in good agreement with strip theory corrected for pressure gradient effects, following the same general trend as the data from the 80 degree wing tested at Mach 18.5.

(C) Figure 293 compares upper surface centerline heating distributions on an AFFDL high L/D configuration (Ref. 16) with laminar strip theory. The local

flow expansion angles were four and nine degrees. Flow properties were based on an isentropic expansion of stagnation point properties to the pressure given by Eq. (4). Strip theory, corrected for pressure gradient, is consistently higher than the measured heating rates by from 45 to 70 percent.

(C) Leeward surface spanwise heating distributions on the 80-degree delta wing at stations 9 and 12 are plotted in Figure 294. Several of the data points shown were obtained by fairing a curve through the longitudinal heating data from other stations. In contrast to windward surface heating distributions, the leeward surface heating rates consistently decrease in the spanwise direction. The heating rates decrease much more rapidly than the pressure (Figure 283), suggesting that the dropoff is primarily a boundary layer, rather than a flow field phenomenon.

3   (U) CONCLUSIONS

Significant results of the delta wing pressure and heating data correlations are summarized below:

1. (C) For angles of attack of 15 degrees or more, lower surface pressure data are in good agreement with Newtonian theory, although minor pressure variations occur due to bluntness effects.

2. (C) For angles of attack between zero and five degrees, delta wing lower surface pressures can be approximated by adding the nose bluntness induced pressure to the Newtonian pressure.

3. (U) Pressure distributions on the leeward surfaces of highly swept delta wings are correlated by a parameter based on blast wave theory.

4. (C) For angles of attack between 10 and 20 degrees, lower surface centerline heating data are in good agreement with strip theory corrected for outflow, with local flow properties based on an isentropic expansion of the stagnation point conditions to the Newtonian pressure.

5. (U) Leeward surface centerline heating data for flow expansion angles of five and ten degrees are in fair agreement with strip theory corrected for pressure gradient with local flow properties based on an isentropic expansion from the stagnation point conditions.

APPENDIX II

(U) THE HEAT CAPACITY AND DENSITY OF 304 STAINLESS STEEL

(U) During preparation for the wind tunnel tests, a purchase order was issued
to Southern Research Institute (SRI) of Birmingham, Alabama to measure the
heat capacity and density of the 304 stainless steel sheet used to fabricate
the thin-skin Tunnel C heat transfer model. These quantities were required
for data reduction and experience has shown that considerable deviations in
these properties may occur in commercially available sheets. The SRI final
test report is reproduced in this Appendix.

THE HEAT CAPACITY AND
DENSITY OF 304 STAINLESS STEEL SHEET

INTRODUCTION

This is the final report under Purchase Order TK-3987-DDX for the determination of the heat capacity of 304 stainless steel sheet from 400°R to 1200°R and the density at room temperature. Two sheets of 304 stainless steel were furnished by Micro Craft, Inc., of Tullahoma, Tennessee. The sheets were approximately 4 inches x 12 inches x 0.049 inch. The sheets were designated "A" and "B," and the determinations were made with specimens from each sheet.

HEAT CAPACITY

Apparatus and Procedure

Heat capacity was derived from the slope of the enthalpy versus temperature data obtained using an adiabatic calorimeter. The adiabatic calorimeter, described in the Appendix, was used to measure enthalpy at specimen temperatures from -64°F (396°R) to 747°F (1207°R). The heated (or cooled) specimen was dropped into a thermally guarded, calibrated cup, and the enthalpy was measured as a function of the temperature change of the cup. The measurements were referenced to zero enthalpy at 85 °F using a linear interpolation. The accuracy of the adiabatic calorimeter was confirmed by making calibration determinations using synthetic sapphire. The overall uncertainty of the enthalpy measurements has been established previously at $\pm$ 3%.

The heat capacity was determined graphically from the slope of the enthalpy versus temperature curve, and also by differentiating an equation for enthalpy obtained using the least squares method. The enthalpy data were first fitted to an equation of the form

$$h_{85} = aT + bT^2 + cT^{-1} + d \tag{1}$$

The derivative of this equation was adjusted to agree with the graphically determined heat capacity at a selected temperature to obtain an equation for heat capacity of the form

$$HC = a + 2bT - c*T^{-2} \qquad\qquad (2)$$

Temperatures (T) are in degrees Rankine. Values determined from the equation are generally valid over a range extending from about 100°F from each end point and cannot be used to extrapolate the data.

Data and Results

Small $\frac{3}{4}$ inch squares were cut from each of the two sheets and used as heat capacity specimens. From two to five pieces were used to obtain the data, with the number of pieces selected to obtain the optimum signal at the various temperatures. The enthalpy data obtained with the adiabatic calorimeter are given in Table II-1 and Figure II-1.

The heat capacity of the material was determined graphically and from the derivative of the equation fitted to the enthalpy data. A curve for heat capacity which considered both the graphical and analytical solutions was determined and is shown in Figure II-1. The heat capacity increased\ from 0.104 Btu/lb/°F at 400°R (-60°F) to about 0.120 Btu/lb/°F at 660°R (200°F). Above this temperature the heat capacity increased slightly with temperature to 0.122 Btu/lb/°F at 1200°R (740°F).

The least squares treatment of the enthalpy data resulted in the following equation for the enthalpy of the material above an 85°F reference from about 400°R to 1200°R. The temperatures in the equation are in degrees Rankine

$$h_{85} = 0.1667\,T - 1823 \times 10^{-8}\,T^2 + 8502\,T^{-1} - 101.3 \qquad\qquad (3)$$

The derivative of Equation 3 was adjusted to agree with the graphically determined heat capacity at 150°F (610°R) to obtain the following equation for heat capacity

$$HC = 0.1667 - 3646 \times 10^{-8}T - 9453\,T^{-2} \qquad\qquad (4)$$

Enthalpies and heat capacities calculated with Equations 3 and 4 are plotted in Figure 1. Equation 4 provides a good definition of the heat capacity from about 500°R to 1000°R. Outside of this temperature range the graphical

solutions, which were higher, were given more weight in plotting the curve for heat capacity.

The heat capacity of the **304** stainless steel sheet is compared in Figure II-2 to the heat capacities for several other stainless steels from various literature sources. The Metals Handbook and Allegheny Ludlum Steel Corporation's Stainless Steel Handbook give the heat capacity of Type **304** and several other stainless steels as **0.12** Btu/lb/°F over the temperature range from 32°F to 212°F. The heat capacities of Type AISI **301**, **316**, and **347** stainless steel from WADC-TR-58-476 are also plotted in Figure II-2. These data increased from about **0.107** Btu/lb/°F at **500**°R (40°F) to from **0.120** to **0.125** Btu/lb/°F at **800**°R (340°F) and from **0.130** to **0.137** Btu/lb/°F at 1200°R (740°F).

DENSITY

Apparatus and Procedure

Density of the **304** stainless steel sheet was determined from measurements of the weights of samples suspended both in air and in distilled water. A confirming measurement was made by hand-lapping a small square of the material and then measuring its weight and volume to determine density.

The following procedure was used to determine density with the water displacement technique. Three pieces from each sheet, which were used in the heat capacity determination, were weighed together using an analytical balance sensitive to **0.0001** gram. The pieces were about $\frac{3}{4}$ inch square, **0.049** inch thick, and each had a small hole drilled in one corner for the suspension wire. A chromel wire of **0.005** inch diameter was inserted through these holes and used to suspend the specimens in air from the beam of the balance. The three pieces and the wire were then weighed while suspended in air and also while suspended slightly below the surface in distilled water. The specimens were then removed from the wire and the wire alone was weighed in air. The wire was then weighed with the same portion immersed in water as before when used to suspend the three specimens. The following calculation was then used to determine density:

$$\text{Specific Gravity} = \frac{W_a D_w}{W_a - W_w + W_s}$$

where

Wa = weight of specimen in air, grams

Ww = weight of specimen and support wire with all of specimen and part of wire immersed in distilled water, grams

Ws = weight of wire with part immersed in distilled water, grams

Dw = specific gravity of water at room temperature

Density was determined from the specific gravity by multiplying by 0.9975 to account for the buoyancy of air in accordance with ASTM test methods.

Data and Results

Three of the $\frac{3}{4}$ inch squares of the 304 stainless steel sheet were used in the density determinations on each sheet. The following data and calculations were for the specimens from Sheets A and B.

		Sheet A	Sheet B
Wa	=	11.1681 grams	11.3305 grams
Ww	=	9.7765 grams	9.9200 grams
Ws	=	0.0203 grams	0.0203 grams
Temperature	=	24°C	24°C
Dw	=	0.9997	0.9997

For Sheet A,

$$S.G. = \frac{11.1681 \times 0.9997}{11.1681 - 9.7765 + 0.0203} = 7.9076$$

Density = 7.9076 x 0.9975 = 7.888 gm/cc

For Sheet B,
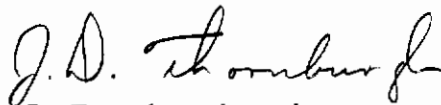
$$S.G. = \frac{11.3305 \times 0.9997}{11.3305 - 9.9200 + 0.0203} = 7.9166$$

Density = $7.9166 \times 0.9975 = 7.897$ gm/cc

One piece from Sheet A was machined to $\frac{3}{4}$ inch by $\frac{3}{4}$ inch. The eight surfaces were then hand-lapped to remove all rough or rounded edges. The piece was weighed using the analytical balance, and the dimensions were measured with a micrometer. The weight was 3.5346 grams and the dimensions were 0.0490 inch by 0.7491 inch by 0.7452 inch. The density calculated with these data was 7.886 gm/cc.

The difference between the densities of the two sheets from the water displacement method was less than 0.12 percent, and the maximum difference between the largest and smallest measurement was about 0.14 percent. The average of the three densities determined was 7.89 grams per cubic centimeter. Most literature sources give 7.9 grams per cubic centimeter for the density of 304 stainless steel.

Submitted by:

J. D. Thornburgh
Associate Engineer

C. M. Pyron, Jr., Head
Thermodynamics Section

Approved:

C. D. Pears, Head
Mechanical Engineering Division

8507-1996-I
(5:12)lw

Temperature - °R

HEAT CAPACITY

— Best fit of graphical and analytical
  solutions
O Graphical solution
+ Analytical solution (from 500°R to
  1000°F)
  HC = 0.1667 - 3646 x 10⁻⁸T - 9453T⁻²

$$HC = 0.1667 - 3646 \times 10^{-8}T - 9453T^{-2}$$

  (T in degrees Rankine)

Temperature - °F

Temperature - °R

ENTHALPY

Adiabatic Calorimeter in Air
O Sheet A
△ Sheet B
+ Least squares curve fit (from 400°R
  to 1200°R)

$$h_{85} = 0.1667\,T - 1823 \times 10^{-8}\,T^2 + 8502\,T^{-1} - 101.3$$

85°F Reference

UNCLASSIFIED

Temperature - °F

Figure II-1. The Enthalpy and Heat Capacity of 304 Stainless Steel
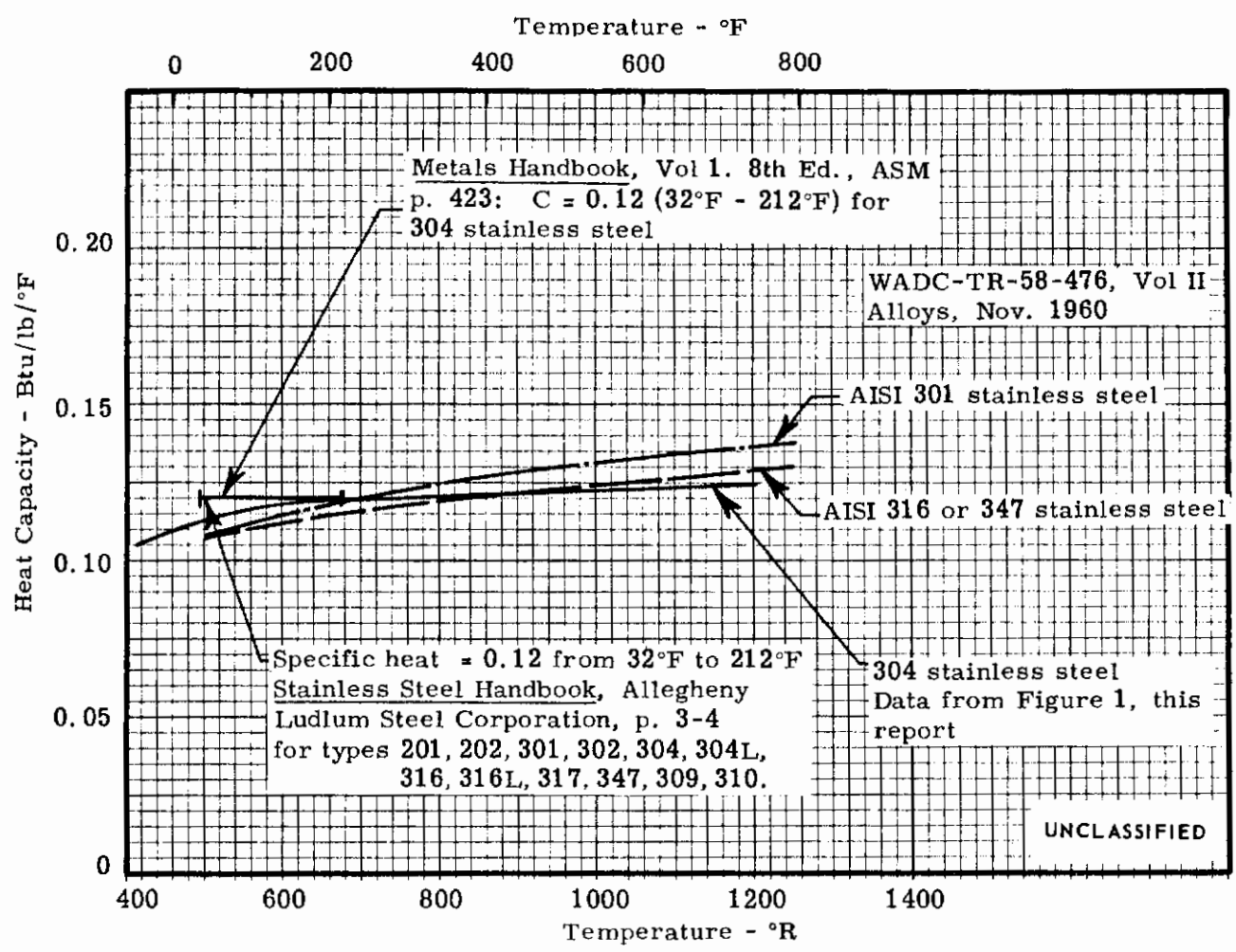
Figure II-2. The Heat Capacities of Some Stainless Steels from Several Sources

Table II-1 (U)

The Enthalpy of 304 Stainless Steel Sheet

Spec. and Run No.	Initial Cup Temp. °F (t_1)	Final Cup Temp. °F (t_2)	Change in Cup Temp. °F	Initial Sample Temp. °F (t_3)	Time to Temp. Min	Initial Wt. of Sample gm	Final Wt. of Sample gm	Enthalpy $h = \frac{K}{W_s}(t_2 - t_1)$ Btu/lb	Enthalpy Above 85°F Reference Btu/lb
Samples from Sheet A									
Run 1	74.00	71.43	-2.57	-64.0	30	18.5895	18.5901	-16.6	-18.3
2	71.43	72.83	1.40	151	30	18.5901	18.5900	9.01	7.61
3	74.32	79.55	5.23	362	30	18.5900	18.5892	33.8	33.2
4	76.83	81.83	5.00	534	45	11.0795	11.0790	54.3	54.9
5	80.00	84.70	4.70	746	35	7.3385	7.3379	77.1	77.1
6	84.65	88.83	4.17	642	30	7.3379	7.3382	68.5	68.9
7	75.70	80.52	4.83	720	30	7.3382	7.3387	79.2	78.6
Samples from Sheet B									
Run 1	73.48	71.22	-2.26	-64.5	30	19.1700	19.1702	-14.2	-15.6
2	72.82	74.45	1.63	163	30	19.1702	19.1698	10.3	9.06
3	79.18	84.13	4.95	350	40	19.1702	19.1685	31.1	31.0
4	80.57	85.70	5.13	531	35	11.5755	11.5749	53.4	53.4
5	80.39	85.52	5.13	747	35	7.7508	7.7511	79.7	79.8
6	76.35	81.09	4.74	662	30	7.7495	7.7508	73.6	73.1
7	88.61	94.13	5.52	806	30	7.7251	7.7448	85.8	86.9

Notes:

1. A calorimeter constant (k) equal to 0.2654 Btu/°F was used to determine specimen enthalpy above final cup temperature (t_2).

2. Enthalpy was referred to a common base temperature of 85°F using the following linear interpolation:

$$h_{85} = h \frac{(t_3 - 85)}{(t_3 - t_2)}$$

ADDENDUM TO SRI FINAL REPORT

HEAT CAPACITY TO 1000°F

The heat capacity to 1000°F is determined from data obtained in an adiabatic calorimeter. In this apparatus the heated specimen is dropped into a thermally guarded, calibrated cup, and the enthalpy is measured as a function of the increase in temperature of the cup. The heat capacity is the slope of the enthalpy versus temperature curve. A picture of the apparatus is shown in Figure II-3.

A tubular furnace and a cold box are used to bring the specimens to temperature. By pivoting this equipment on a common post near the calorimeter, the samples are transferred to a position directly over the calorimeter cup. At this position the specimen is released from a suspension assembly that is triggered externally. Thermocouples located near the specimen are used to measure specimen temperature. The normal specimen size is about 1" x 1" x 1".

Elevated specimen temperatures are maintained by a manual setting of a variable voltage transformer, which controls the power input to the furnace. Cold sample temperatures are obtained by filling the cold box with dry ice and, when required, injecting liquid nitrogen vapors. The cold box consists of two concentric cylinders enclosed in a housing. The smaller cylinder (3" diameter by 16" high) is constructed of $\frac{1}{4}$" mesh hardware cloth. The larger cylinder is made of galvanized sheet metal (15" diameter and 16" high). The annulus is partially filled with dry ice.

Specimens of the materials are heated or cooled to the desired temperature, and following a stabilization period, are dropped into the calorimeter cup. Adiabatic conditions are maintained during each run by manually adjusting the cup guard bath temperature.

The covered cup of the drop-type adiabatic calorimeter is approximately $2\frac{1}{2}$" in diameter by 2" deep. Three thermocouple wells are located in the bottom wall of the cup. The cup is mounted on cork supports, which rest in a silver-plated copper jacket. The jacket is immersed in a bath of ethylene glycol which is maintained at the temperature of the cup by means of a heater and copper cooling coils immersed in the liquid. Chilled trichloroethylene is circulated through the coils to cool the bath below ambient temperature when cold enthalpy measurements are made. A double-bladed stirrer maintains uniform bath temperature.

In the calorimeter six copper-constantan thermocouples, differentially connected between calorimeter cup and jacket, indicate temperature difference between cup and bath. The six thermocouples enable a difference of 0.03°F to be detected. This difference is maintained to within 0.15°F. During the runs, absolute temperature measurements of the cup are determined by means of the three thermocouple junctions, series connected, in the bottom of the calorimeter cup. All of the thermocouple readings are taken with instruments which permit readout to within 0.1°F; however, the system uncertainty is about 0.5°F.

The enthalpy of the specimen at any initial temperature is calculated from the following equation:

$$h = \frac{K}{W_S} (t_2 - t_1) \tag{1}$$

where

h = enthalpy above t_2
K = calorimeter constant, 0.2654 Btu/°F
W_S = sample weight in lbs
t_1 = initial cup temperature in °F
t_2 = final cup temperature in °F

The calorimeter constant of 0.2654 Btu/°F was determined by measuring the enthalpy of an electrolytic copper specimen of known specific heat.

The enthalpy is referred to a common base temperature of 85°F using the following linear interpolation:

$$h_{85} = h \frac{(t_3 - 85)}{(t_3 - t_2)} \tag{2}$$

where

h_{85} = enthalpy above the reference temperature of 85°F in Btu/lb
t_3 = initial sample temperature in °F

The base of 85°F is used because this is usually near the actual final cup temperature.

The enthalpy-temperature curve established is used to determine heat capacity (specific heat) by measuring its slope at different temperatures. This is done both graphically and by analytical methods which first fit the enthalpy data to an equation of the following type:

$$h_{85} = aT + bT^2 + cT^{-1} + d \qquad (3)$$

The temperature (T) employed usually is in degrees Rankine. While this equation may not provide the best definition of the enthalpy data over the entire temperature range, it does anticipate the theoretical behavior and is consistent with methods recommended in WADC TR **57-308** and by **K. K. Kelley.**[1] The derivative of this equation, the heat capacity, is used with the constant "c" adjusted so that the analytical solution agrees with the value determined graphically at **150°F**. This technique is similar to that of Kelley in forcing the heat capacity equation through a known value. The equations are developed using a digital computer.

The accuracy of the apparatus has been confirmed by measuring the enthalpy of sapphire and other standard specimens and comparing the results to literature values. The results of the comparison on sapphire are shown in Table II-2. From these and other data the overall uncertainty of the apparatus was established at $\pm$ **3%**.

---

1. Kelley, K. K., "Contributions to Data on Theoretical Metallurgy," Vol. XIII High Temperature Heat Content, Heat Capacity, and Enthalpy Data for Elements and Inorganic Compounds, Bulletin **584**, U. S. Bureau of Mines, Nov. **1958**.
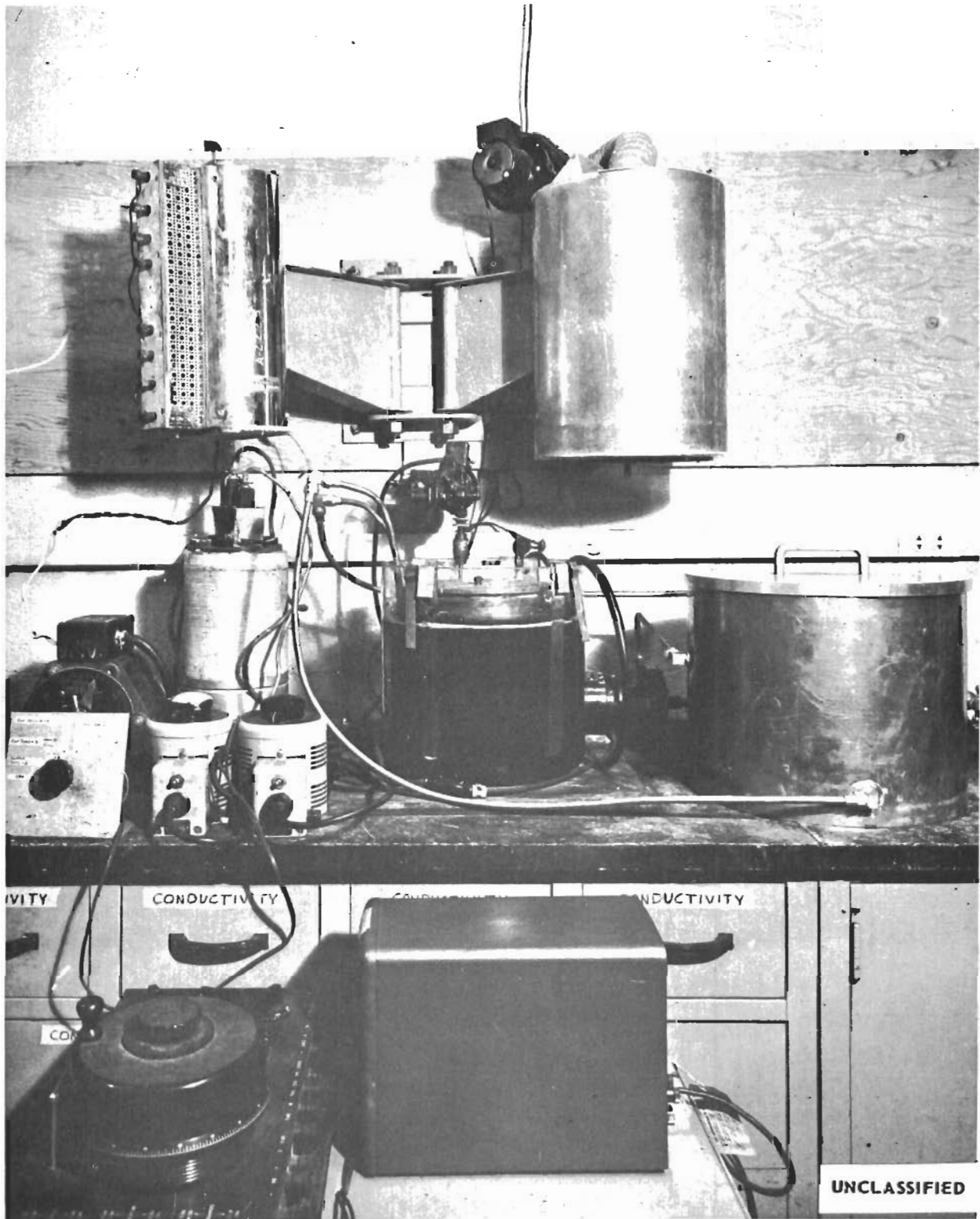
Figure II-3. Heat Capacity Apparatus

Table II-2 (U)

Comparison of the Specific Heat of Sapphire Obtained by the Adiabatic Calorimeter to Several Other Sources

SRI Adiabatic Calorimeter		SRI Ice Calorimeter		Armour Research Foundation		Linde Company		International Critical Tables	
Temp. °F	Specific Heat Btu/lb °F	Temp. °F	Specific Heat Btu/lb °F	Approx. Temp. °F	Specific Heat Btu/lb °F	Approx. Temp. °F	Specific Heat Btu/lb °F	Temp. °F	Specific Heat Btu/lb °F
490	0.233	497	0.210	500	0.263	500	0.2125		
996	0.240	1008	0.241	1000	0.280	1000	0.2265	922	0.239

63

(REVERSE SIDE IS BLANK)

REFERENCES

1   C. F. Hansen, Approximations for the Thermodynamic and Transport
    Properties of High Temperature Air, NASA TR R-50, 1959

2   J. A. Fay and F. R. Riddell, "Theory of Stagnation Point Heat Transfer
    in Dissociated Air, "Journal of Aeronautical Society, Volume 25, No. 2,
    February 1958

3   J. C. Boison and H. A. Curtiss, "An Experimental Investigation of Blunt
    Body Stagnation Point Velocity Gradient, "ARS Journal, February 1959

4   I. Beckwith, Similar Solutions for the Compressible Boundary Layer on a
    Yawed Cylinder with Transpiration Cooling, NASA TR R-42, 1959

5   J. Gaz, Leading Edge Heat Transfer Testing Analysis (U), Boeing Company
    Report D2-81319-1, September 1965 (C)

6   J. T. Lloyd, et al, Preliminary Design of Hypersonic High L/D Test
    Vehicles, AFFDL-TR-66-12, May 1966 (C)

7   H. D. Schultz, Thermal Analyzer Computer Program for the Solution of
    General Heat Transfer Problems, Lockheed-California Company, LR 18902,
    July 1965

8   E. R. van Driest, Investigation of Laminar Boundary Layer in Compressible
    Fluids Using the Crocco Method, NACA TN 2597, January 1959

9   E. R. van Driest, Turbulent Boundary Layer in Compressible Fluids, Journal
    of Aeronautical Society, Volume 18, No. 3, March 1951

10 R. D. Neumann and P. G. Renfroe, Evaluation of the Heat Transfer and Flow
    Fields about Highly Swept Delta Wings in Hypersonic Flow (U),
    ASD TDR 64-76, April 1964 (C)

11 L. Lees, Laminar Heat Transfer Over Blunt Nosed Bodies at Hypersonic
    Speeds, Jet Propulsion, April 1956

12 A. Thomas, et al, Advanced Reentry Systems Heat Transfer Handbook for
    Hypersonic Flight, AFFDL-TR-65-195, June 1966

13 D. T. Nowlan, Pressure and Heat Transfer Distribution on ASD Elliptic
    Cone (W3) and ASD Sortie (W4) in the CAL 48-inch Hypersonic Shock
    Tunnel (U), CAL Report AM-1800-Y-2, December 1963 (C)

14 R. Archer, et al, Experimental Pressure and Heat Transfer Distributions on Blunt-Nose Delta Wings for Angles of Attack up to 30° at Mach Number 7, Aerospace Research Laboratory Report ARL 63-231, December 1965

15 J. C. Dunavant, Investigation of Heat Transfer and Pressures on Highly Swept Flat and Dihedraled Delta Wings at Mach Numbers of 6.8 and 9.6 and Angles of Attack to 90° (U), NASA TM X-688, January 1962 (C)

16 E. C. Knox, Pressure and Heat Transfer Distributions on an AFFDL High Lift-to-Drag Ratio Reentry Configuration at Angles of Attack for Freestream Mach Number of 19 and Unit Reynolds Number to 600,000 per Foot (U), AEDC-TR-62-220, October 1965 (C)

17 R. Beckman, Shock Tunnel Heat Transfer and Pressure Distributions on a High L/D Reentry Vehicle Configuration (U), Lockheed-California Company Report LR 20321, December 1966 (C)

18 ASSET Program Final Summary (U), Technical Report No. AFFDL-TR-65-31, Volume IV, April 1966 (C)

19 D. R. Chapman, D. M. Chapman and H. K. Larson, Investigation of Separated Flows in Supersonic and Subsonic Streams with Emphasis on the Effect of Transition, NASA Report 1356, 1958.

20 H. D. Schultz, Heat Transfer Distributions on a Hypersonic High L/D Configuration, Lockheed-California Company, LR 19277, April 1966

21 M. H. Bertram and W. V. Feller, A Simple Method for Determining Heat Transfer, Skin Friction, and Boundary-Layer Thickness for Hypersonic Laminar Boundary-Layer Flows in a Pressure Gradient, NASA Memo 5-24-59L, June 1959

22 Test Facilities Handbook, Sixth Edition, Arnold Engineering Development Center, November 1966.

23 C. Onspaugh, Wind Tunnel Models and Design Report - Preliminary Design of Two High Volumetrically Efficient, High L/D, Unmanned Flight Test Vehicles, Lockheed-California Company Report LR 20872, June 1967

24 C. J. Spurlin, Force, Pressure, and Heat-Transfer Tests of a Volumetrically Efficient High L/D Configuration at Mach Numbers 1.5 to 10 (U), AEDC-TR-67-230, Nov. 1967 (C)

25 C. J. Spurlin, Tunnel C Pressure Data for Project VTO 618, Groups 399 through 447 (U) Von Karman Gas Dynamics Facility, ARO, Inc., Arnold Air Force Station, Tennessee, 4 August 1967 (C)

26 C. J. Spurlin, Tabulated Tunnel C Heat Transfer Data for Project VTO 618, Groups 324 through 398 (U), Von Karman Gas Dynamics Facility, ARO, Inc., Arnold Air Force Station, Tennessee, 29 July 1967 (C)

27 D. S. Bynum, <u>Instrumentation for the AEDC/VKF 100-in. Hotshot (Tunnel F)</u>, AEDC-TR-66-209, January 1967

28 R. Ledford, W. Smotherman, and C. Kidd, <u>Recent Developments in Heat Transfer Rate, Pressure and Force Measurements for Hotshot Tunnels</u>, AEDC-TR-66-228, January 1967

29 Letter from R. Eaves, VKF Hypervelocity Branch, to F. Guard, Lockheed-California Company, dated Dec. 11, 1967

30 J. Sims, <u>Tables for Supersonic Flow About Right Circular Cones at Zero Angle of Attack</u>, NASA SP-3004, 1964

31 W. Francis, F. Malvestuto, and J. Stuart, <u>Study to Determine Skin-Friction Drag in Hypersonic Low-Density Flow</u>, Vol. I Summary Analysis, ASD-TR-61-433, April 1962

32 M. O. Creager, <u>The Effect of Leading Edge Sweep and Surface Inclination on the Hypersonic Flow Field Over a Blunt Flat Plate</u>, NASA Memo 12-26-58A, January 1959

33 E. R. G. Eckert, <u>Survey on Heat Transfer at High Speeds</u>, WADC TR 54-70, April 1954

34 K. Stetson and G. Rushton, <u>A Shock Tunnel Investigation of the Effects of Nose Bluntness, Angle of Attack and Boundary Layer Cooling on Boundary Layer Transition at a Mach Number of 5.5</u>, AIAA Paper 66-495, June 1966

35 J. Lukasiewicz, Blast-Hypersonic Flow Analogy Theory and Application, <u>ARS Journal</u>, September 1962

36 M. H. Bertram and P. E. Everhart, <u>An Experimental Study of the Pressure and Heat-Transfer Distribution on a 70° Sweep Slab Delta Wing in Hypersonic Flow</u>, NASA TR R-153, December 1963

(REVERSE SIDE IS BLANK)
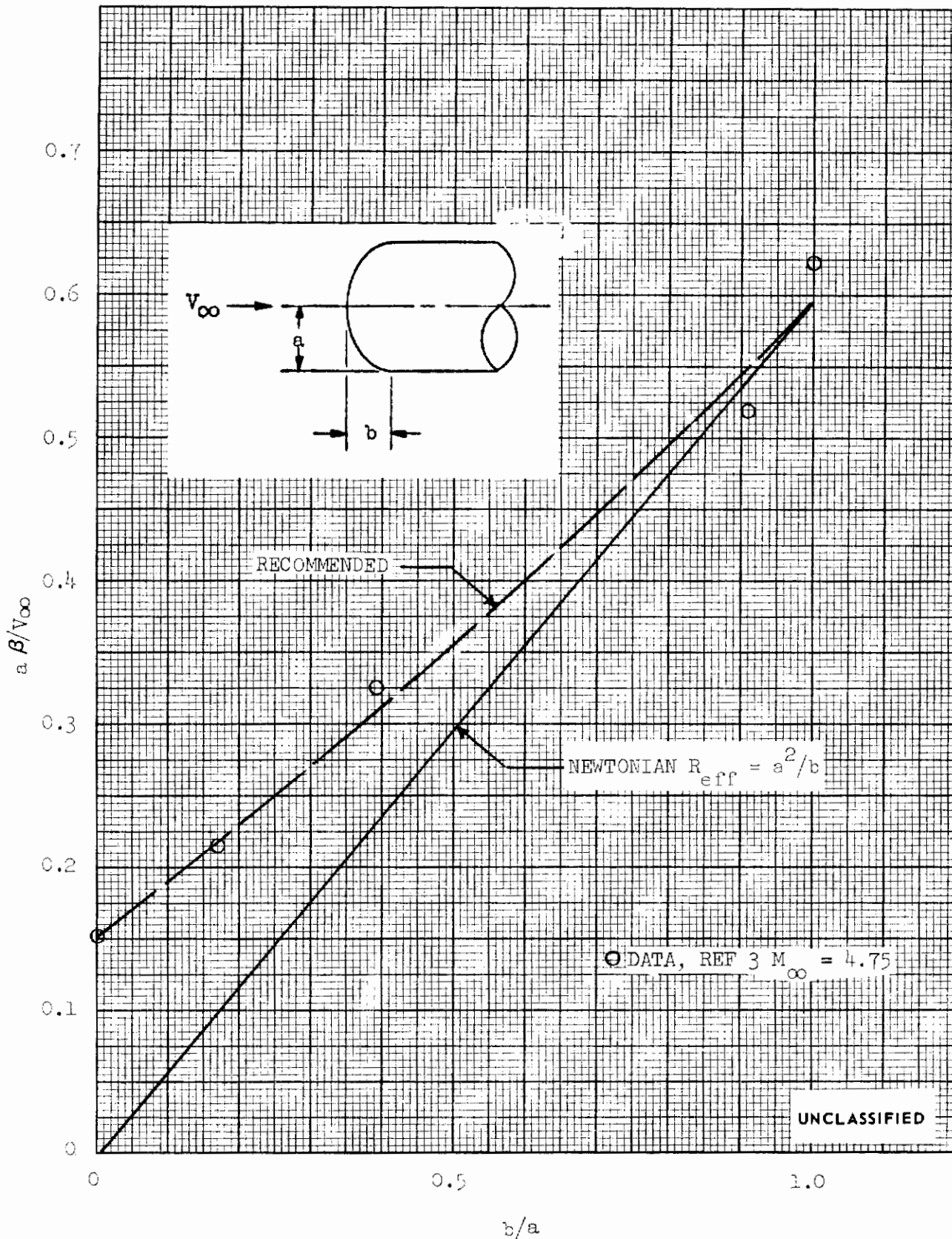
FIGURE 1   (U) STAGNATION POINT VELOCITY GRADIENT PARAMETER FOR
ELLIPSOIDAL SHAPES

69

$M_\infty = 22$ $Re_\infty/FT = 9.5 \times 10^4$
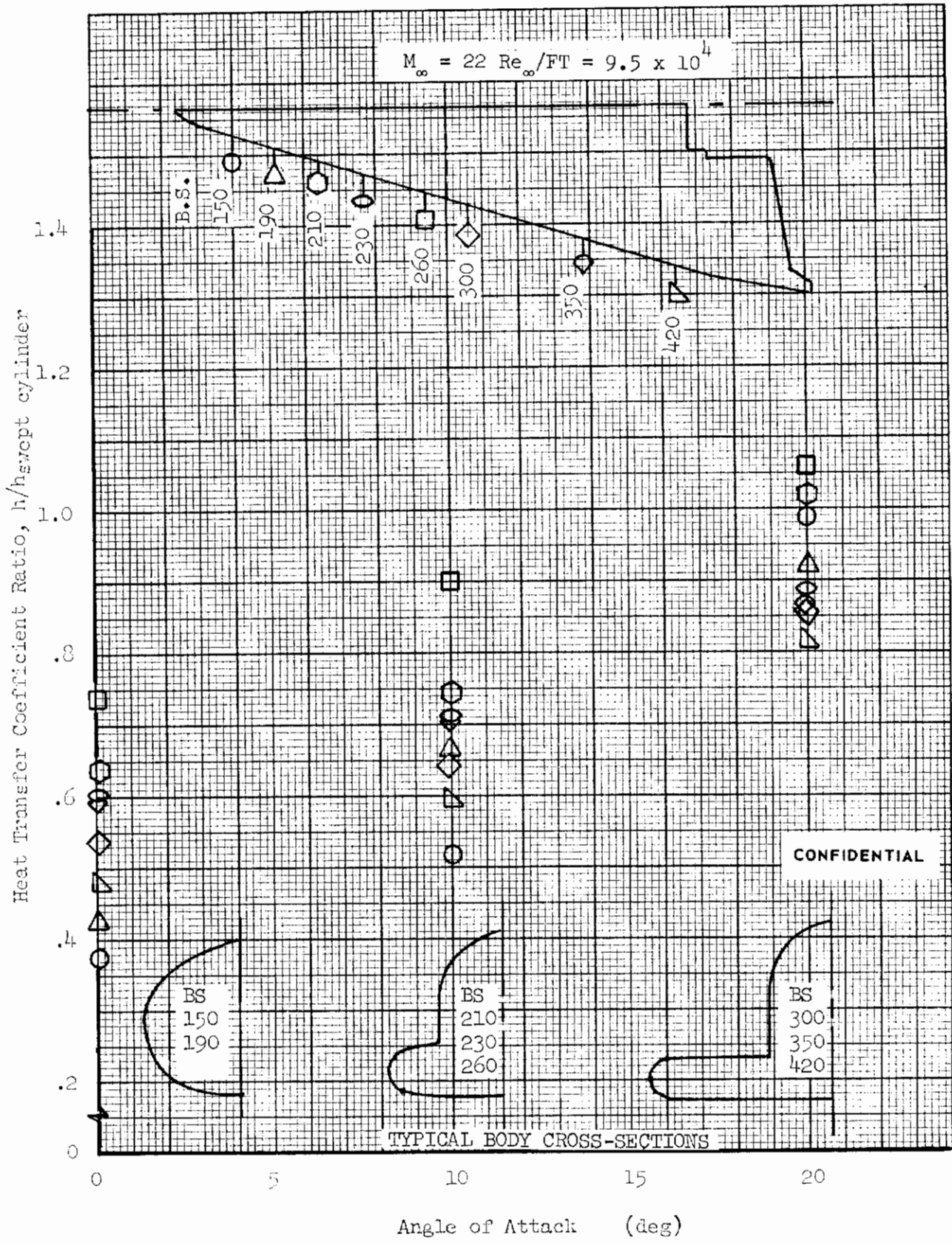
FIGURE 2 (U) CORRELATION OF LEADING EDGE HEAT TRANSFER DATA FROM
X-20 MODEL

70
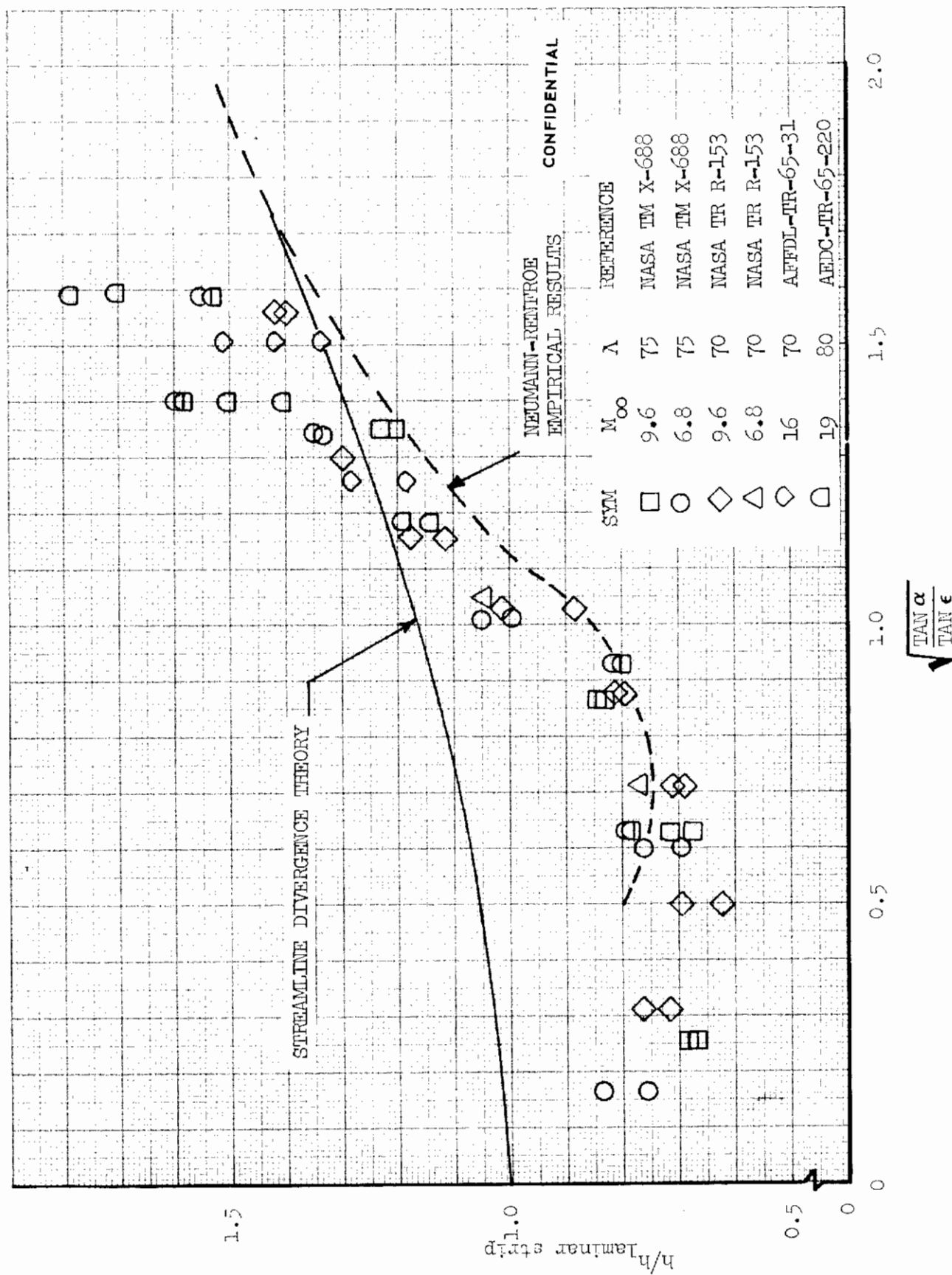
FIGURE 3 (U) RATIO OF EXPERIMENTAL TO LAMINAR STRIP HEATING ON DELTA WING CENTERLINE

71
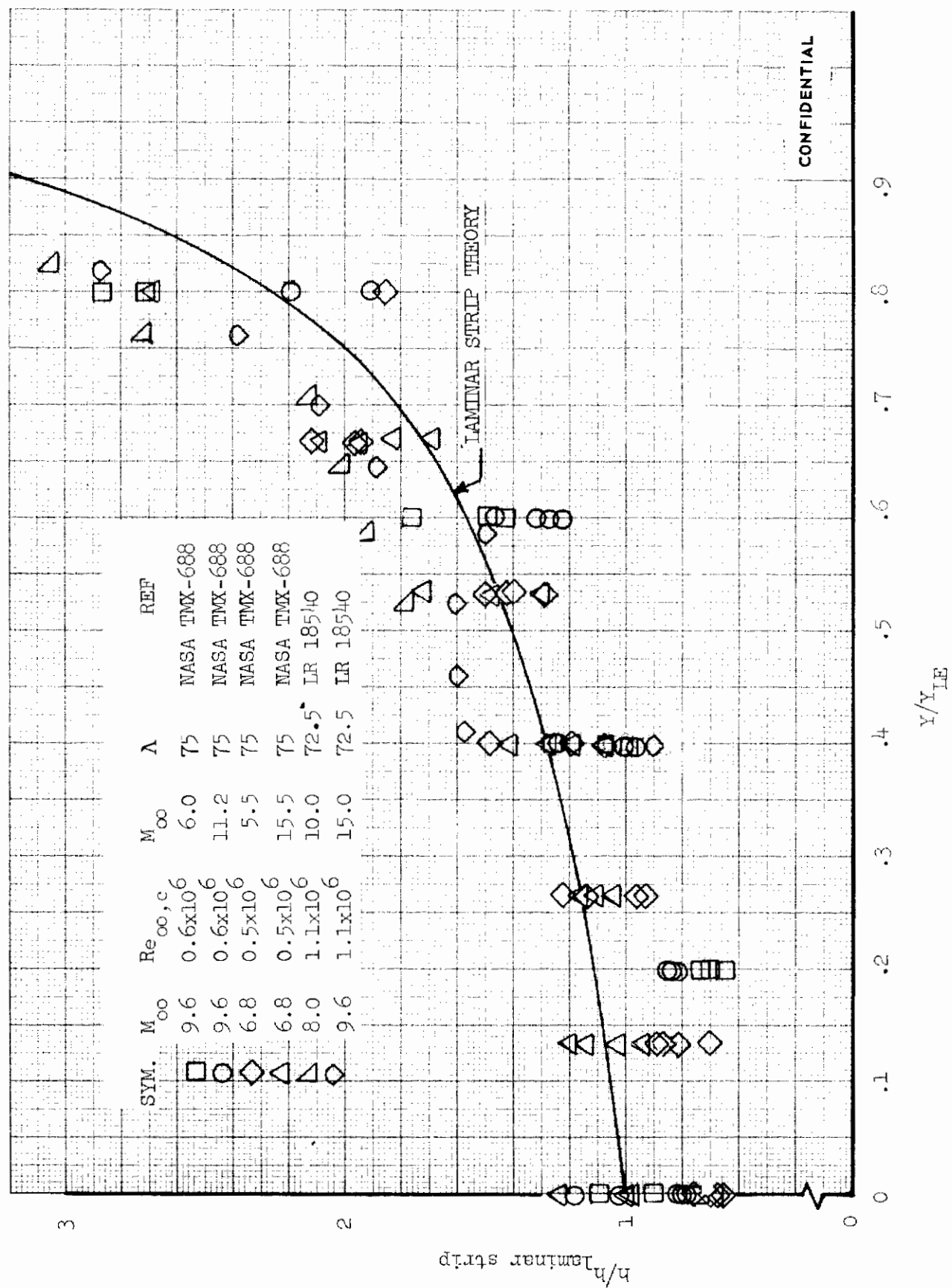
FIGURE 4 (U) COMPARISON OF EXPERIMENTAL AND THEORETICAL SPANWISE HEATING ON FLAT DELTA WINGS
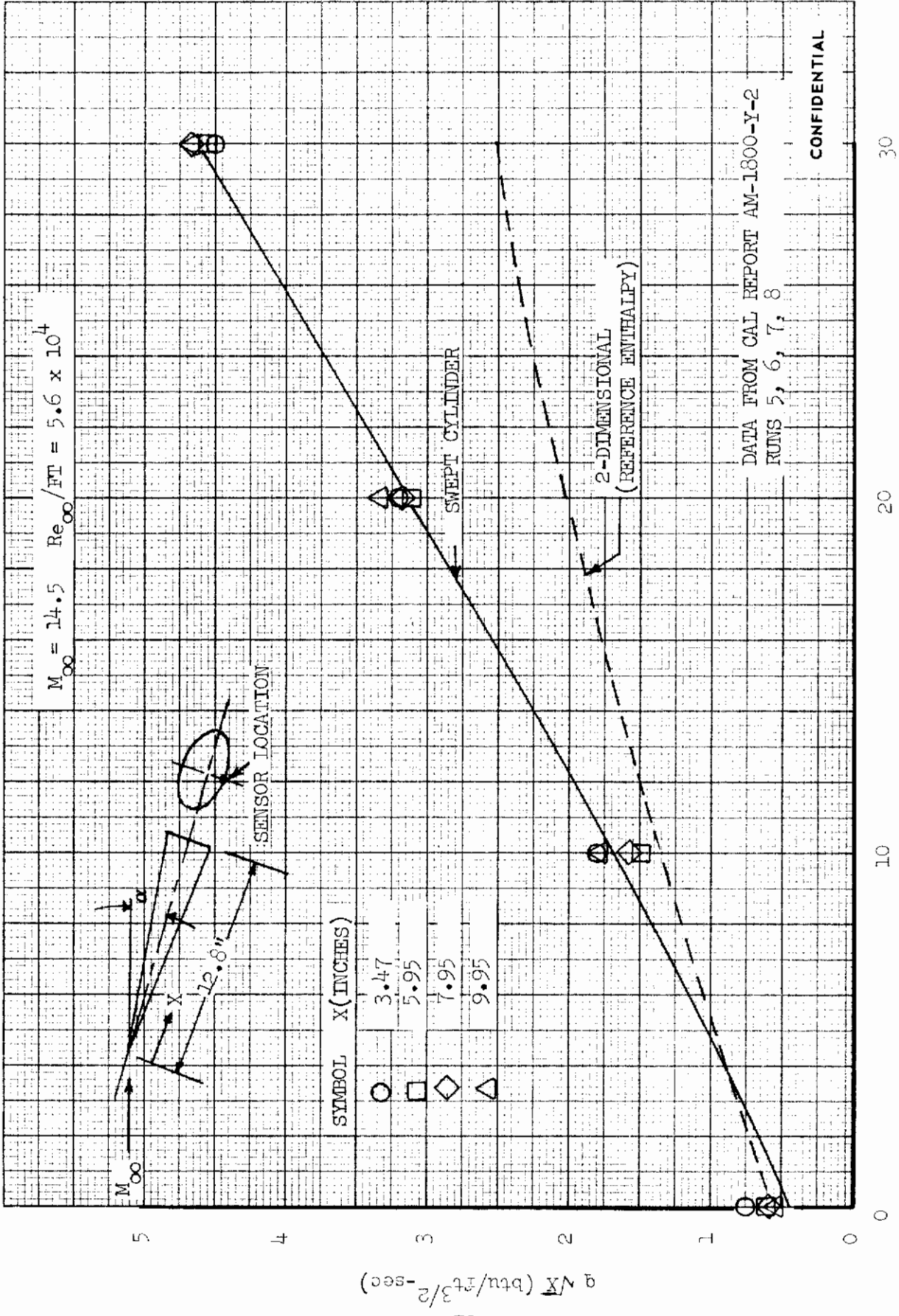
FIGURE 5 (U) CORRELATION OF CENTERLINE HEATING DATA ON AN ELLIPTIC CONE (ASD MODEL W3)

$M_\infty = 14.5$ $Re_\infty/FT = 5.6 \times 10^4$

SENSOR LOCATION

12.8"

SWEPT CYLINDER

2-DIMENSIONAL
(REFERENCE ENTHALPY)

DATA FROM CAL REPORT AM-1800-Y-2
RUNS 5, 6, 7, 8

CONFIDENTIAL

SYMBOL	X (INCHES)
○	3.47
□	5.95
◇	7.95
△	9.95

Angle of Attack (deg)

$q\sqrt{X}$ (btu/ft$^{3/2}$-sec)
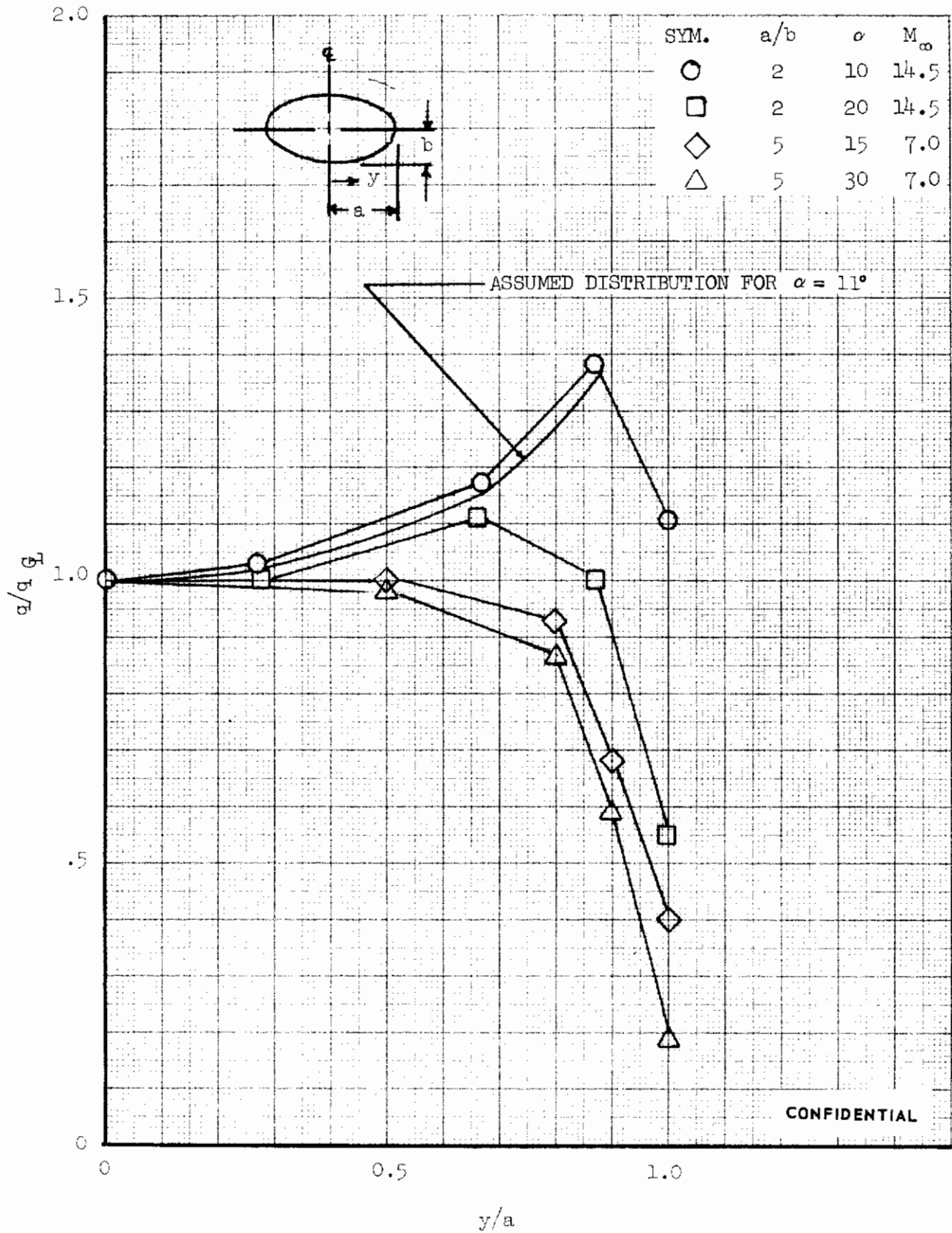
FIGURE 6   (U) EXPERIMENTAL HYPERSONIC SPANWISE HEATING DISTRIBUTIONS
ON TWO ELLIPTIC CONES

74
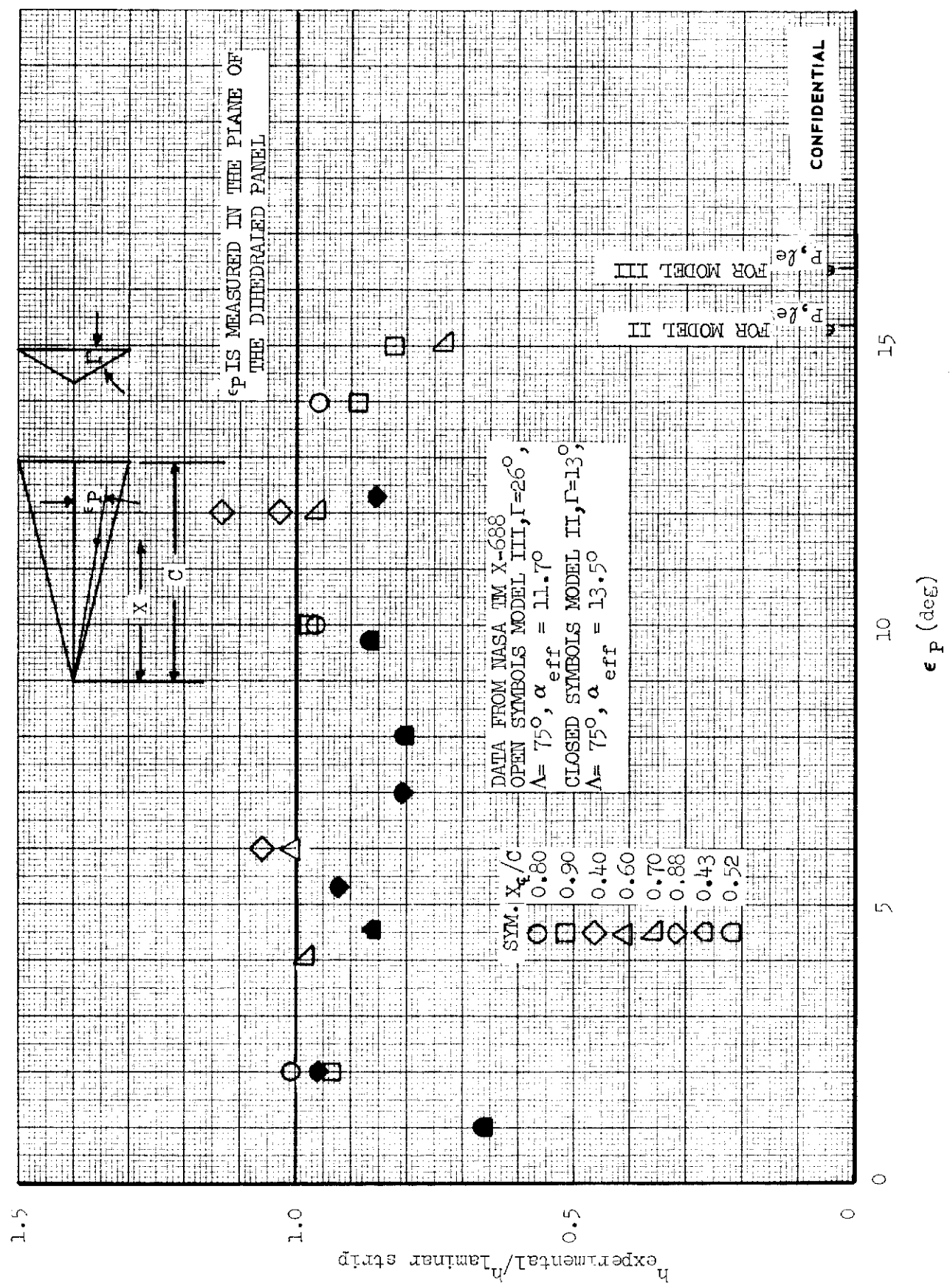
FIGURE 7 (U) CORRELATION OF HEAT TRANSFER MEASUREMENTS ON DIHEDRALED DELTA WING CONFIGURATIONS
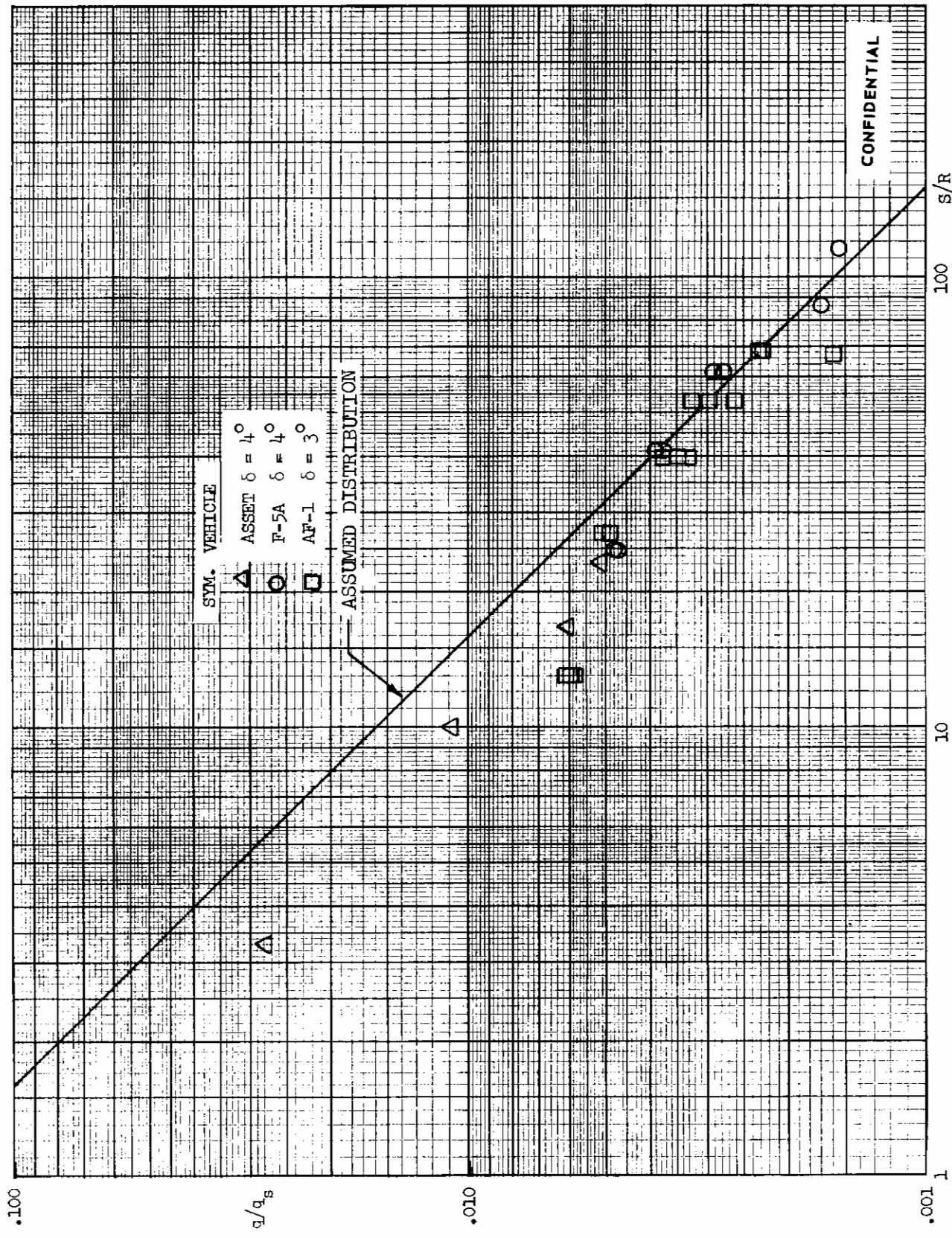
FIGURE 8 (U) CORRELATION OF UPPER SURFACE CENTERLINE HEATING DATA ON HIGH L/D REENTRY CONFIGURATIONS
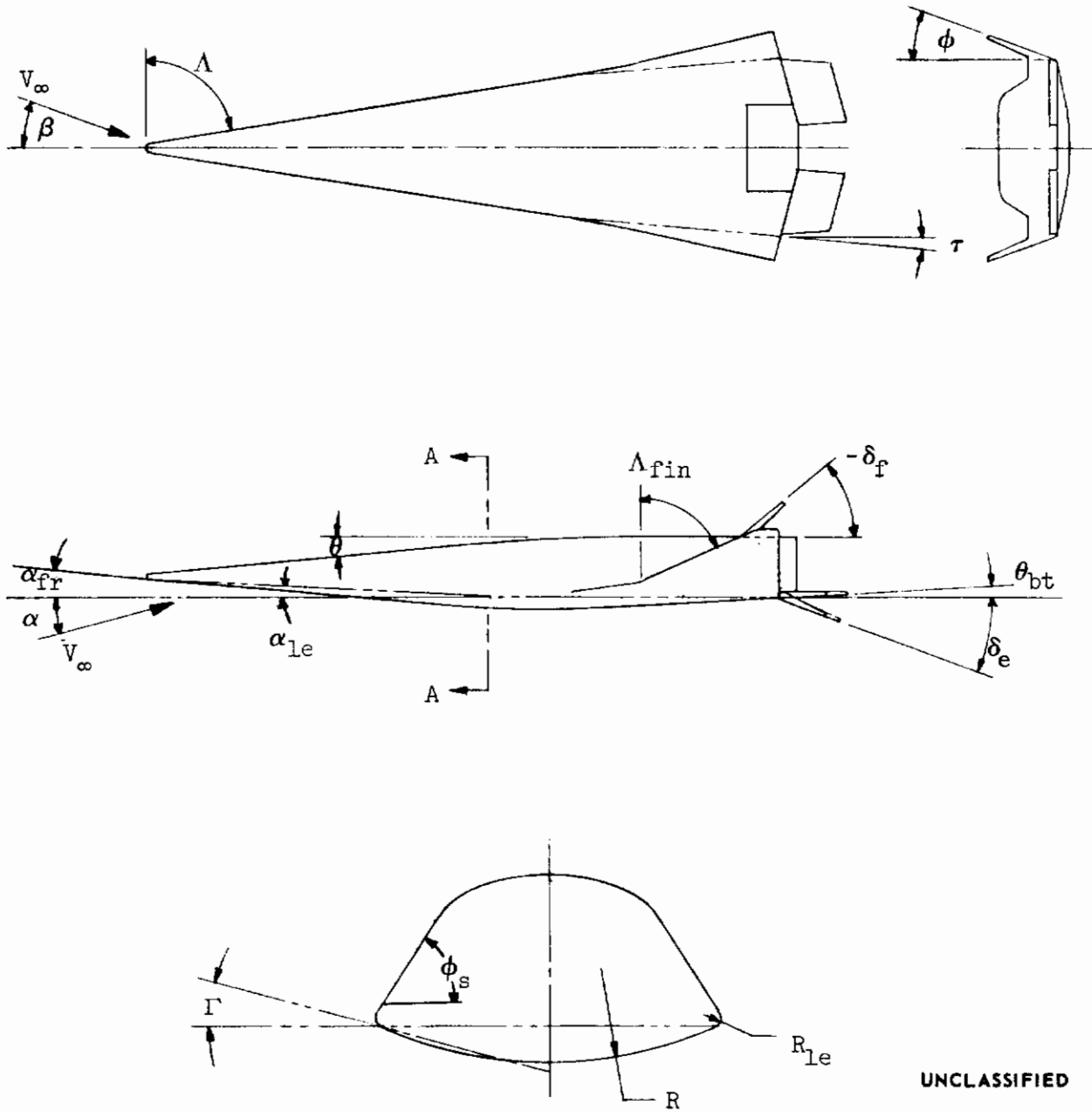
FIGURE 9 (U) AEROTHERMODYNAMIC CONFIGURATION PARAMETERS

UNCLASSIFIED
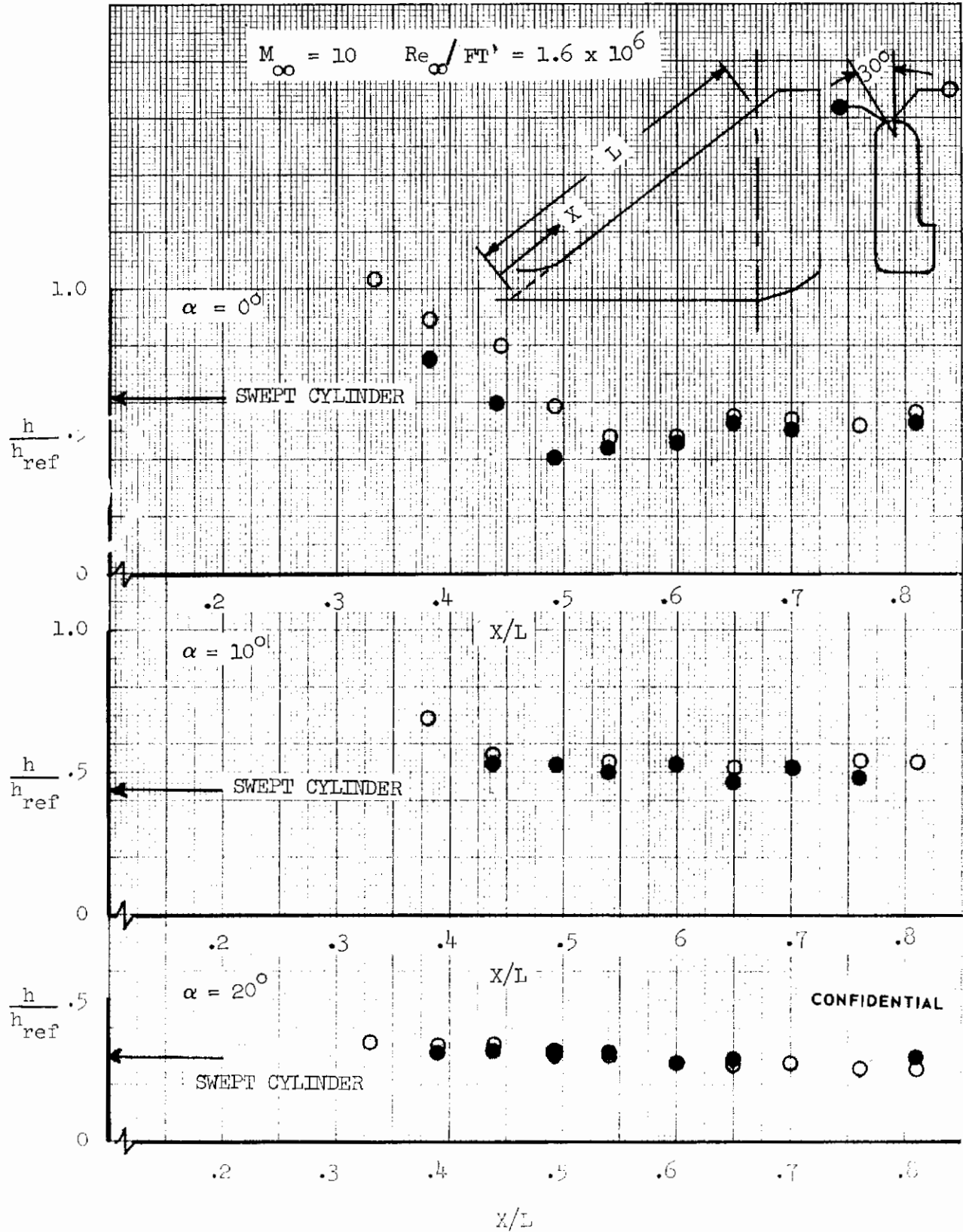
FIGURE 10 (U) HEAT TRANSFER DISTRIBUTIONS ON X-20 MODEL FIN LEADING EDGE

78
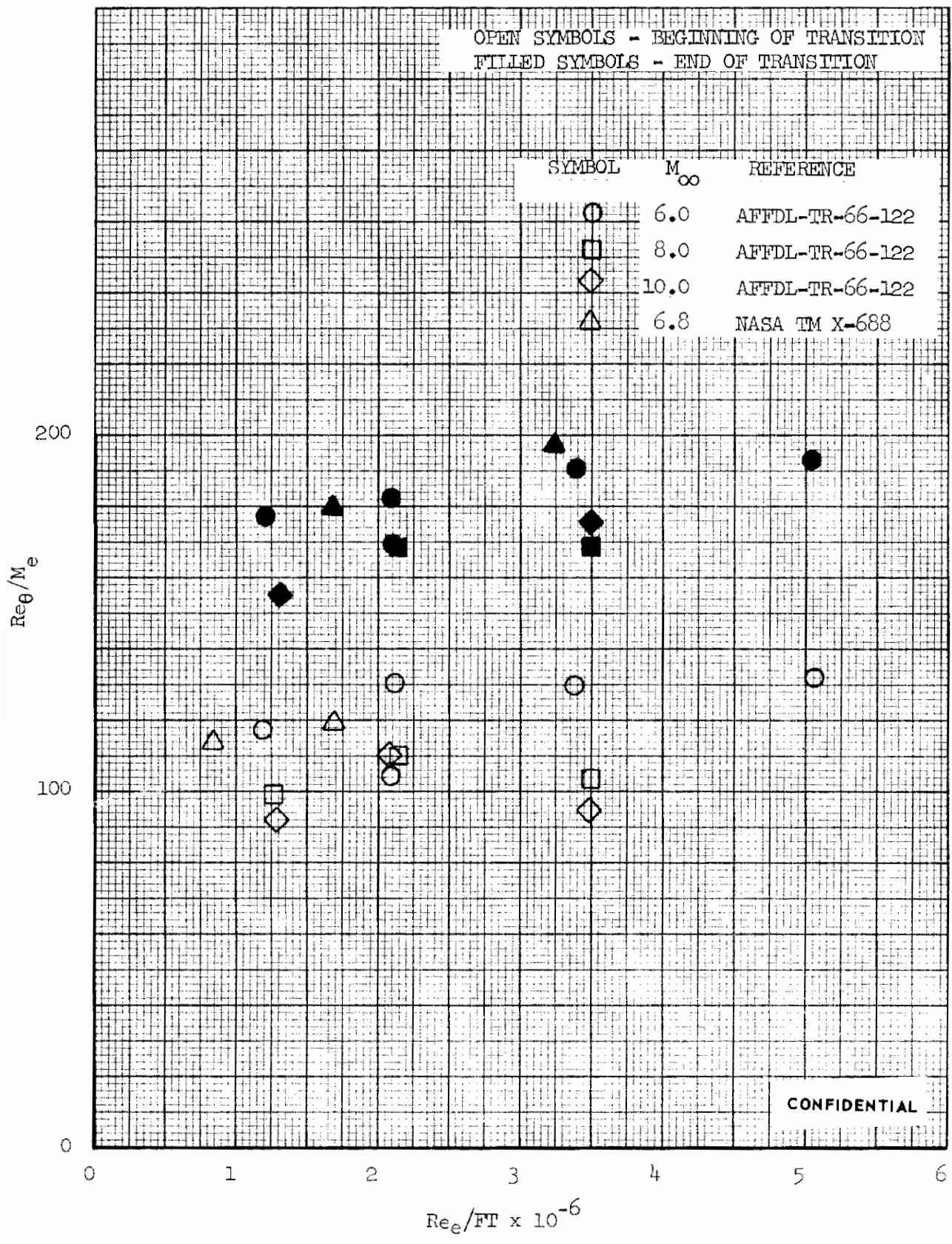
FIGURE 11 (U) CORRELATION OF DELTA WING TRANSITION DATA

79
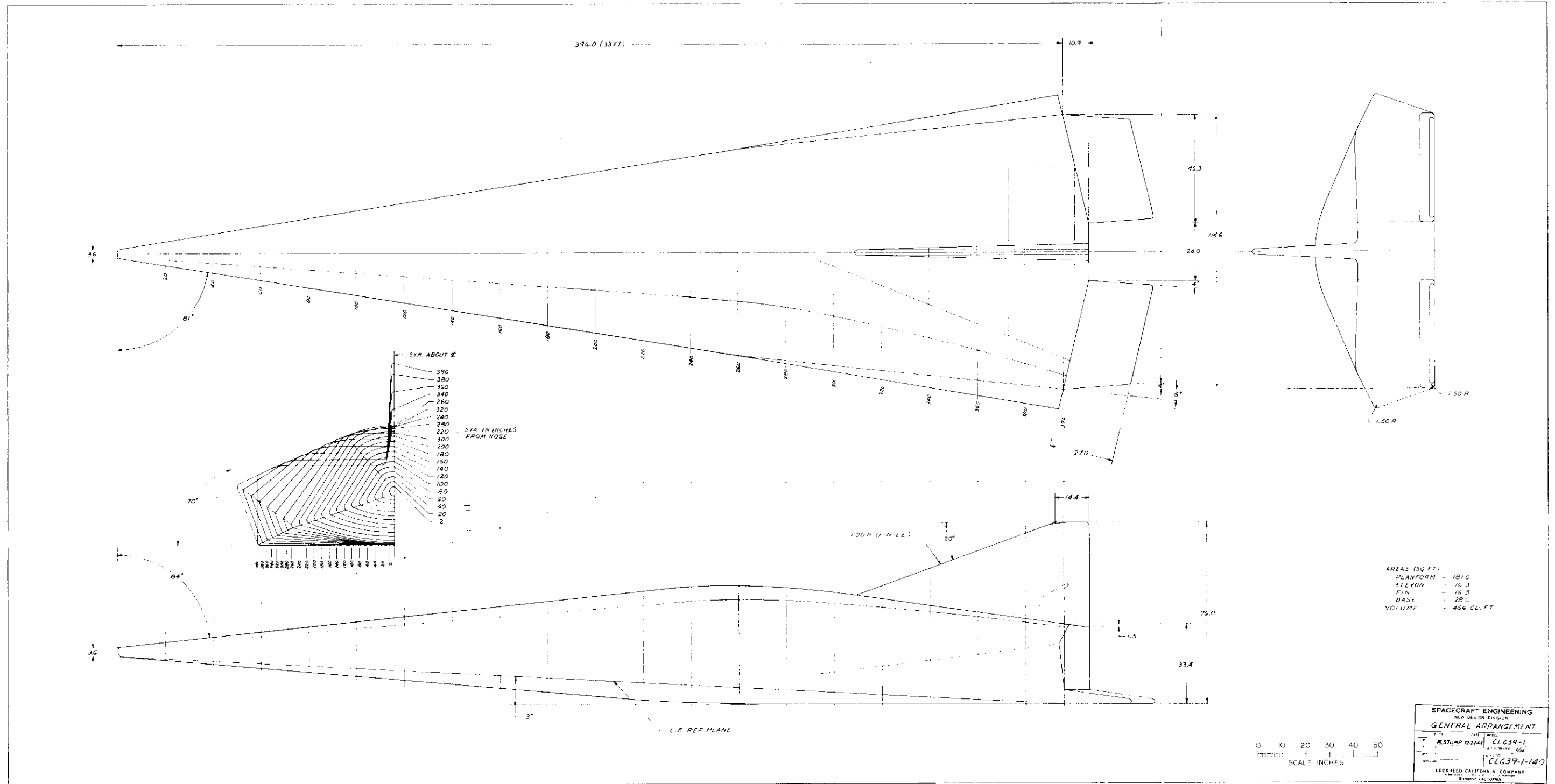
FIGURE 12 (U) FDL-5 CONFIGURATION

81   (REVERSE SIDE IS BLANK)
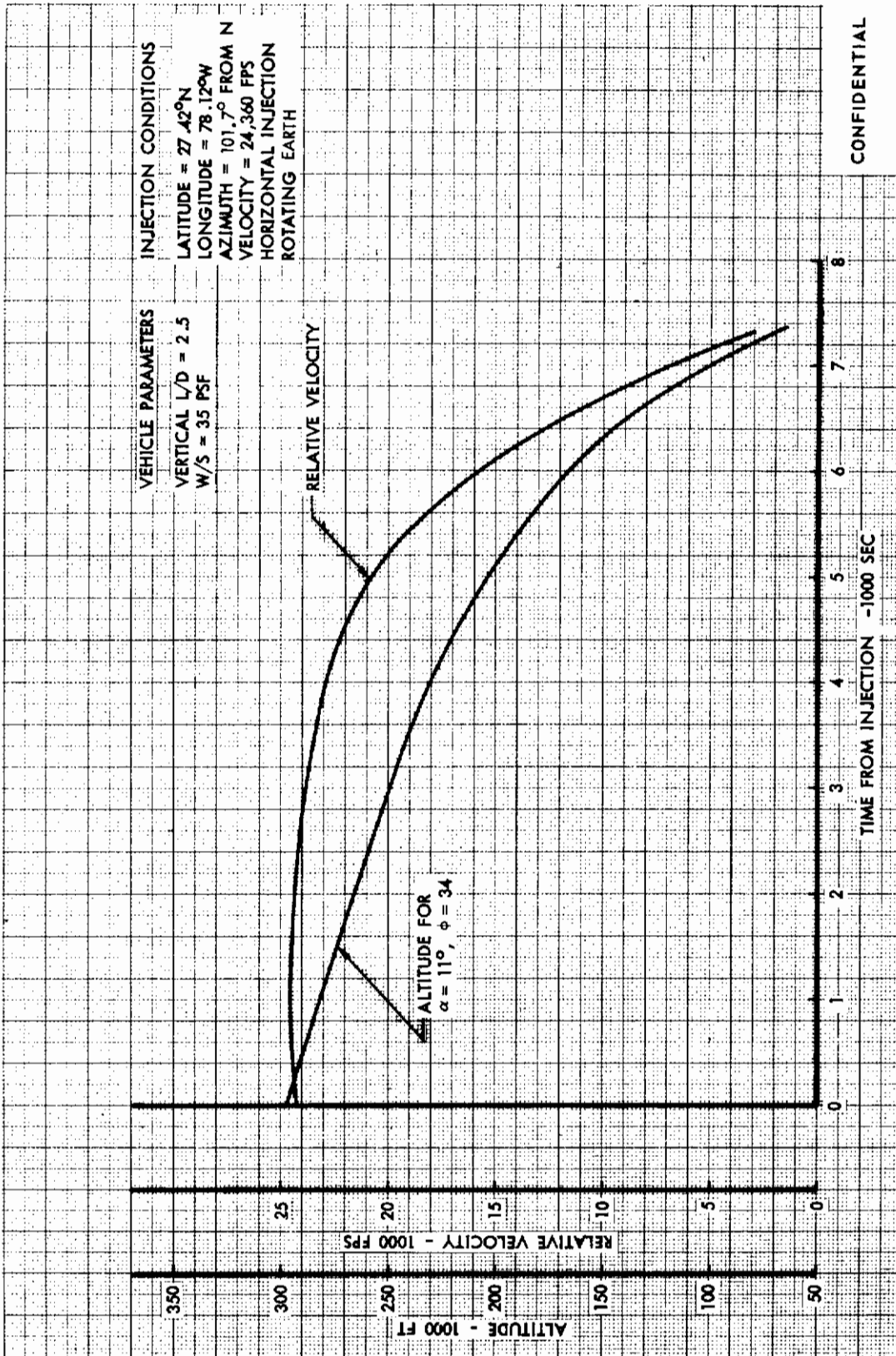
FIGURE 13 (U) REFERENCE TRAJECTORY

HEATING RATES BASED ON F-5

LOW ALTITUDE REFERENCE

TRAJECTORY $\alpha = 11°$

NOSE STAGNATION POINT

LEADING EDGE

LOWER SURFACE AT STATION 100

LOWER SURFACE AT STATION 396

CONFIDENTIAL

TIME FROM INJECTION - SECONDS
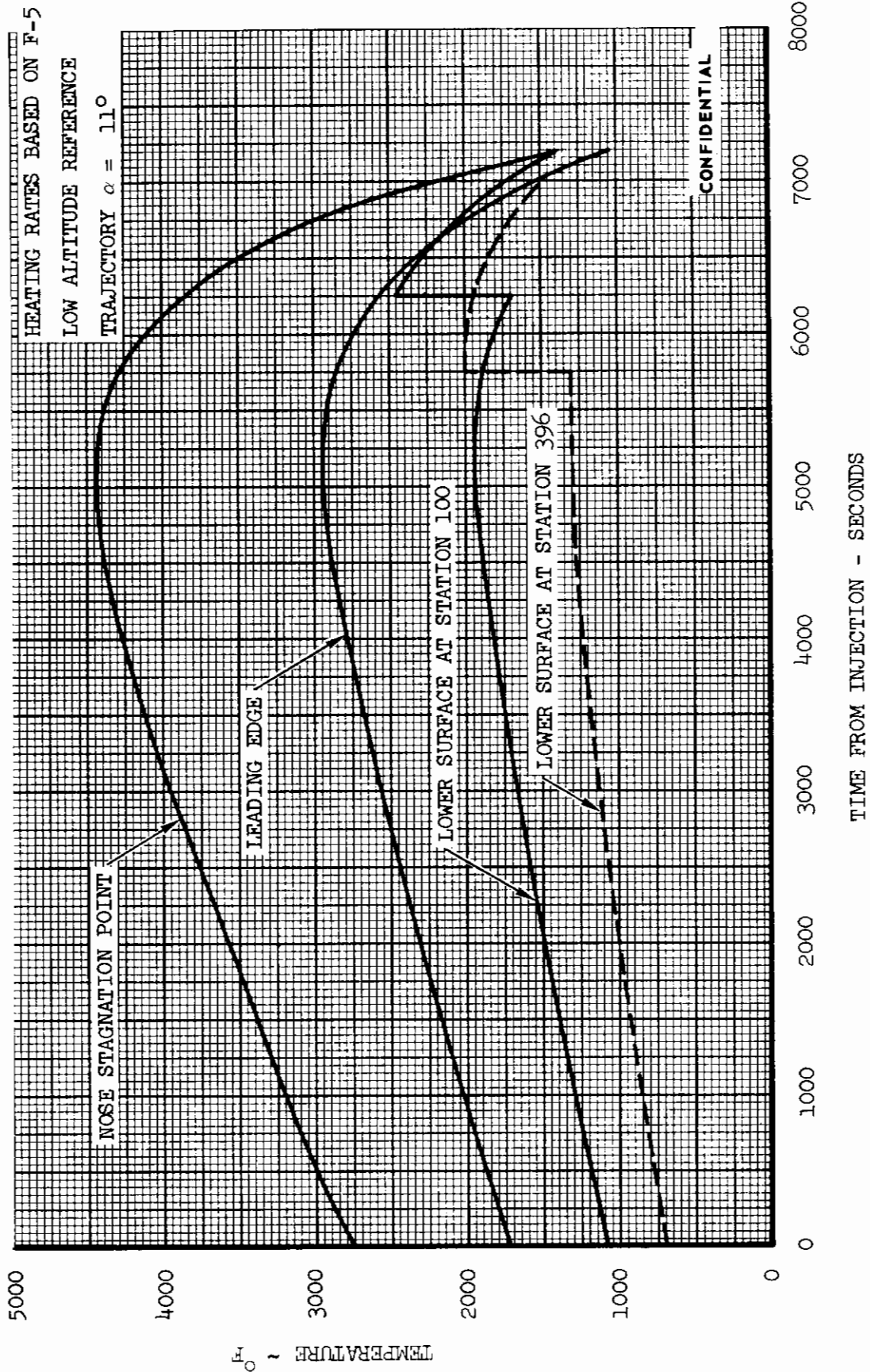
TEMPERATURE ~ $°F$

FIGURE 14 (U) TEMPERATURE HISTORIES AT VARIOUS VEHICLE LOCATIONS

84
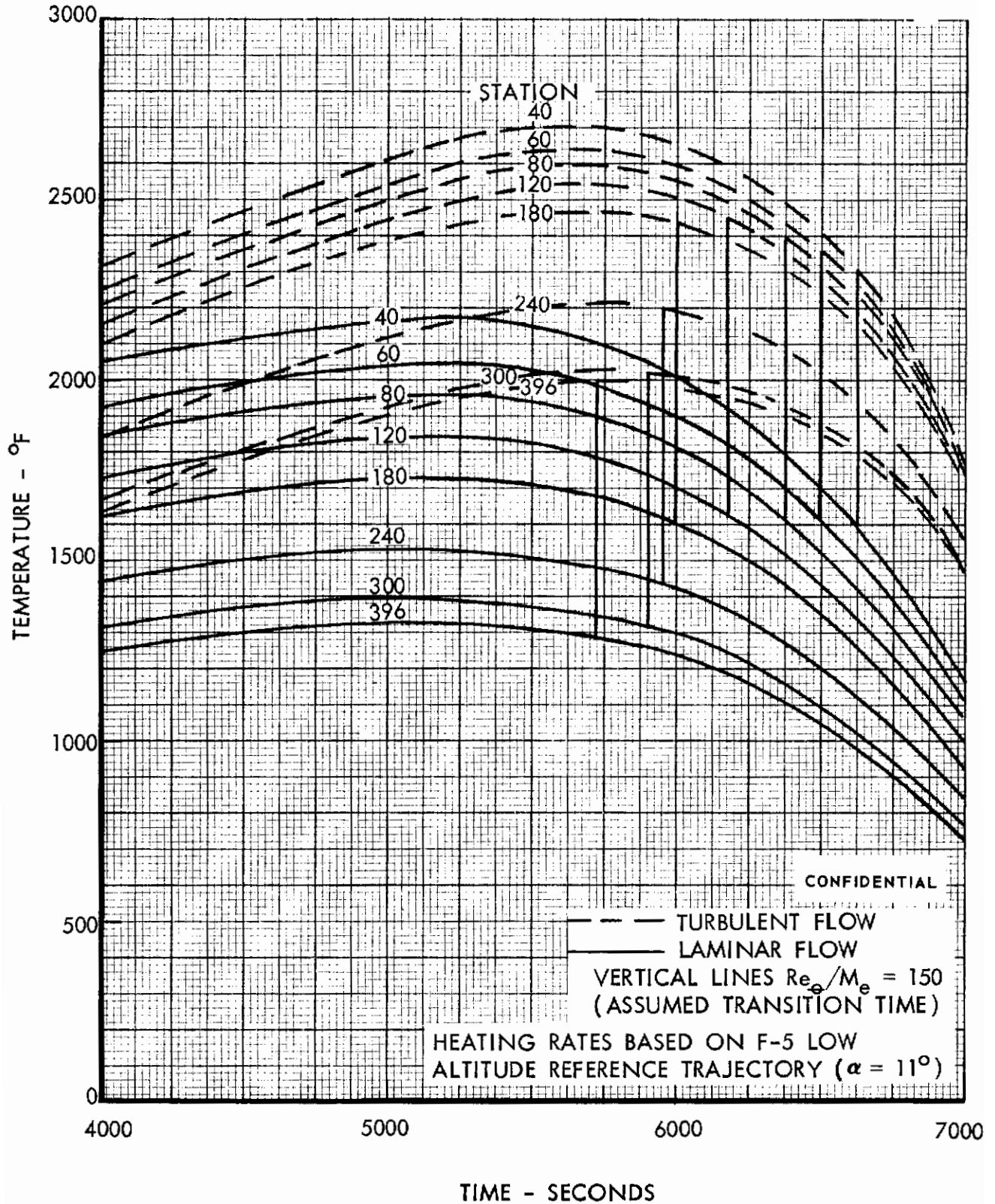
FIGURE 15   (U)   TEMPERATURE HISTORIES AT VARIOUS LOCATIONS ON
LOWER SURFACE CENTERLINE FOR LAMINAR AND TURBULENT
FLOW

85
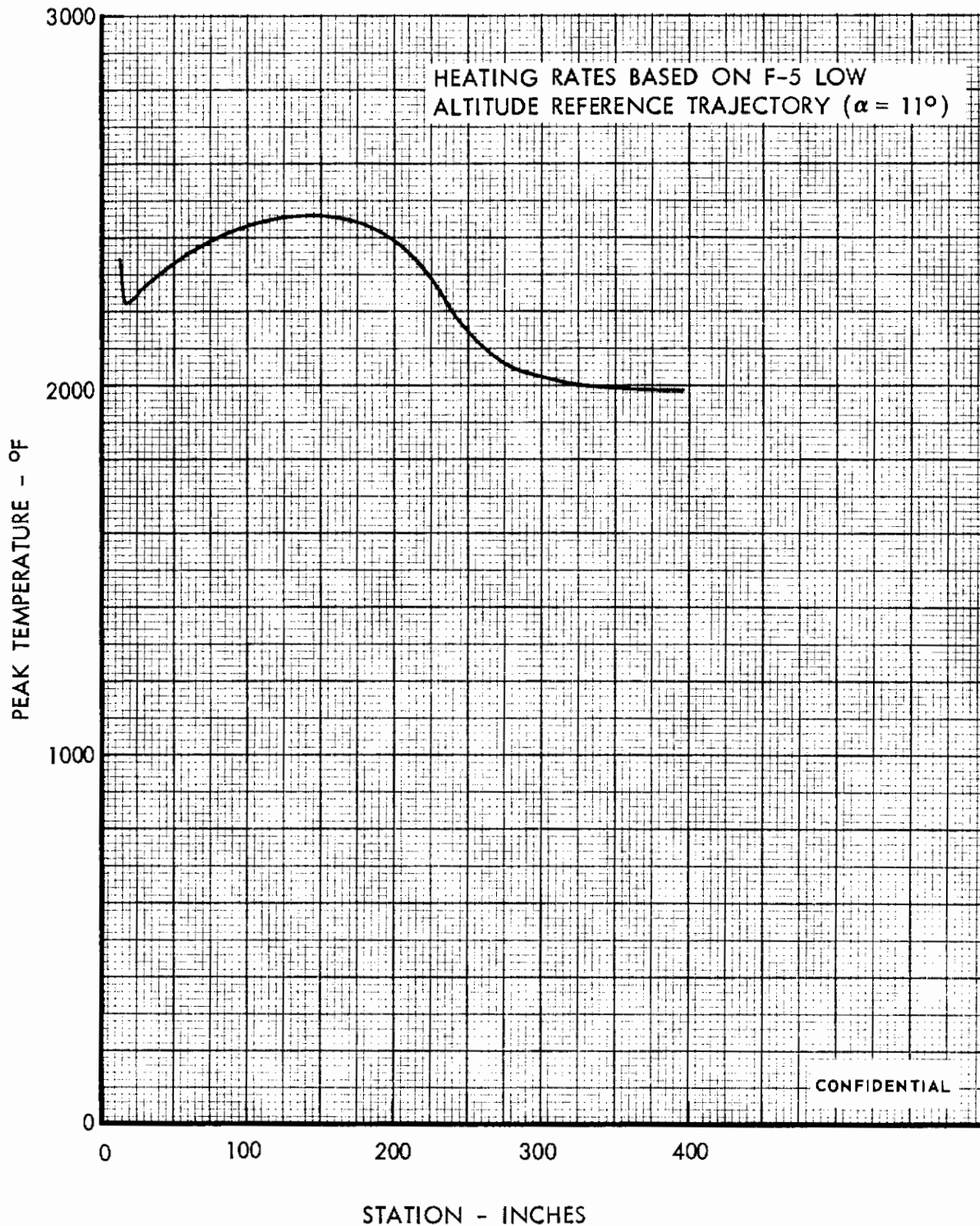
FIGURE 16 (U) PEAK LOWER SURFACE CENTERLINE TEMPERATURES

TEMPERATURES IN °F
LAMINAR FLOW ,
$\epsilon = 0.7$

$T_{STAG. LINE} = 2790$

$T_{STAG. LINE} = 2870$

LOWER
SURFACE

UPPER
SURFACE

$T_{NOSE} = 4330$

$T_{STAG. LINE} = 3200$

STATION O   100   200   300   CONFIDENTIAL   396

$74°(REF)$
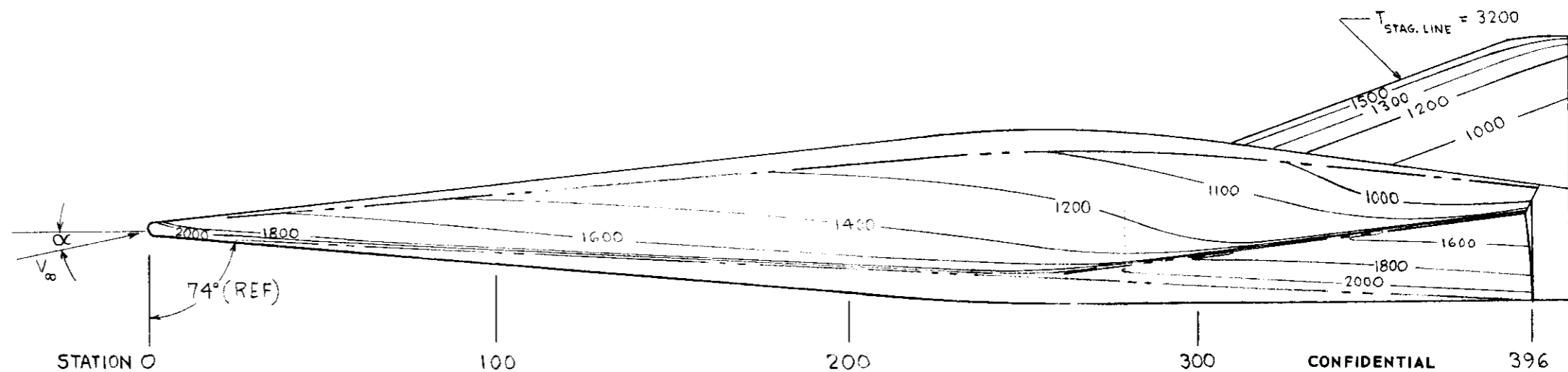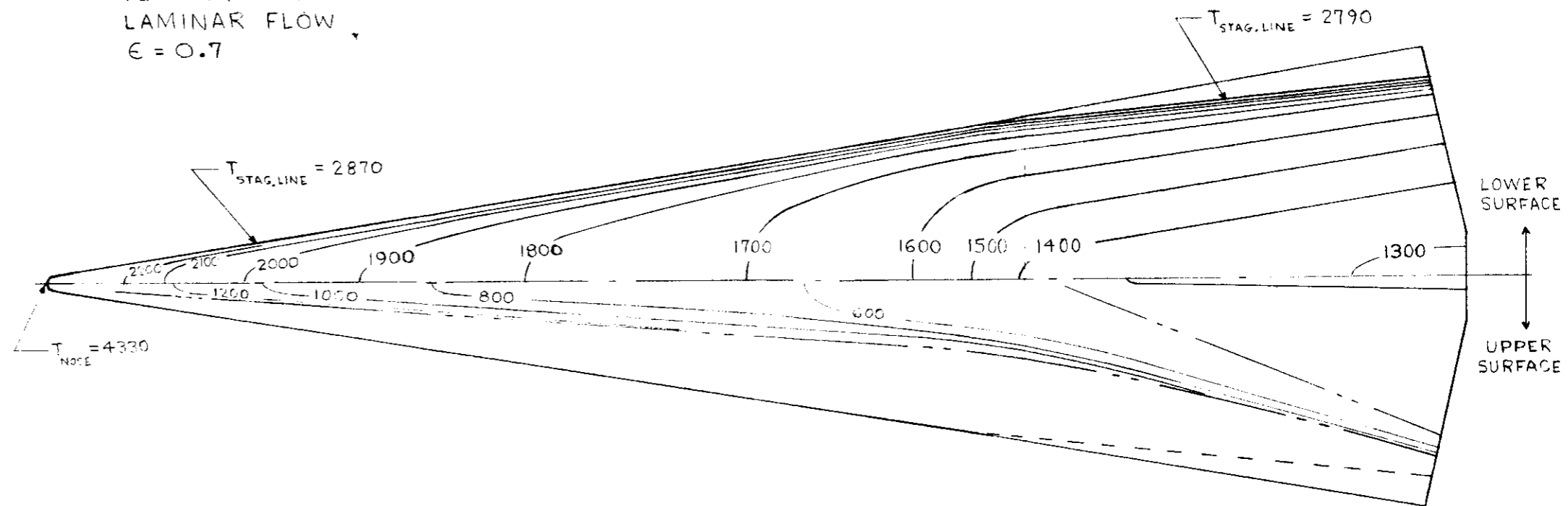
SURFACE TEMPERATURE DISTRIBUTION AT DESIGN CONDITION $\left(V_\infty = 20000 \text{ FPS}, H = 200000 \text{ FT}, \alpha = 11° \right)$

FIGURE 17   (U) SURFACE TEMPERATURE DISTRIBUTION AT DESIGN CONDITION (V_∞ = 20,000 fps, H = 200,000 ft, α = 11°)
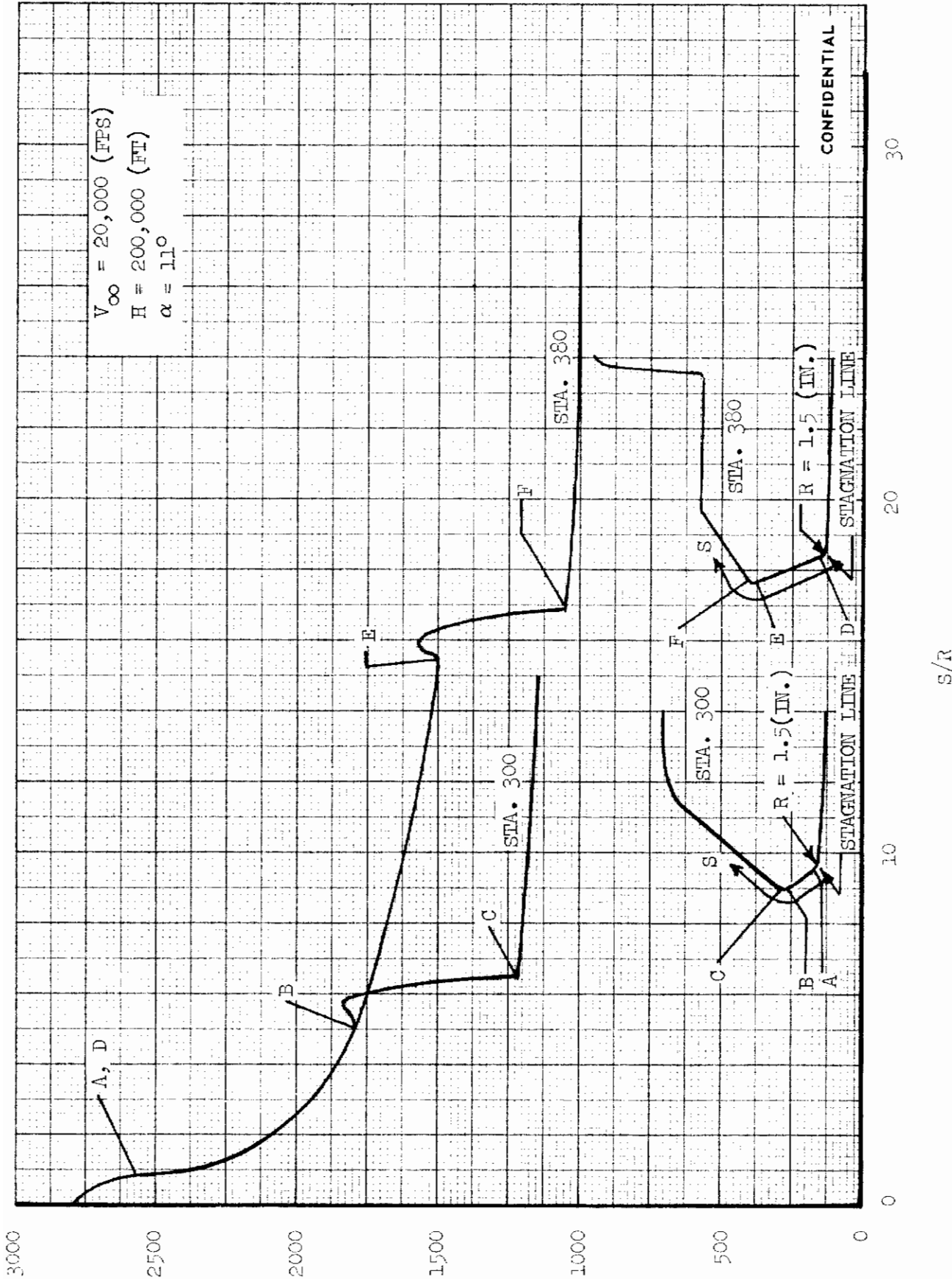
FIGURE 18 (U) TEMPERATURE DISTRIBUTIONS ON AFT LOWER COMPRESSION SURFACE

$V_\infty = 20,000$ (FPS)
$H = 200,000$ (FT)
$\alpha = 11°$

TEMPERATURES IN °F
$\alpha = 11°$, $\beta = 0$
$\epsilon = 0.7$

$T_{STAG\ LINE} = 2750$ $(R = 1.5")$

$T_{STAG\ LINE} = 2940$ $(R = 1.5")$

LOWER SURFACE

UPPER SURFACE

2500
2450
2400
2300
1200 1400
1000
900
2450 2400 2300 2200 2100 2000

$T_{NOSE} = 4420$

$T_{STAG\ LINE} = 3270$ $(R = 1")$

1700 1500 1300 1200

1400
1900 1800 1700 1600 1500
2200 2000 1900

STATION 0
100
200
300
396

CONFIDENTIAL
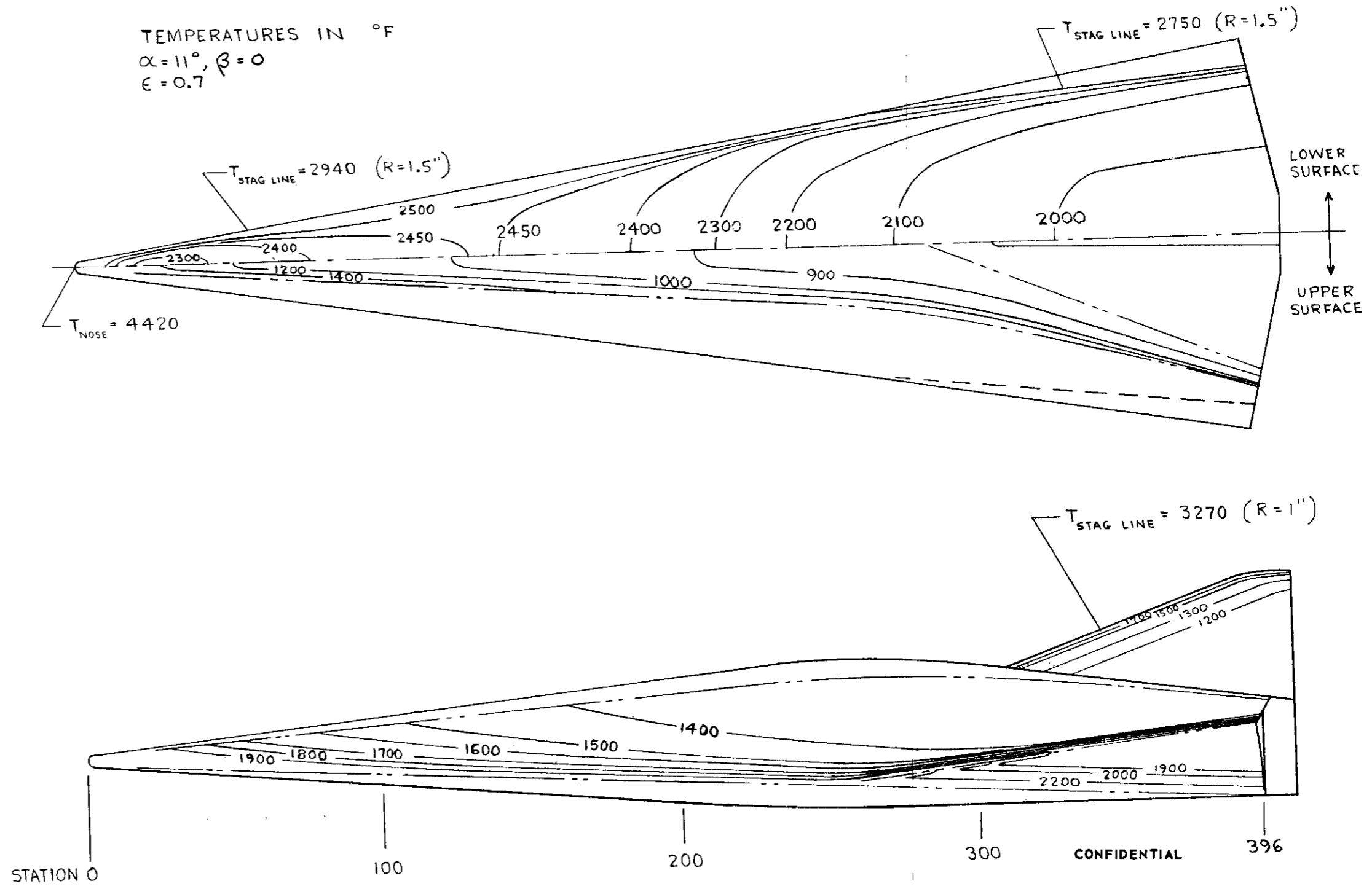
FIGURE 19   (U) FDL-5 PEAK SURFACE TEMPERATURES

91   (REVERSE SIDE IS BLANK)
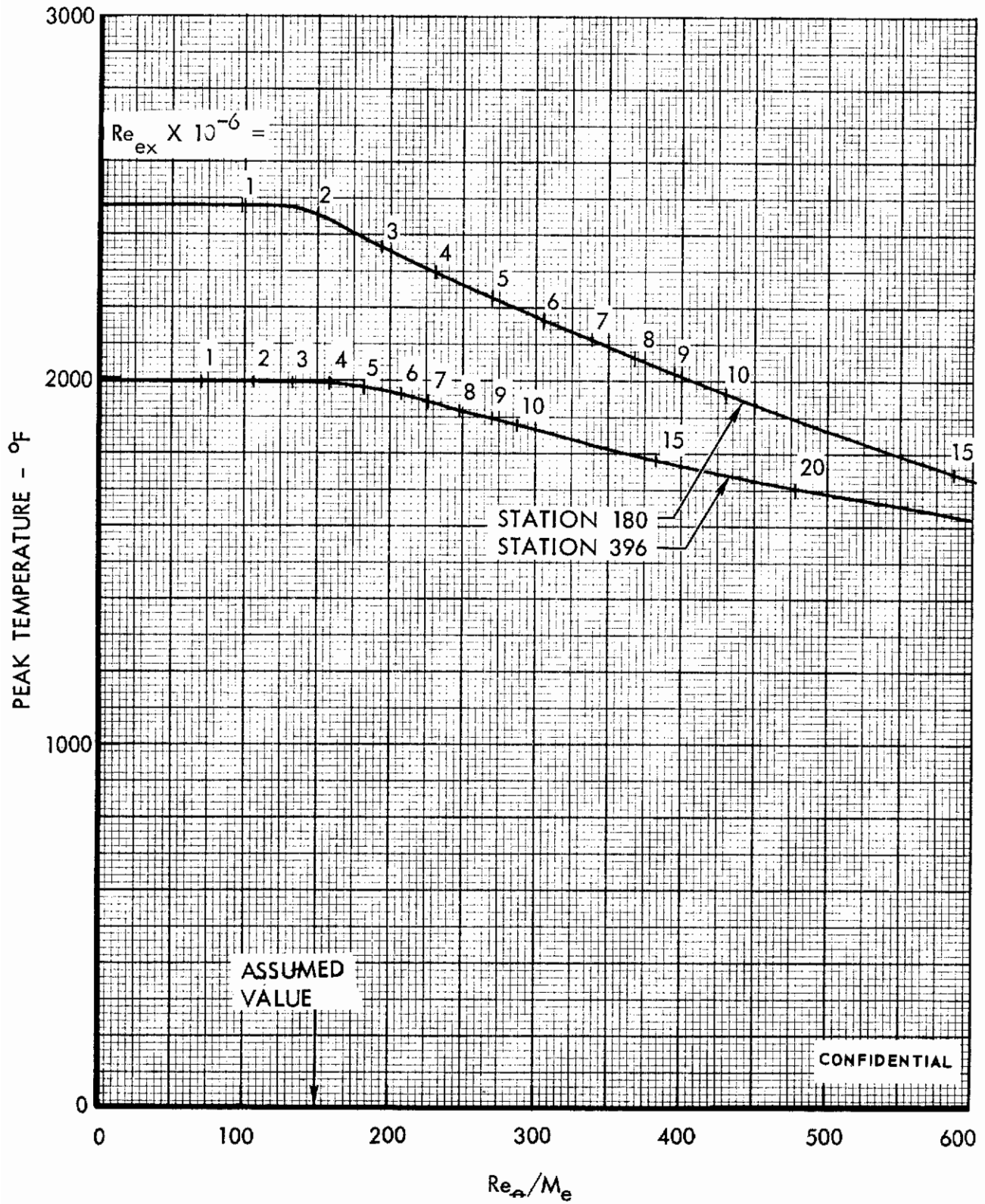
FIGURE 20 (U) EFFECT OF TRANSITION CRITERION ON PEAK LOWER
SURFACE CENTERLINE TEMPERATURES

93
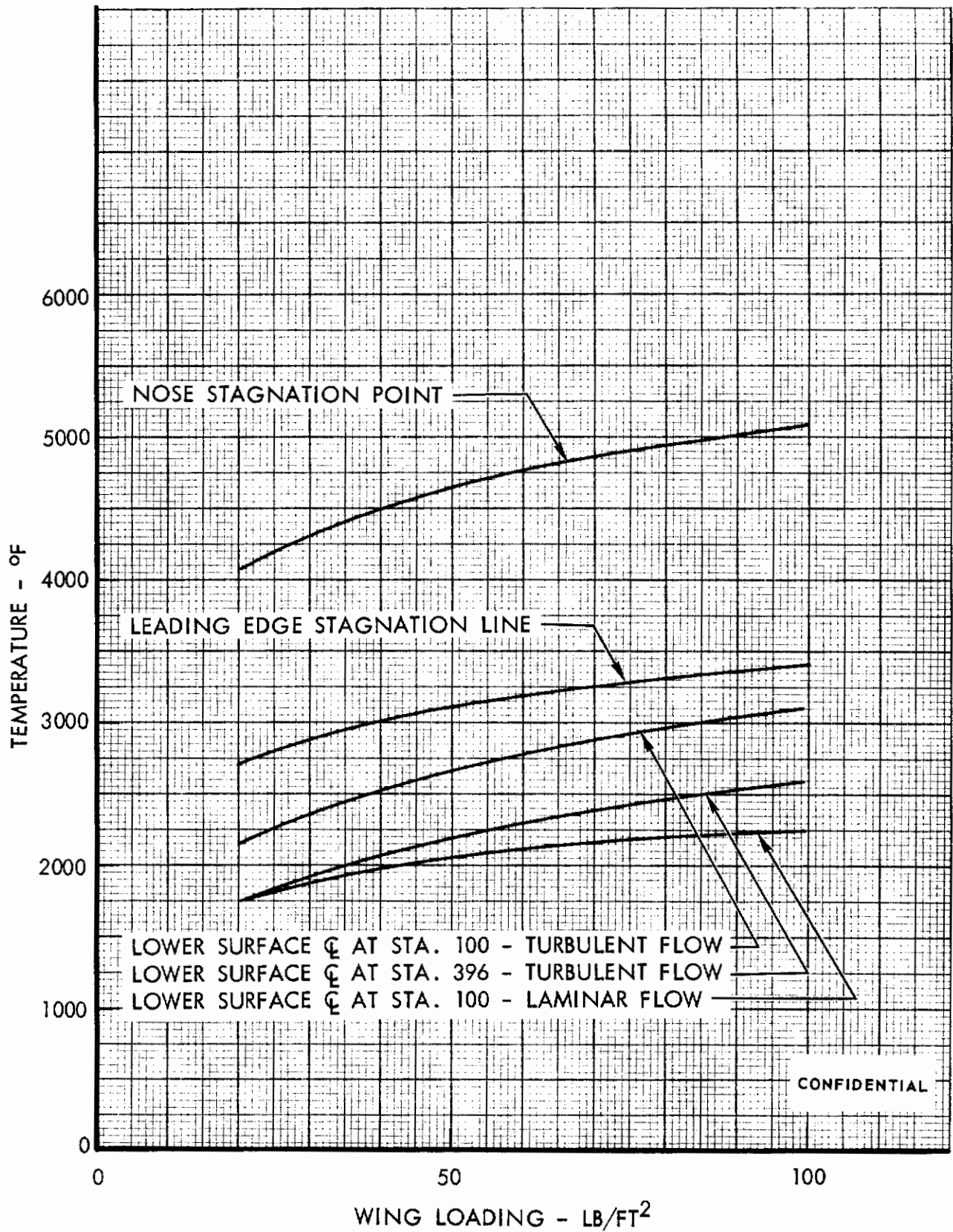
FIGURE 21 (U) EFFECT OF WING LOADING ON PEAK TEMPERATURES
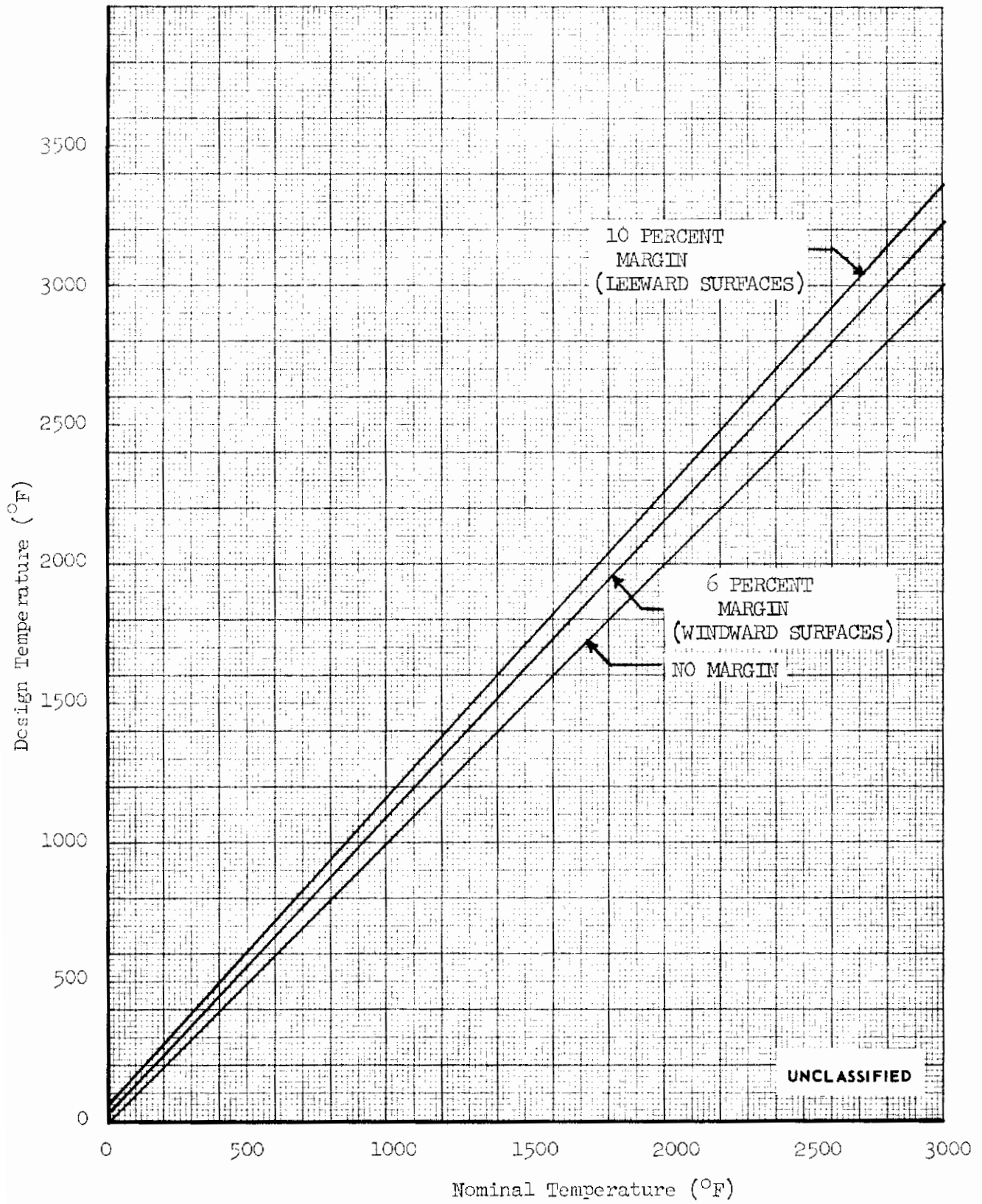
FIGURE 22 (U) EFFECT OF DESIGN MARGINS ON TEMPERATURE

95
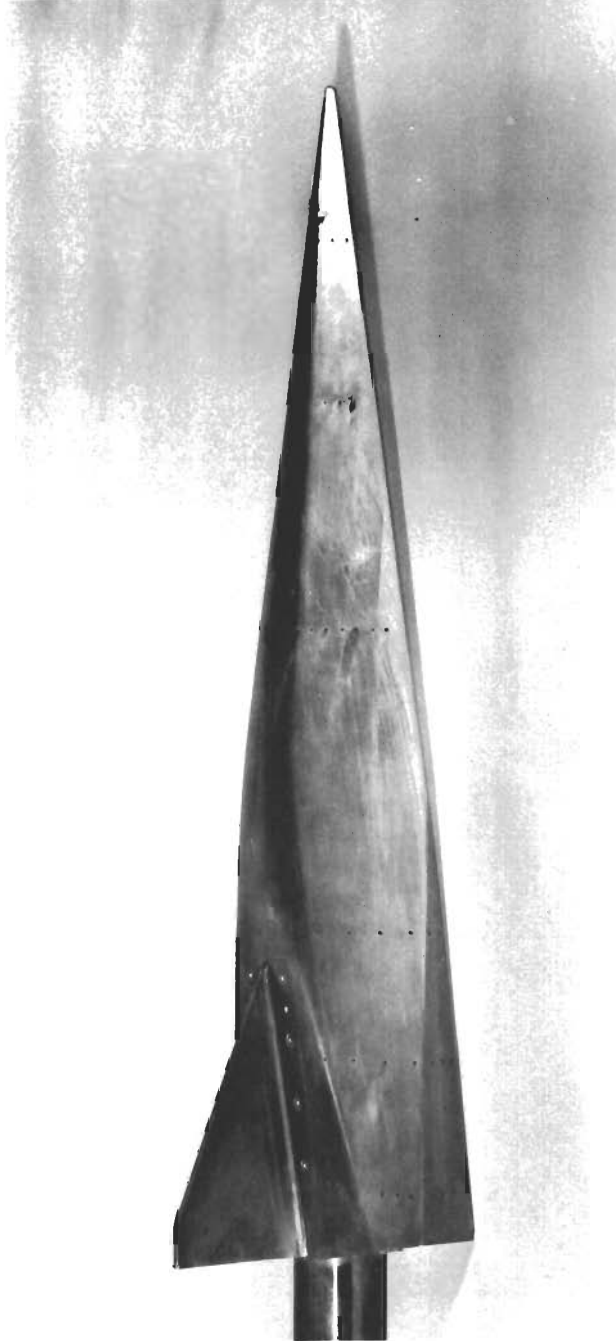
FIGURE 23 (U) 20-INCH STEEL PRESSURE MODEL FOR TUNNEL C

FIGURE 24 (U) TUNNEL C PRESSURE MODEL
INSTRUMENTATION LOCATIONS
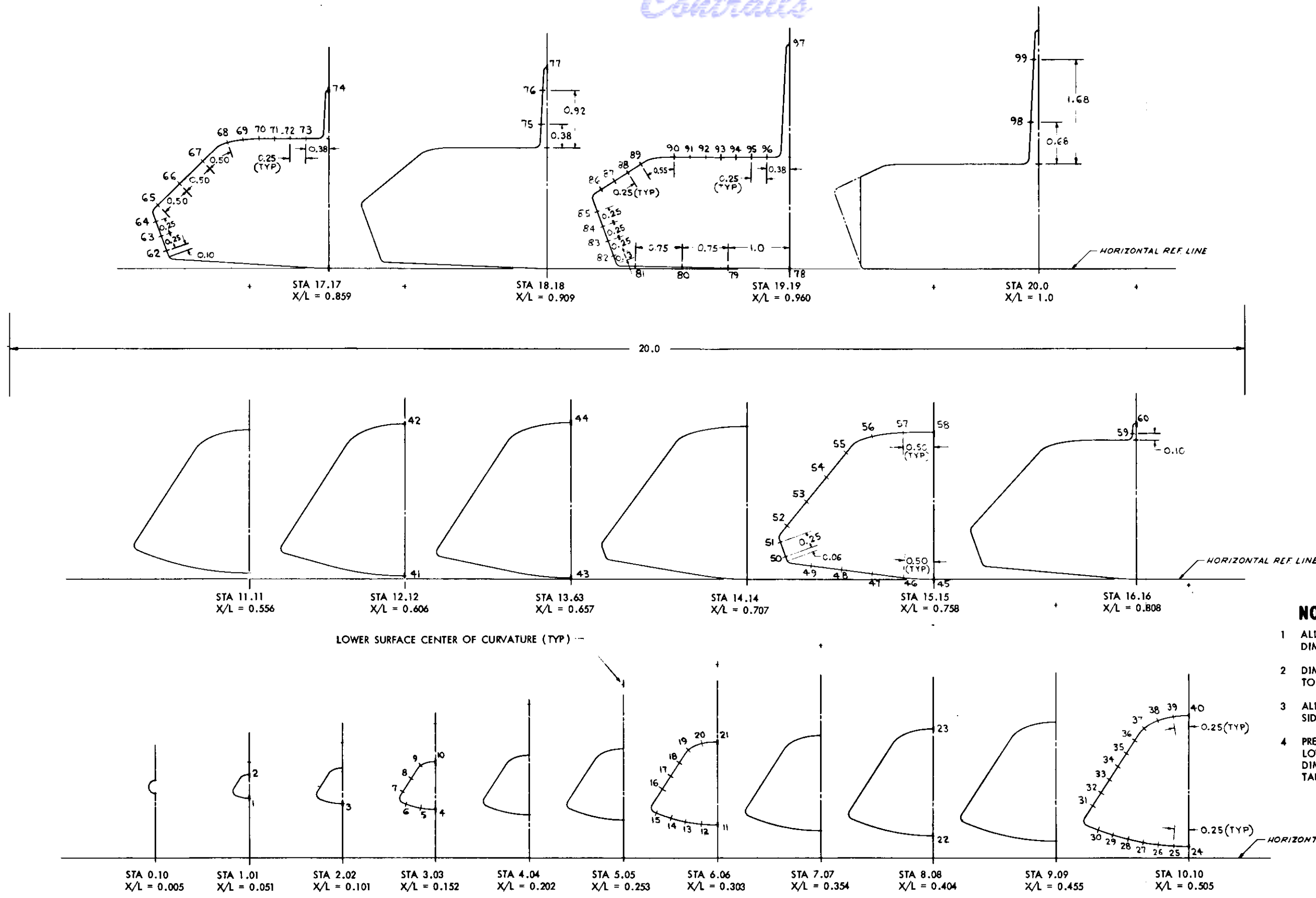
NOTE

1 ALL PRESSURE TAP LOCATIONS ARE DIMENSIONED ALONG SURFACE CONTOURS

2 DIMENSIONS AT STA 10.1 ALSO APPLY TO STA 3.03 AND 6.06

3 ALL PRESSURE TAPS ARE ON RIGHT SIDE OF MODEL

4 PRESSURE TAP LOCATIONS ON AFT LOWER COMPRESSION SURFACE ARE DIMENSIONED FROM LEADING EDGE TANGENCY POINT.
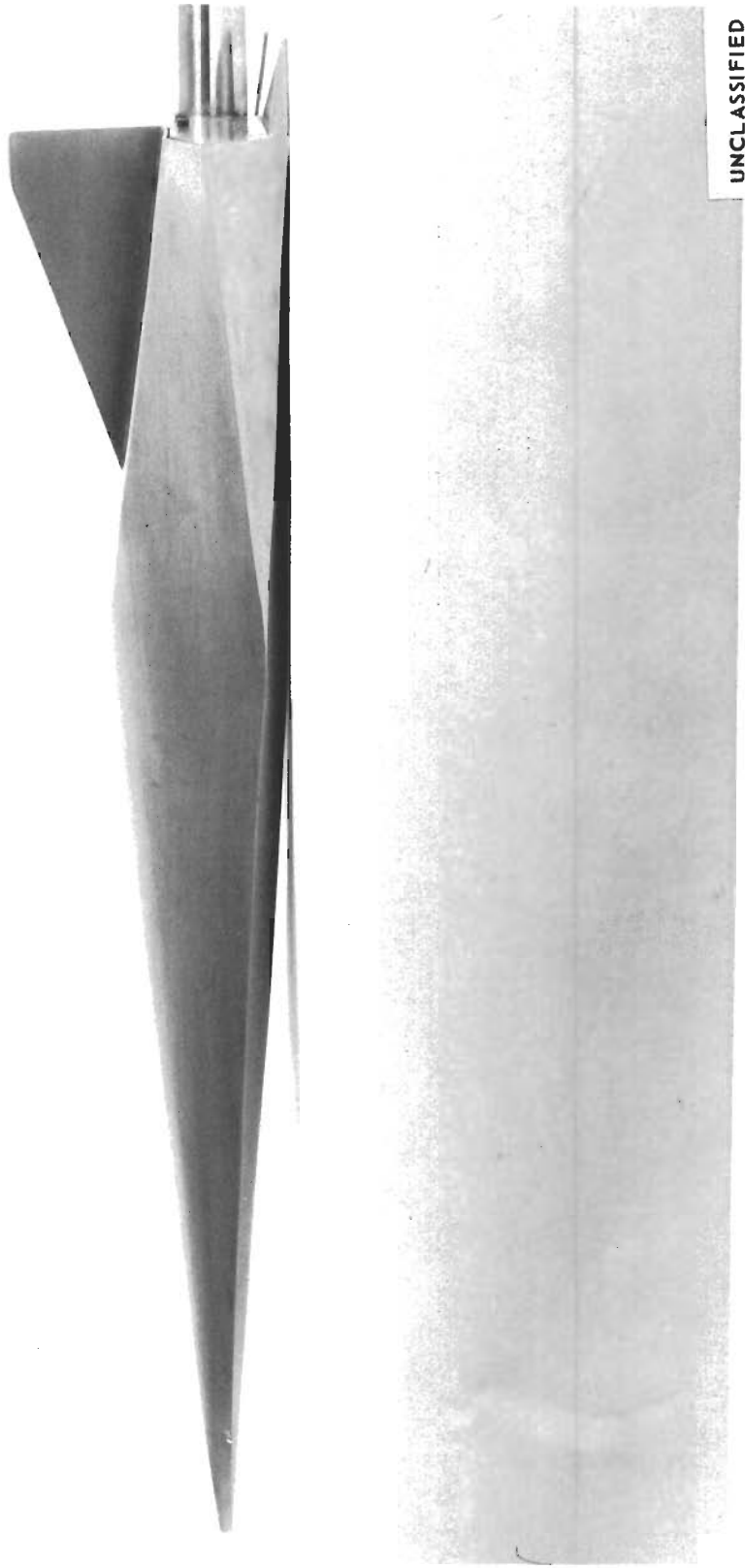
FIGURE 25 (U) 20-INCH THIN SKIN HEAT TRANSFER MODEL FOR TUNNEL C

(REVERSE SIDE IS BLANK)
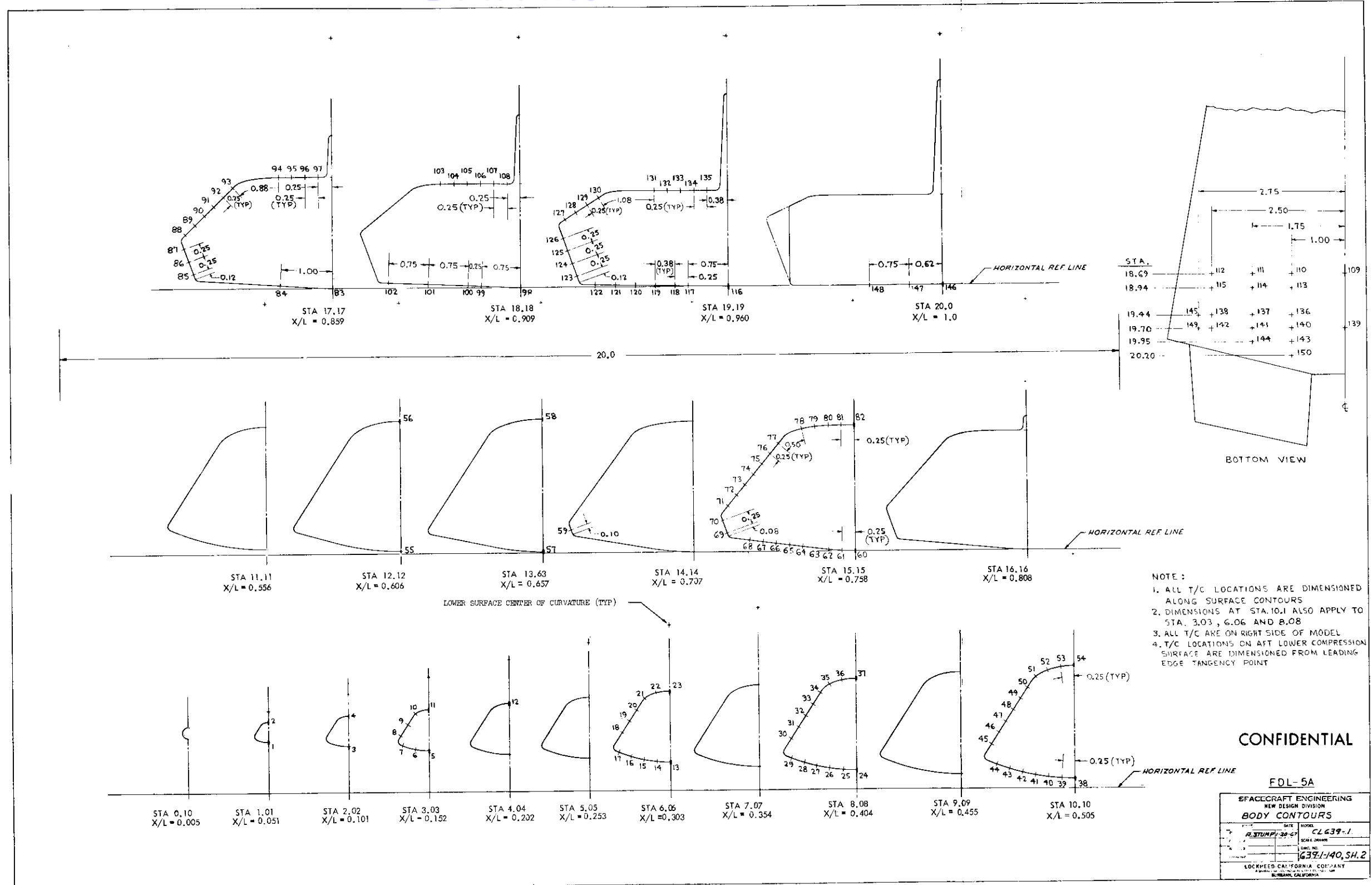
FIGURE 26 (U) TUNNEL C HEAT TRANSFER MODEL INSTRUMENTATION LOCATIONS

101 (REVERSE SIDE IS BLANK)
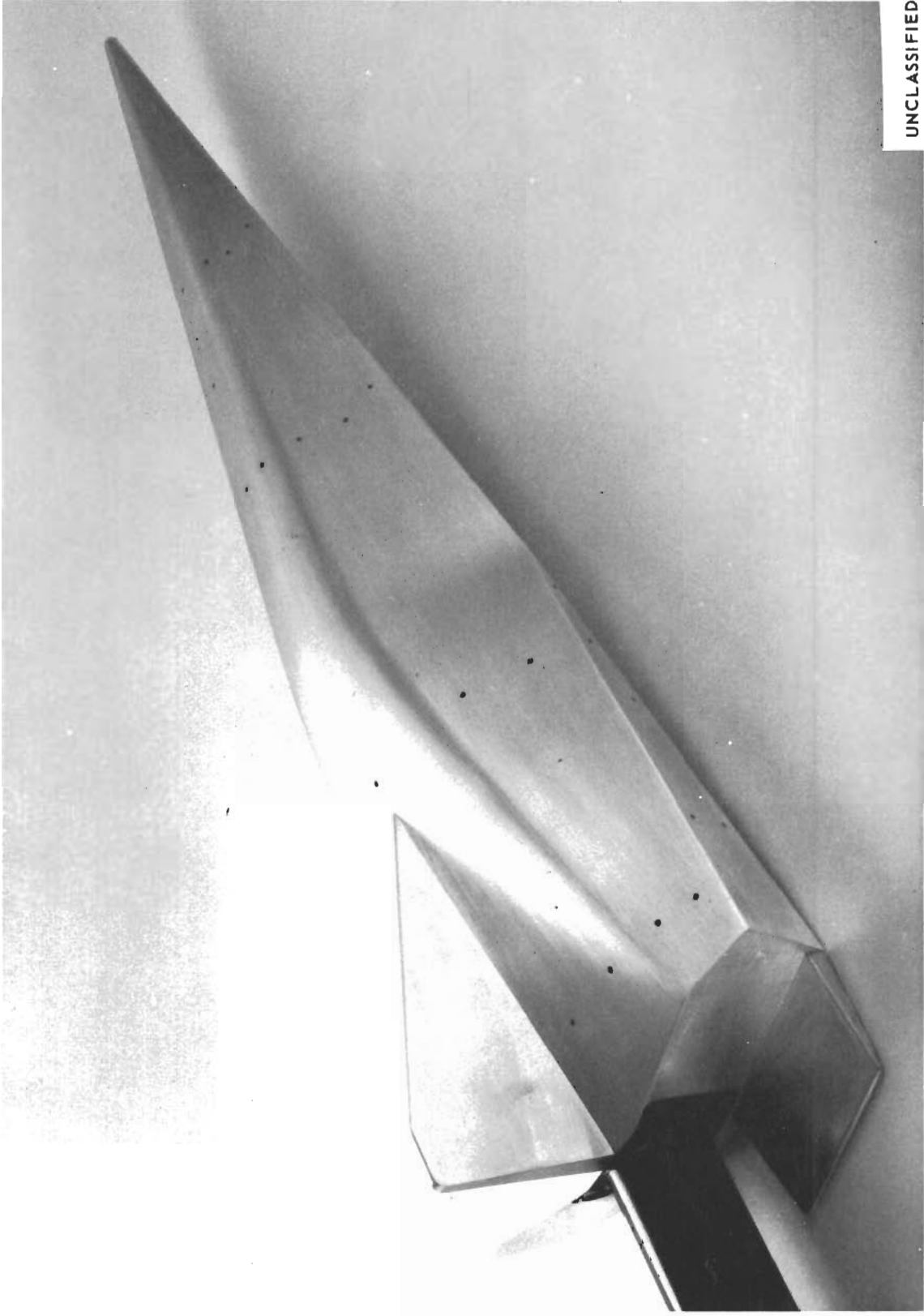
FIGURE 27 (U) 20-INCH ALUMINUM PRESSURE/HEAT TRANSFER MODEL FOR TUNNEL F (PRESSURE PLUGS INSTALLED)

UNCLASSIFIED

(REVERSE SIDE IS BLANK)
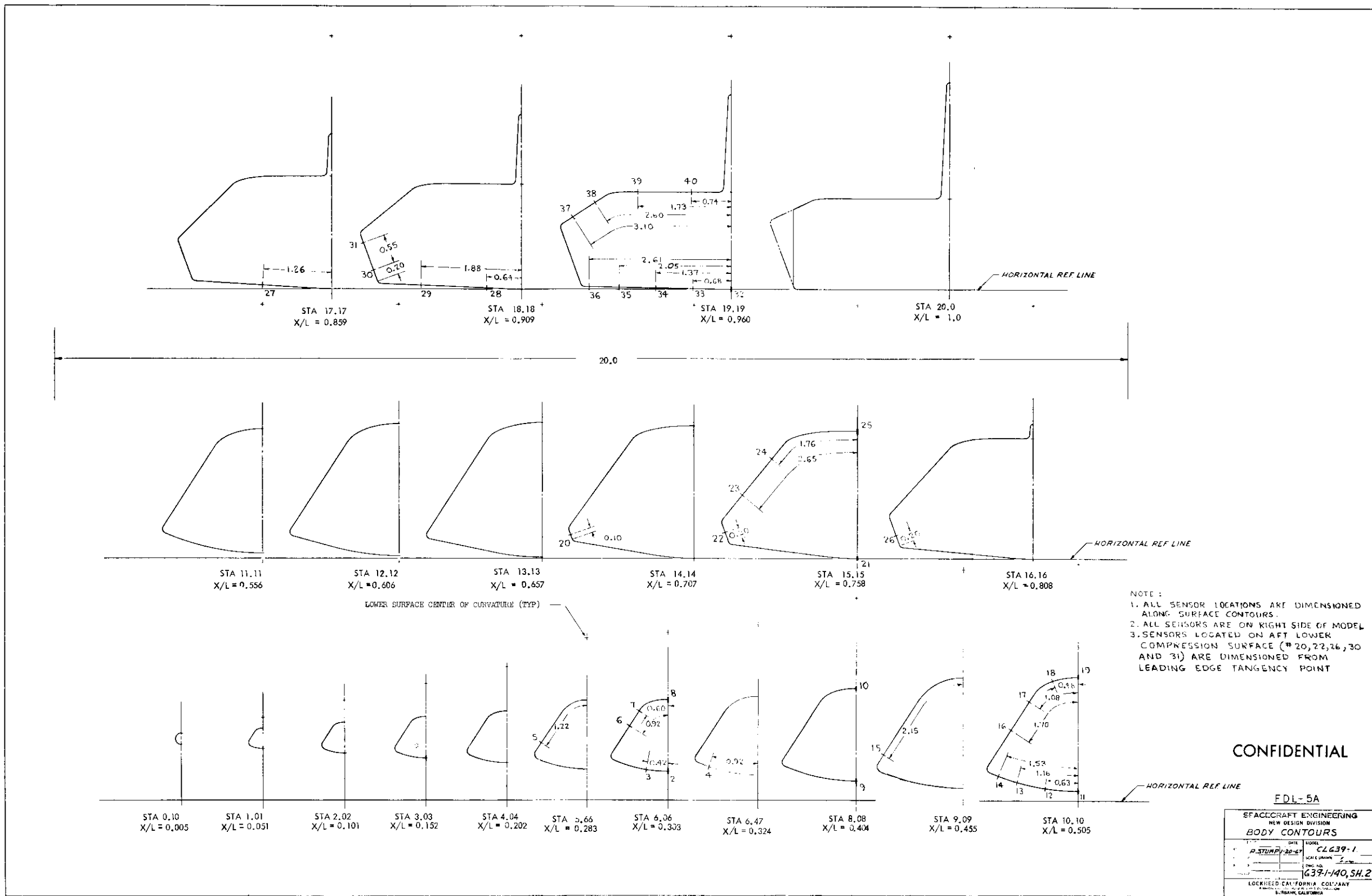
FIGURE 28 (U) TUNNEL F PRESSURE/HEAT TRANSFER
MODEL INSTRUMENTATION LOCATIONS

105 (REVERSE SIDE IS BLANK)
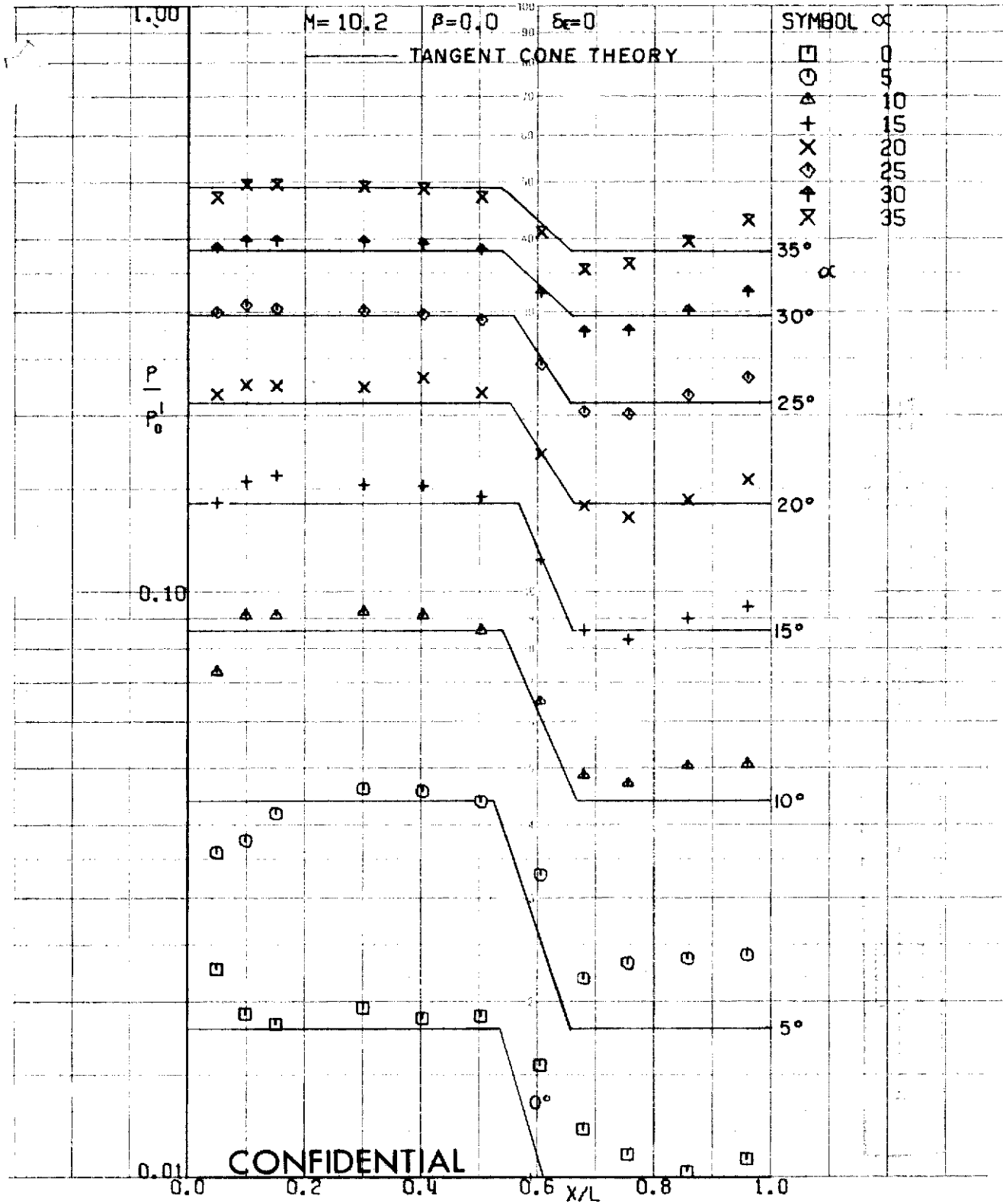
FIGURE 29 (U) TUNNEL C LOWER SURFACE CENTERLINE PRESSURES, β=0
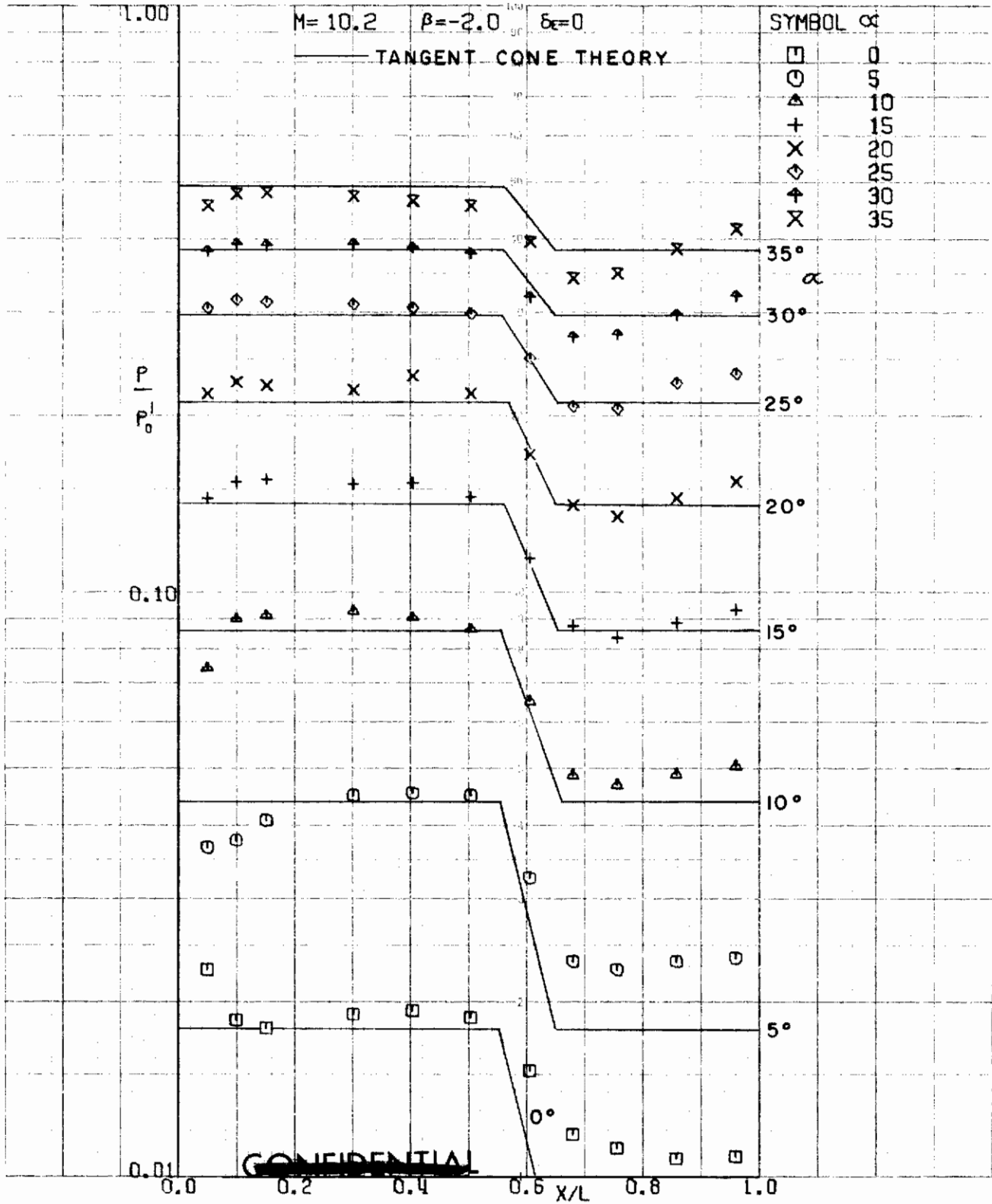
FIGURE 30   (U) TUNNEL C LOWER SURFACE CENTERLINE PRESSURES, β= -2
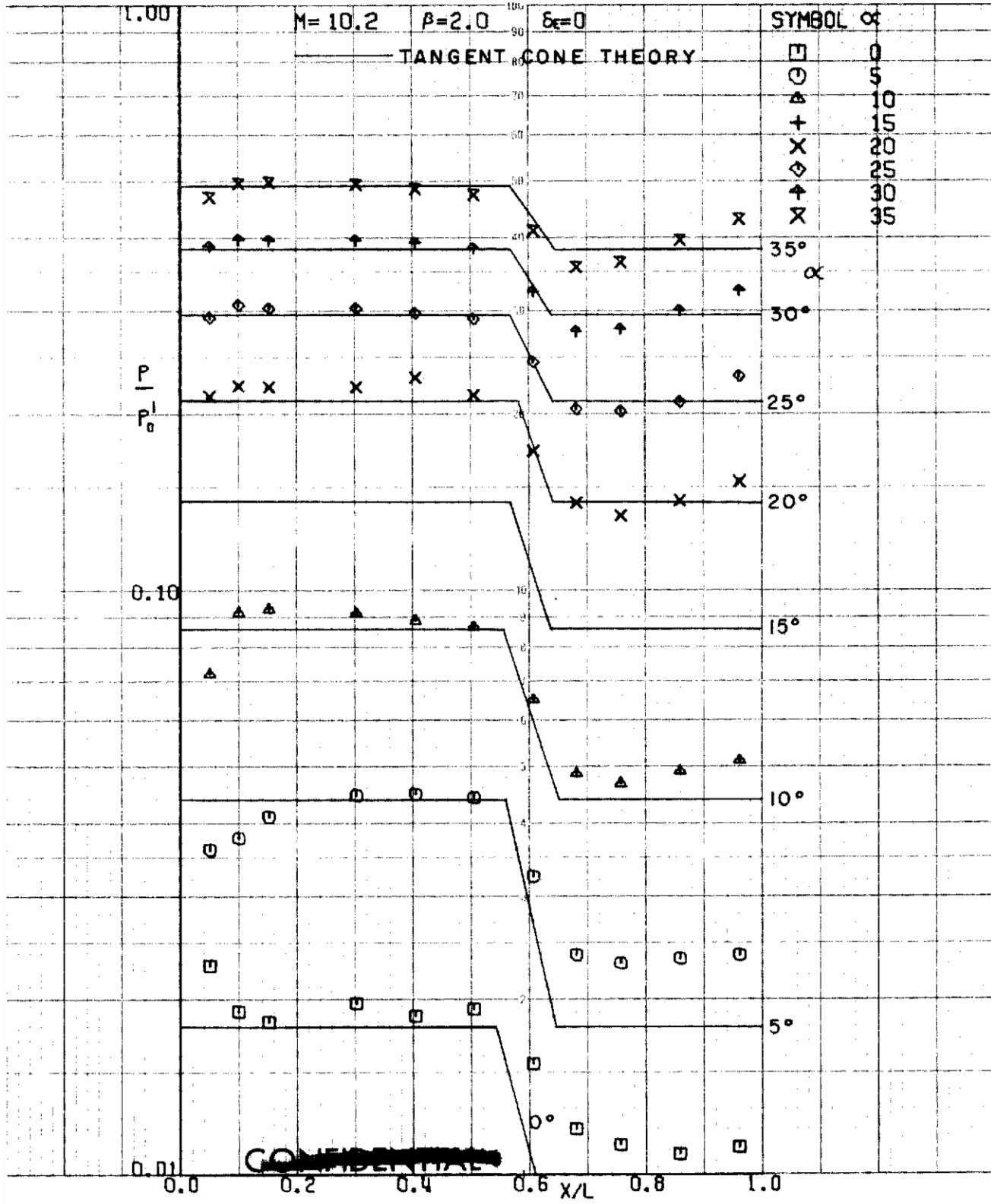
FIGURE 31 (U) TUNNEL C LOWER SURFACE CENTERLINE PRESSURES, β=2
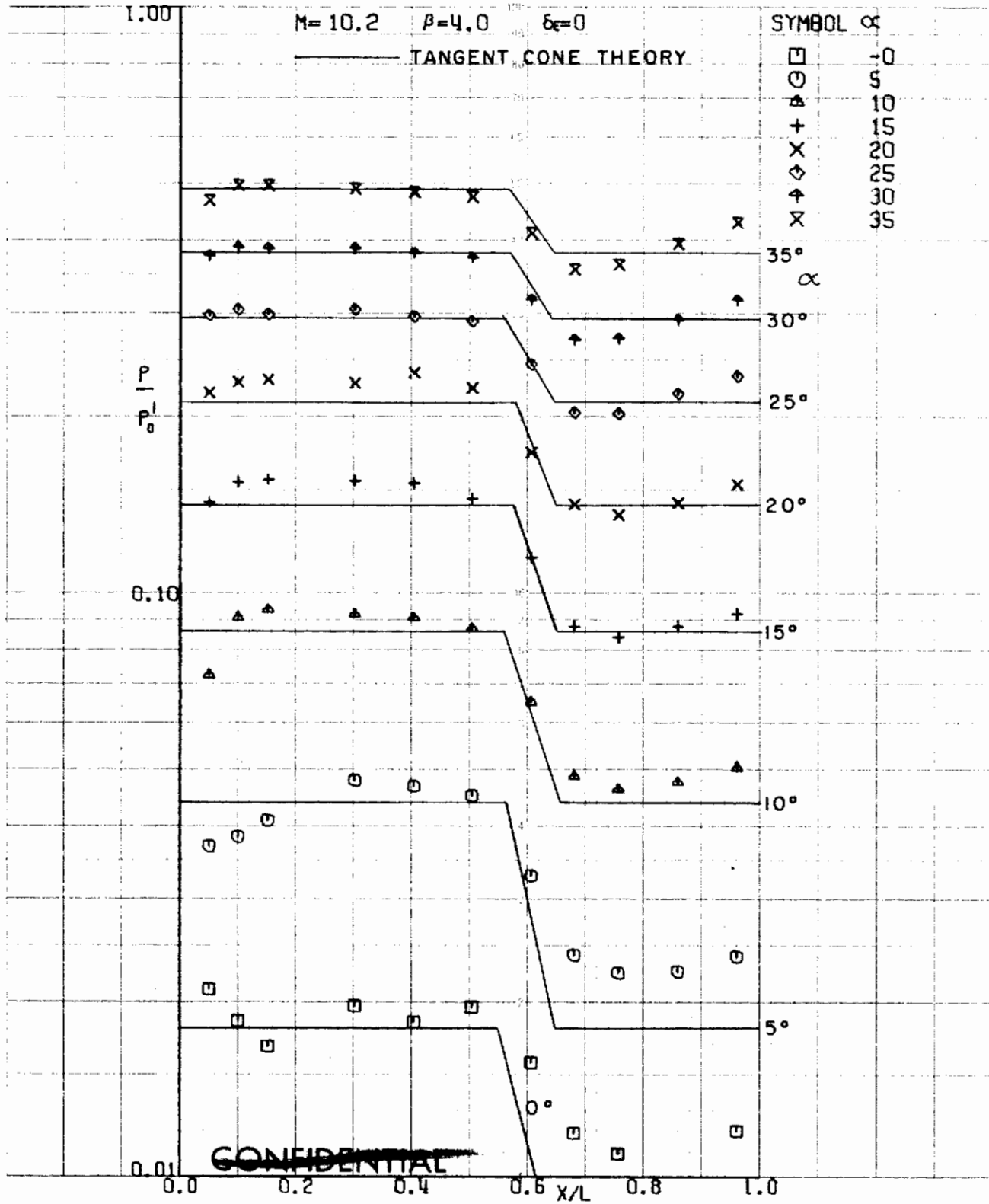
FIGURE 32 (U) TUNNEL C LOWER SURFACE CENTERLINE PRESSURES, β=4
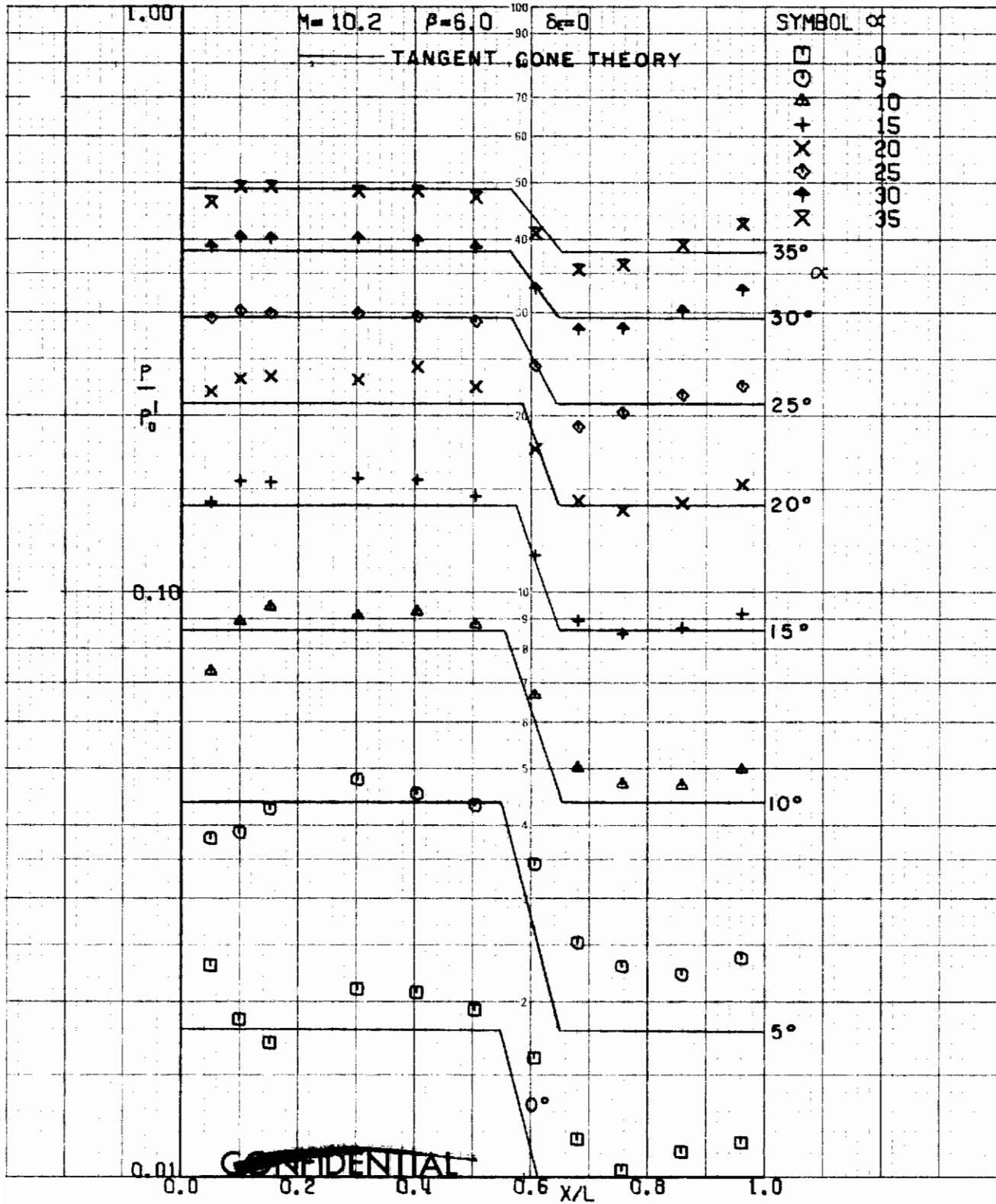
FIGURE 33   (U) TUNNEL C LOWER SURFACE CENTERLINE PRESSURES, β=6

111
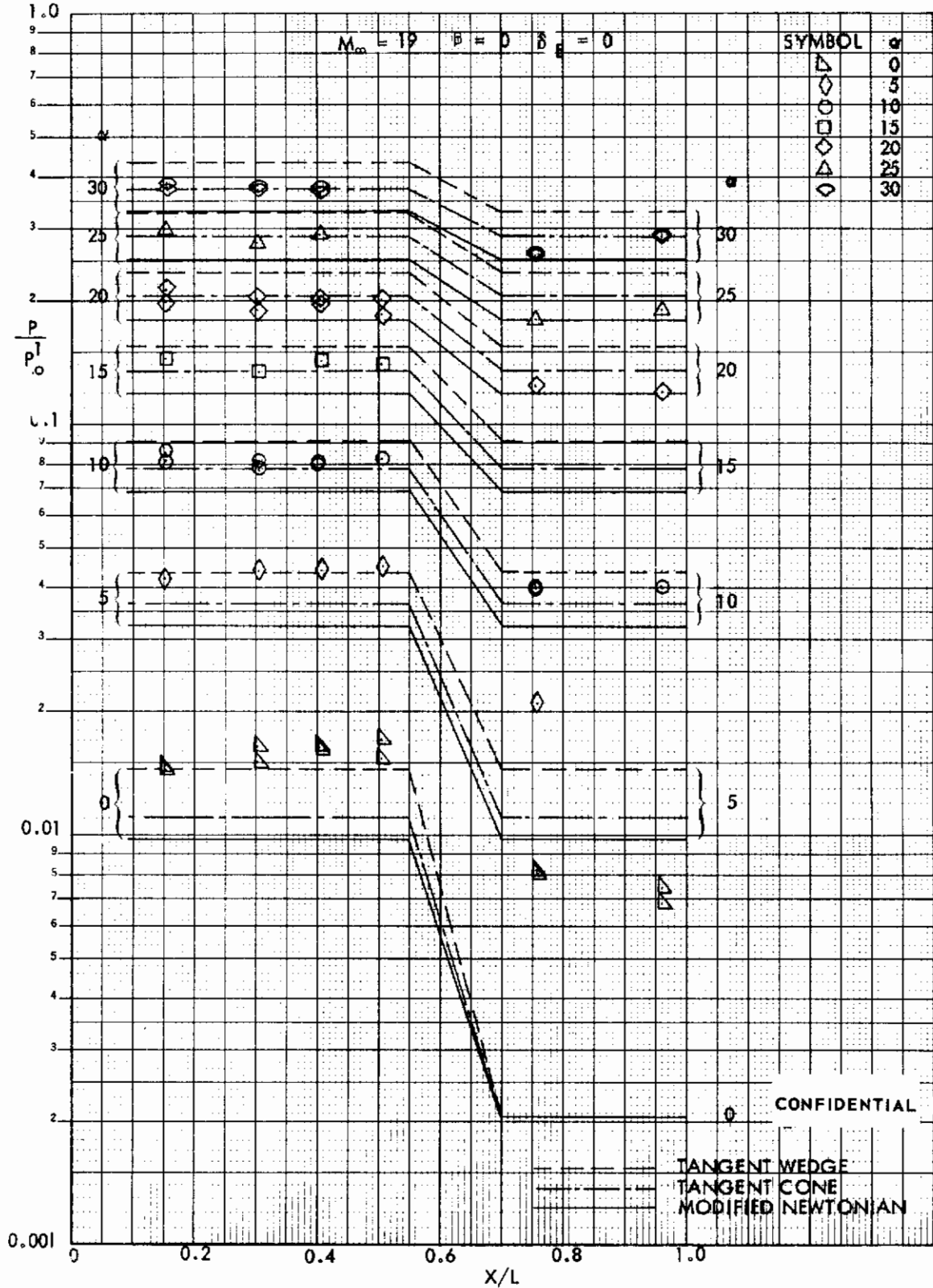
FIGURE 34 (U) TUNNEL F LOWER SURFACE CENTERLINE PRESSURES, $\beta = 0$
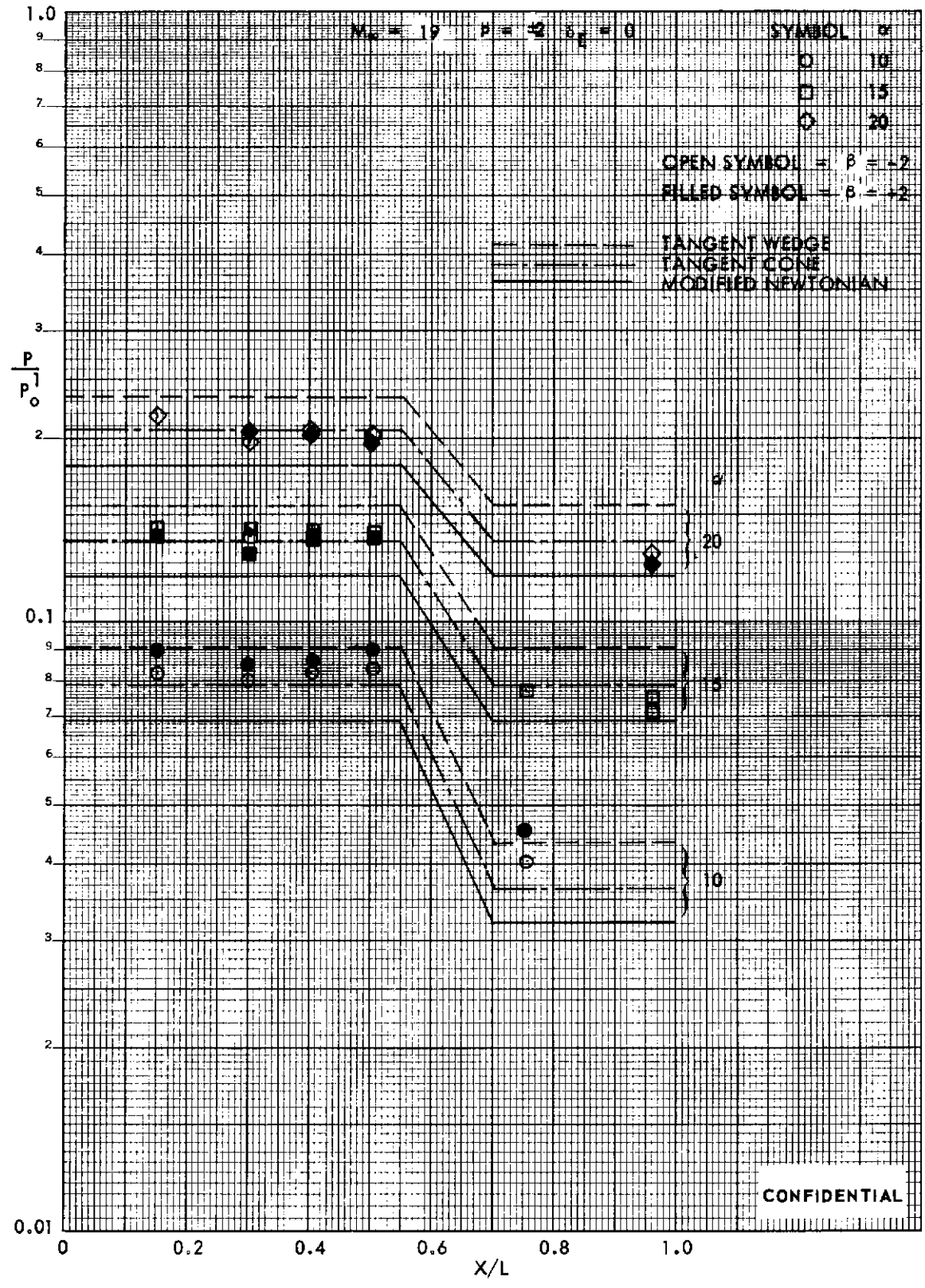
FIGURE 35 (U) TUNNEL F LOWER SURFACE CENTERLINE PRESSURES, β=±2

113
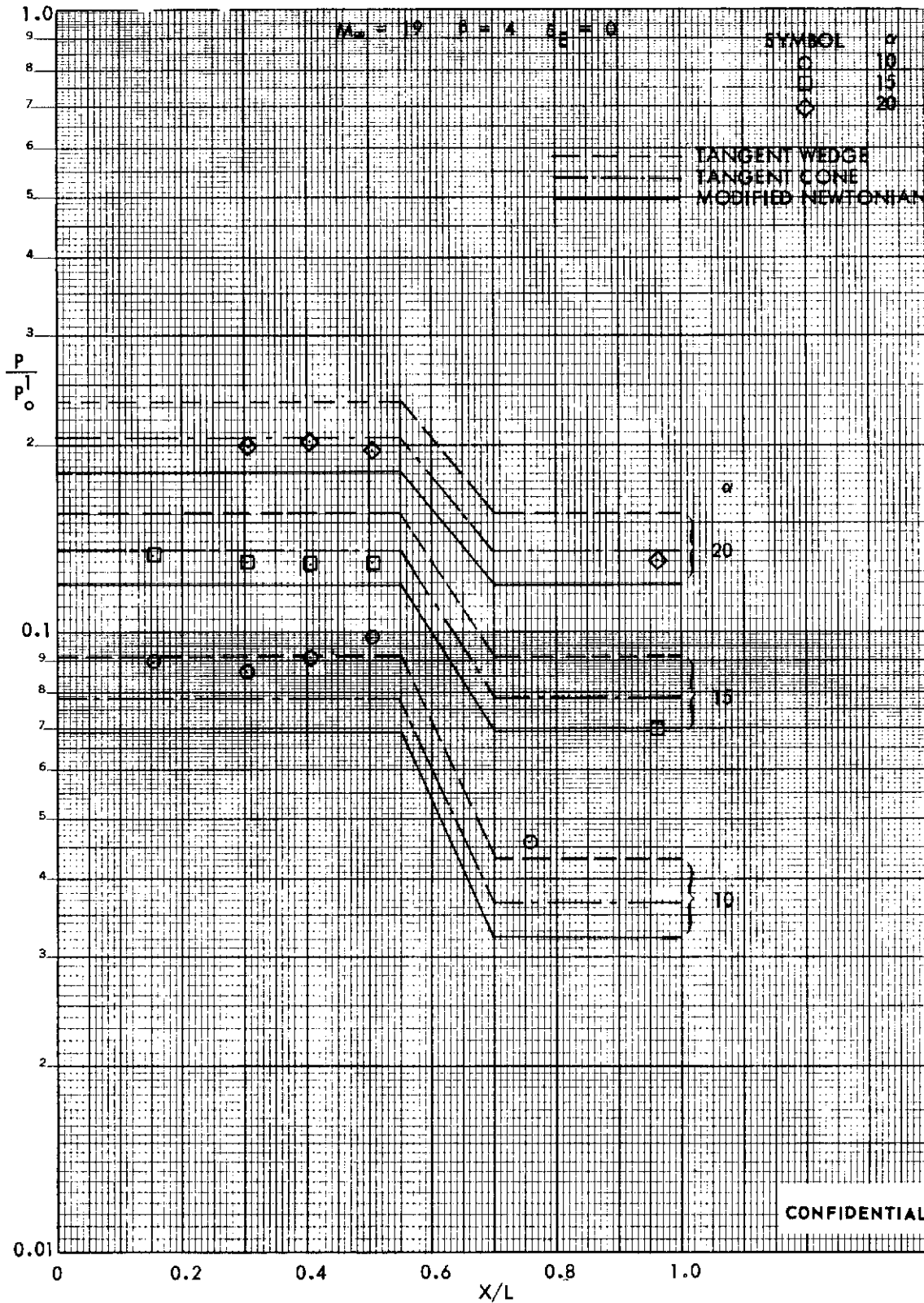
FIGURE 36   (U) TUNNEL F LOWER SURFACE CENTERLINE PRESSURES, $\beta = 4$

114
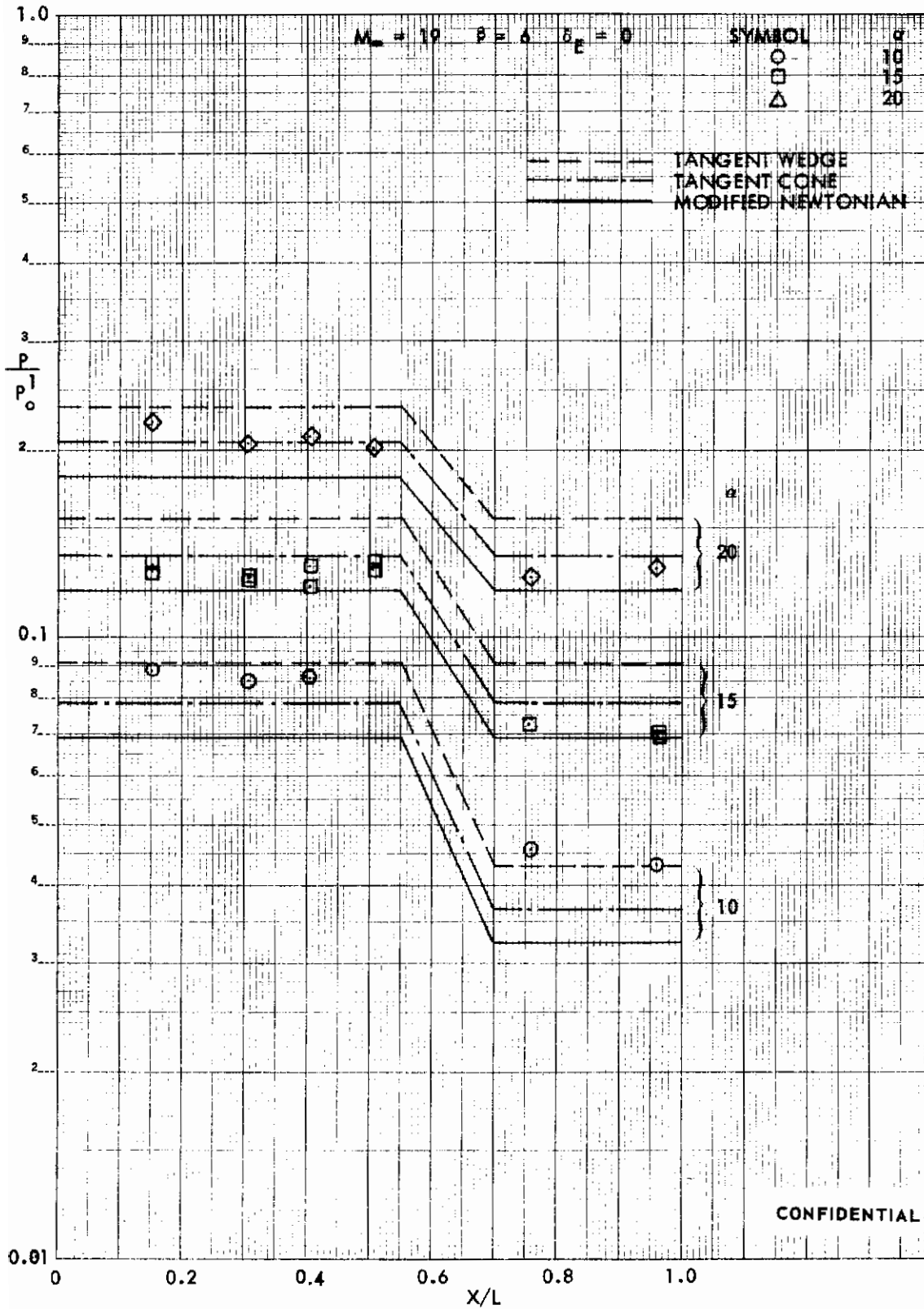
FIGURE 37 (U) TUNNEL F LOWER SURFACE CENTERLINE PRESSURES, $\beta=6$
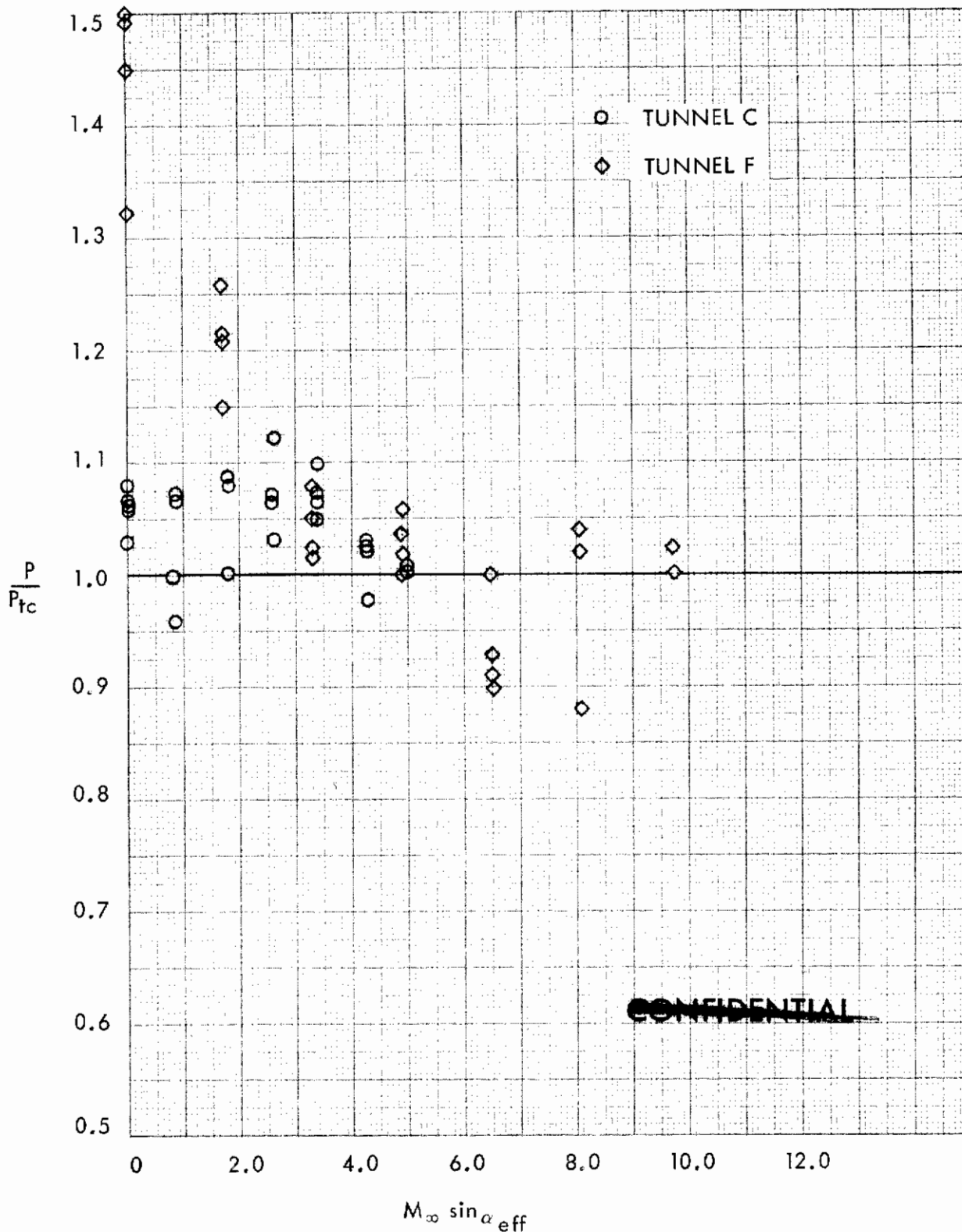
FIGURE 38 (U) COMPARISON OF FORWARD RAMP CENTERLINE PRESSURES
FROM TUNNELS C AND F

116
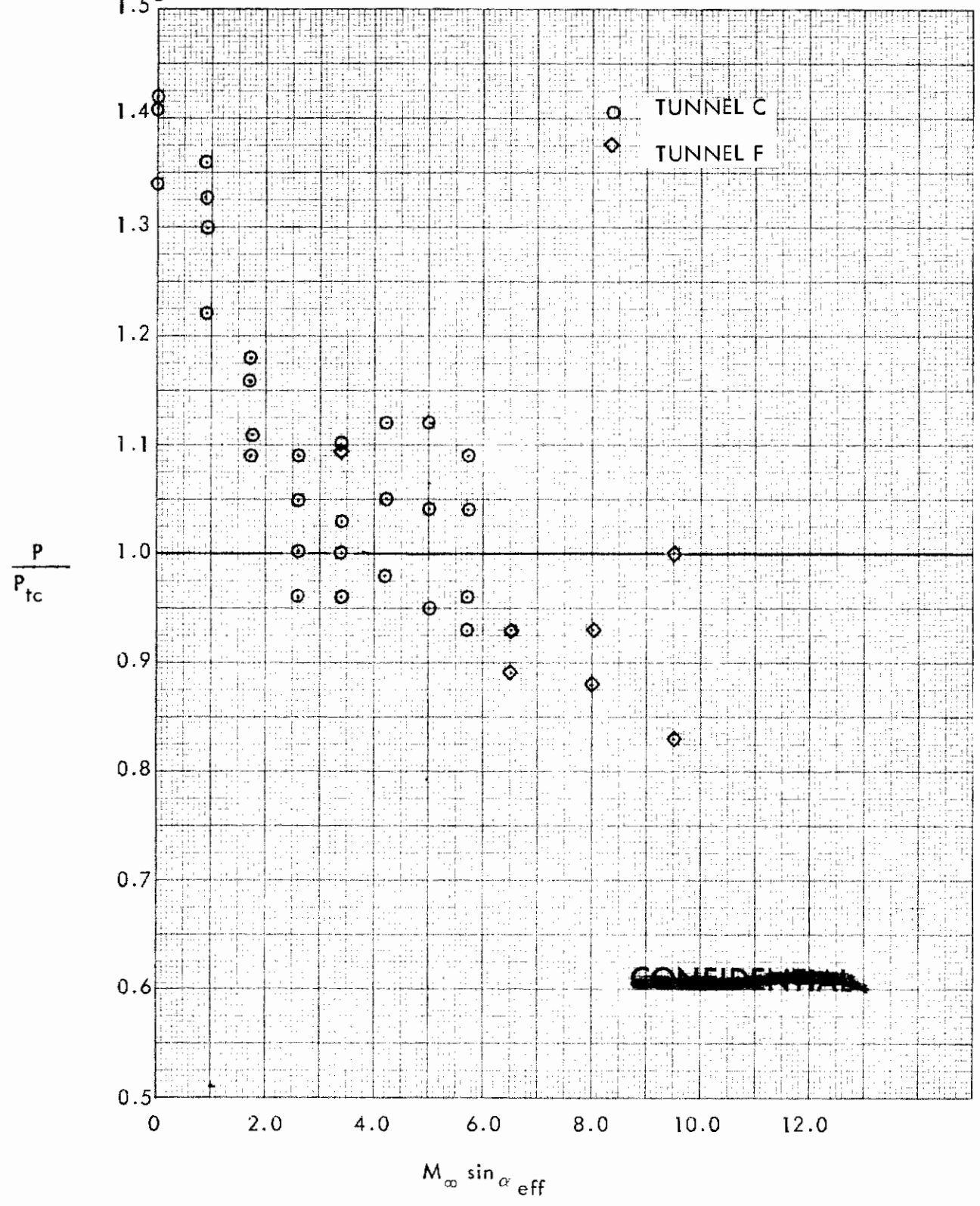
FIGURE 39 (U) COMPARISON OF AFT LOWER SURFACE CENTERLINE PRESSURES FROM TUNNELS C AND F

117
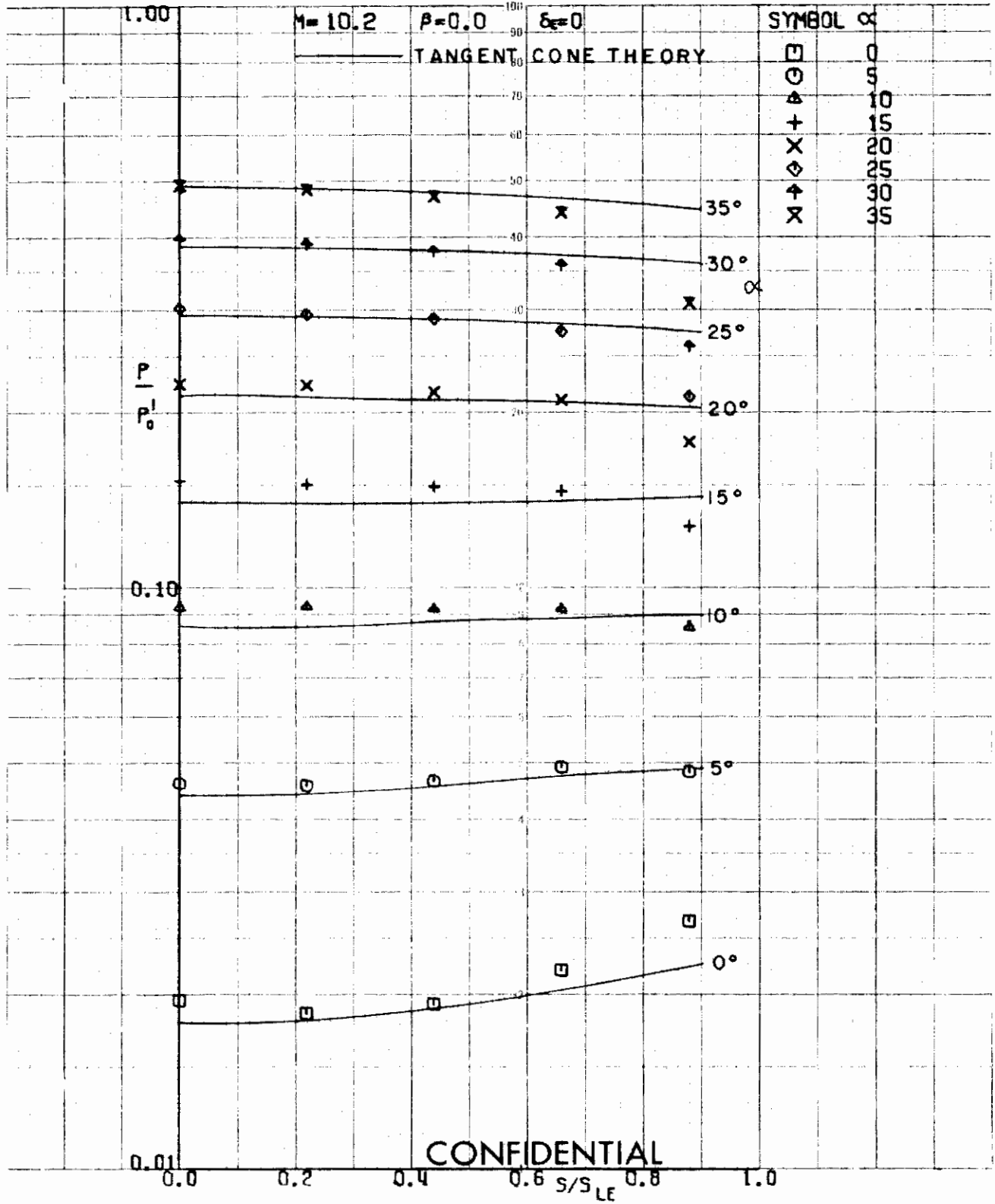
FIGURE 40   (U) TUNNEL C LOWER SURFACE SPANWISE PRESSURES AT/X L = 0.30, β=0
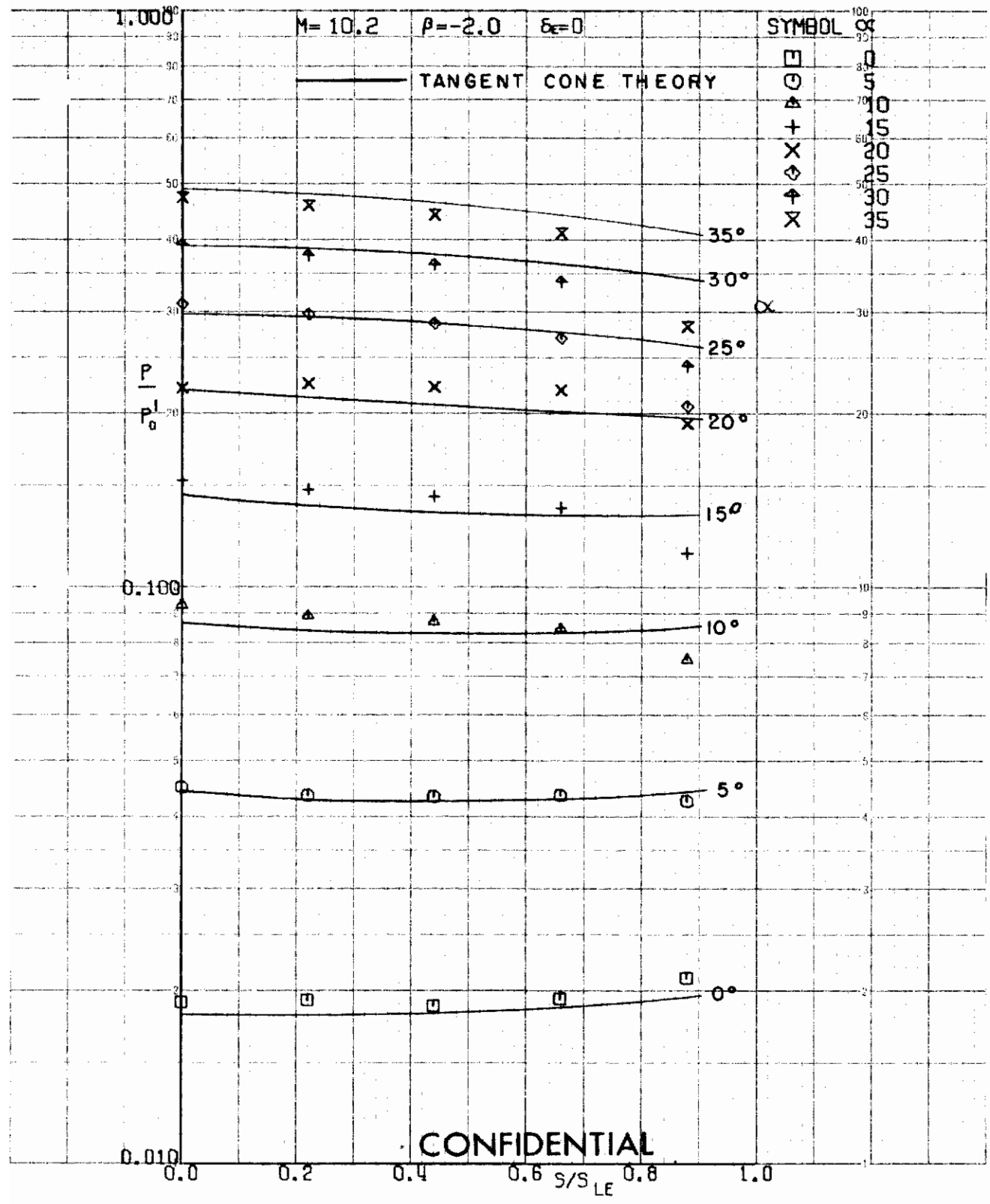
FIGURE 41 (U) TUNNEL C LOWER SURFACE SPANWISE PRESSURES AT X/L = 0.30, β= -2
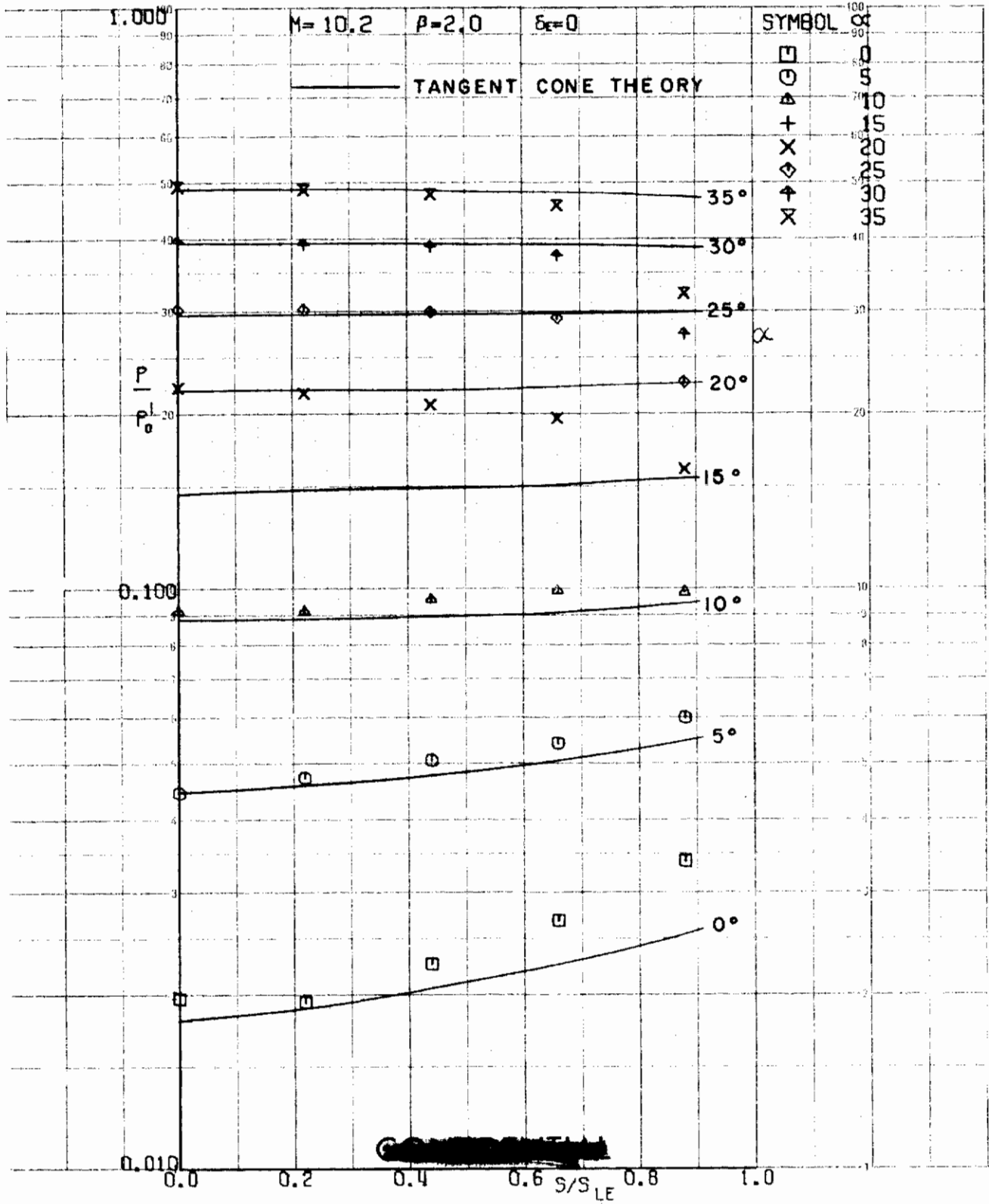
FIGURE 42 (U) TUNNEL C LOWER SURFACE SPANWISE PRESSURES AT X/L =0.30, β=2

120
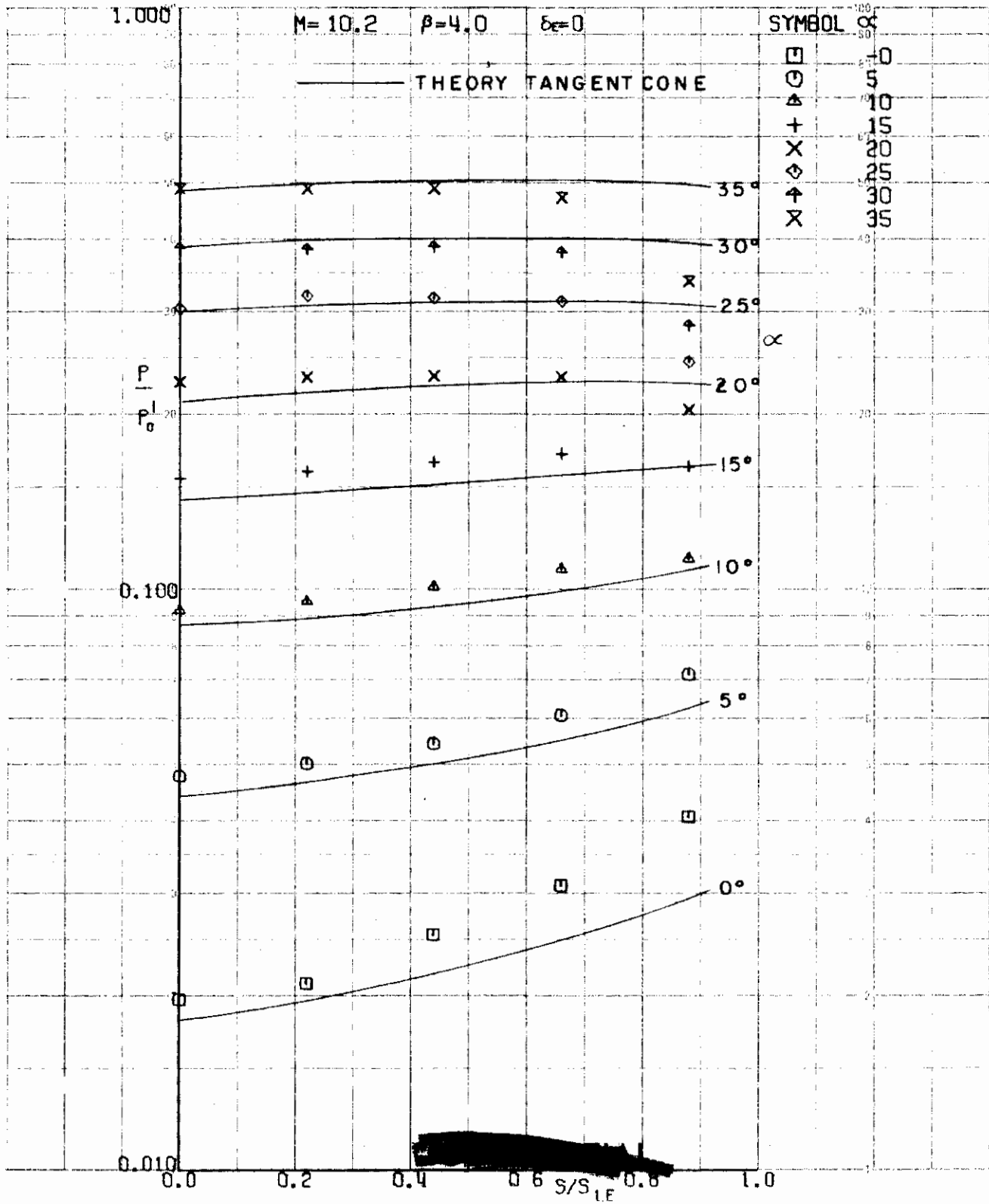
FIGURE 43 (U) TUNNEL C LOWER SURFACE SPANWISE PRESSURES AT X/L = 0.30, β=4
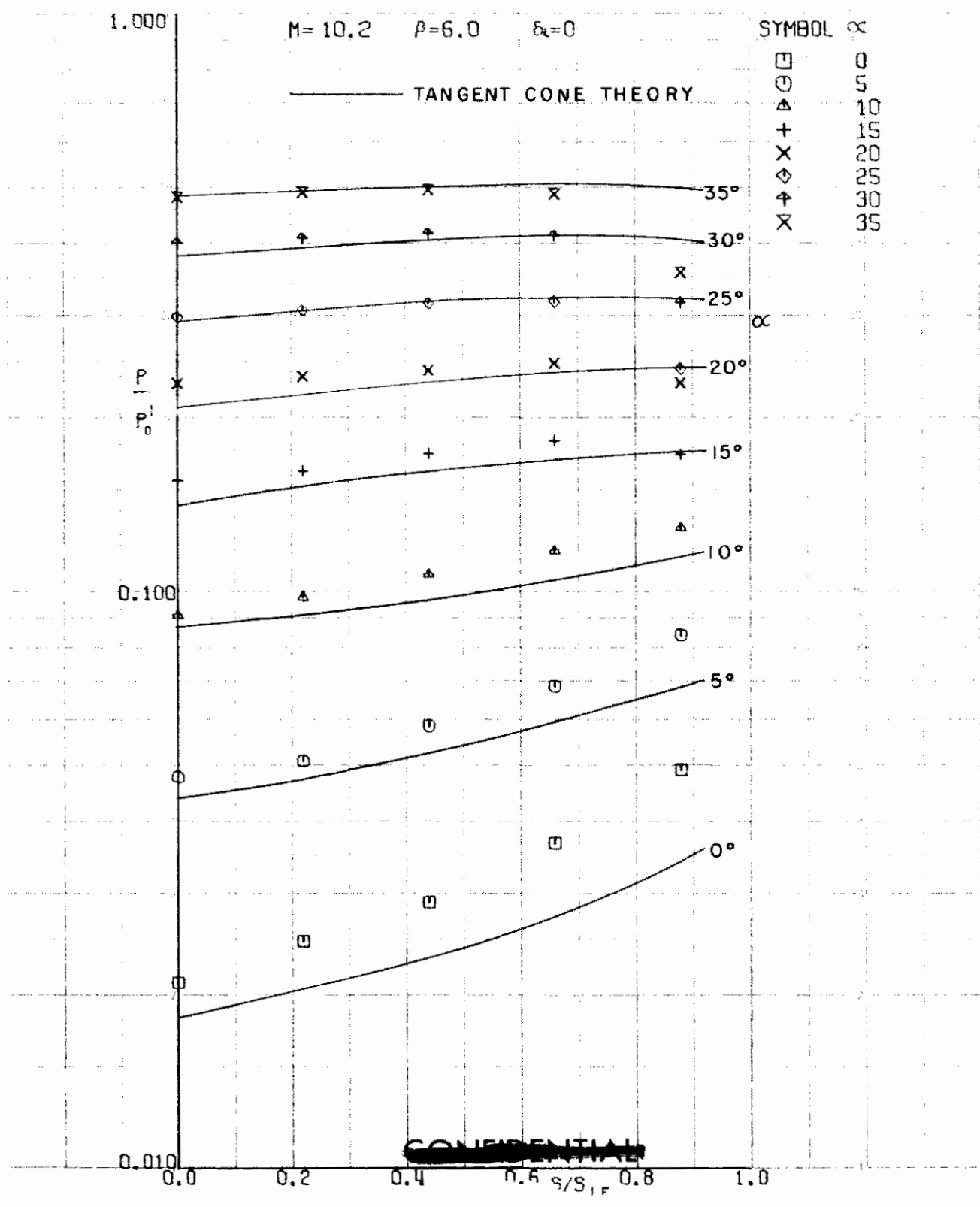
FIGURE 44 (U) TUNNEL C LOWER SURFACE SPANWISE PRESSURES AT X/L = 0.30, β=6

122

FIGURE 45 (U) TUNNEL F LOWER SURFACE SPANWISE PRESSURES AT X/L = 0.30, β=0
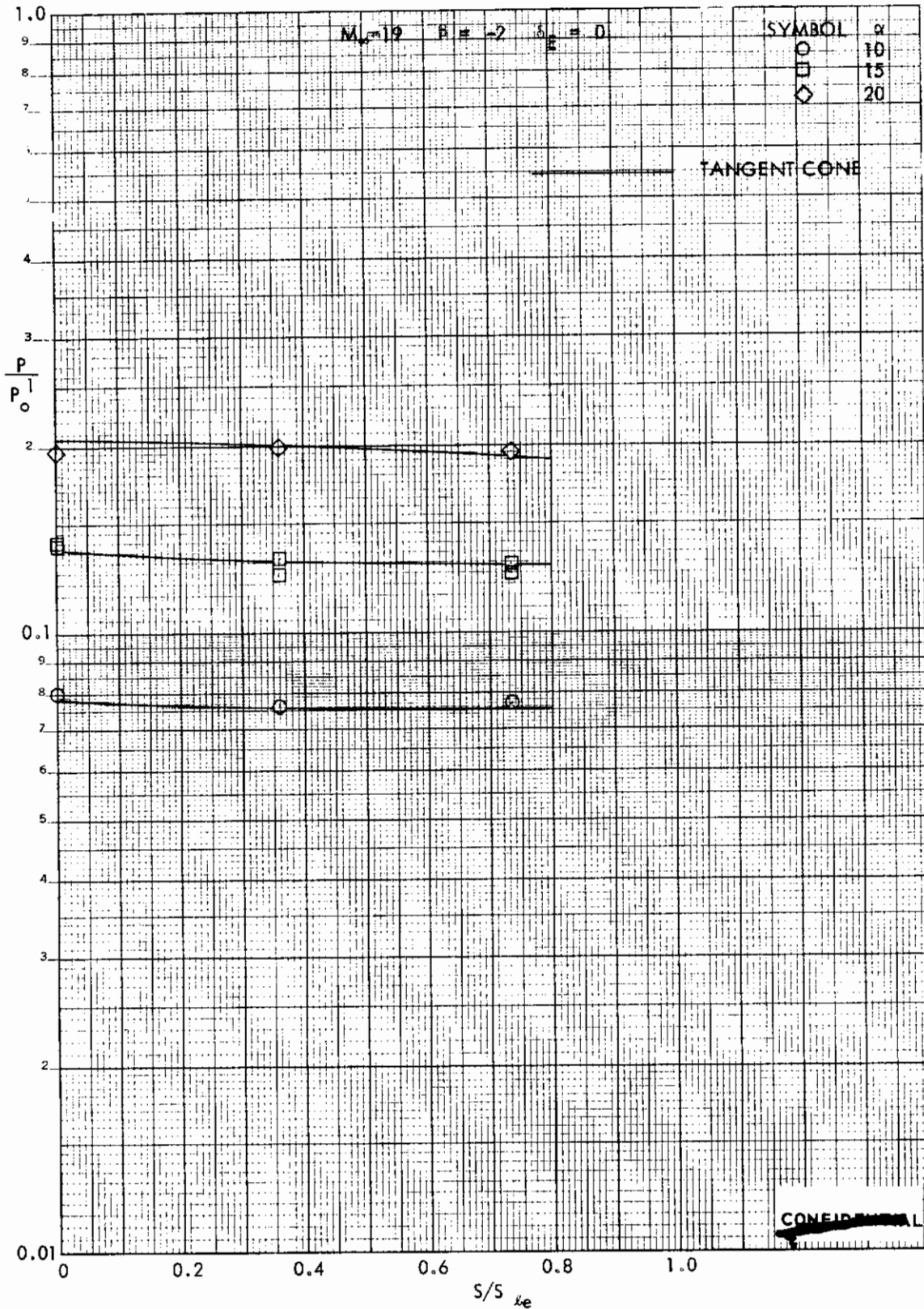
FIGURE 46 (U) TUNNEL F LOWER SURFACE SPANWISE PRESSURES AT X/L = 0.30, β=-2

124
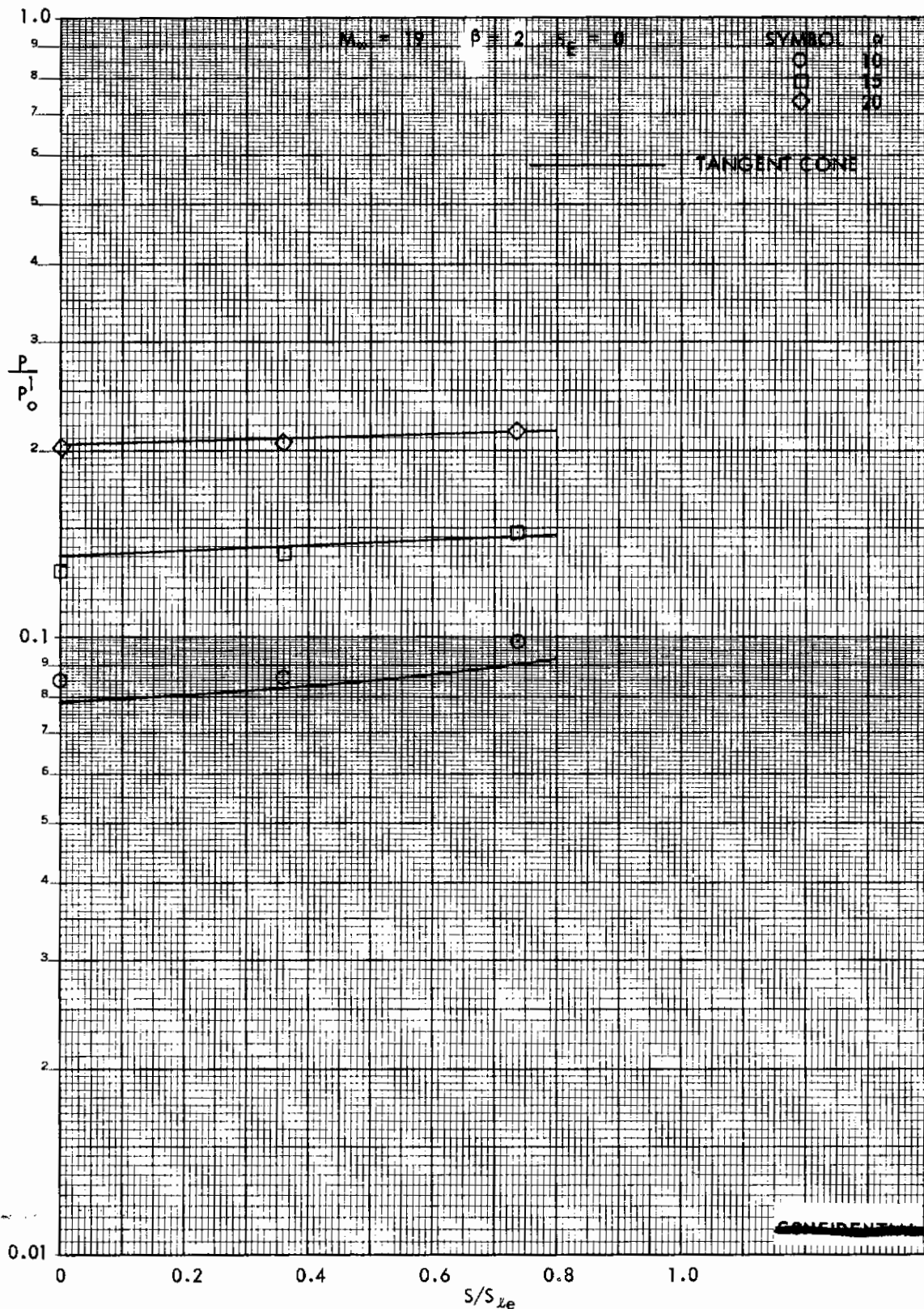
FIGURE 47 (U) TUNNEL F LOWER SURFACE SPANWISE PRESSURES AT X/L = 0.30, β=2
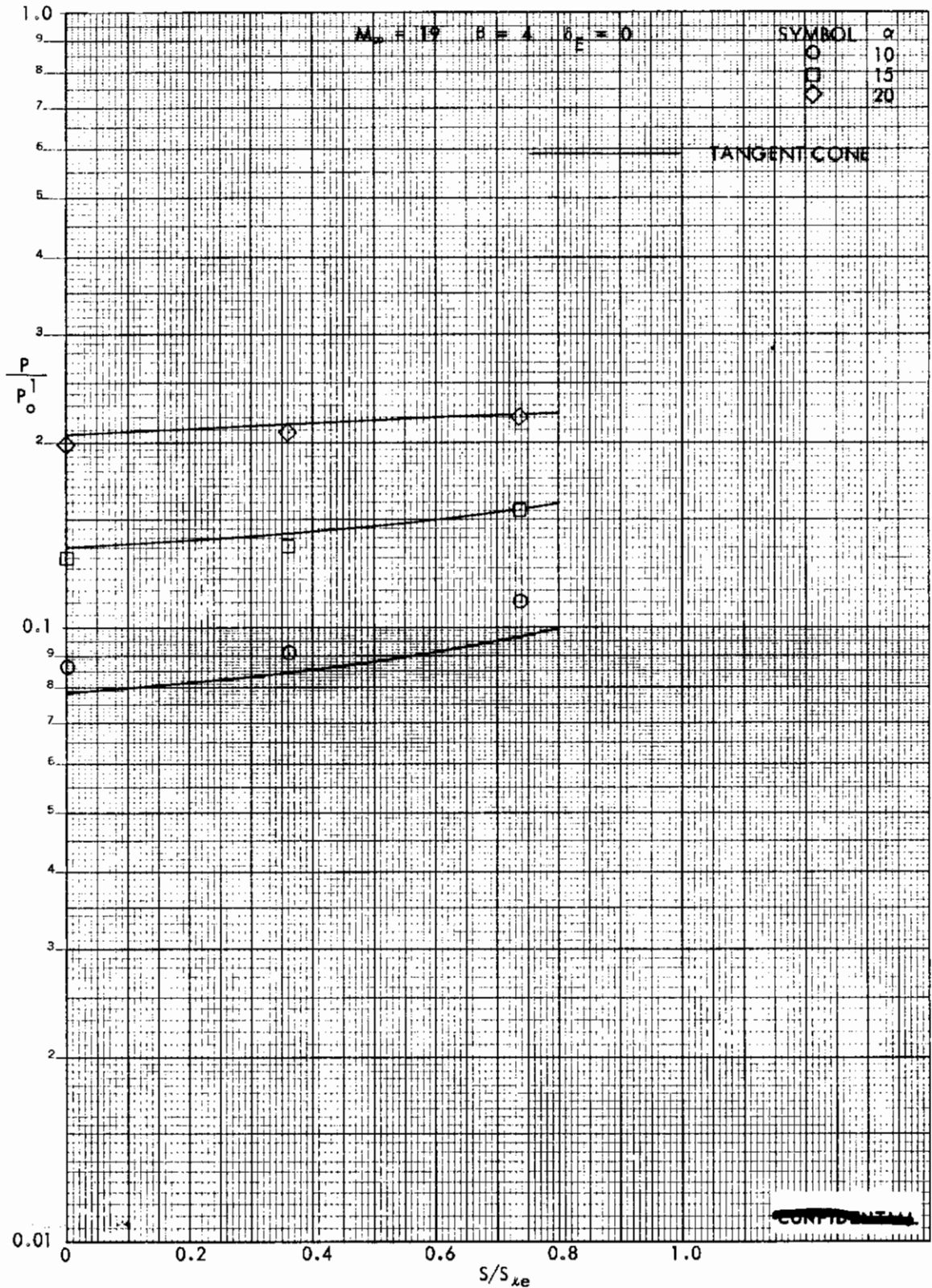
FIGURE 48 (U) TUNNEL F LOWER SURFACE SPANWISE PRESSURES AT X/L = 0.30, β=4
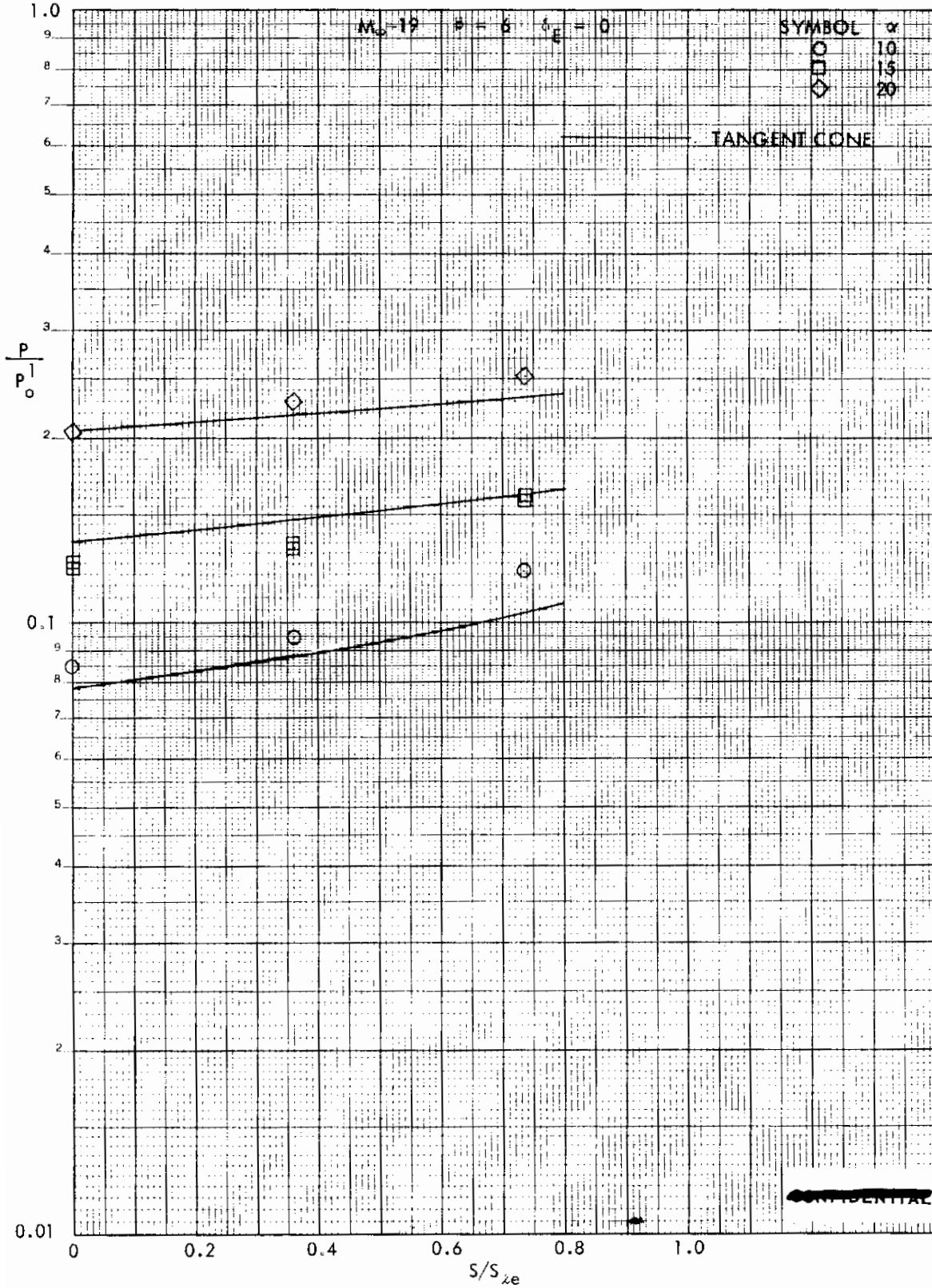
FIGURE 49 (U) TUNNEL F LOWER SURFACE SPANWISE PRESSURES AT X/L = 0.30, β=6
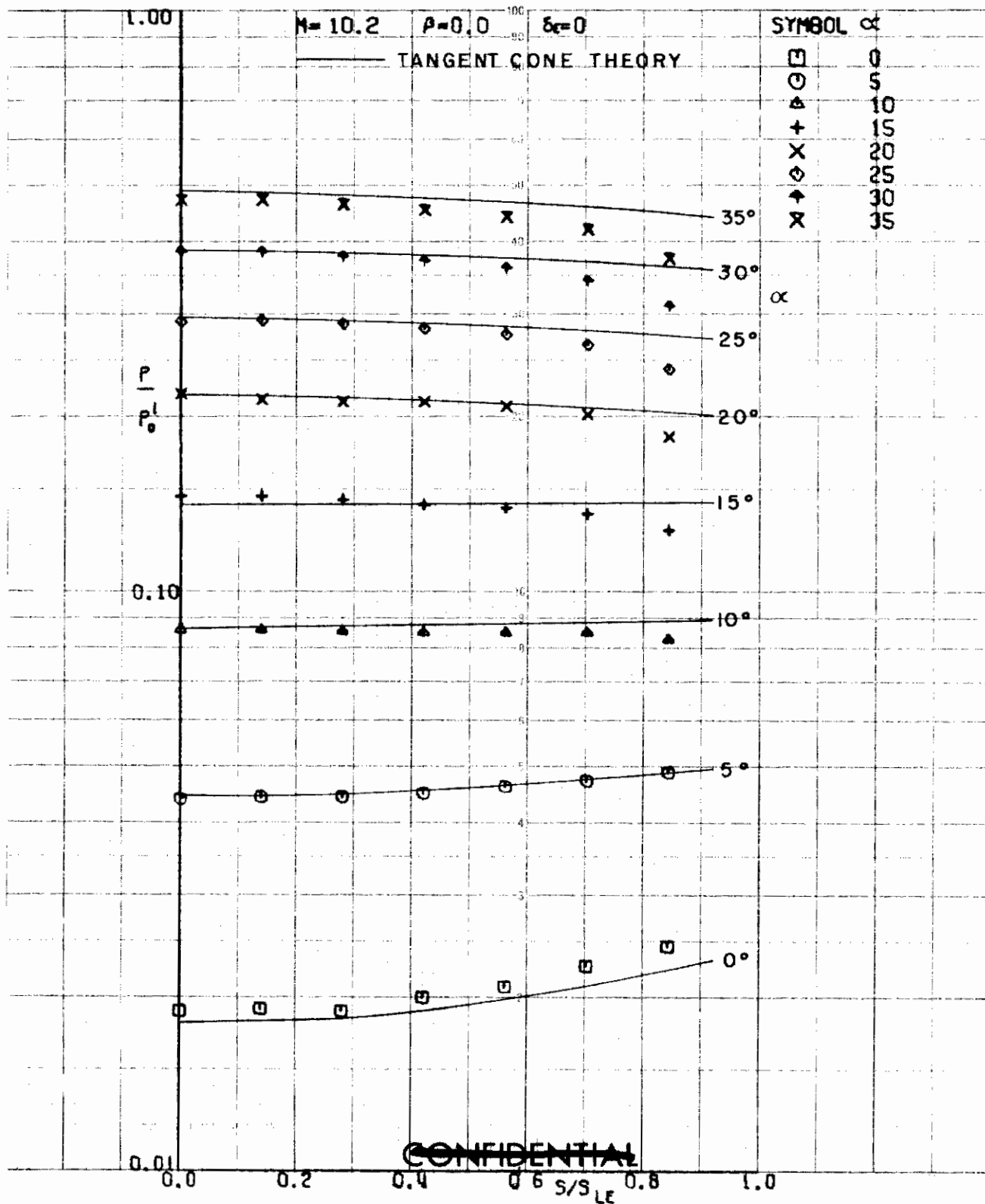
FIGURE 50 (U) TUNNEL C LOWER SURFACE SPANWISE PRESSURES AT X/L = 0.50, β=0

FIGURE 51 (W) TUNNEL C LOWER SURFACE SPANWISE PRESSURES AT X/L = 0.50, β=-2

129
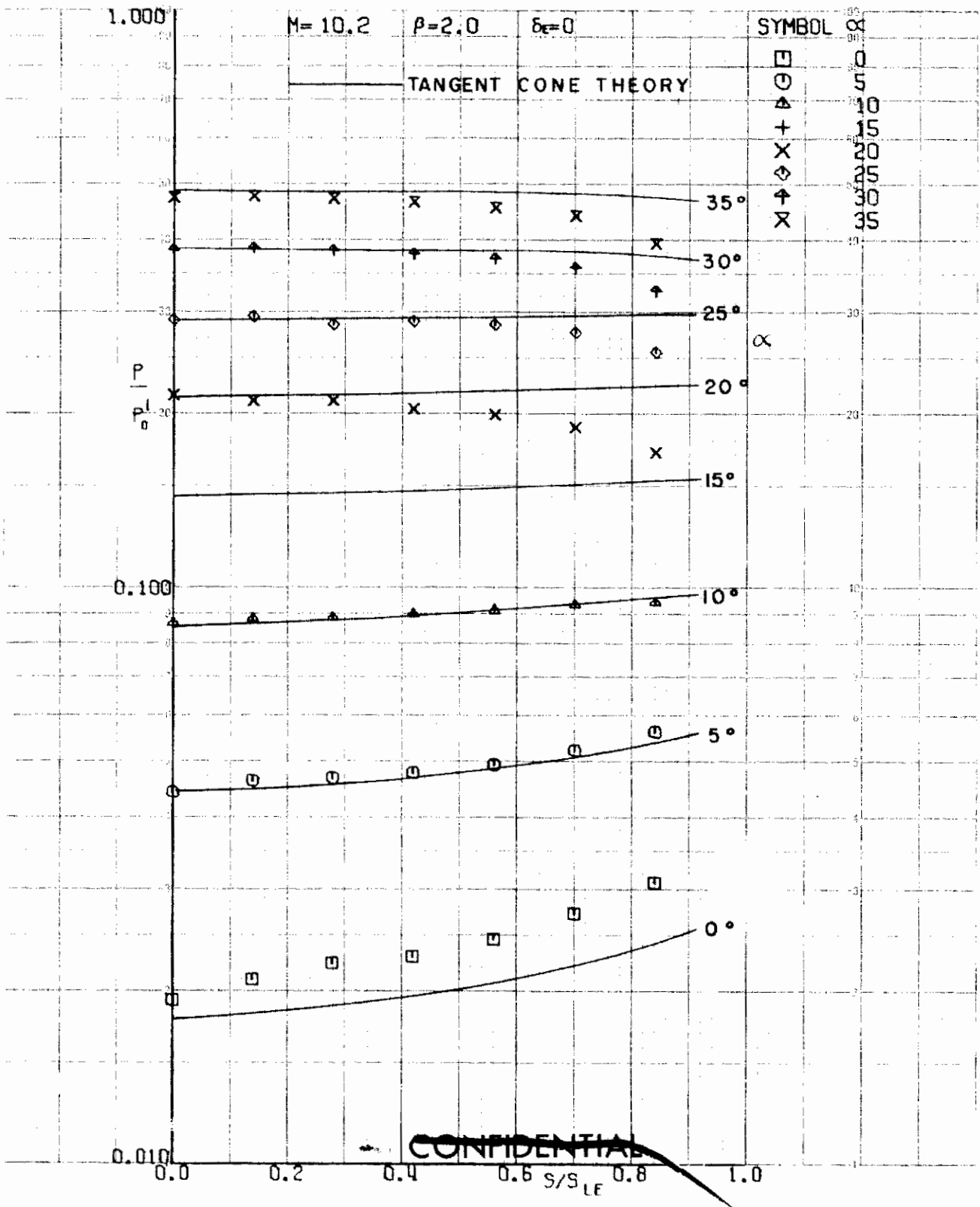
FIGURE 52 (U) TUNNEL C LOWER SURFACE SPANWISE PRESSURES AT X/L = 0.50, β=2
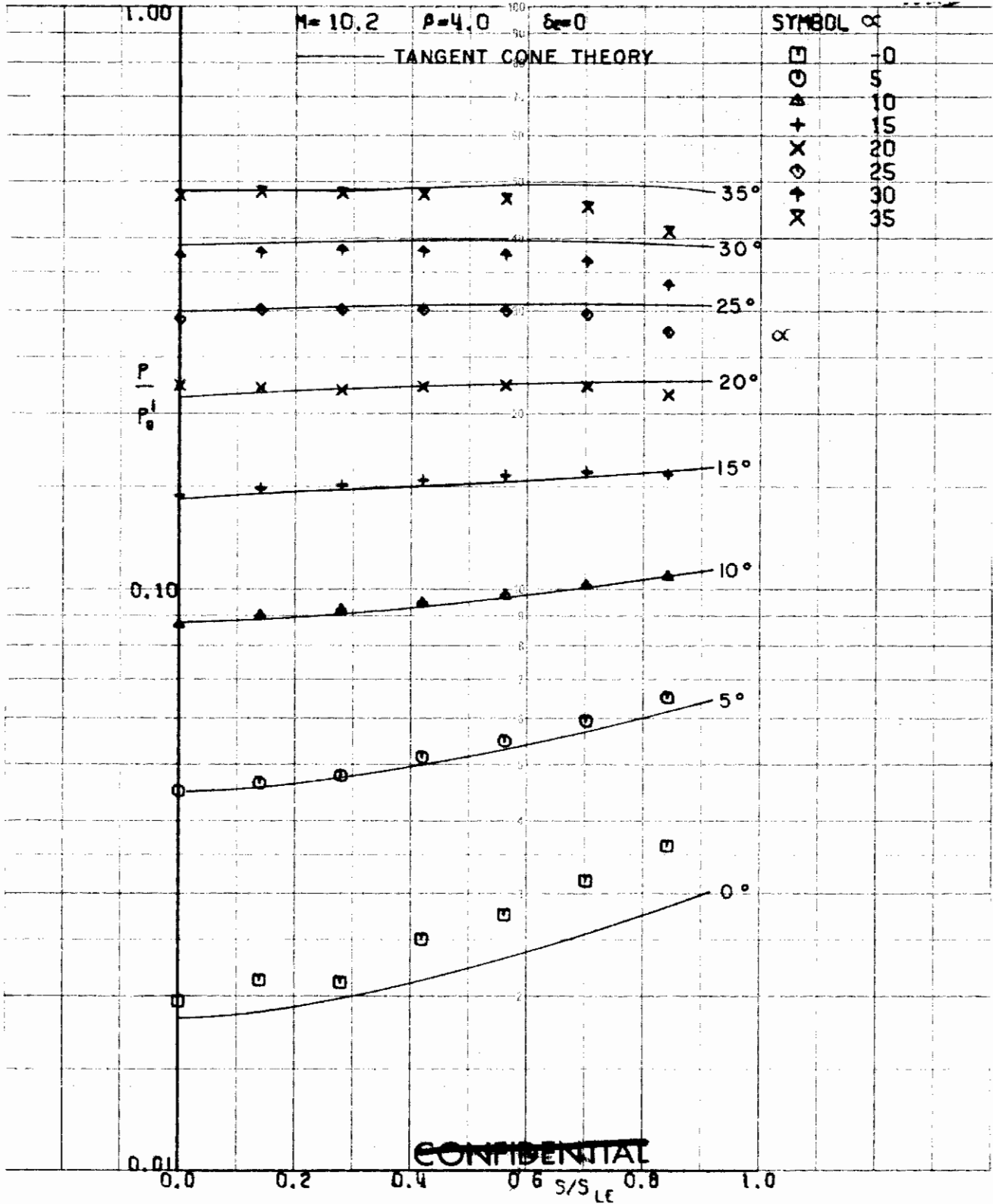
FIGURE 53 (U) TUNNEL C LOWER SURFACE SPANWISE PRESSURES AT X/L = 0.50, β=4
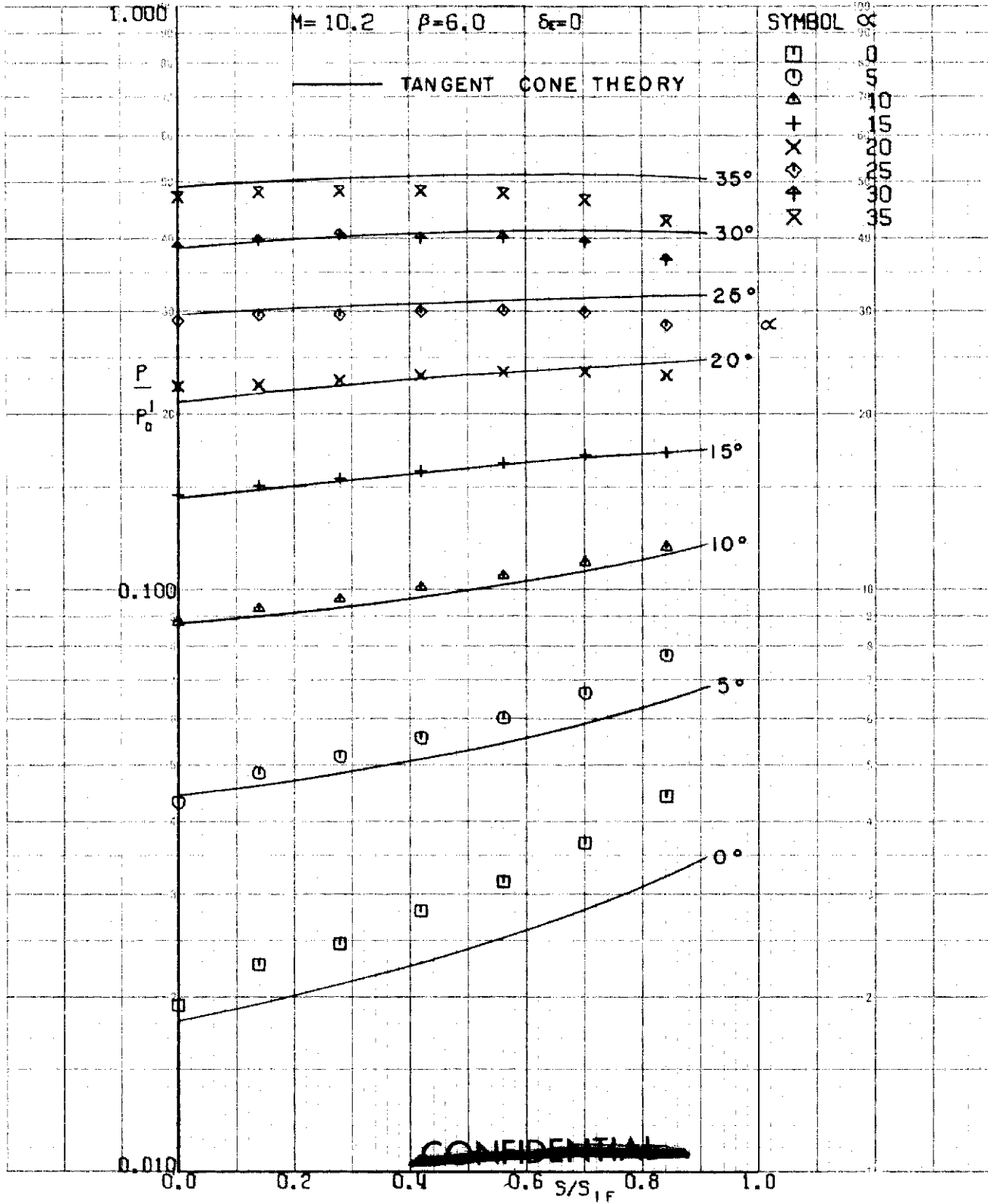
FIGURE 54 (U) TUNNEL C LOWER SURFACE SPANWISE PRESSURES AT X/L = 0.50, β=6
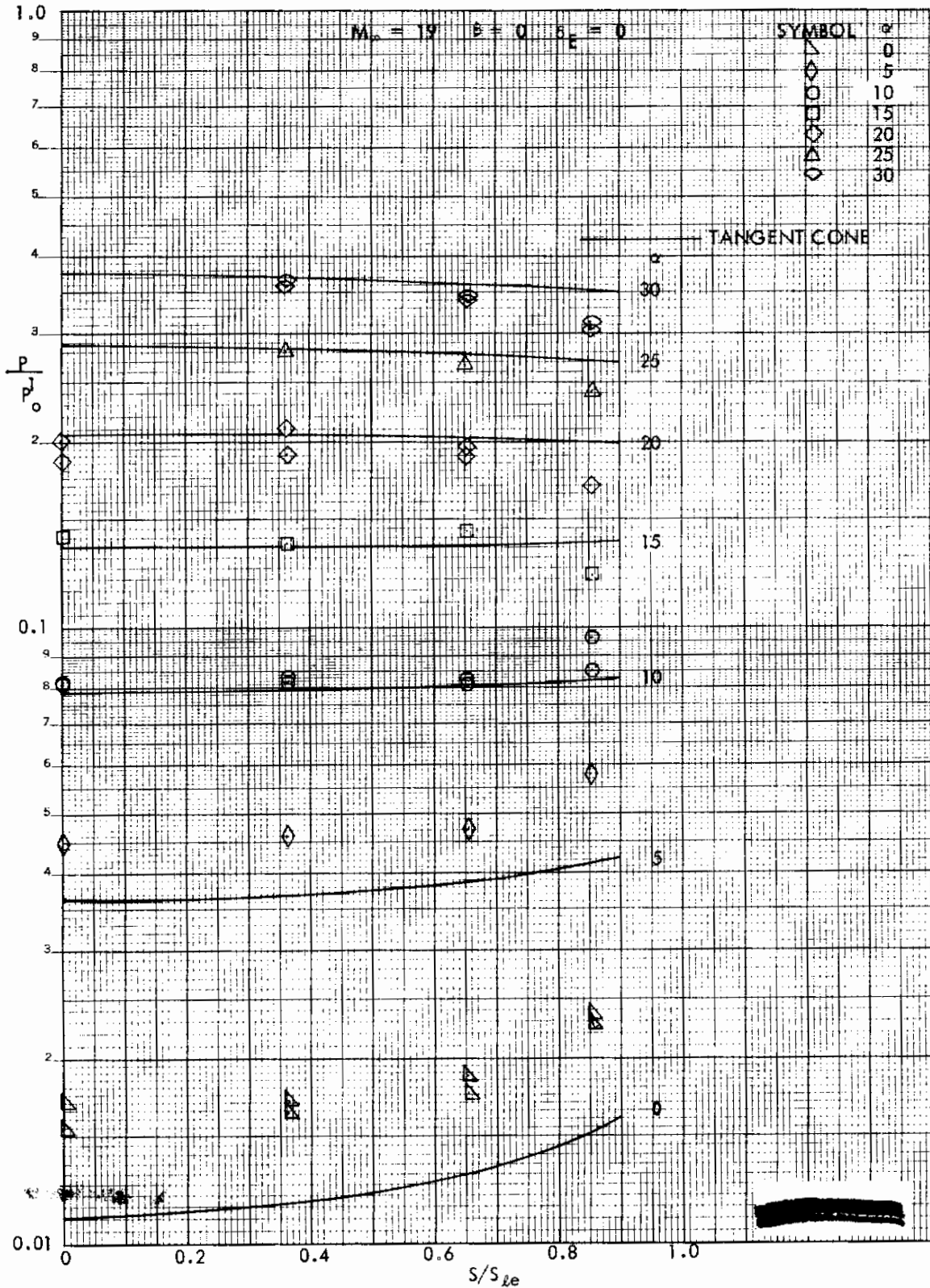
FIGURE 55   (U) TUNNEL F LOWER SURFACE SPANWISE PRESSURES AT X/L = 0.50, β=0
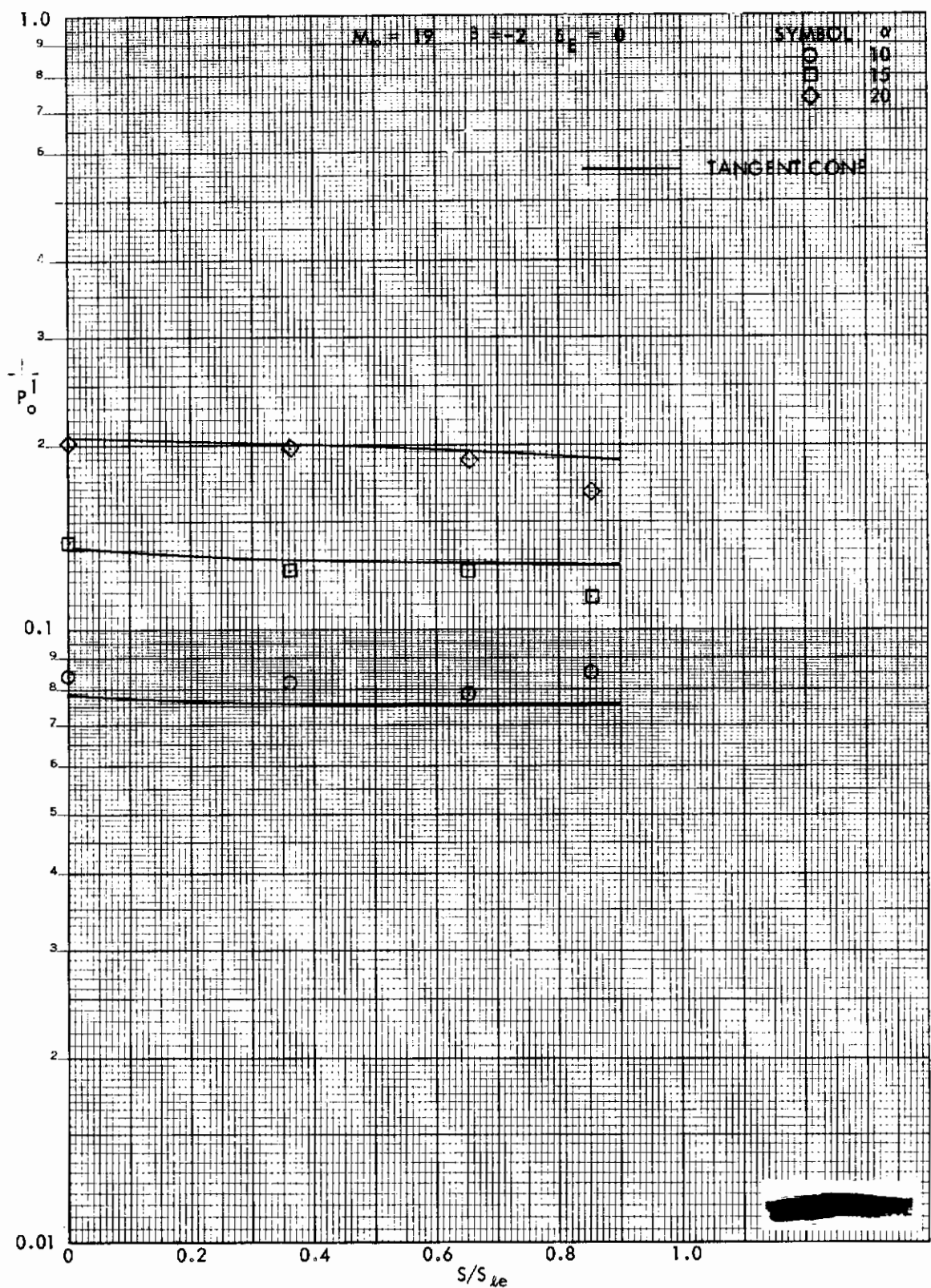
FIGURE 56 (U) TUNNEL F LOWER SURFACE SPANWISE PRESSURES AT $x/L = 0.50$, $\beta = -2$
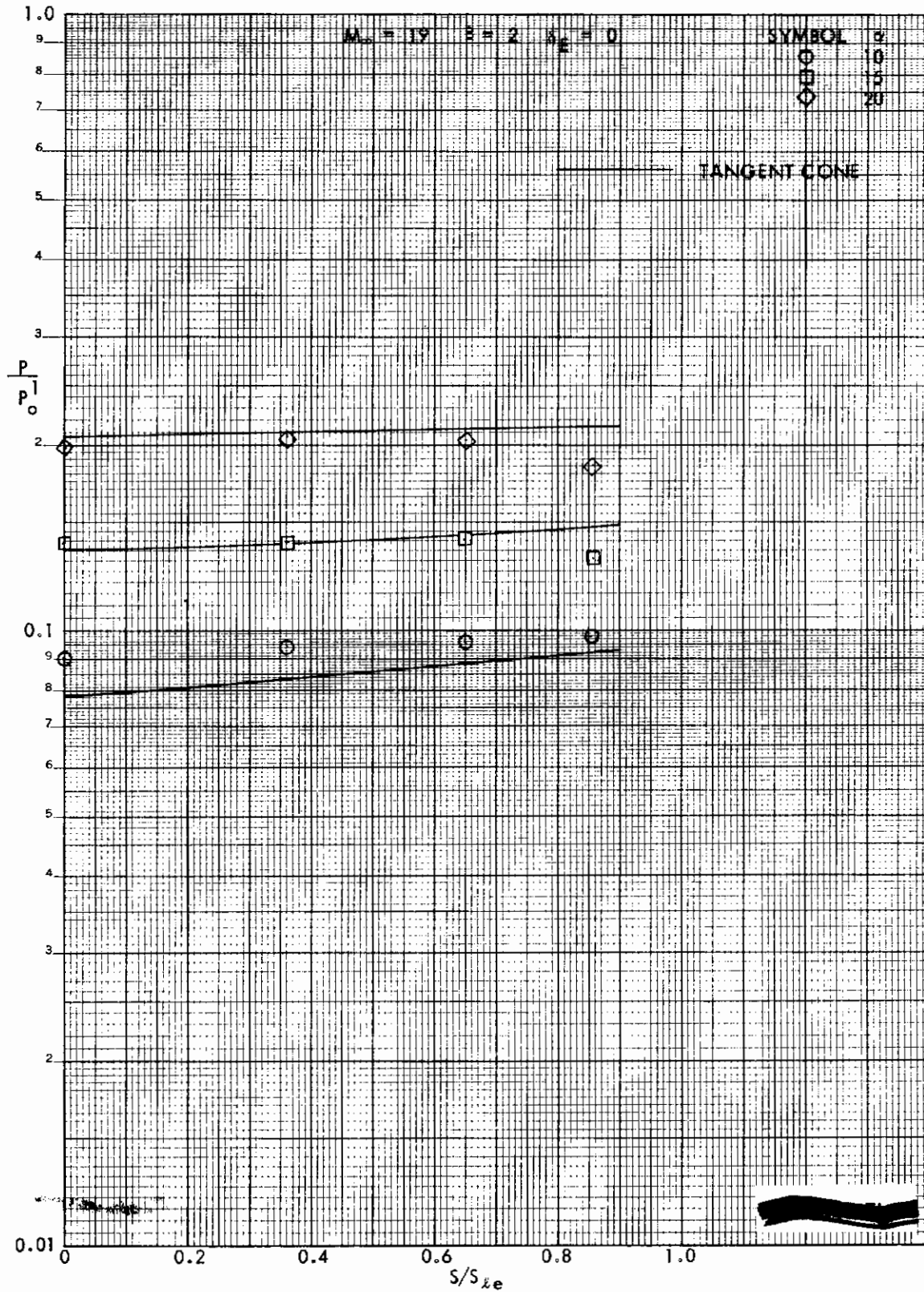
FIGURE 57 (U) TUNNEL F LOWER SURFACE SPANWISE PRESSURES AT X/L = 0.50, β=2
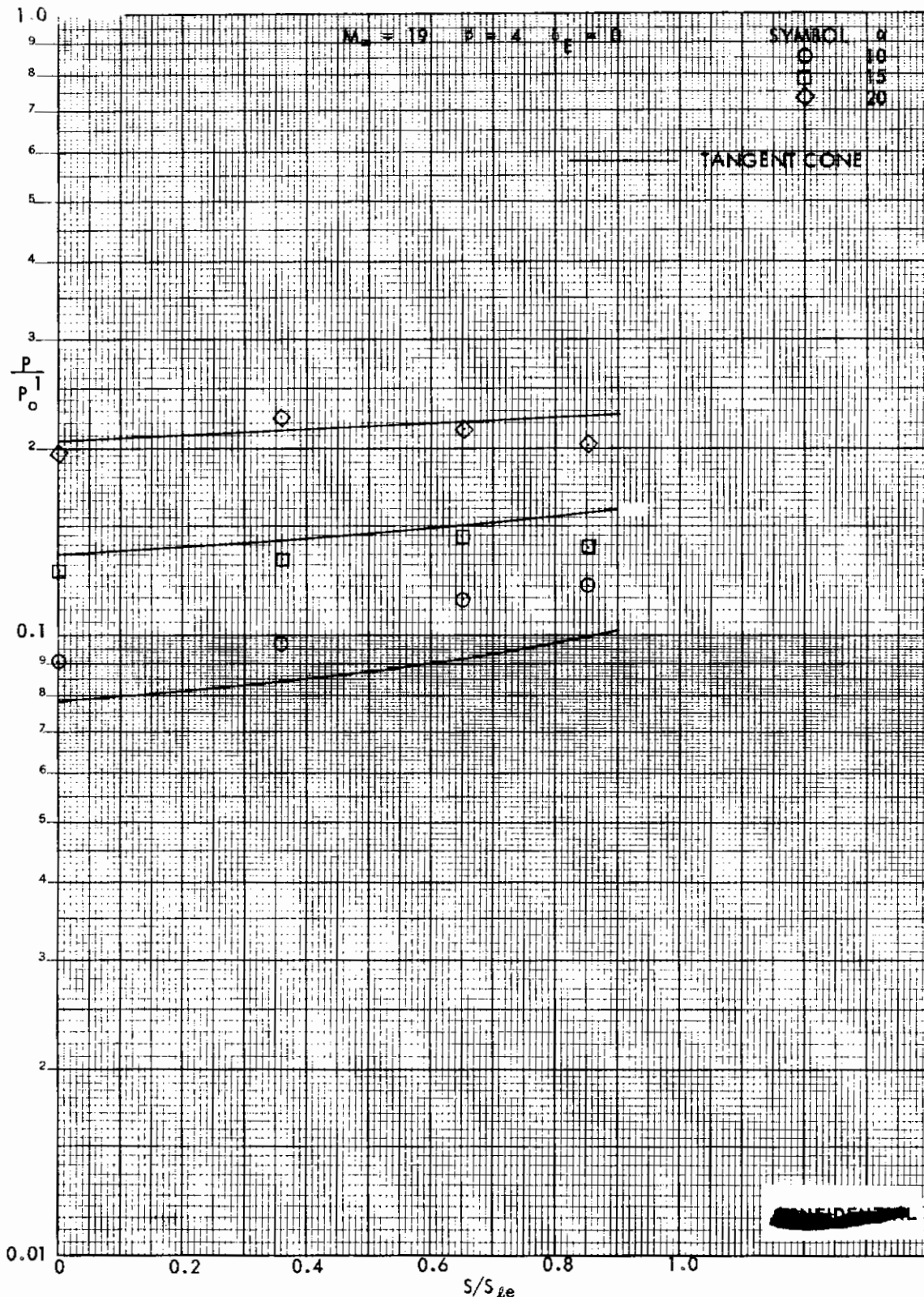
FIGURE 58 (U) TUNNEL F LOWER SURFACE SPANWISE PRESSURES AT X/L = 0.50, β=4

136
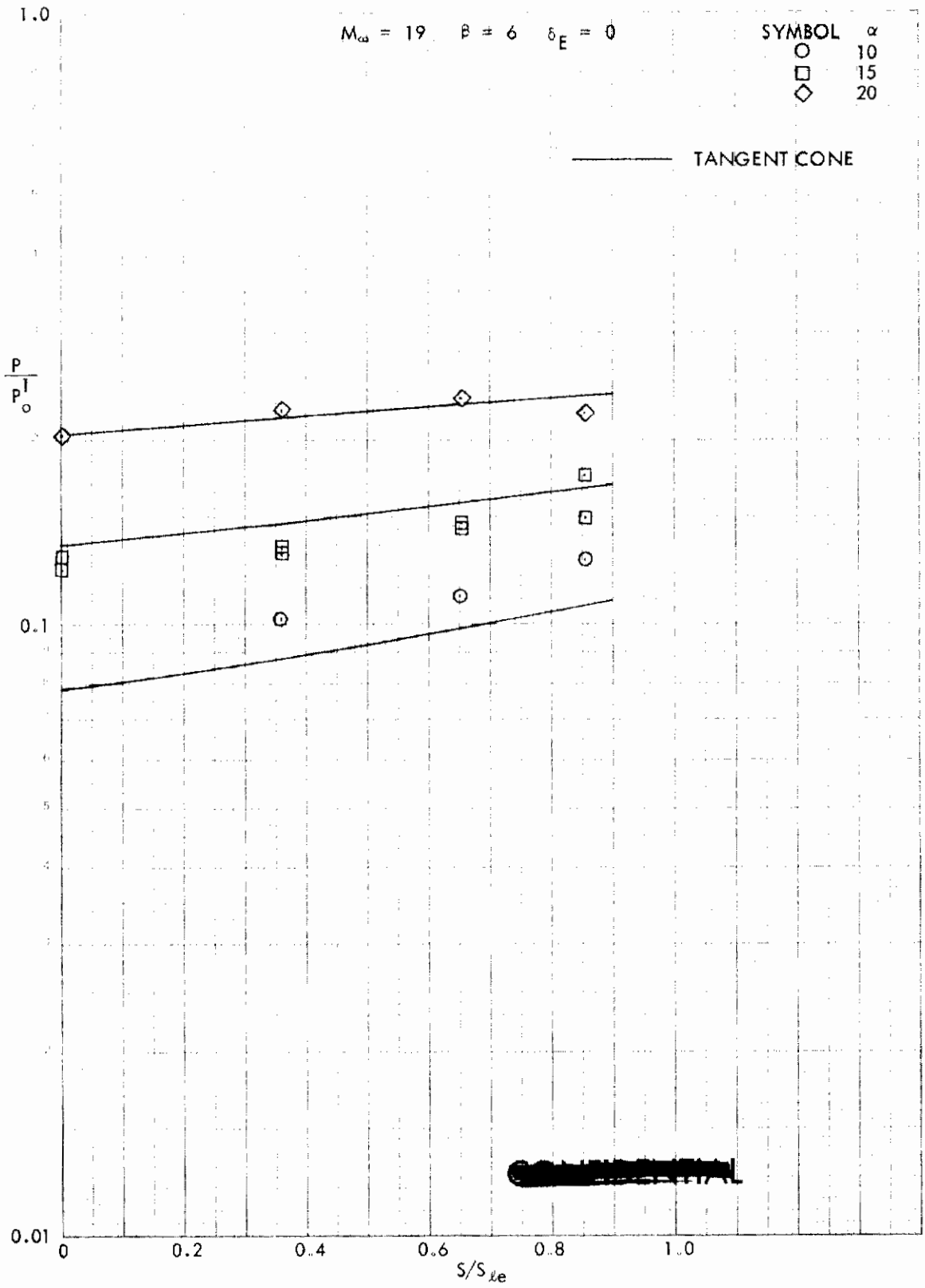
FIGURE 59 (U) TUNNEL F LOWER SURFACE SPANWISE PRESSURES AT X/L = 0.50, β=6

$M_\infty = 19$ $X/L = 0.50$ $\delta_E = 0$

SYMBOL	S/S_{le}	SENSOR
◯	0	11
▢	.36	12
◇	0.86	14

OPEN SYMBOL $\alpha = 10$
FILLED SYMBOL $\alpha = 15$

FIGURE 60 (U) EFFECT OF YAW ON LOWER SURFACE PRESSURES AT $X/L = 0.50$

138
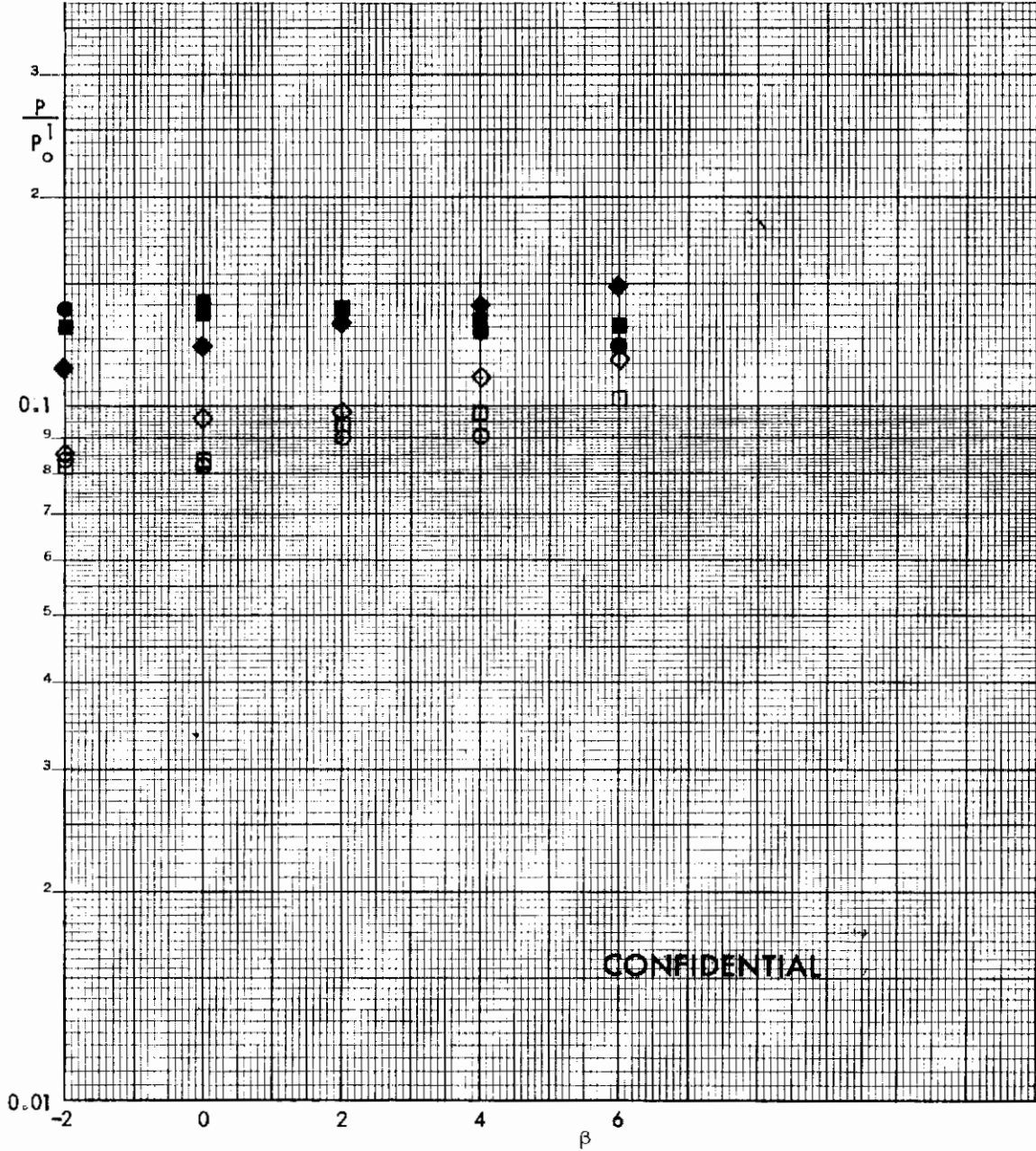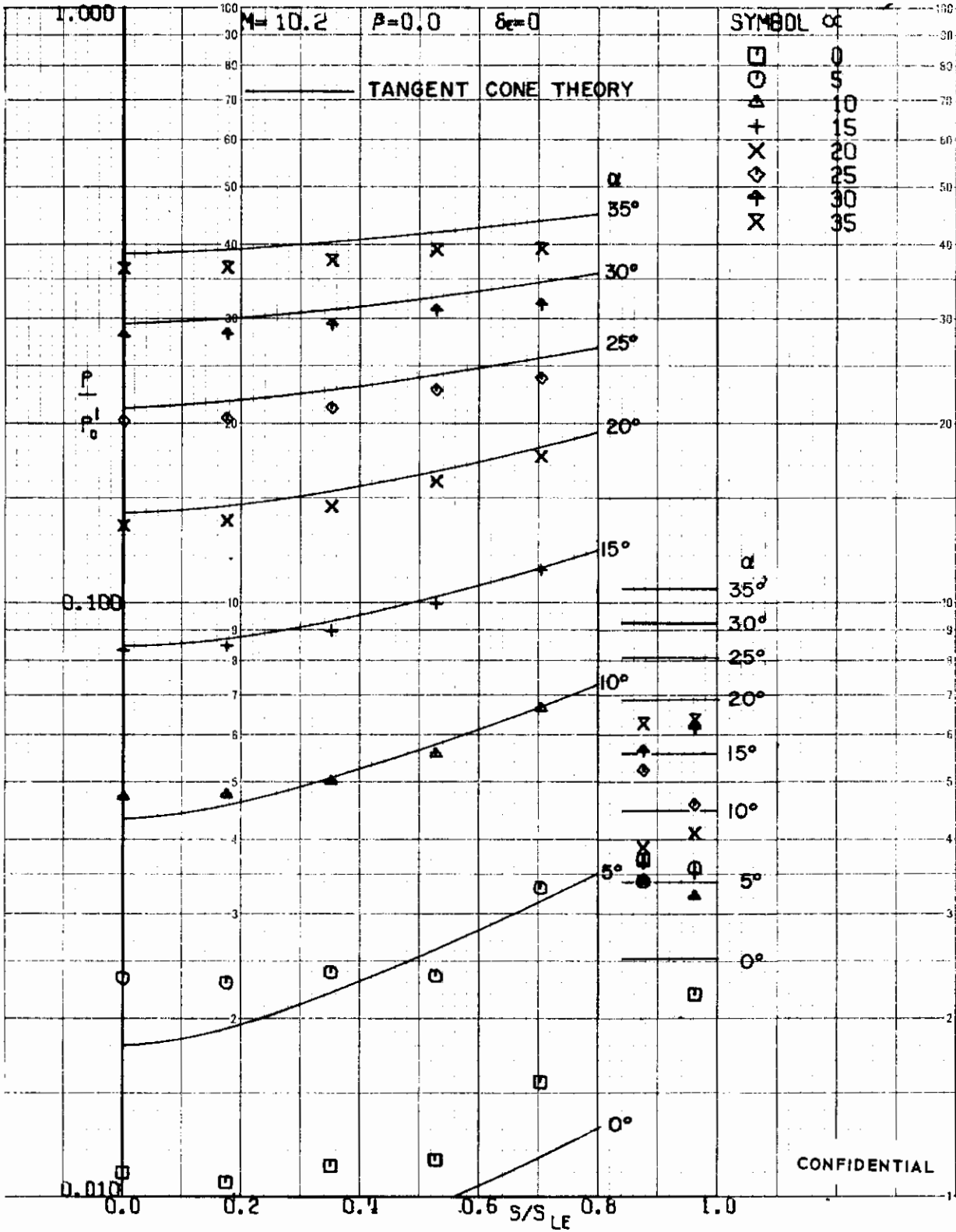
FIGURE 61 (U) TUNNEL C LOWER SURFACE SPANWISE PRESSURES AT X/L = 0.75, β=0
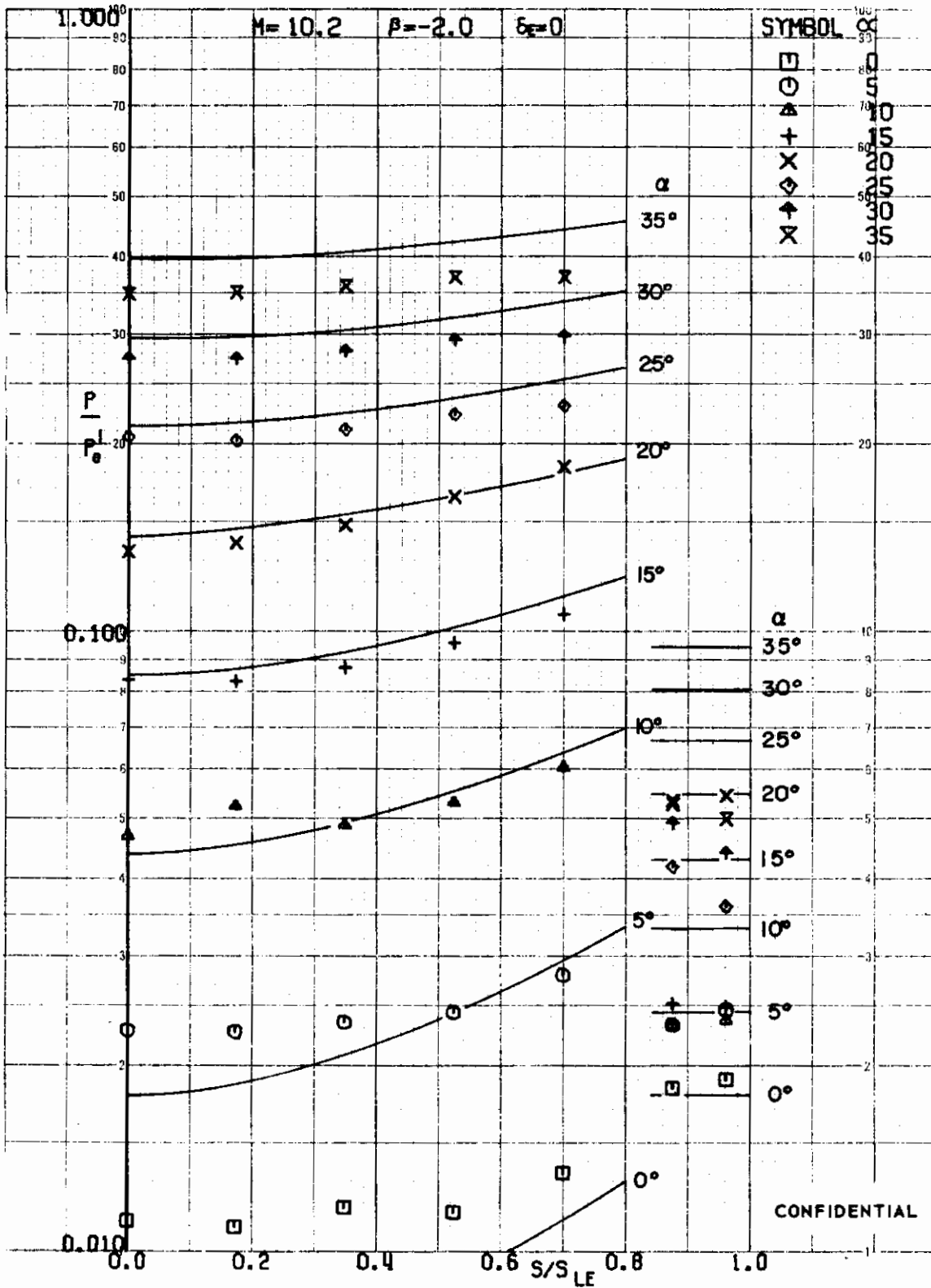
FIGURE 62 (U) TUNNEL C LOWER SURFACE SPANWISE PRESSURES AT X/L = 0.75, β=-2
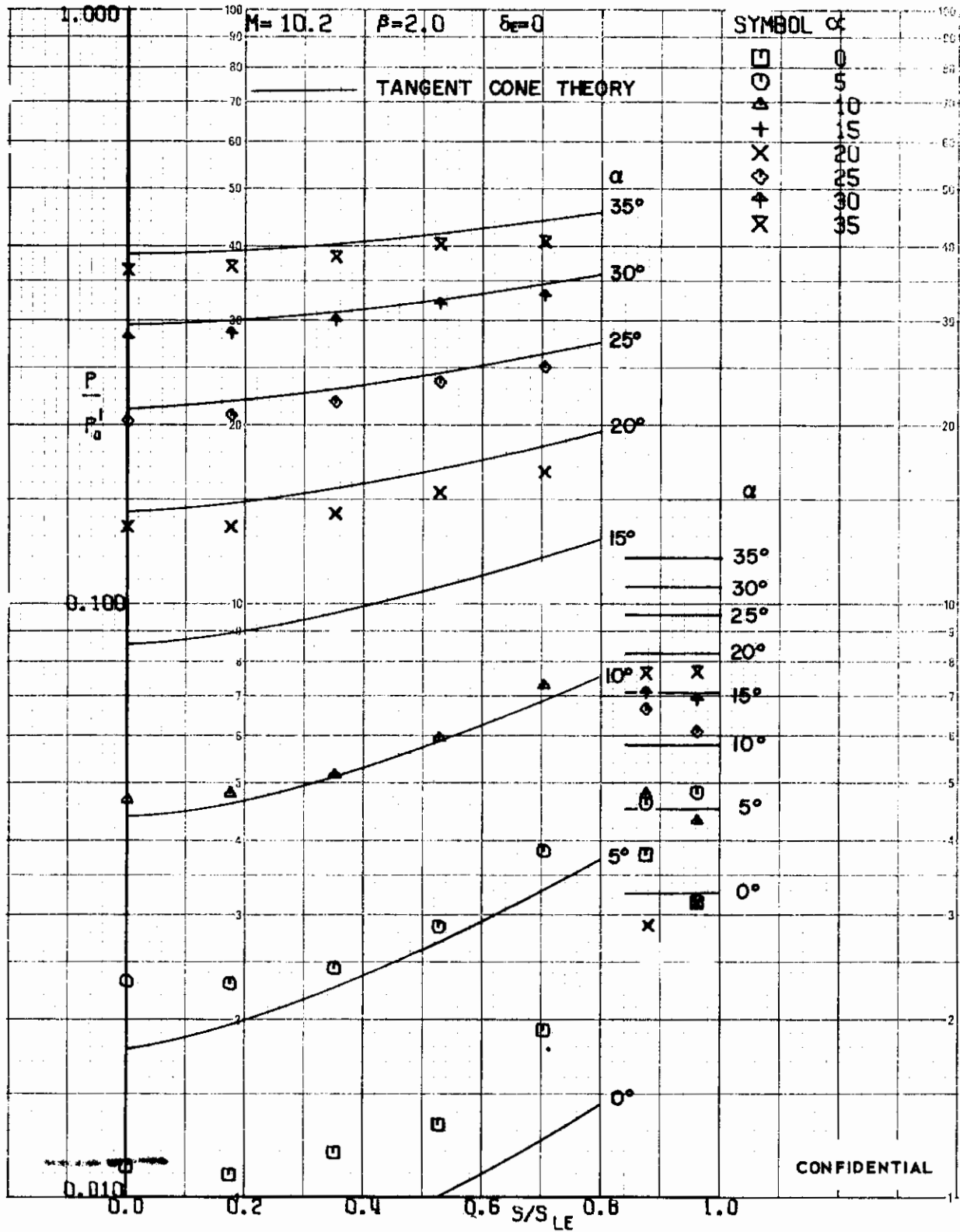
FIGURE 63 (U) TUNNEL C LOWER SURFACE SPANWISE PRESSURES AT X/L = 0.75, β=2

141
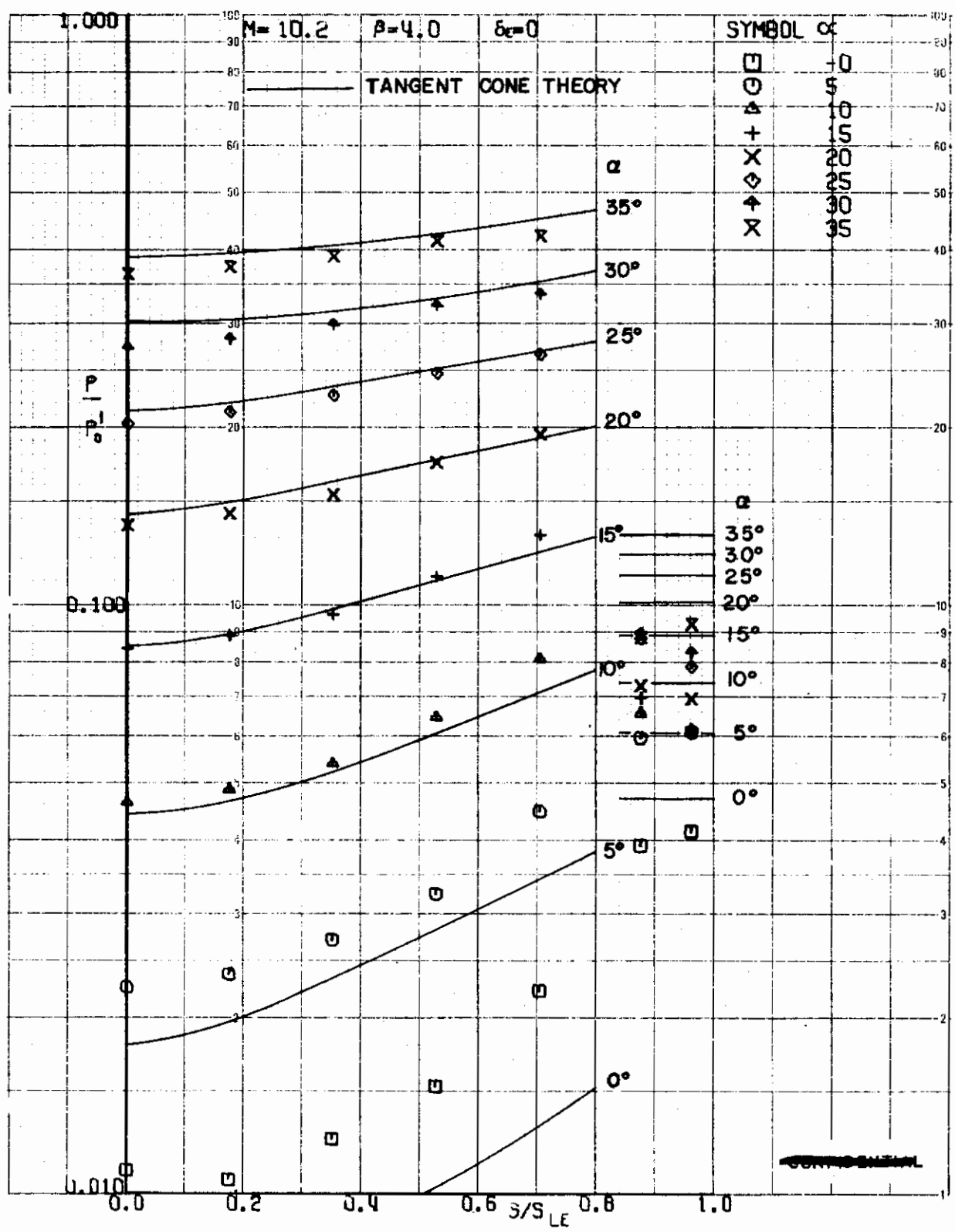
FIGURE 64 (U) TUNNEL C LOWER SURFACE SPANWISE PRESSURES AT X/L = 0.75, β=4
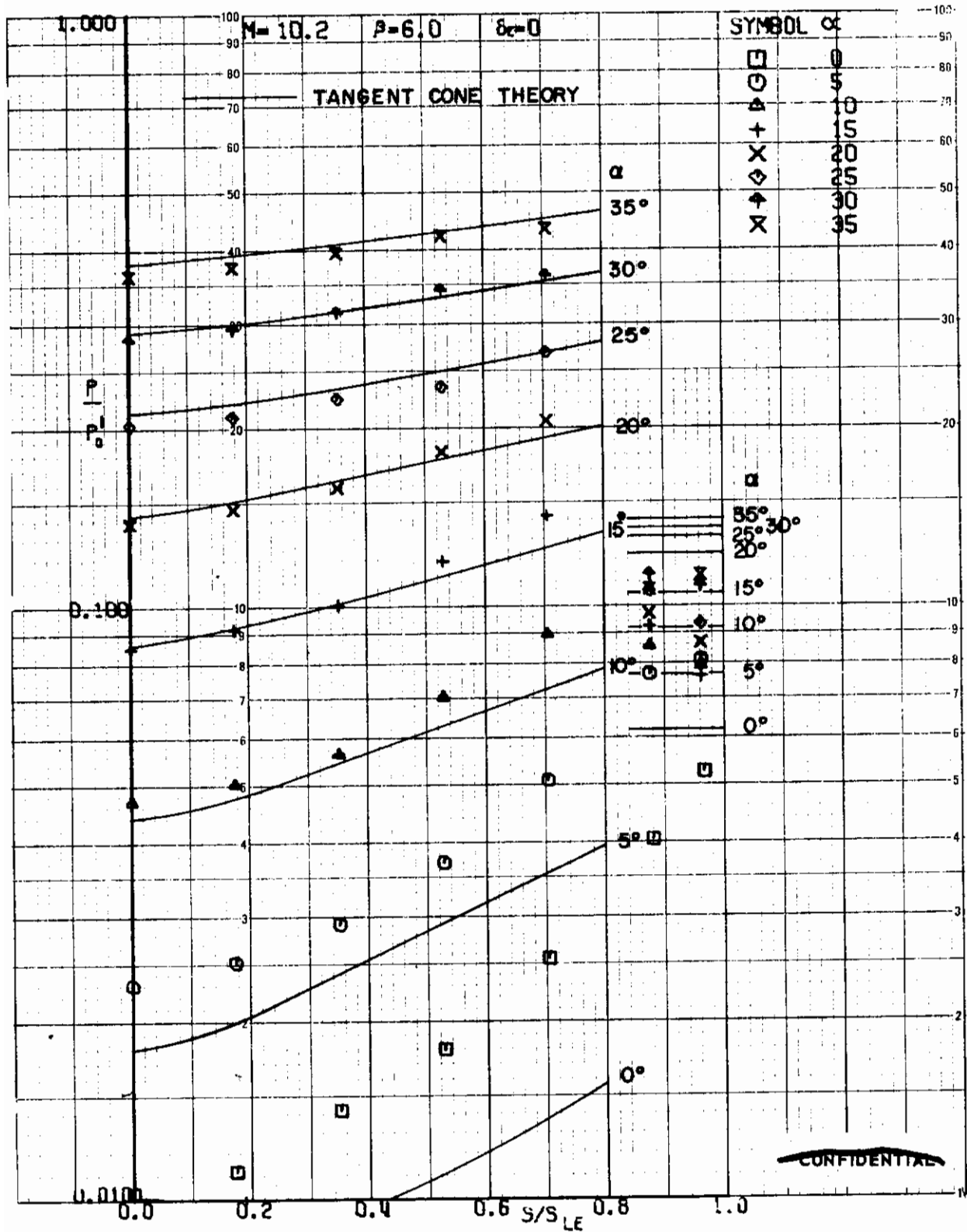
FIGURE 65 (U) TUNNEL C LOWER SURFACE SPANWISE PRESSURES AT X/L = 0.75, β=6

143
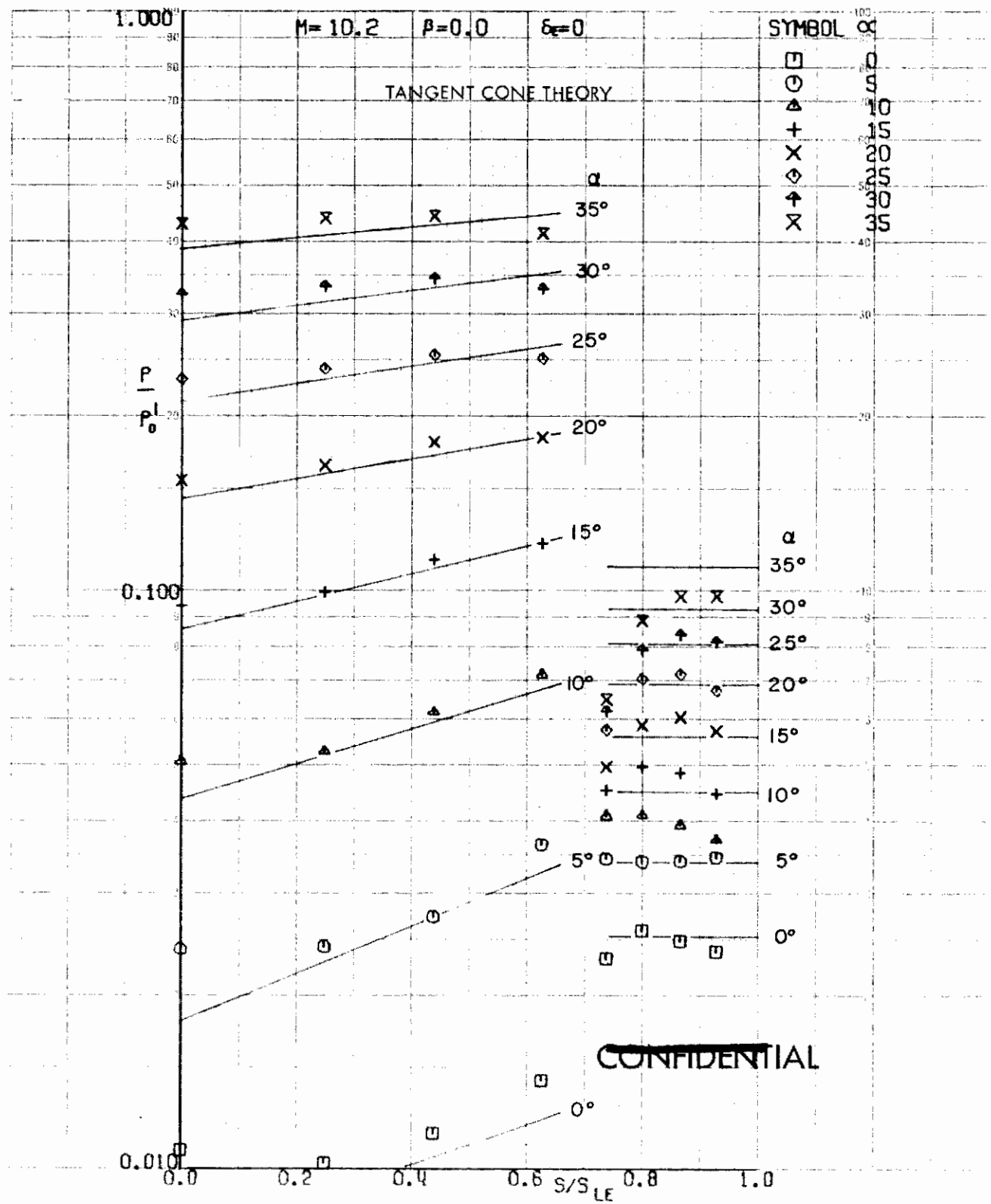
FIGURE 66 (U) TUNNEL C LOWER SURFACE SPANWISE PRESSURES AT X/L = 0.96, β=0
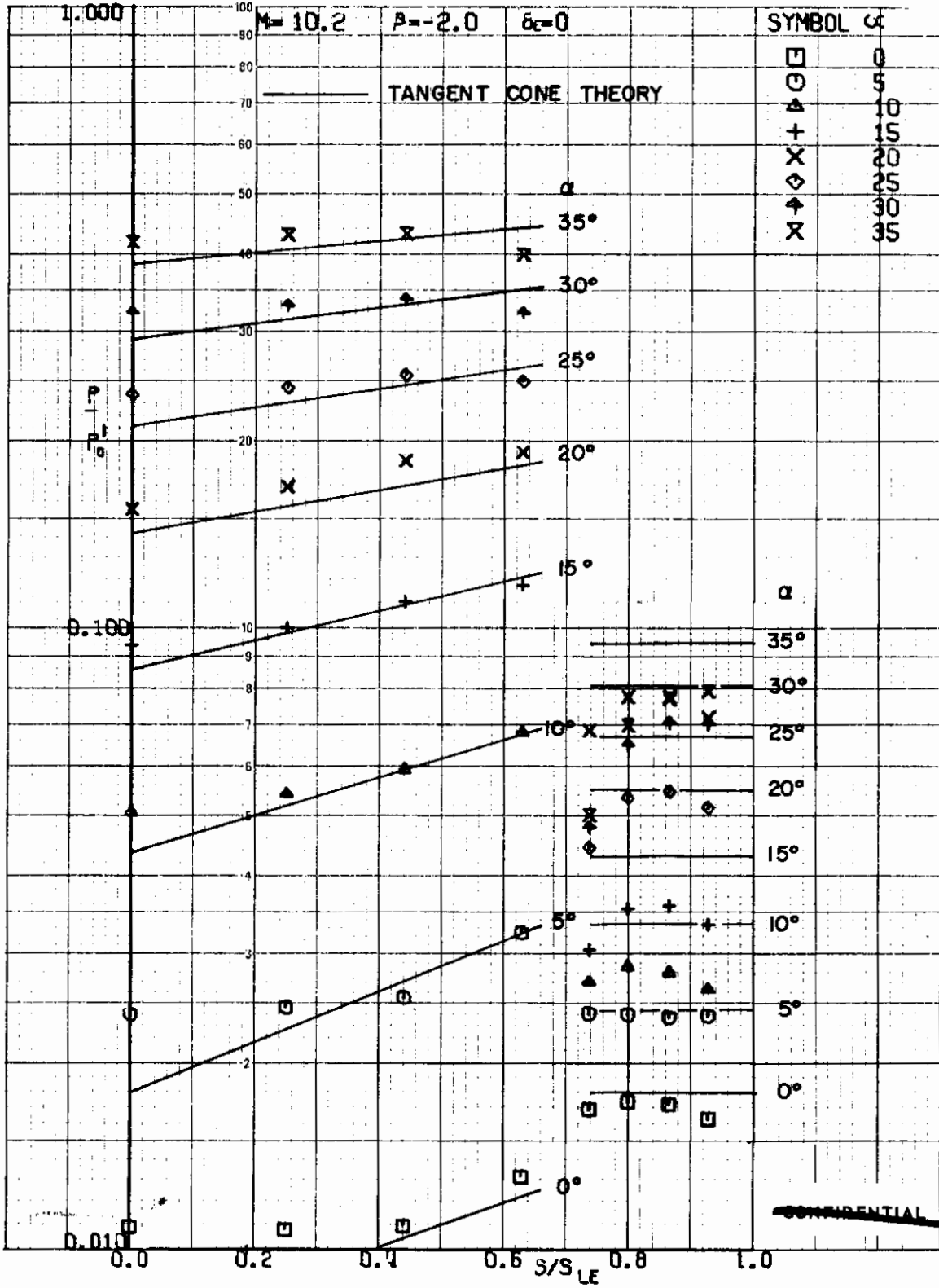
FIGURE 67 (U) TUNNEL C LOWER SURFACE SPANWISE PRESSURES AT X/L = 0.96, β=-2

145
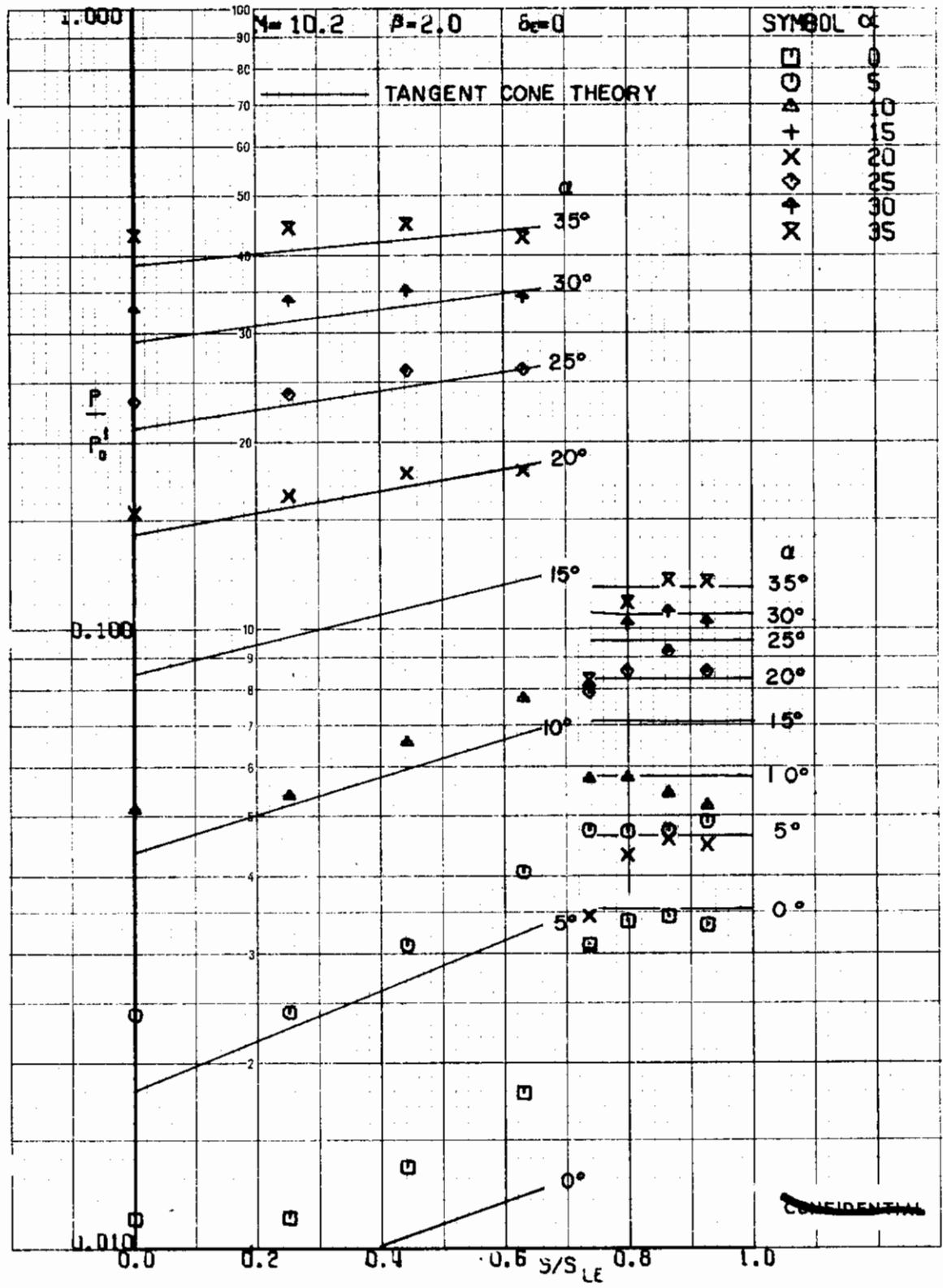
FIGURE 68 (U) TUNNEL C LOWER SURFACE SPANWISE PRESSURES AT X/L = 0.96, β=2
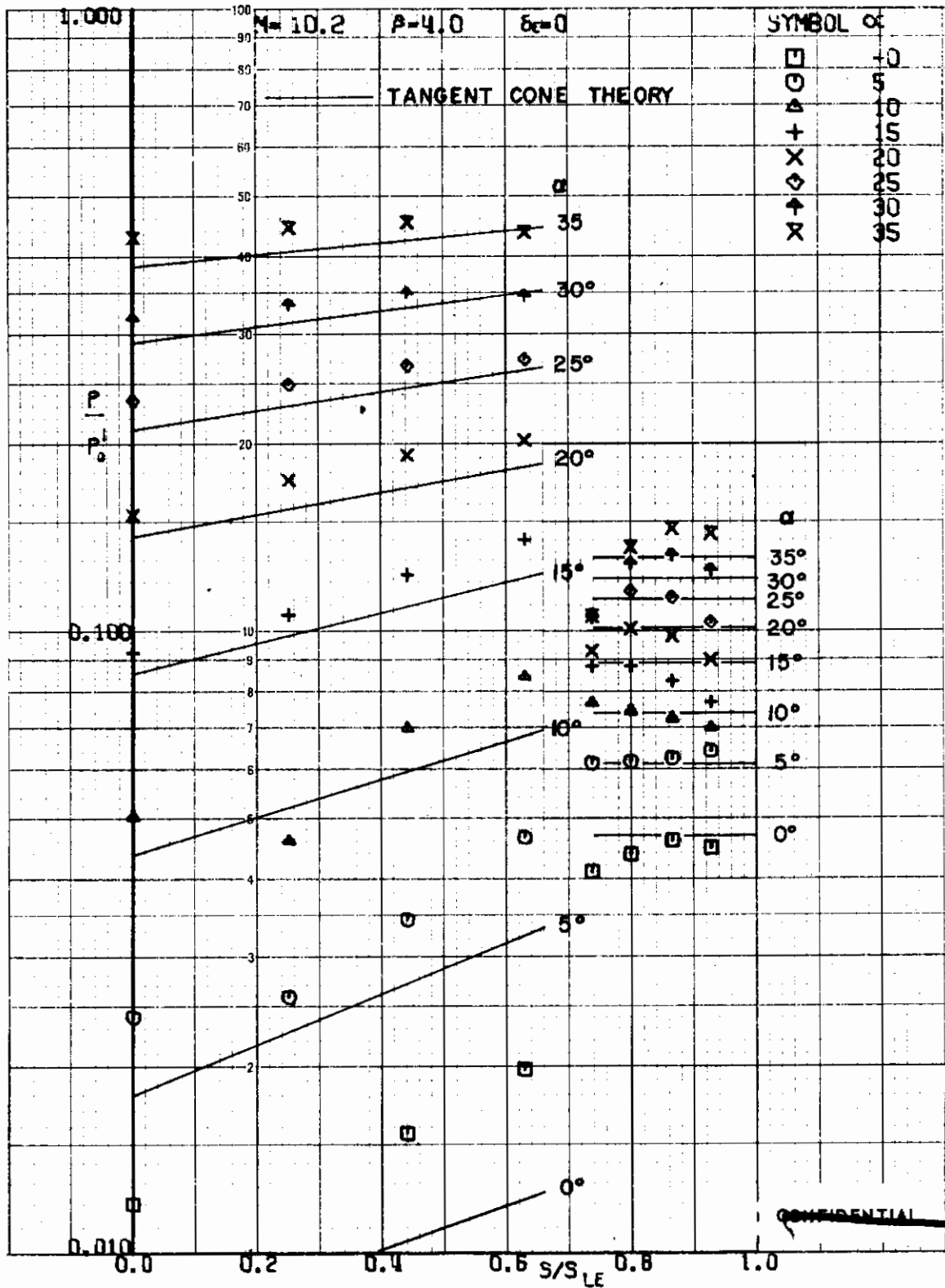
FIGURE 69 (U) TUNNEL C LOWER SURFACE SPANWISE PRESSURES AT X/L = 0.96, β=4
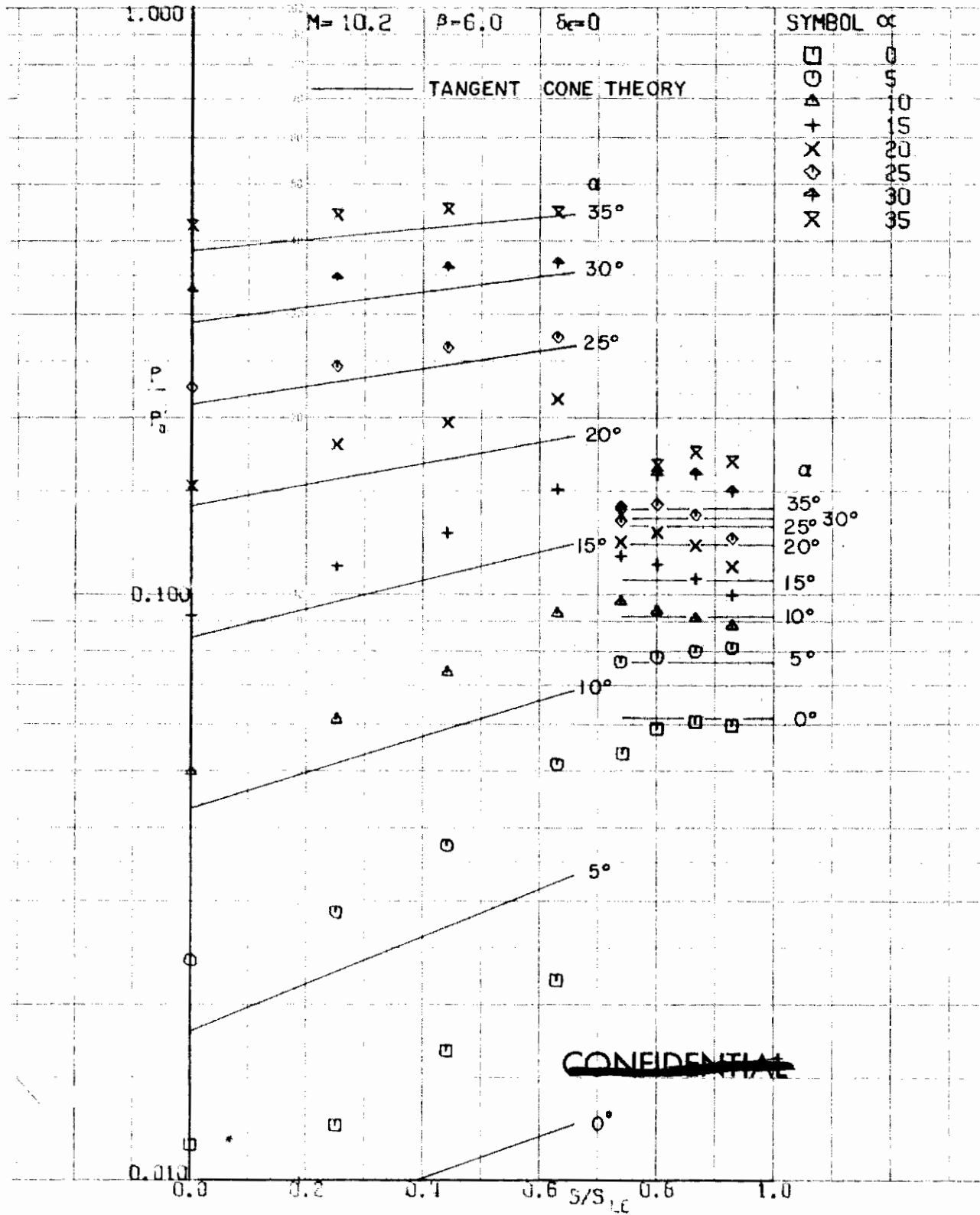
FIGURE 70 (U) TUNNEL C LOWER SURFACE SPANWISE PRESSURES AT X/L = 0.96, β=6

148

FIGURE 71 (U) TUNNEL F LOWER SURFACE SPANWISE PRESSURES AT X/L = 0.96, β=0
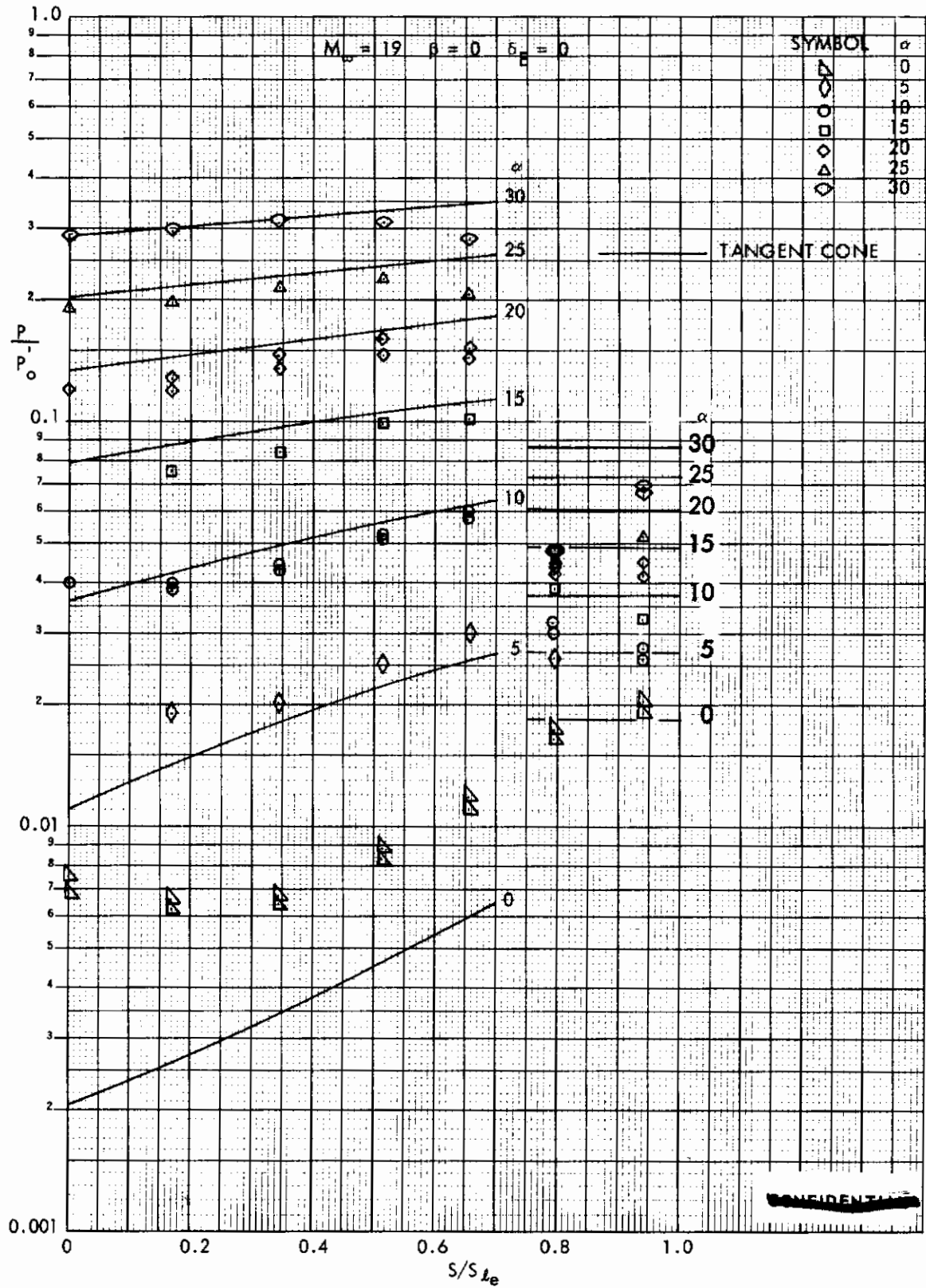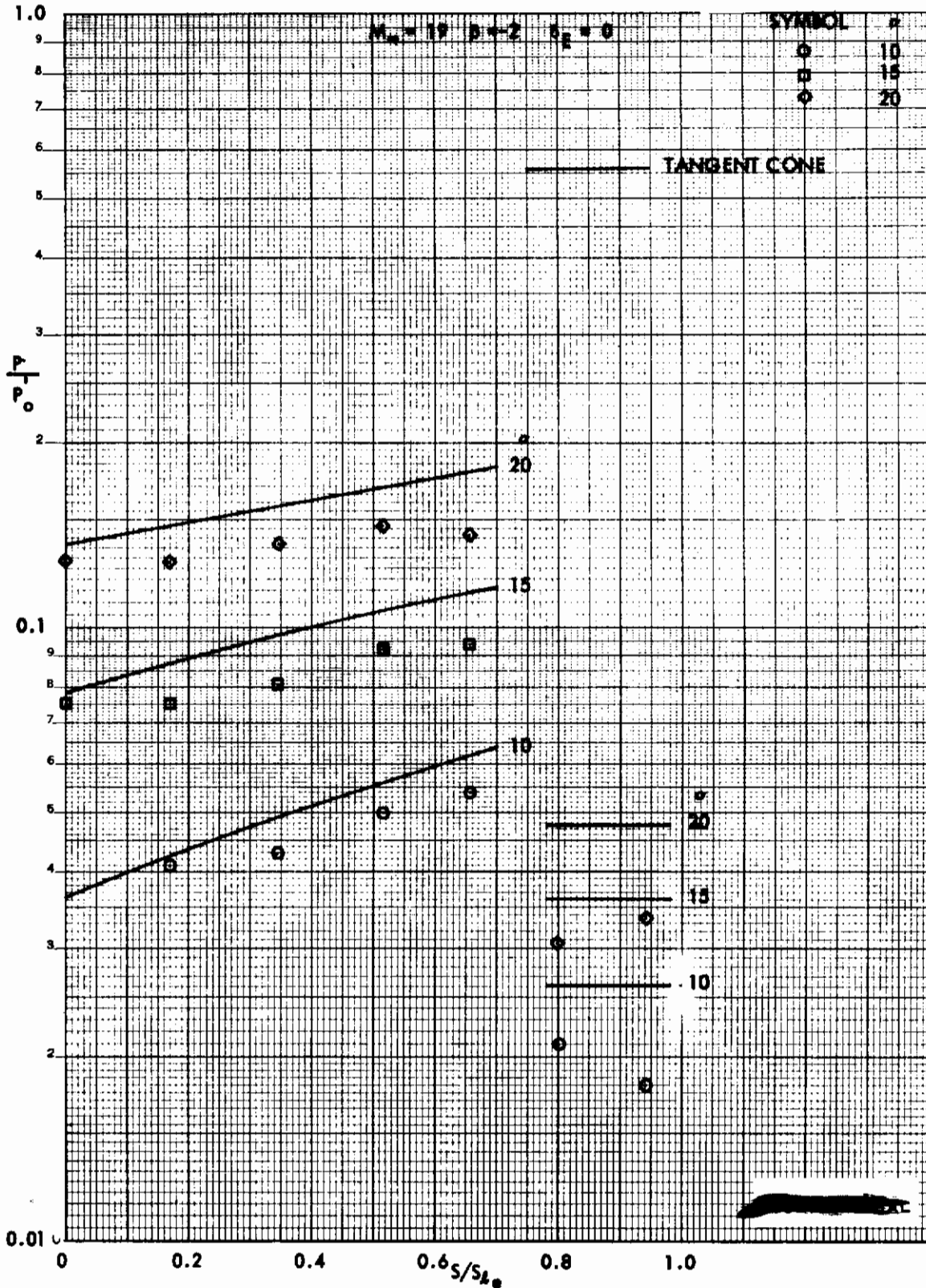
FIGURE 72 (U) TUNNEL F LOWER SURFACE SPANWISE PRESSURES AT X/L = 0.96, β=-2
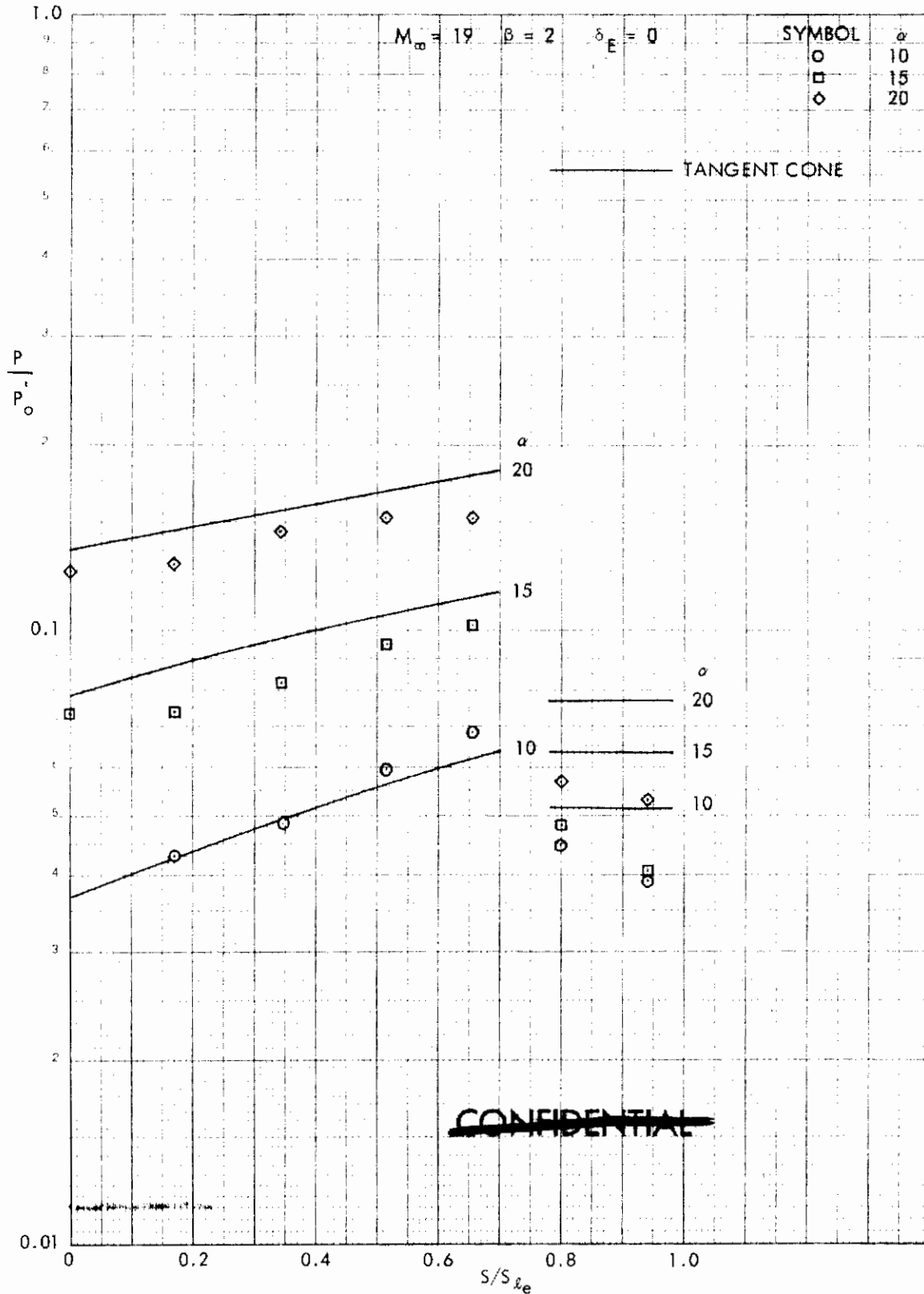
FIGURE 73 (U) TUNNEL F LOWER SURFACE SPANWISE PRESSURES AT X/L = 0.96, β=2

151
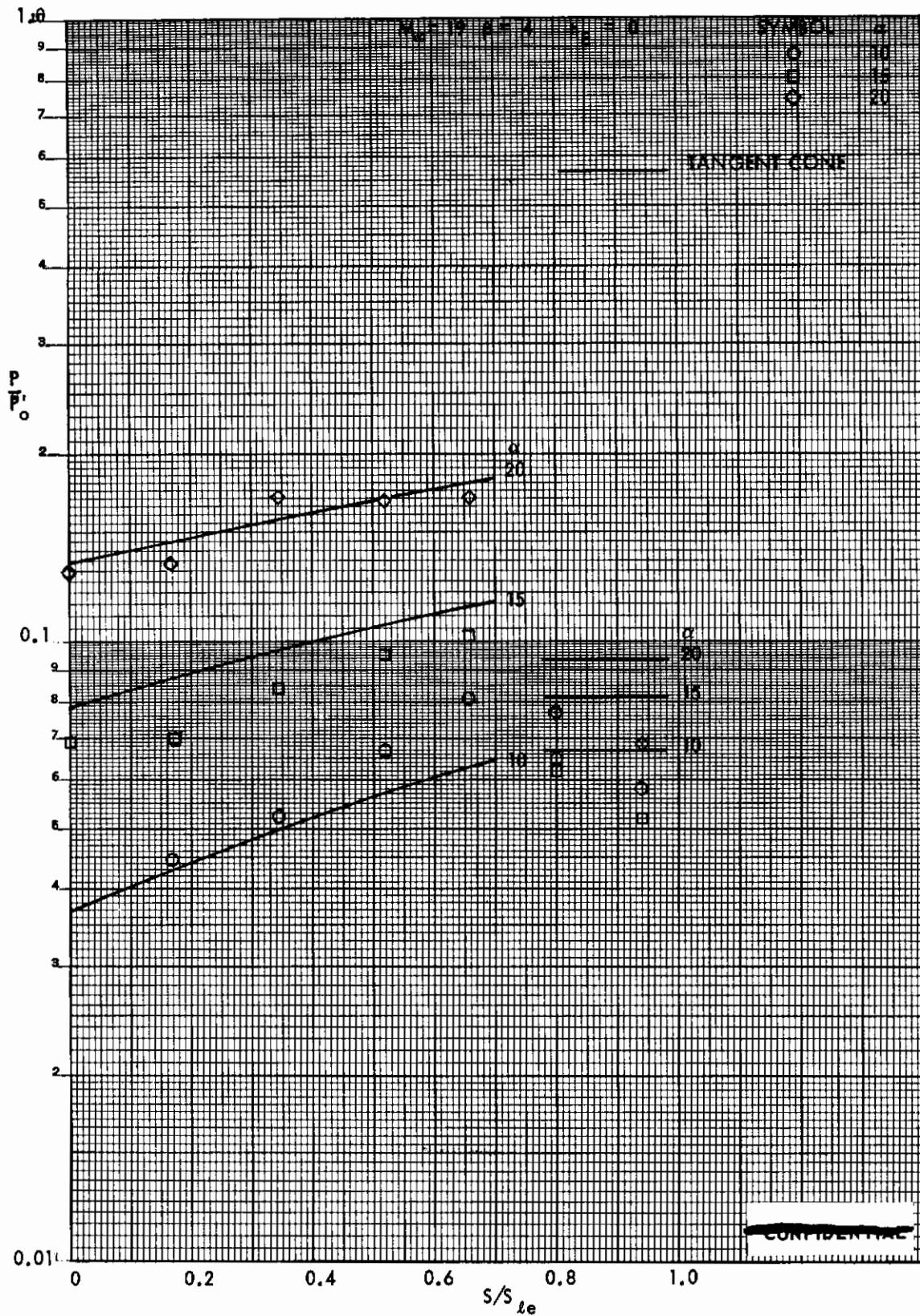
FIGURE 74   (U) TUNNEL F LOWER SURFACE SPANWISE PRESSURES AT X/L = 0.96, β=4
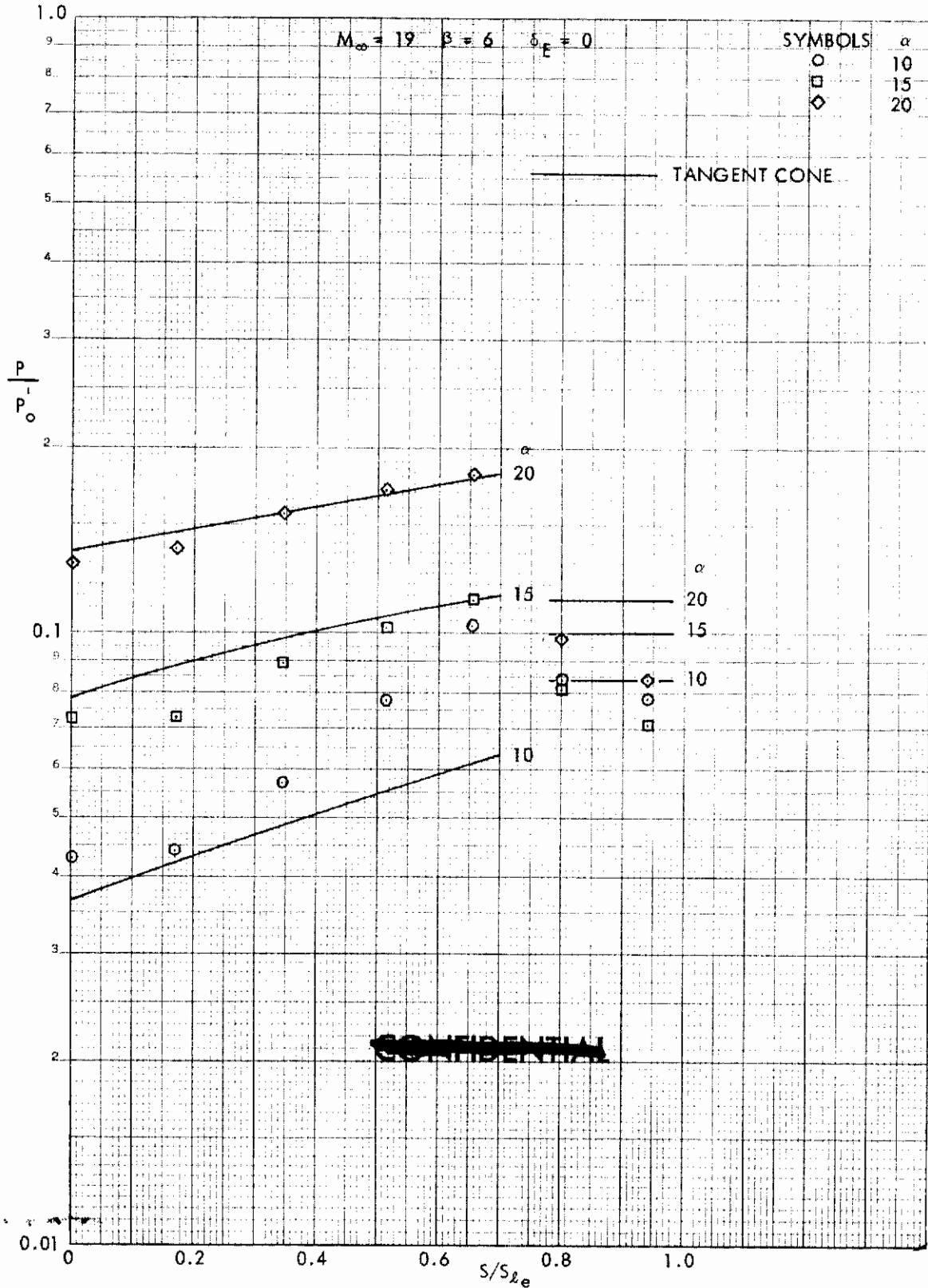
FIGURE 75 (U) TUNNEL F LOWER SURFACE SPANWISE PRESSURES AT X/L = 0.96, β=6
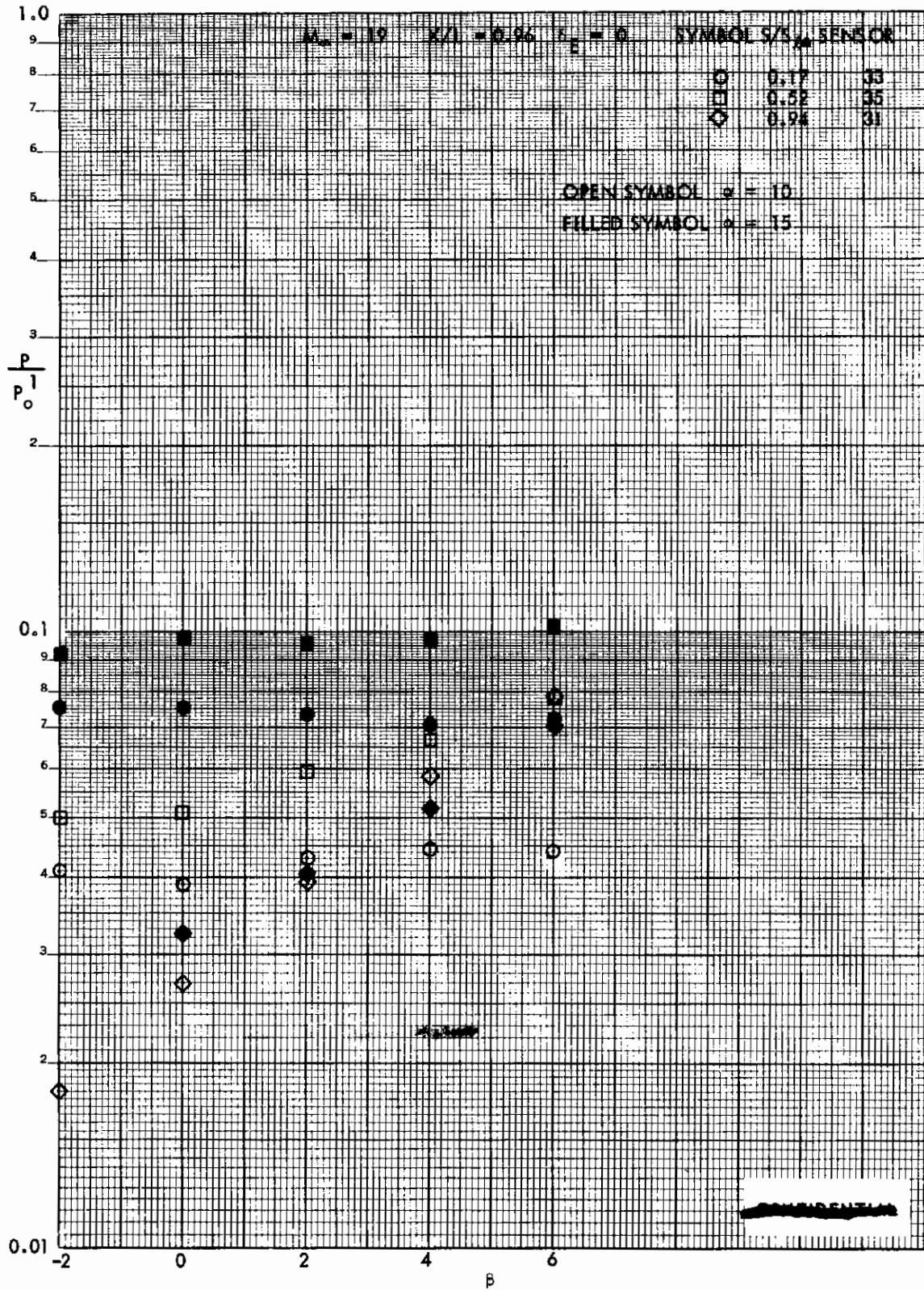
FIGURE 76 (U) EFFECT OF YAW ON LOWER SURFACE PRESSURES AT X/L = 0.96
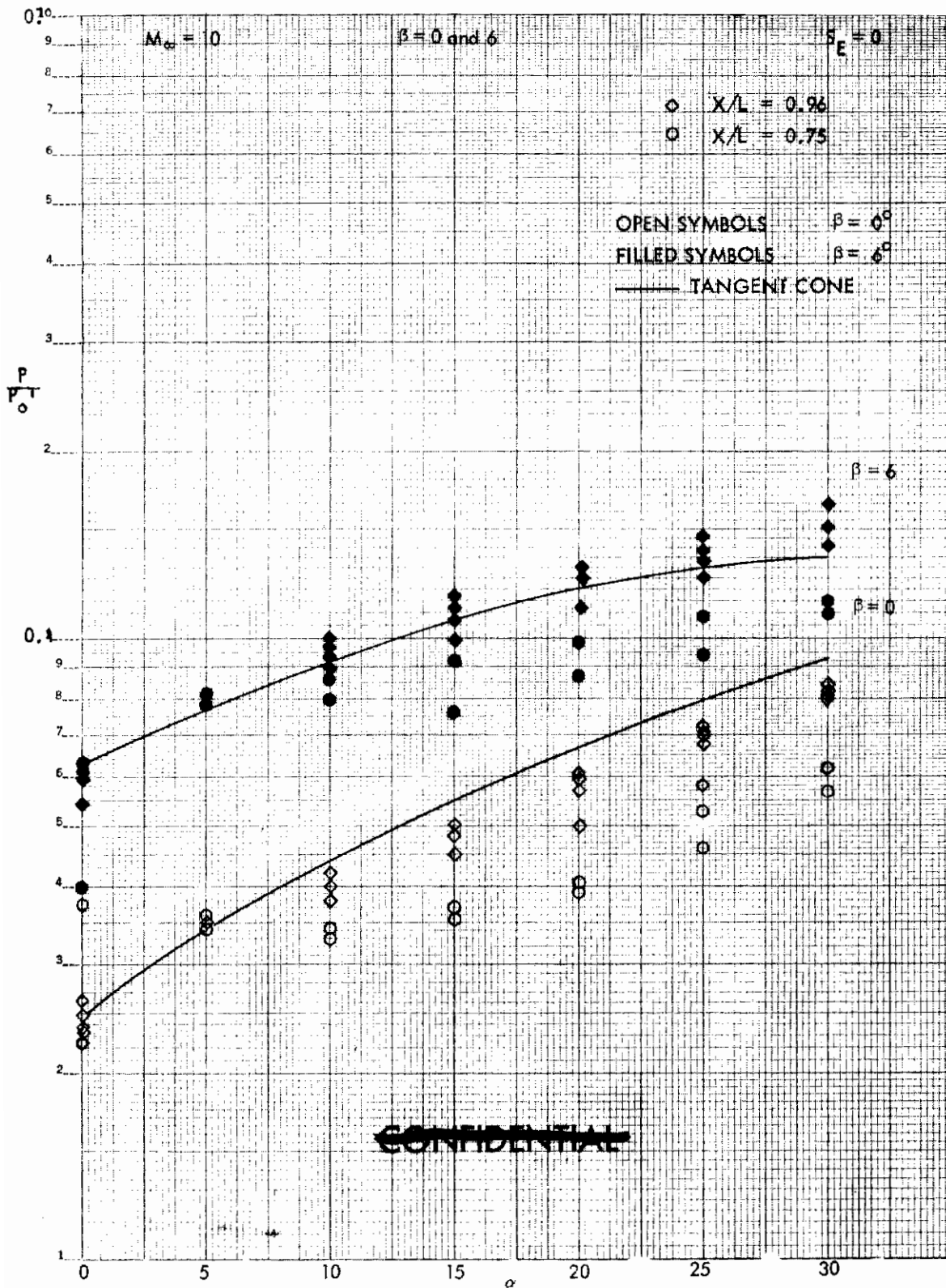
FIGURE 77 (C) TUNNEL C AFT LOWER COMPRESSION SURFACE PRESSURE
VERSUS ANGLE OF ATTACK
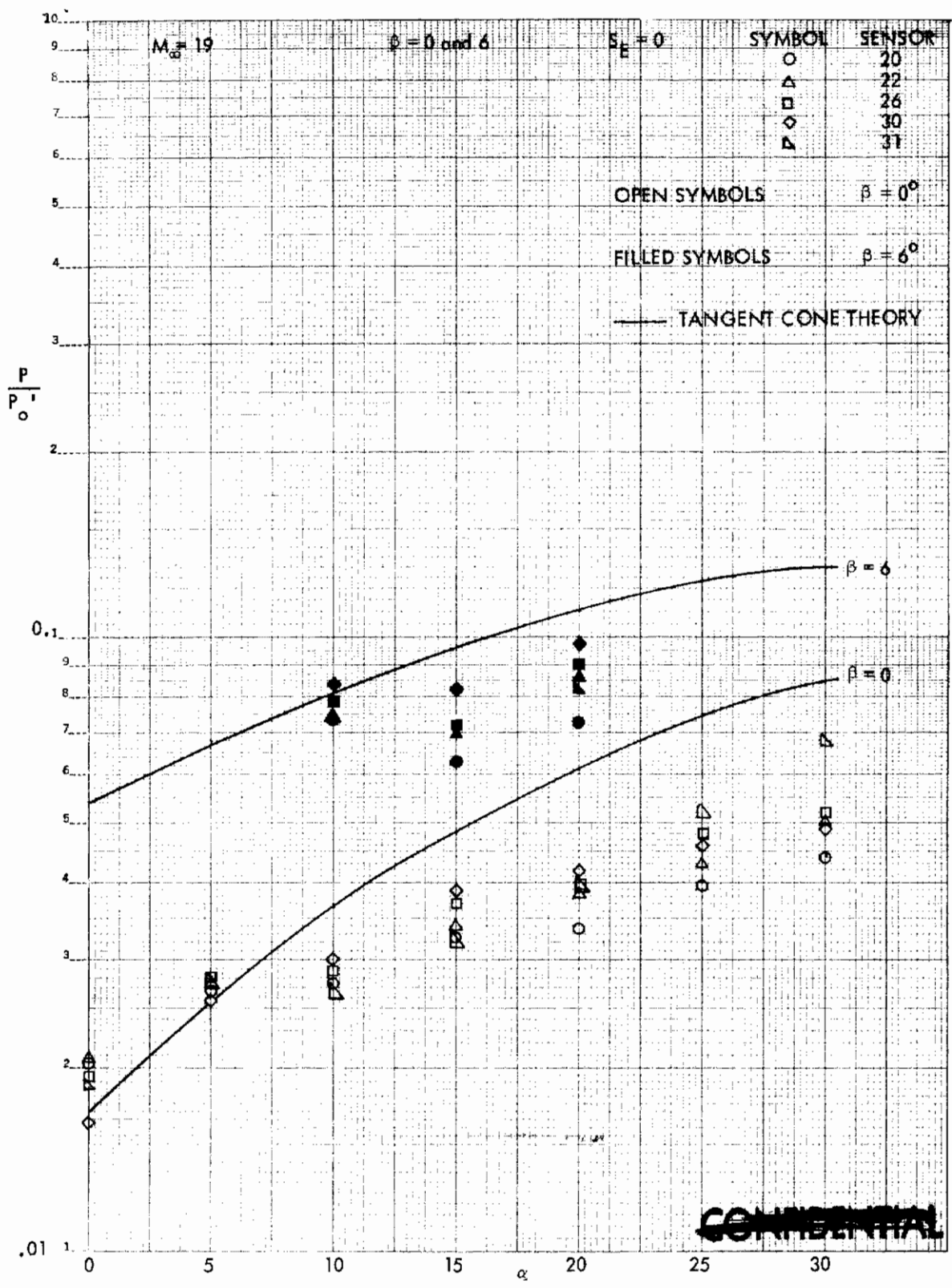
155

FIGURE 78 (U) TUNNEL F AFT LOWER COMPRESSION SURFACE PRESSURE
VERSUS ANGLE OF ATTACK

156
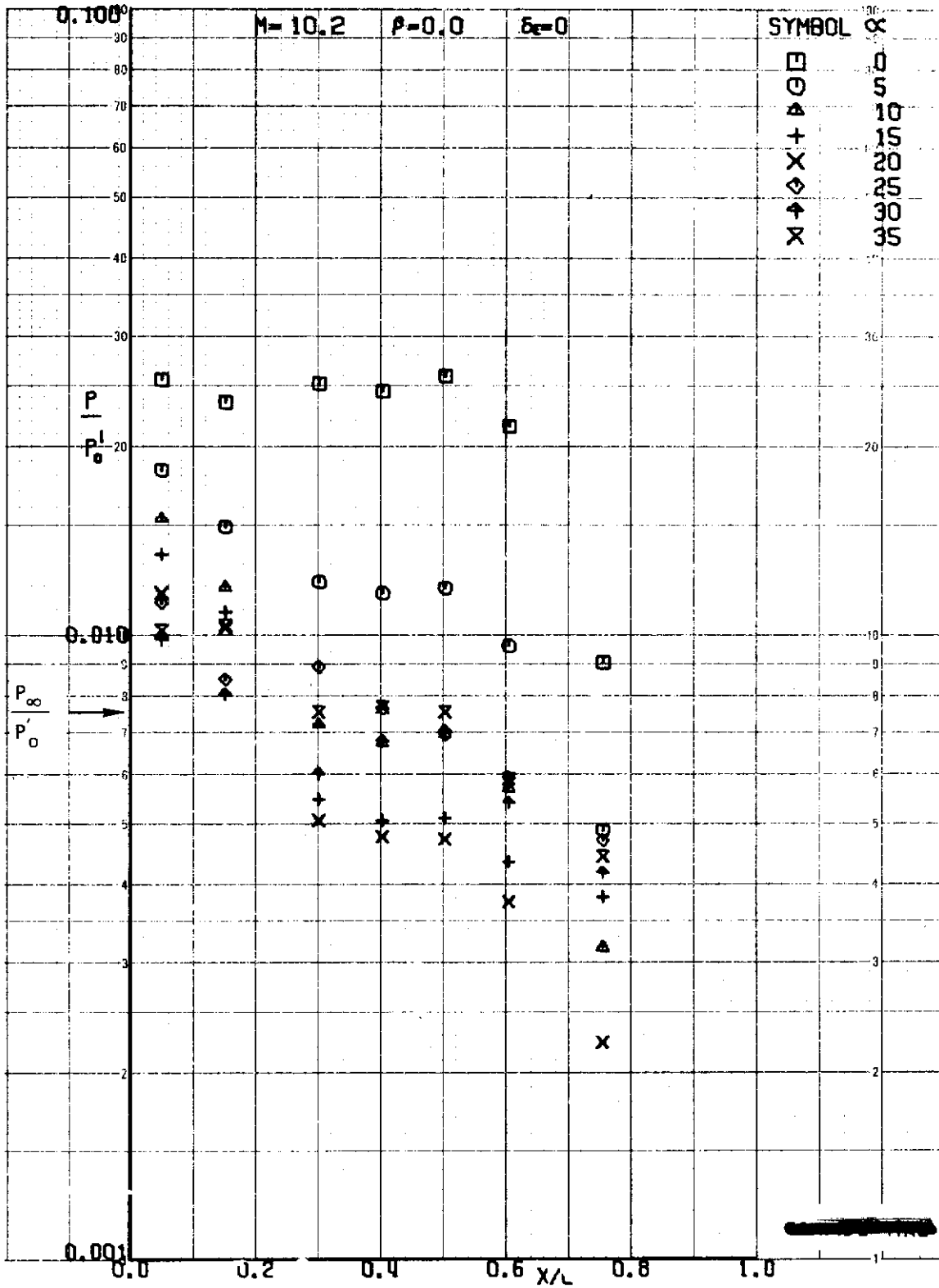
FIGURE 79 (U) TUNNEL C UPPER SURFACE CENTERLINE PRESSURES, β=0
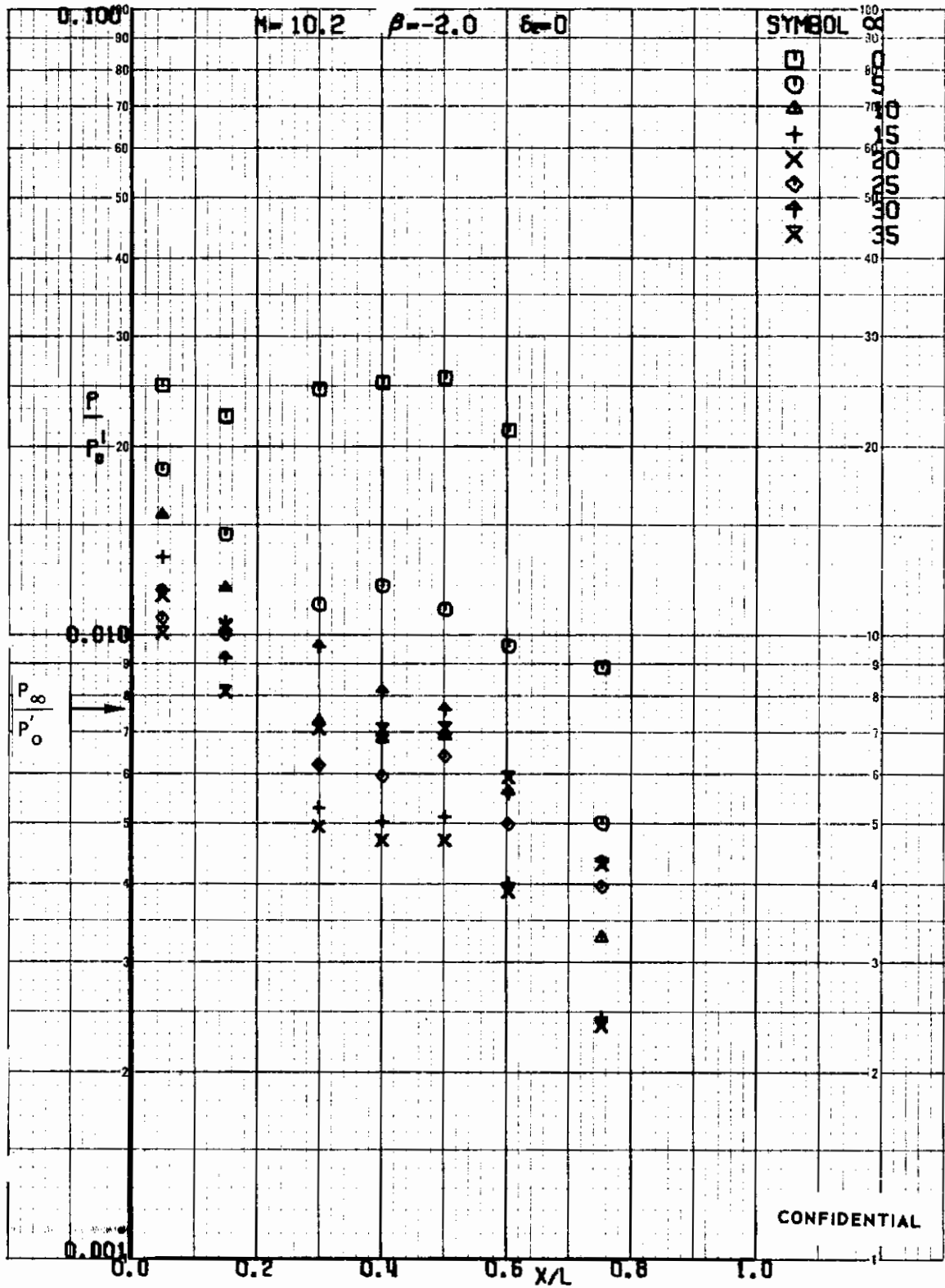
FIGURE 80 (U) TUNNEL C UPPER SURFACE CENTERLINE PRESSURES, β=-2
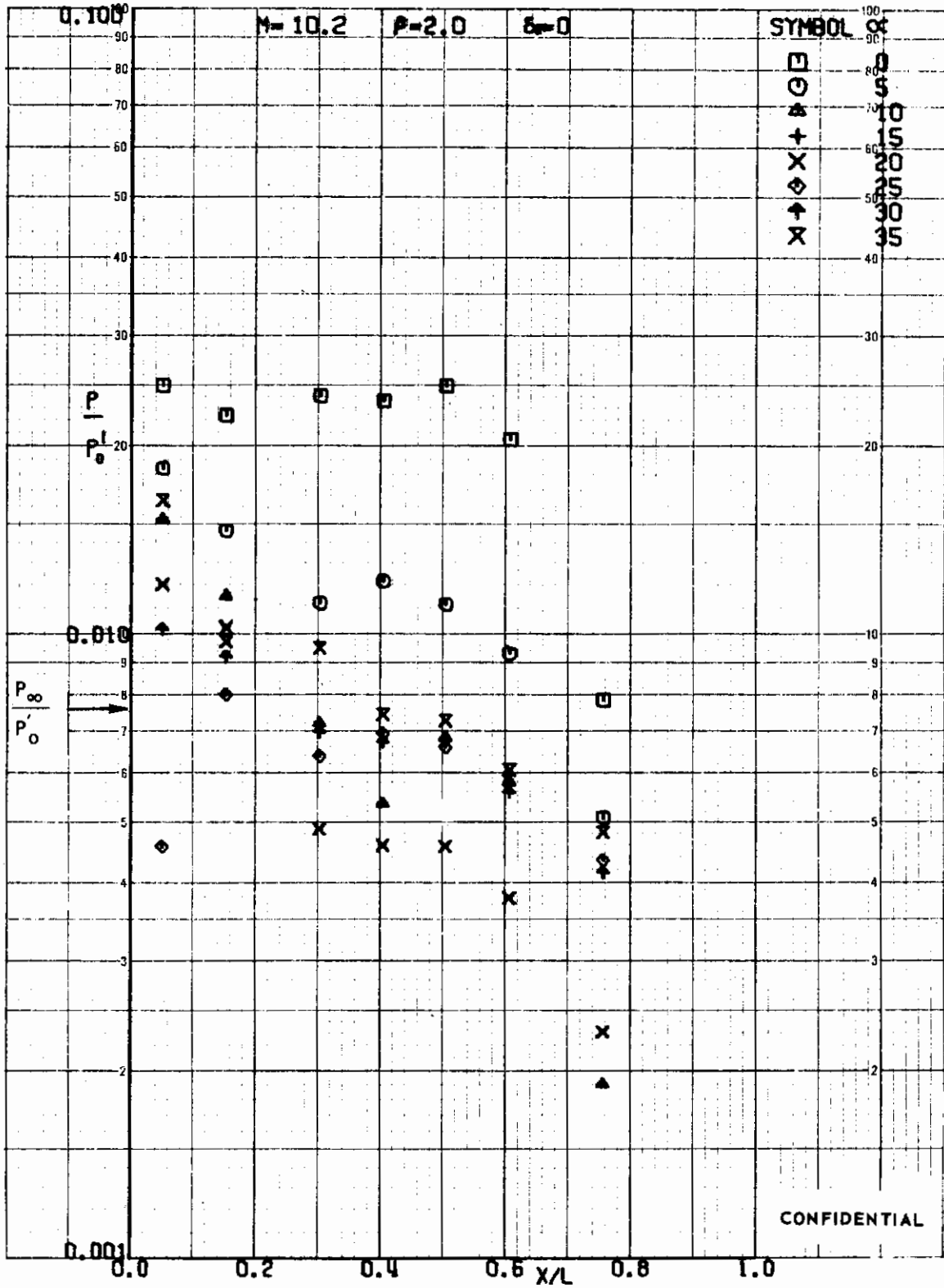
FIGURE 81. (U) TUNNEL C UPPER SURFACE CENTERLINE PRESSURES, β=2

159
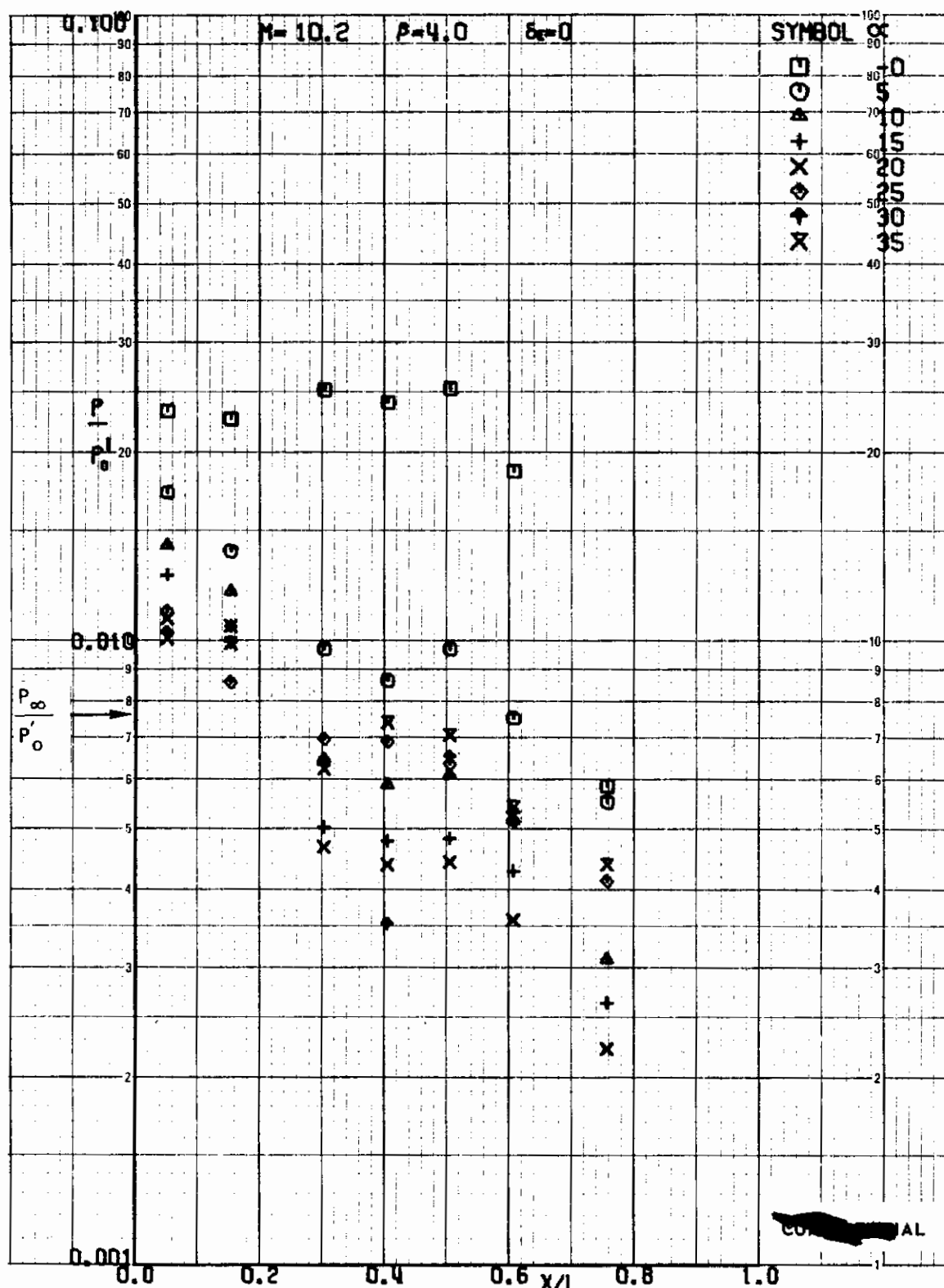
FIGURE 82 (U) TUNNEL C UPPER SURFACE CENTERLINE PRESSURES, β=4

160
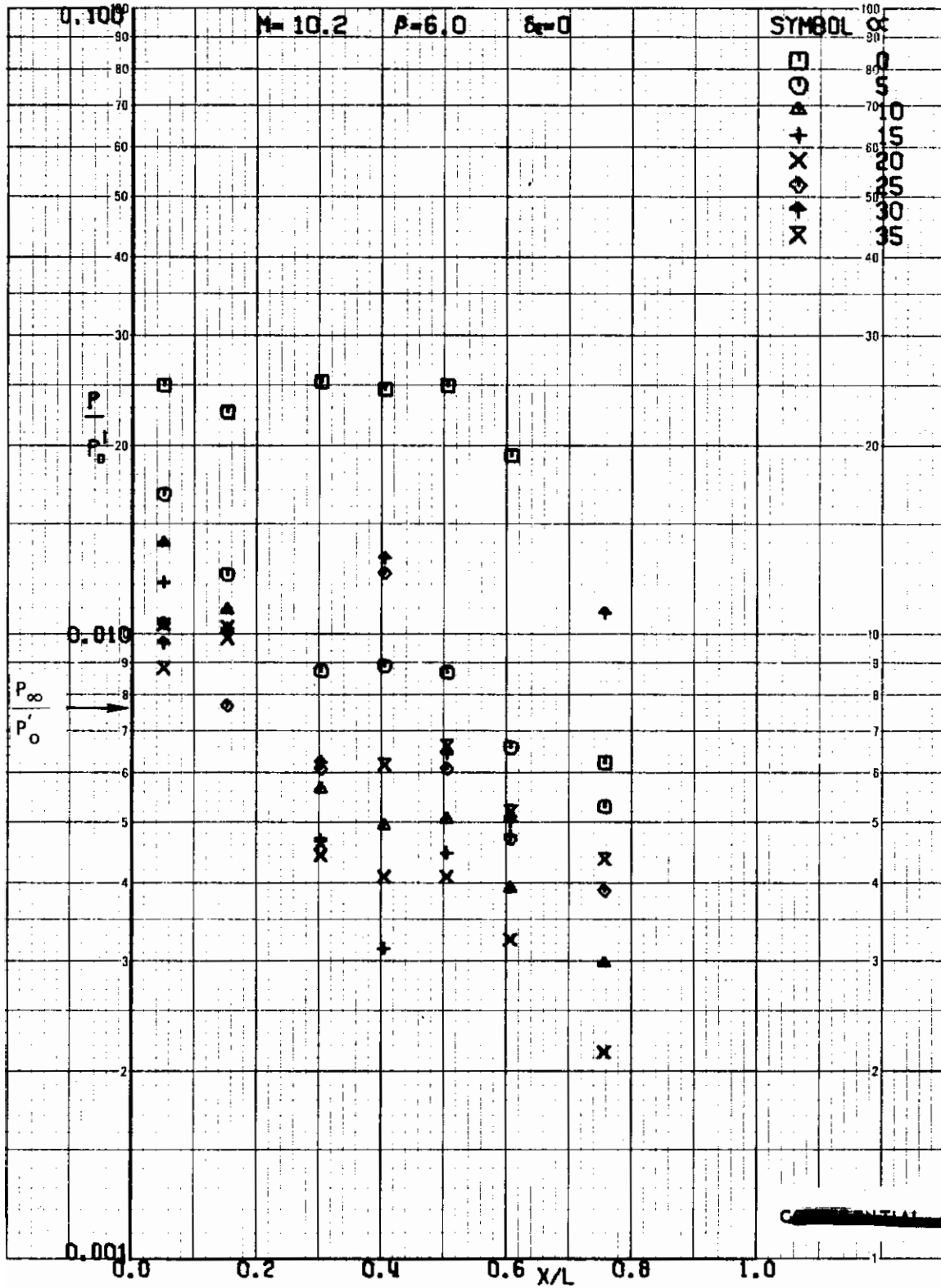
FIGURE 83   (U) TUNNEL C UPPER SURFACE CENTERLINE PRESSURES, β=6
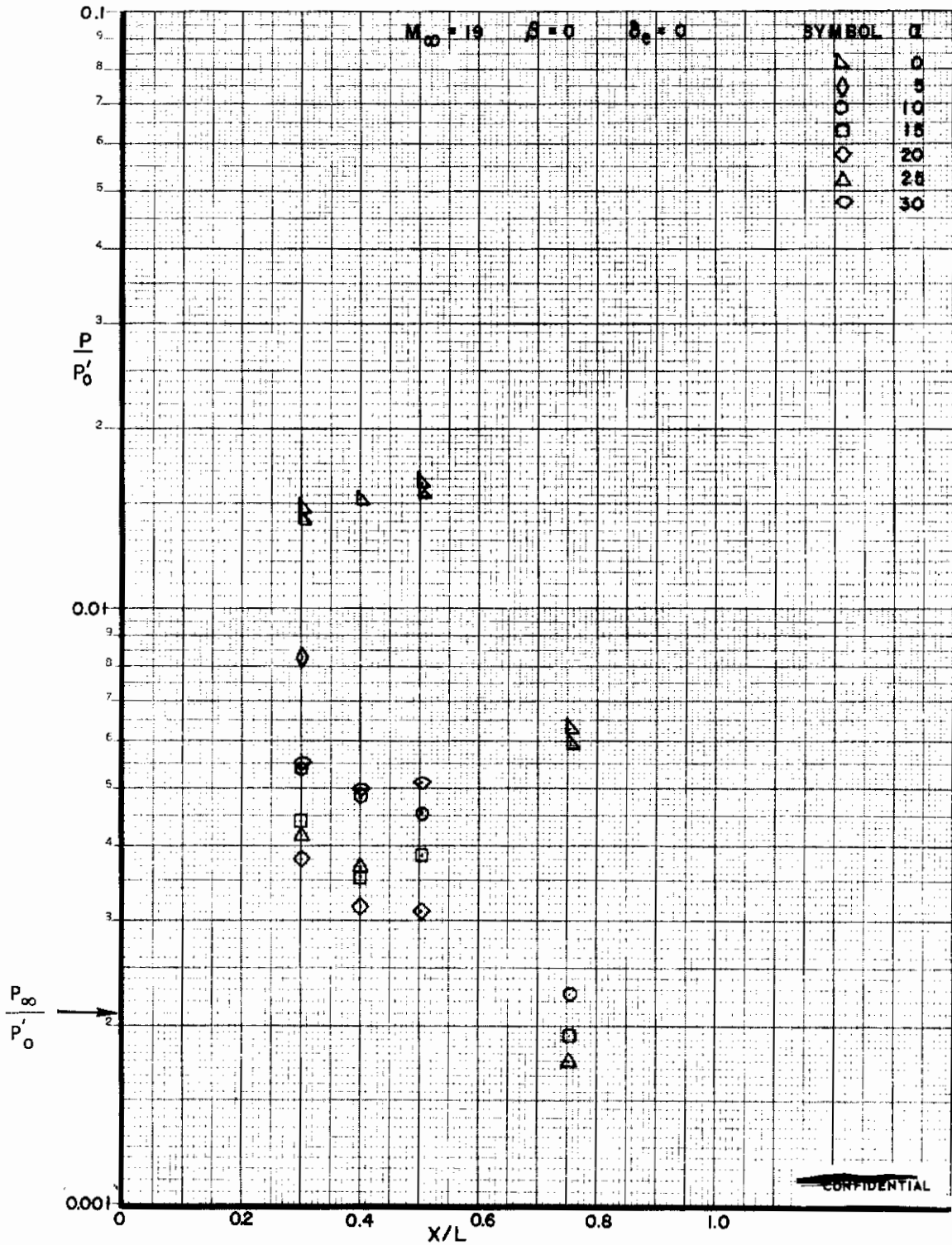
FIGURE 84 (U) TUNNEL F UPPER SURFACE CENTERLINE PRESSURES, β=0
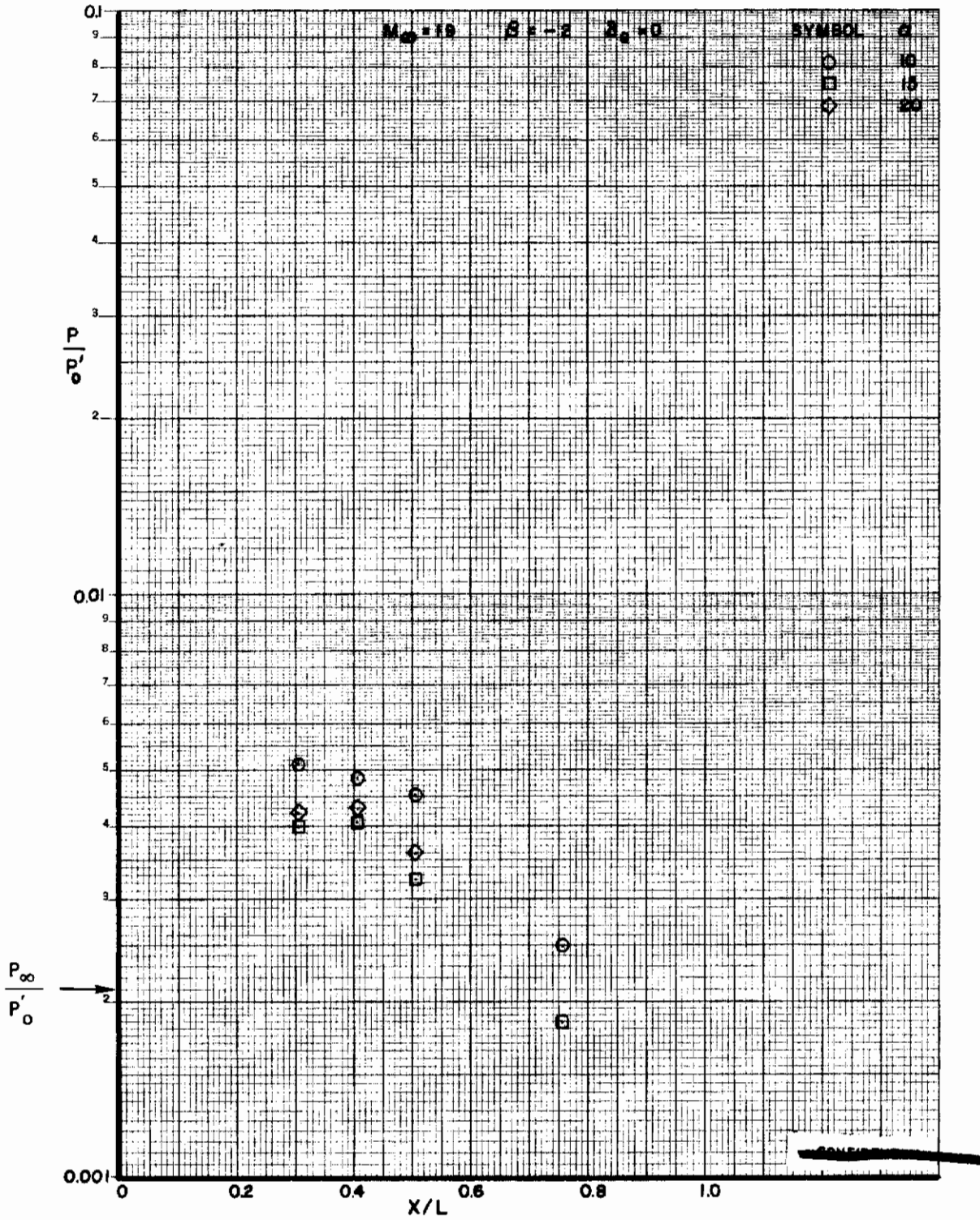
FIGURE 85 (U) TUNNEL F UPPER SURFACE CENTERLINE PRESSURES, β=-2
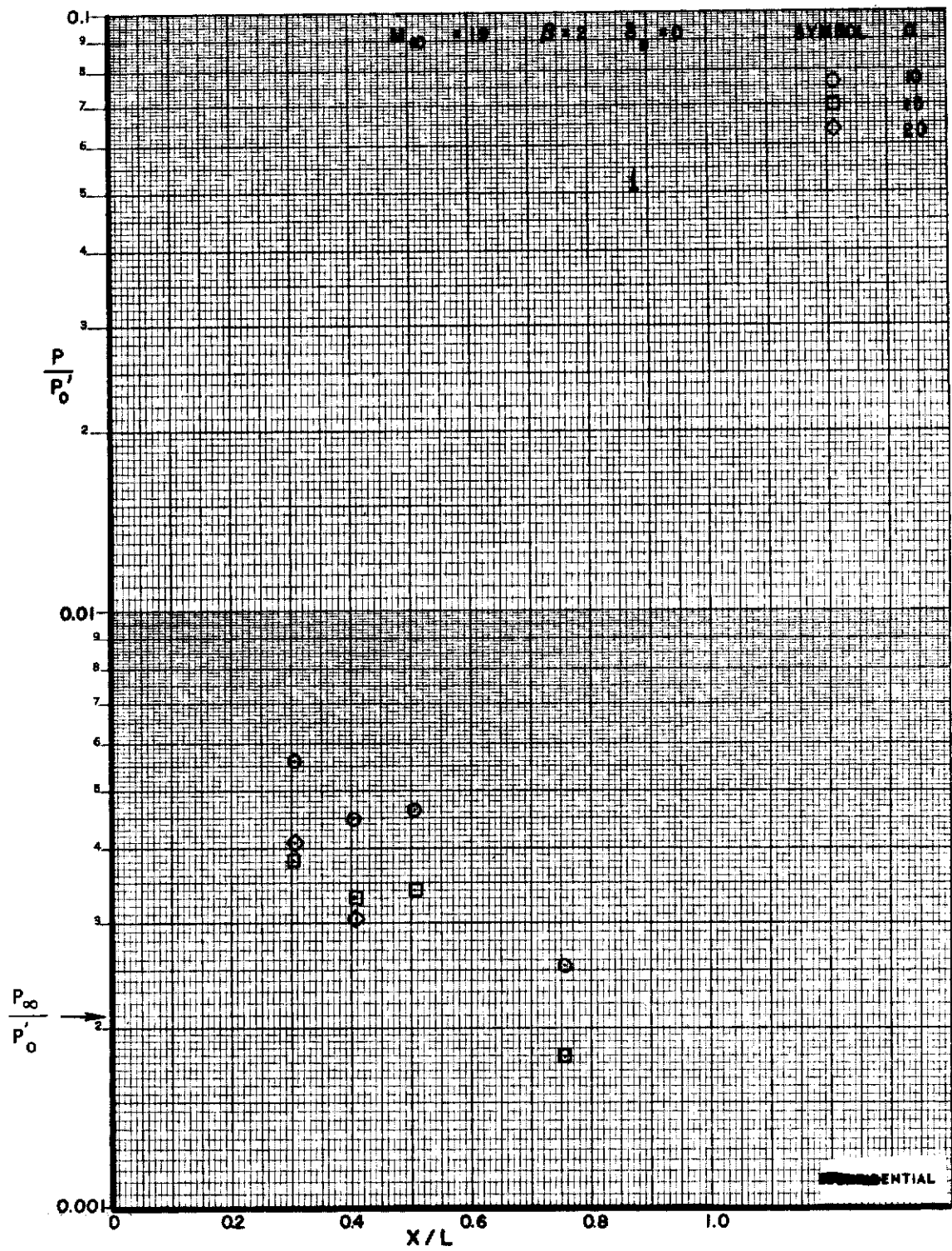
FIGURE 86   (U) TUNNEL F UPPER SURFACE CENTERLINE PRESSURES, β=2

164
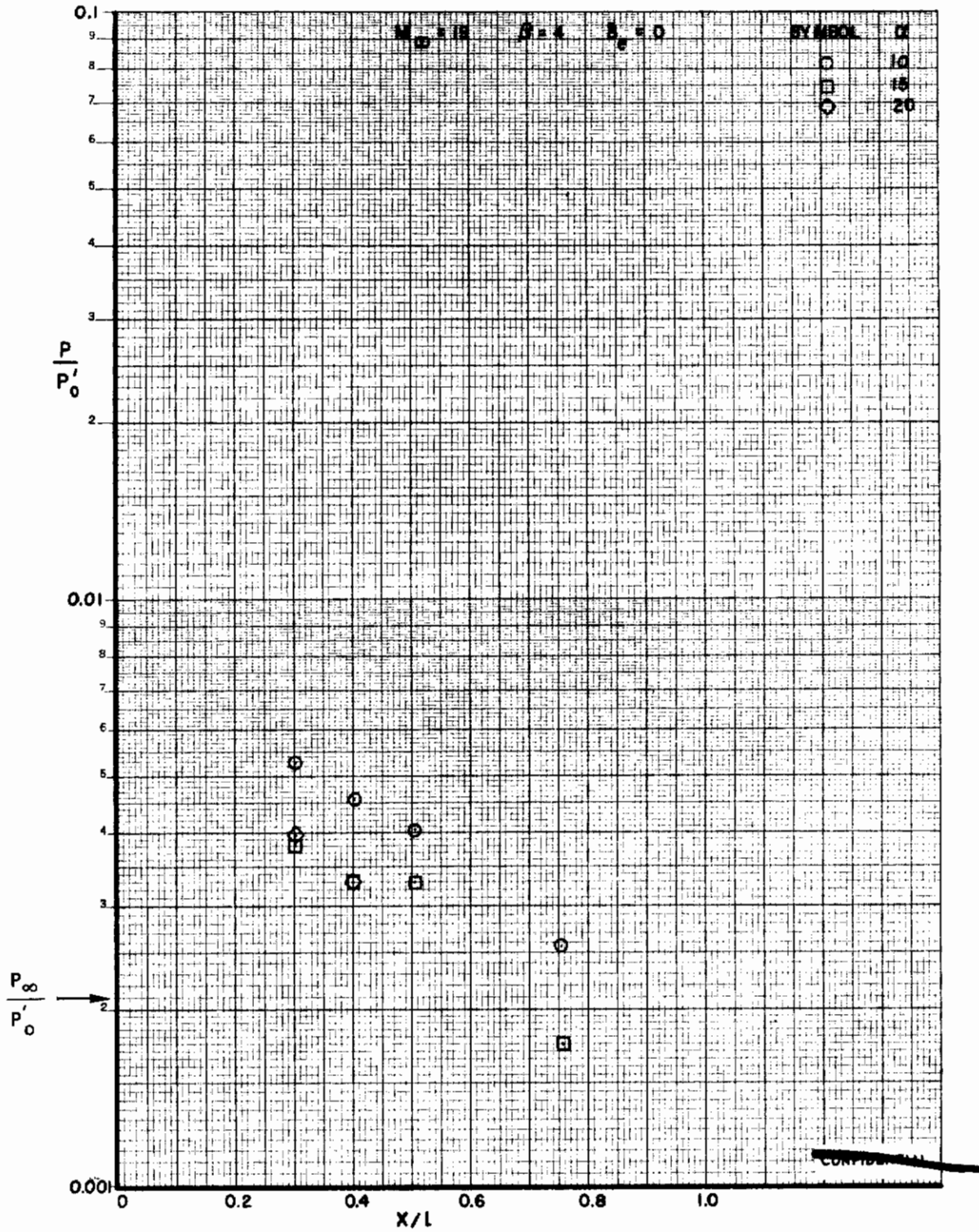
FIGURE 87 (U) TUNNEL F UPPER SURFACE CENTERLINE PRESSURES, β=4

165
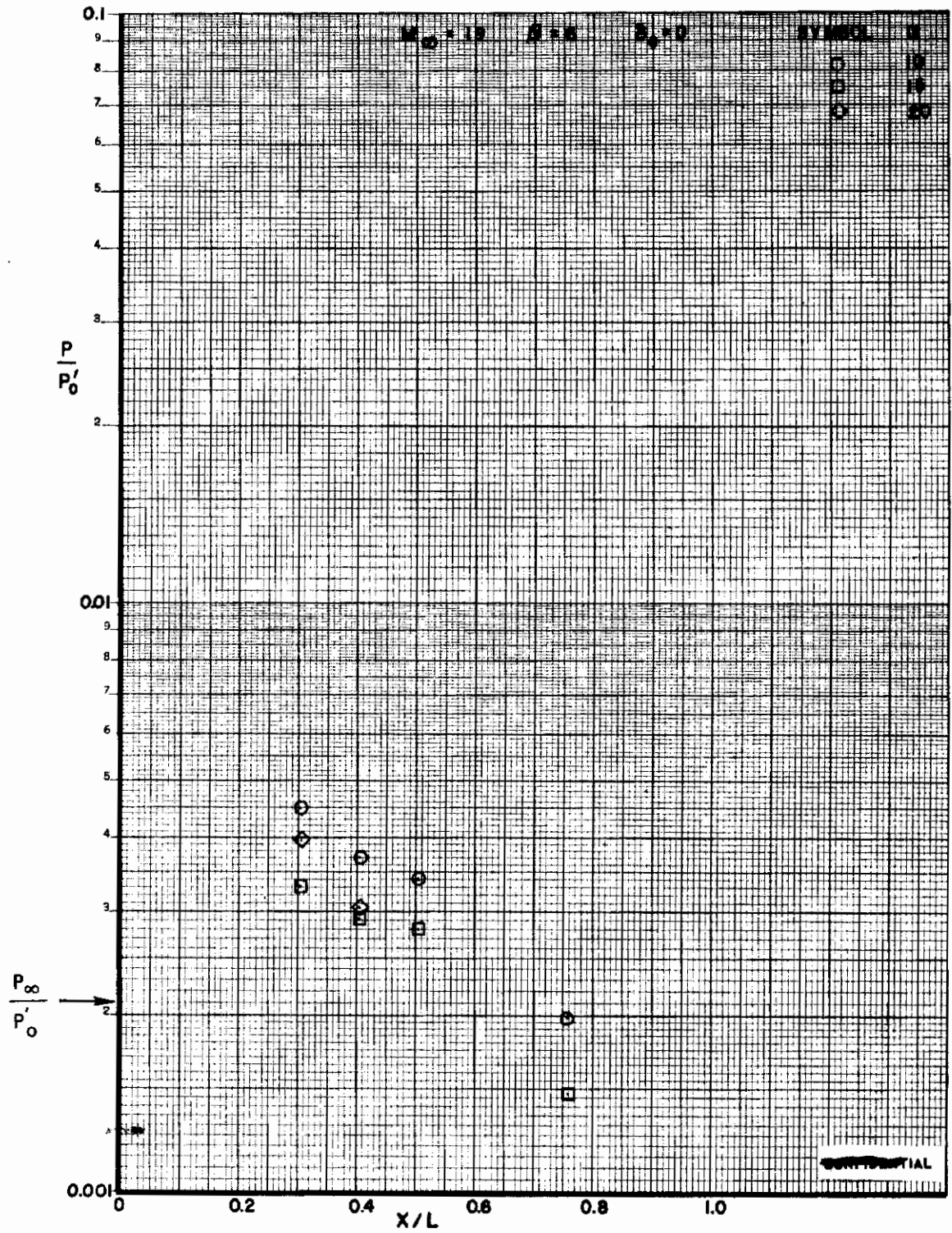
FIGURE 88 (U) TUNNEL F UPPER SURFACE CENTERLINE PRESSURES, β=6
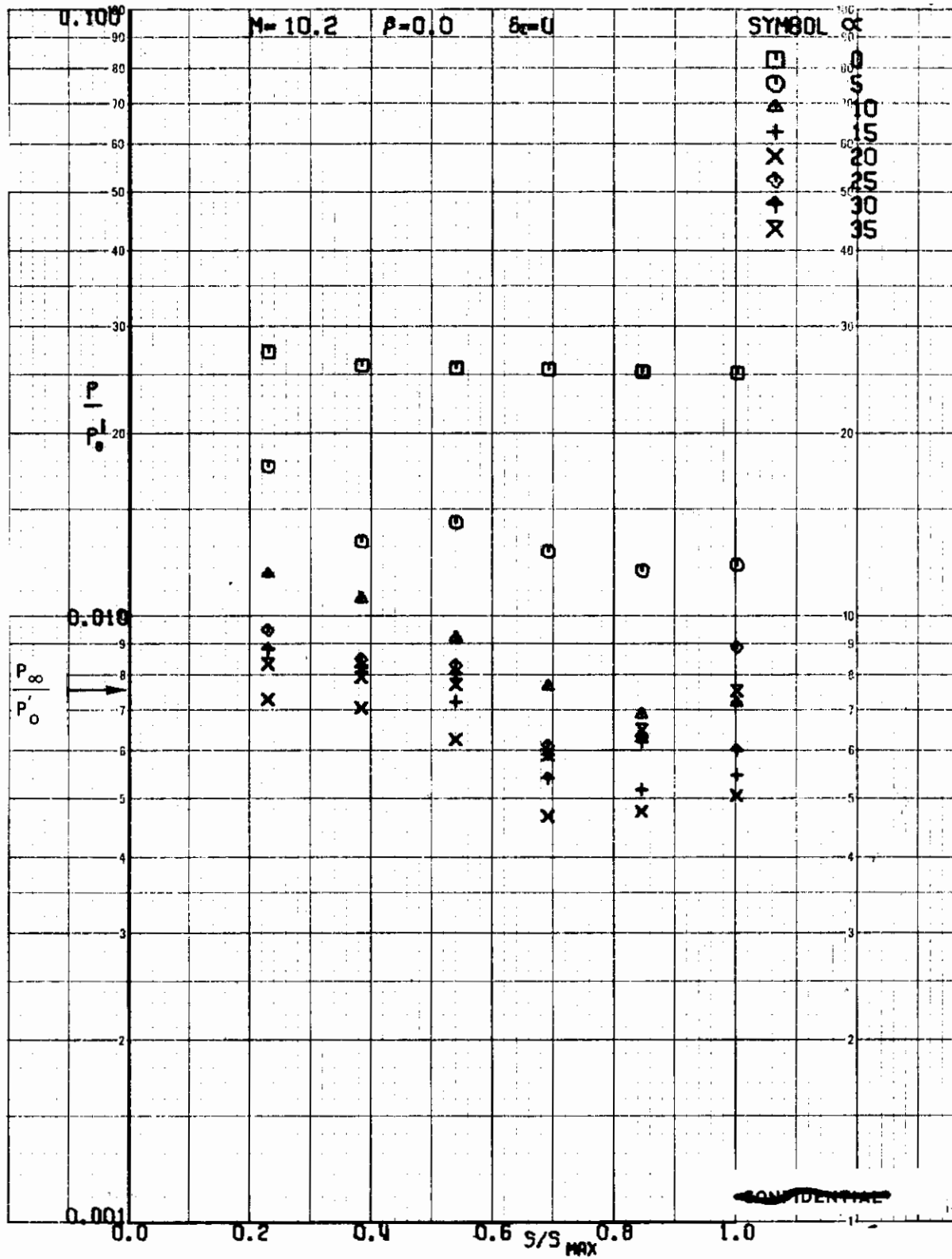
FIGURE 89 (U) TUNNEL C UPPER SURFACE SPANWISE PRESSURES AT X/L = 0.30, β=0
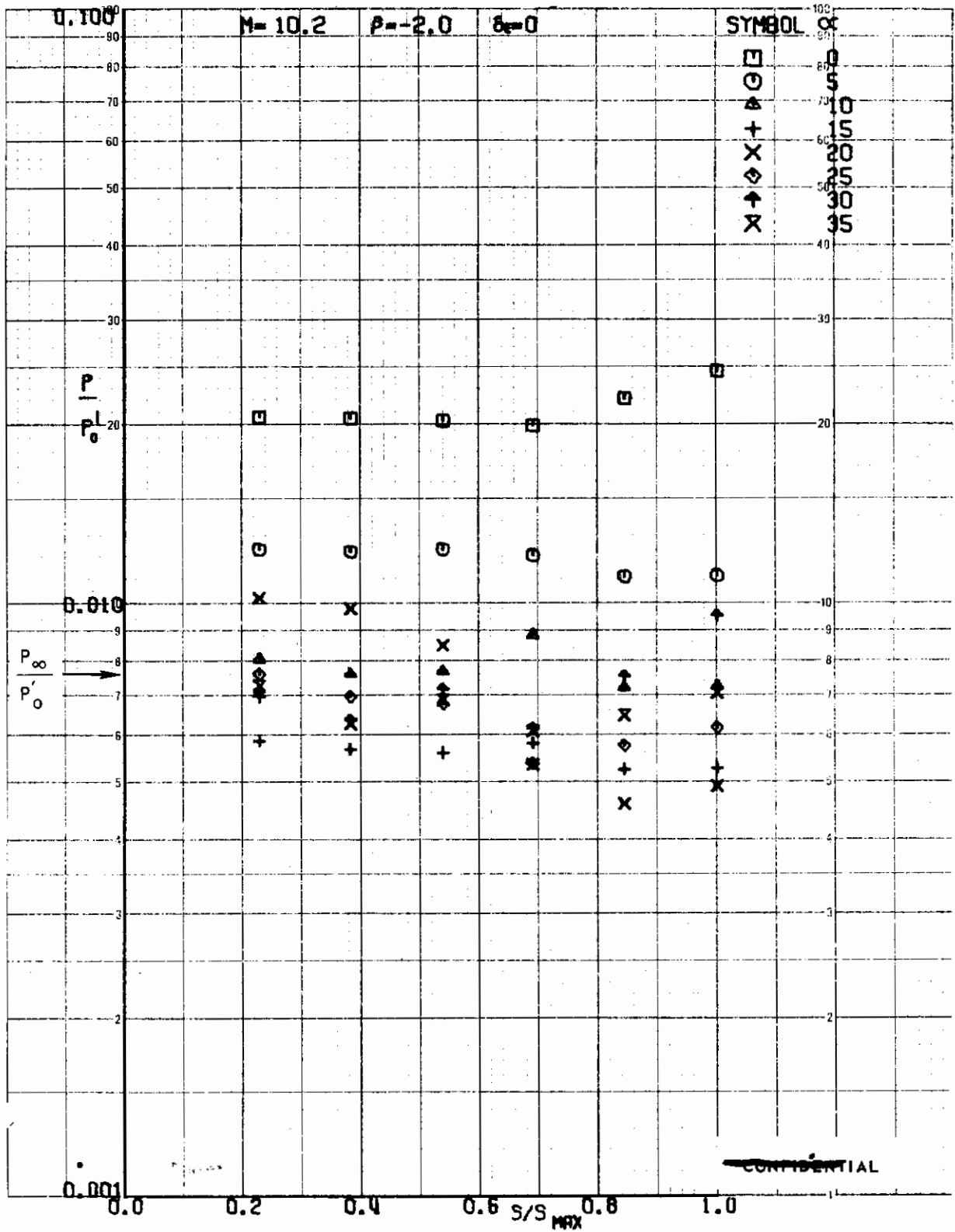
FIGURE 90   (U) TUNNEL C UPPER SURFACE SPANWISE PRESSURES AT X/L = 0.30, β=-2
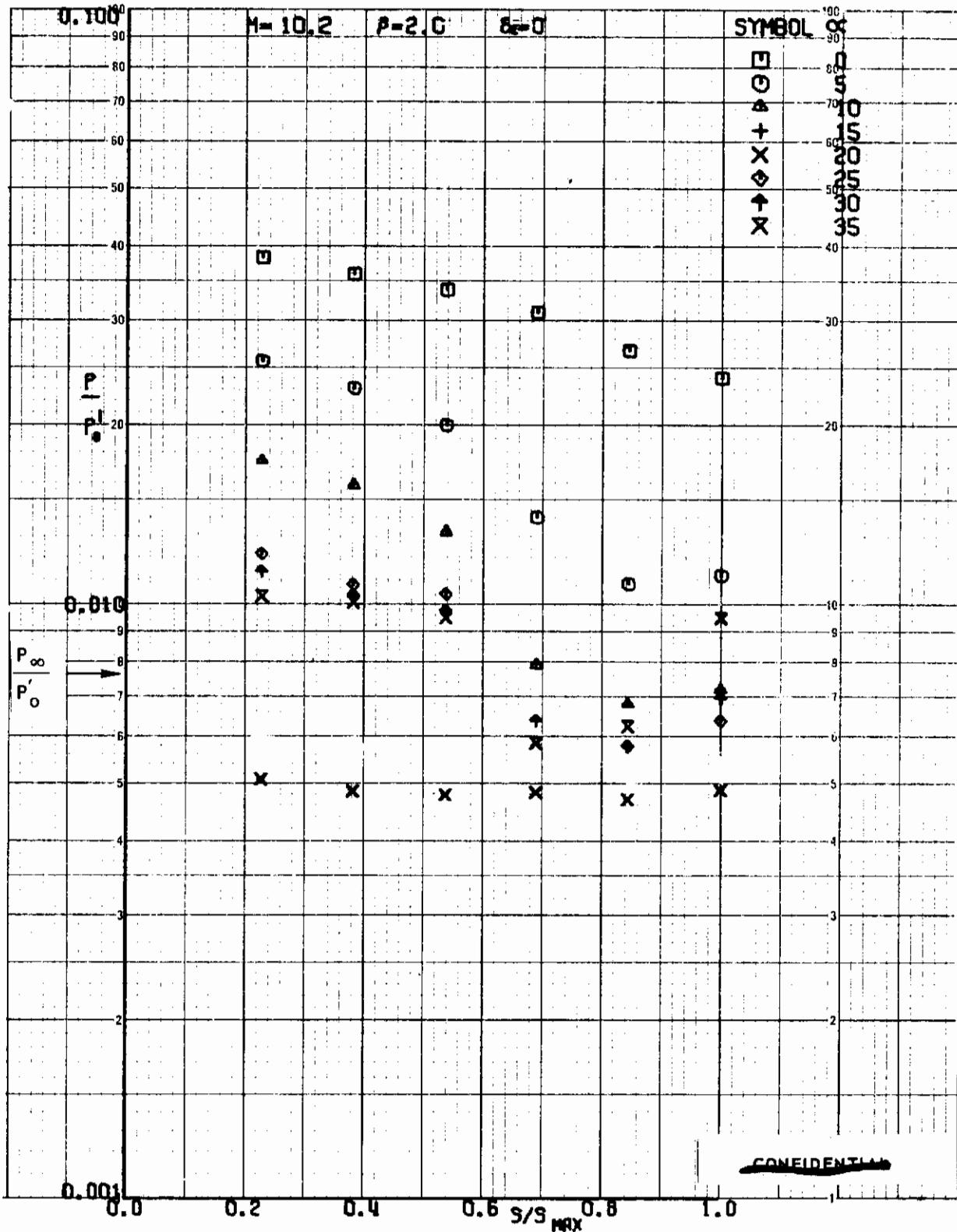
FIGURE 91 (U) TUNNEL C UPPER SURFACE SPANWISE PRESSURES AT X/L = 0.30, β=2

169
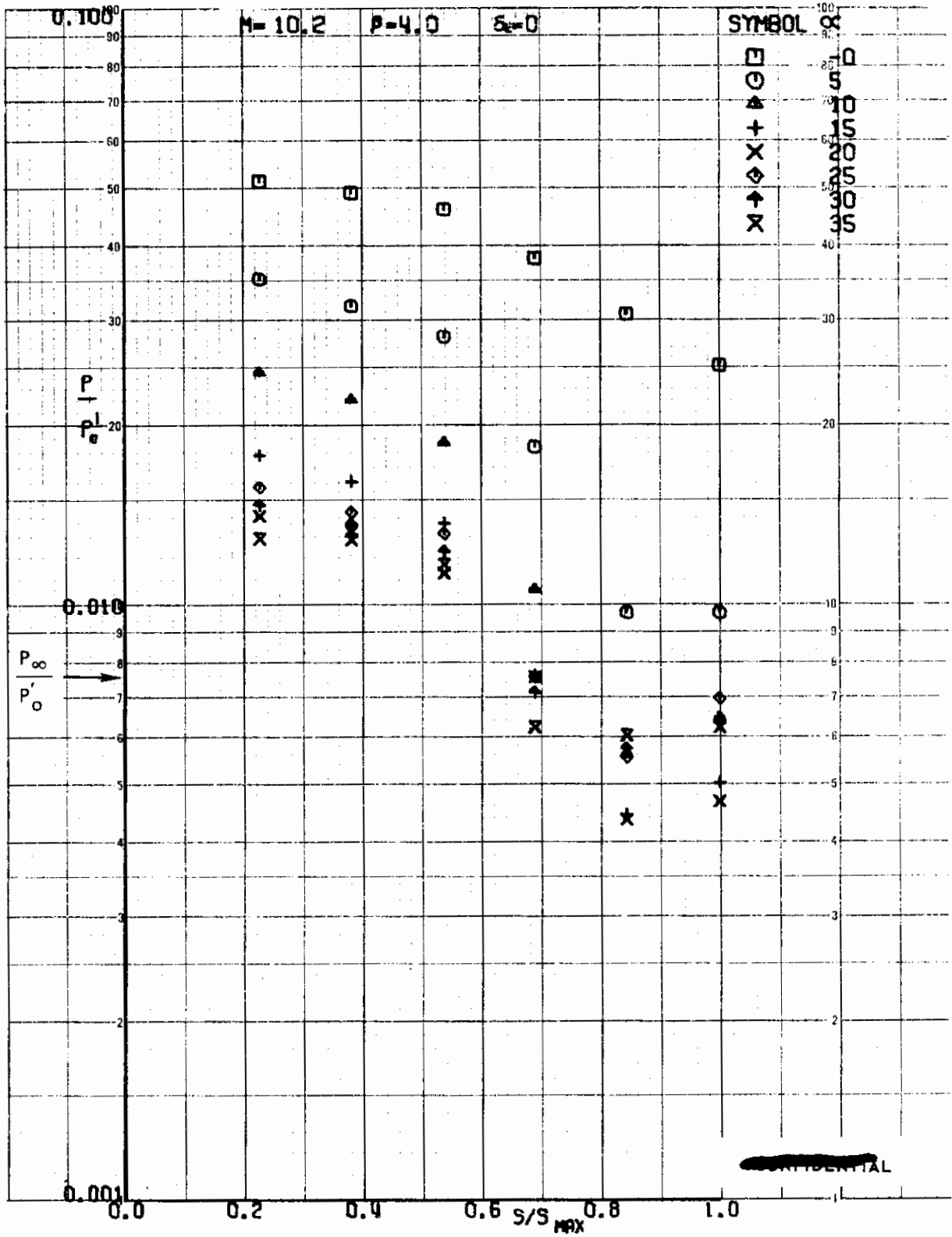
FIGURE 92 (U) TUNNEL C UPPER SURFACE SPANWISE PRESSURES AT X/L = 0.30, β=4

170
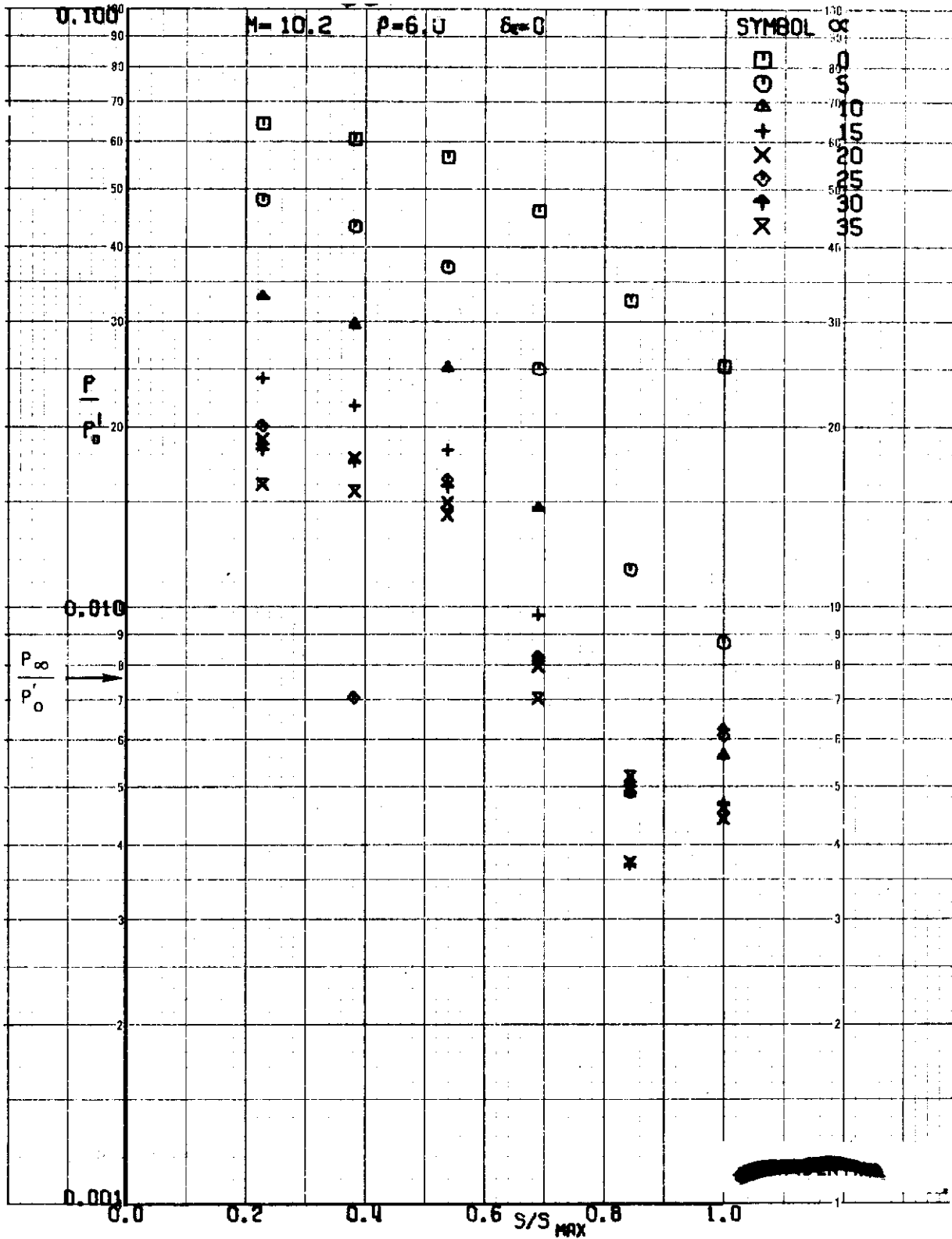
FIGURE 93 (U) TUNNEL C UPPER SURFACE SPANWISE PRESSURES AT X/L = 0.30, β=6

171
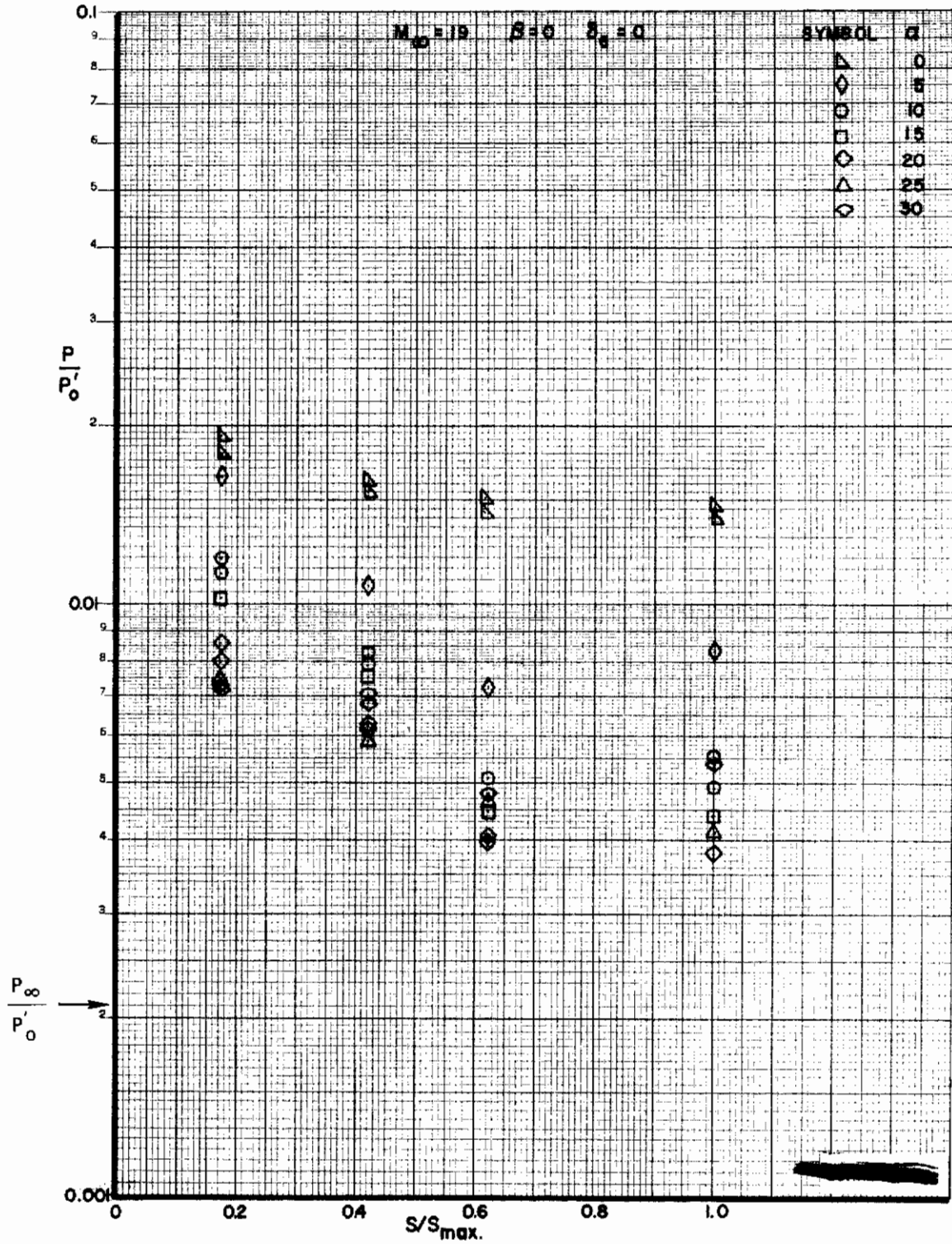
FIGURE 94 (U) TUNNEL F UPPER SURFACE SPANWISE PRESSURES AT X/L = 0.30, β=0
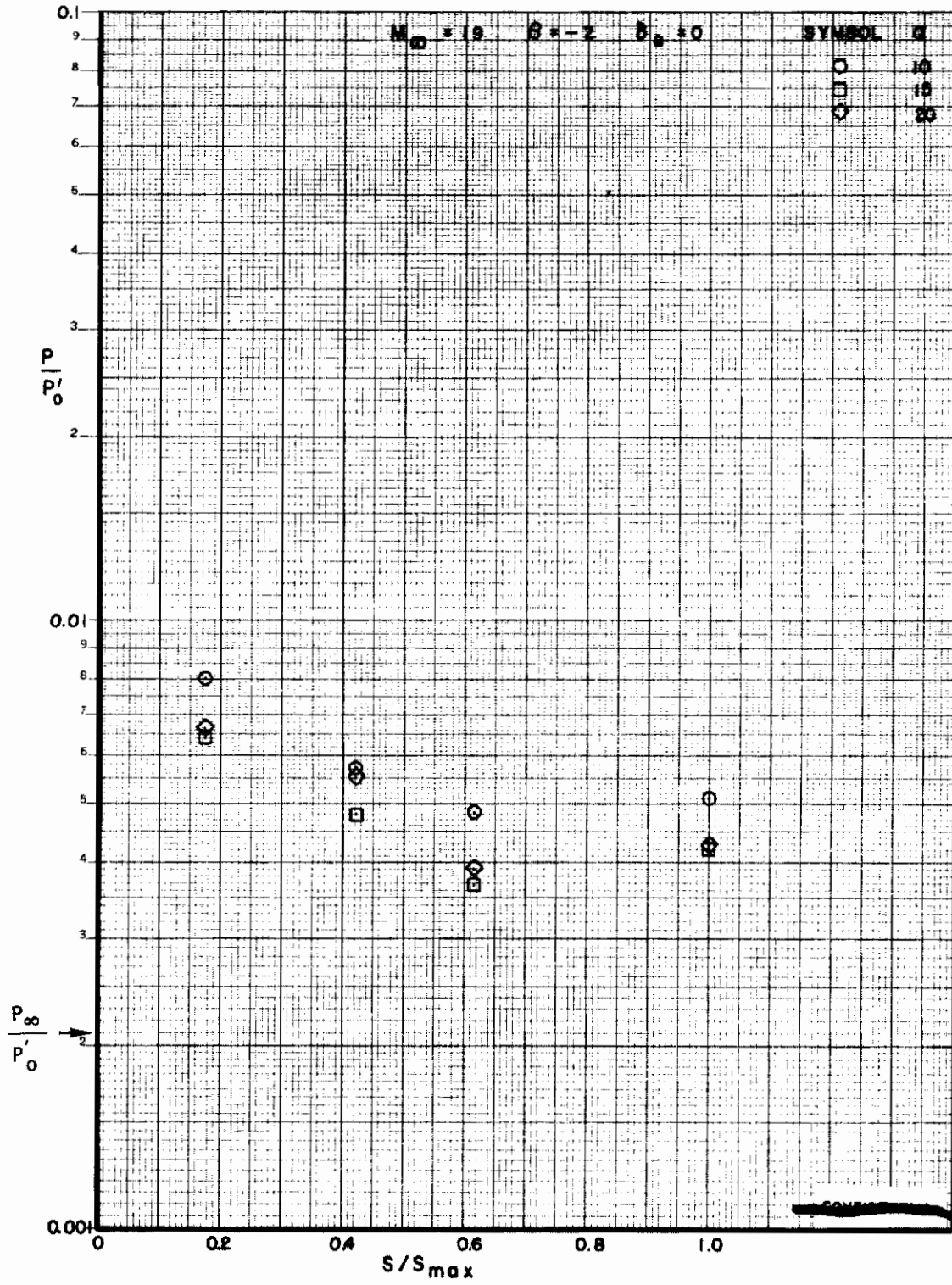
FIGURE 95 (U) TUNNEL F UPPER SURFACE SPANWISE PRESSURES AT X/L = 0.30, β=-2

173
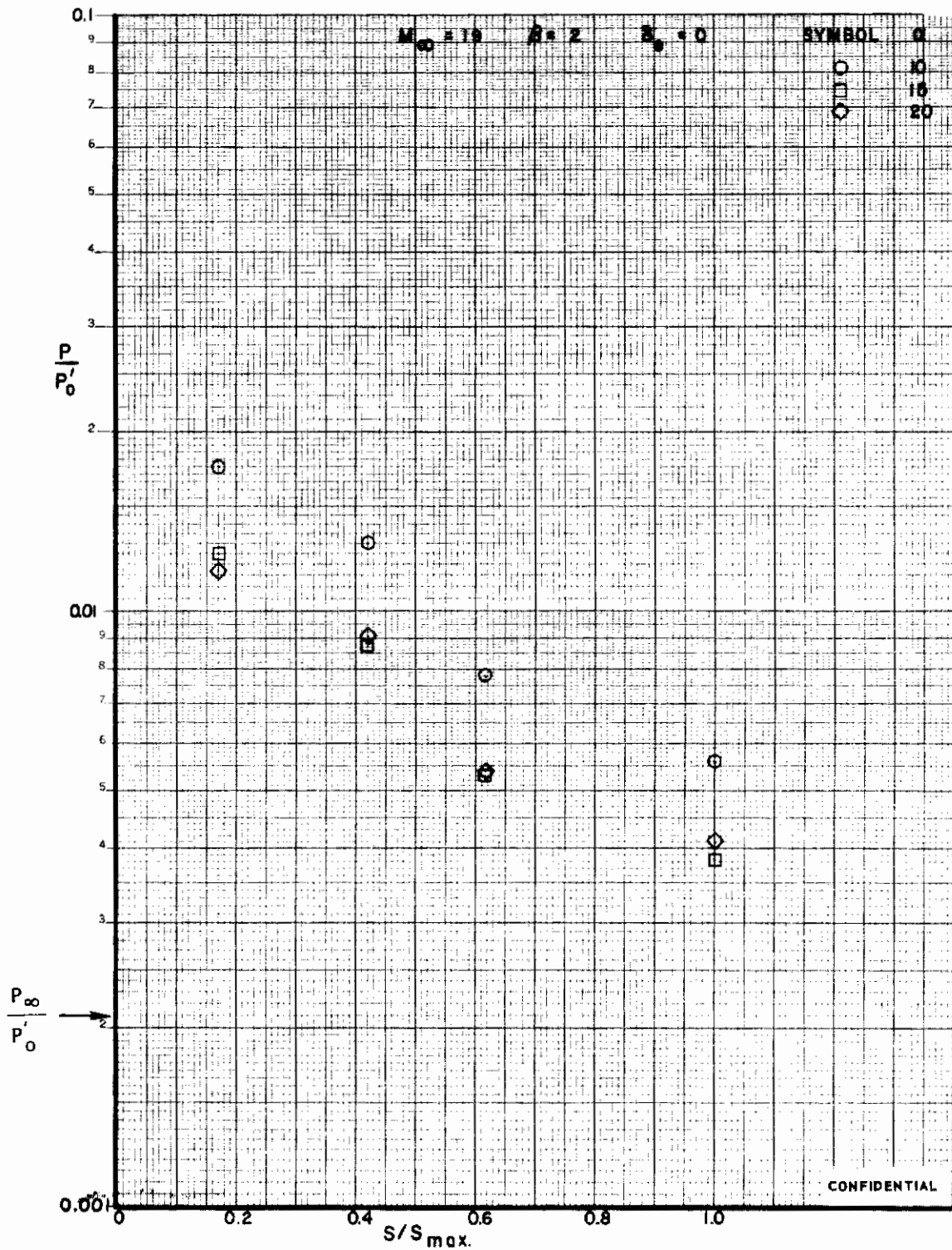
FIGURE 96 (U) TUNNEL F UPPER SURFACE SPANWISE PRESSURES AT X/L = 0.30, β=2

174
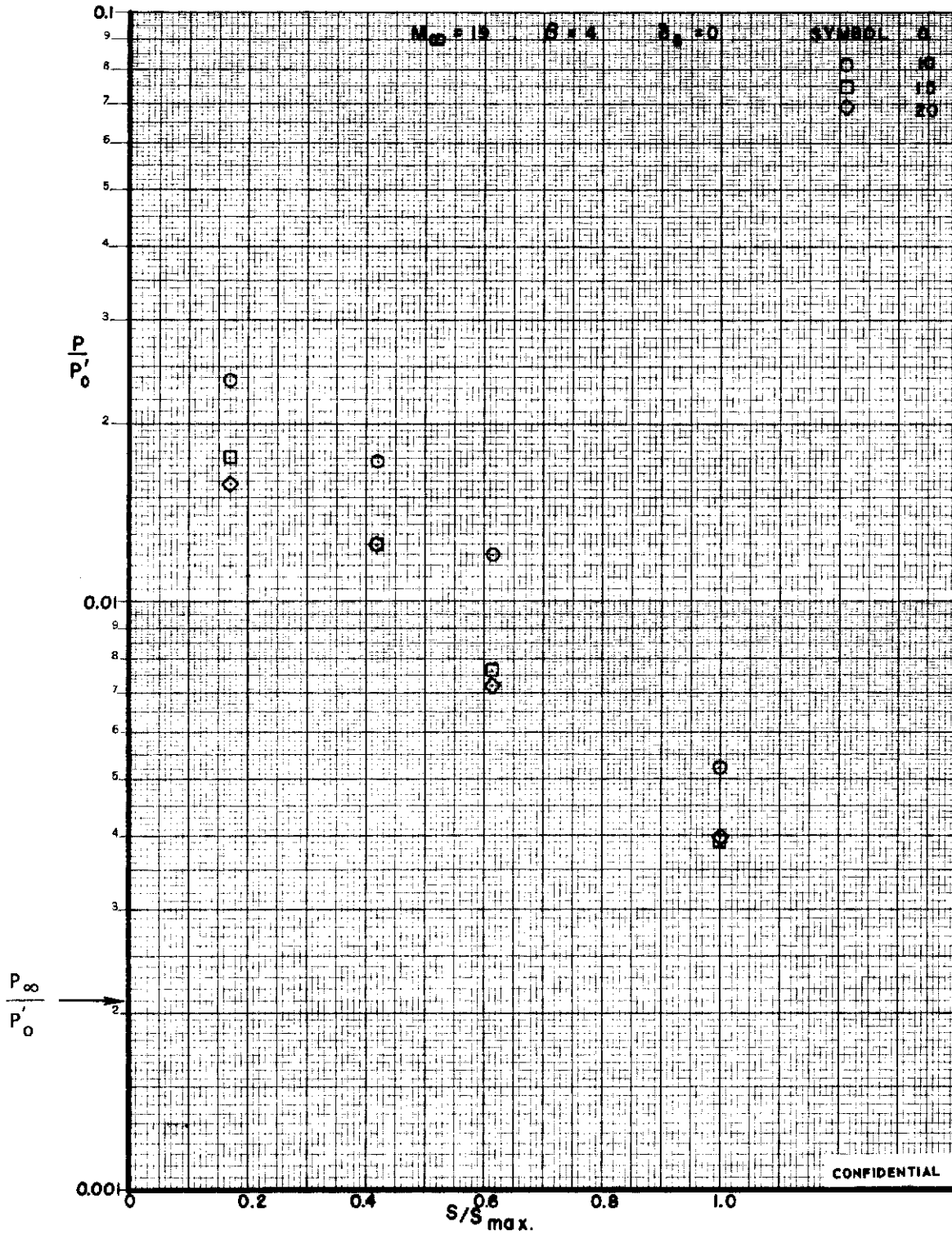
FIGURE 97 (U) TUNNEL F UPPER SURFACE SPANWISE PRESSURES AT X/L = 0.30, β=4
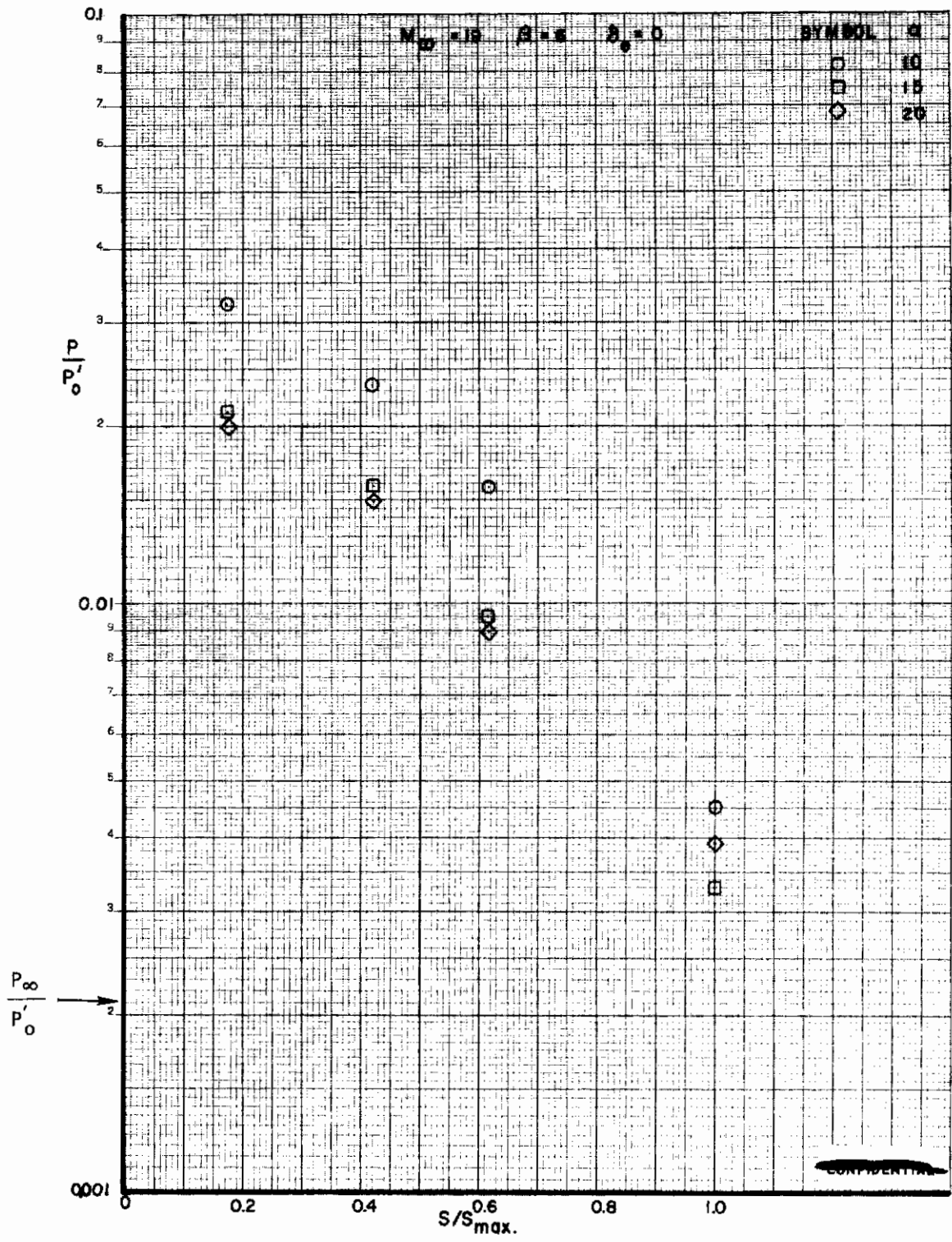
FIGURE 98 (U) TUNNEL F UPPER SURFACE SPANWISE PRESSURES AT X/L = 0.30, β=6
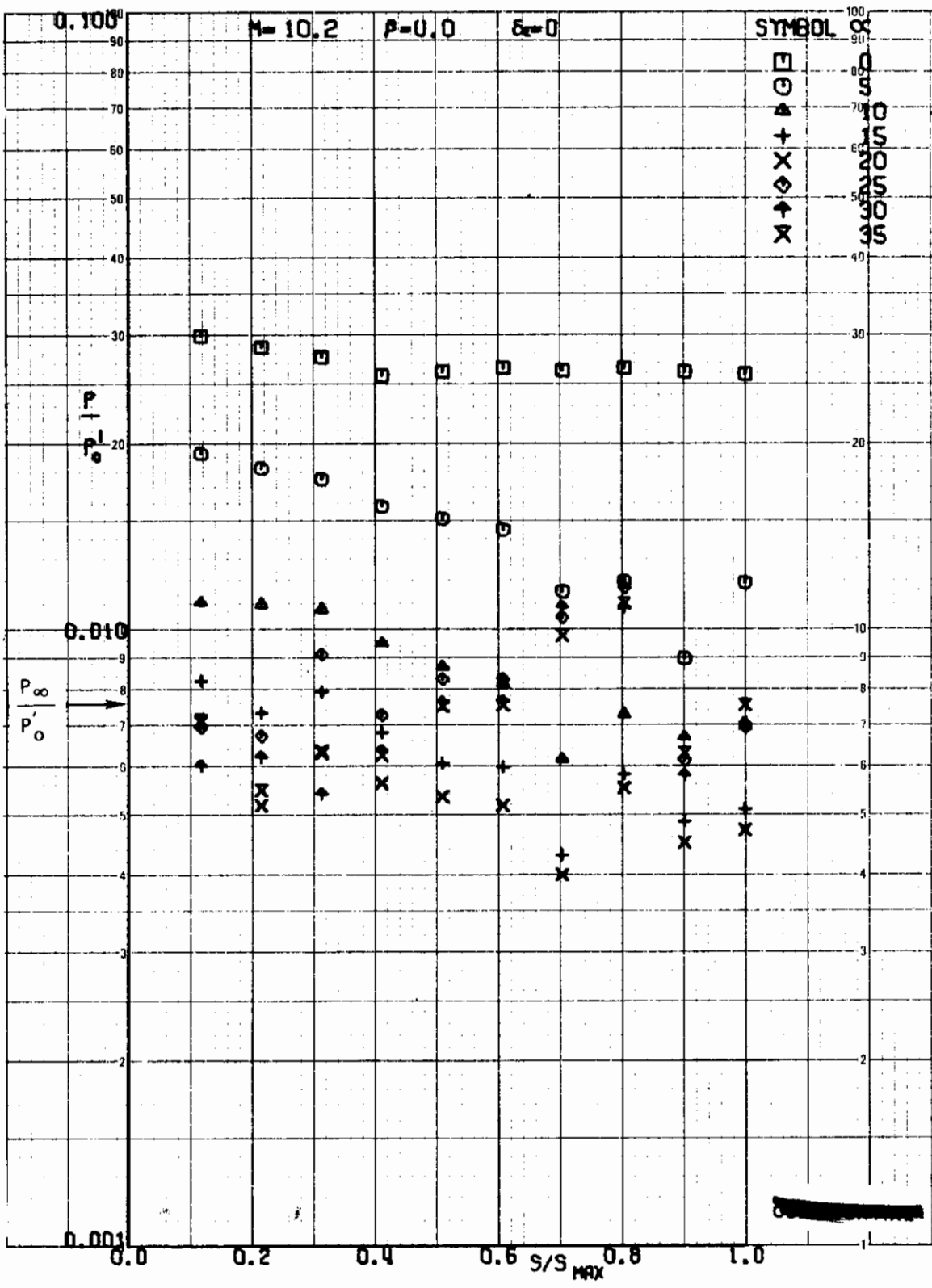
FIGURE 99 (U) TUNNEL C UPPER SURFACE SPANWISE PRESSURES AT X/L = 0.50, β=0

177
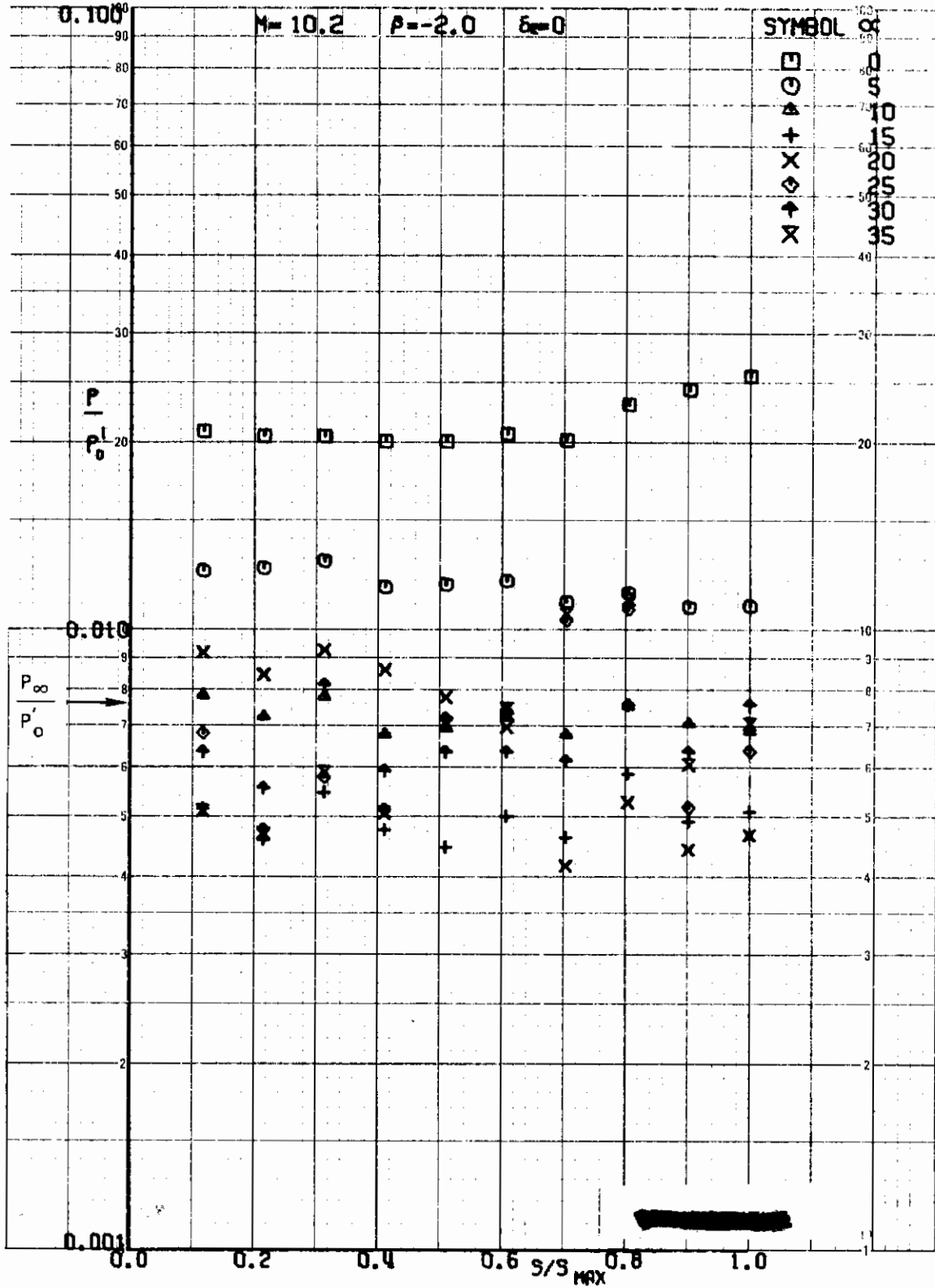
FIGURE 100 (U) TUNNEL C UPPER SURFACE SPANWISE PRESSURES AT X/L = 0.50, β=-2
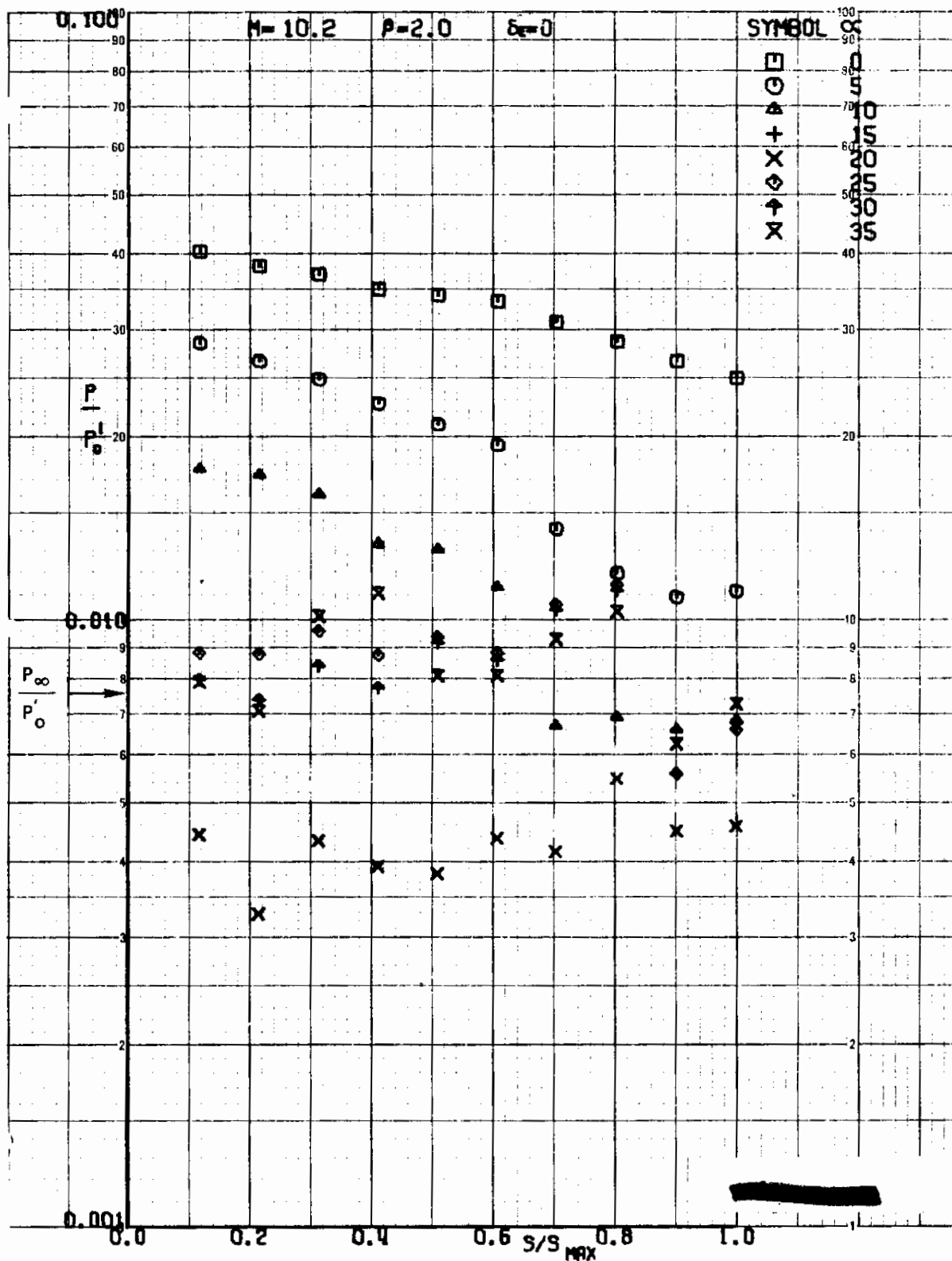
FIGURE 101 (U) TUNNEL C UPPER SURFACE SPANWISE PRESSURES AT X/L = 0.50, β=2
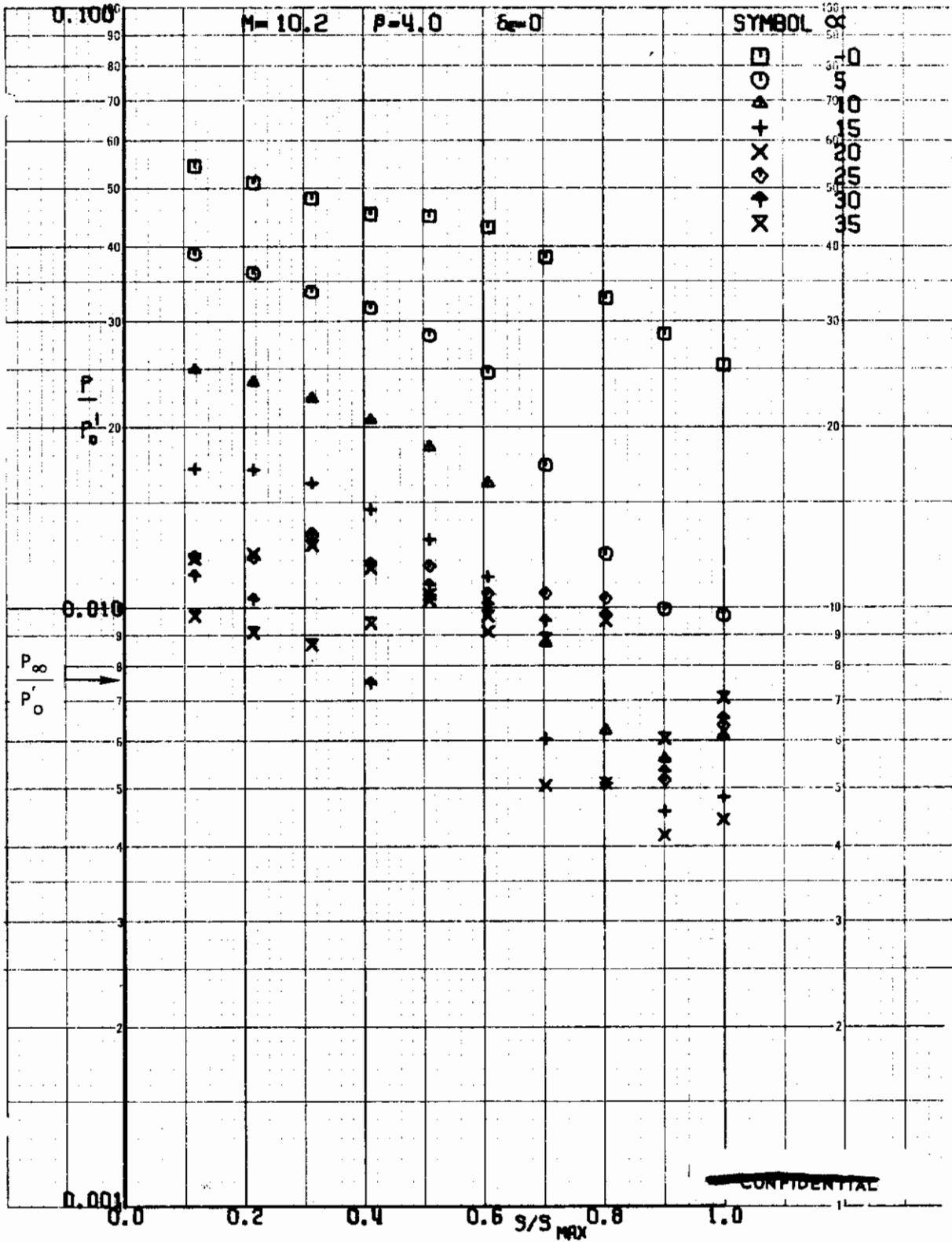
FIGURE 102   (U) TUNNEL C UPPER SURFACE SPANWISE PRESSURES AT X/L = 0.50, β=4
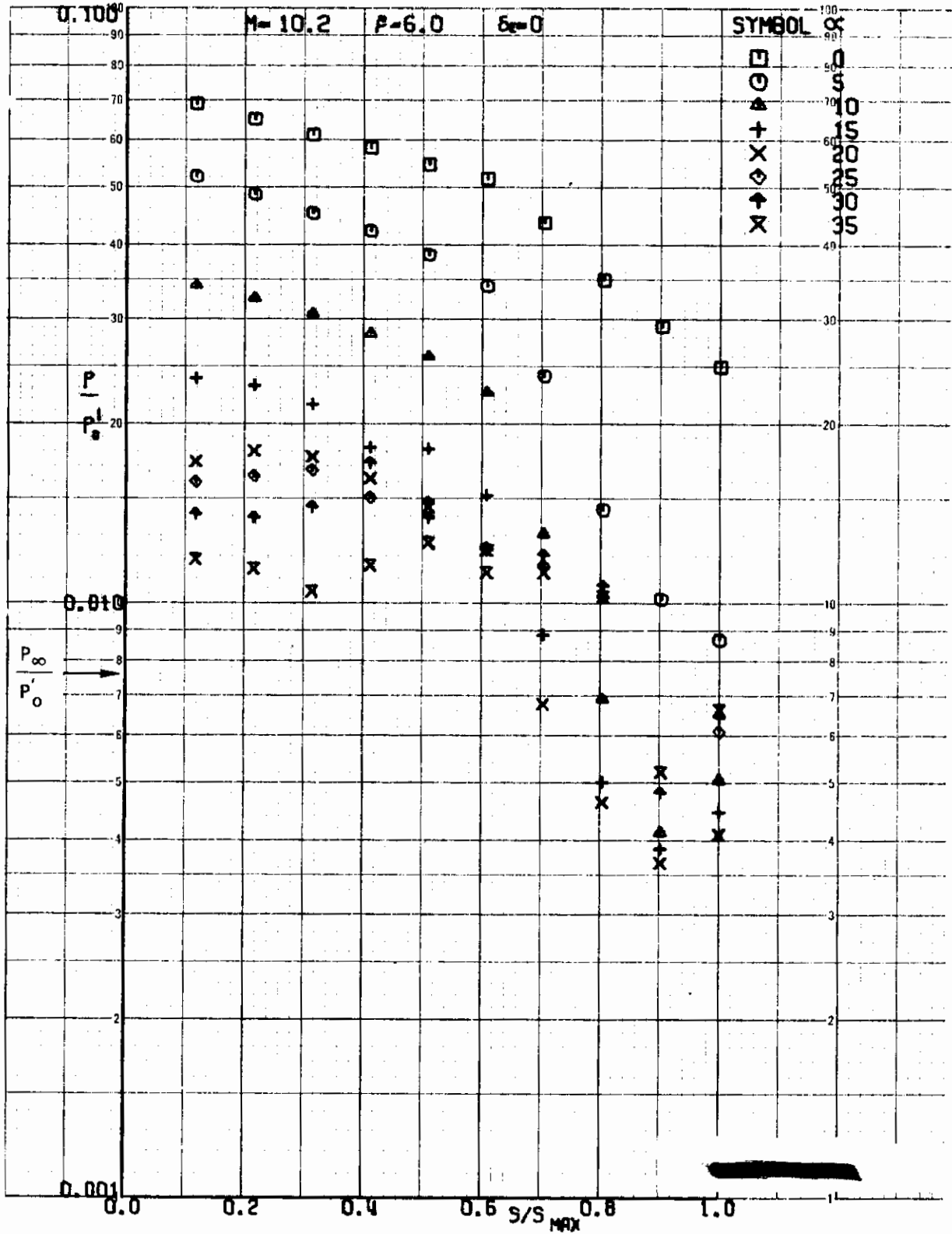
FIGURE 103   (U) TUNNEL C UPPER SURFACE SPANWISE PRESSURES AT X/L = 0.50, β=6
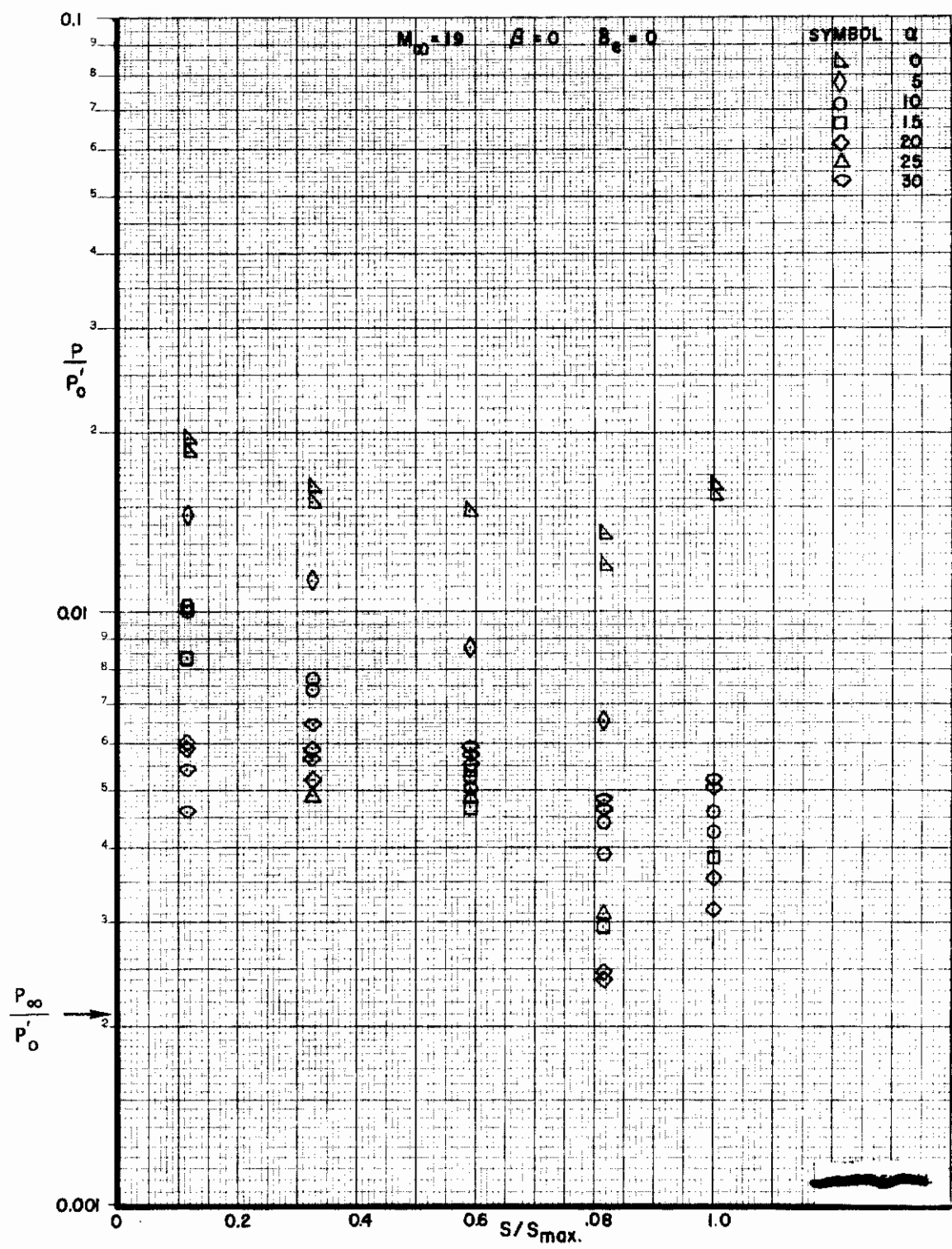
FIGURE 104 (U) TUNNEL F UPPER SURFACE SPANWISE PRESSURES AT X/L = 0.50, β=0
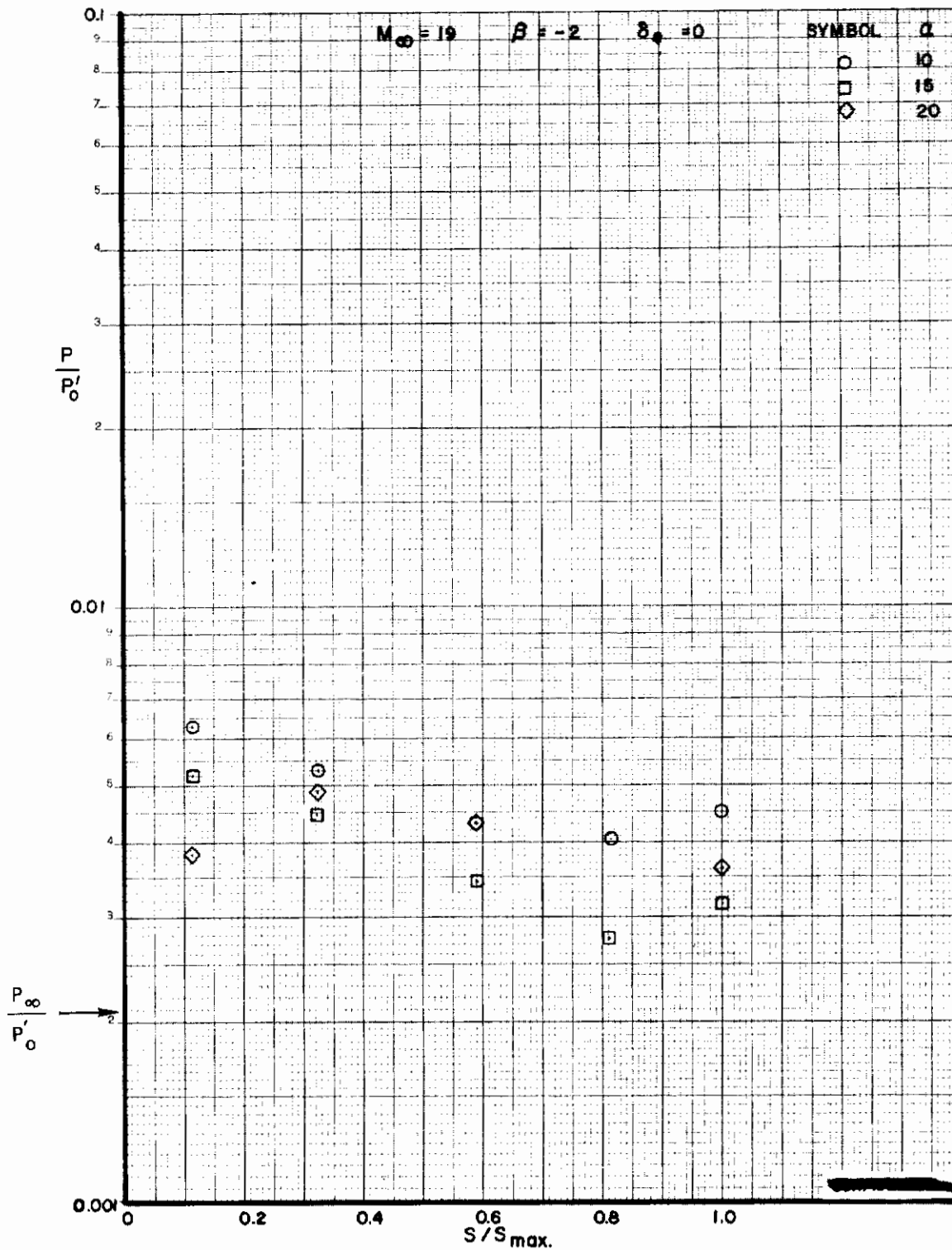
FIGURE 105 (U) TUNNEL F UPPER SURFACE SPANWISE PRESSURES AT X/L = 0.50, β=-2
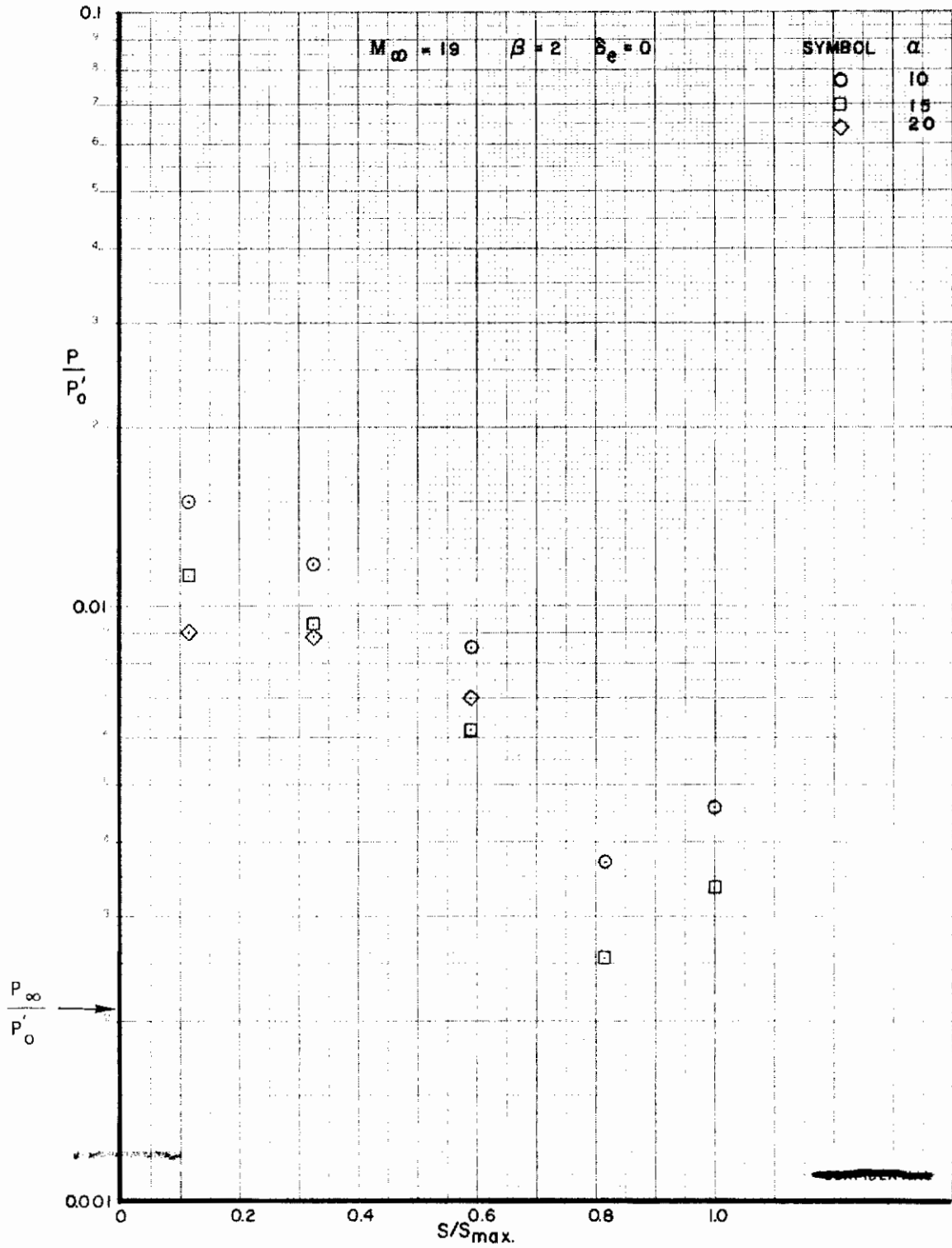
FIGURE 106 (U) TUNNEL F UPPER SURFACE SPANWISE PRESSURES AT X/L = 0.90, β = 2

184
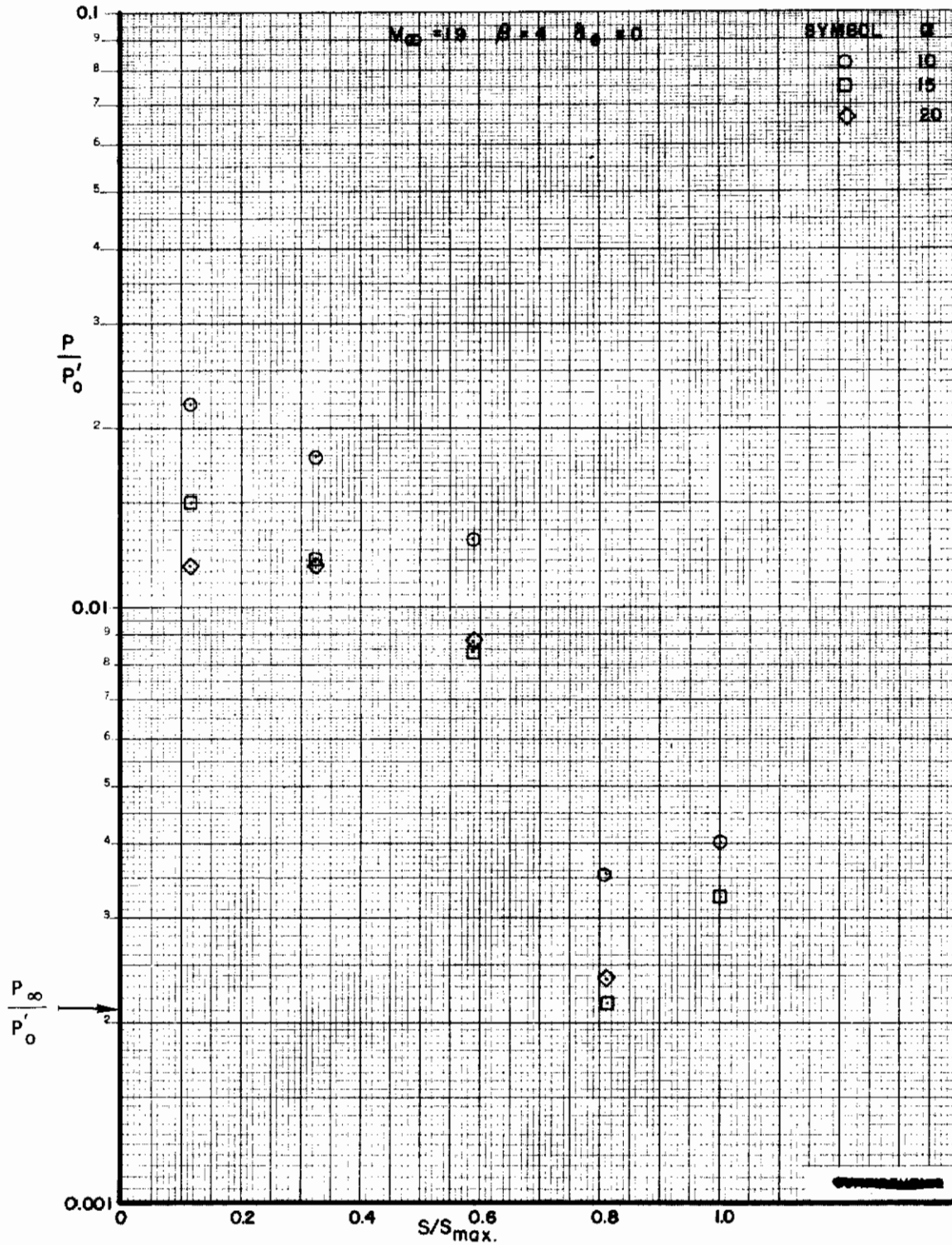
FIGURE 107 (U) TUNNEL F UPPER SURFACE SPANWISE PRESSURES AT X/L = 0.50, β=4
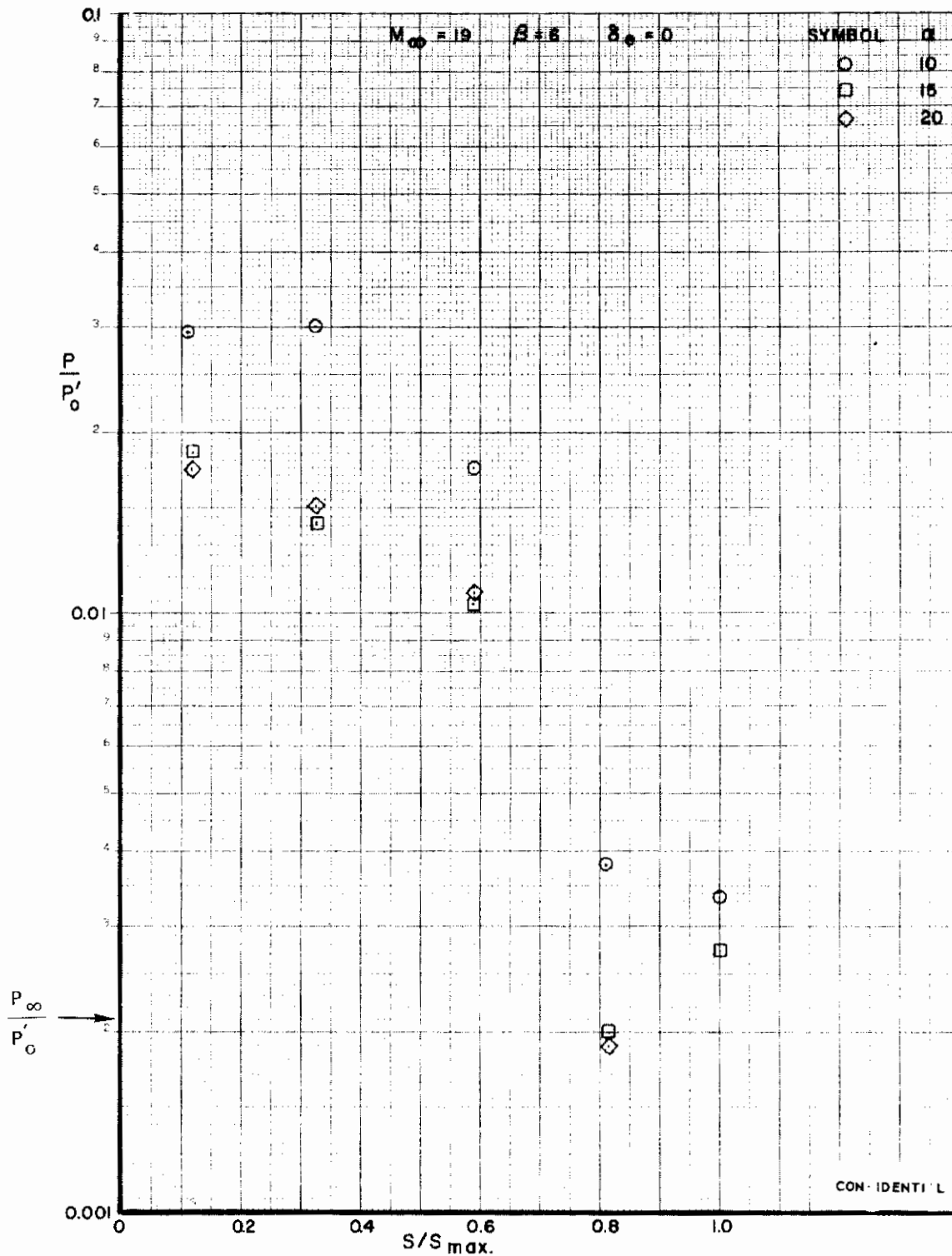
FIGURE 108 (U) TUNNEL F UPPER SURFACE SPANWISE PRESSURES AT X/L = 0.50, β = 6
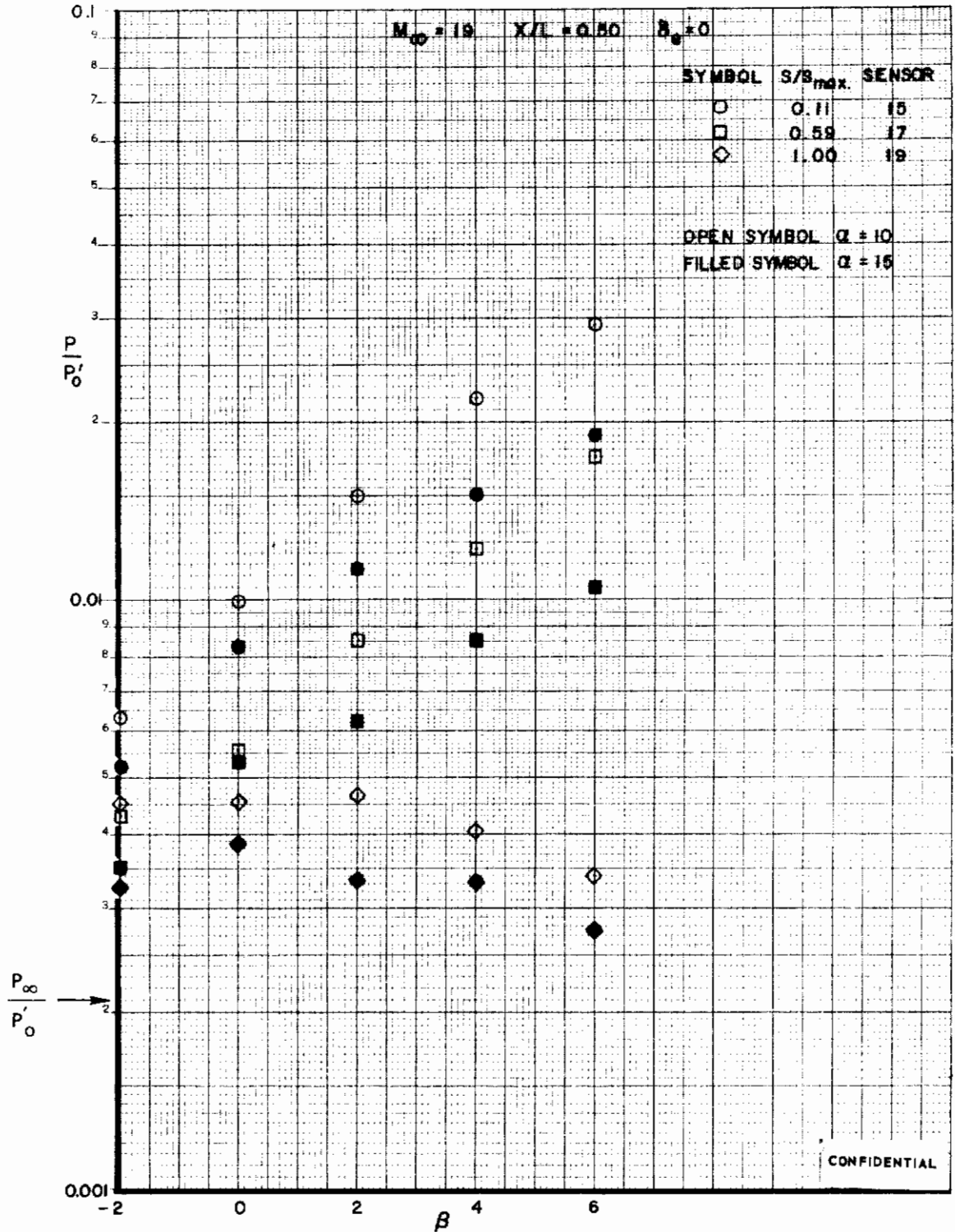
FIGURE 109 (U) EFFECT OF YAW ON UPPER SURFACE PRESSURES AT X/L = 0.50
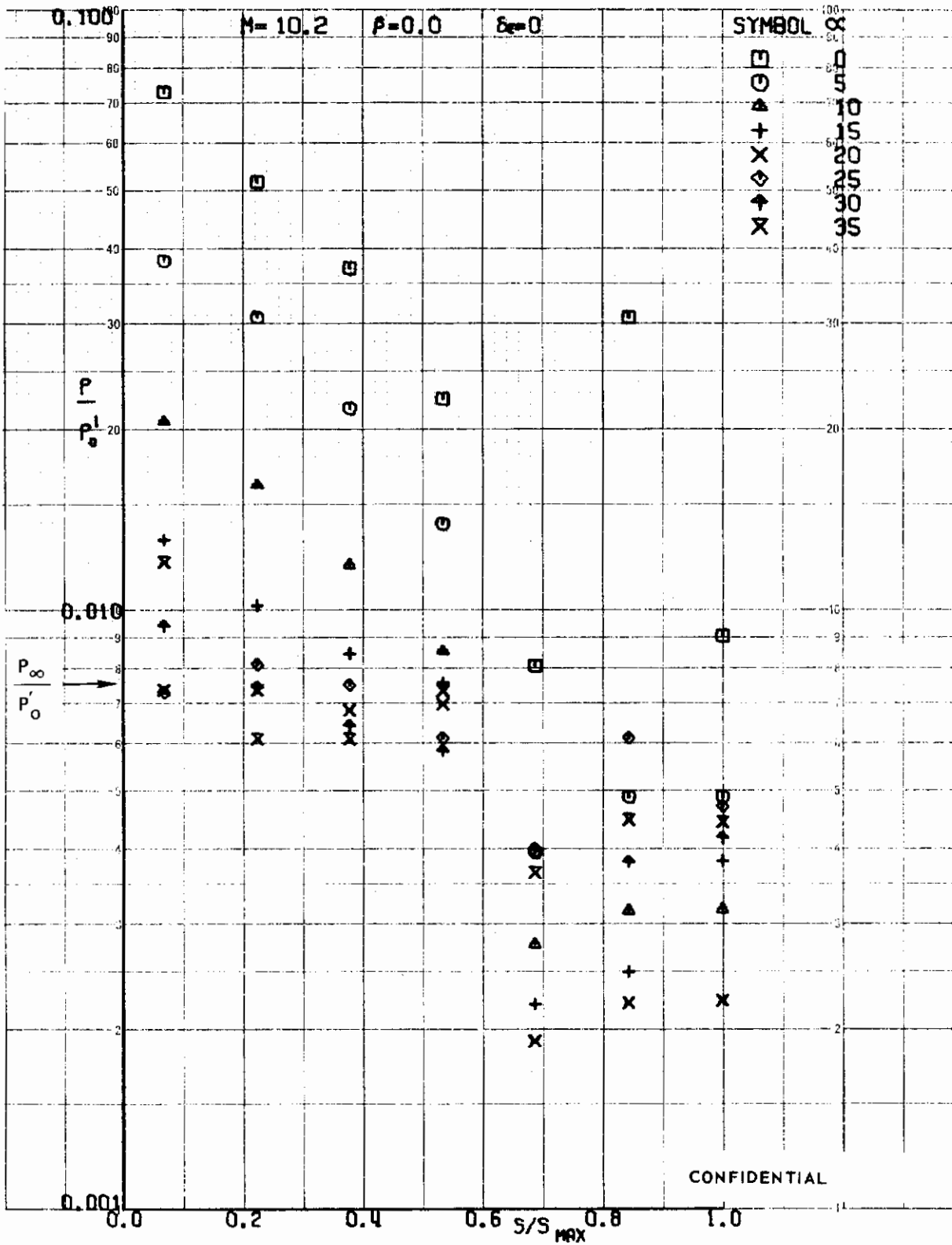
FIGURE 110 (U) TUNNEL C UPPER SURFACE SPANWISE PRESSURES AT X/L = 0.75, β=0
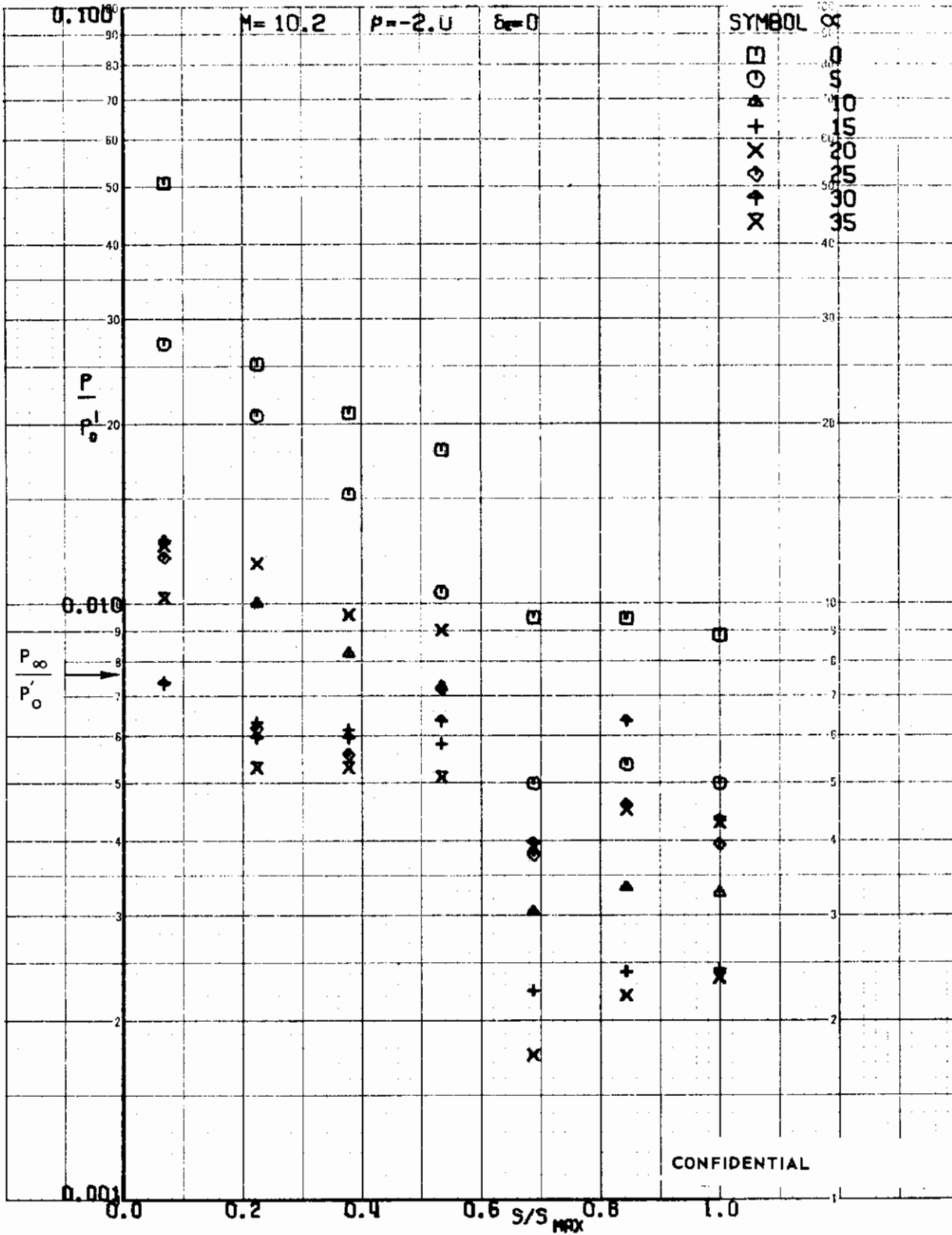
FIGURE 111 (U) TUNNEL C UPPER SURFACE SPANWISE PRESSURES AT X/L = 0.75, β=-2

189
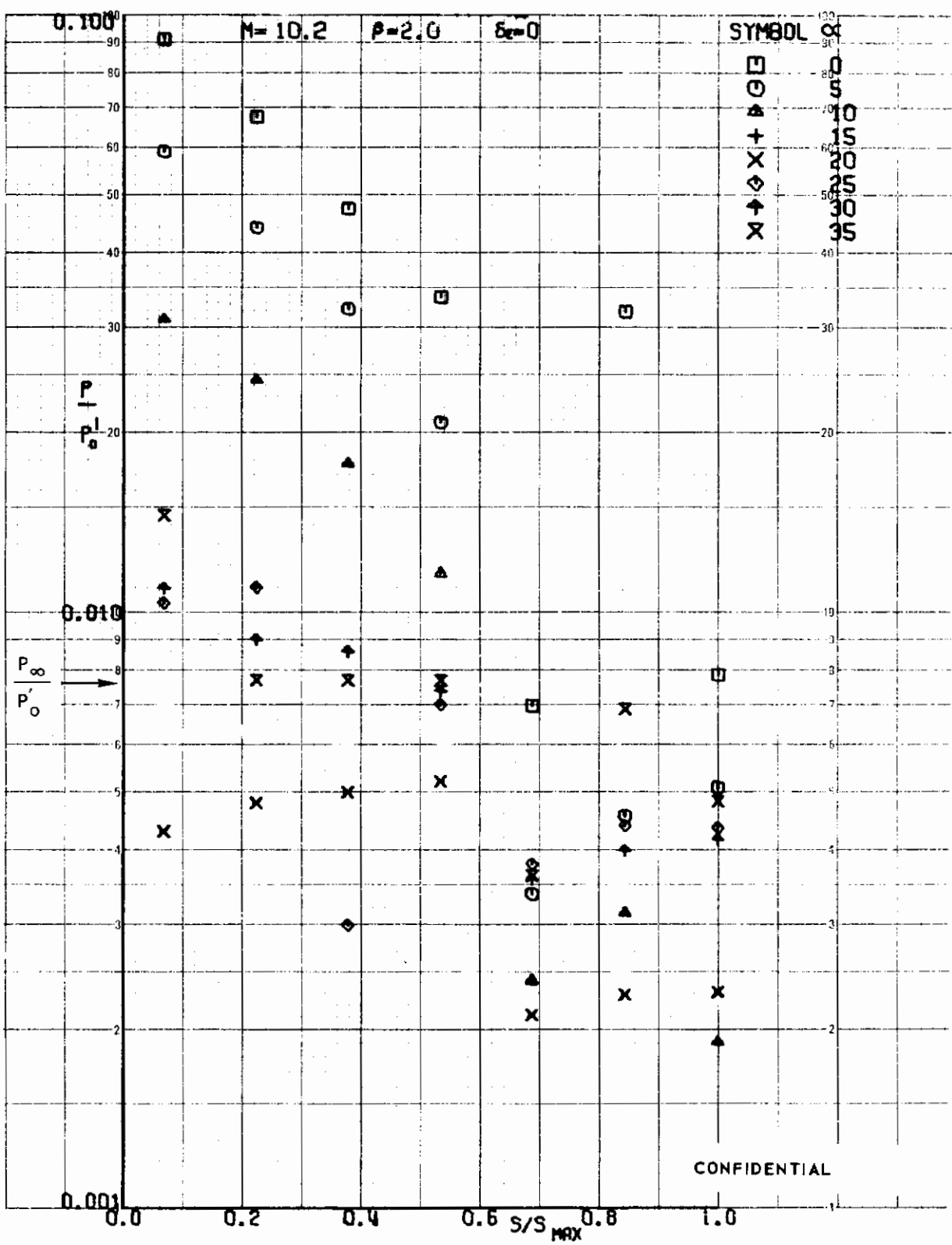
FIGURE 112 (U) TUNNEL C UPPER SURFACE SPANWISE PRESSURES AT X/L = 0.75, β=2

190
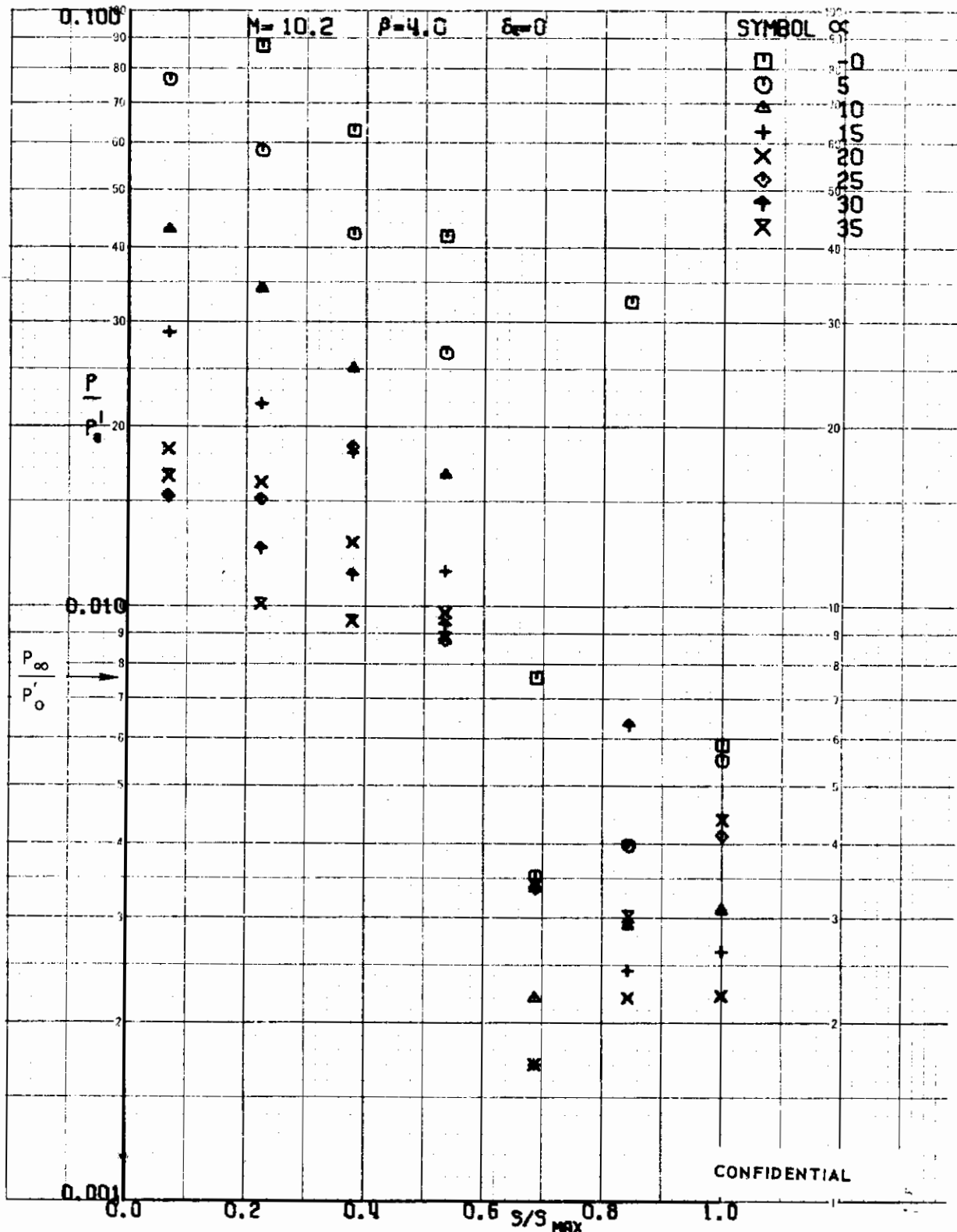
FIGURE 113 (U) TUNNEL C UPPER SURFACE SPANWISE PRESSURES AT X/L = 0.75, β=4
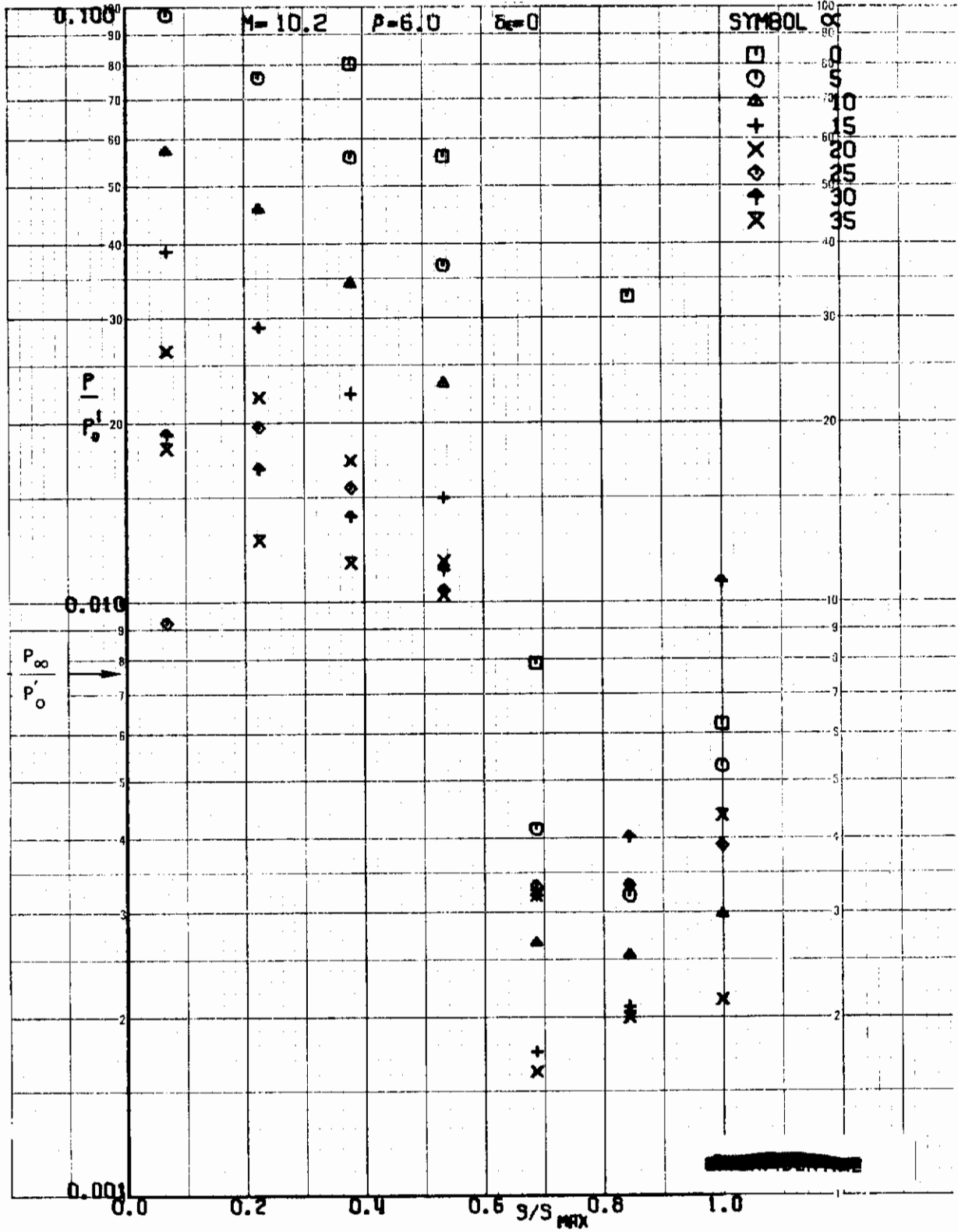
FIGURE 114 (U) TUNNEL C UPPER SURFACE SPANWISE PRESSURES AT X/L = 0.75, β=6
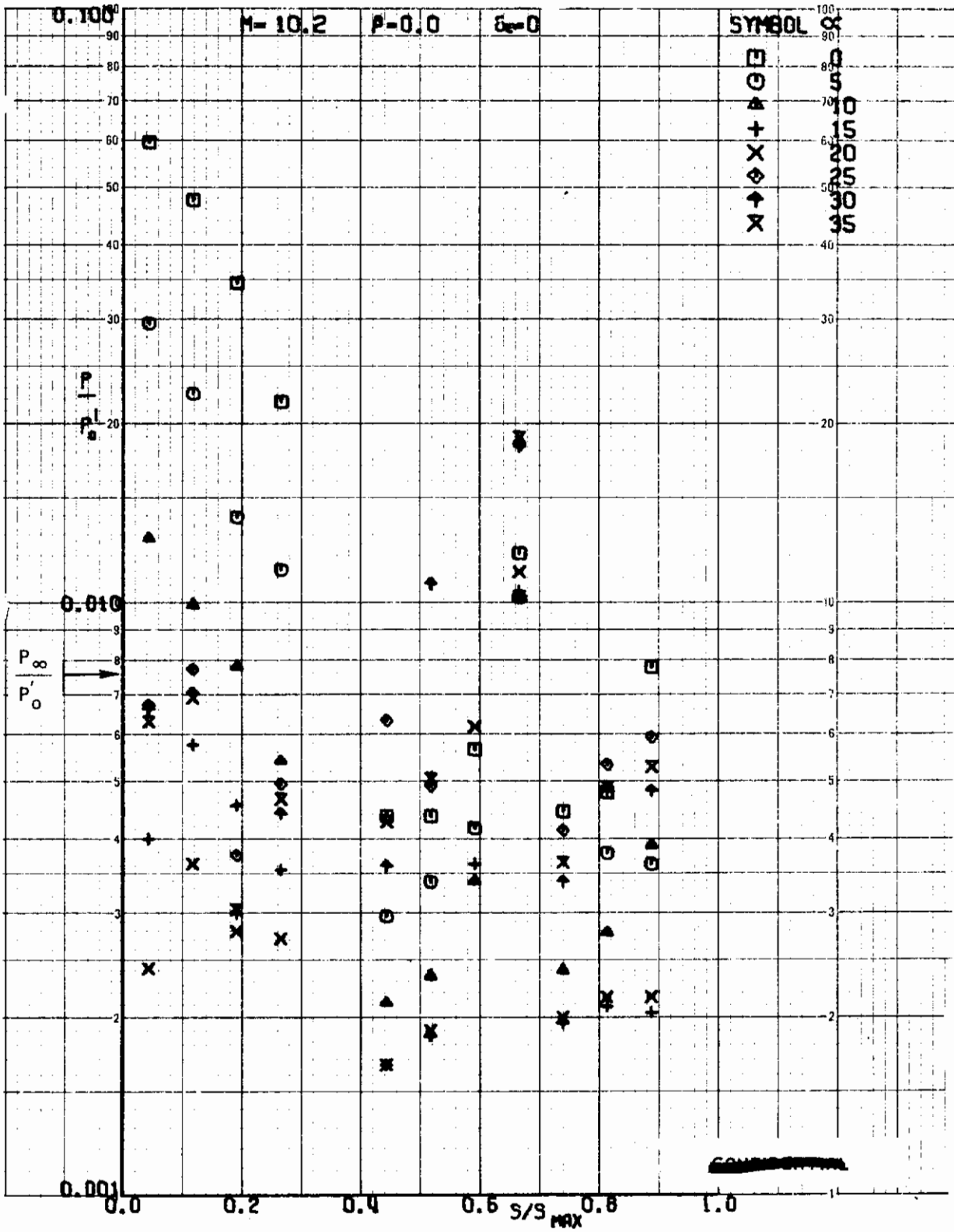
FIGURE 115 (U) TUNNEL C UPPER SURFACE SPANWISE PRESSURES AT X/L = 0.96, β=0
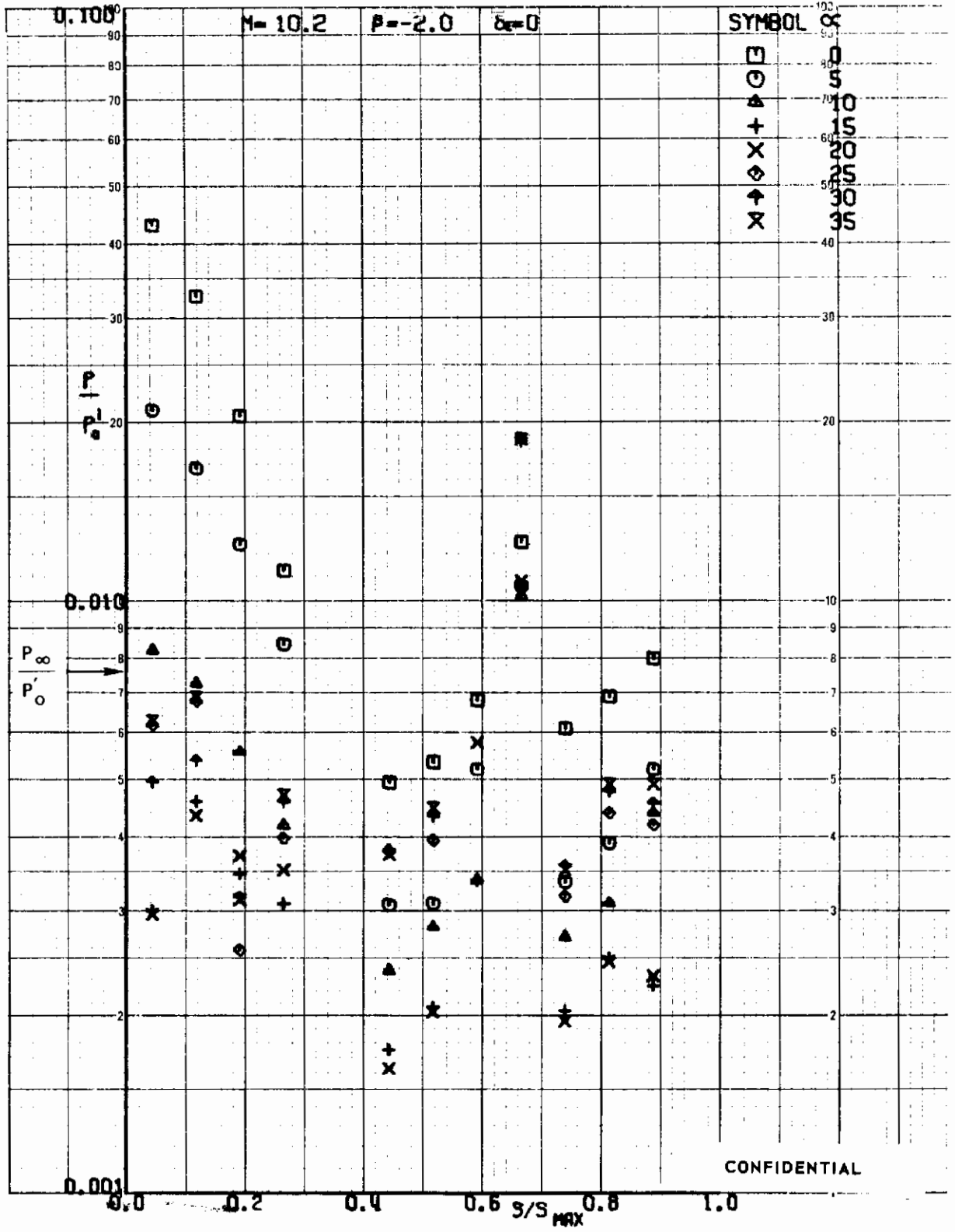
FIGURE 116 (U) TUNNEL C UPPER SURFACE SPANWISE PRESSURES AT X/L = 0.96, β=-2
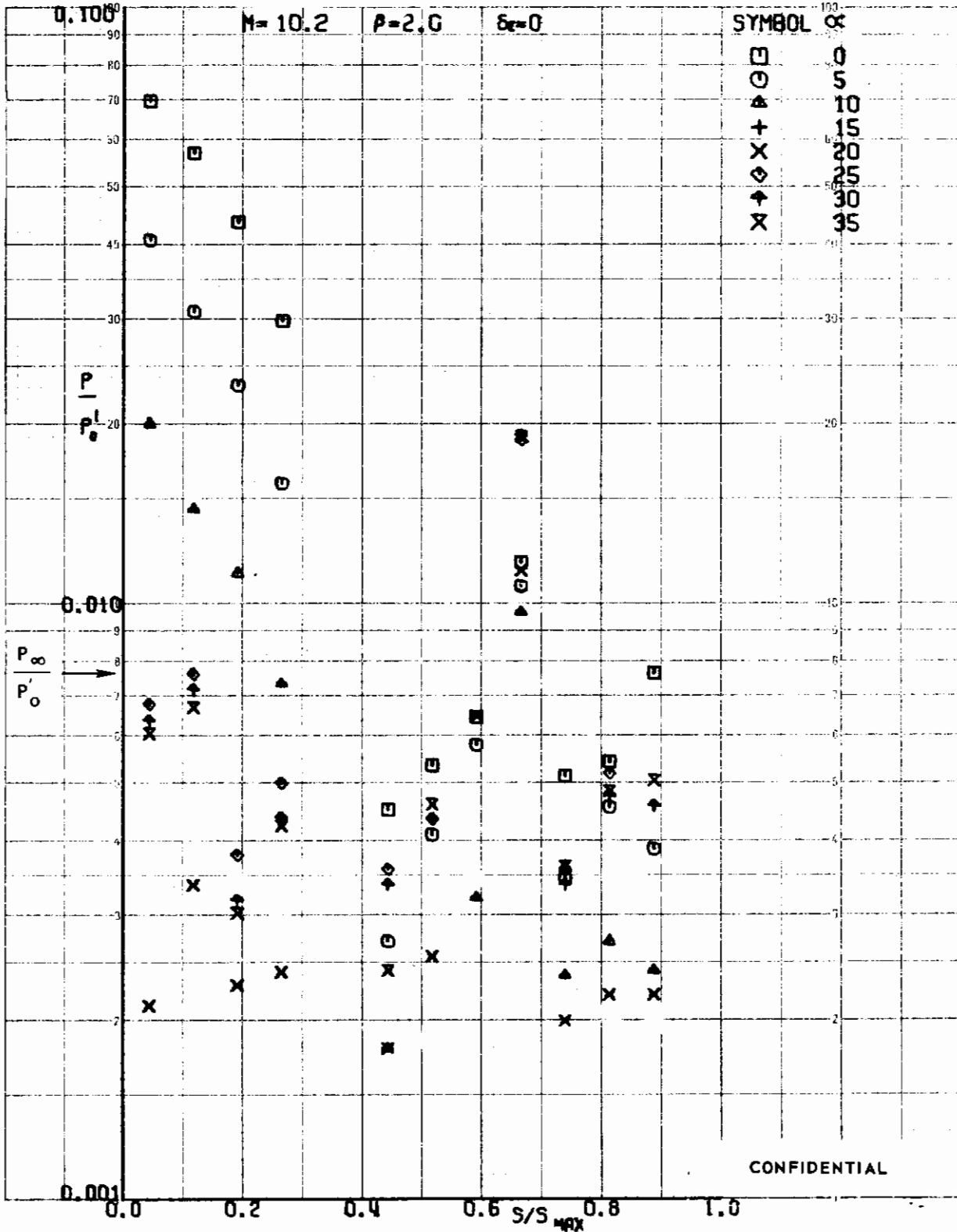
FIGURE 117 (U) TUNNEL C UPPER SURFACE SPANWISE PRESSURES AT X/L = 0.96, β=2
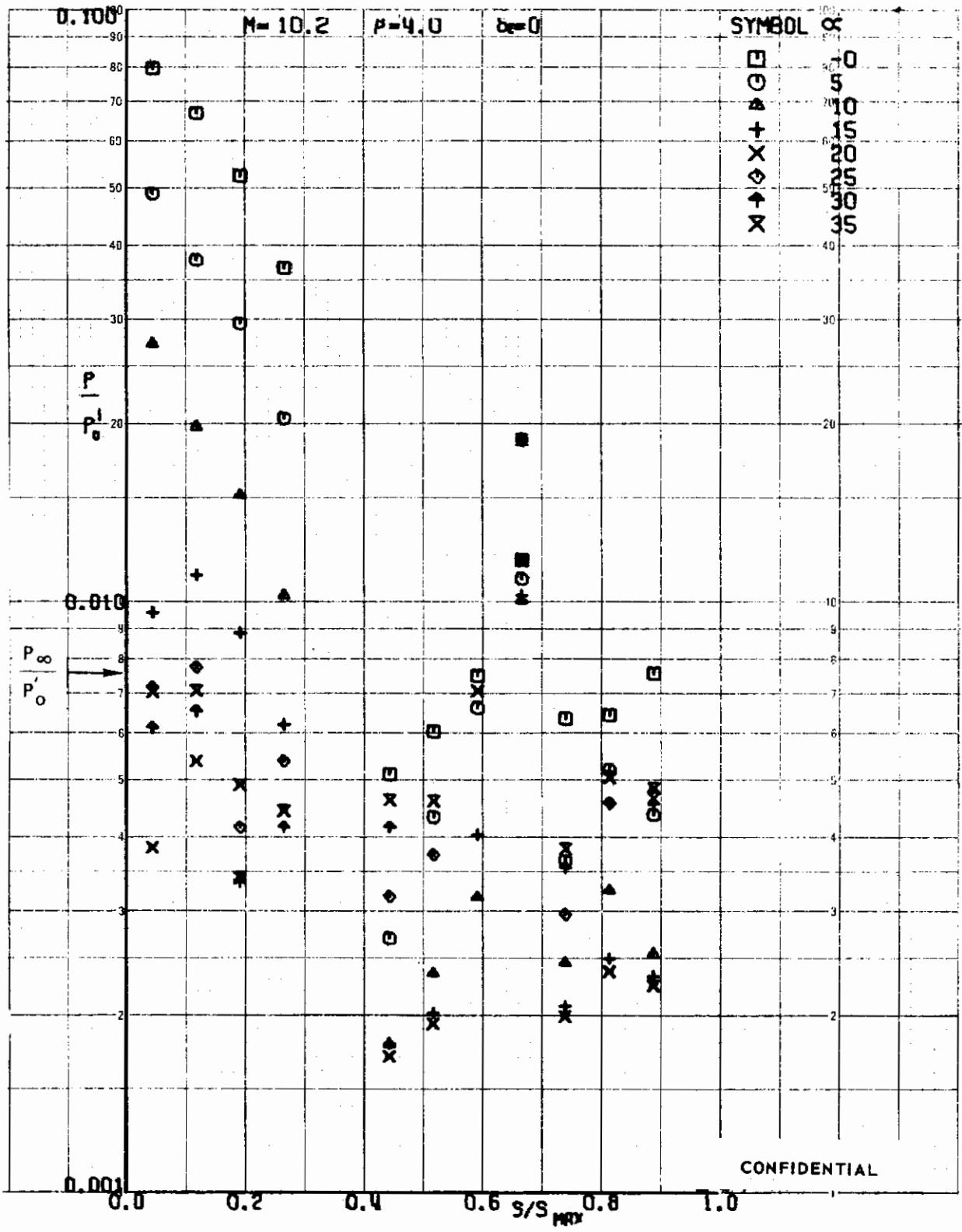
FIGURE 118   (U) TUNNEL C UPPER SURFACE SPANWISE PRESSURES AT X/L = 0.96, β=4
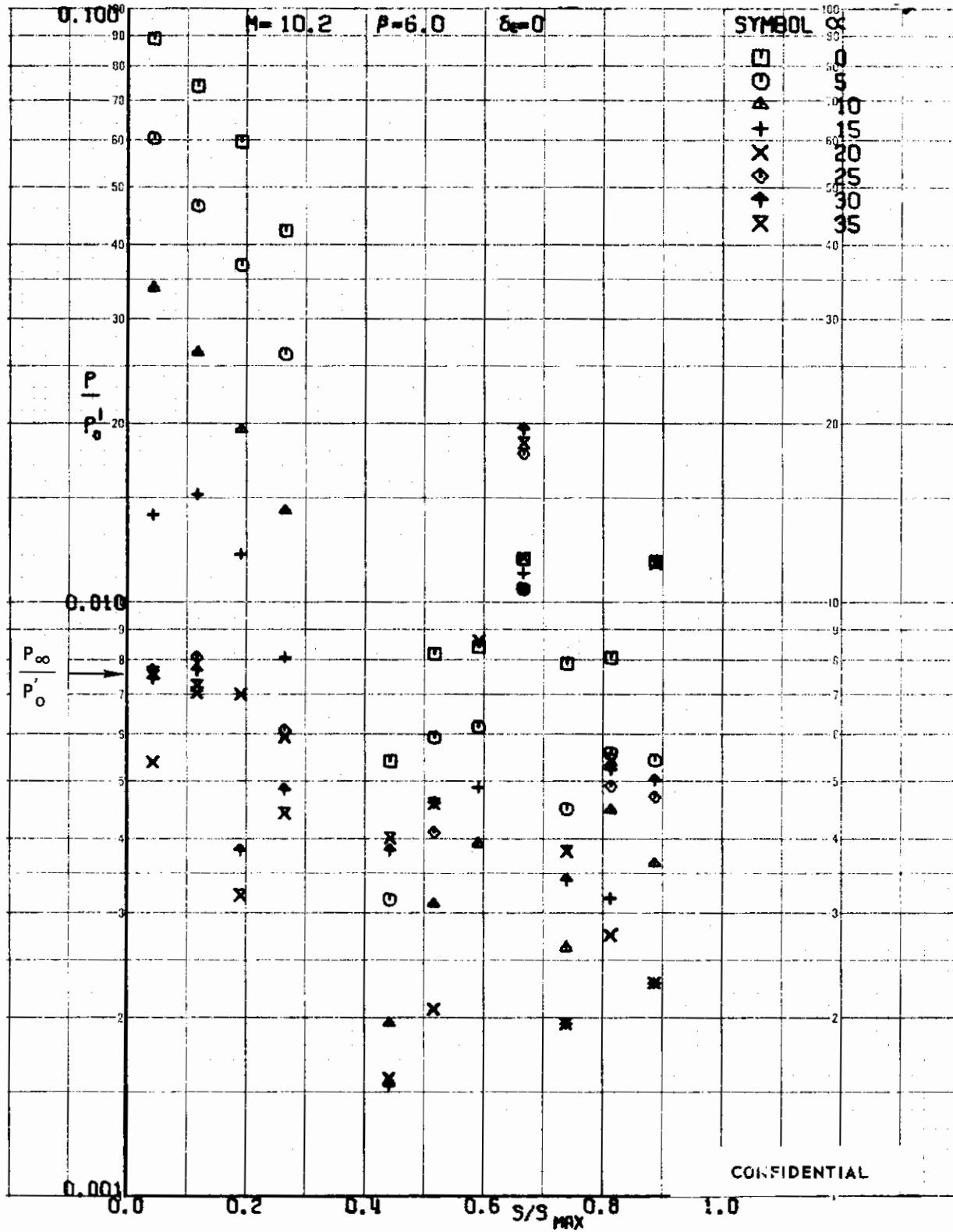
FIGURE 119 (U) TUNNEL C UPPER SURFACE SPANWISE PRESSURES AT X/L = 0.96, β=6

197
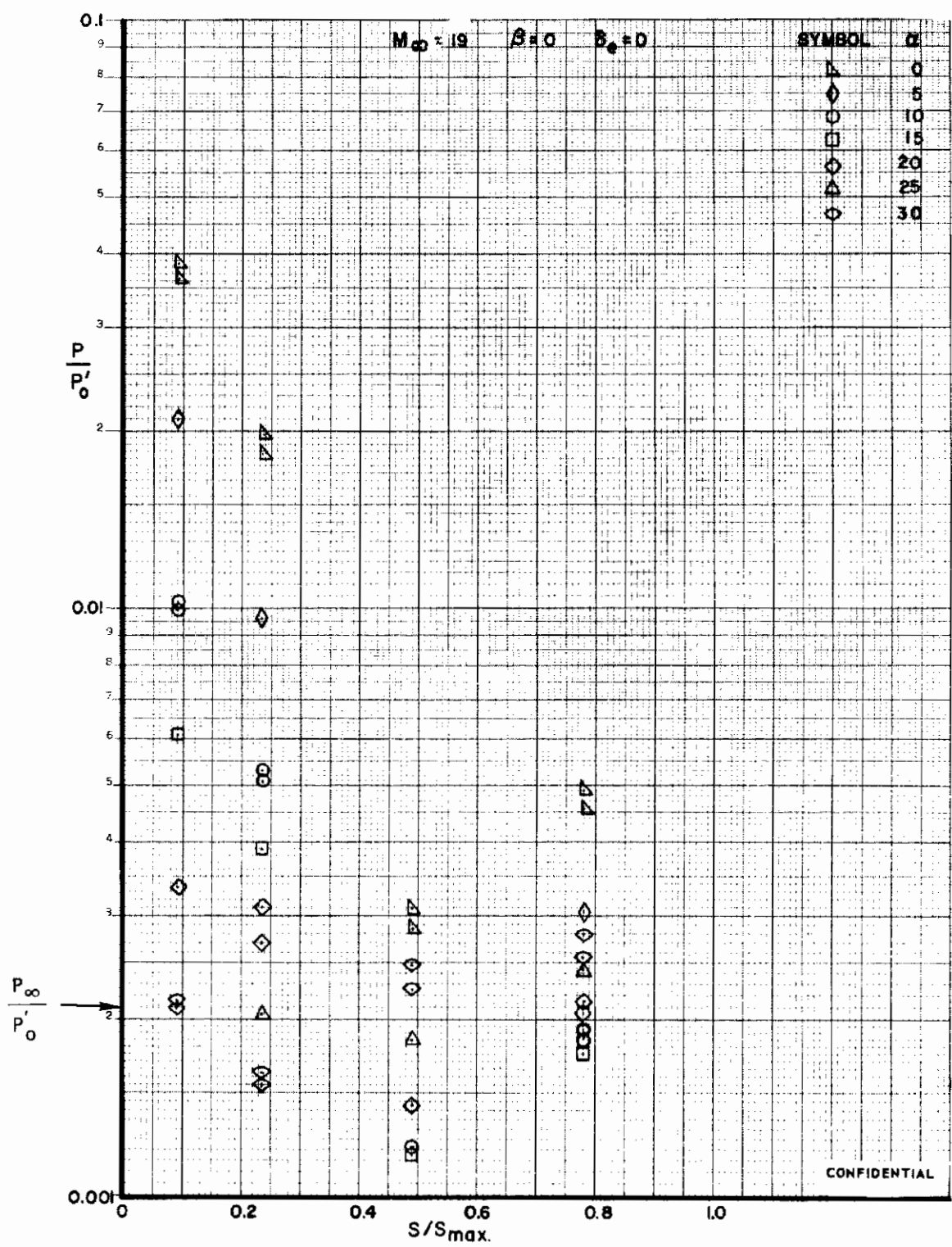
FIGURE 120 (U) TUNNEL F UPPER SURFACE SPANWISE PRESSURES AT X/L = 0.96, β=0
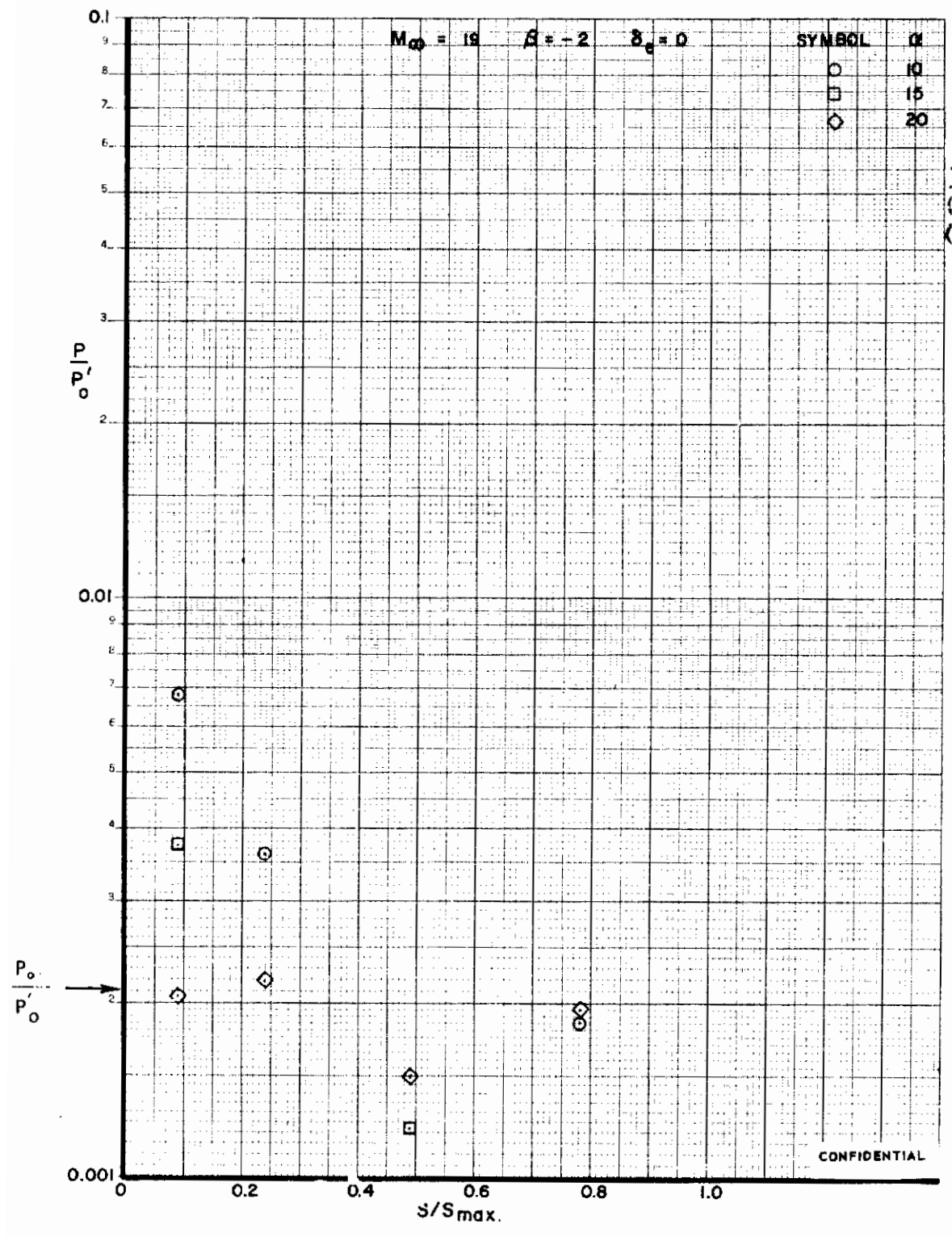
FIGURE 121 (U) TUNNEL F UPPER SURFACE SPANWISE PRESSURES AT X/L = 0.96, β=-2
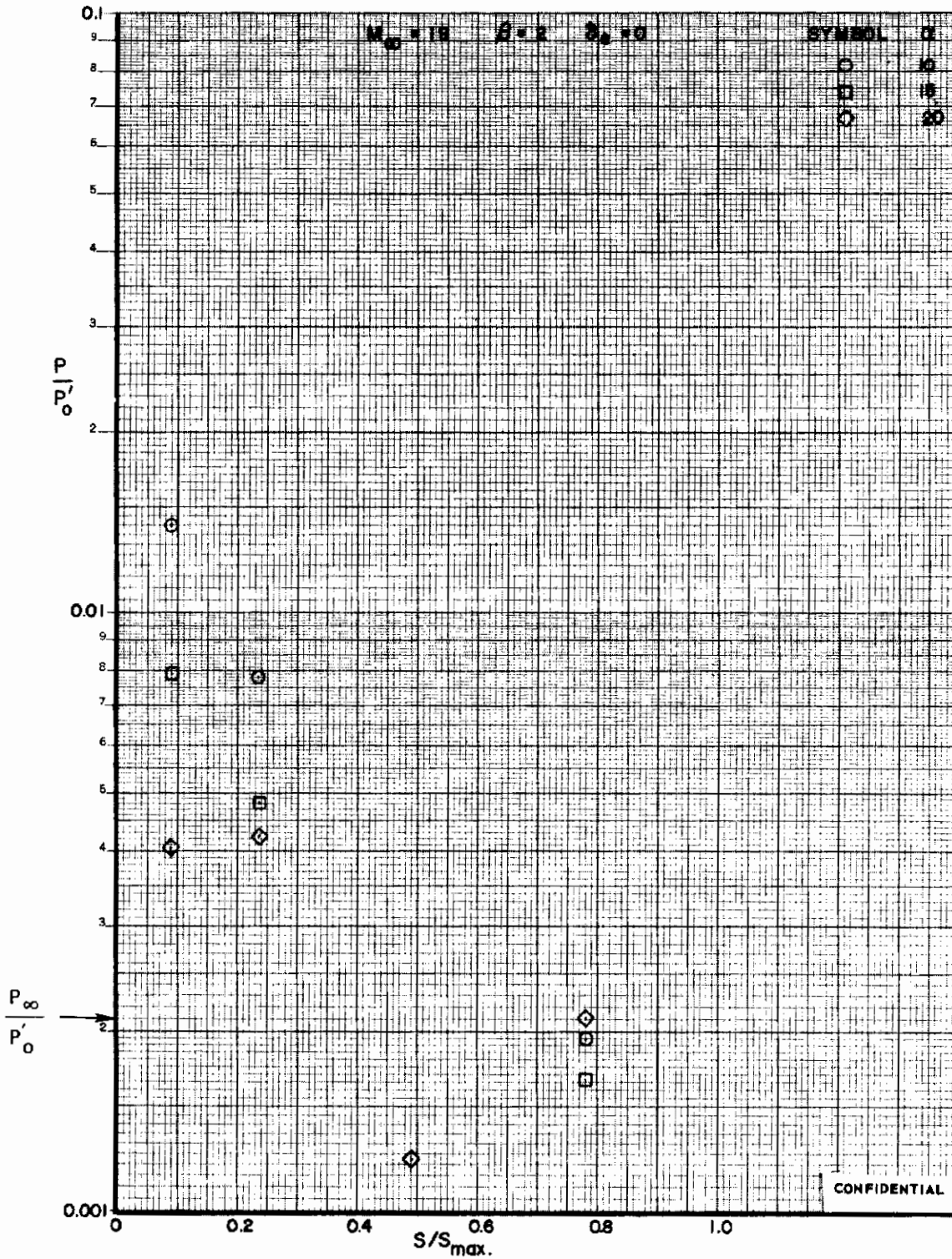
FIGURE 122 (U) TUNNEL F UPPER SURFACE SPANWISE PRESSURES AT X/L = 0.96, β=2

200
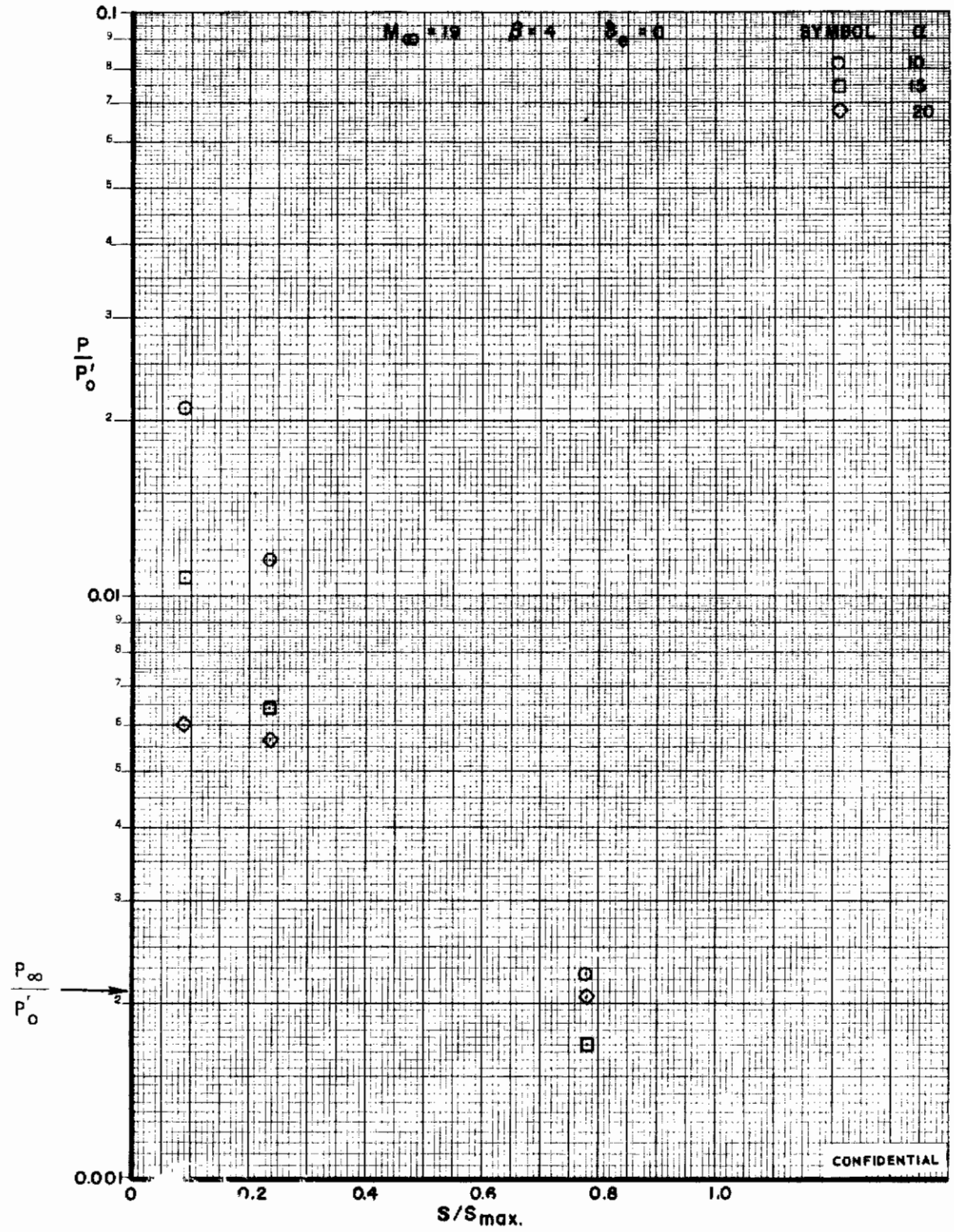
FIGURE 123 (U) TUNNEL F UPPER SURFACE SPANWISE PRESSURES AT X/L = 0.96, $\beta = 4$

201
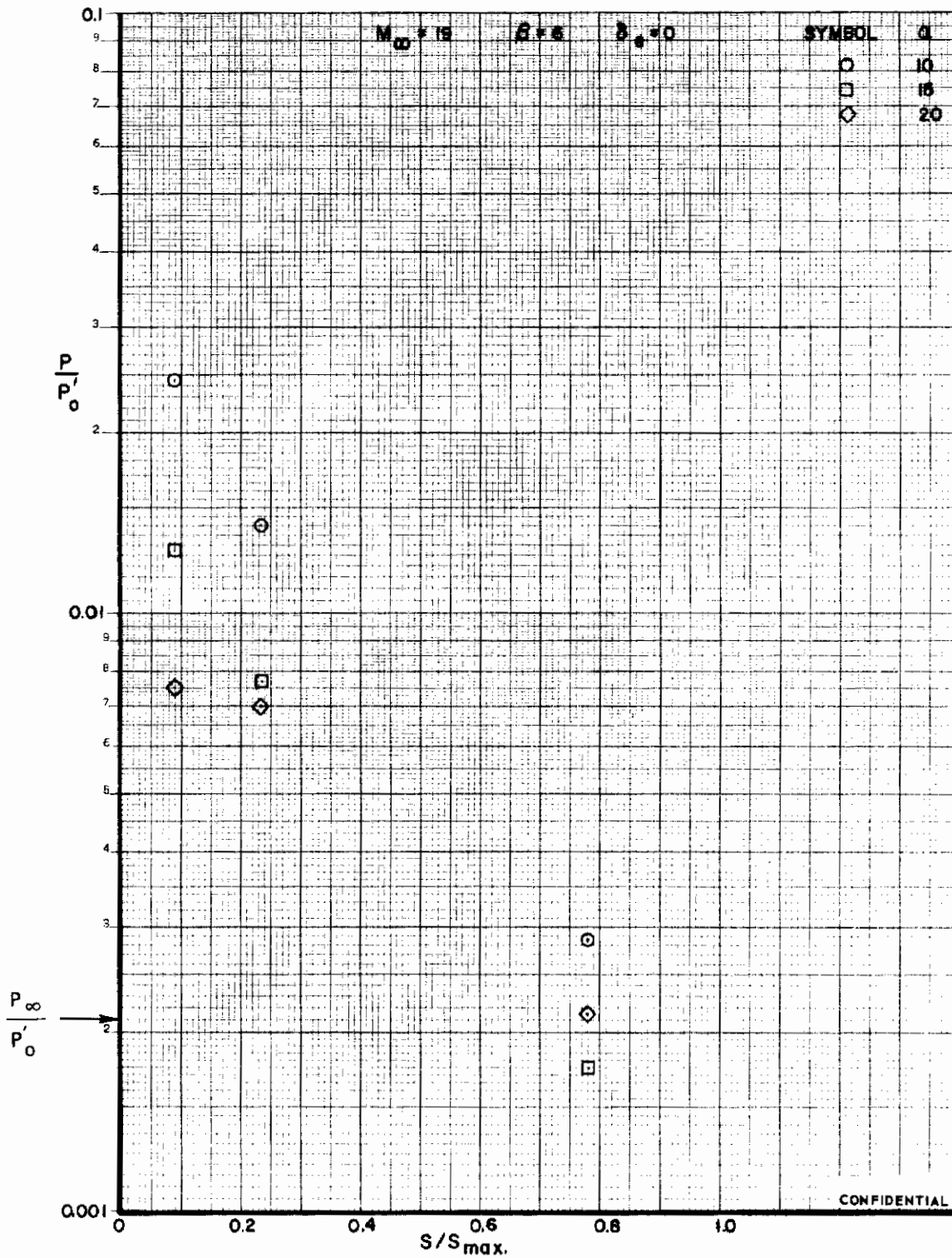
FIGURE 124   (U) TUNNEL F UPPER SURFACE SPANWISE PRESSURES AT X/L = 0.96, β = 6
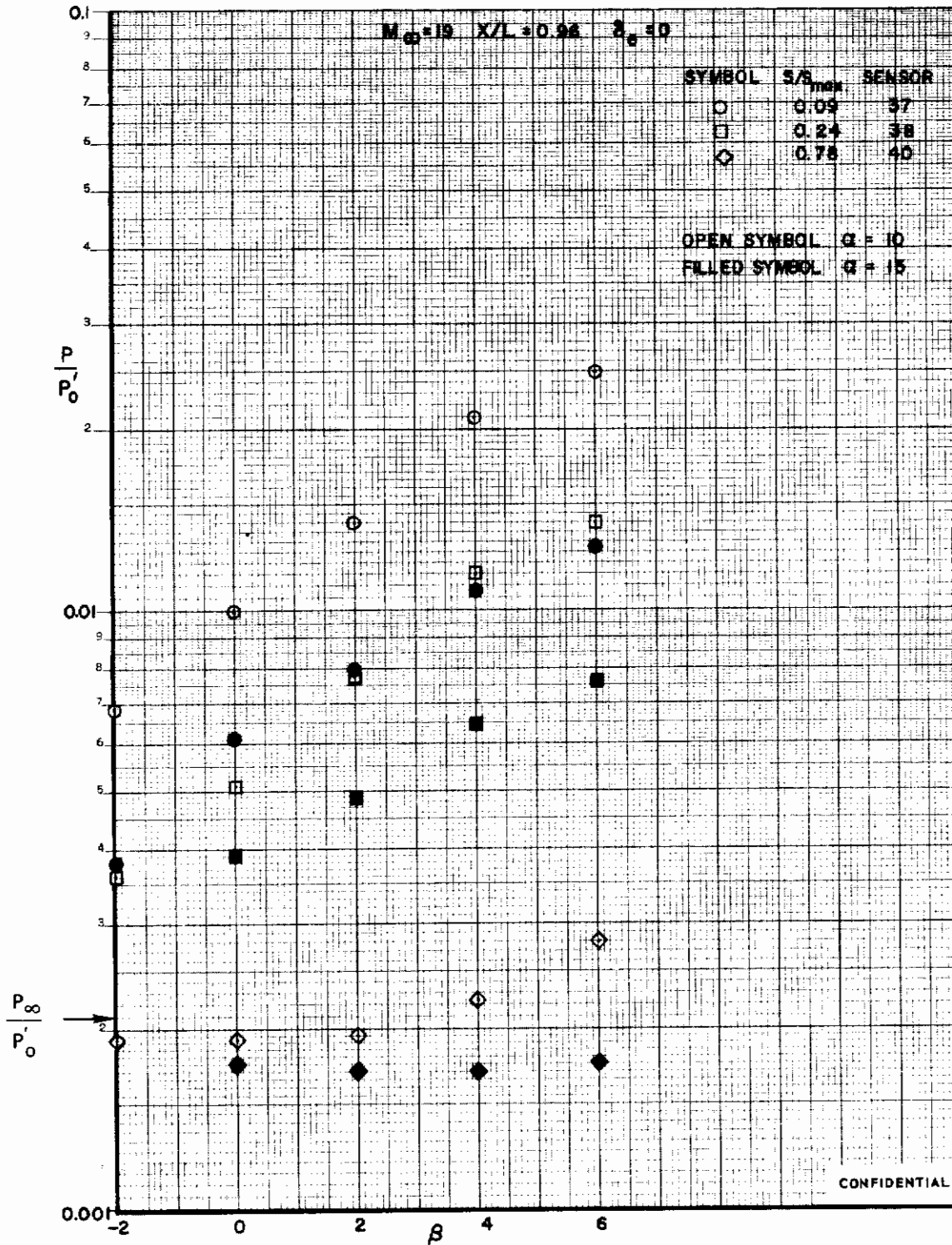
FIGURE 125 (U) EFFECT OF YAW ON UPPER SURFACE PRESSURES AT X/L = 0.96
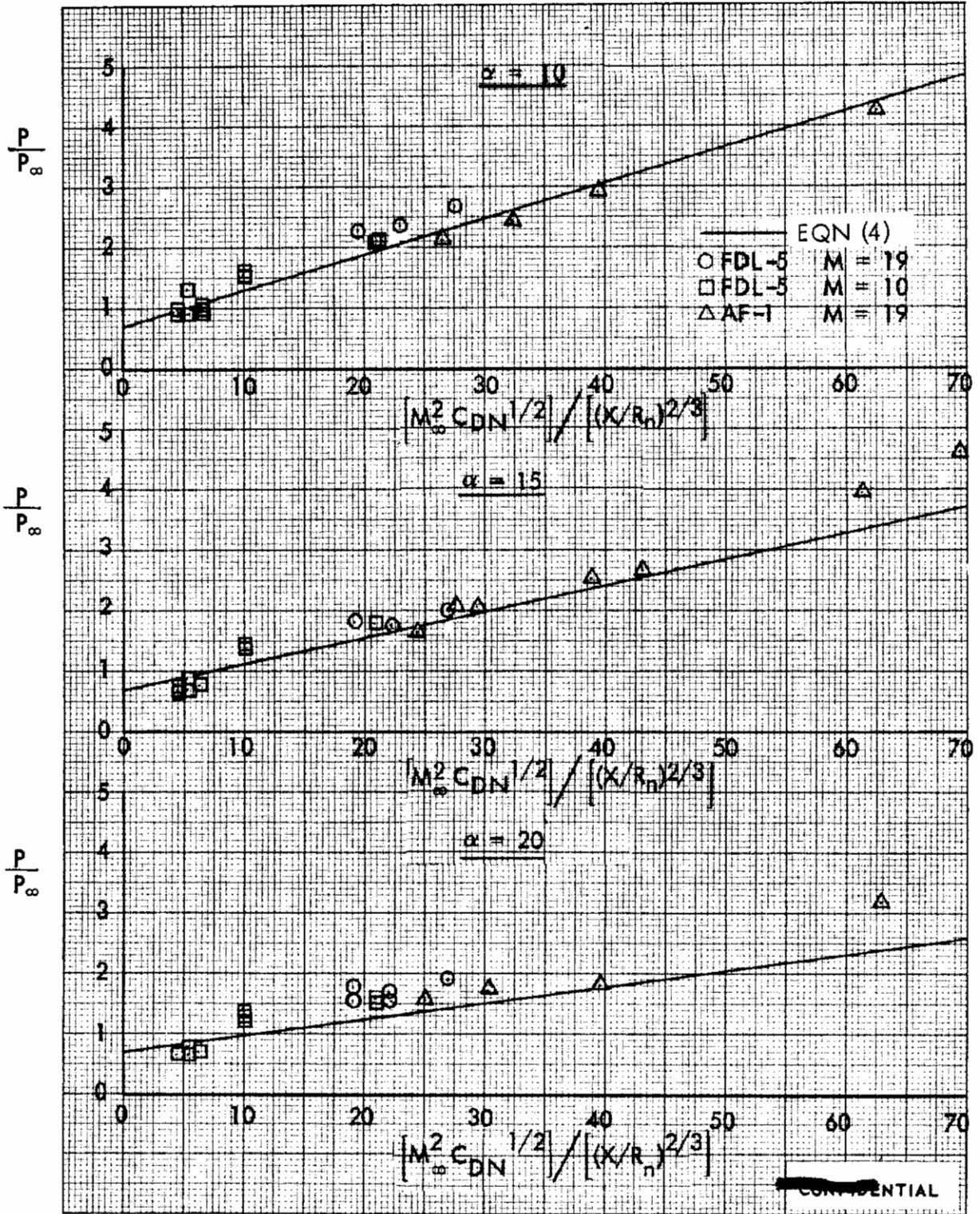
FIGURE 126 (U) COMPARISON OF UPPER SURFACE CENTERLINE PRESSURES FROM THREE SOURCES

204

EQN. (4)

X/L = 0.05

X/L = 0.15

X/L = 0.30
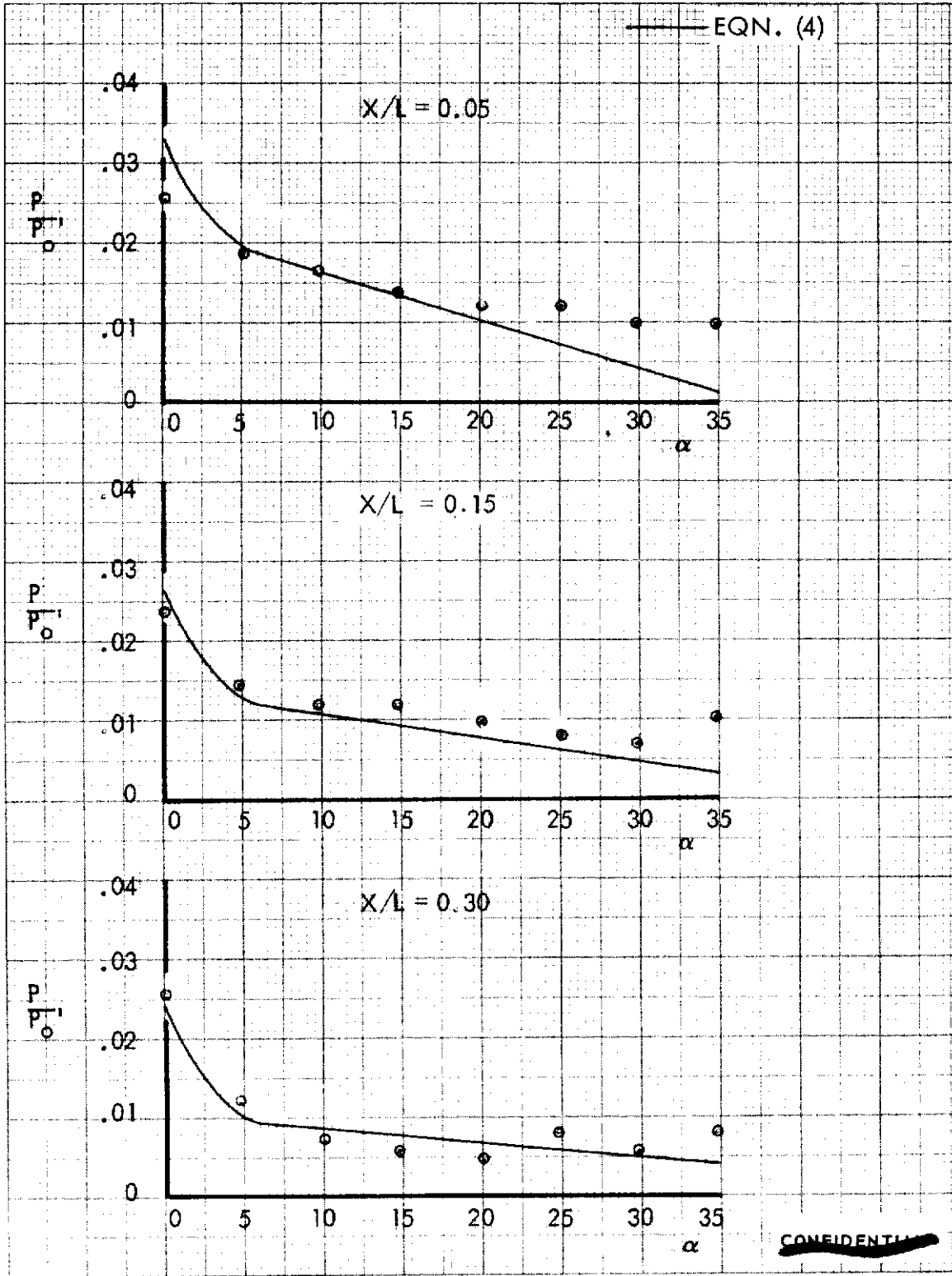
FIGURE 127 (U) CORRELATION OF TUNNEL C UPPER SURFACE CENTERLINE PRESSURES
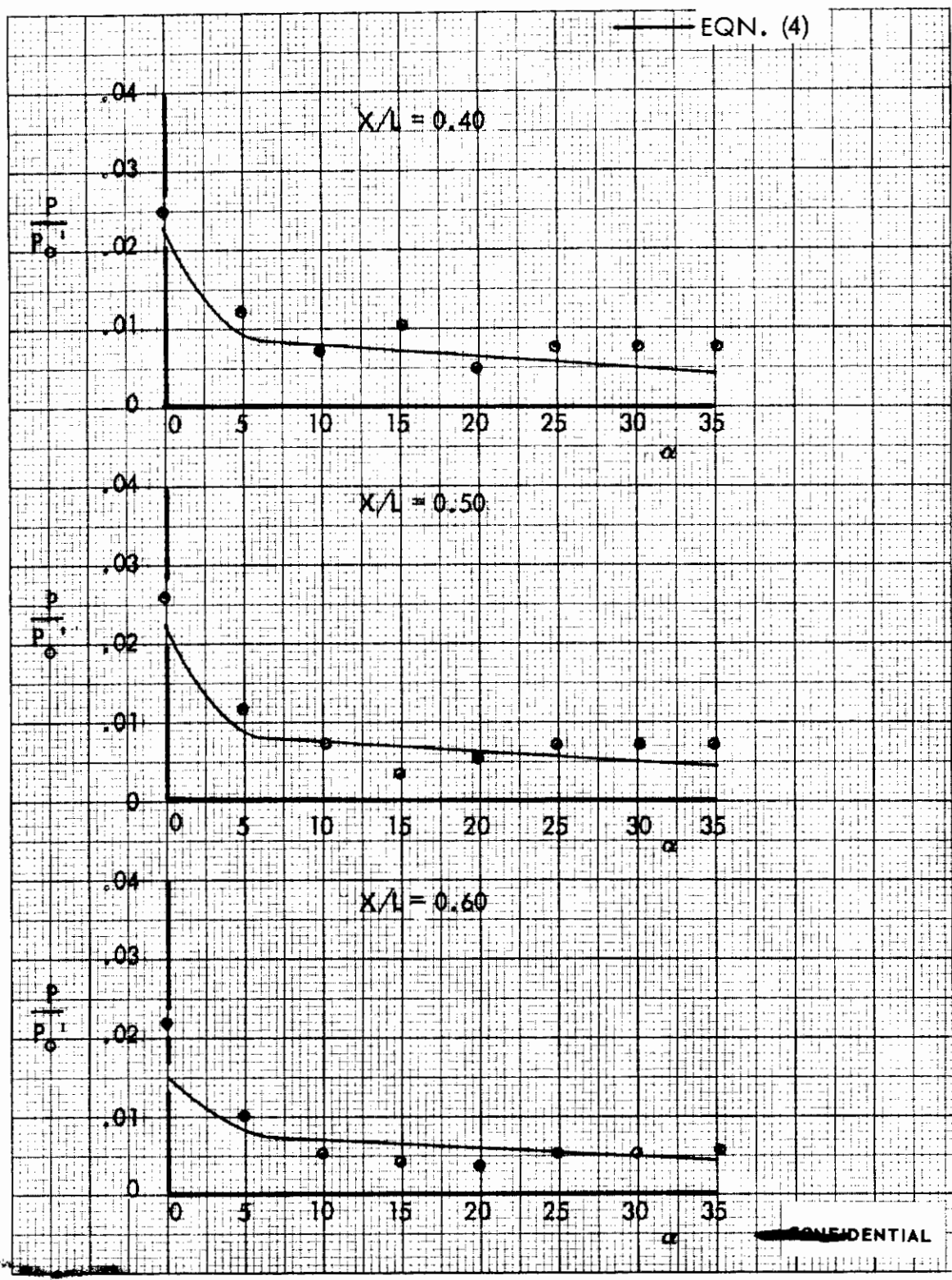
FIGURE 127   (U) (CONCLUDED) CORRELATION OF TUNNEL C UPPER SURFACE
CENTERLINE PRESSURES
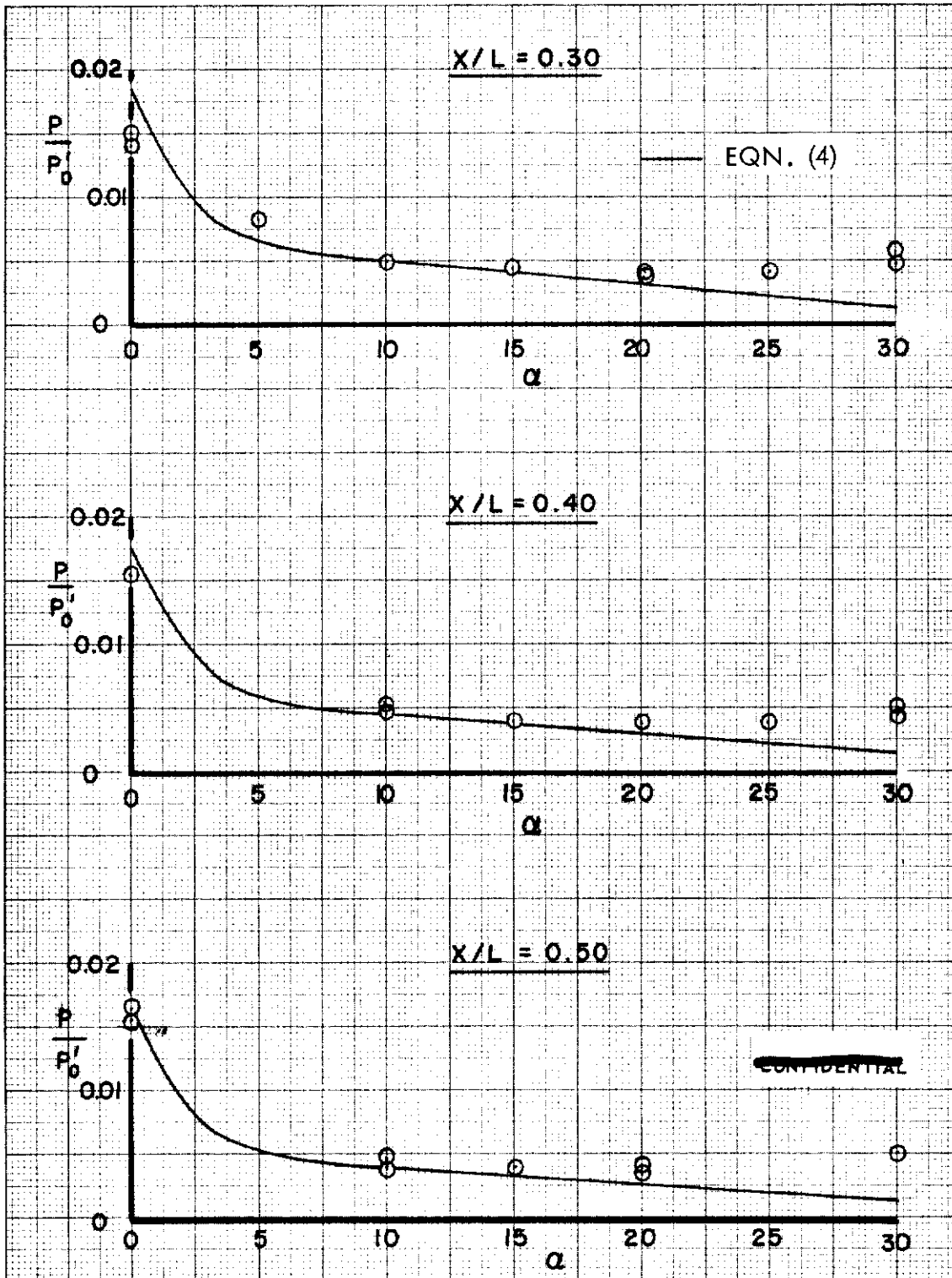
FIGURE 128 (ᵘ) CORRELATION OF TUNNEL F UPPER SURFACE CENTERLINE PRESSURES

207
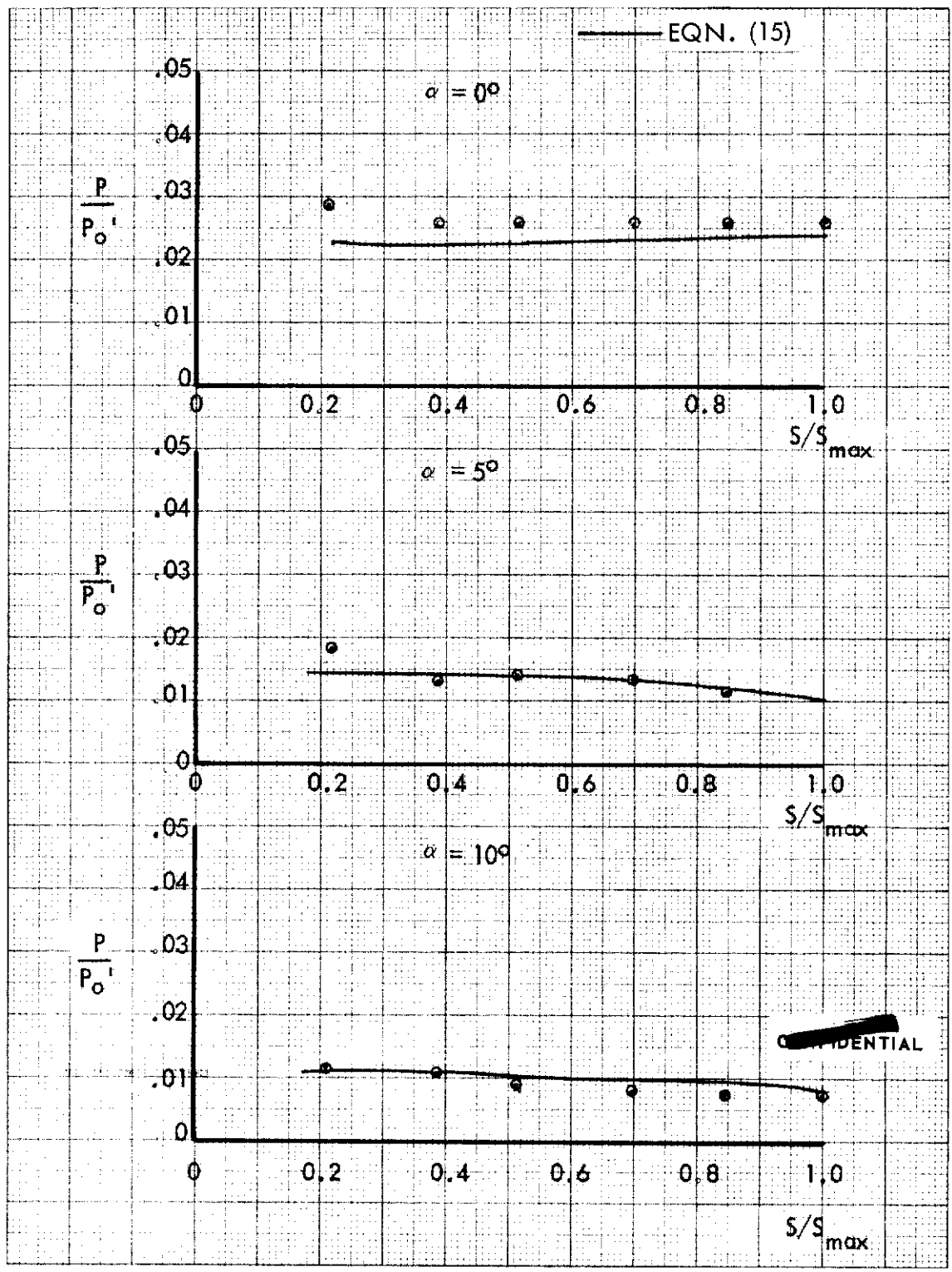
FIGURE 129 (U) CORRELATION OF TUNNEL C UPPER SURFACE SPANWISE PRESSURES AT X/L = 0.30
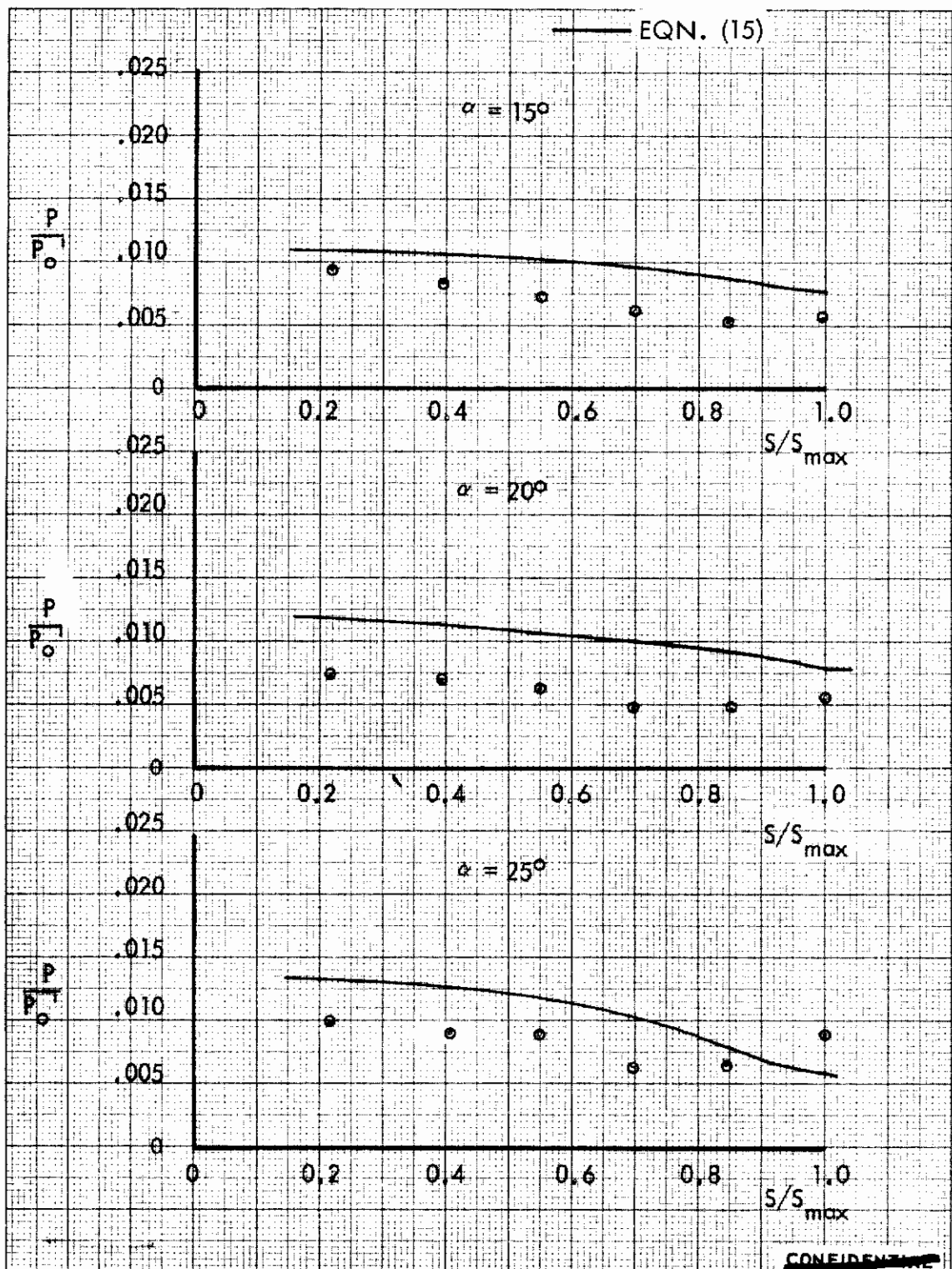
FIGURE 129 (U) (CONCLUDED) CORRELATION OF TUNNEL C UPPER SURFACE
SPANWISE PRESSURES AT X/L = 0.30

209
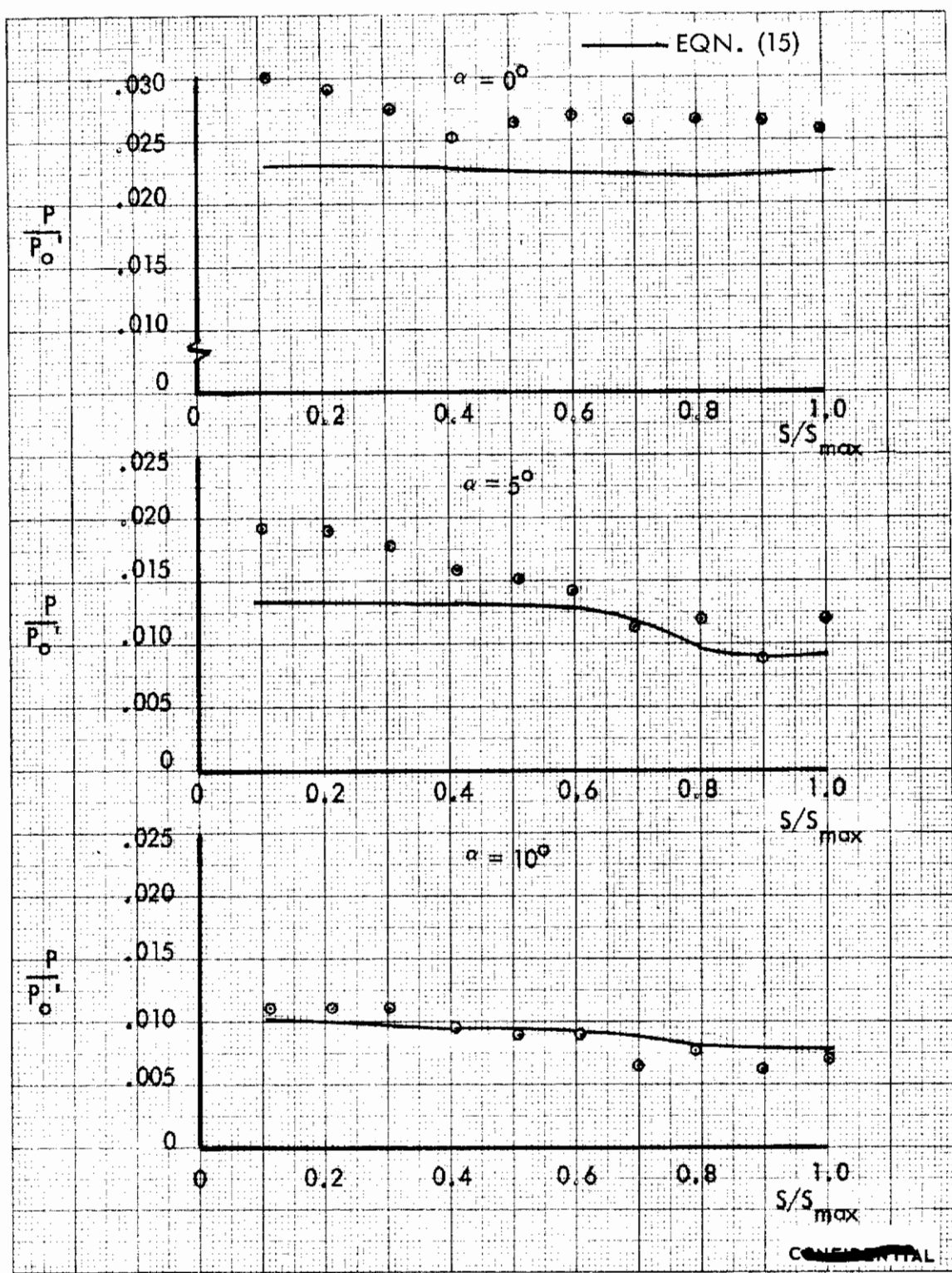
FIGURE 130 (U) CORRELATION OF TUNNEL C UPPER SURFACE
SPANWISE PRESSURES AT X/L = 0.50

210
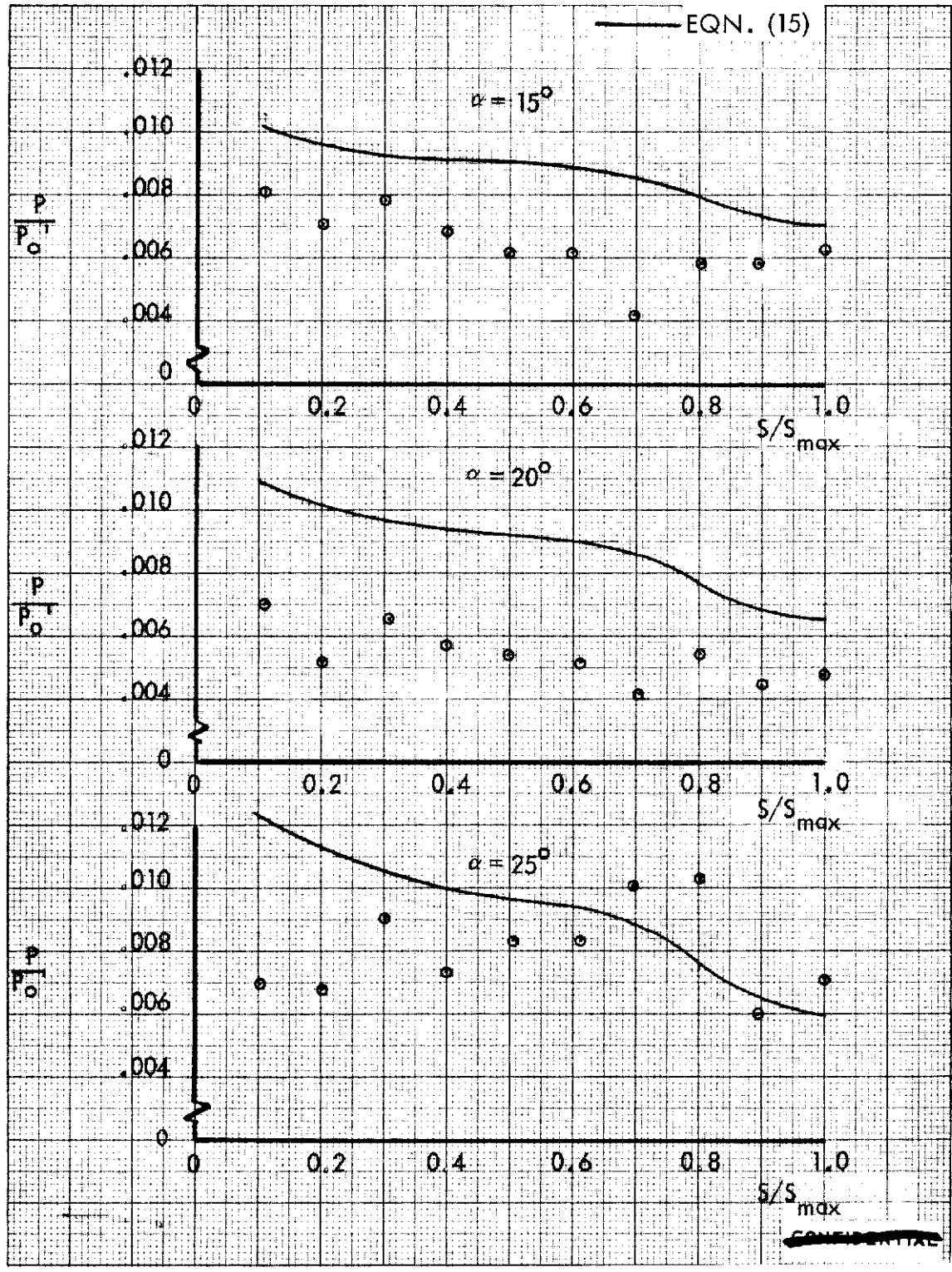
FIGURE 130 (U) (CONCLUDED) CORRELATION OF TUNNEL C UPPER SURFACE
SPANWISE PRESSURES AT X/L = 0.50

211
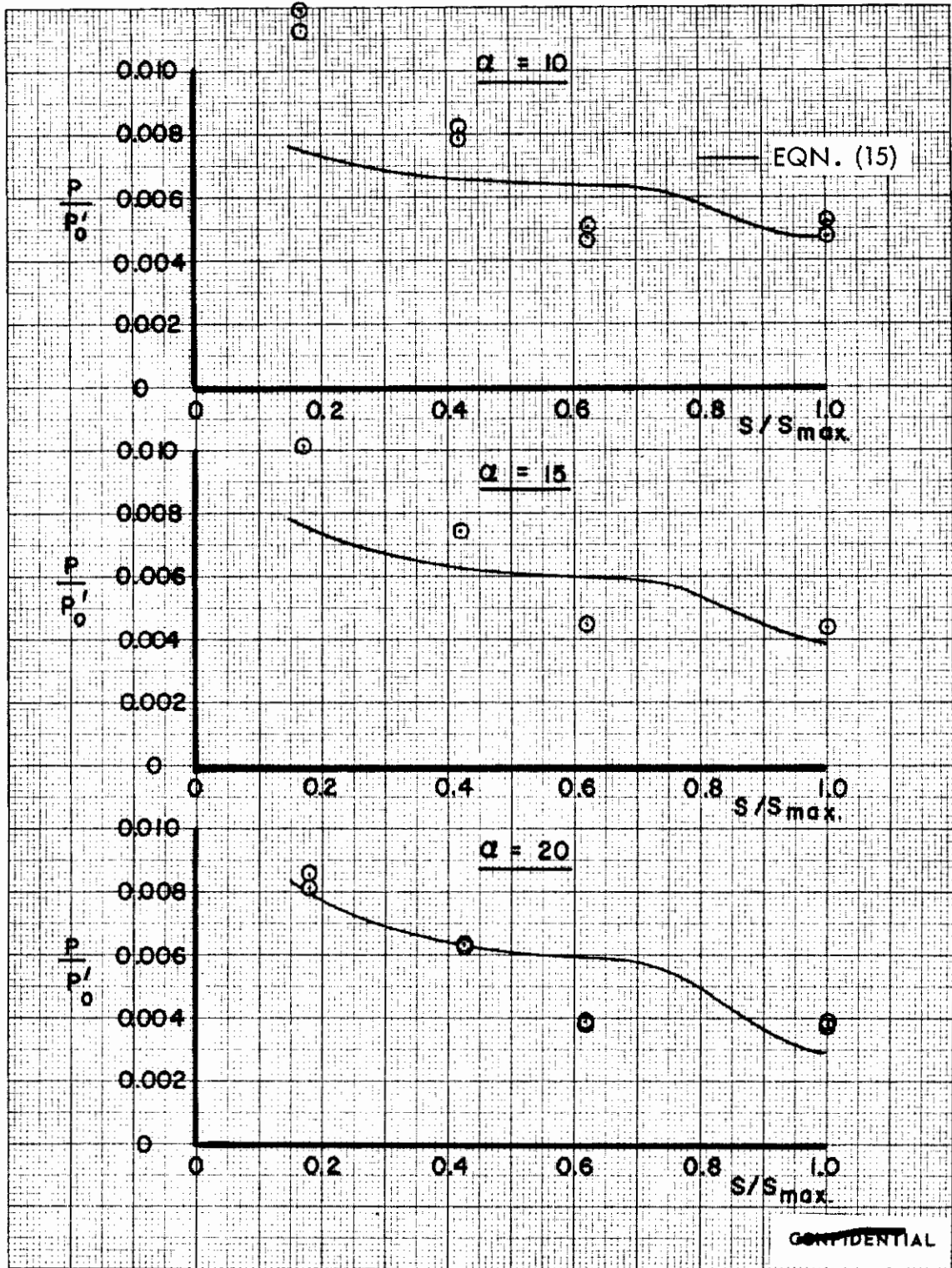
FIGURE 131 (U) CORRELATION OF TUNNEL F UPPER SURFACE SPANWISE PRESSURES
AT X/L = 0.30
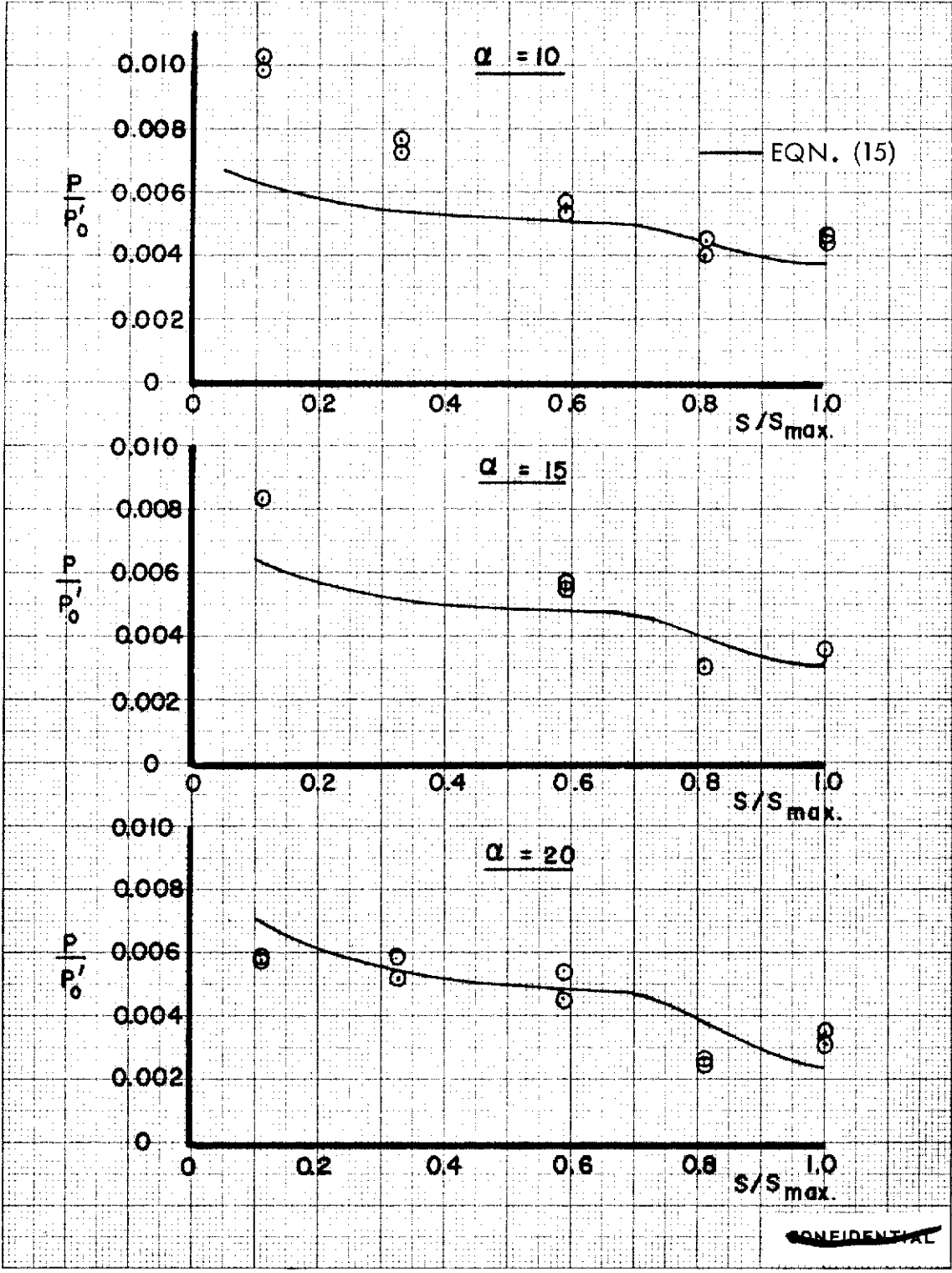
FIGURE 132   (U) CORRELATION OF TUNNEL F UPPER SURFACE SPANWISE PRESSURES
AT X/L = 0.50
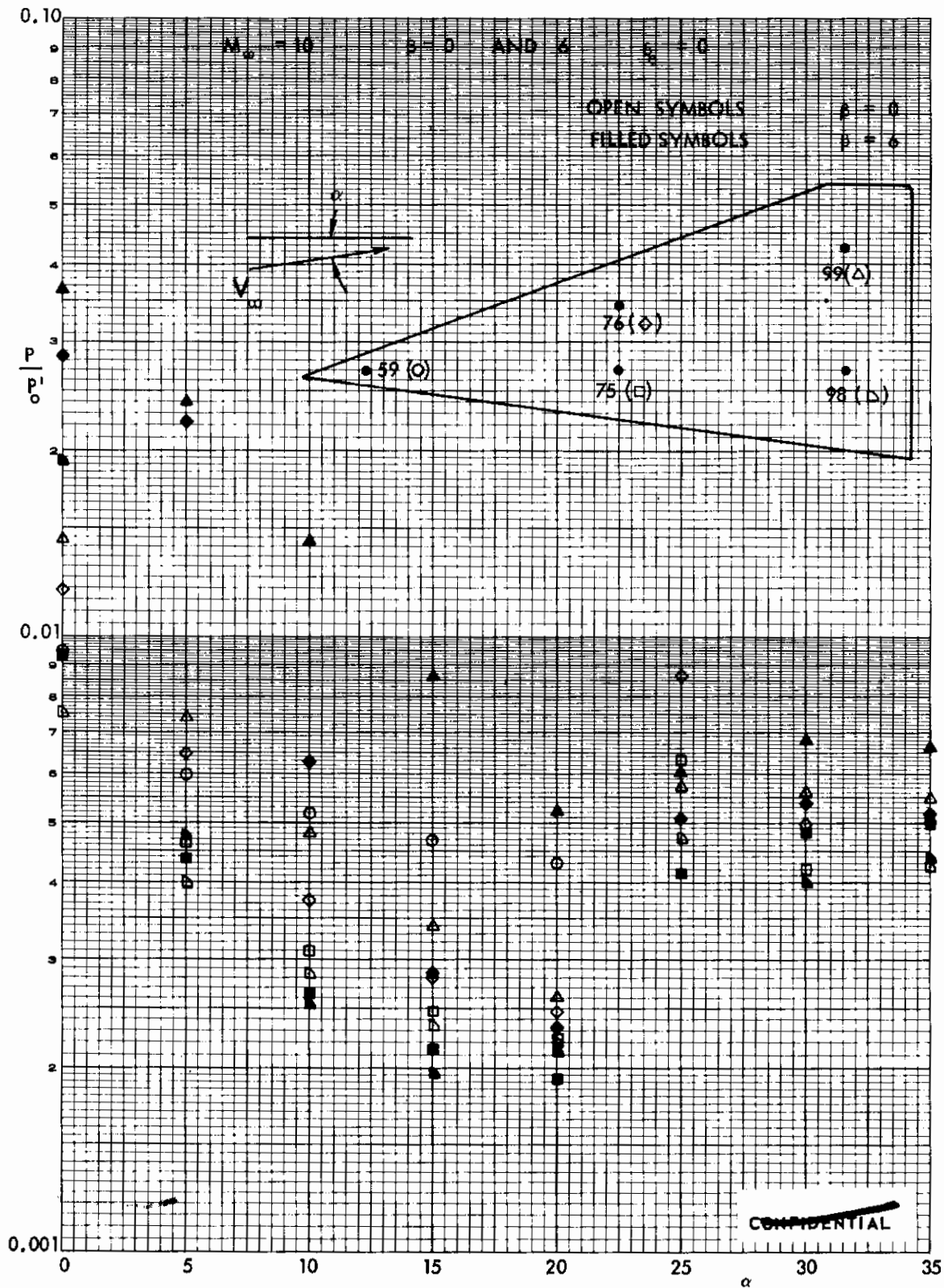
FIGURE 133 (C) FIN SIDE PANEL PRESSURES

214
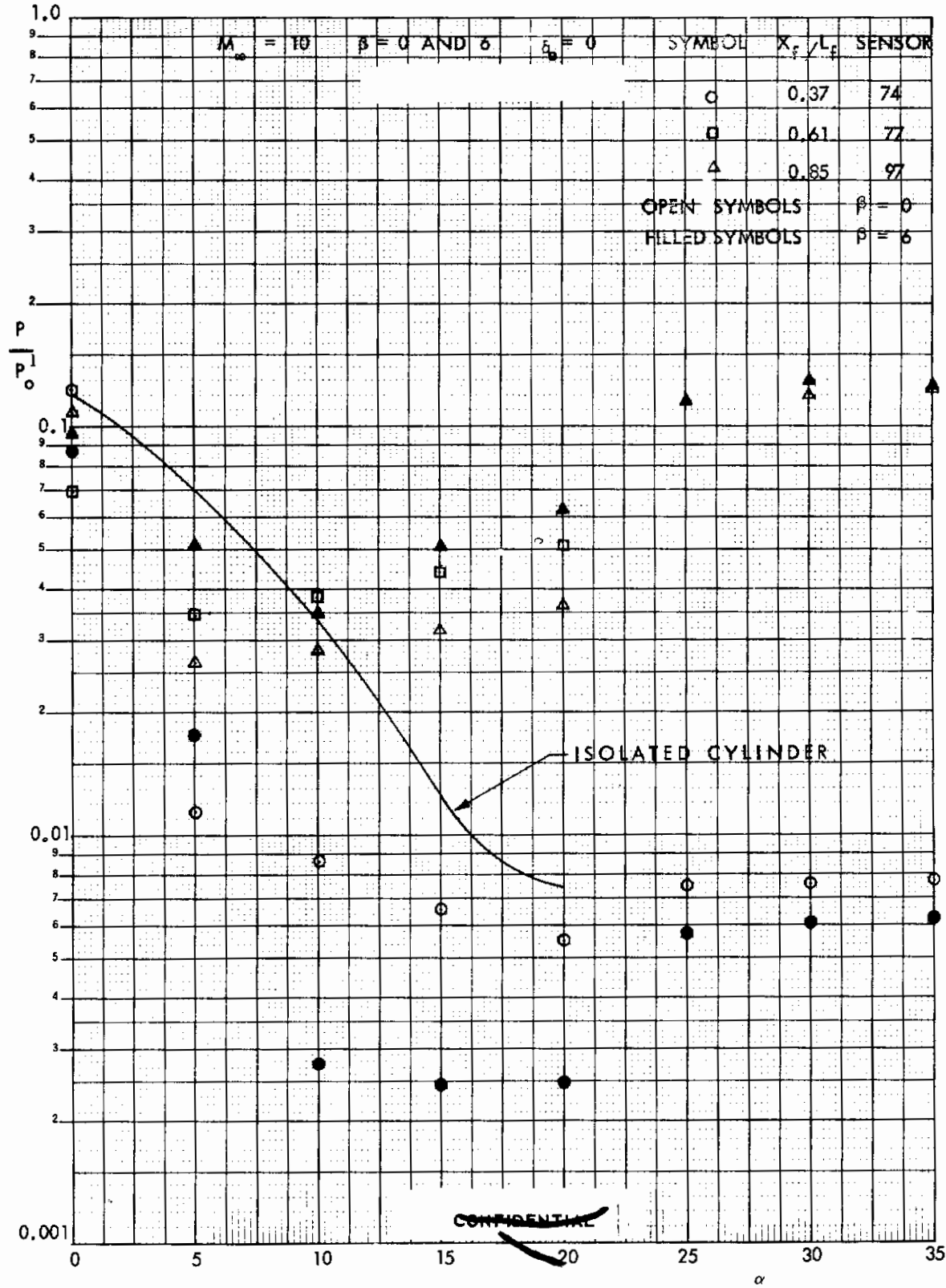
FIGURE 134 (U) FIN STAGNATION LINE PRESSURES

215
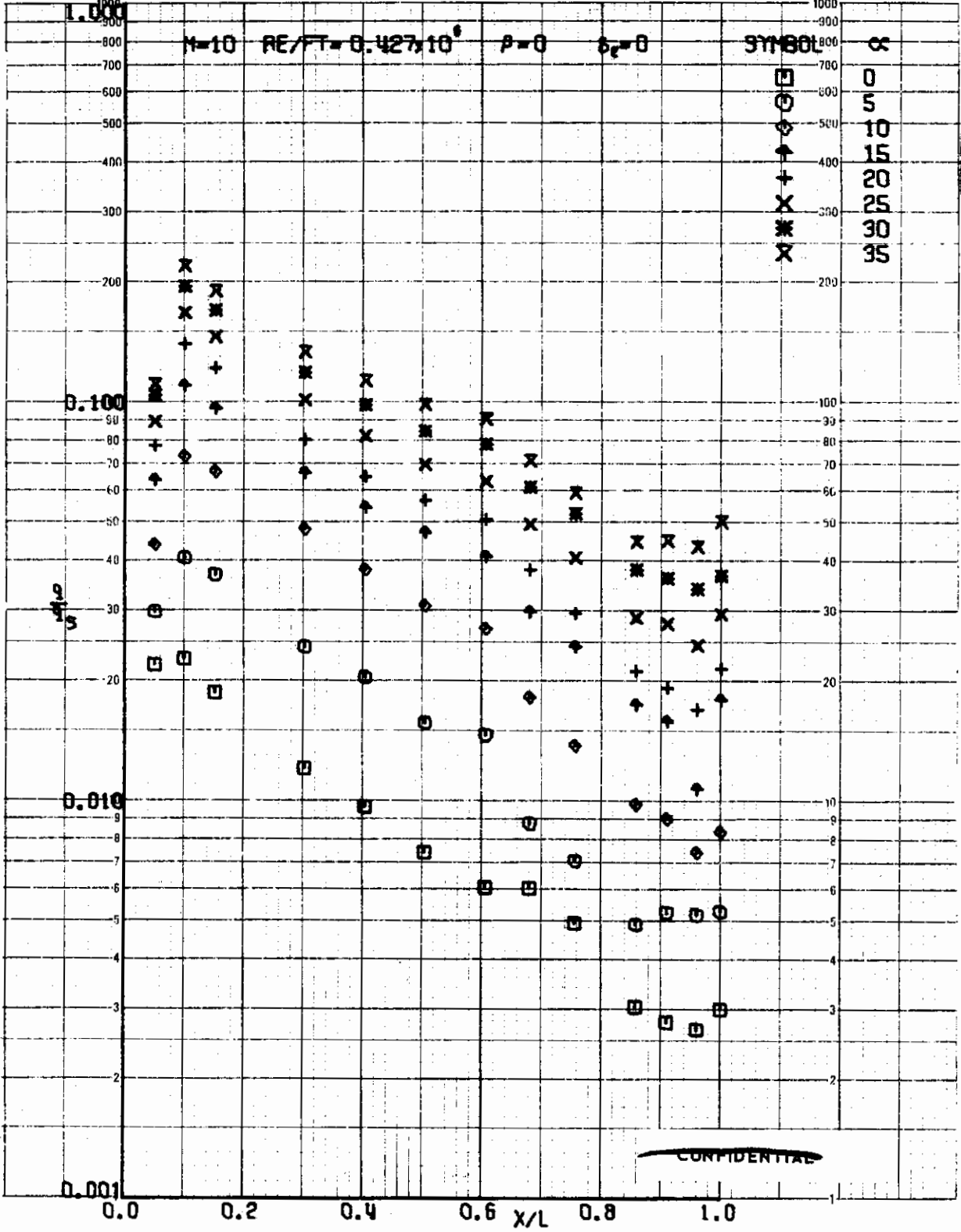
FIGURE 135   (U) TUNNEL C LOWER SURFACE CENTERLINE HEATING RATES, $\beta=0$

216
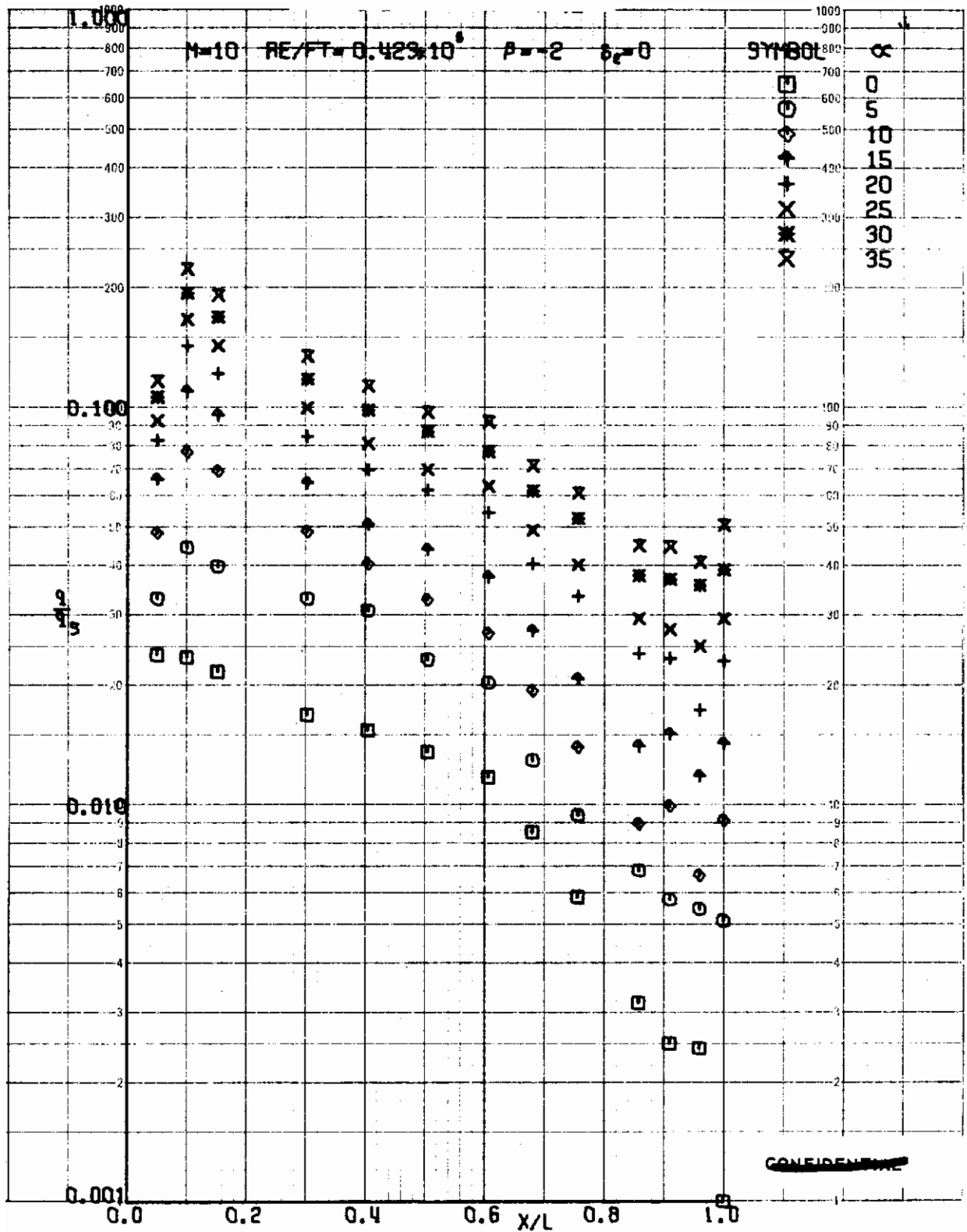
FIGURE 136 (U) TUNNEL C LOWER SURFACE CENTERLINE HEATING RATES, β=-2
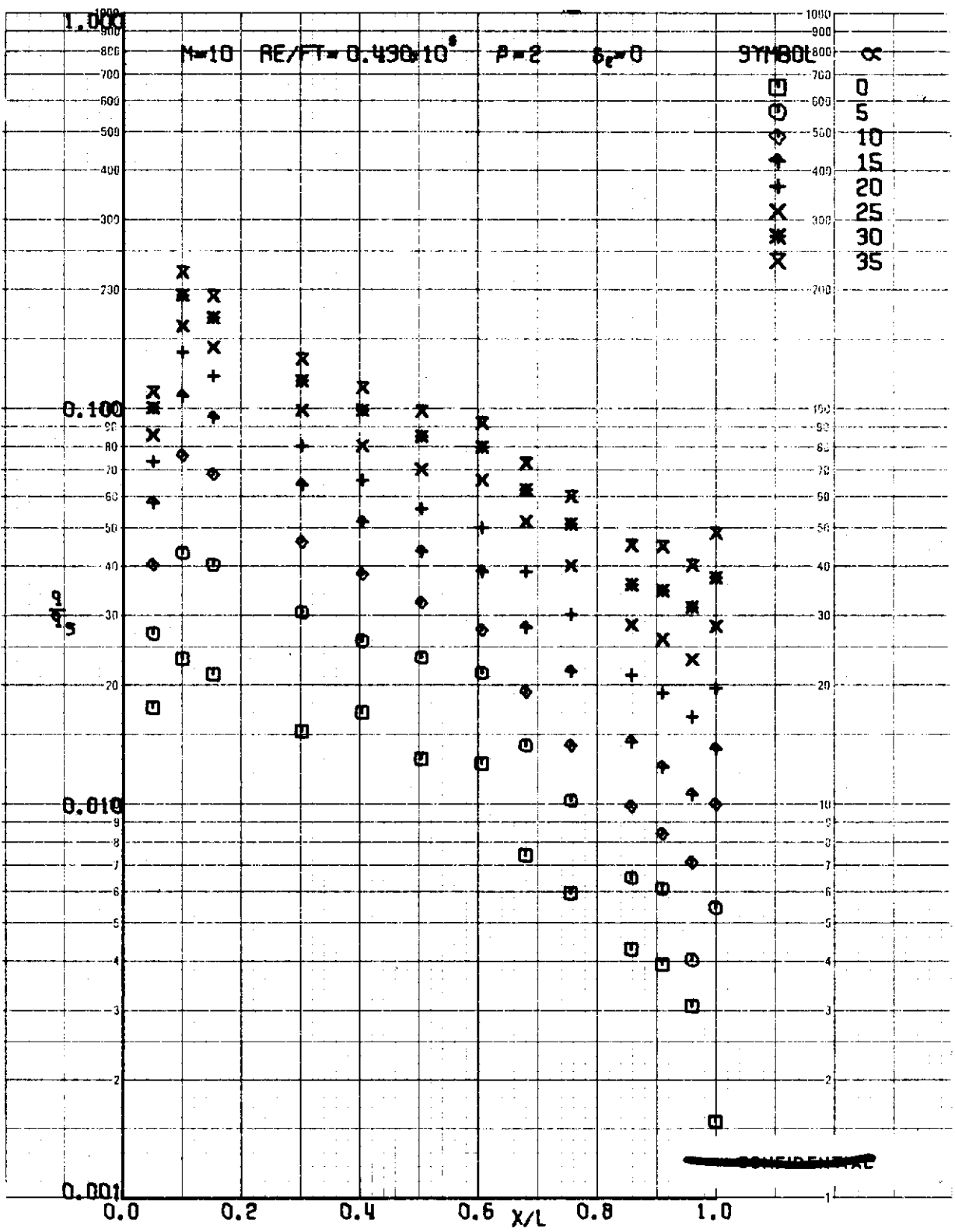
FIGURE 137 (U) TUNNEL C LOWER SURFACE CENTERLINE HEATING RATES, β=2
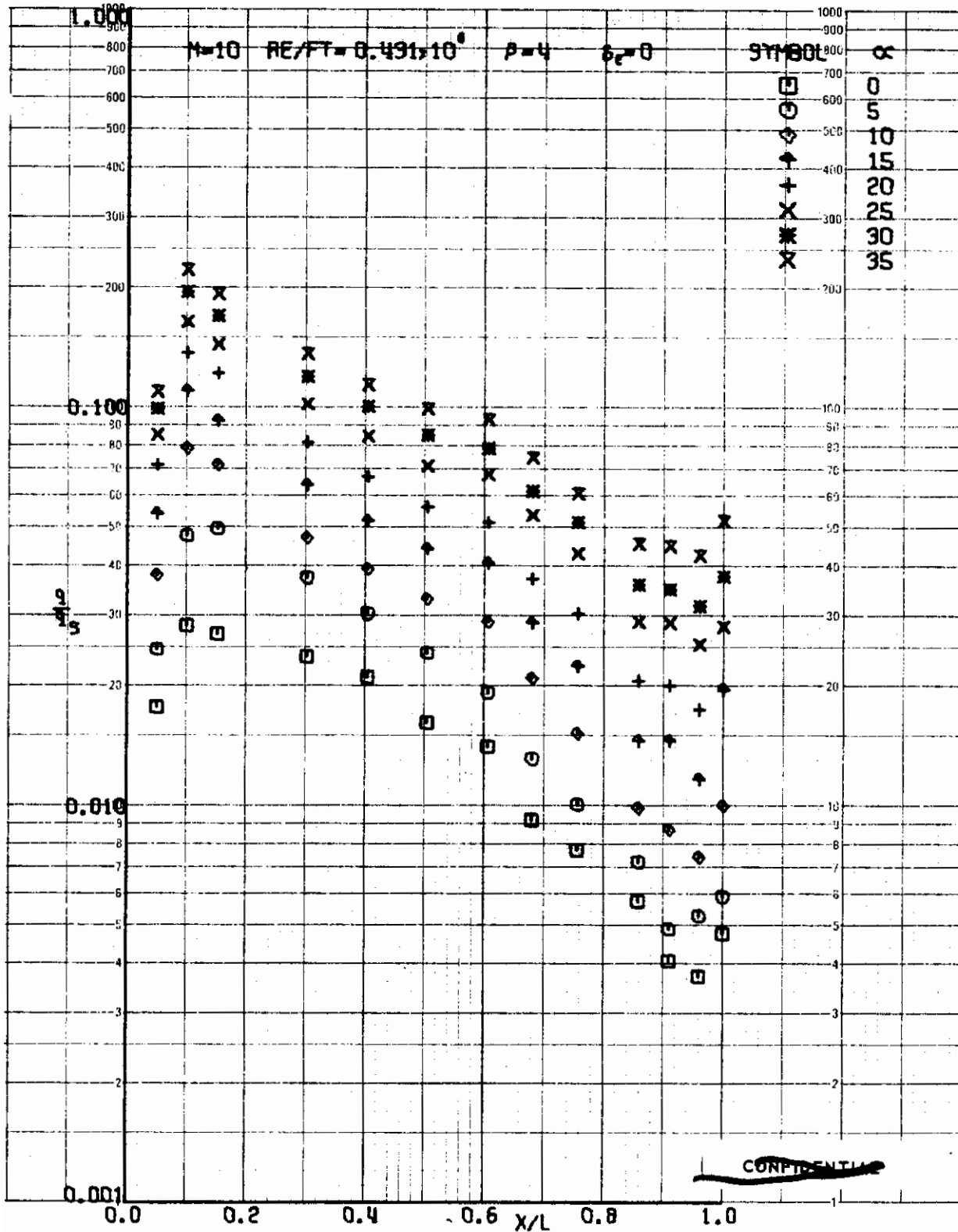
FIGURE 138   (U) TUNNEL C LOWER SURFACE CENTERLINE HEATING RATES, β=4

219

FIGURE 139 (U) TUNNEL C LOWER SURFACE CENTERLINE HEATING RATES, β=6
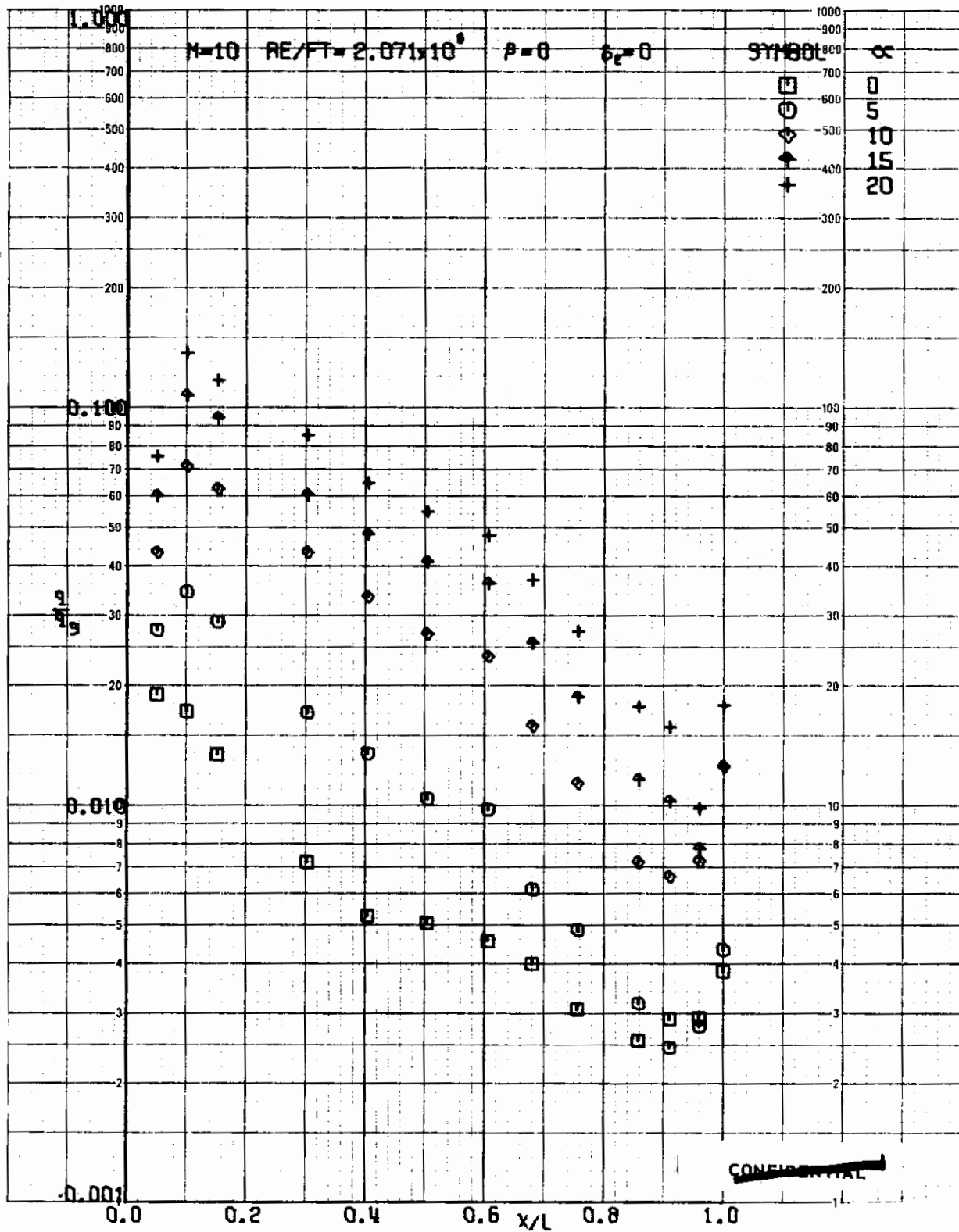
FIGURE 140   (U) TUNNEL C LOWER SURFACE CENTERLINE HEATING RATES, β=0
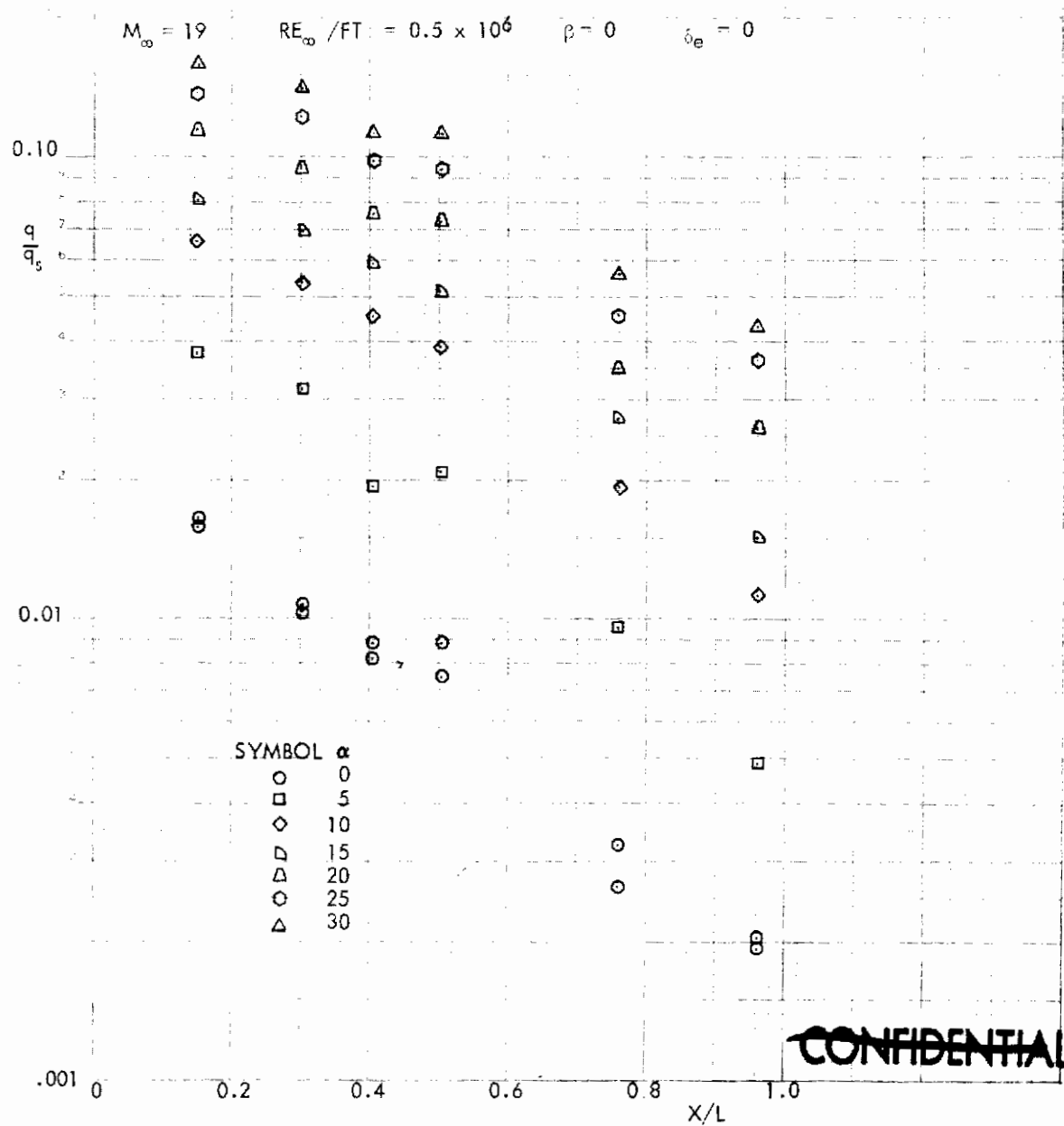
FIGURE 141 (U) TUNNEL F LOWER SURFACE CENTERLINE HEATING RATES, $\beta=0$
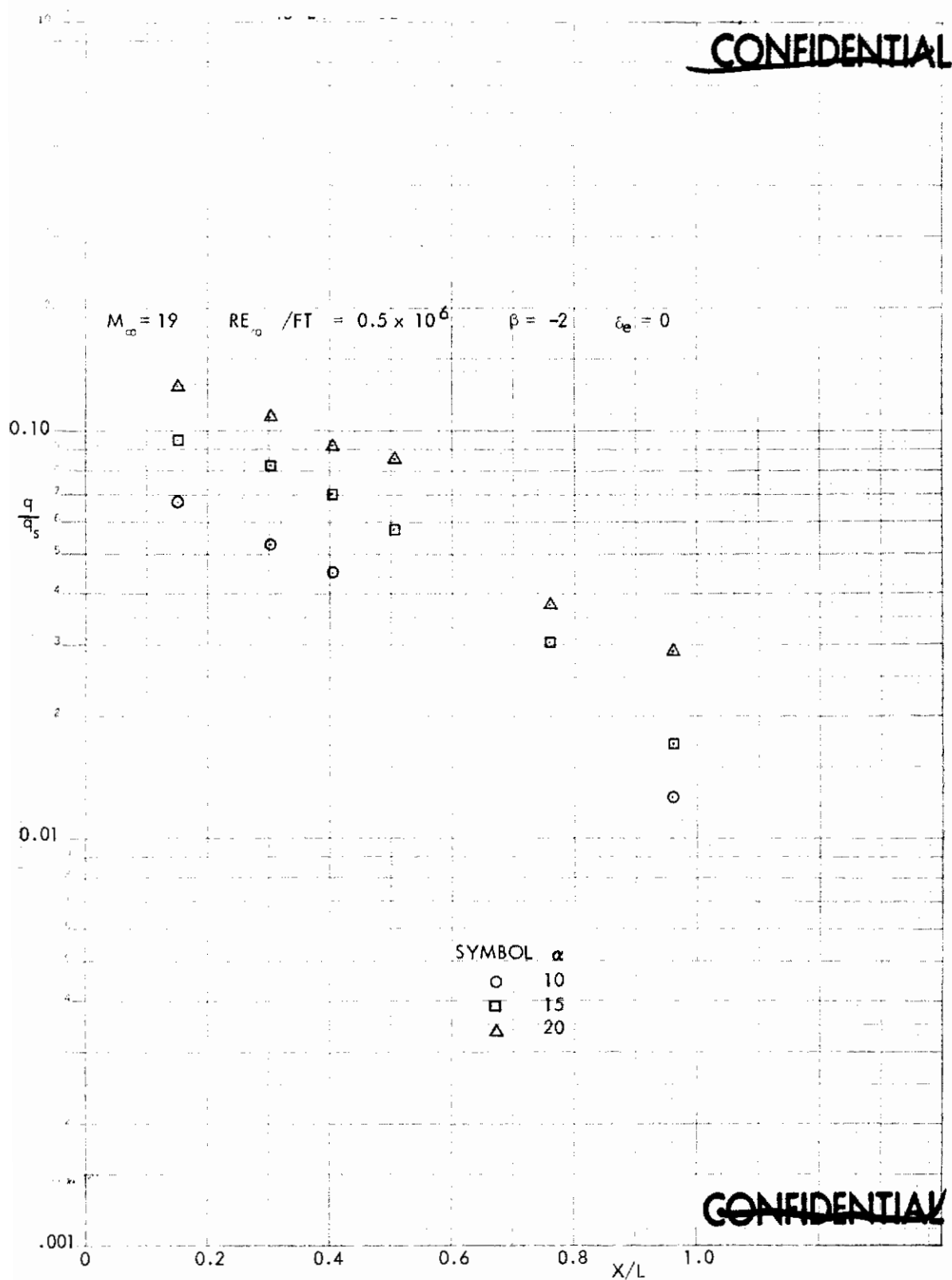
FIGURE 142   (U) TUNNEL F LOWER SURFACE CENTERLINE HEATING RATES, $\beta = -2$
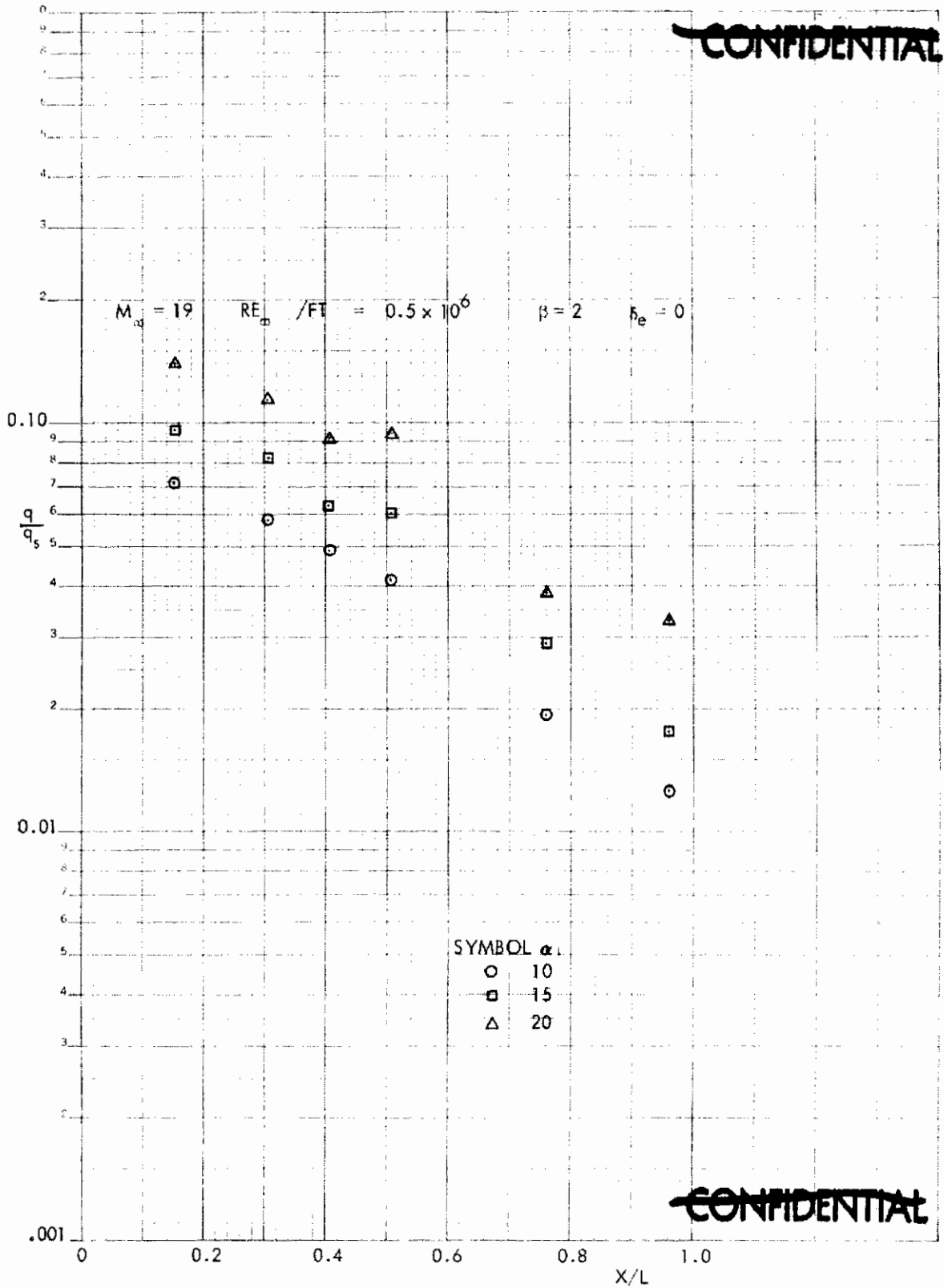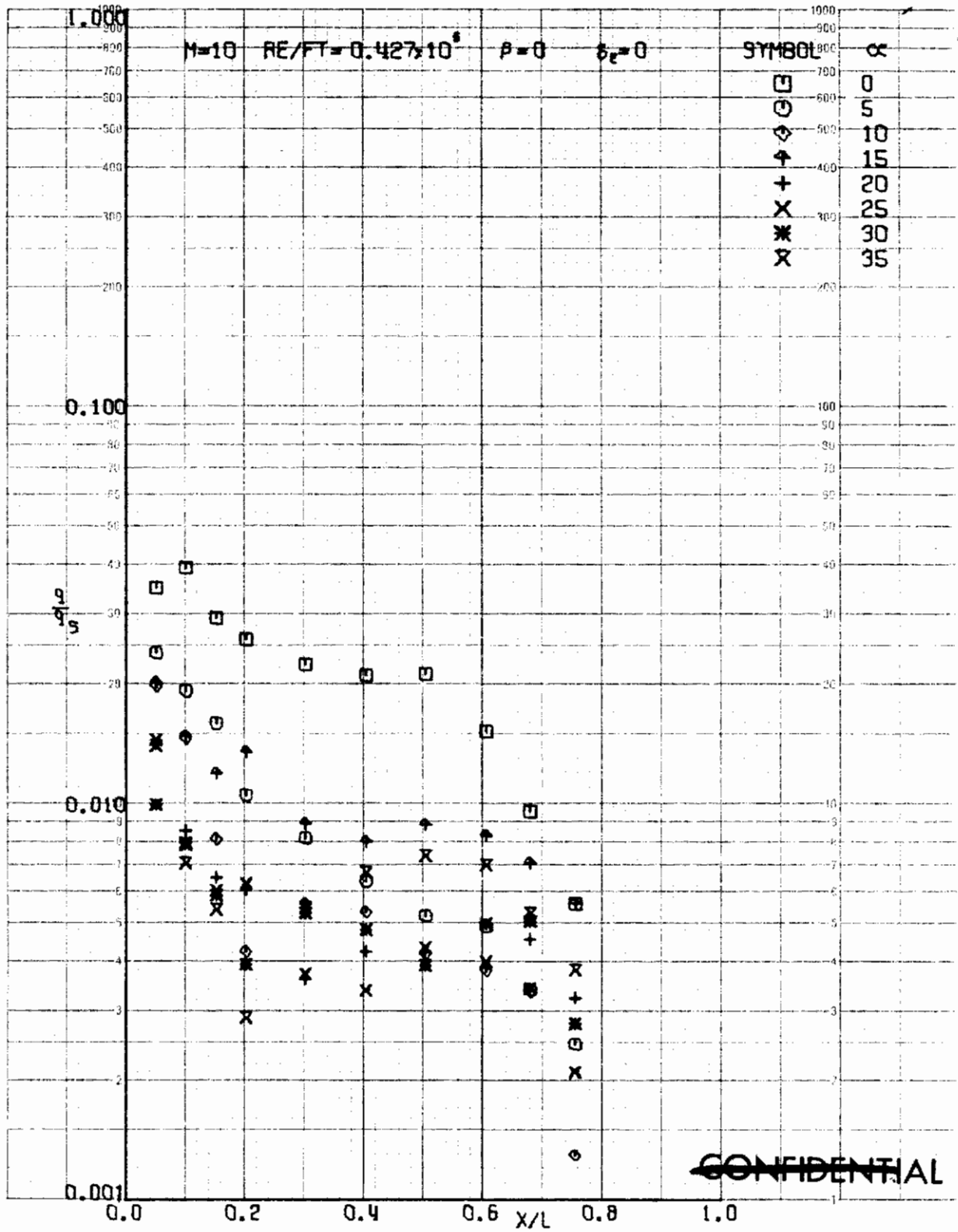
FIGURE 143 (U) TUNNEL F LOWER SURFACE CENTERLINE HEATING RATES, $\beta=2$
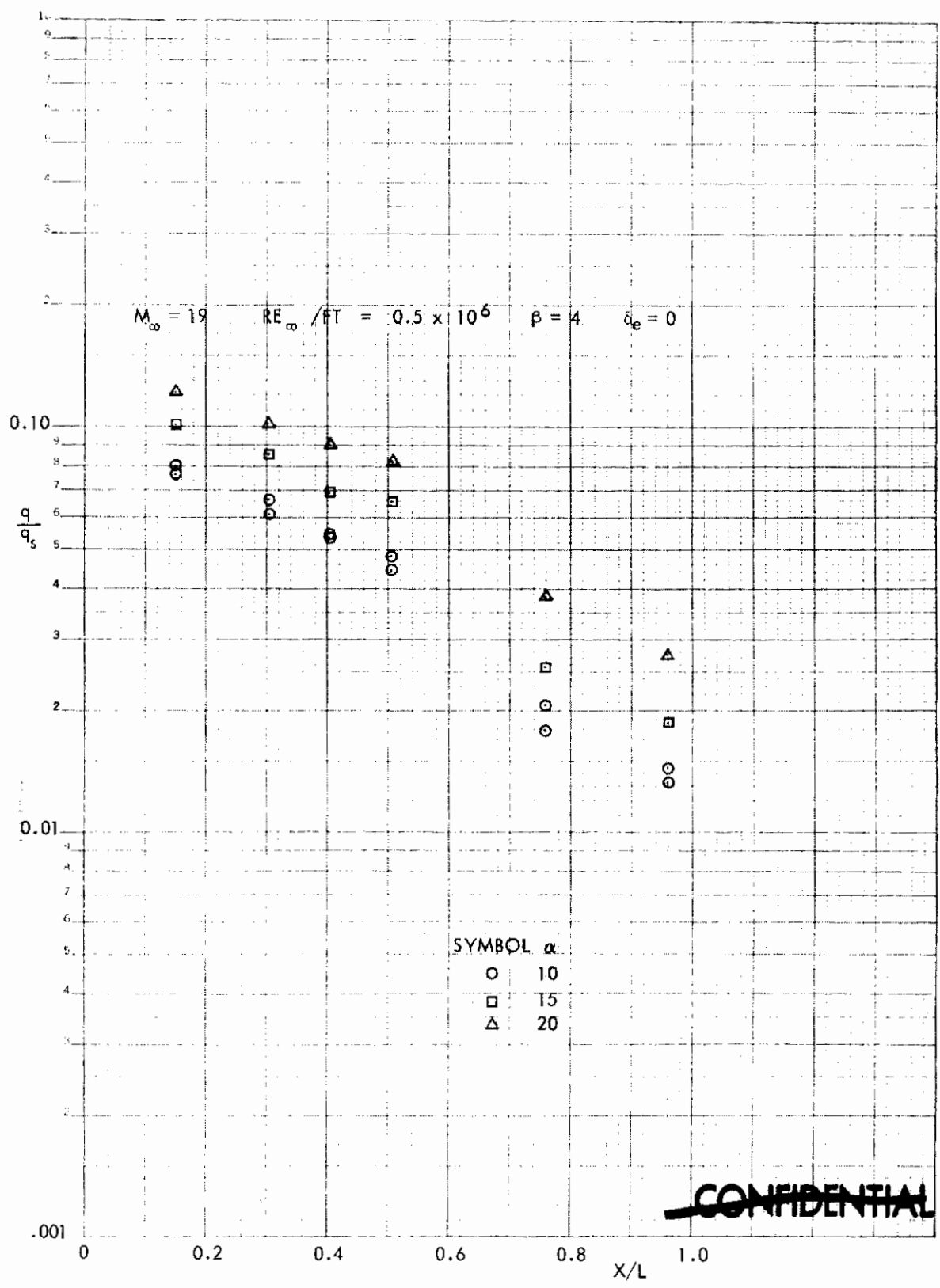
FIGURE 144 (U) TUNNEL F LOWER SURFACE CENTERLINE HEATING RATES, $\beta=4$

225

$M_\infty = 19$ $RE_\infty /FT = 0.5 \times 10^6$ $\beta = 6$ $\delta_e = 0$

SYMBOL	α
○	10
□	15
△	20
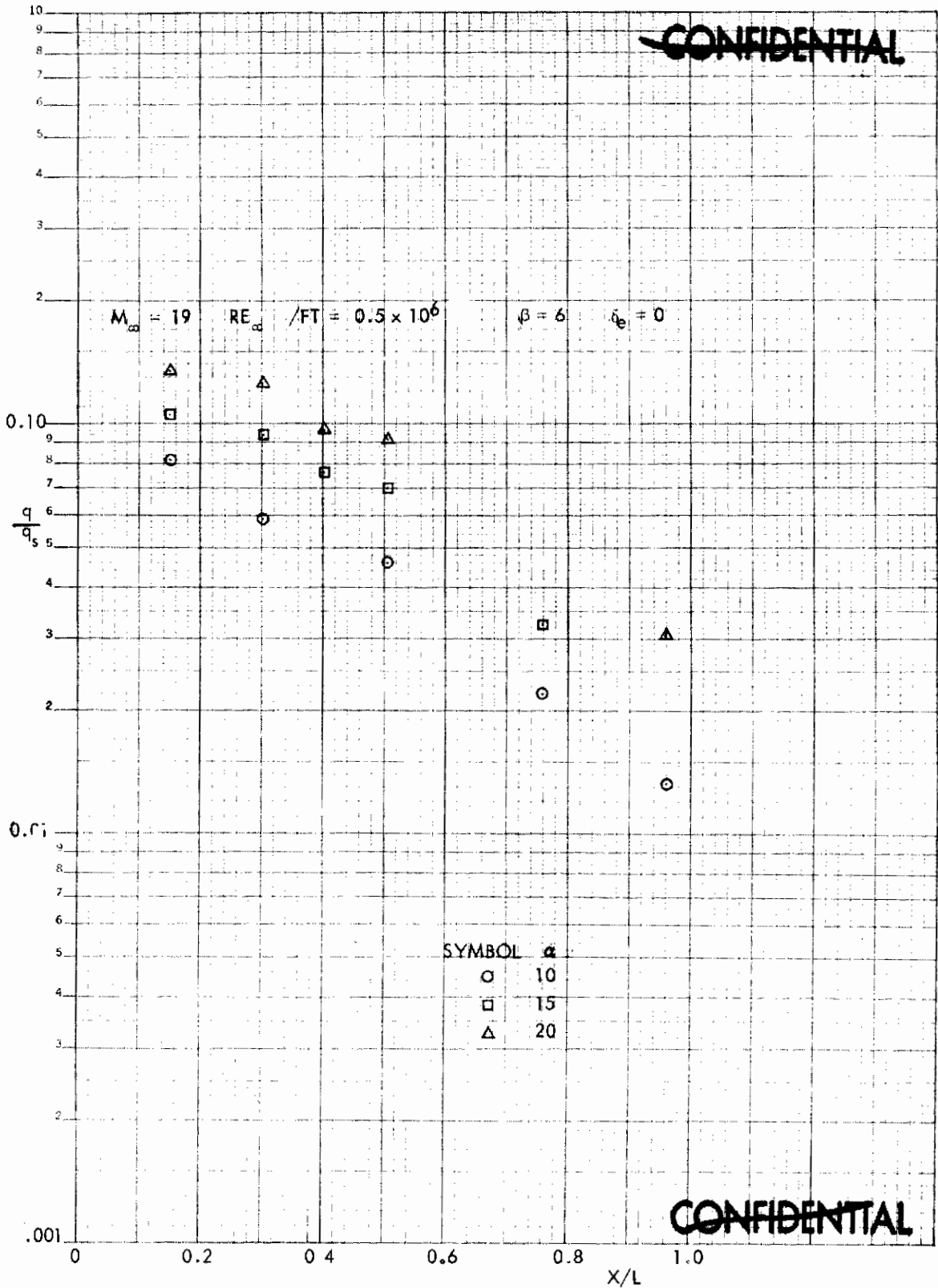
FIGURE 145   (U) TUNNEL F LOWER SURFACE CENTERLINE HEATING RATES, $\beta=6$

226
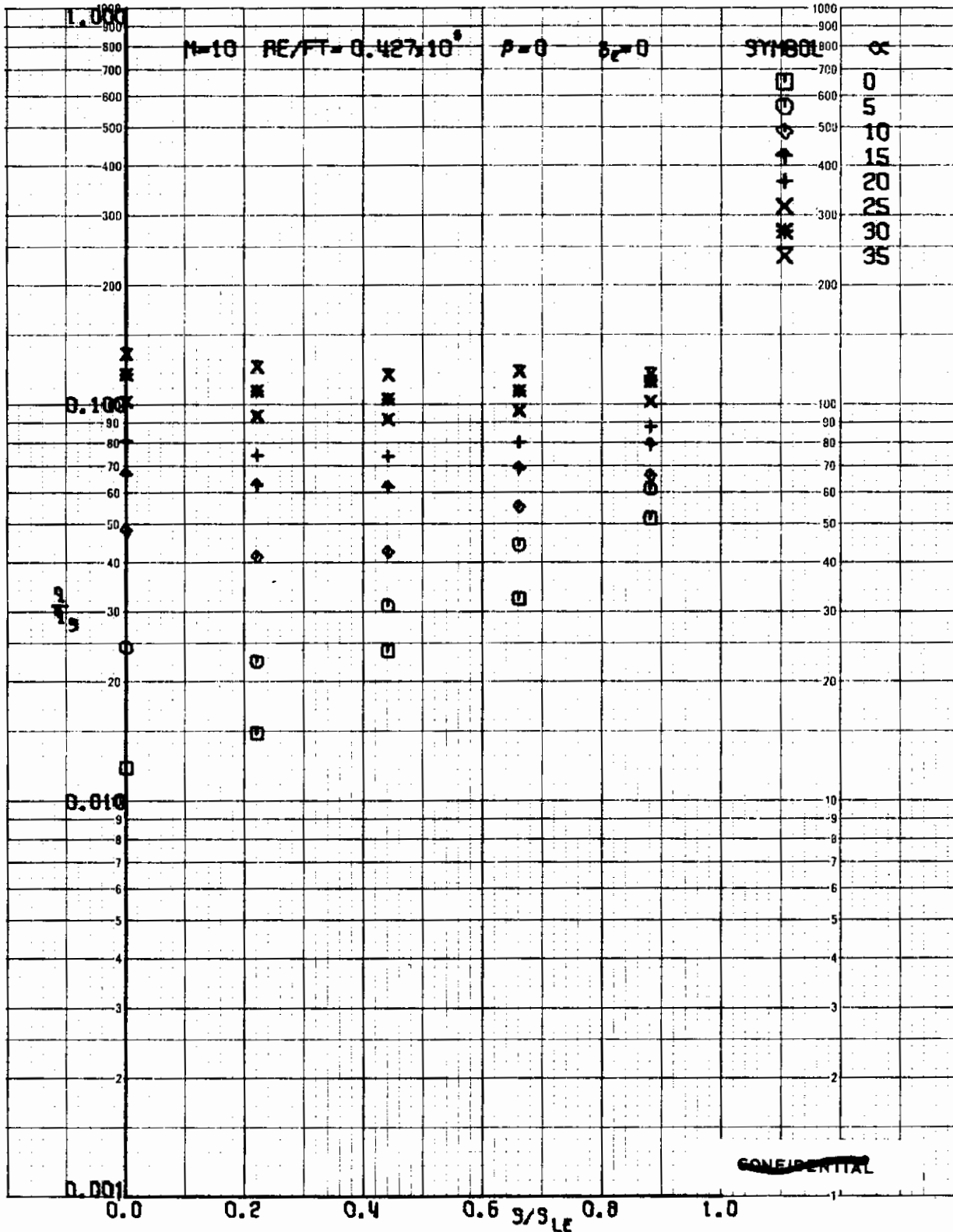
FIGURE 146 (U) TUNNEL C LOWER SURFACE SPANWISE HEATING RATES AT
X/L = 0.30, β=0
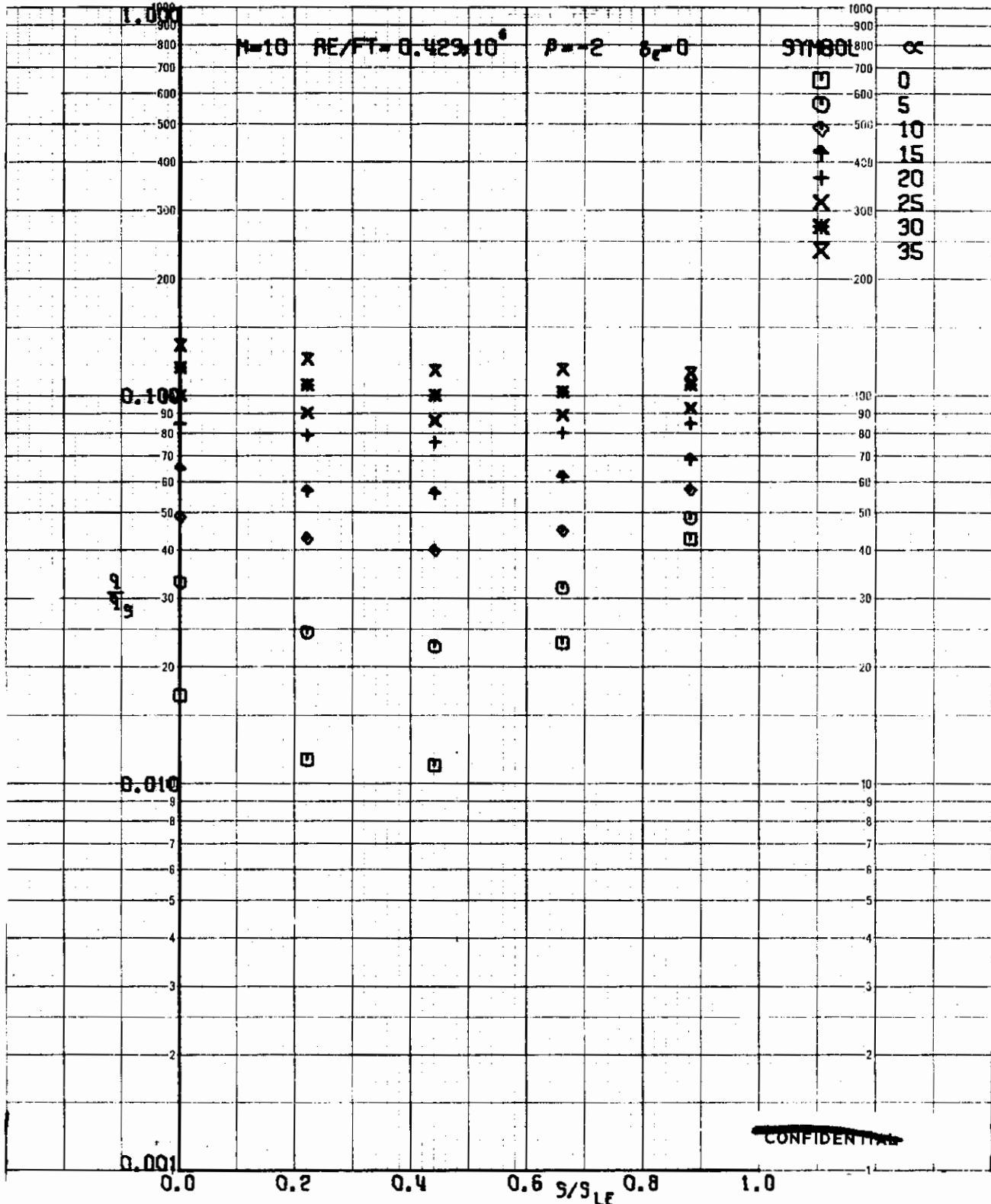
FIGURE 147 (U) TUNNEL C LOWER SURFACE SPANWISE HEATING RATES AT
X/L = 0.30, β=-2

228
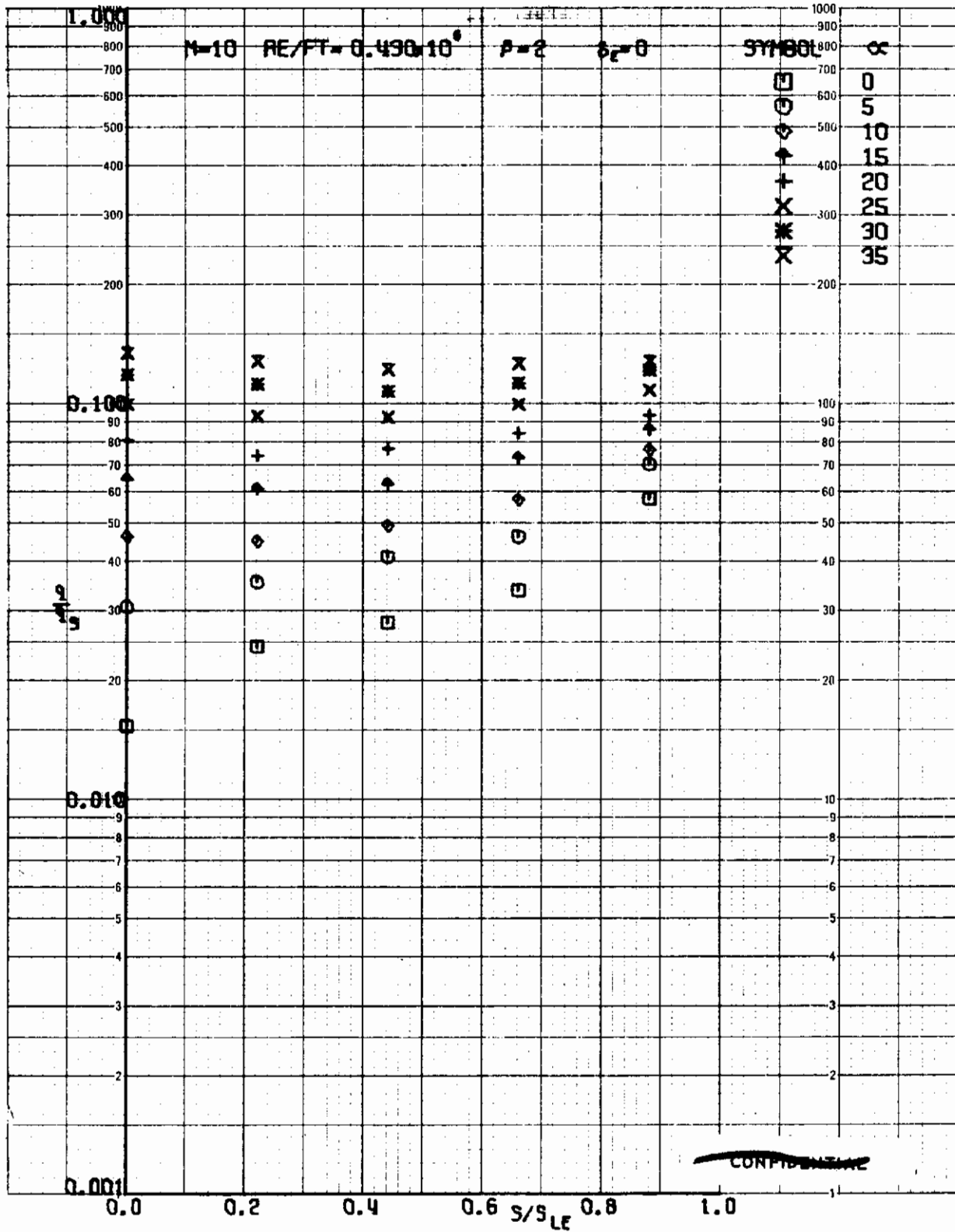
FIGURE 148 (U) TUNNEL C LOWER SURFACE SPANWISE HEATING RATES AT
X/L = 0.30, β=2

FIGURE 149 (U) TUNNEL C LOWER SURFACE SPANWISE HEATING RATES AT
X/L = 0.30, β=4

230
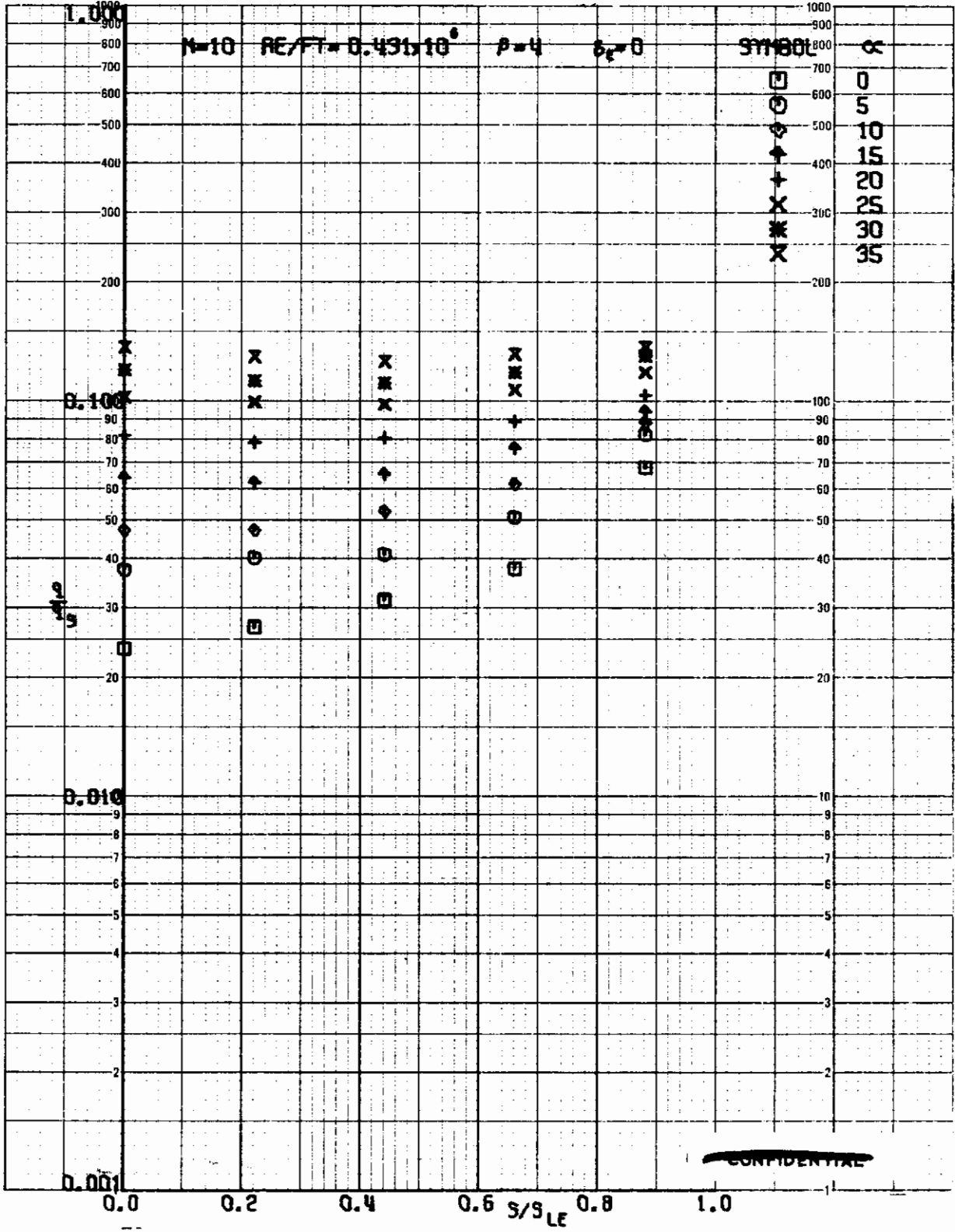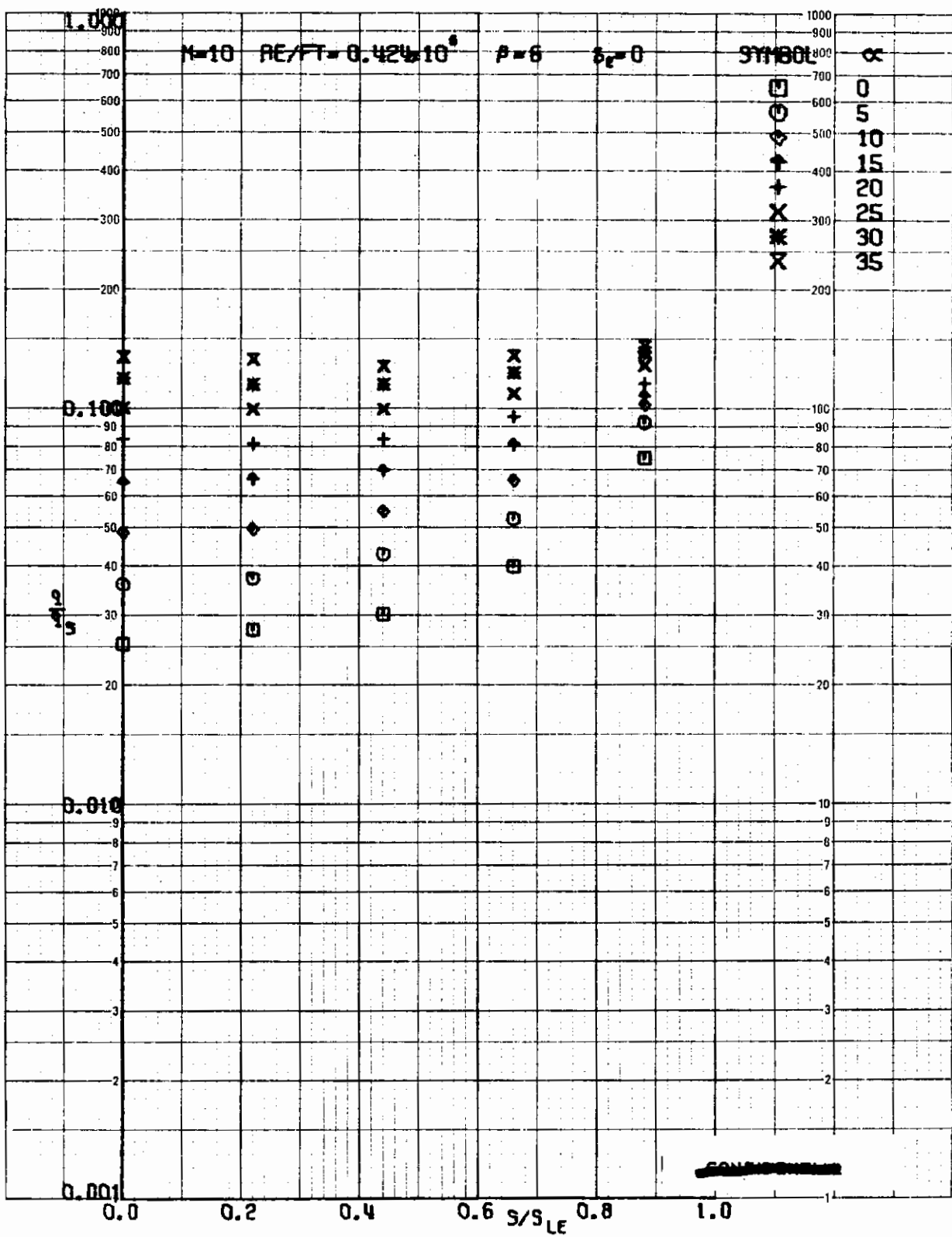
FIGURE 150 (U) TUNNEL C LOWER SURFACE SPANWISE HEATING RATES AT
X/L = 0.30, β=6

231
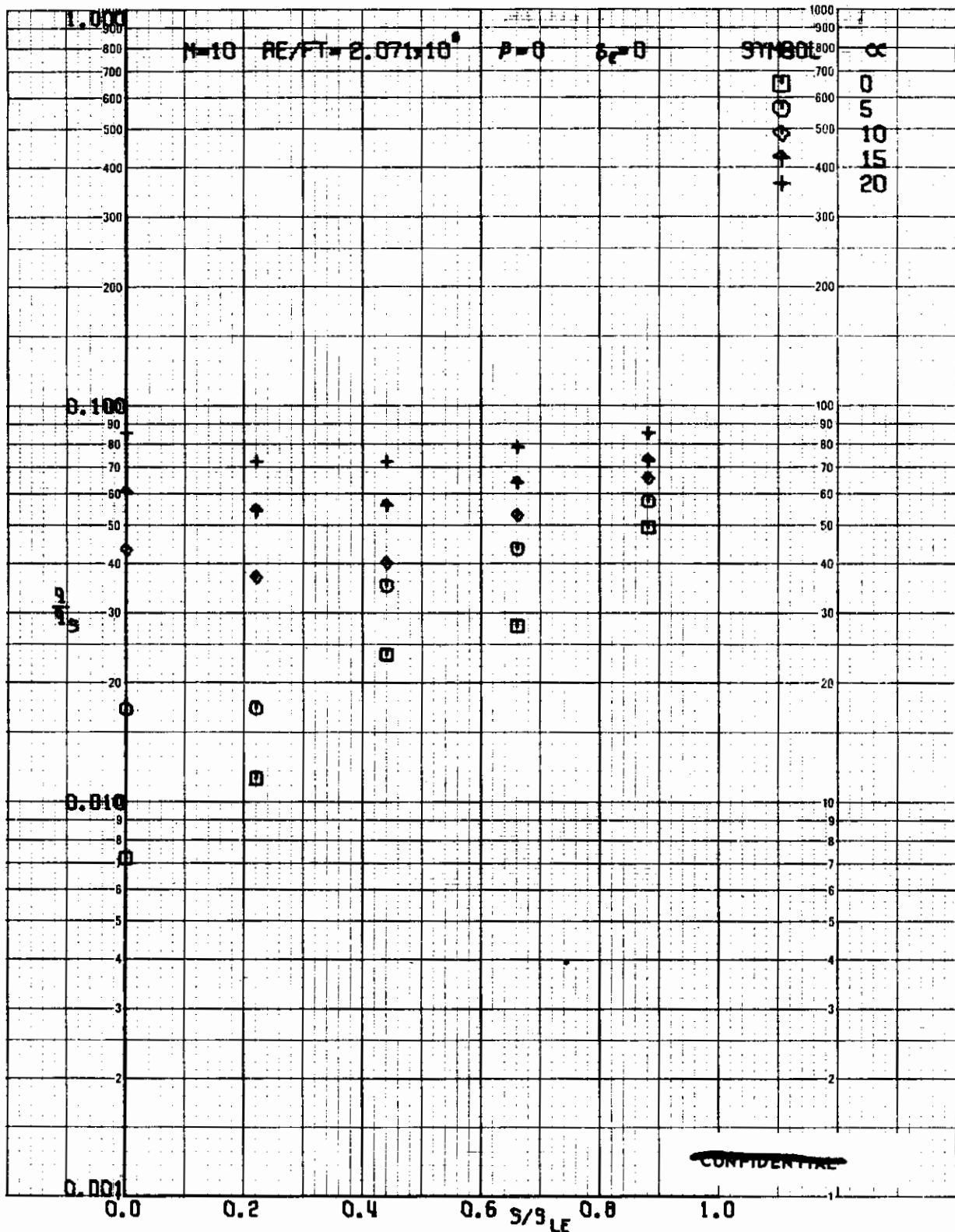
FIGURE 151 (U) TUNNEL C LOWER SURFACE SPANWISE HEATING RATES AT
X/L = 0.30, β=0

$M_\infty = 19$ $RE_\infty / FT = 0.5 \times 10^6$ $\beta = 0$ $\delta_e = 0$

SYMBOL	α
◯	0
☐	5
◇	10
△	15
△	20
⬡	25
△	30
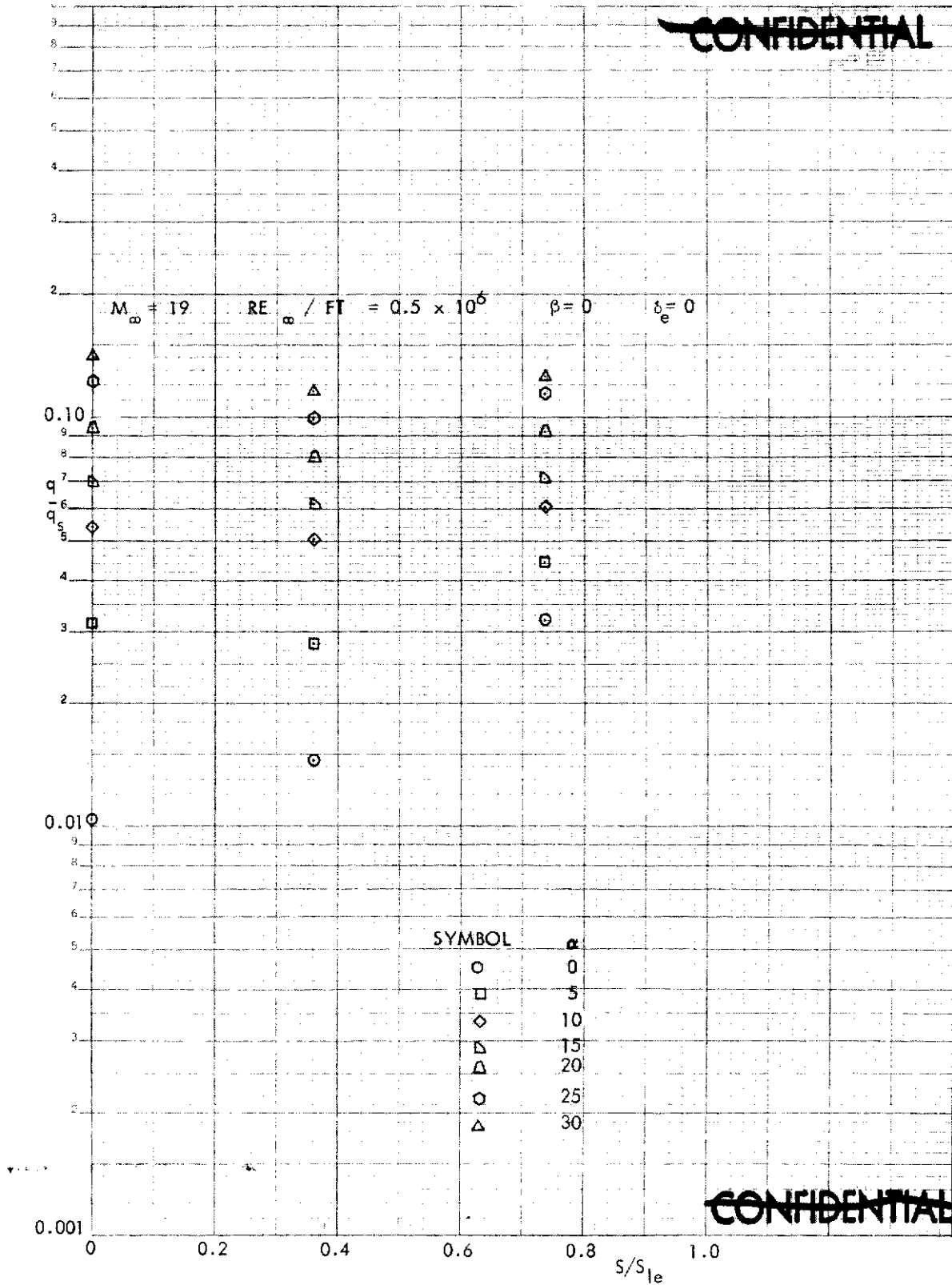
FIGURE 152   (U) TUNNEL F LOWER SURFACE SPANWISE HEATING RATES AT
X/L = 0.30, β=0
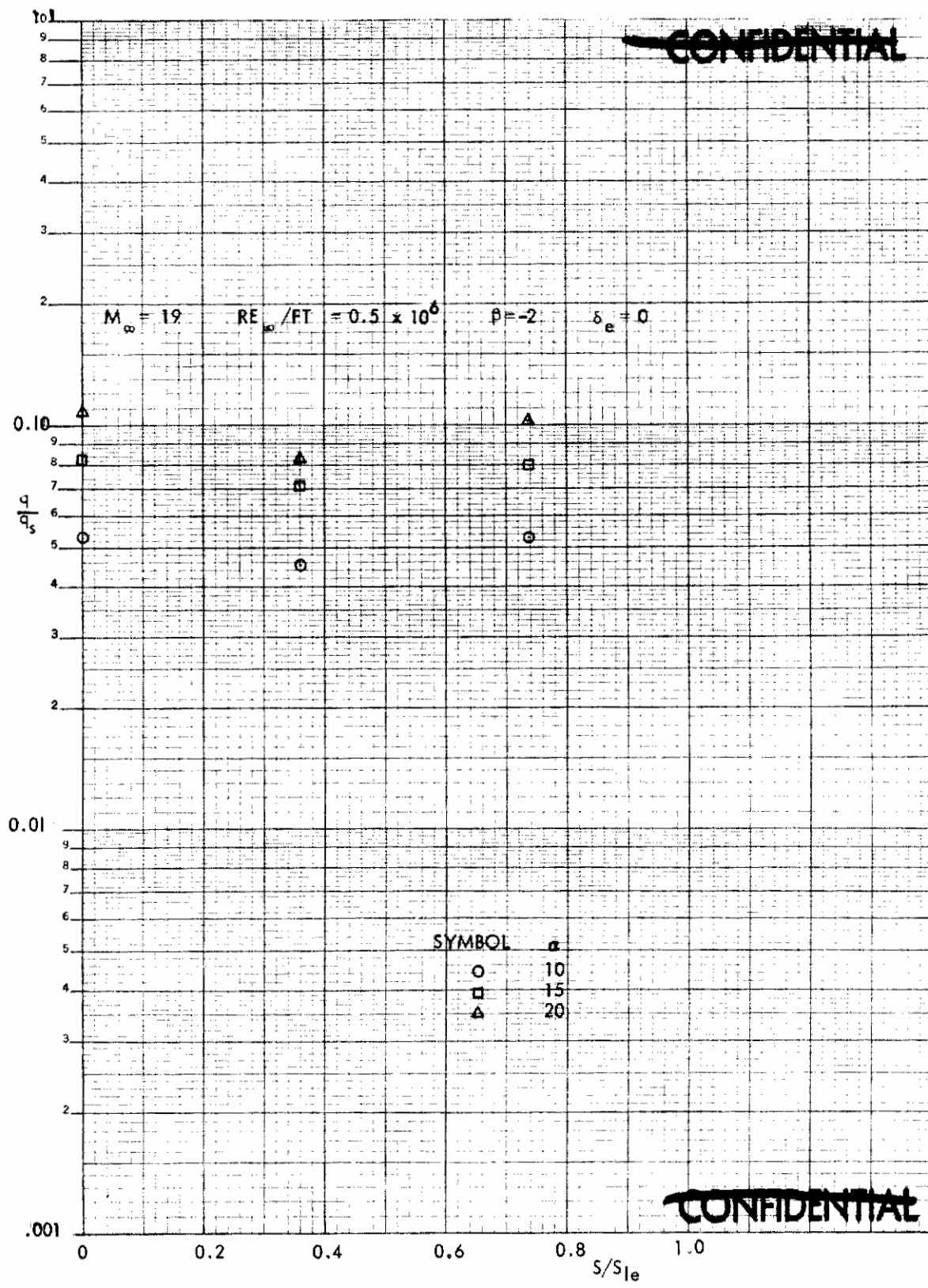
FIGURE 153 (U) TUNNEL F LOWER SURFACE SPANWISE HEATING RATES AT
X/L = 0.30, β=-2

$M_\infty = 19$ $RE_\infty/FT = 0.5 \times 10^6$ $\beta = 2$ $\delta_e = 0$

SYMBOL	α
O	10
□	15
△	20

$\frac{q}{q_s}$

S/S_{le}
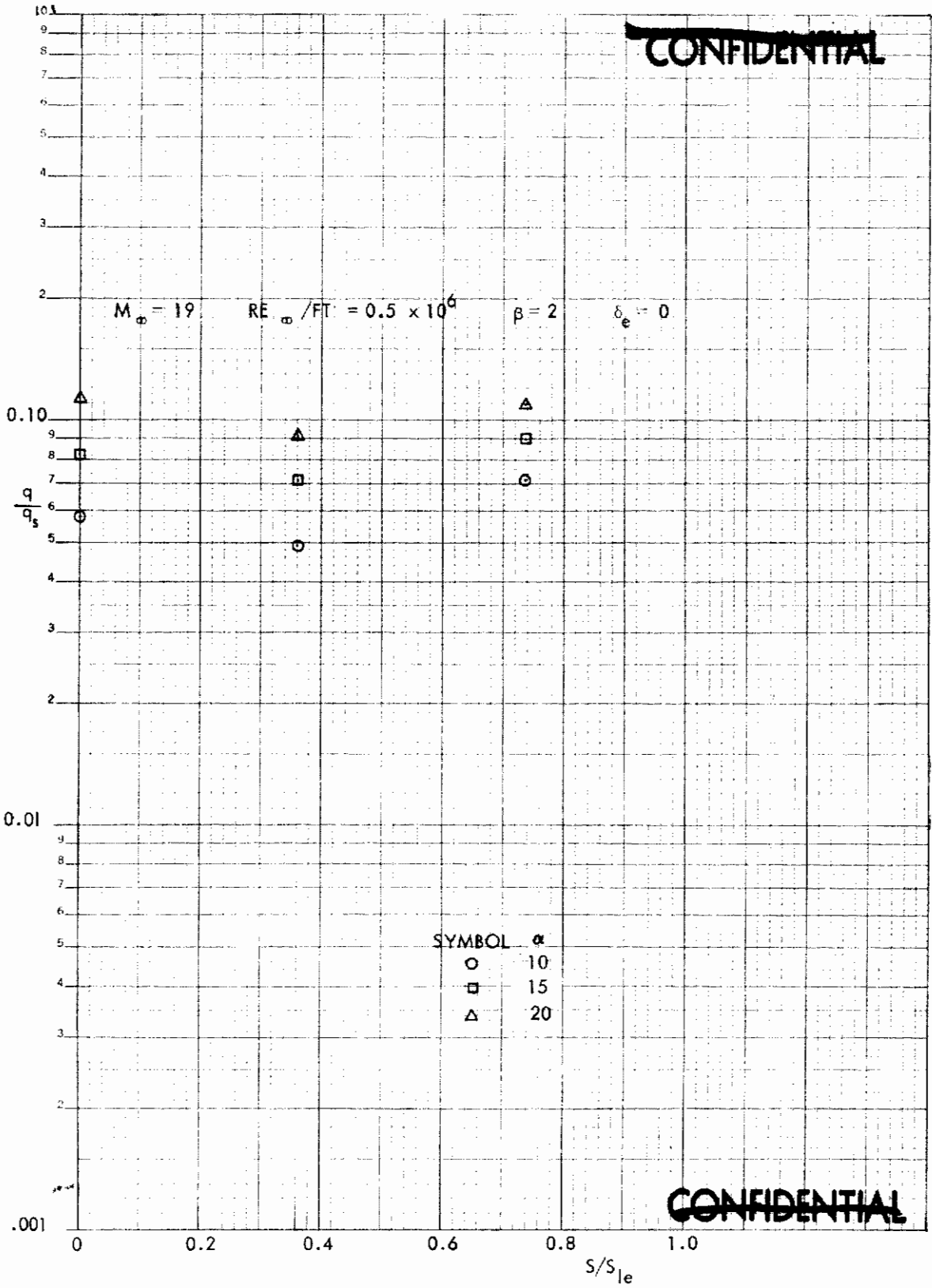
FIGURE 154   (U) TUNNEL F LOWER SURFACE SPANWISE HEATING RATES AT
X/L = 0.30, β=2

235

$M_\infty - 19 \quad RE_\infty/FT = 0.5 \times 10^6 \quad \beta = 4 \quad \delta_e = 0$

SYMBOL	α
○	10
□	15
△	20

$\dfrac{q}{q_s}$

S/S_{le}
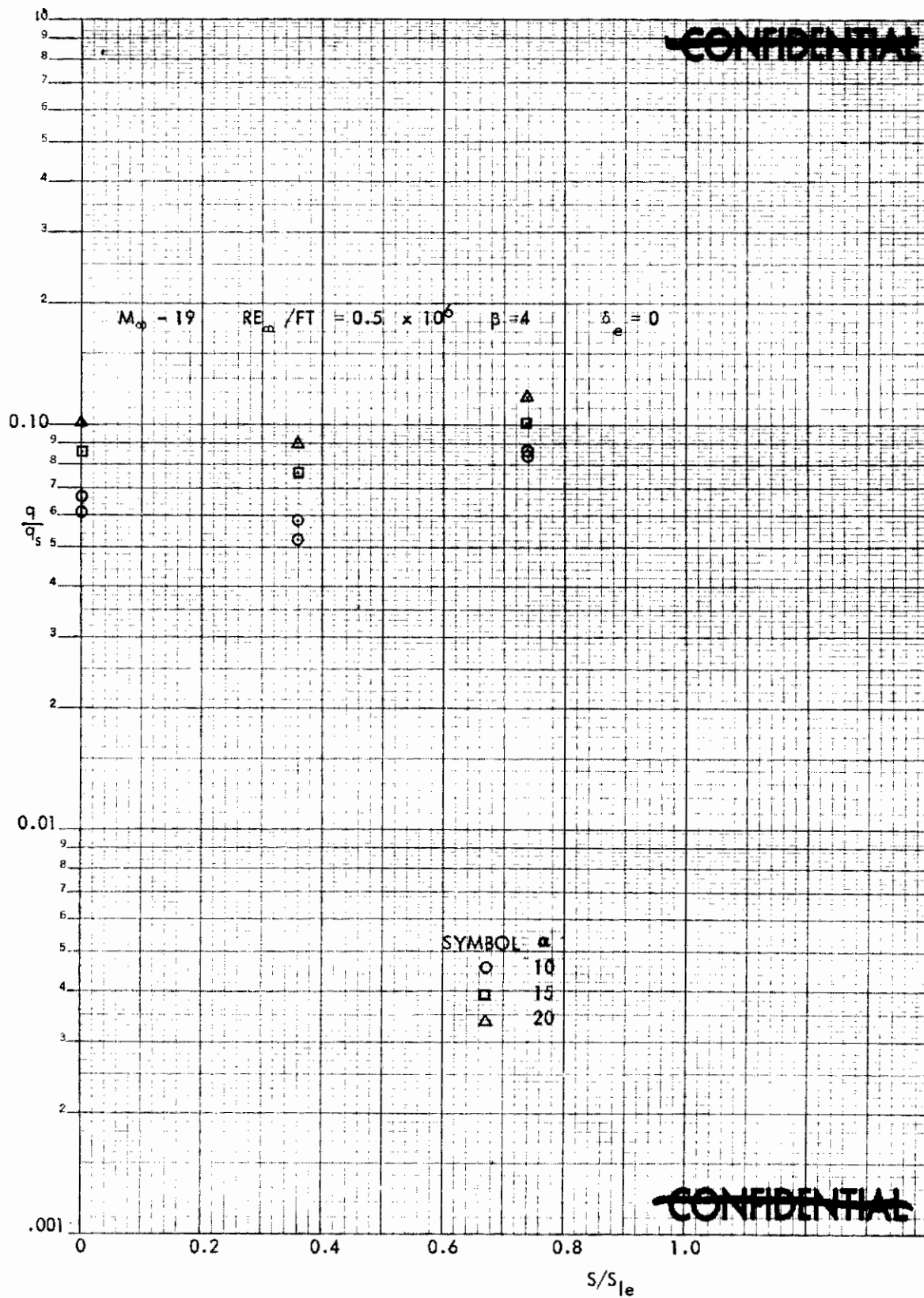
FIGURE 155 (U) TUNNEL F LOWER SURFACE SPANWISE HEATING RATES AT X/L = 0.30, β=4

236

$M_\infty = 19$ $RE_\infty/FT = 0.5 \times 10^6$ $\beta = 6$ $\delta_e = 0$
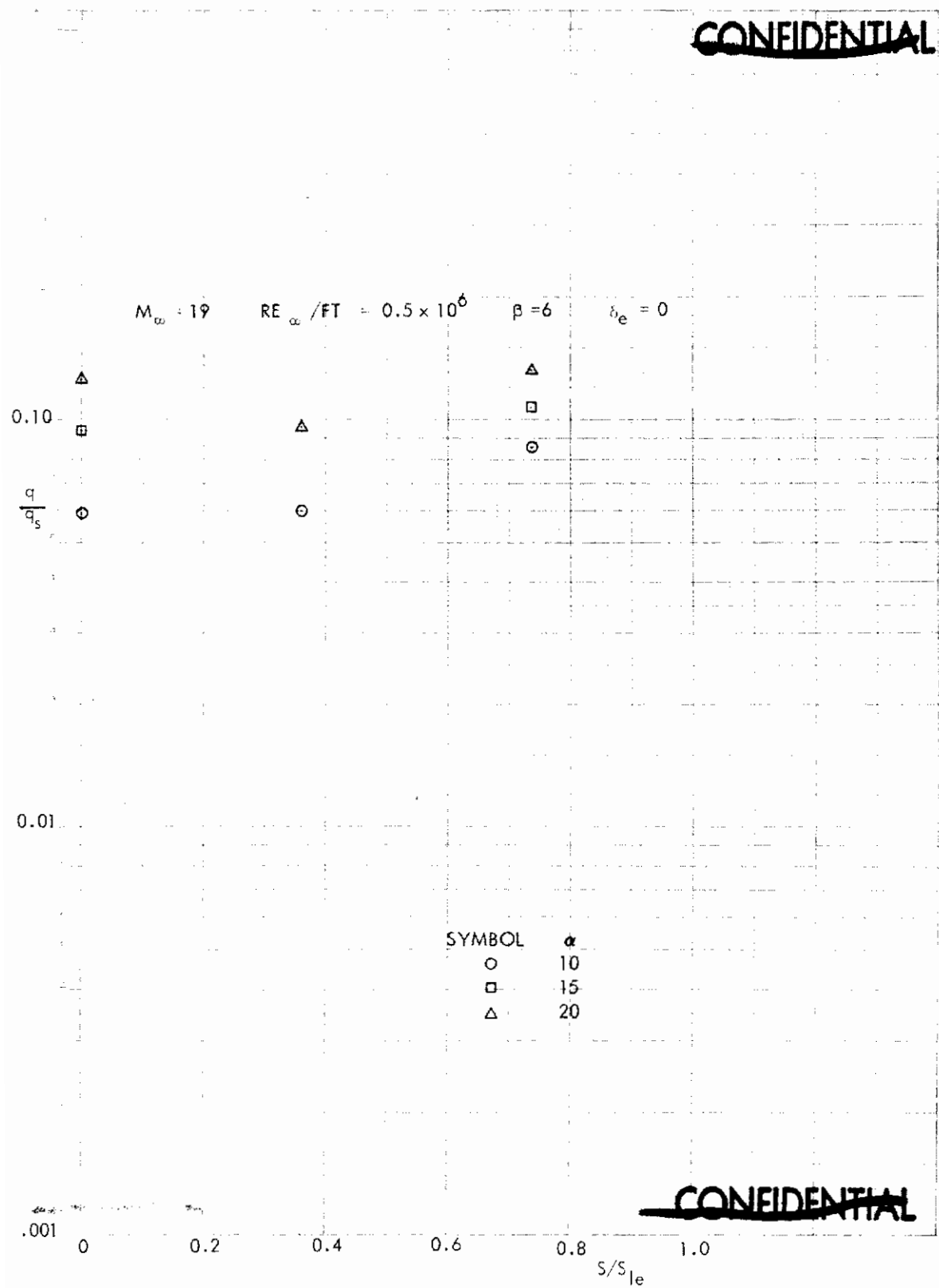
FIGURE 156 (U) TUNNEL F LOWER SURFACE SPANWISE HEATING RATES AT
X/L = 0.30, β=6
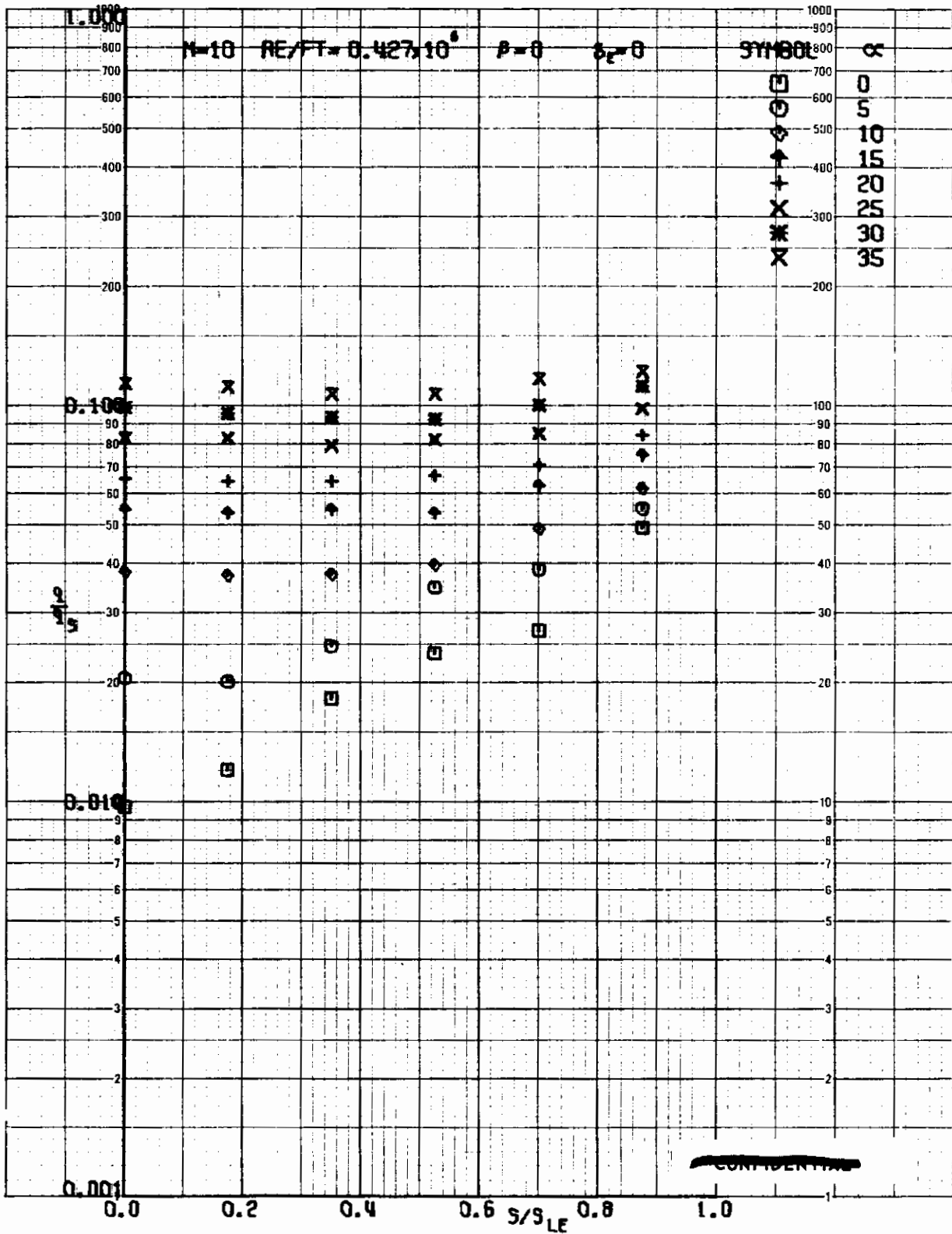
FIGURE 157 (U) TUNNEL C LOWER SURFACE SPANWISE HEATING RATES AT
X/L = 0.40, β=0

238
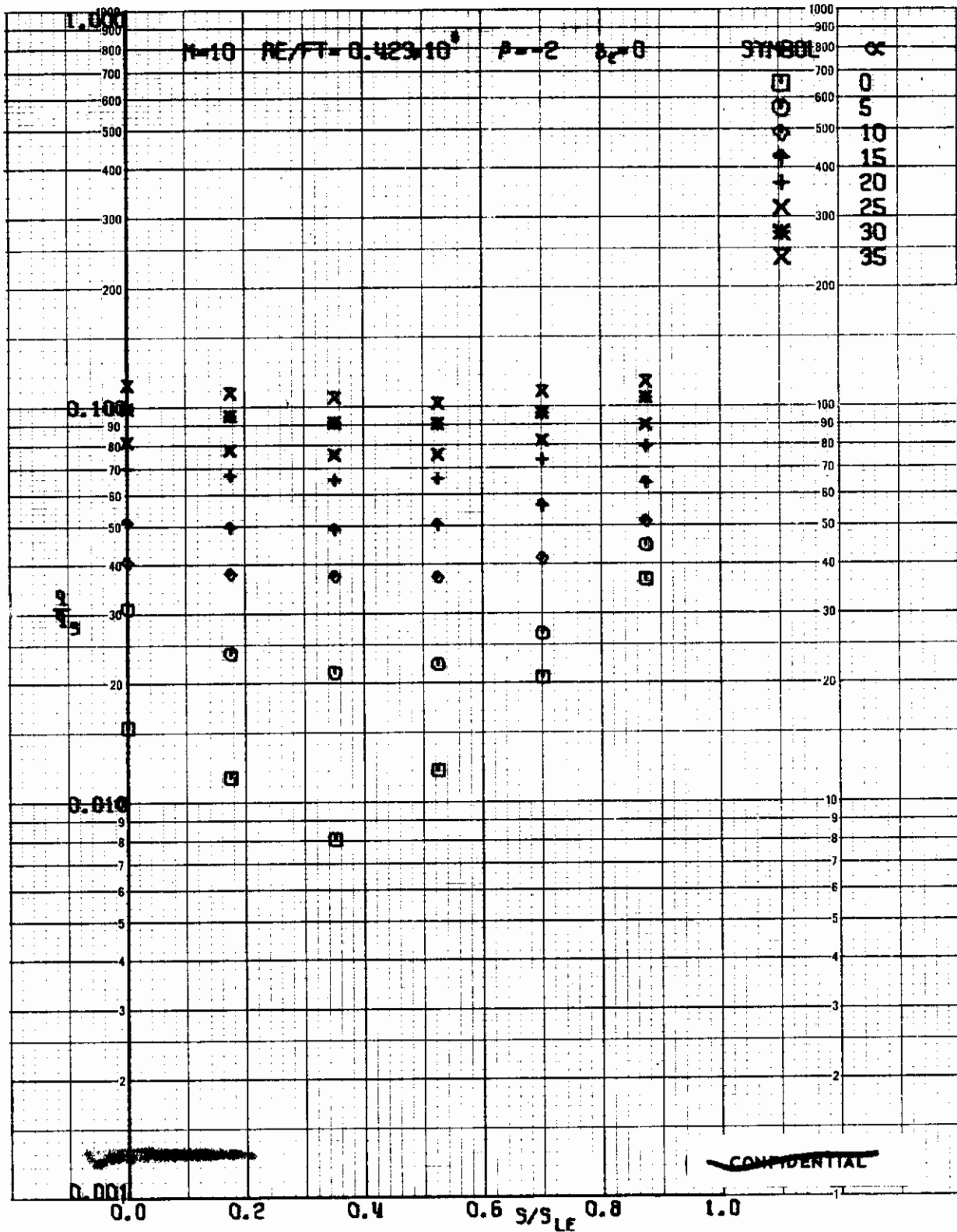
FIGURE 158 (U) TUNNEL C LOWER SURFACE SPANWISE HEATING RATES AT
X/L = 0.40, β=-2
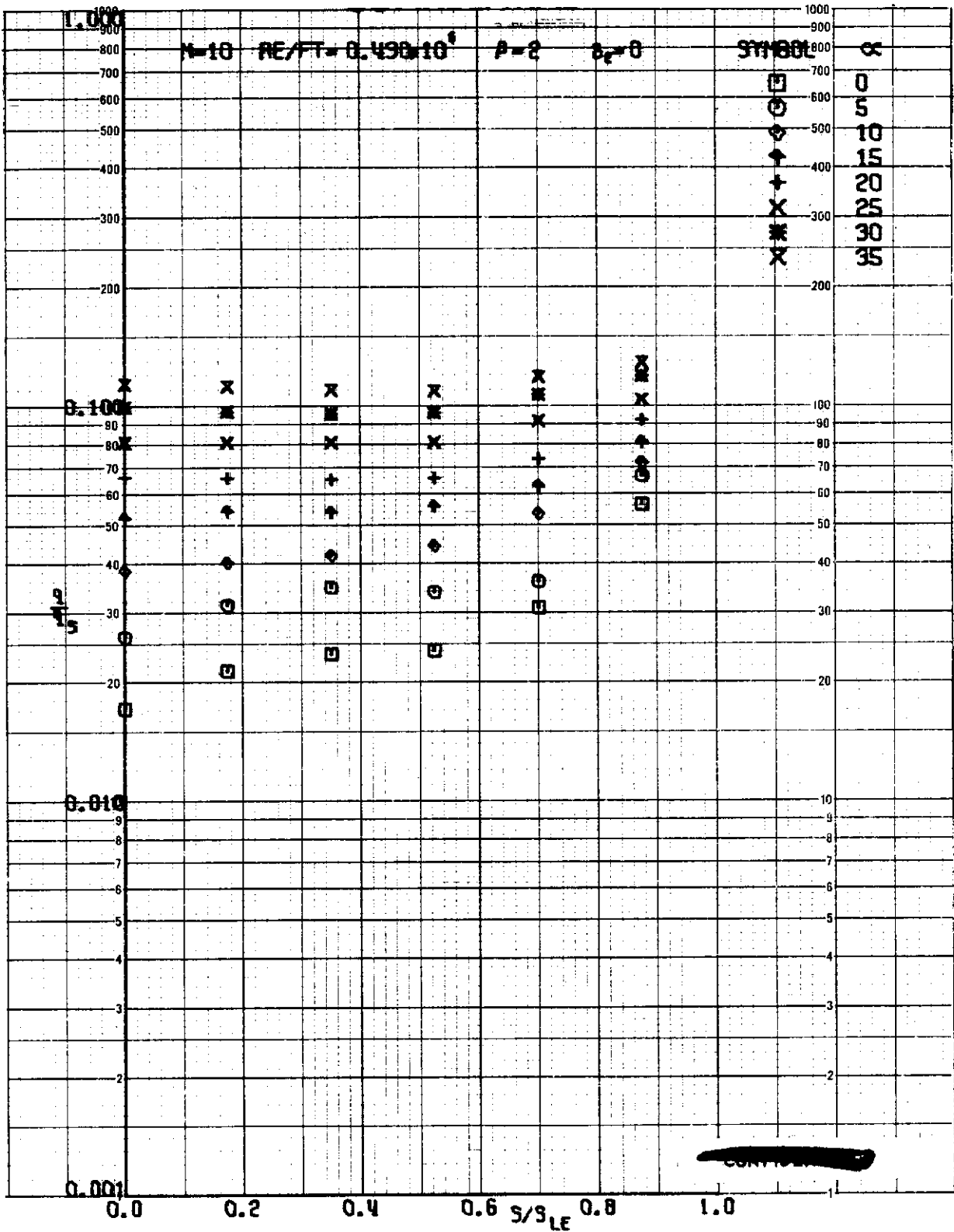
FIGURE 159 (U) TUNNEL C LOWER SURFACE SPANWISE HEATING RATES AT
X/L = 0.40, β=2
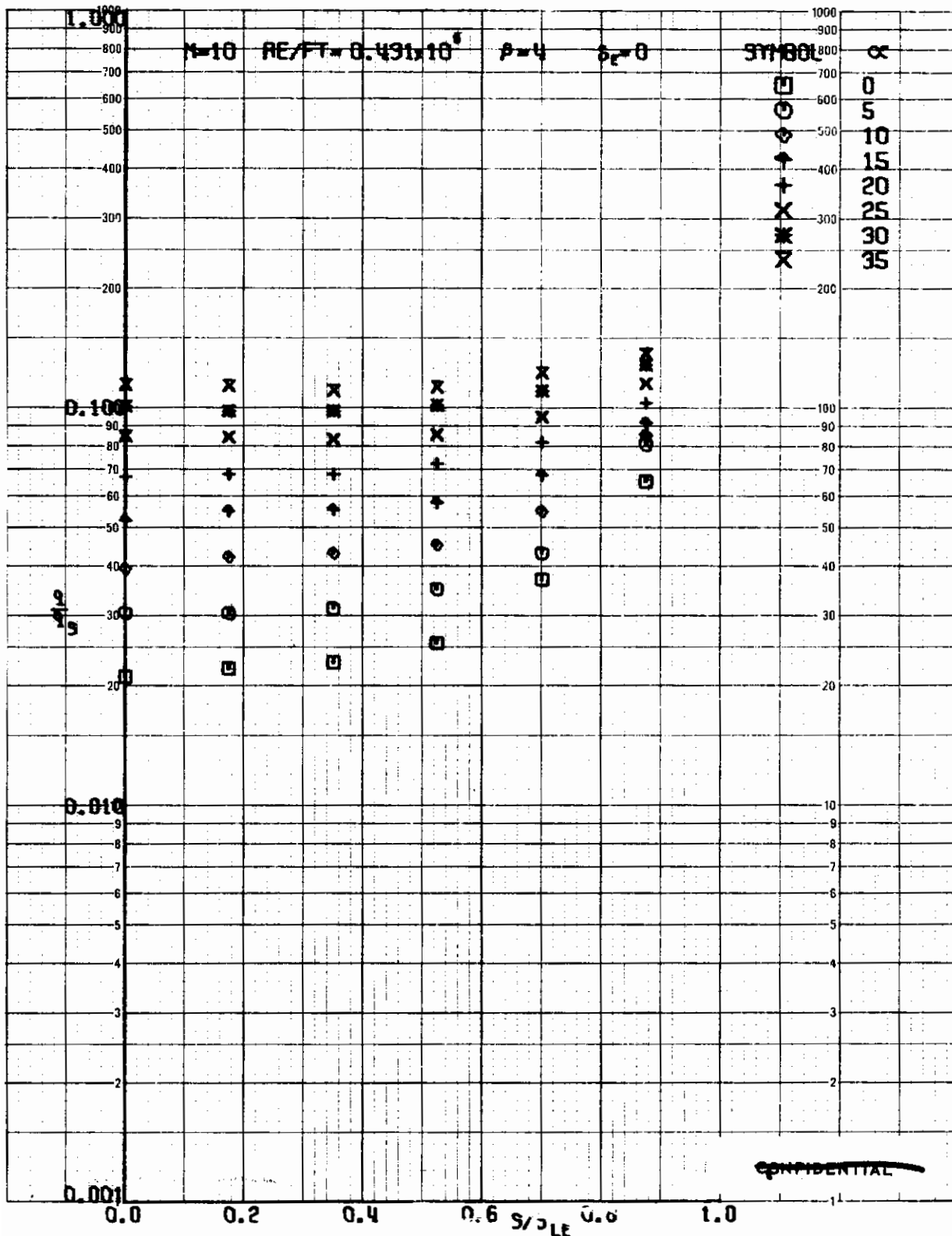
FIGURE 160 (U) TUNNEL C LOWER SURFACE SPANWISE HEATING RATES AT
X/L = 0.40, β=4
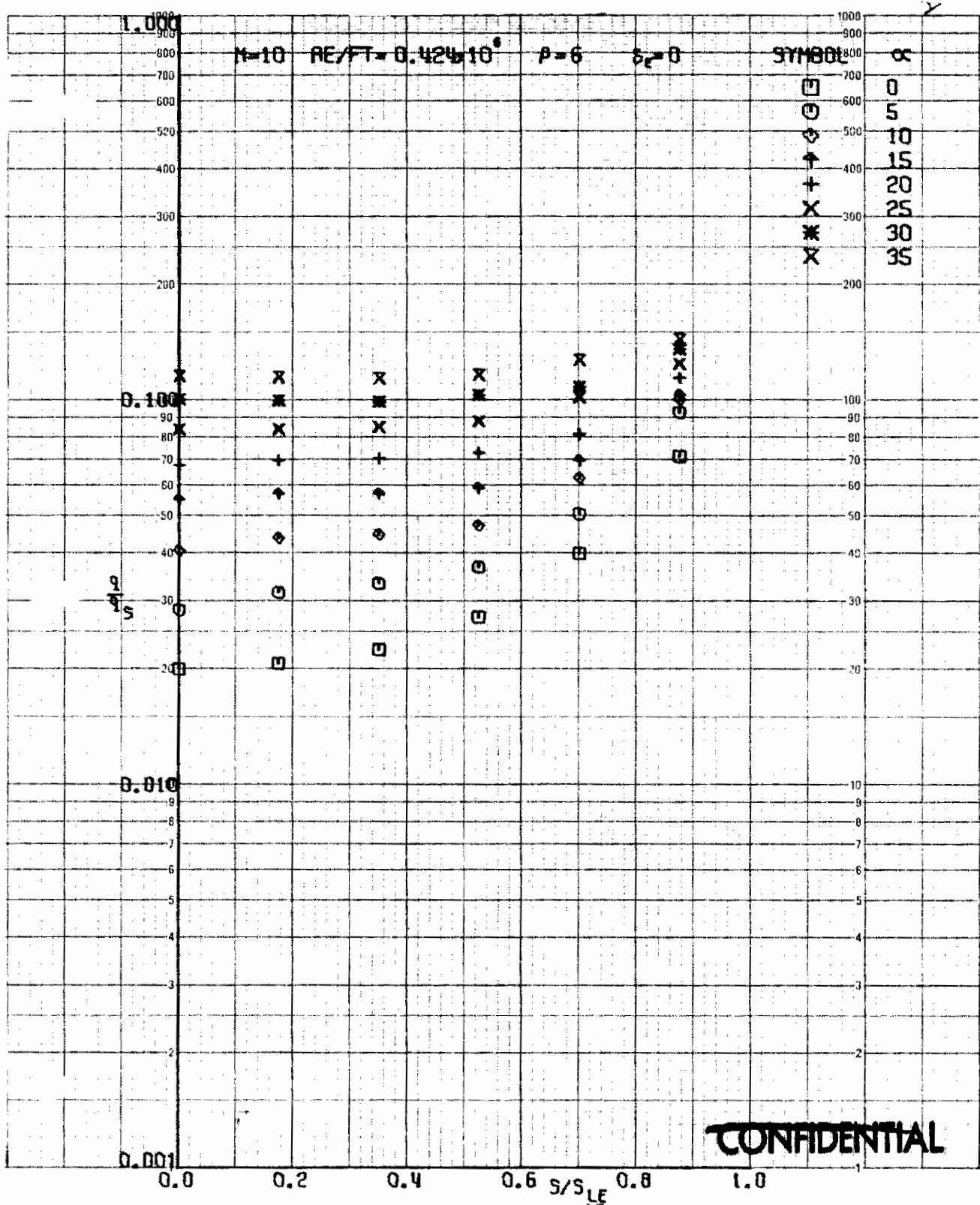
FIGURE 161 (U) TUNNEL C LOWER SURFACE SPANWISE HEATING RATES AT
X/L = 0.40, β=6
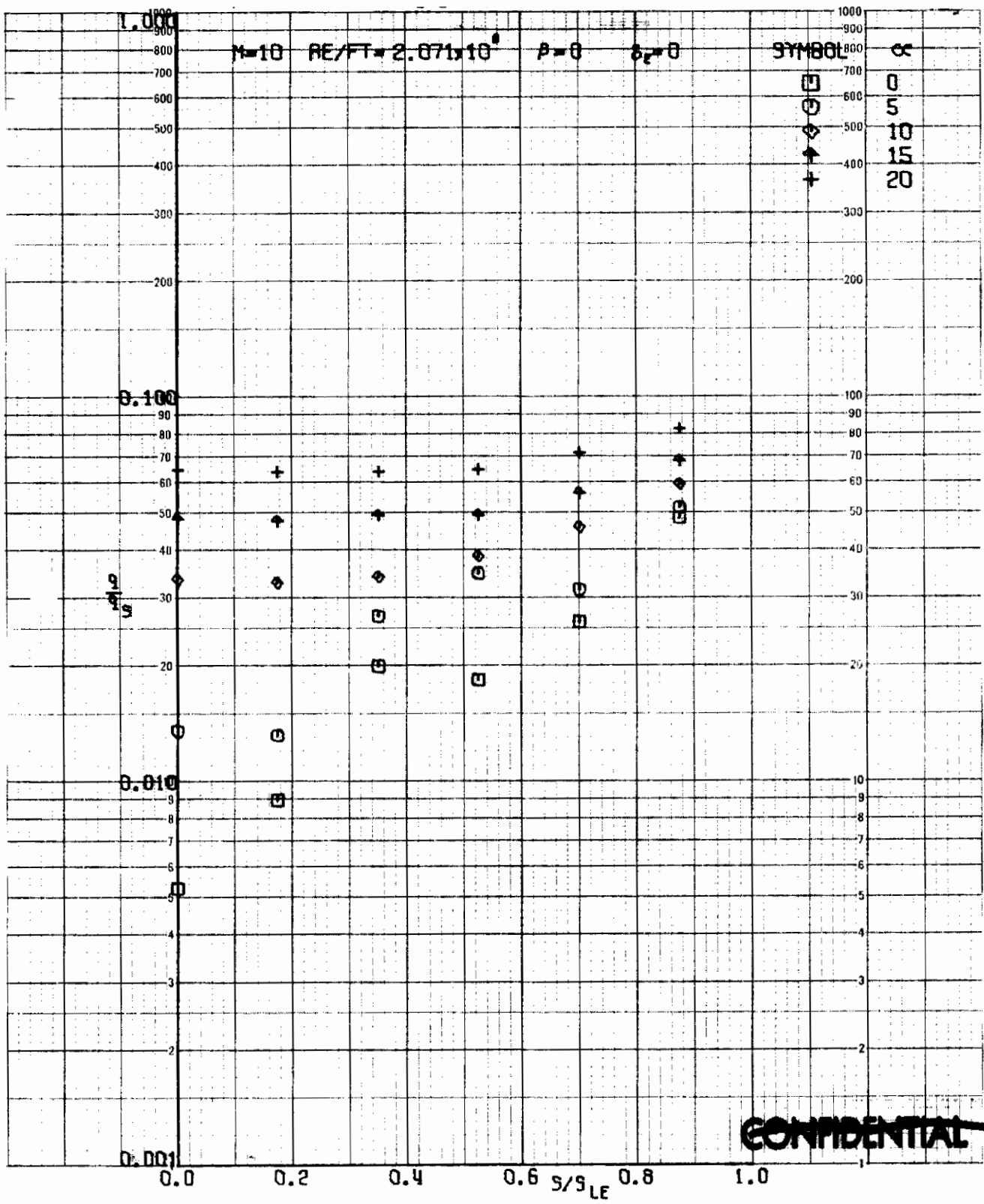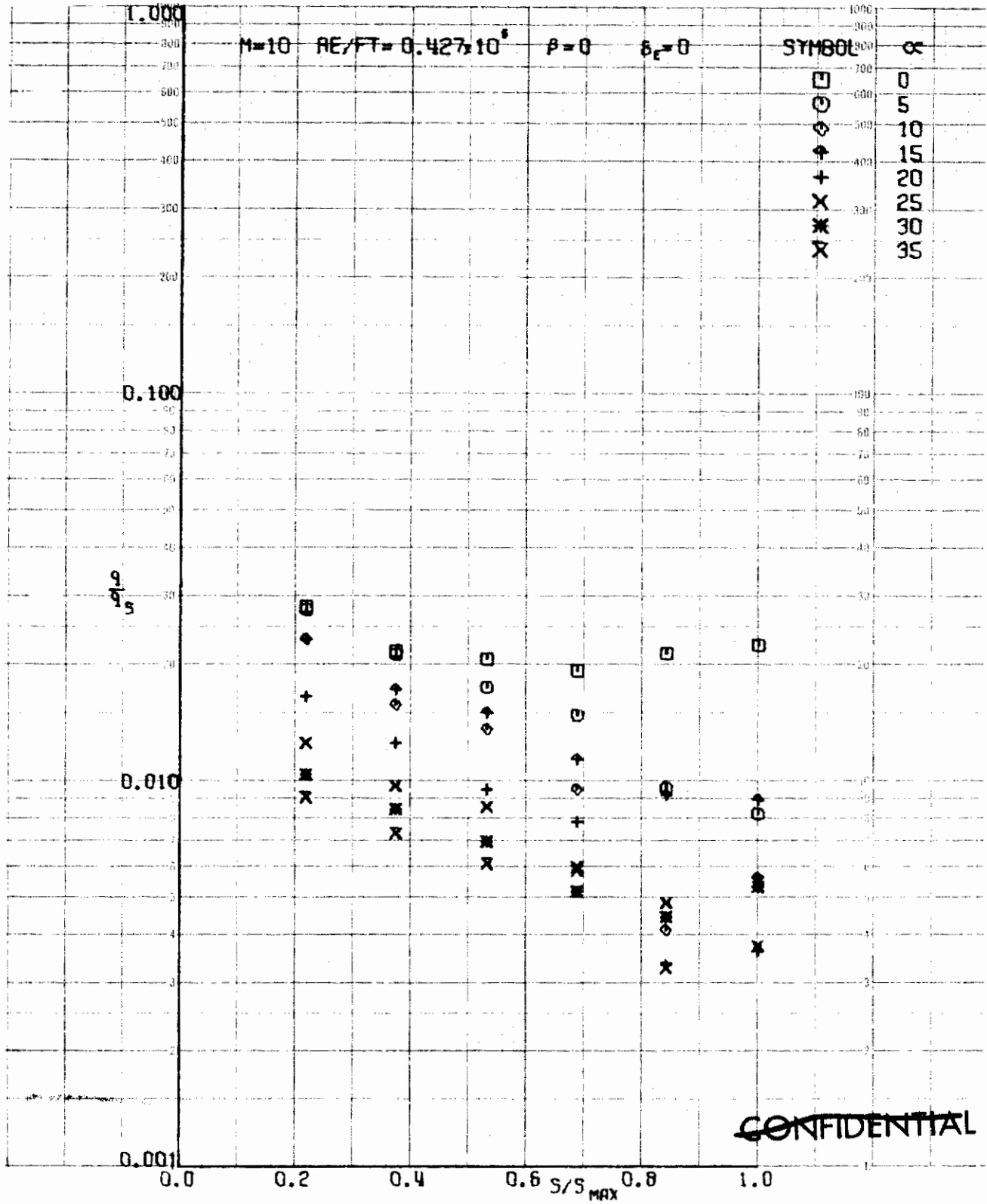
FIGURE 162 (U) TUNNEL C LOWER SURFACE SPANWISE HEATING RATES AT
X/L = 0.40, β=0

243
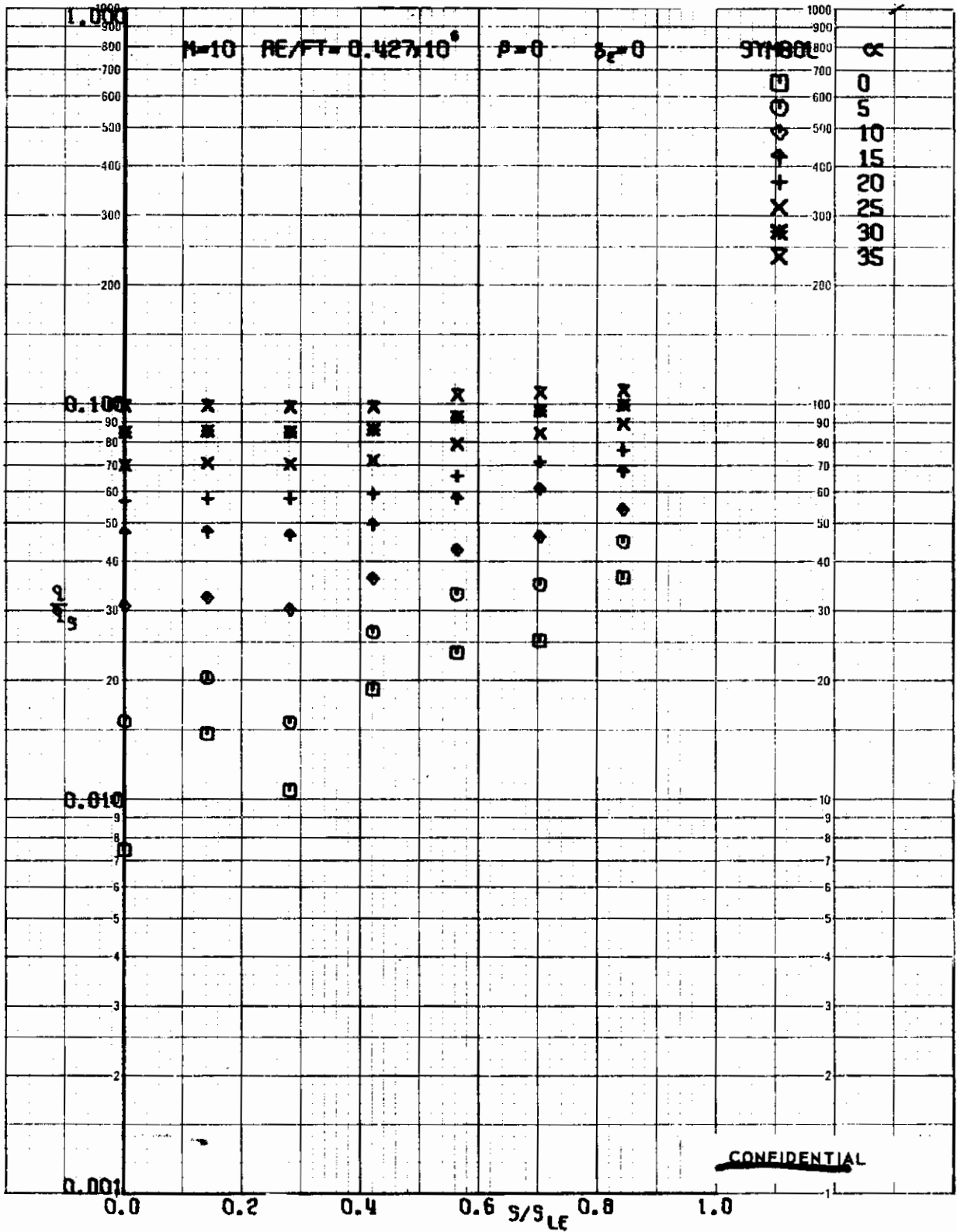
FIGURE 163 (U) TUNNEL C LOWER SURFACE SPANWISE HEATING RATES AT X/L = 0.50, β=0

244
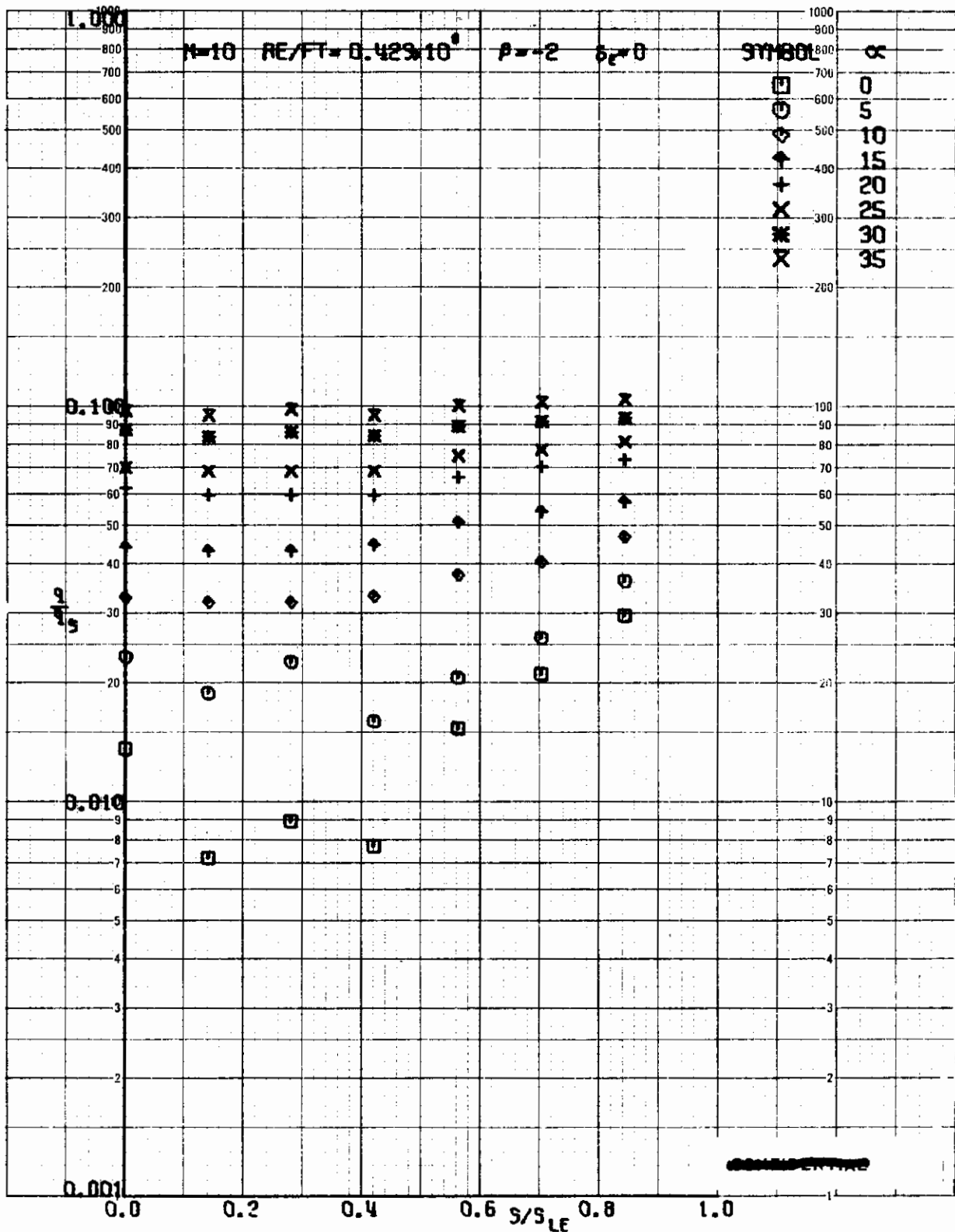
FIGURE 164 (U) TUNNEL C LOWER SURFACE SPANWISE HEATING RATES AT
X/L = 0.50, ρ=-2

245
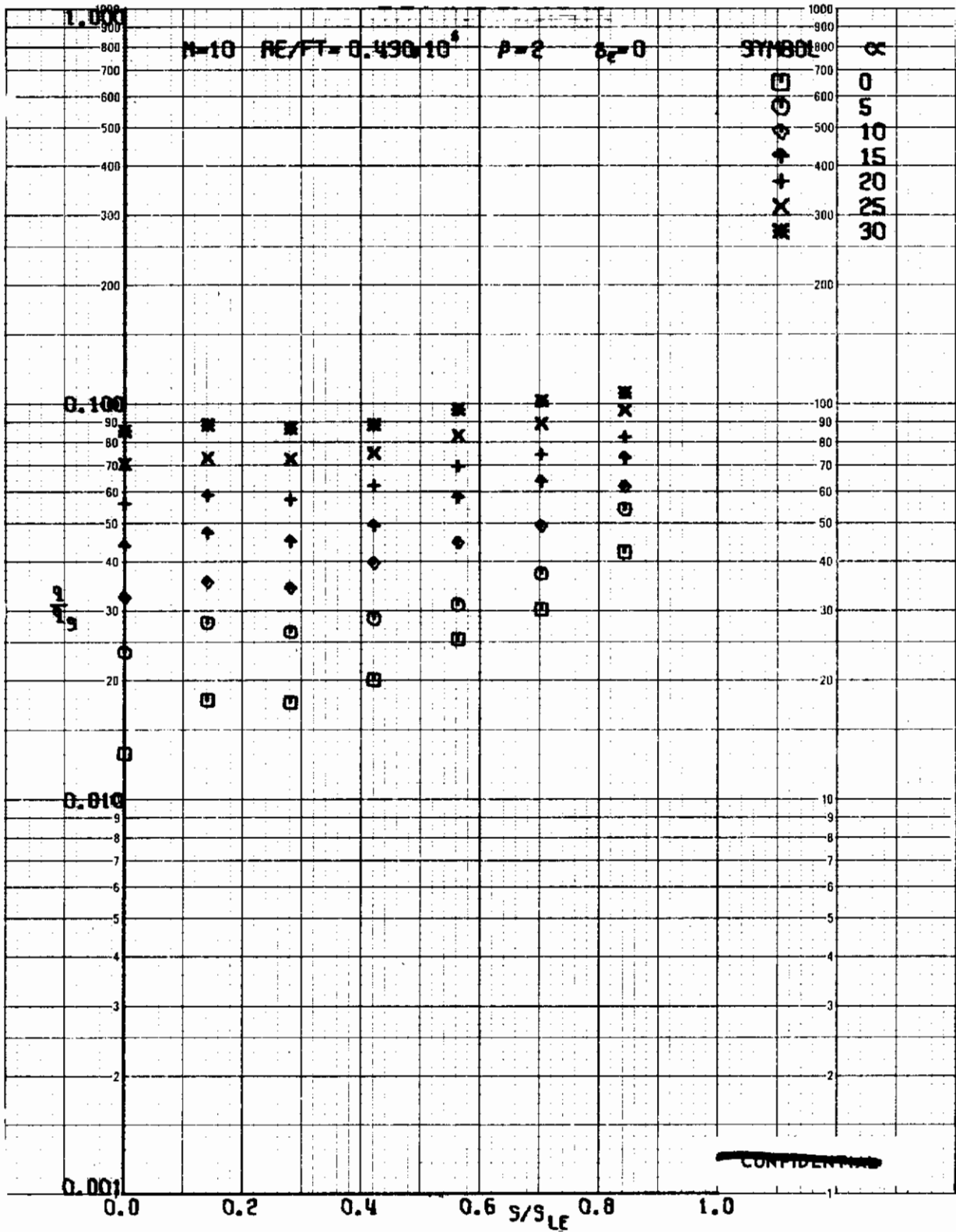
FIGURE 165 (U) TUNNEL C LOWER SURFACE SPANWISE HEATING RATES AT X/L = 0.50, β=2
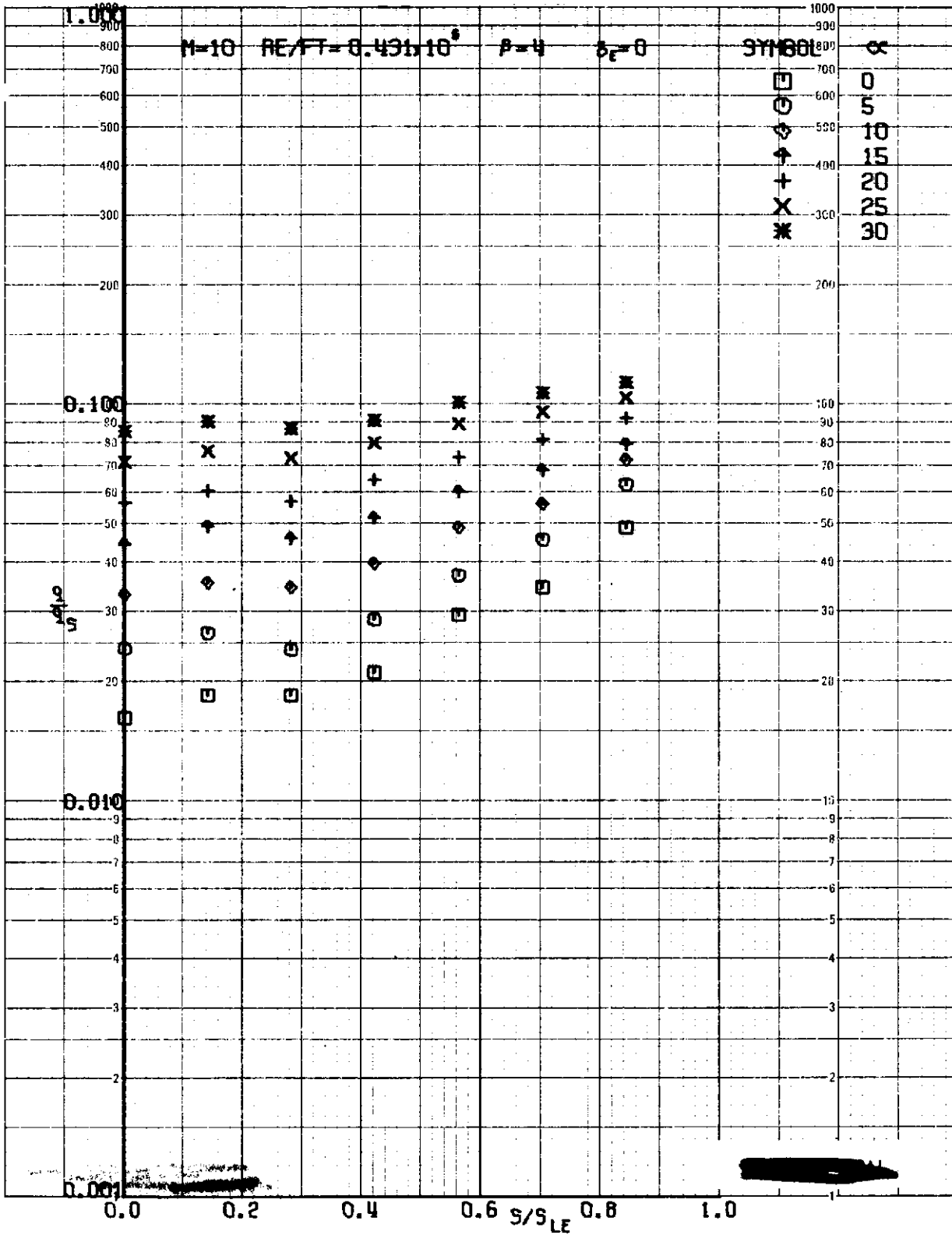
FIGURE 166 (U) TUNNEL C LOWER SURFACE SPANWISE HEATING RATES AT
X/L = 0.50, β=4

247
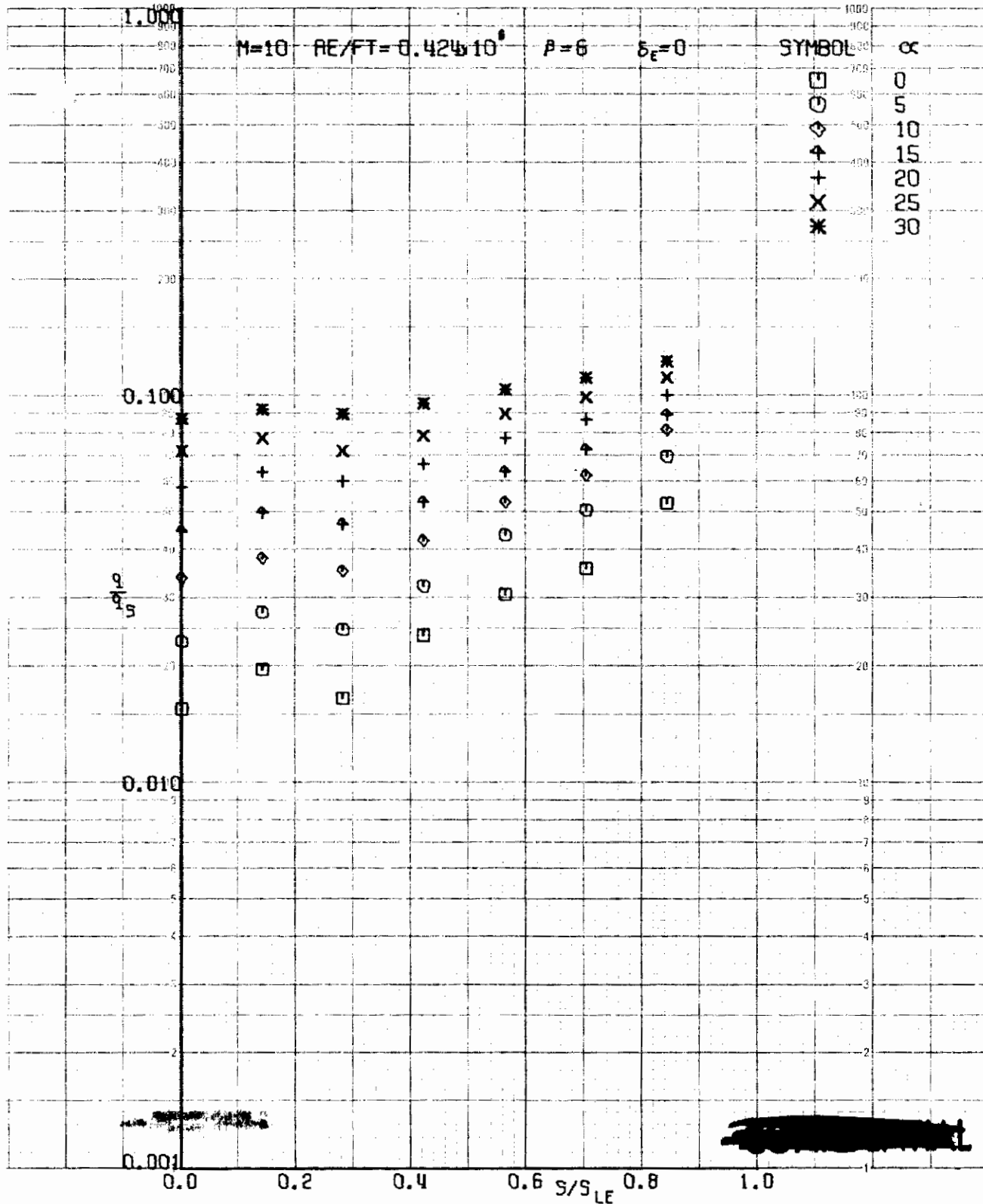
FIGURE 167 (U) TUNNEL C LOWER SURFACE SPANWISE HEATING RATES AT
X/L = 0.50, β=6
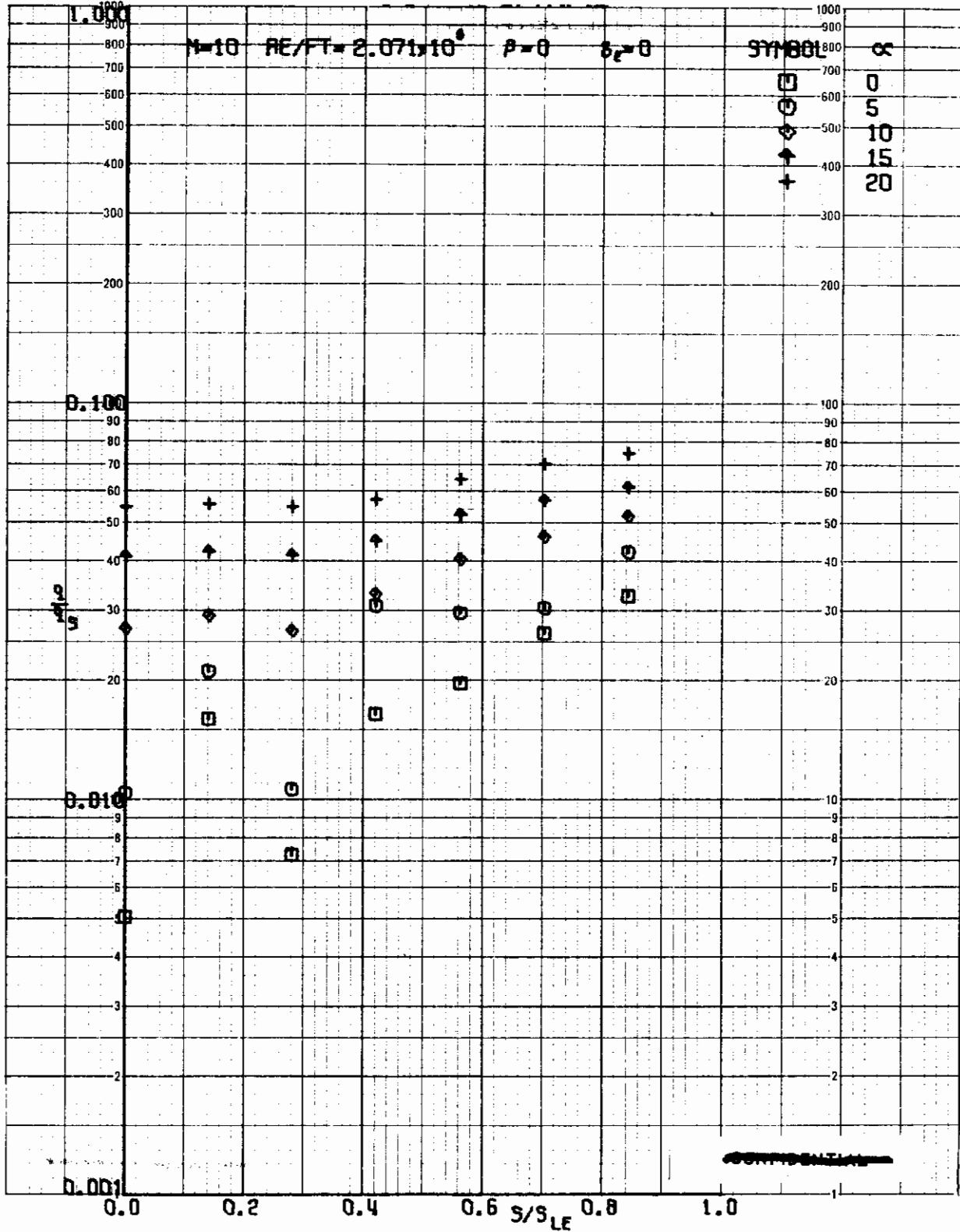
FIGURE 168 (U) TUNNEL C LOWER SURFACE SPANWISE HEATING RATES AT
X/L = 0.50, β=0

249
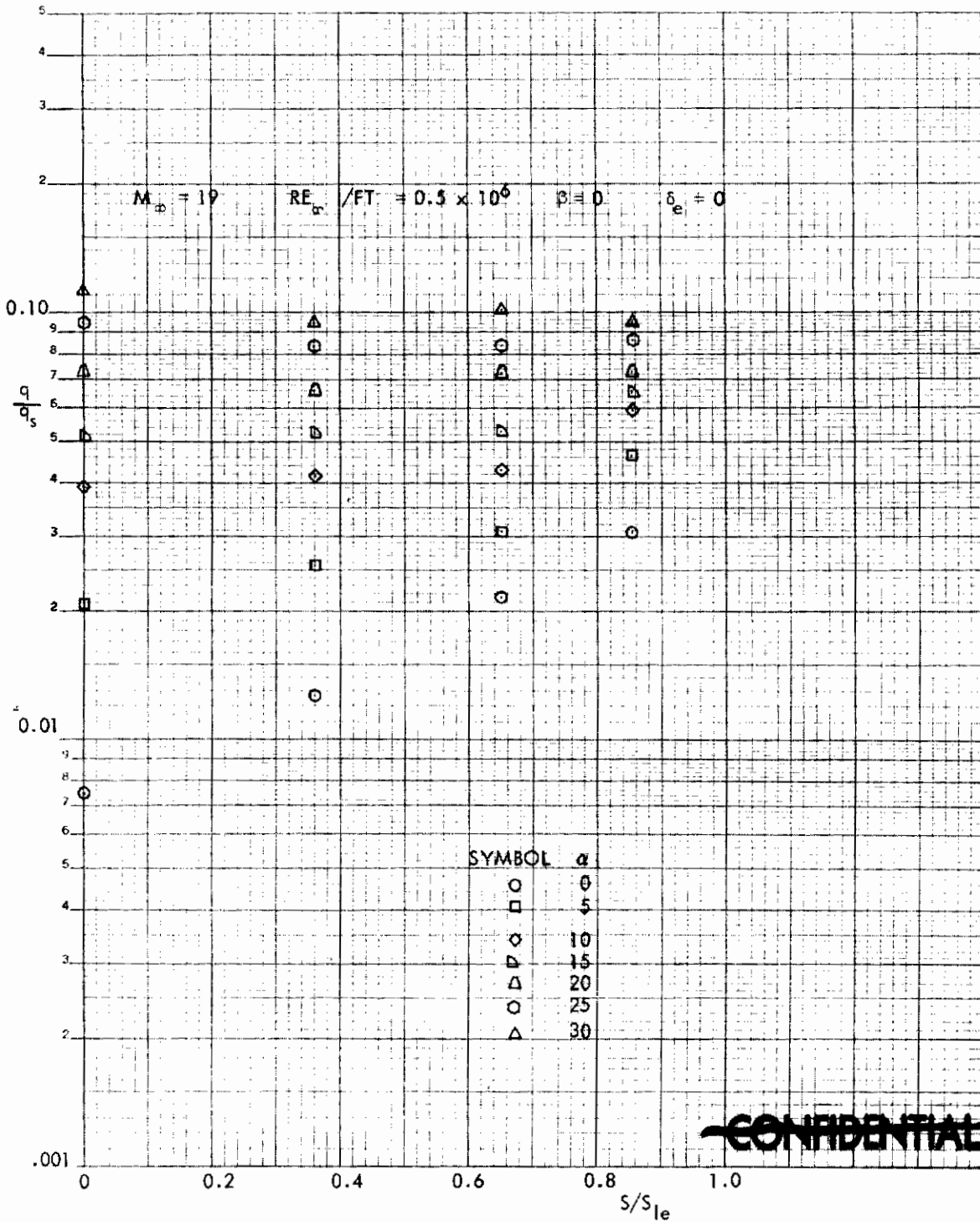
FIGURE 169 (U) TUNNEL F LOWER SURFACE SPANWISE HEATING RATES AT
X/L = 0.50, β=0
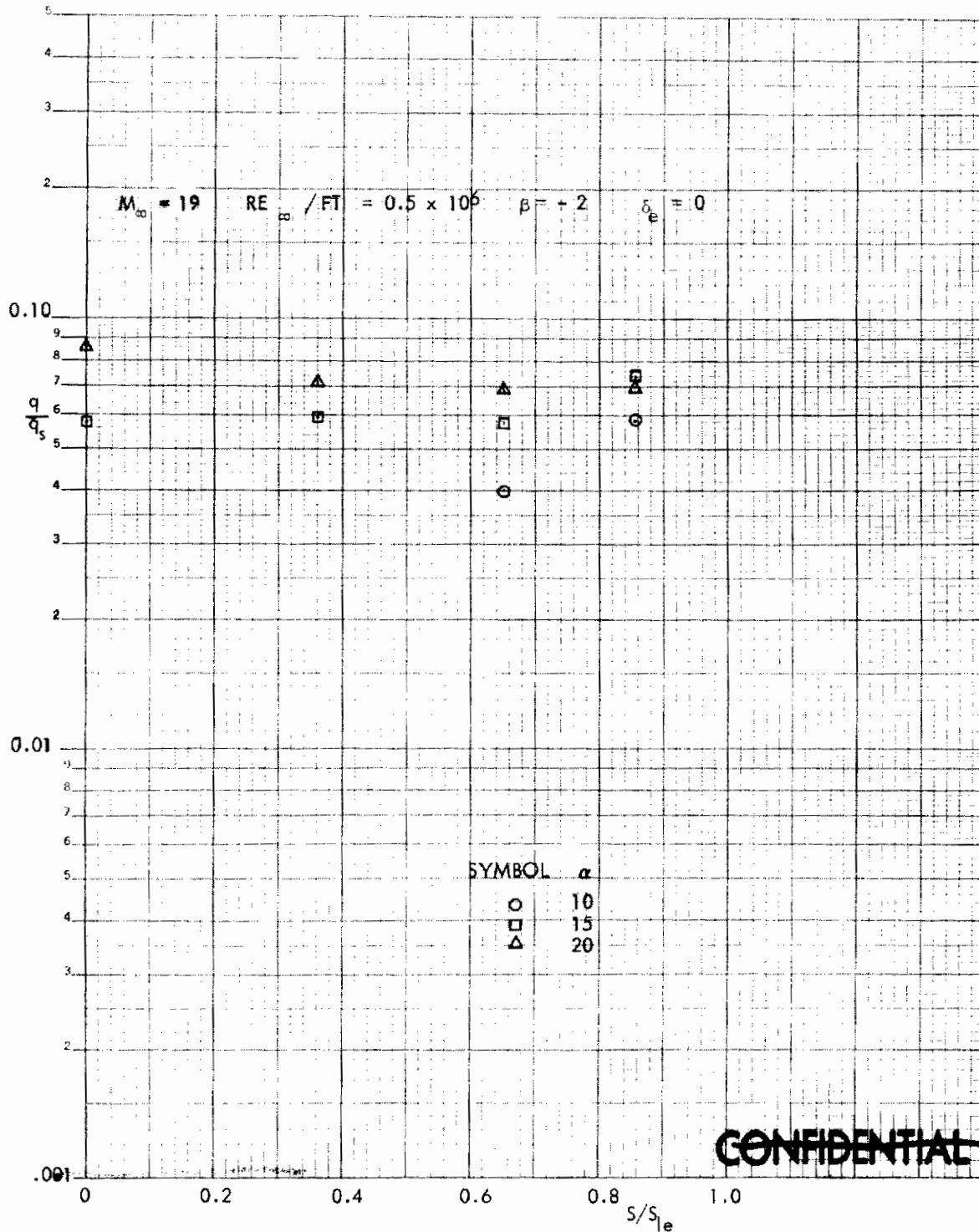
FIGURE 170 (U) TUNNEL F LOWER SURFACE SPANWISE HEATING RATES AT
X/L = 0.50, β=-2

251
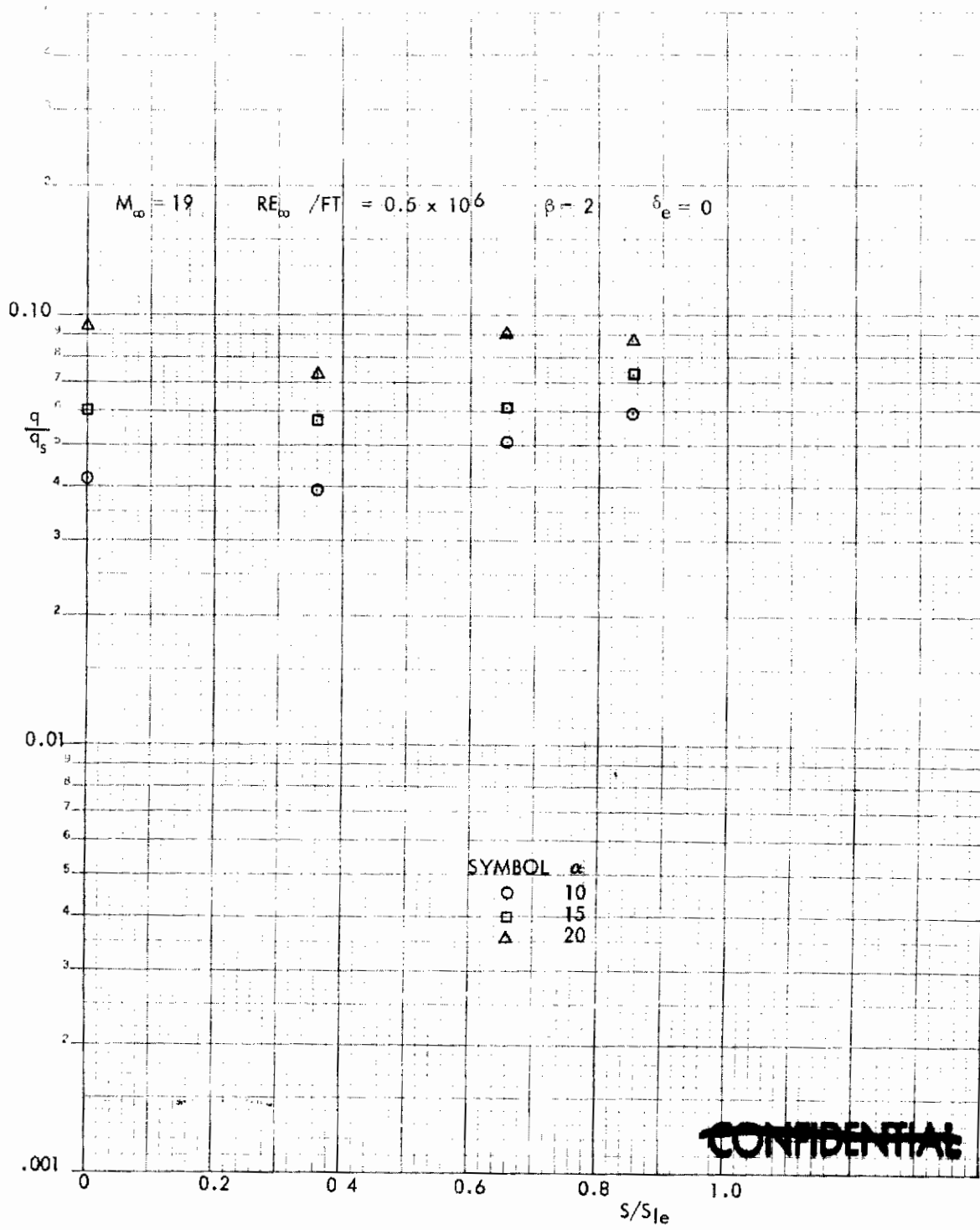
FIGURE 171. (U) TUNNEL F LOWER SURFACE SPANWISE HEATING RATES AT
X/L = 0.50, β=2

$$M_\infty = 19 \qquad RE_\infty /FT = 0.5 \times 10^6 \qquad \beta = 4 \qquad \delta_e = 0$$

SYMBOL	α
$\circ$	10
$\square$	15
$\triangle$	20

$\dfrac{q}{q_s}$

S/S_{le}
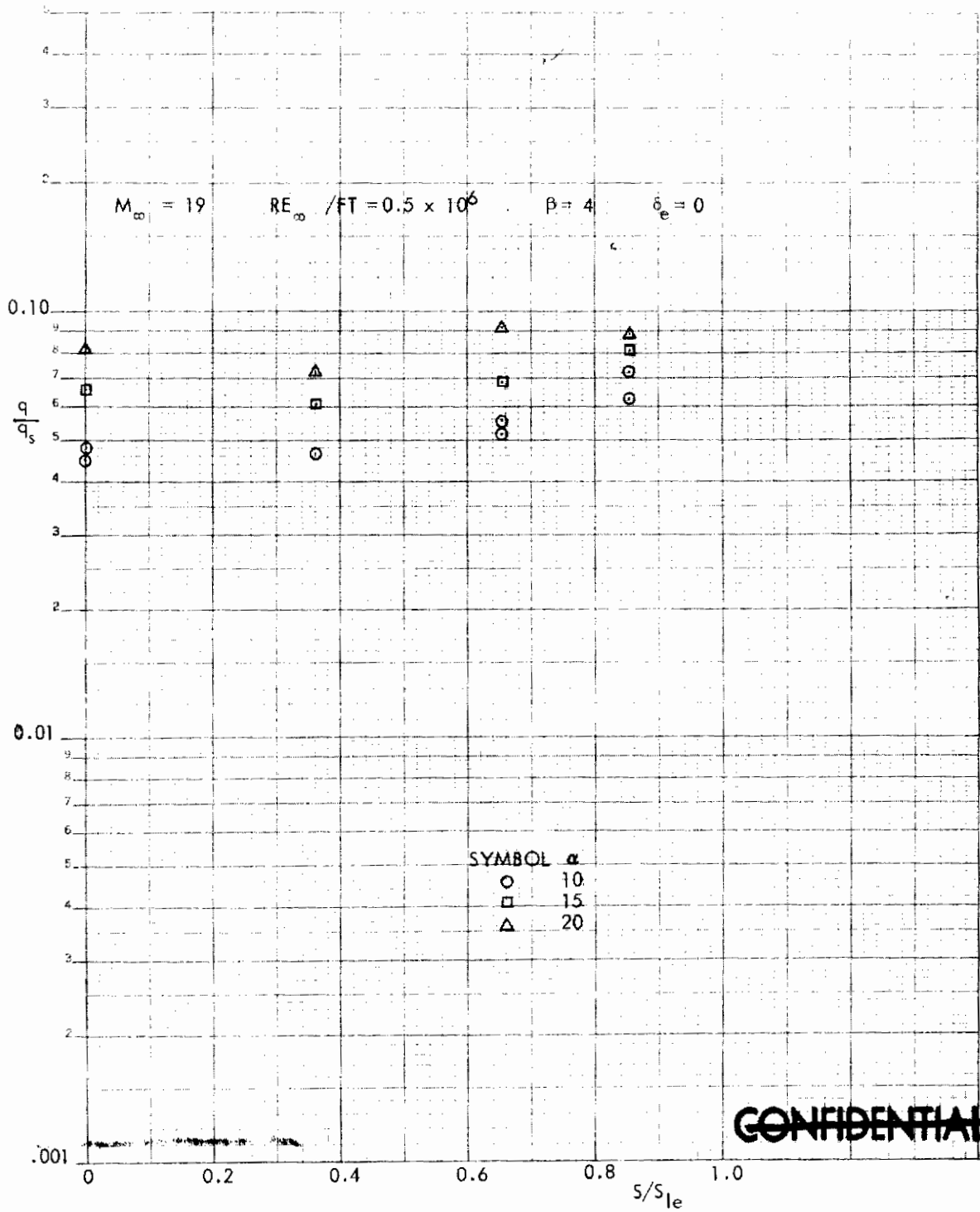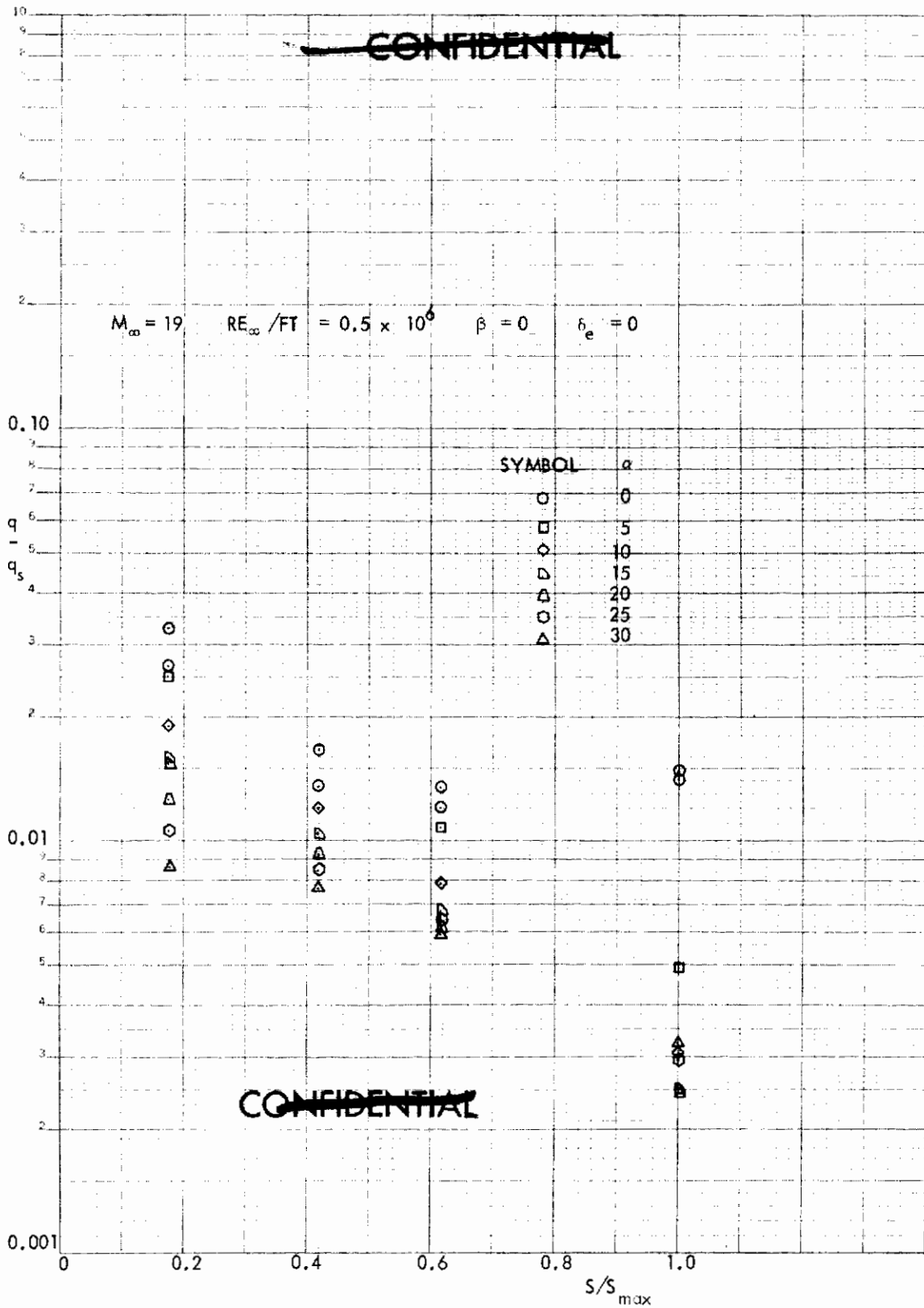
FIGURE 172 (U) TUNNEL F LOWER SURFACE SPANWISE HEATING RATES AT
X/L = 0.50, β=4
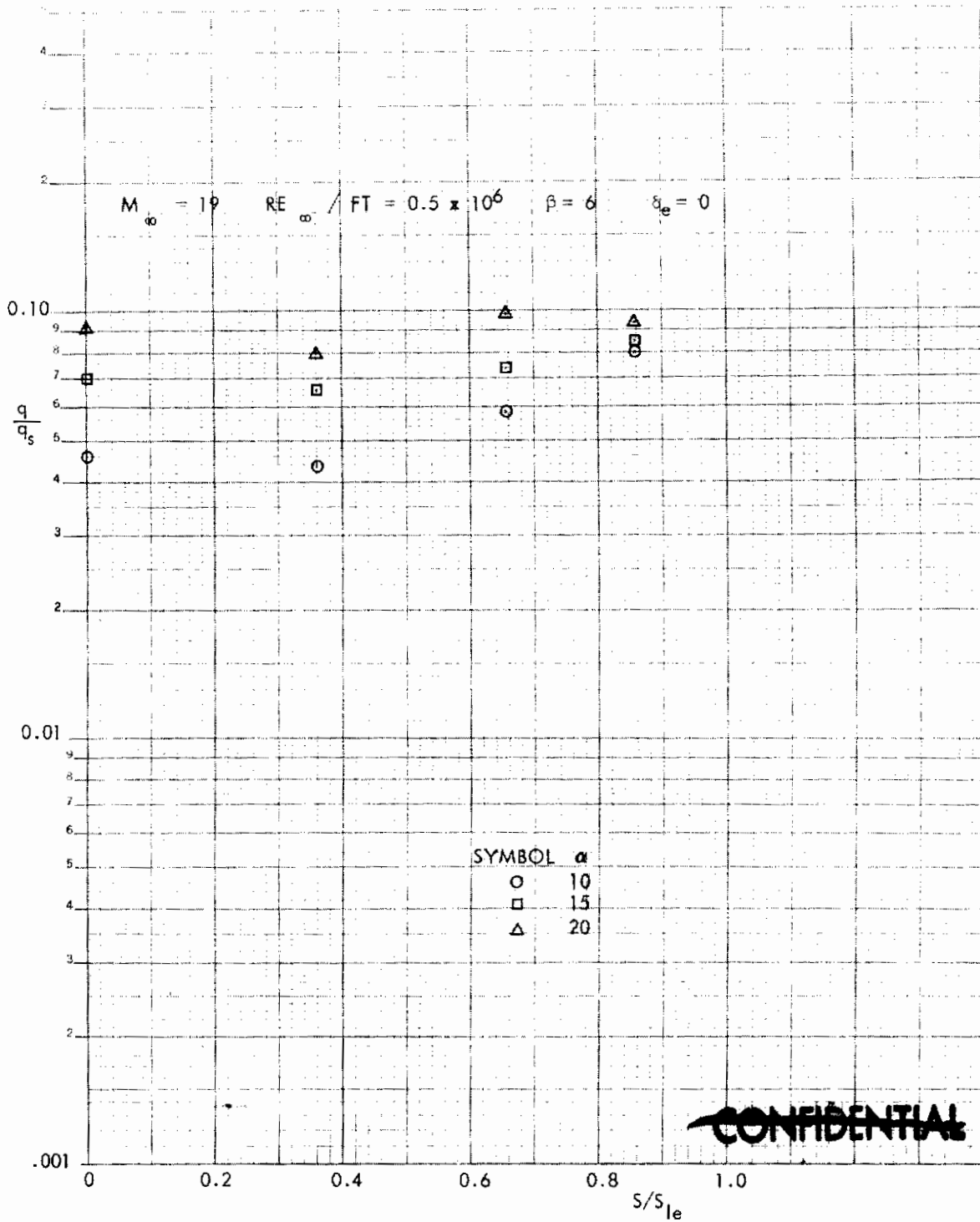
FIGURE 173 (U) TUNNEL F LOWER SURFACE SPANWISE HEATING RATES AT
X/L = 0.50, β=6
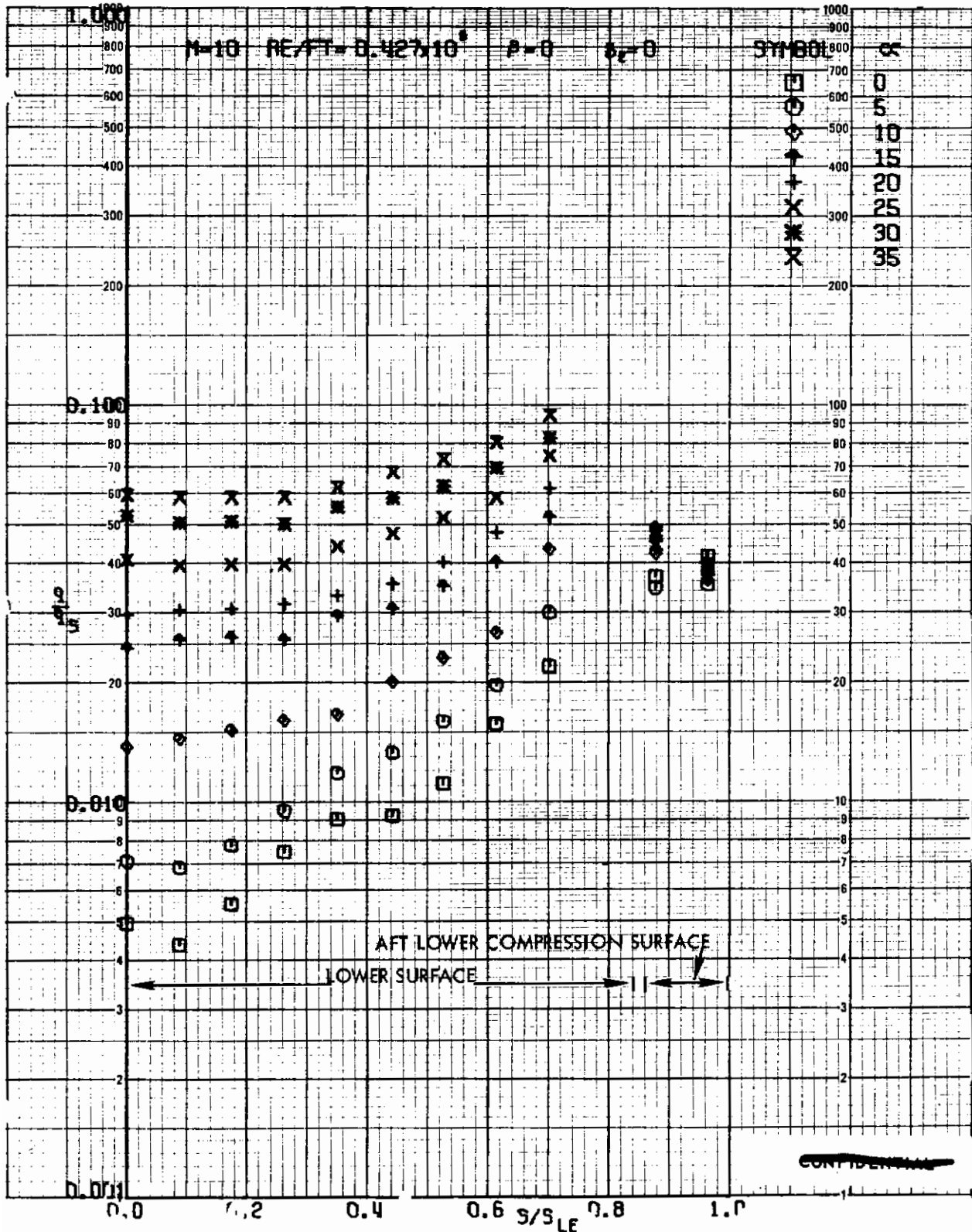
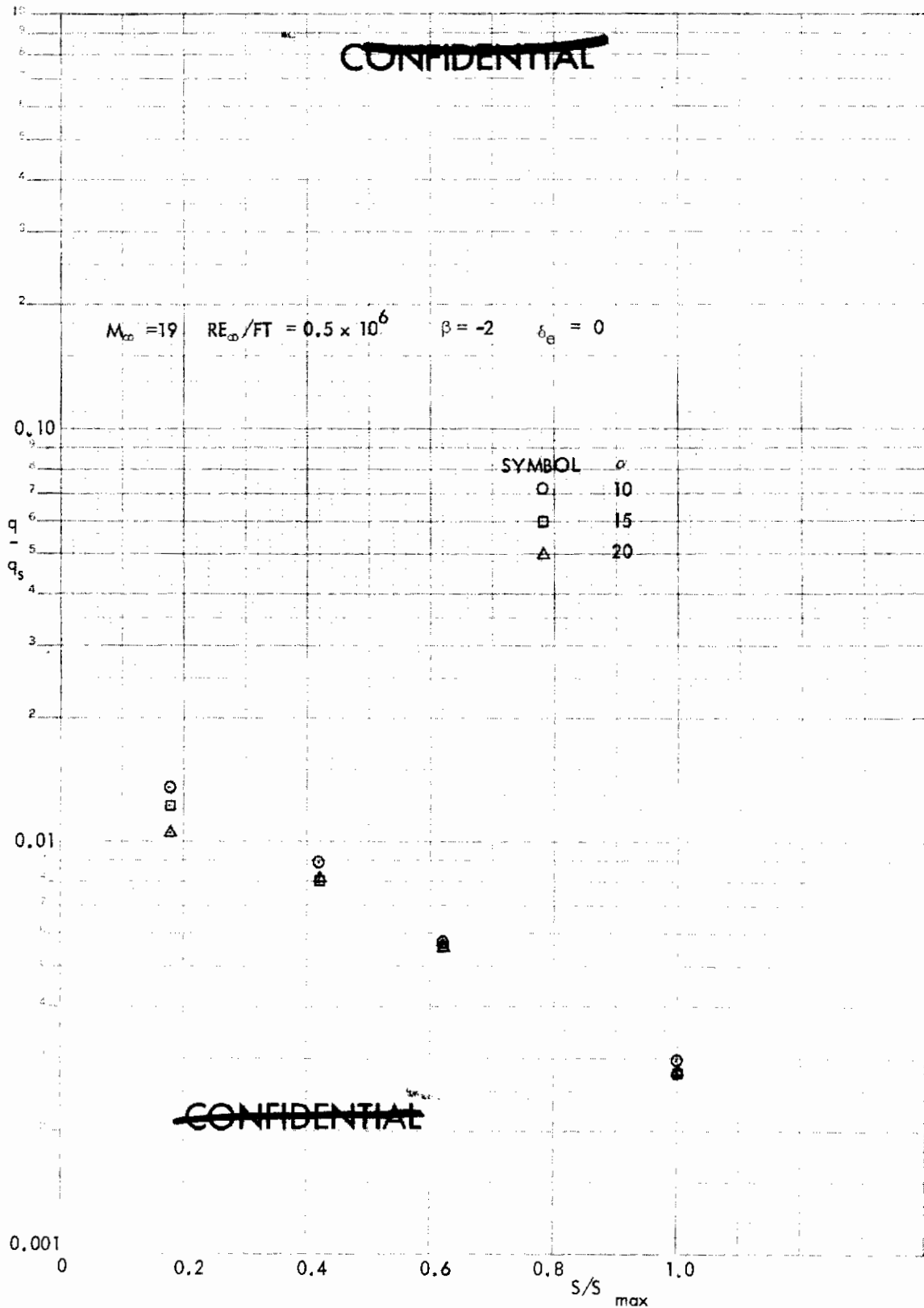FIGURE 174 (C) TUNNEL C LOWER SURFACE SPANWISE HEATING RATES AT
X/L = 0.75, β = 0

255
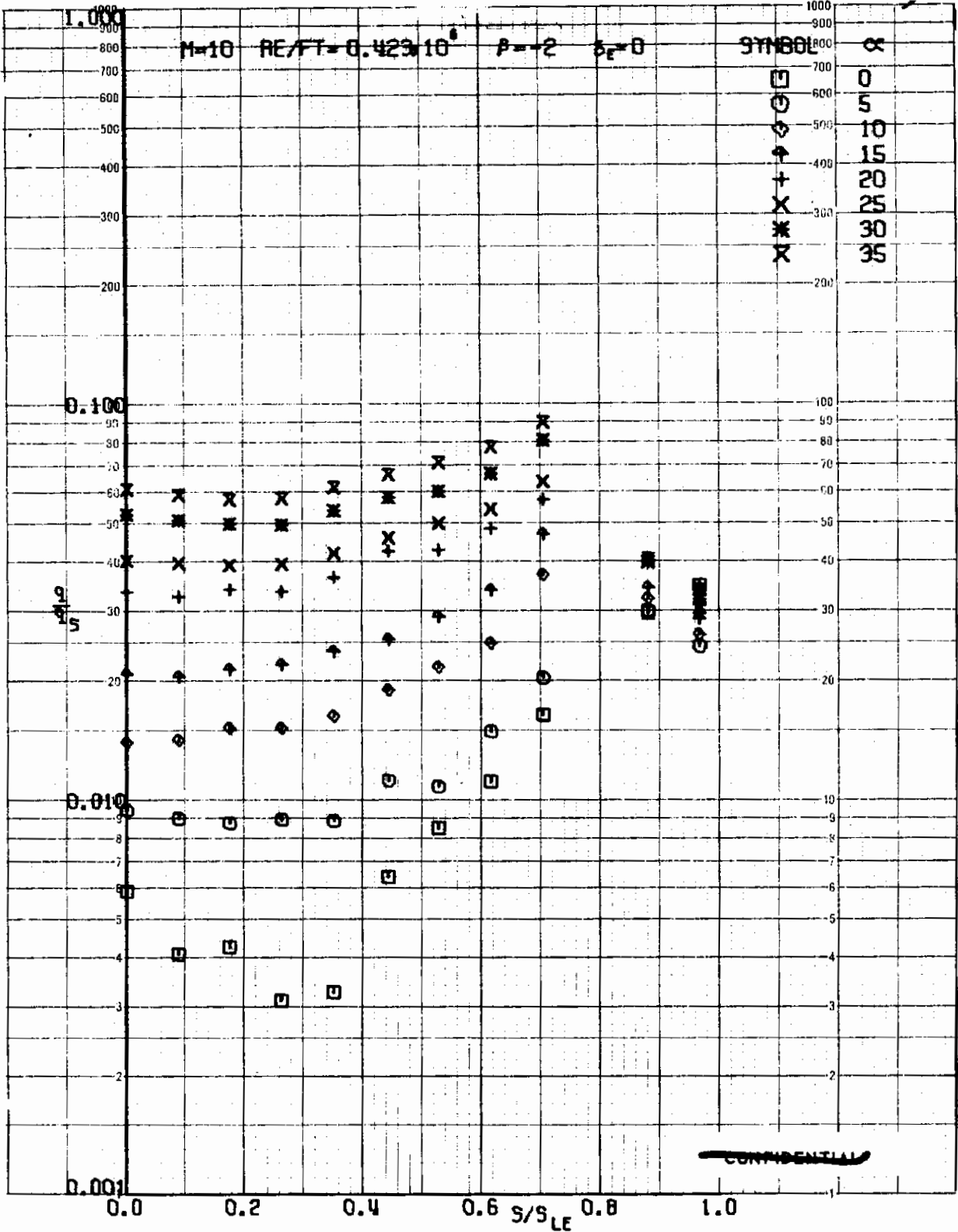
FIGURE 175 (U) TUNNEL C LOWER SURFACE SPANWISE HEATING RATES AT
X/L = 0.75, β=-2
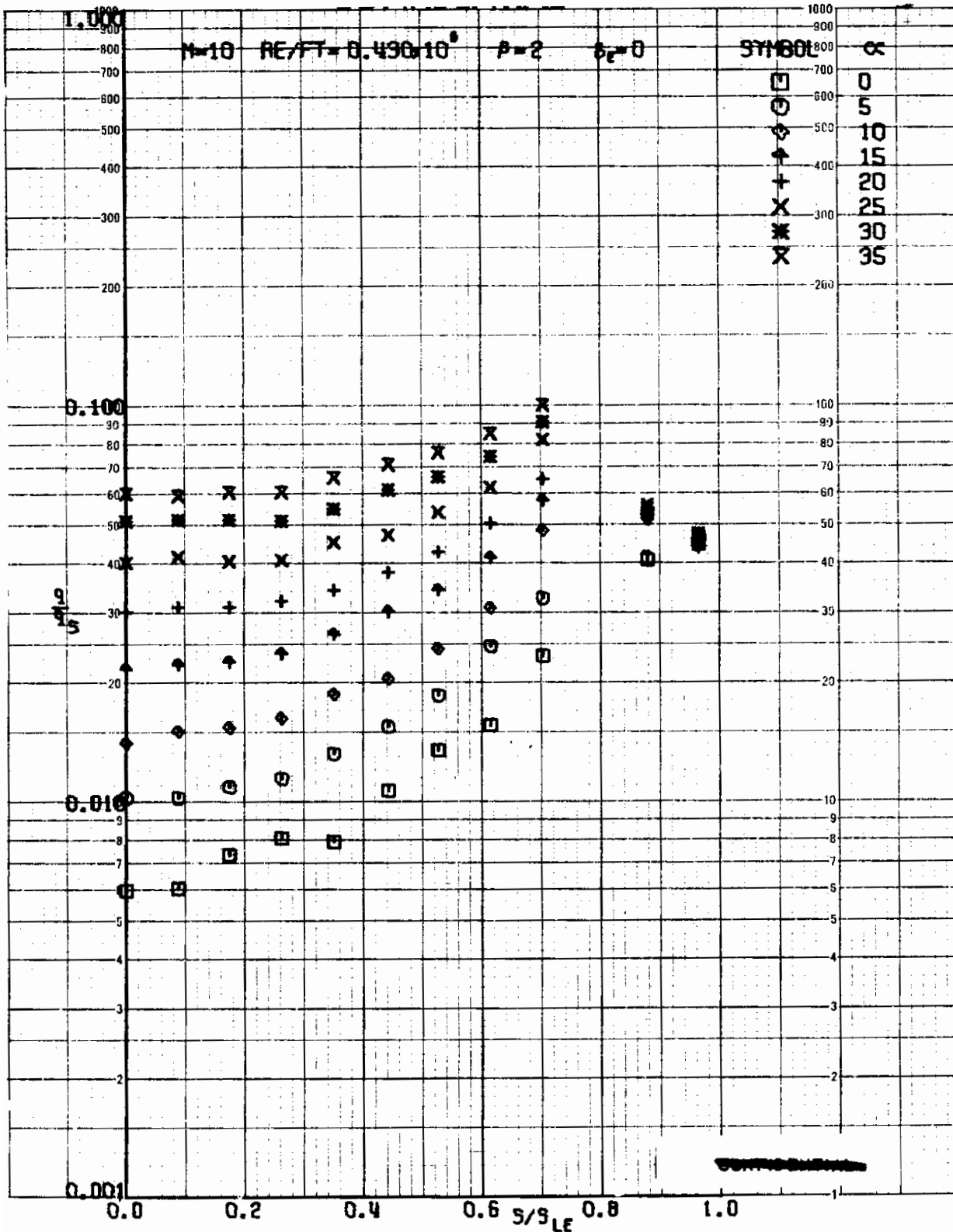
FIGURE 176 (U) TUNNEL C LOWER SURFACE SPANWISE HEATING RATES AT
X/L = 0.75, β=2
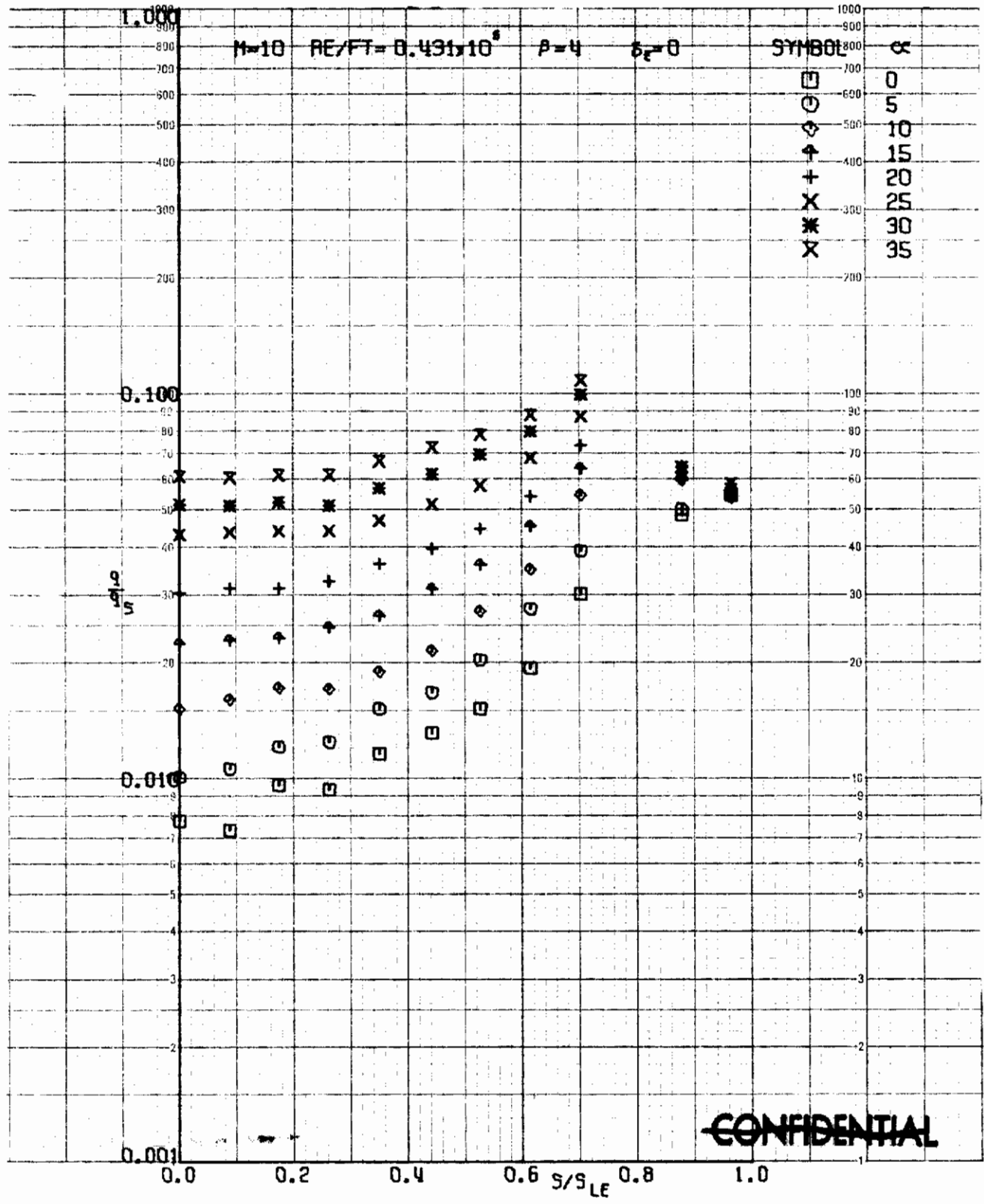
FIGURE 177 (U) TUNNEL C LOWER SURFACE SPANWISE HEATING RATES AT
X/L = 0.75, β=4

258
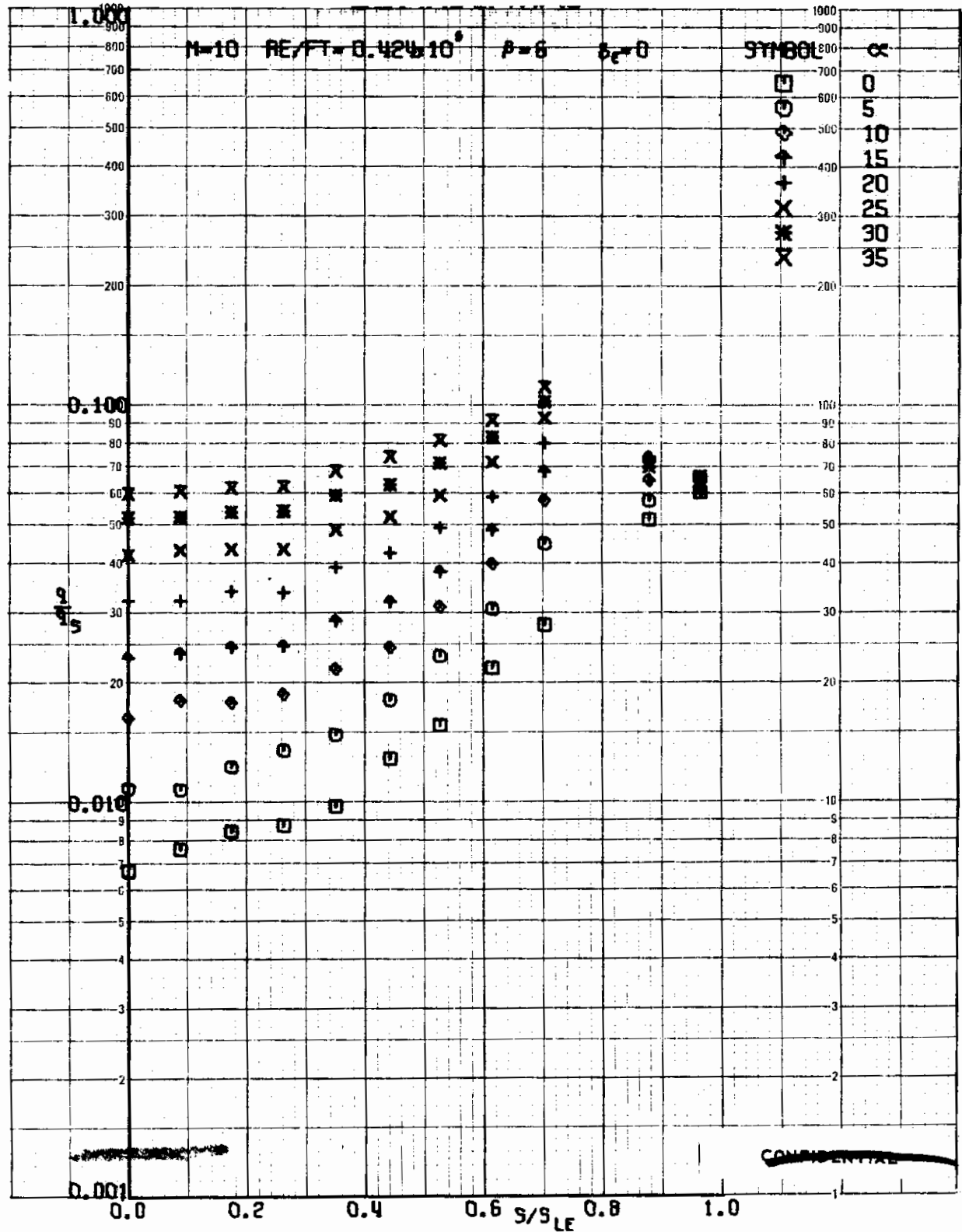
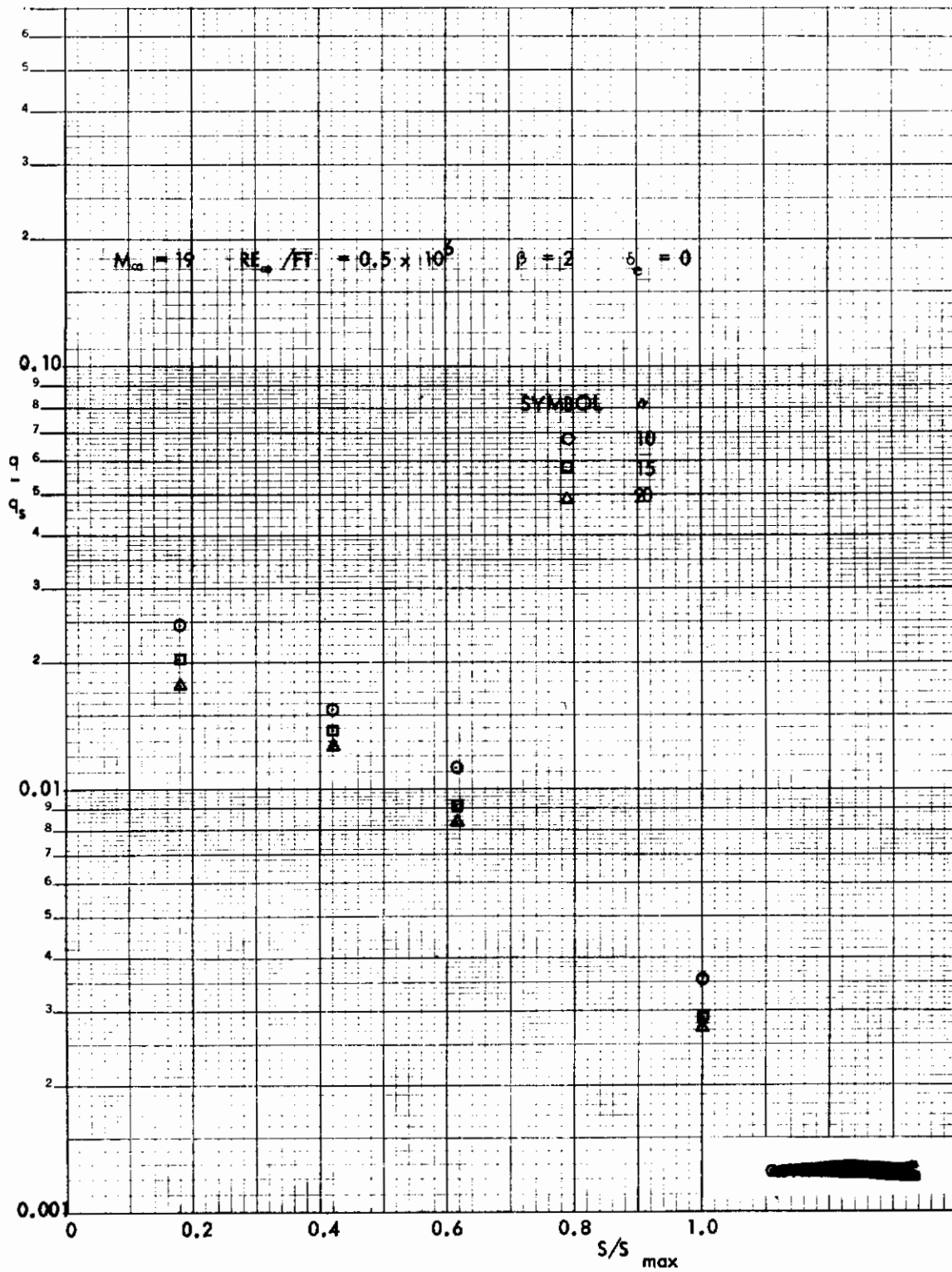FIGURE 178   (U) TUNNEL C LOWER SURFACE SPANWISE HEATING RATES AT
X/L = 0.75, β=6

259
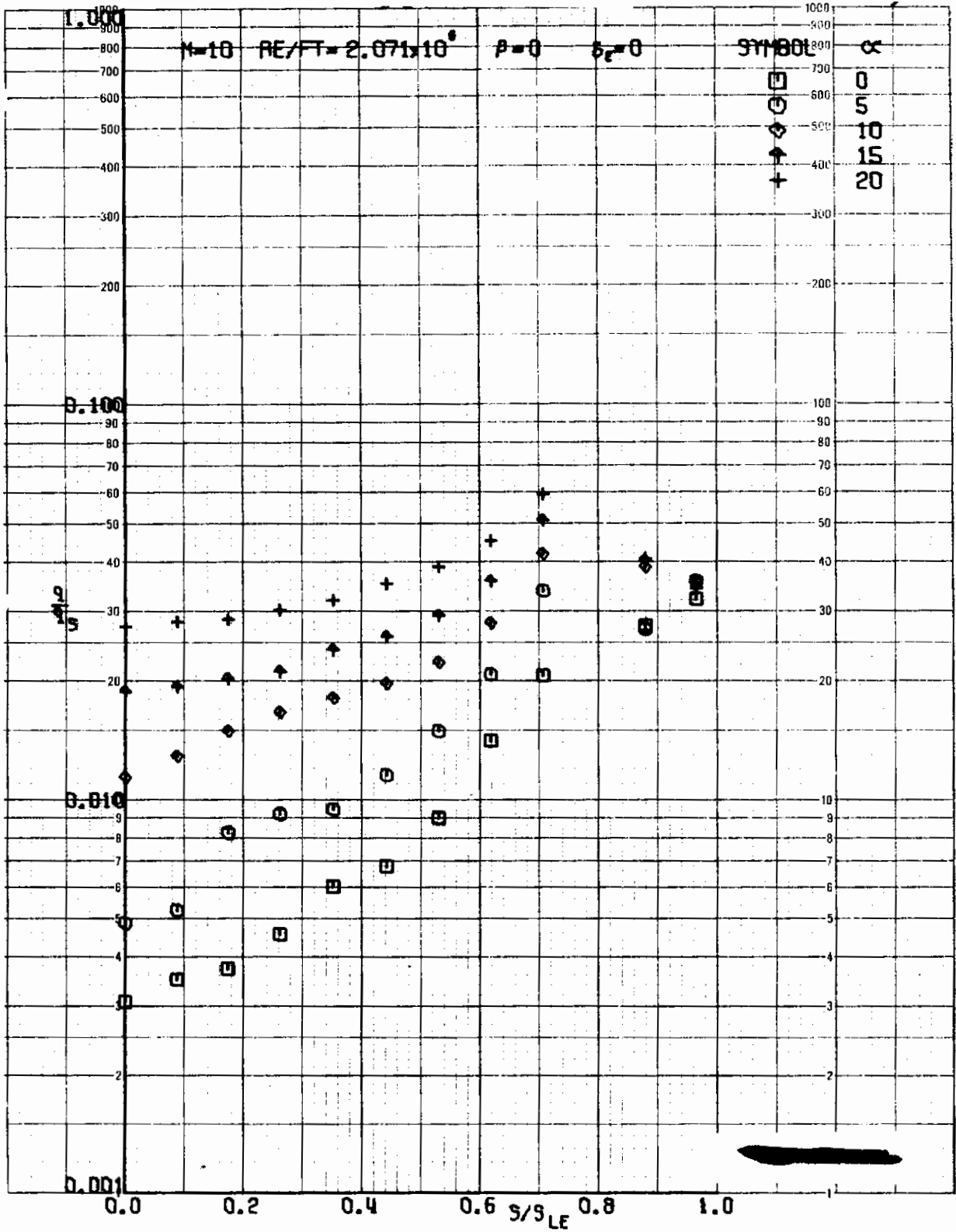
FIGURE 179 (U) TUNNEL C LOWER SURFACE SPANWISE HEATING RATES AT
X/L = 0.75, β=0
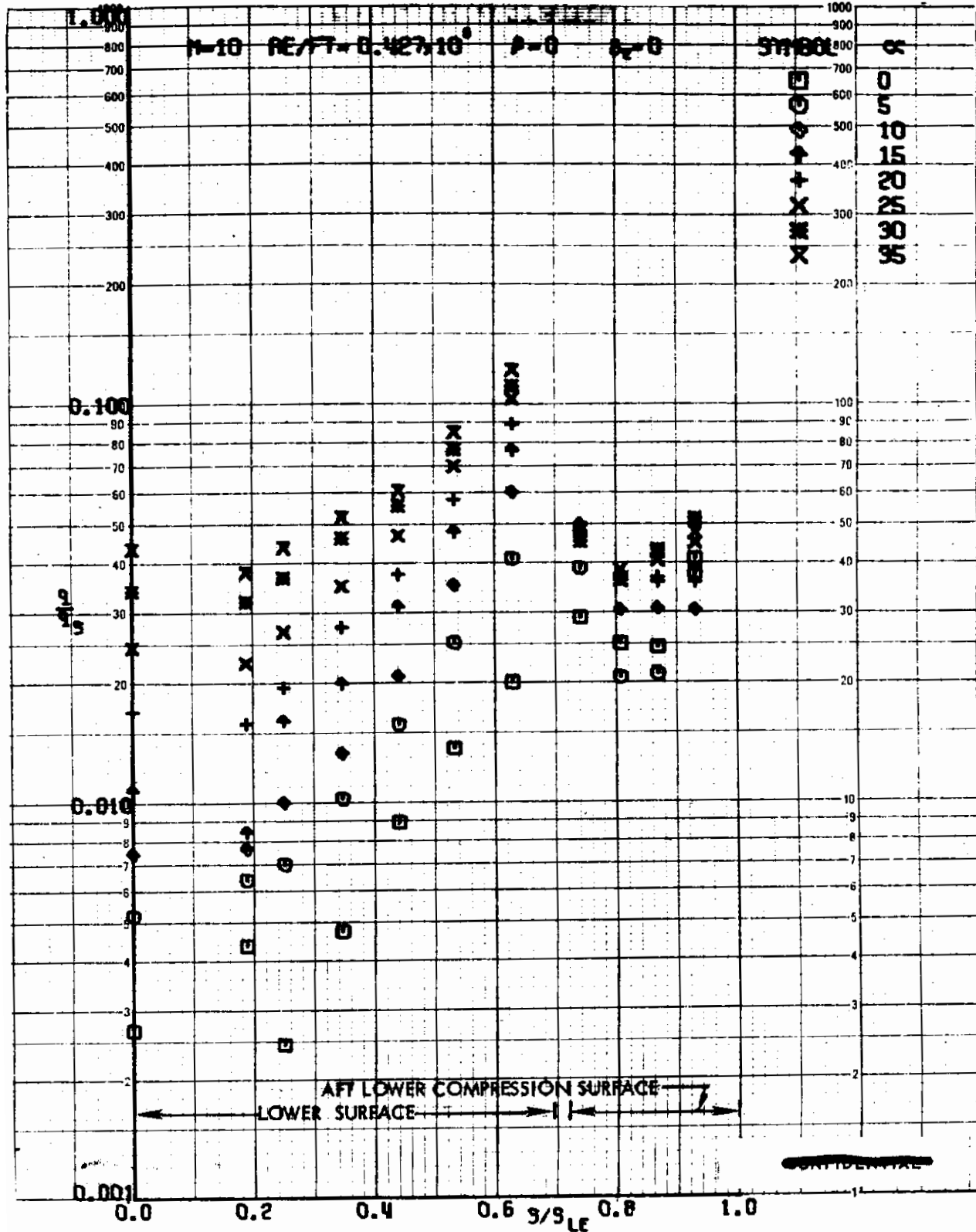
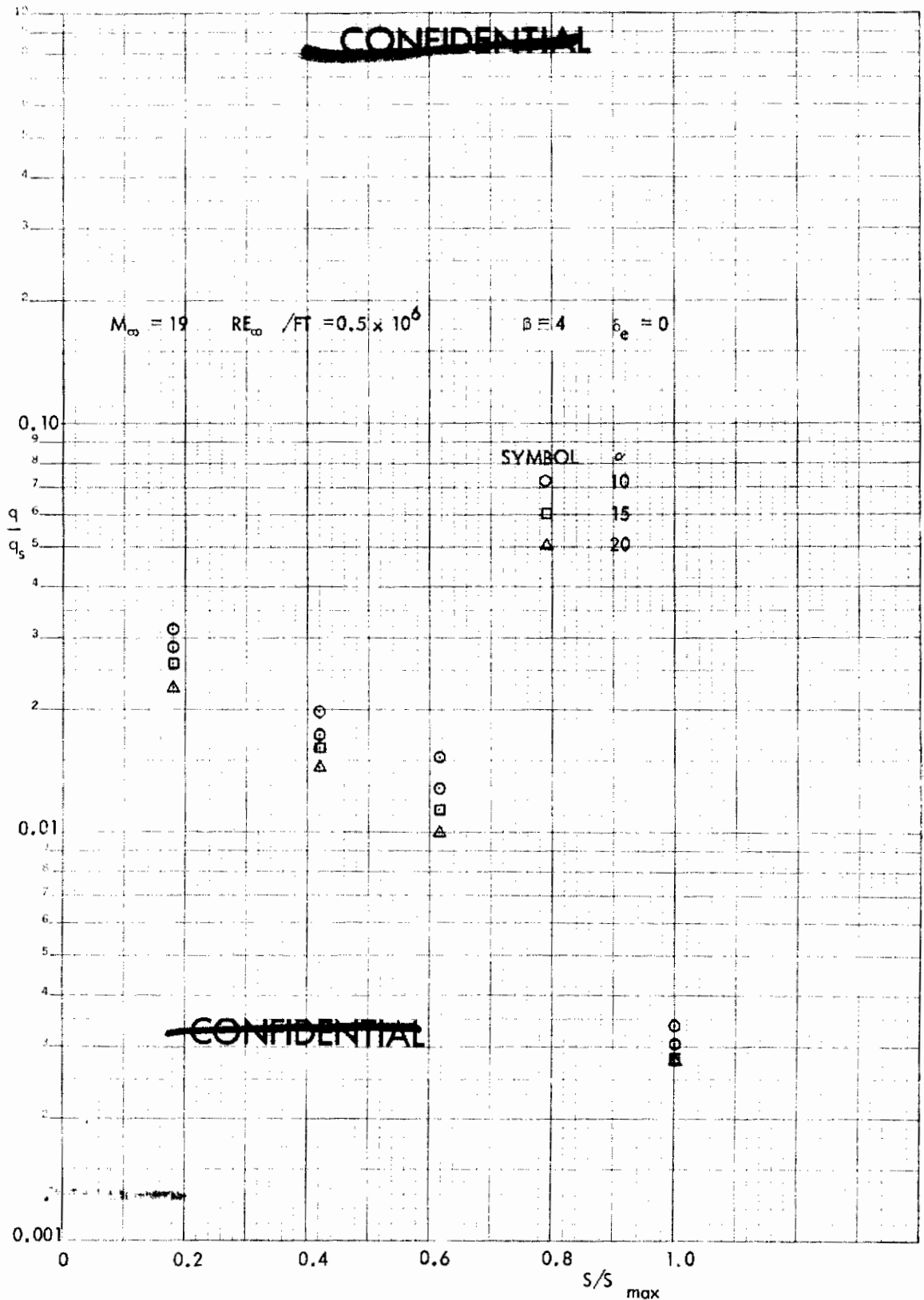FIGURE 130 (U) TUNNEL C LOWER SURFACE SPANWISE HEATING RATES AT
X/L = 0.96, β=0
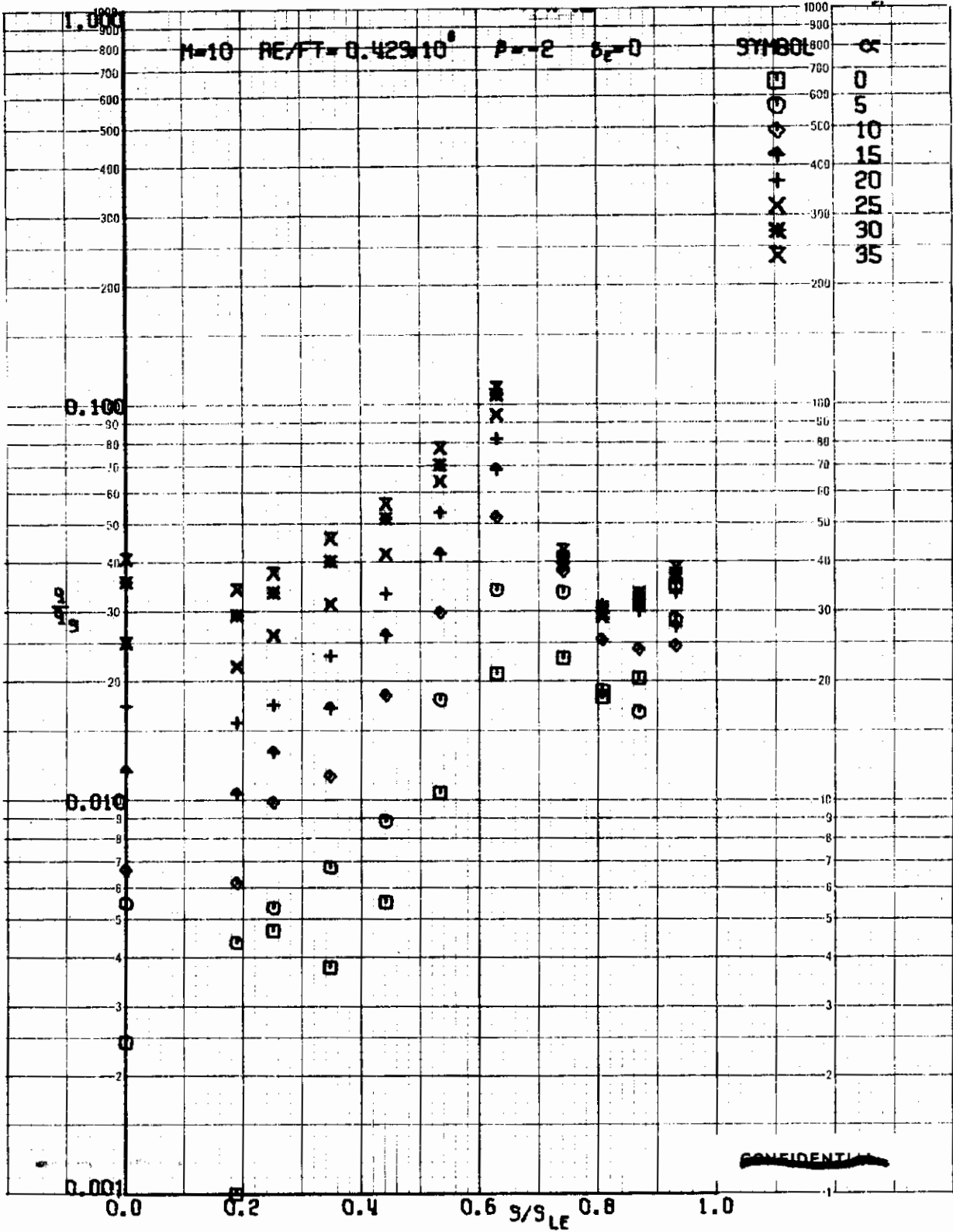
FIGURE 181 (U) TUNNEL C LOWER SURFACE SPANWISE HEATING RATES AT
X/L = 0.96, β=-2
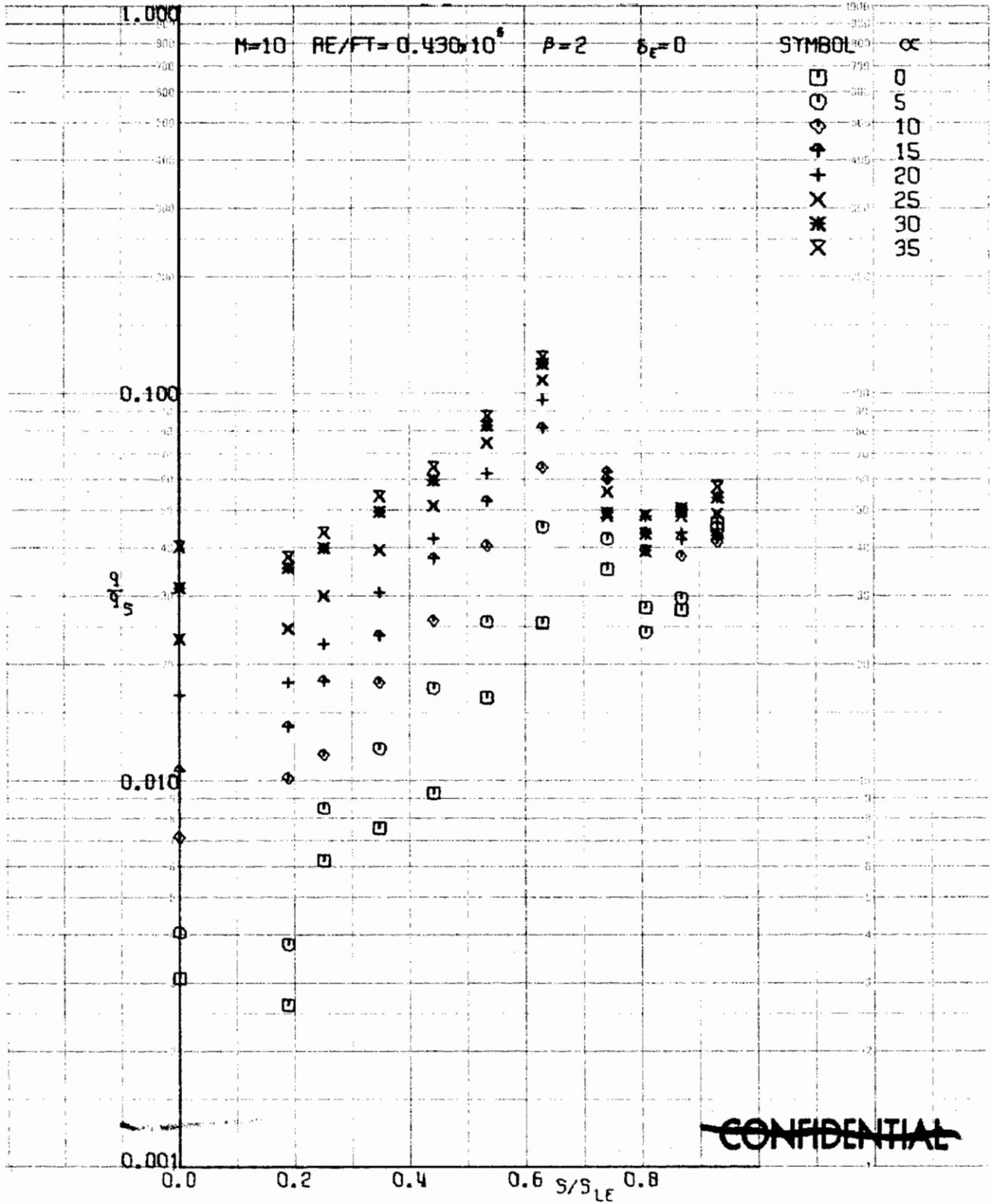
FIGURE 182   (U) TUNNEL C LOWER SURFACE SPANWISE HEATING RATES AT
X/L = 0.96, β=2

263
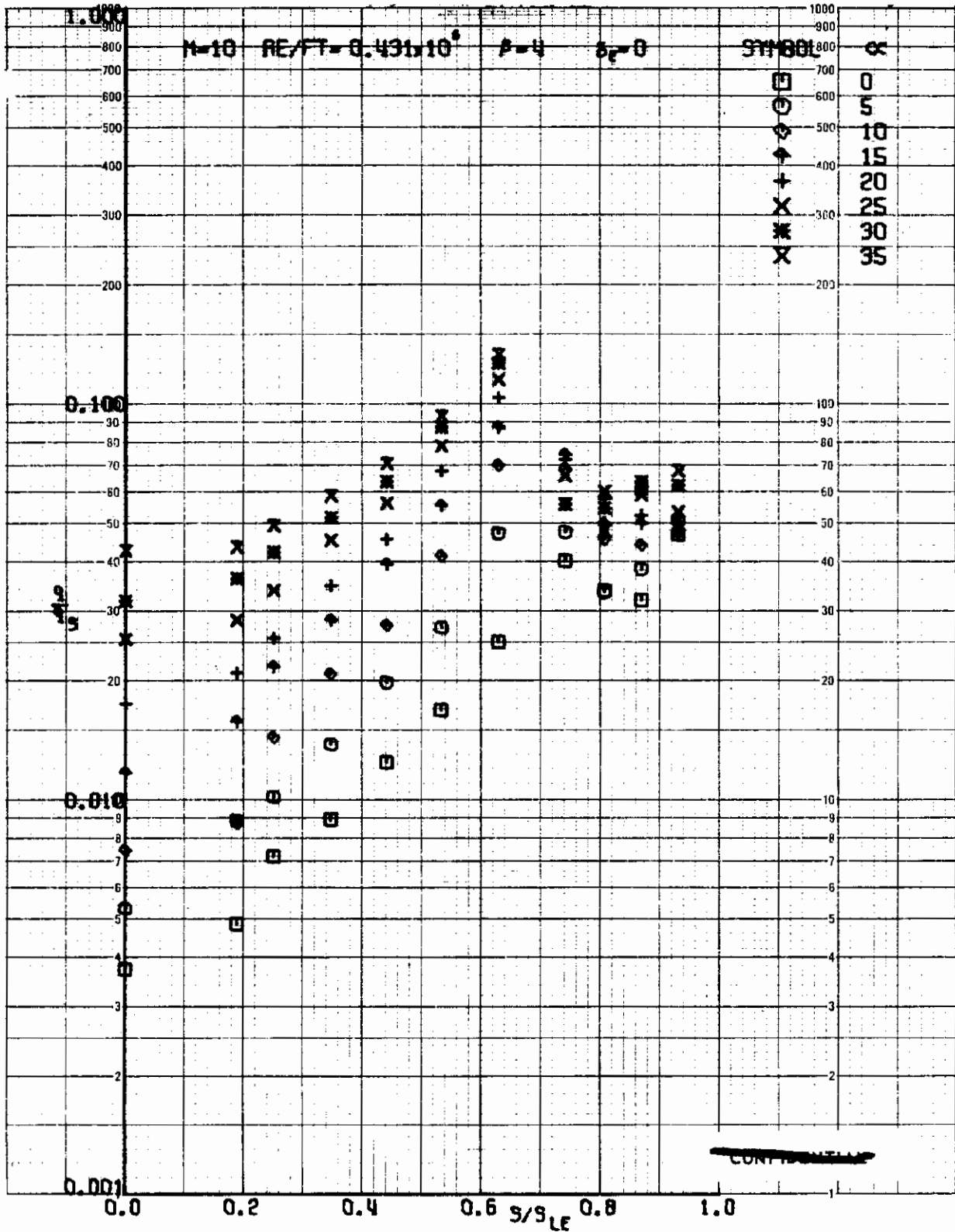
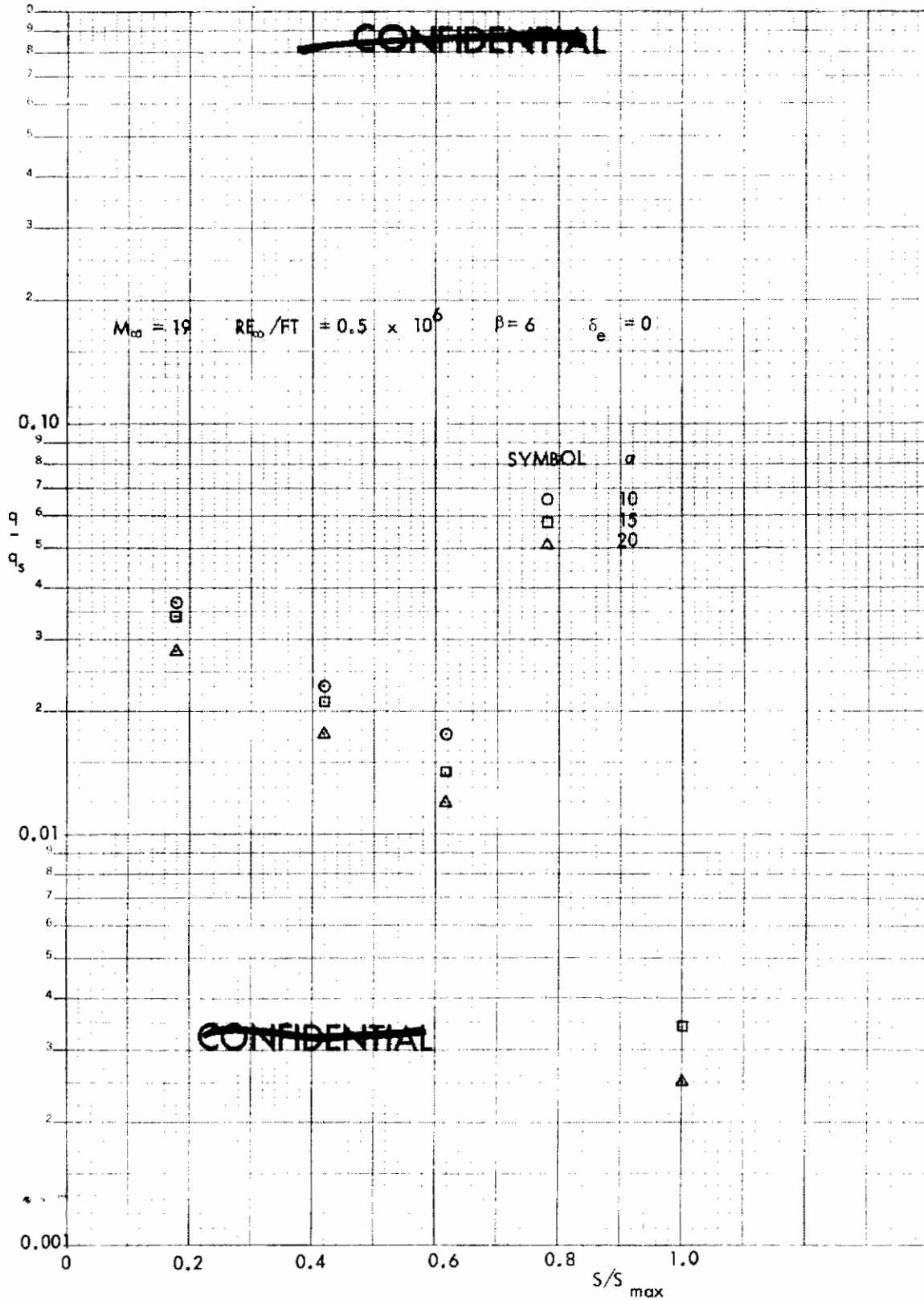FIGURE 183 (U) TUNNEL C LOWER SURFACE SPANWISE HEATING RATES AT
X/L = 0.96, β=4

264
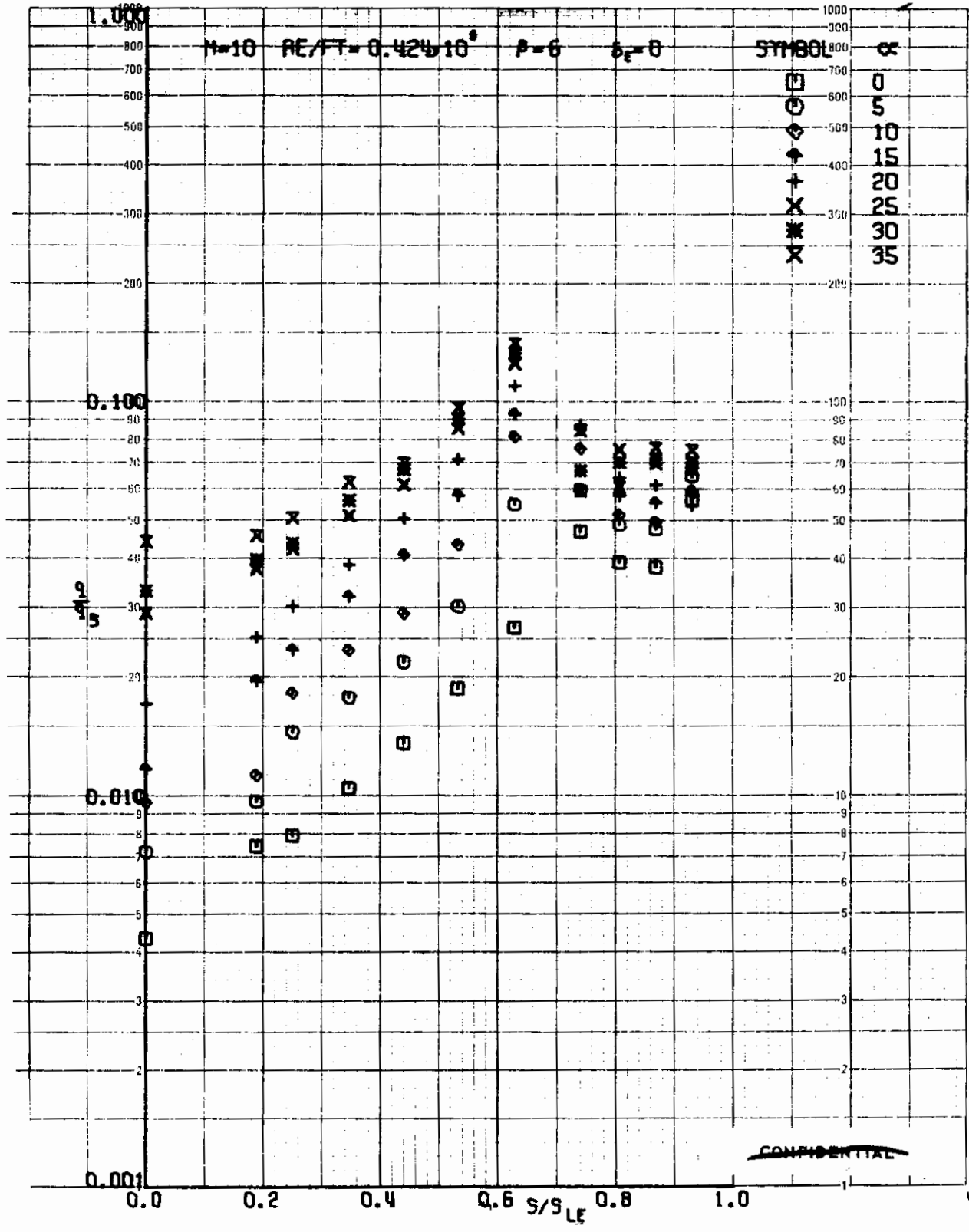
FIGURE 184   (U) TUNNEL C LOWER SURFACE SPANWISE HEATING RATES AT
X/L = 0.96, β=6
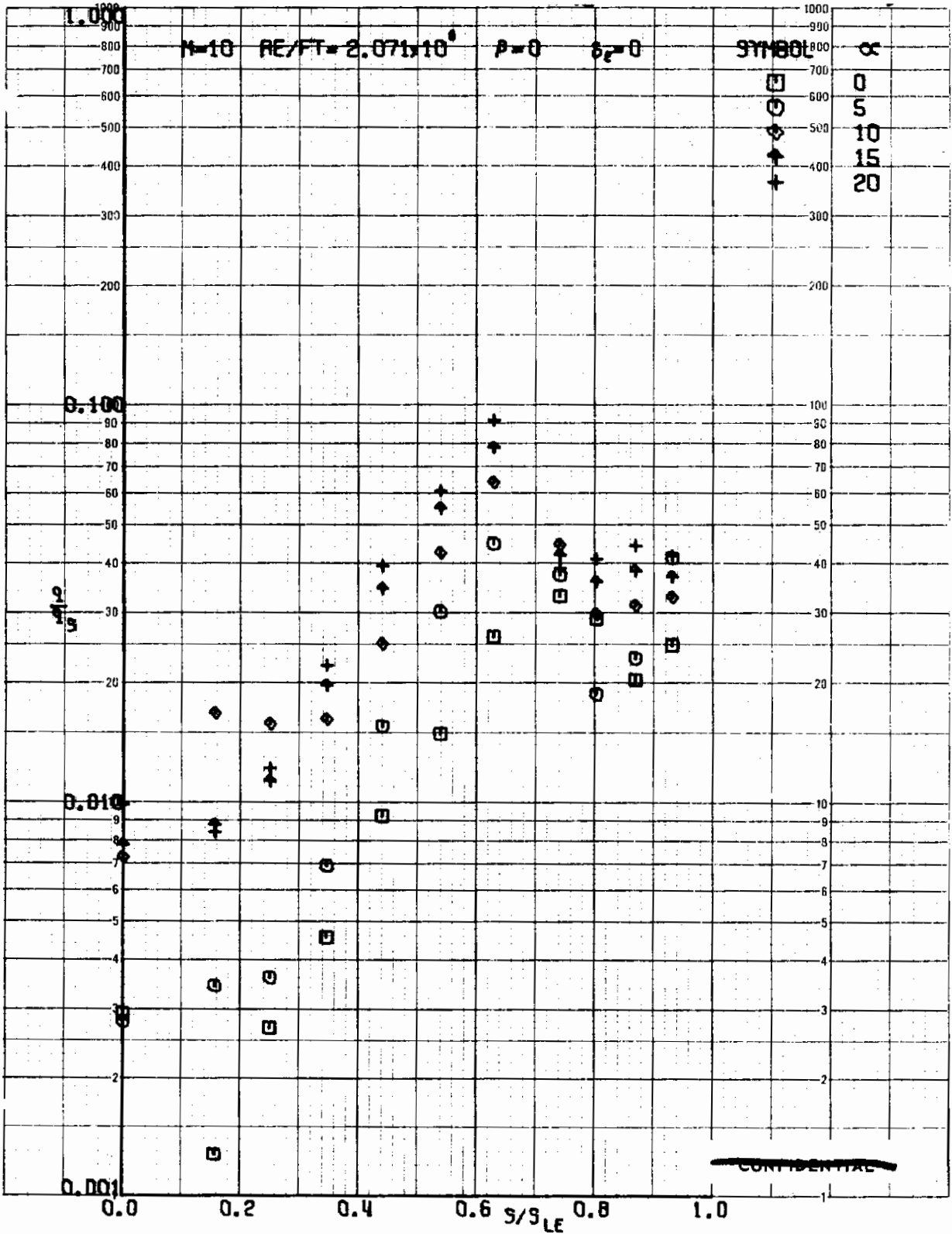
FIGURE 185   (U) TUNNEL C LOWER SURFACE SPANWISE HEATING RATES AT
X/L = 0.96, β=0
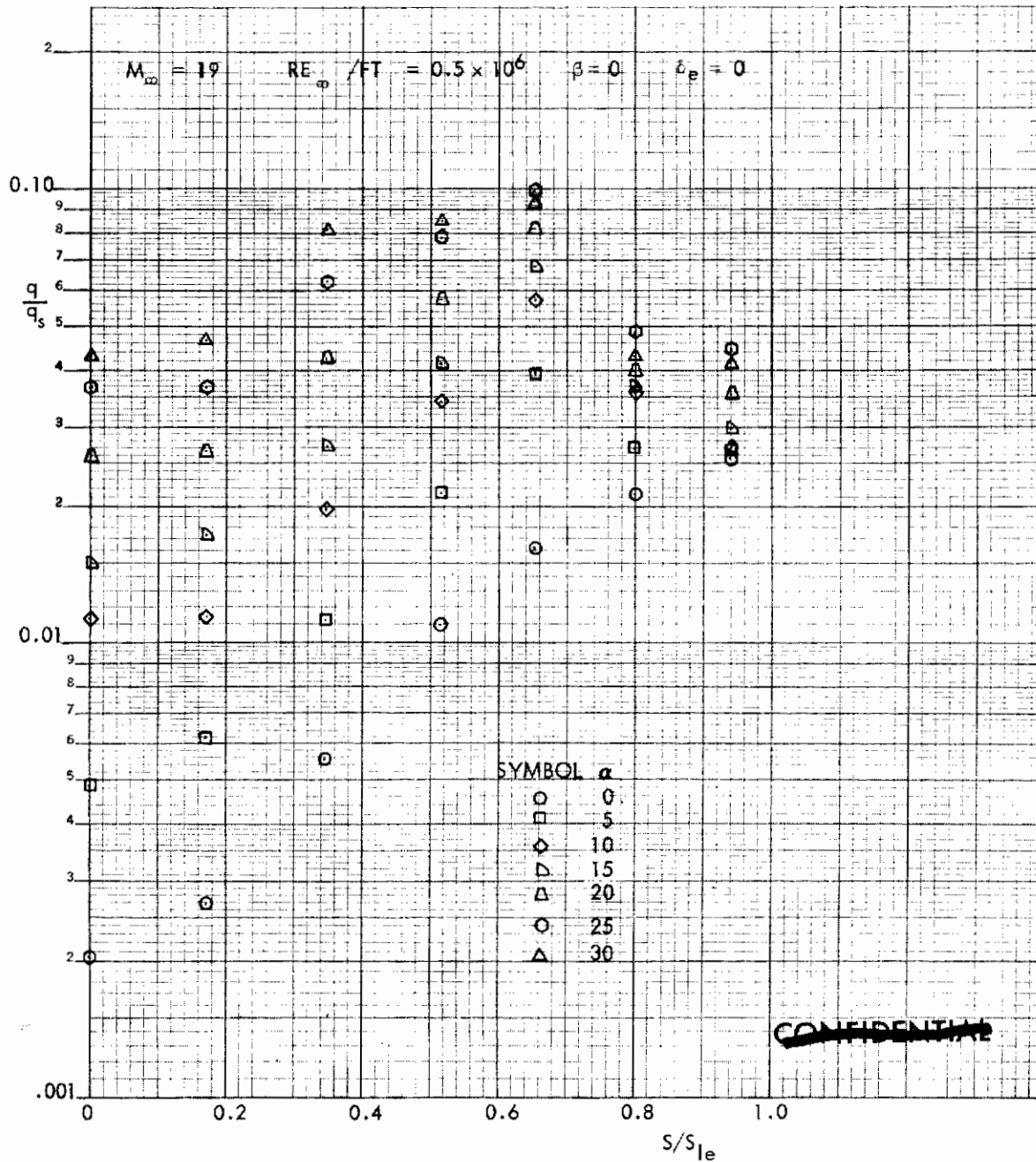
FIGURE 186   (b) TUNNEL F LOWER SURFACE SPANWISE HEATING RATES AT
X/L = 0.96, β=0
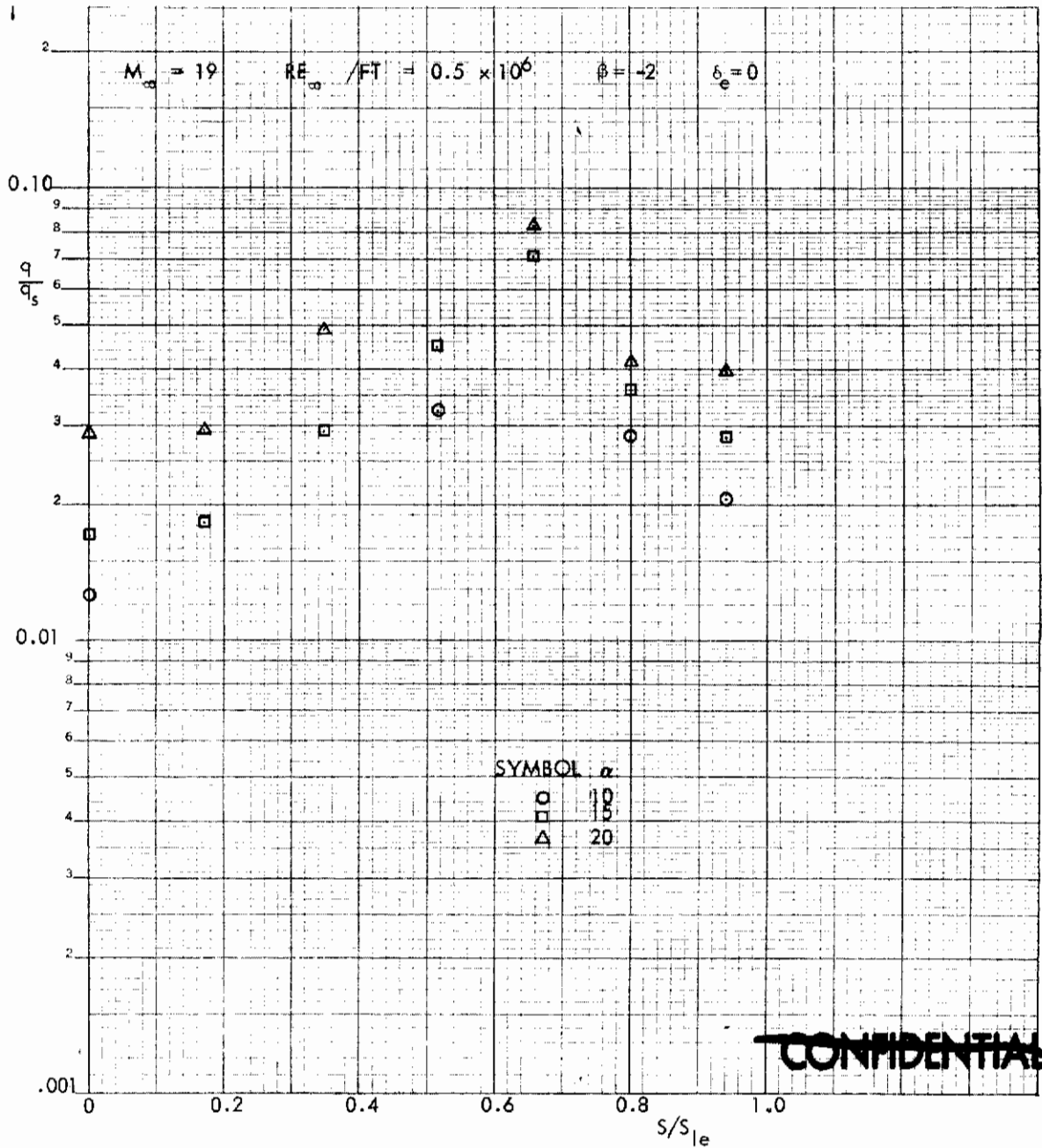
FIGURE 187 (U) TUNNEL F LOWER SURFACE SPANWISE HEATING RATES AT
X/L = 0.96, β=-2
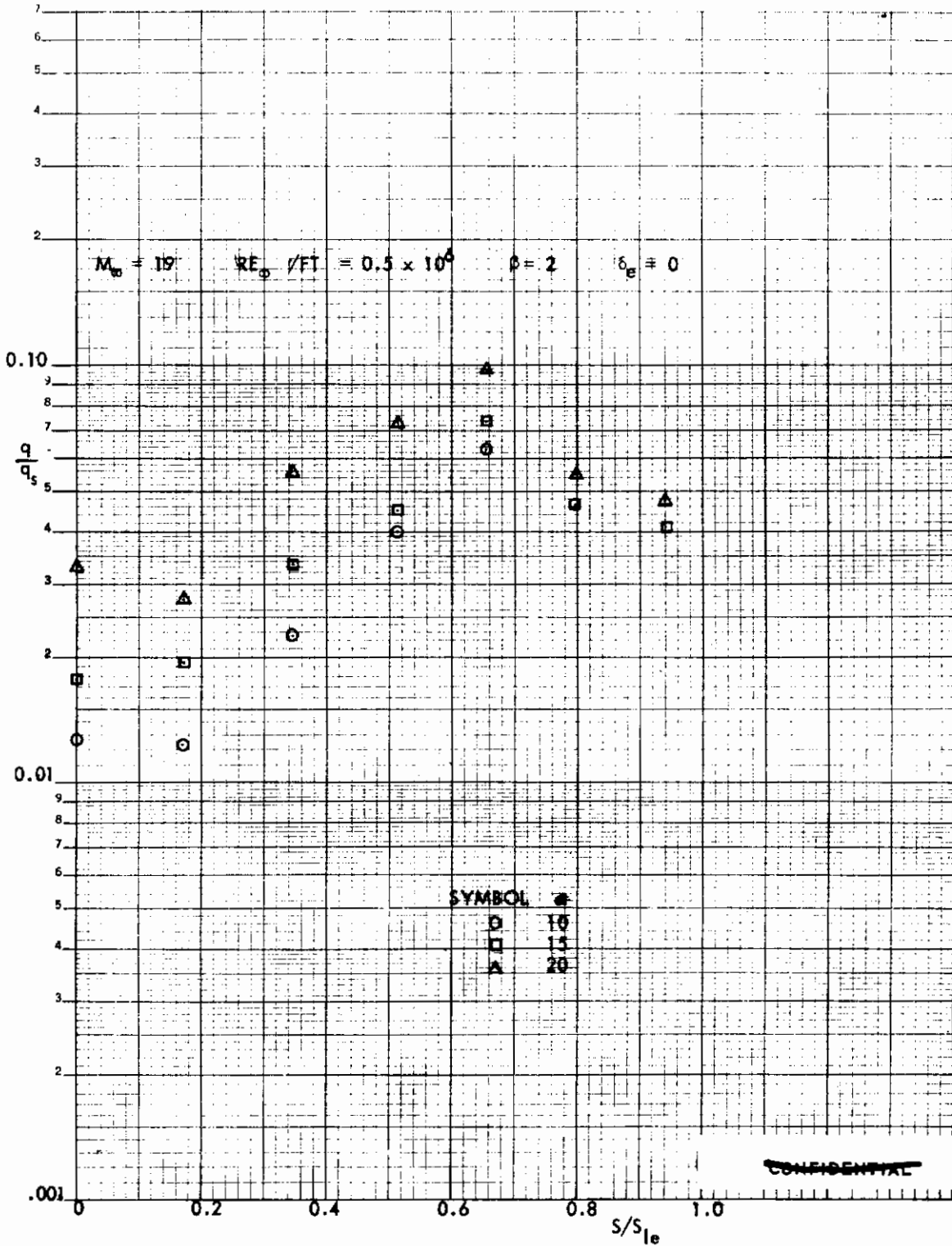
FIGURE 188 (U) TUNNEL F LOWER SURFACE SPANWISE HEATING RATES AT
X/L = 0.96, β=2
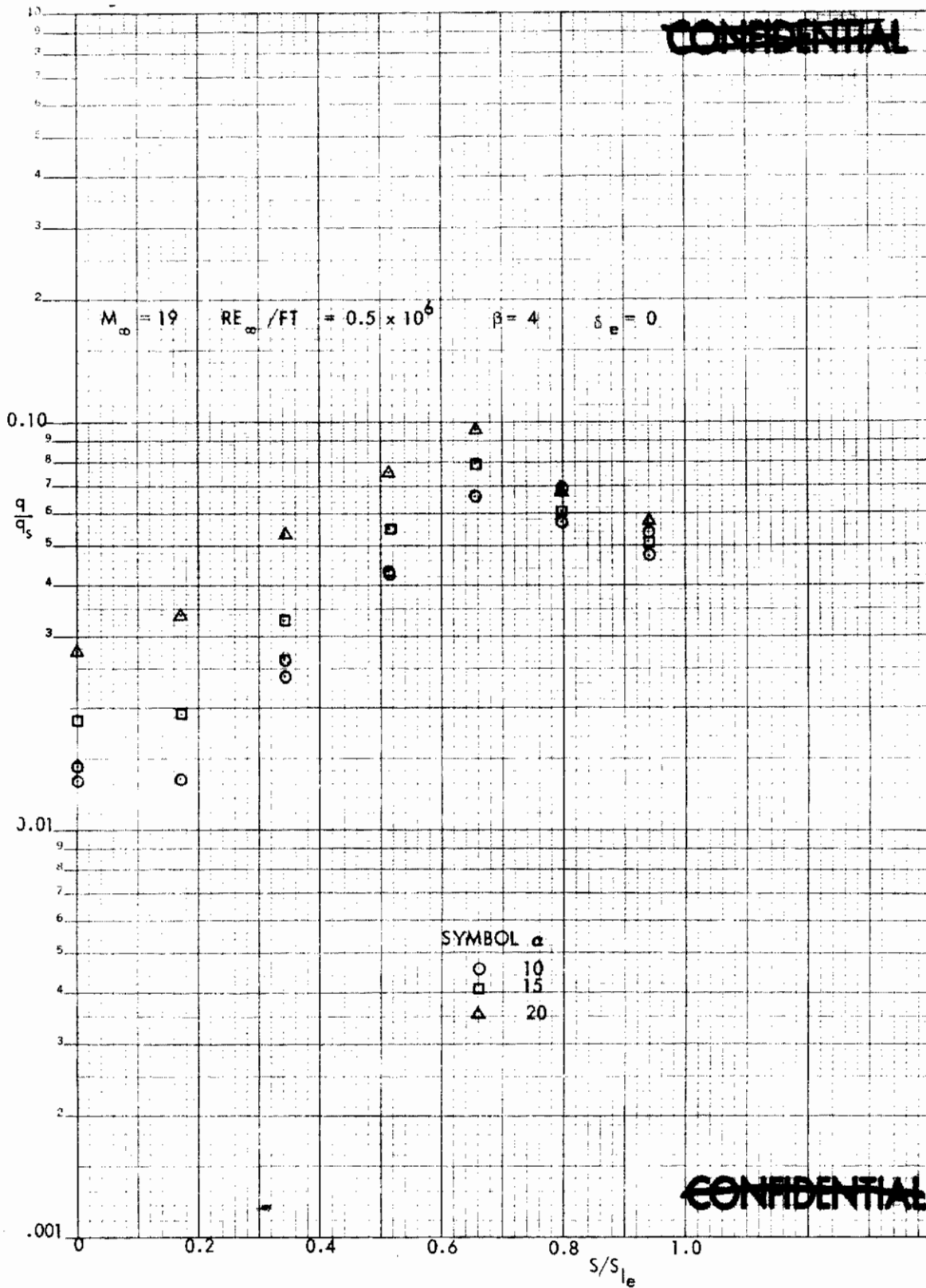
FIGURE 189 (U) TUNNEL F LOWER SURFACE SPANWISE HEATING RATES AT X/L = 0.96, β=4

270
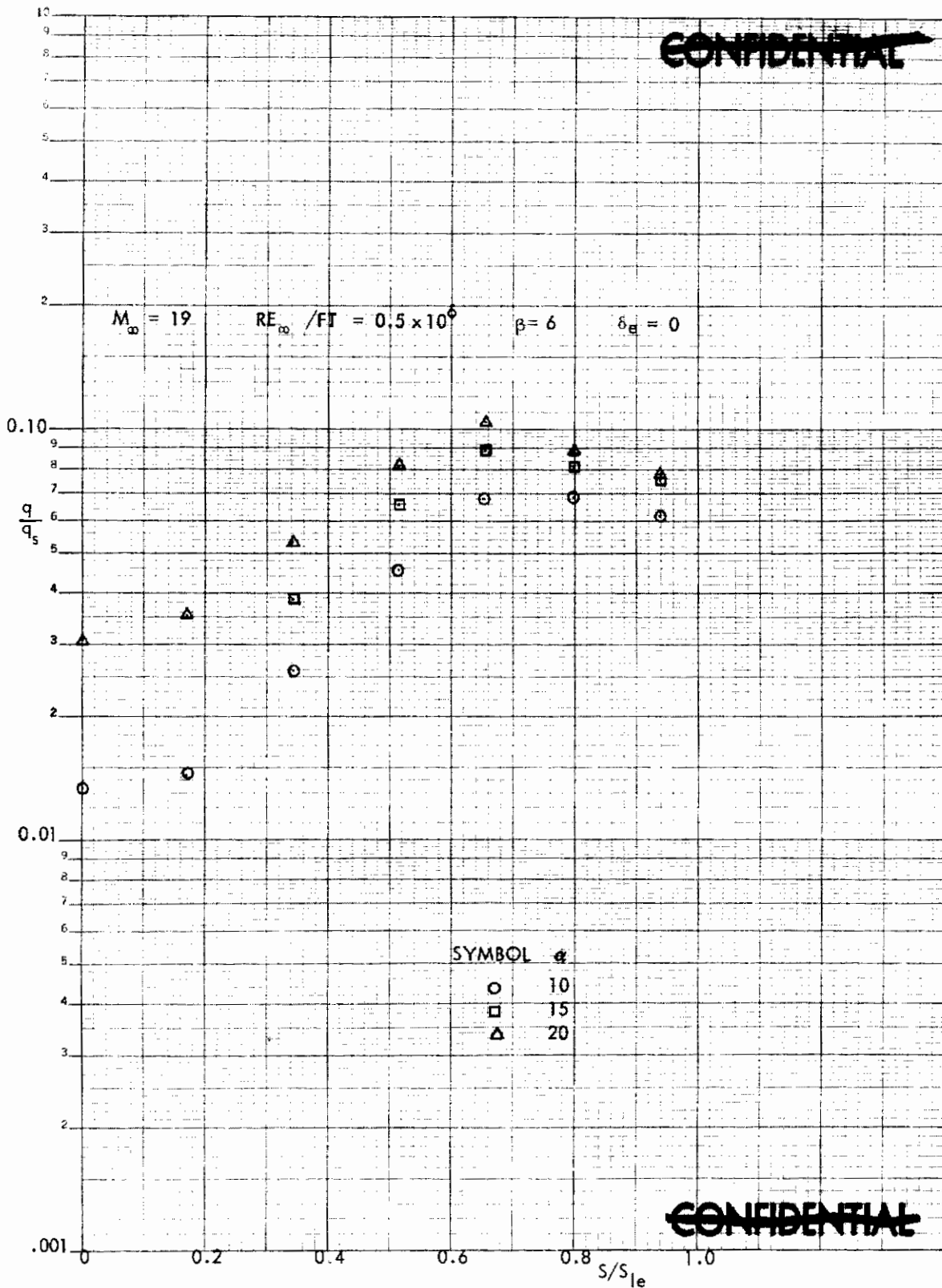
FIGURE 190 (U) TUNNEL F LOWER SURFACE SPANWISE HEATING RATES AT
X/L = 0.96, β=6
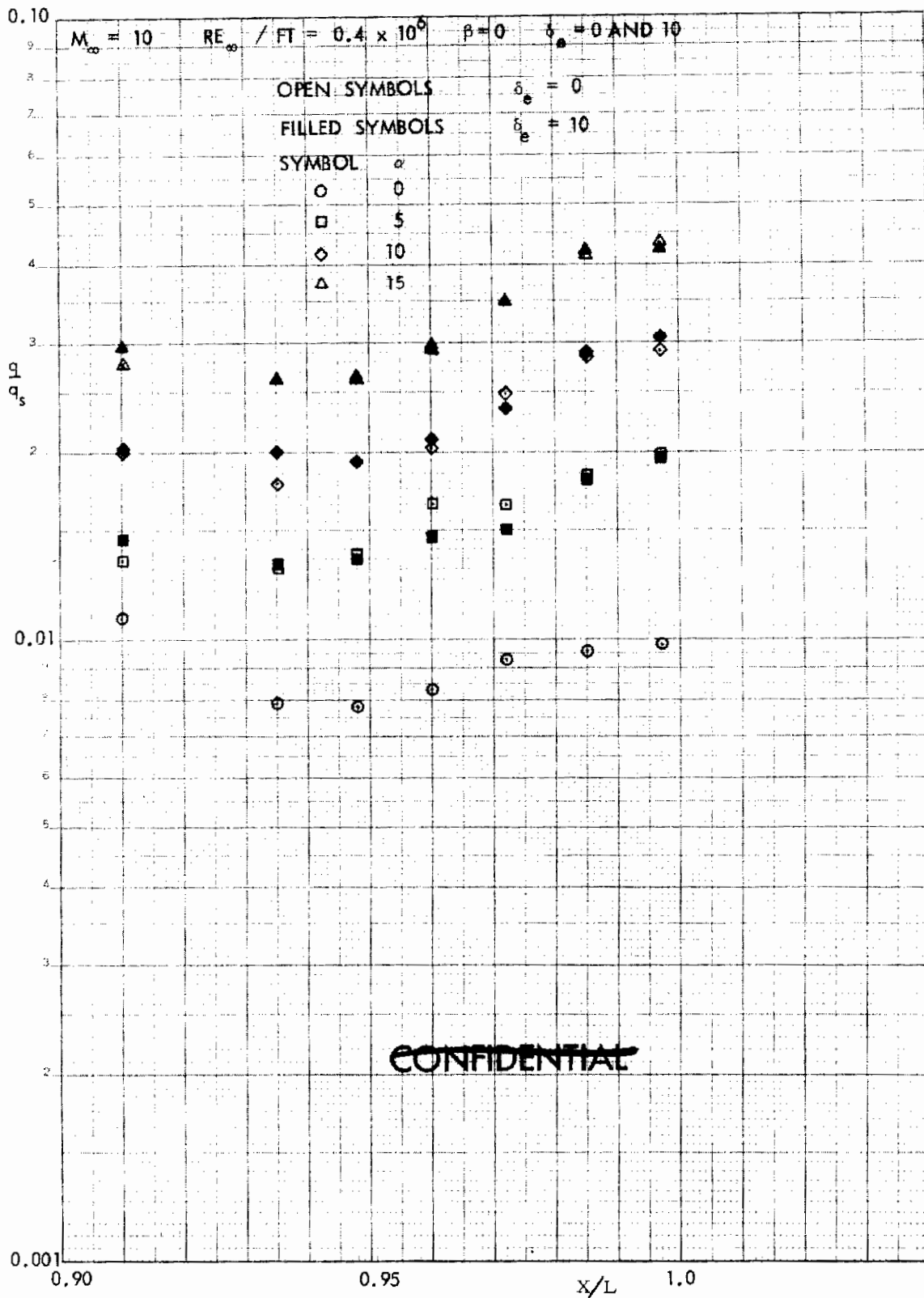
FIGURE 191 (U) EFFECT OF ELEVON DEFLECTION ON LOWER SURFACE HEATING
AT Y/L = 0.0875
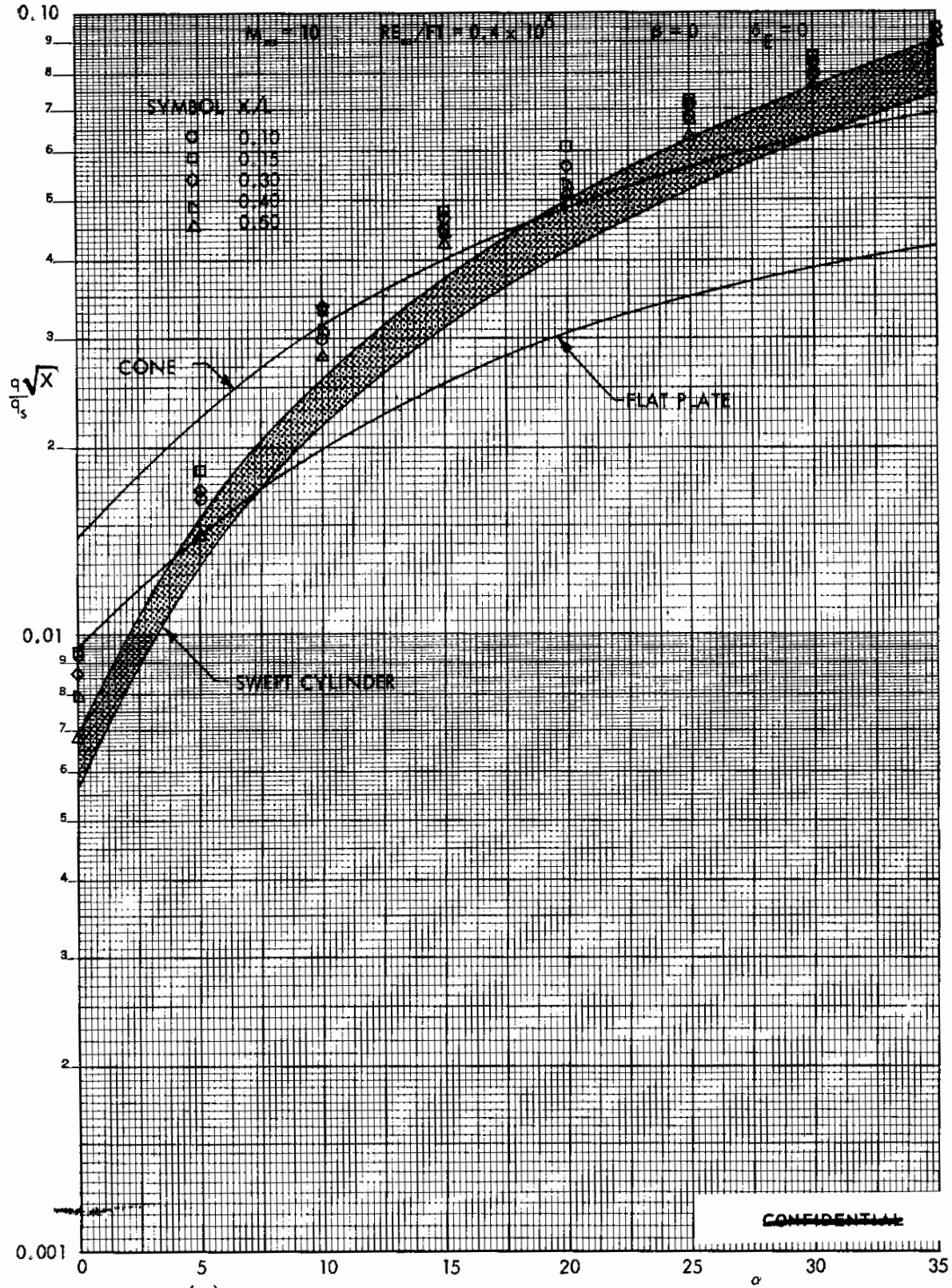
FIGURE 192a (U) CORRELATION OF TUNNEL C FORWARD RAMP CENTERLINE HEATING
DATA, β=0
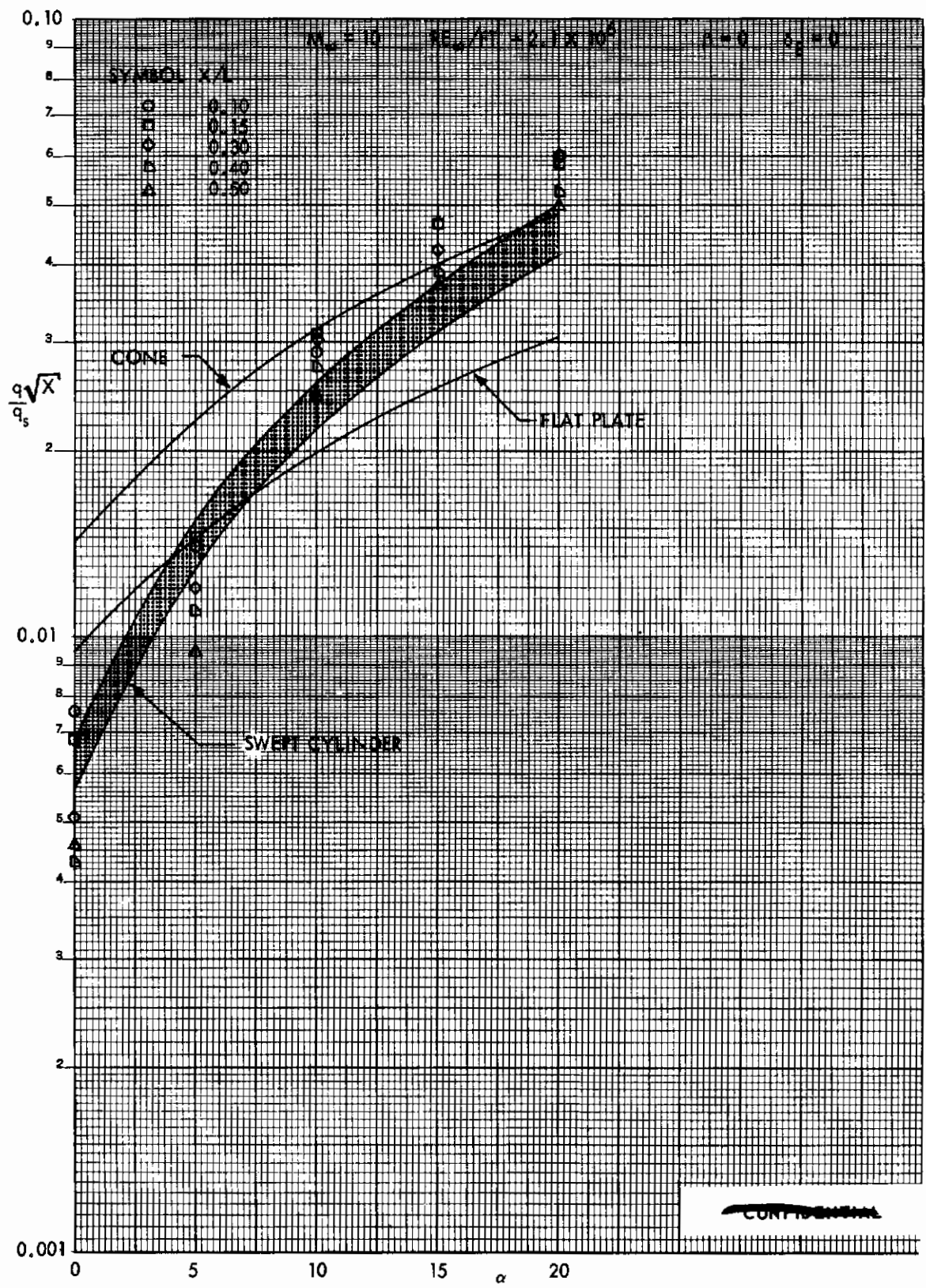
FIGURE 192b (U) CORRELATION OF TUNNEL C FORWARD RAMP CENTERLINE HEATING DATA, β=0
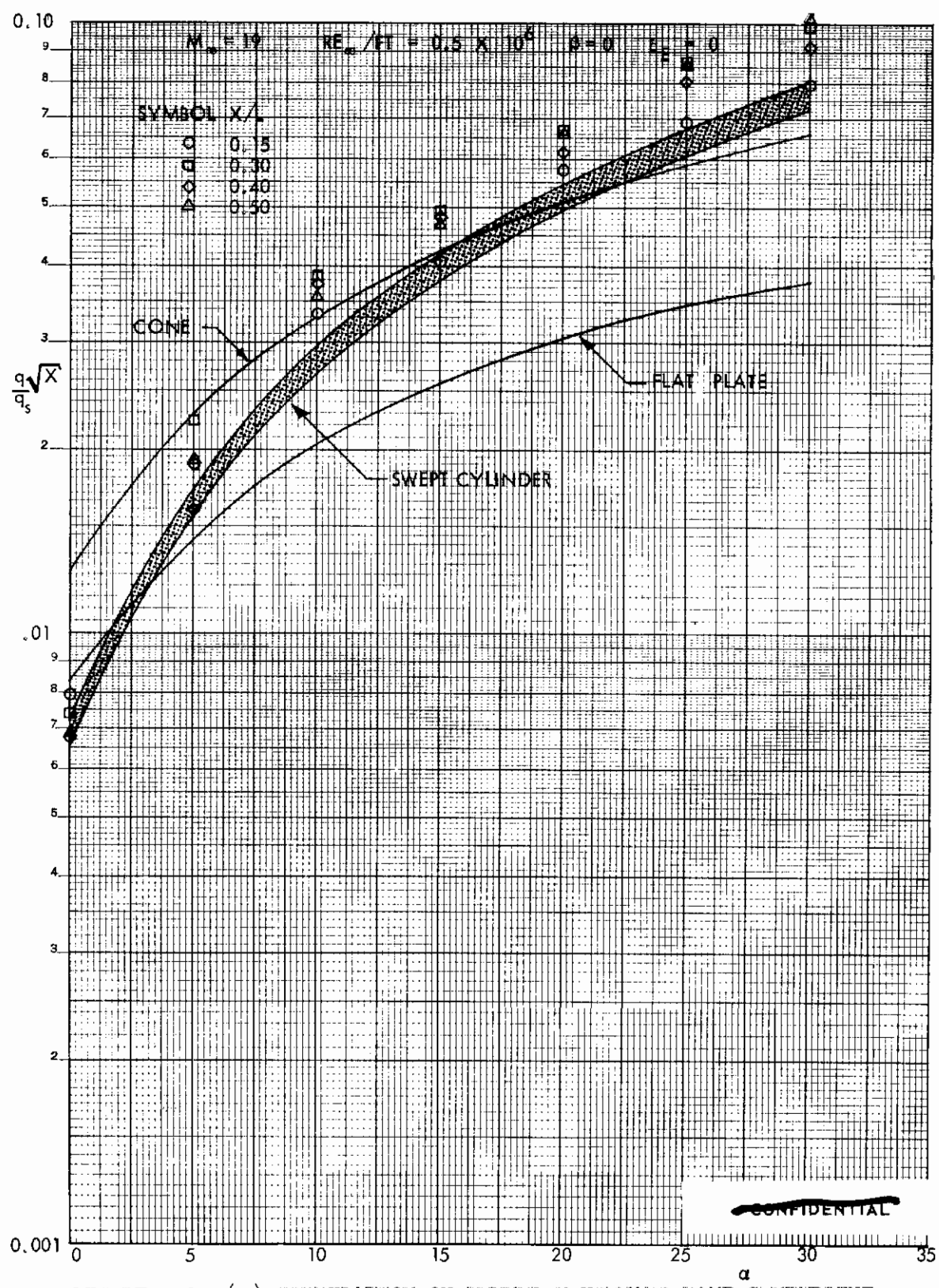
FIGURE 193 (U) CORRELATION OF TUNNEL F FORWARD RAMP CENTERLINE HEATING DATA, β=0
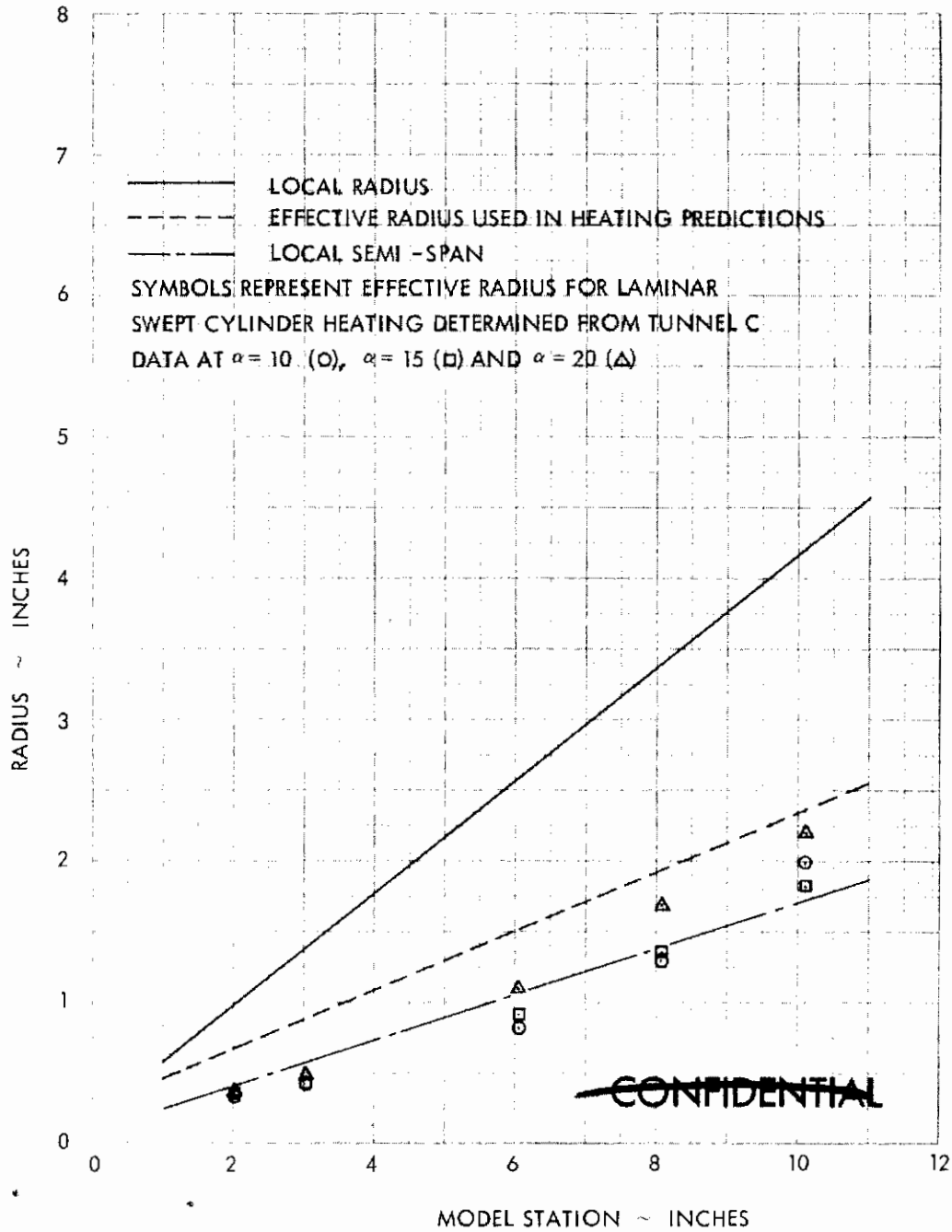
FIGURE 194 (U) EFFECTIVE BODY RADIUS FOR LAMINAR SWEPT CYLINDER
HEATING ON THE FDL-5 MODEL FORWARD RAMP

276
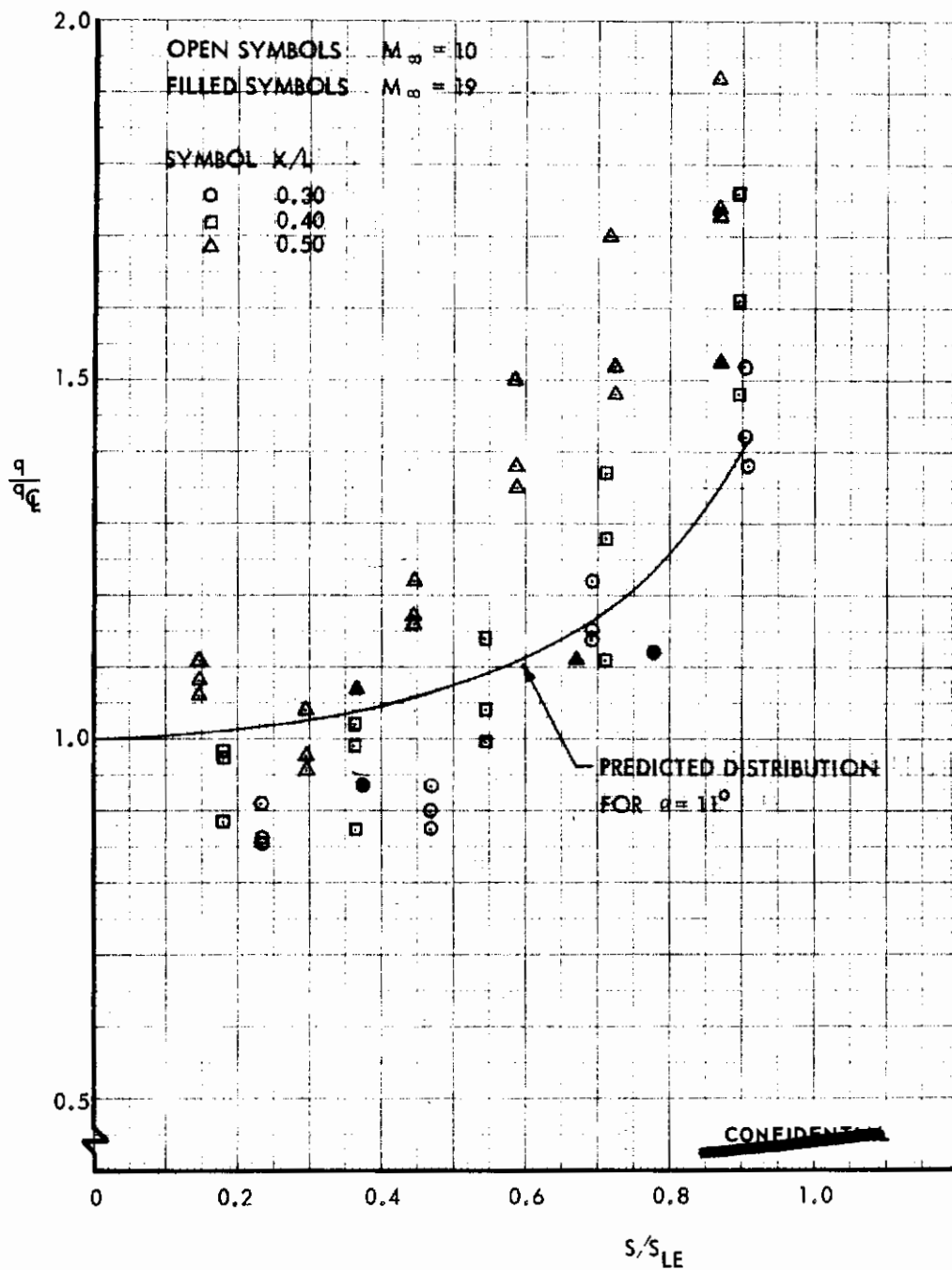
FIGURE 195 (U) COMPARISON OF PREDICTED AND EXPERIMENTAL SPANWISE HEATING DISTRIBUTIONS ON THE FORWARD RAMP
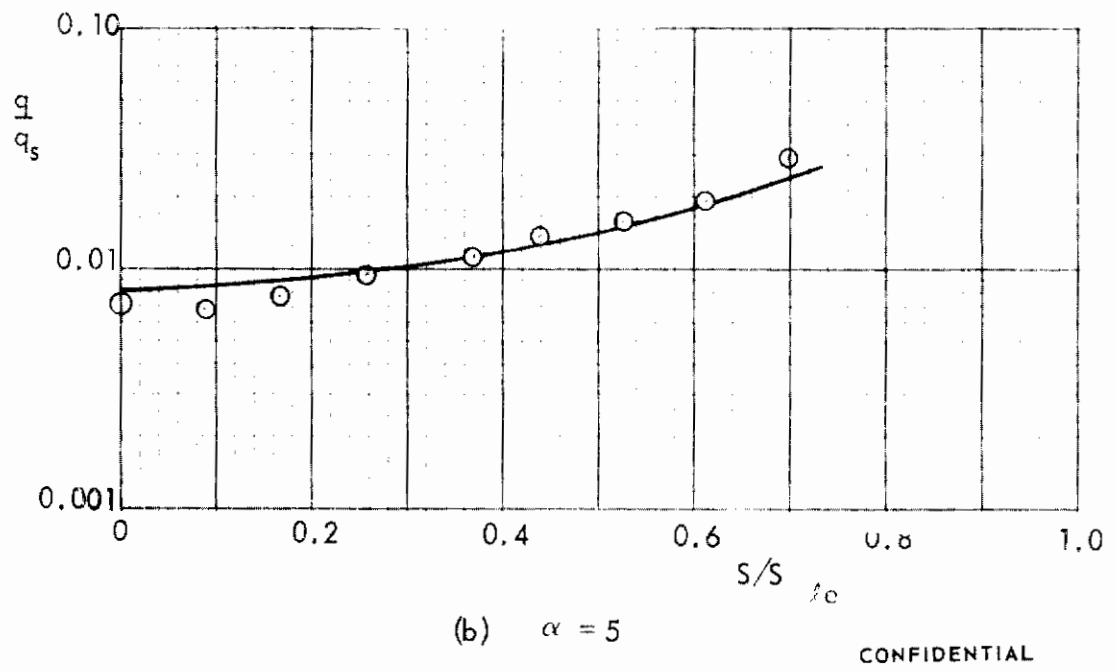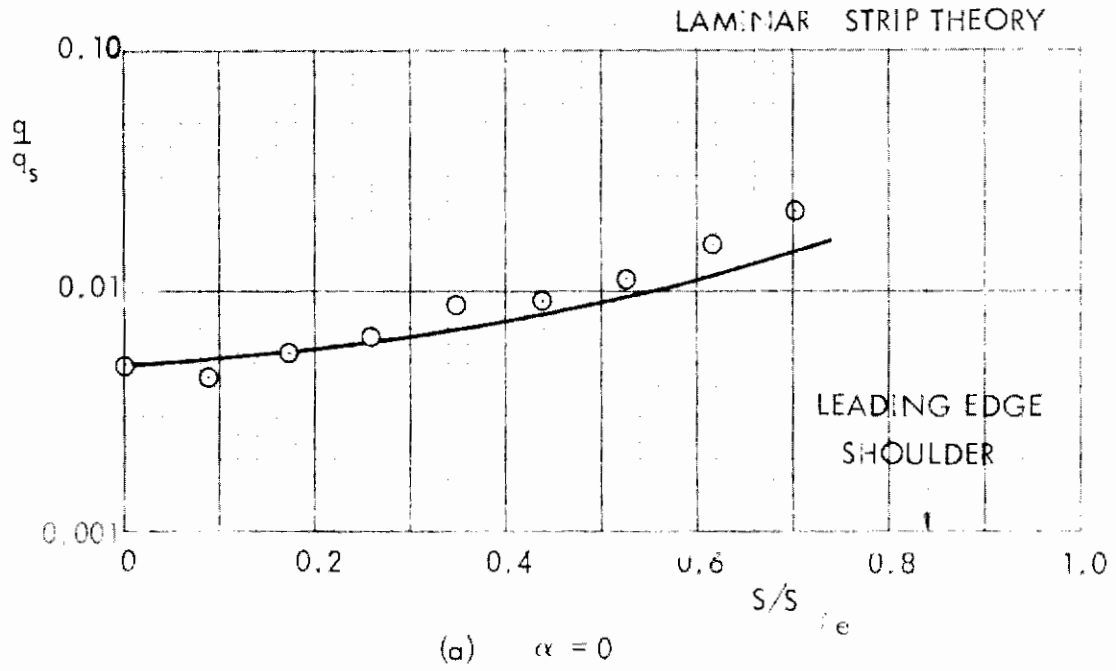
277

(a) $\alpha = 0$

(b) $\alpha = 5$

FIGURE 196   (U) CORRELATION OF TUNNEL C AFT LOWER SURFACE HEATING
DISTRIBUTIONS AT X/L = 0.75

278

(c) $\alpha = 10$

(d) $\alpha = 15$
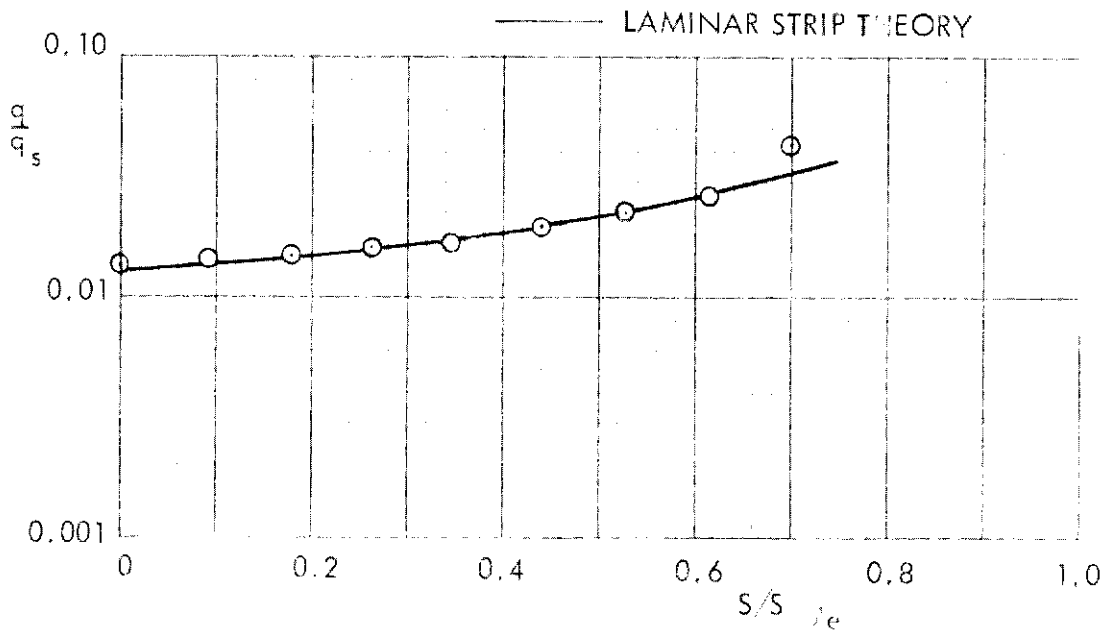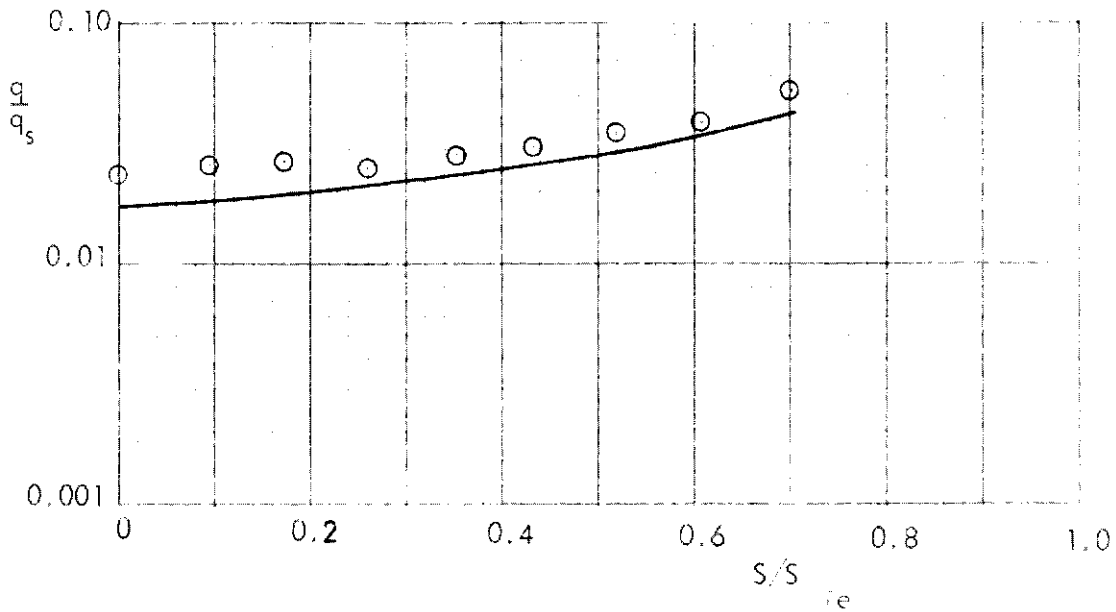
FIGURE 196 (U) CORRELATION OF TUNNEL C AFT LOWER SURFACE HEATING
DISTRIBUTIONS AT X/L = 0.75 (CONTINUED)
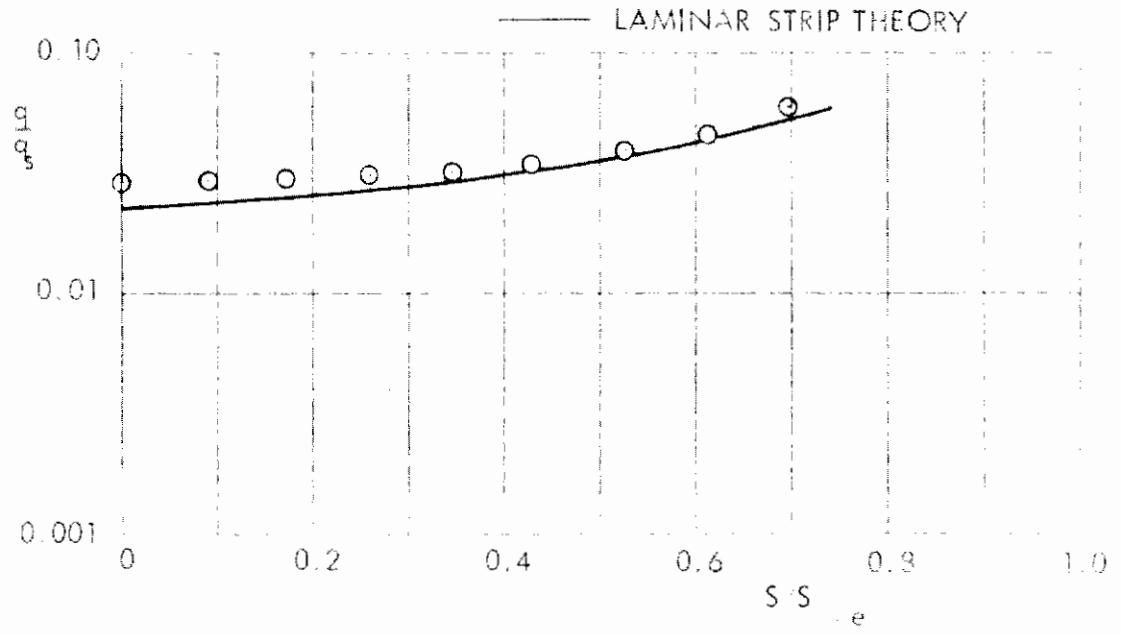
(e) $\alpha = 20$
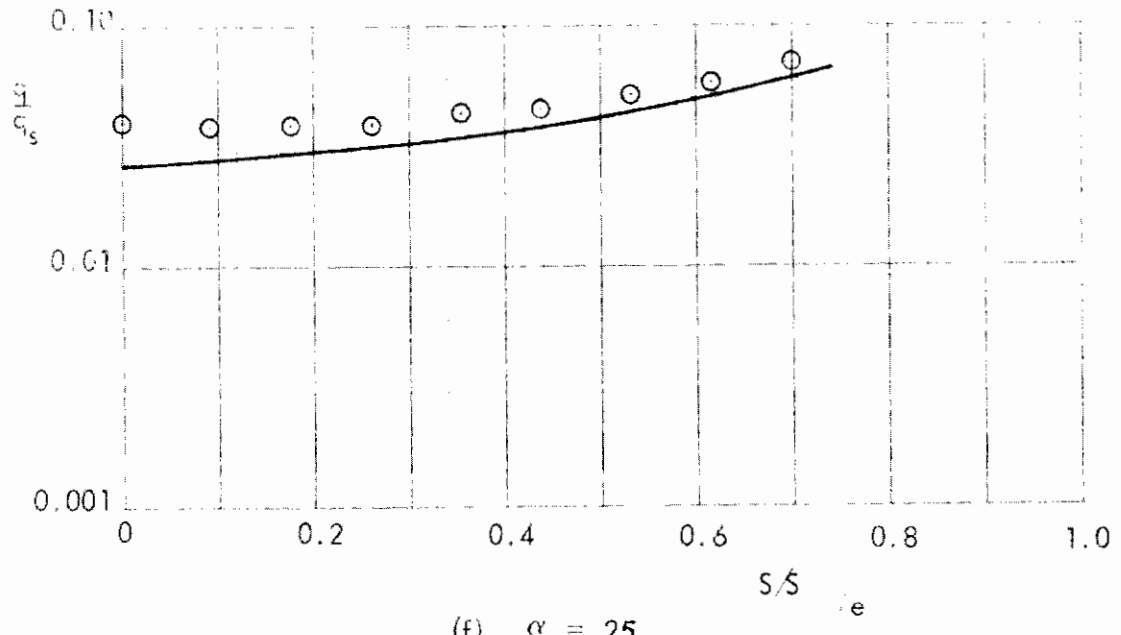
(f) $\alpha = 25$

FIGURE 196 (U) CORRELATION OF TUNNEL C AFT LOWER SURFACE HEATING
DISTRIBUTIONS AT X/L = 0.75 (CONTINUED)

280

(g) $\alpha = 30$

(h) $\alpha = 35$
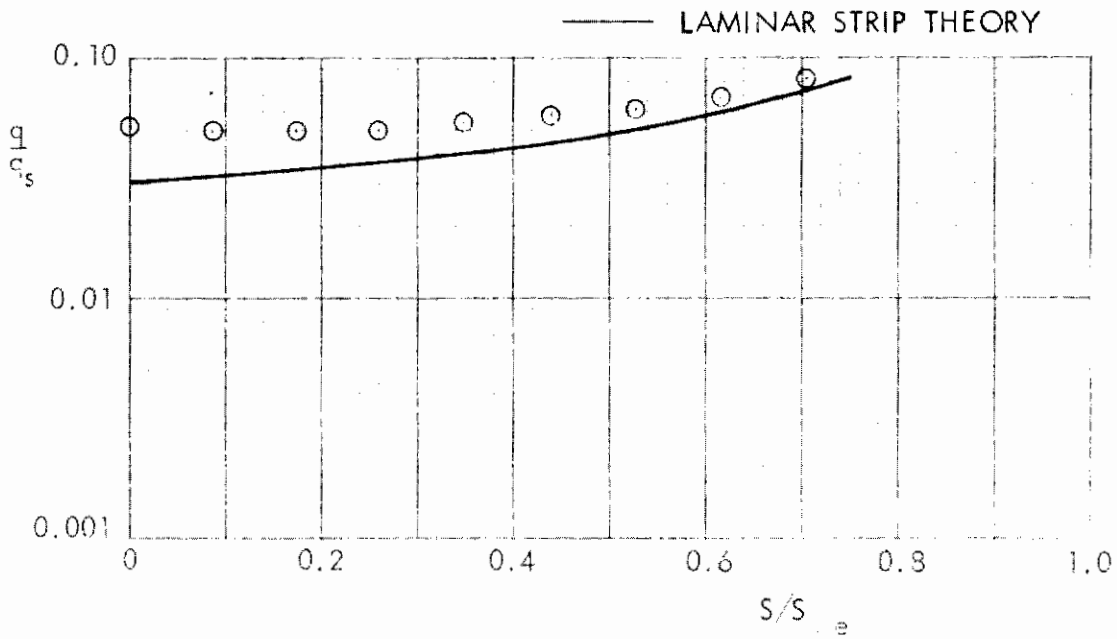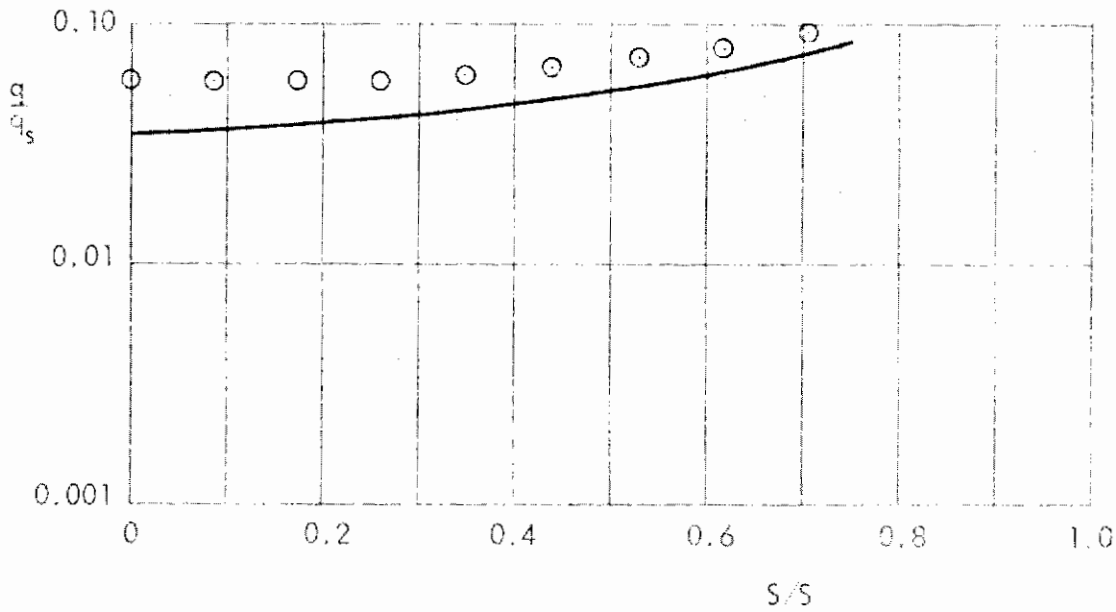
FIGURE 196 (U) CORRELATION OF TUNNEL C AFT LOWER SURFACE HEATING
DISTRIBUTIONS AT $x/L = 0.75$ (CONCLUDED)
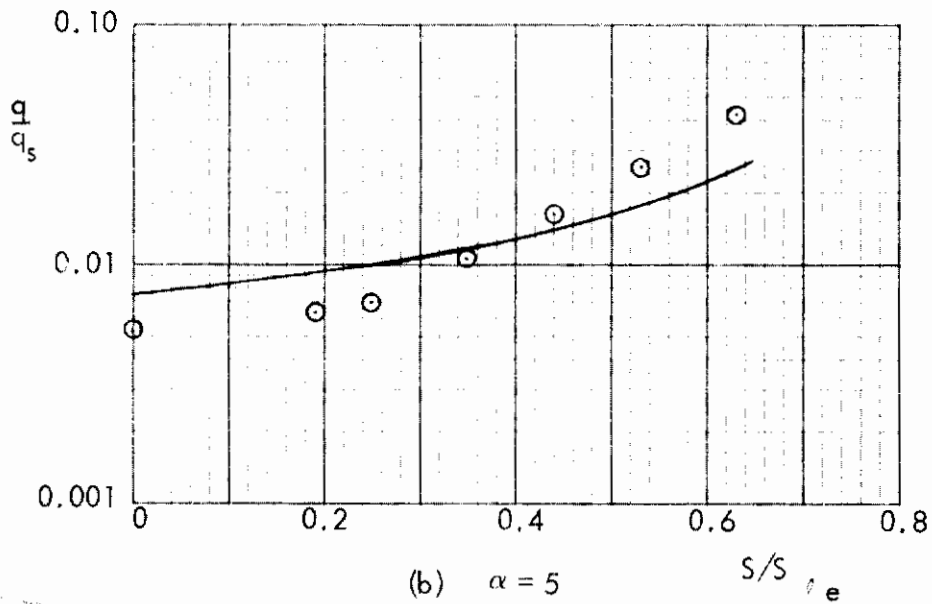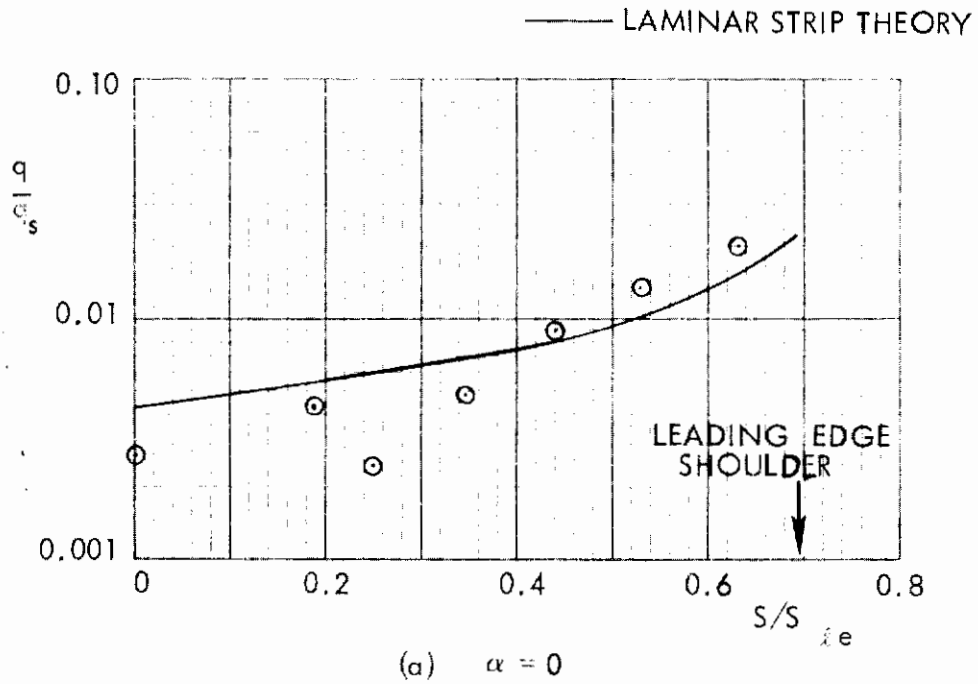
—— LAMINAR STRIP THEORY

(a) $\alpha = 0$

(b) $\alpha = 5$

FIGURE 197   (U) CORRELATION OF TUNNEL C AFT LOWER SURFACE HEATING
DISTRIBUTIONS AT X/L = 0.96

———— LAMINAR STRIP THEORY
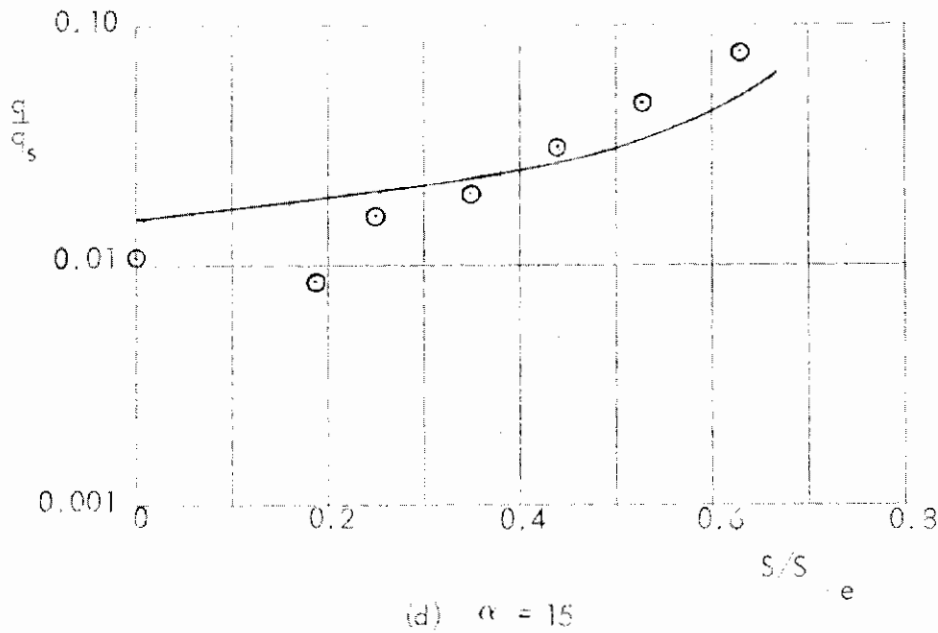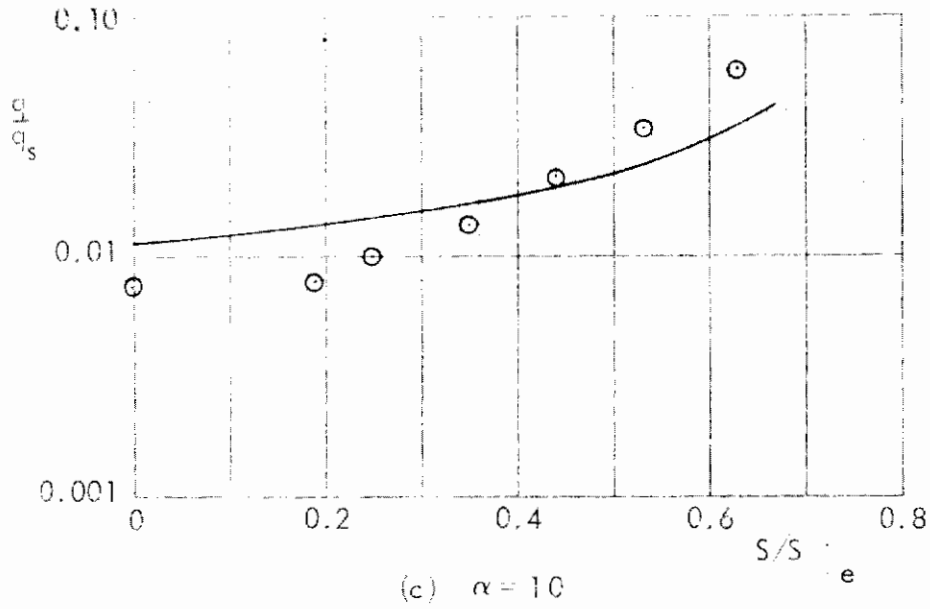
(c) $\alpha = 10$

(d) $\alpha = 15$

FIGURE 197   (U) CORRELATION OF TUNNEL C AFT LOWER SURFACE HEATING
DISTRIBUTIONS AT X/L = 0.96 (CONTINUED)

(e) $\alpha = 20$

(f) $\alpha = 25$

FIGURE 197 (U) CORRELATION OF TUNNEL C AFT LOWER SURFACE HEATING
DISTRIBUTIONS AT X/L = 0.96 (CONTINUED)

FIGURE 197 (U) CORRELATION OF TUNNEL C AFT LOWER SURFACE HEATING
DISTRIBUTIONS AT X/L = 0.96 (CONCLUDED)

FIGURE 198   (U) CORRELATION OF TUNNEL F AFT LOWER SURFACE HEATING
DISTRIBUTIONS AT X/L = 0.96
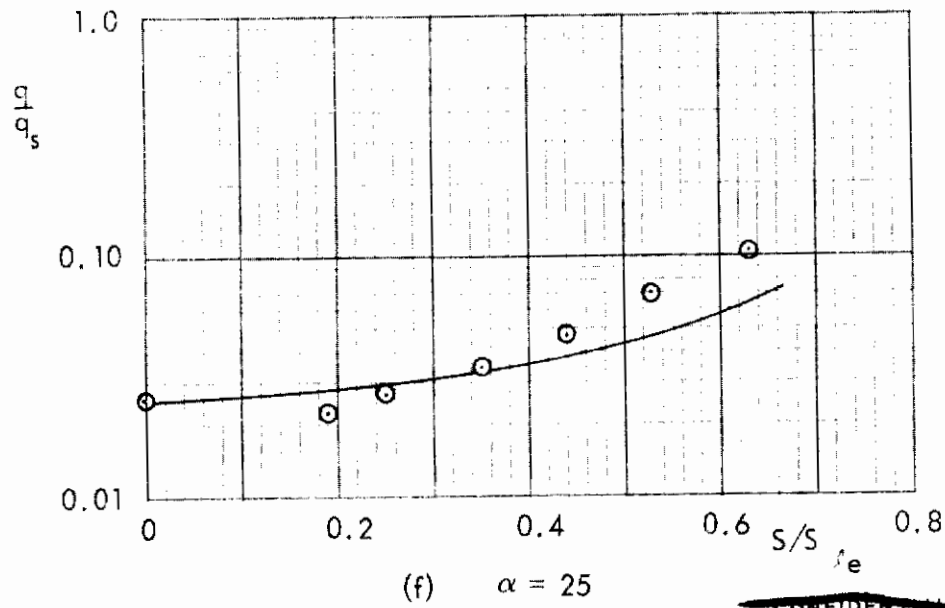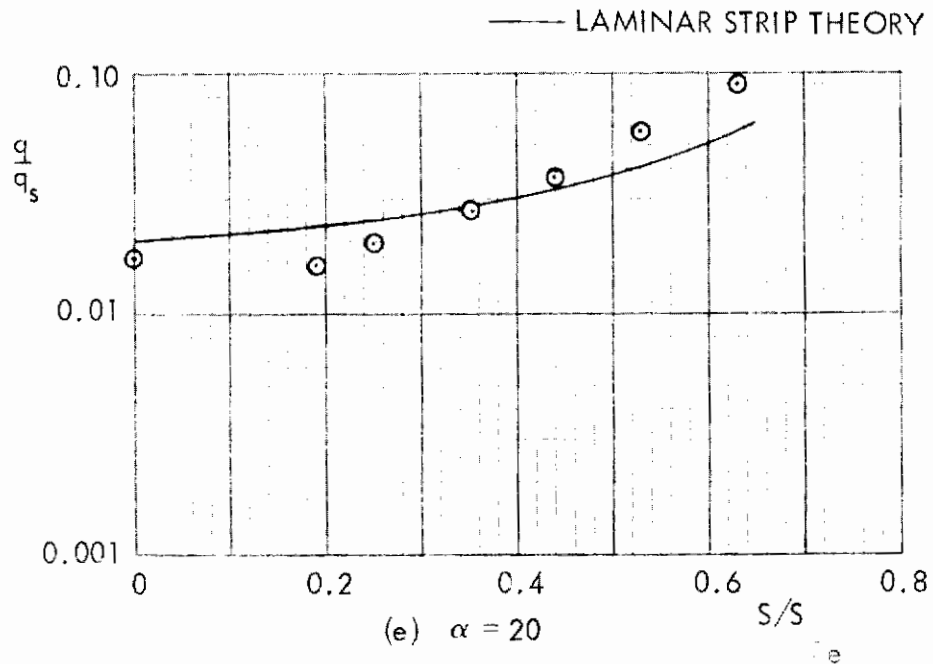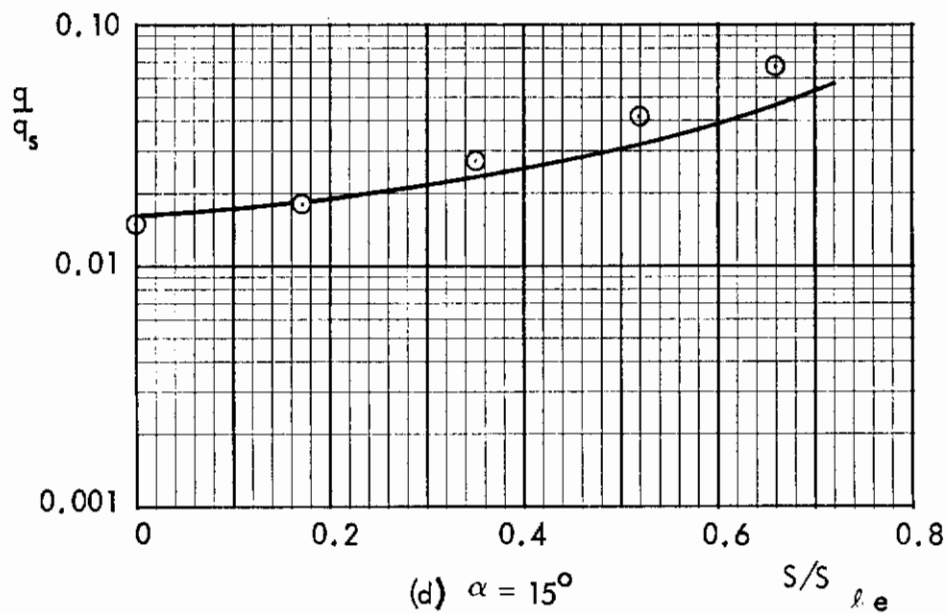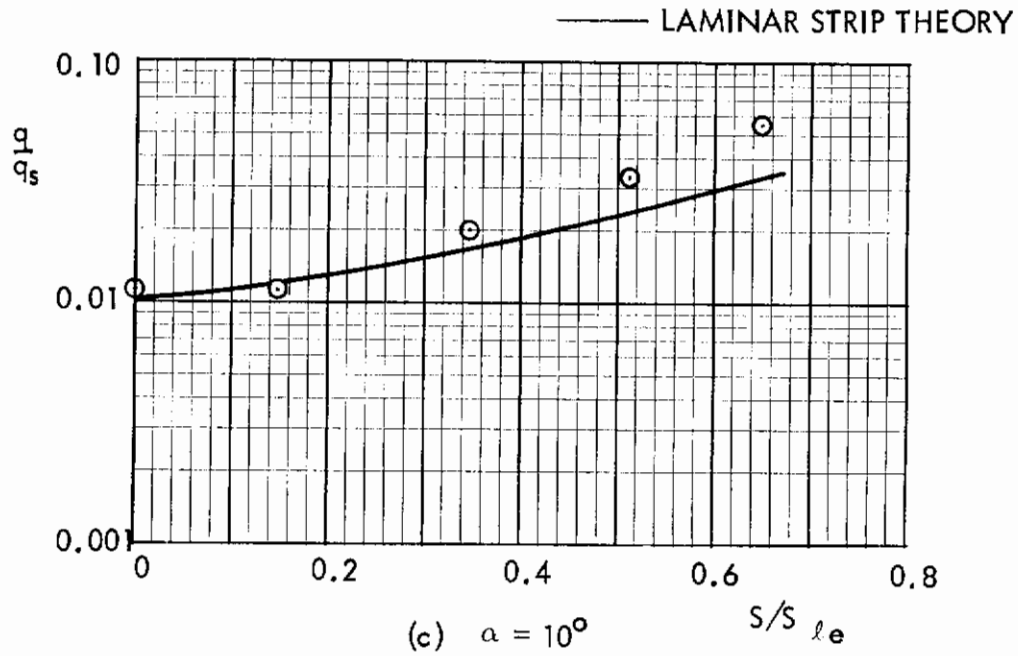
FIGURE 198 (U) CORRELATION OF TUNNEL F AFT LOWER SURFACE HEATING
DISTRIBUTIONS AT X/L = 0.96 (CONTINUED)

LAMINAR STRIP THEORY

(e) $\alpha = 20$

(f) $\alpha = 25^{\circ}$
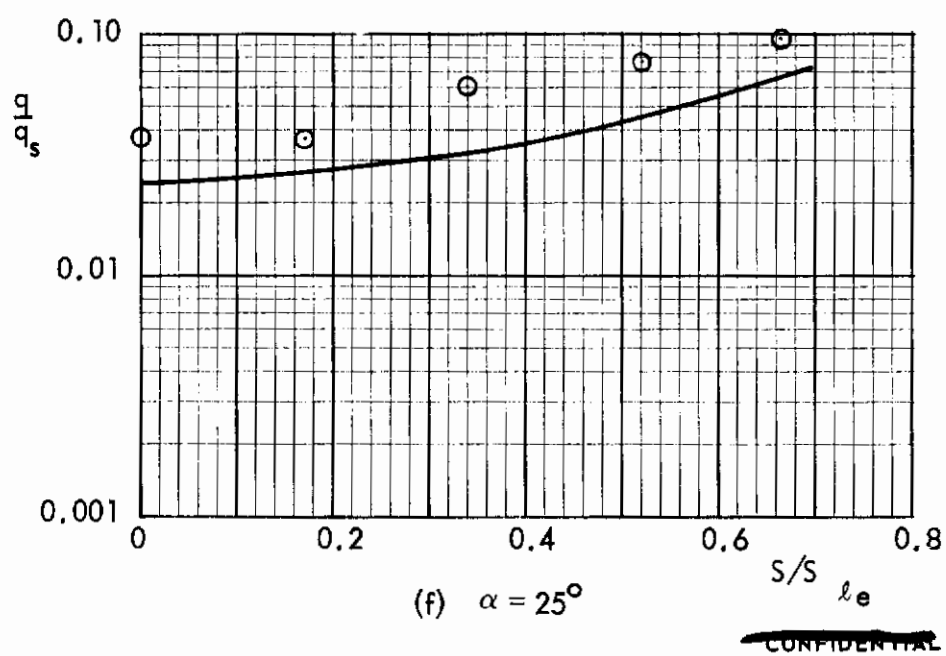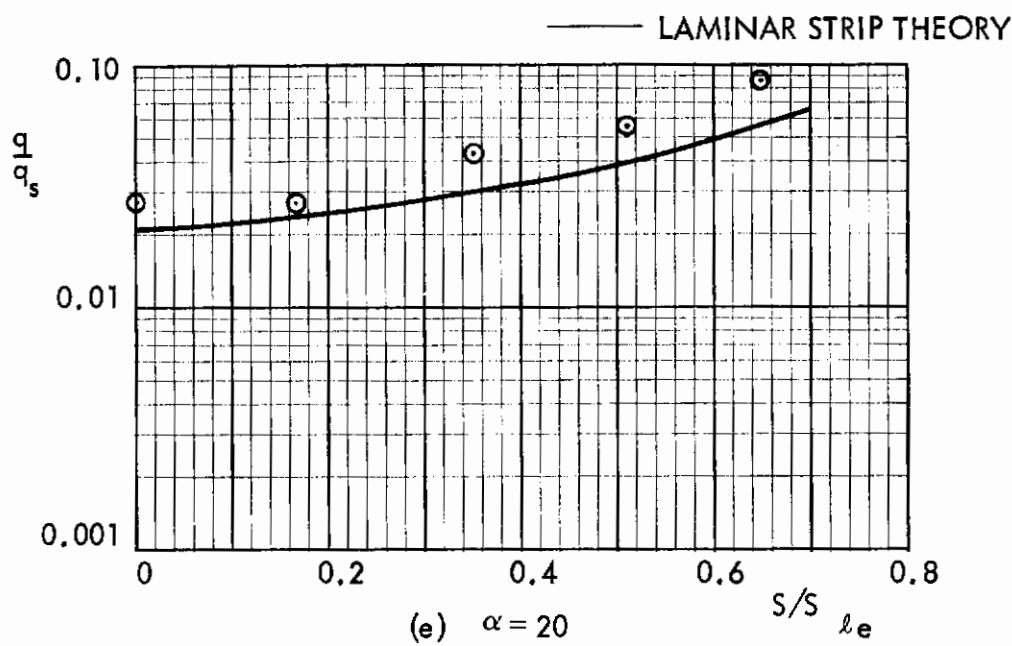
FIGURE 198 (U) CORRELATION OF TUNNEL F AFT LOWER SURFACE HEATING
DISTRIBUTIONS AT X/L = 0.96 (CONTINUED)
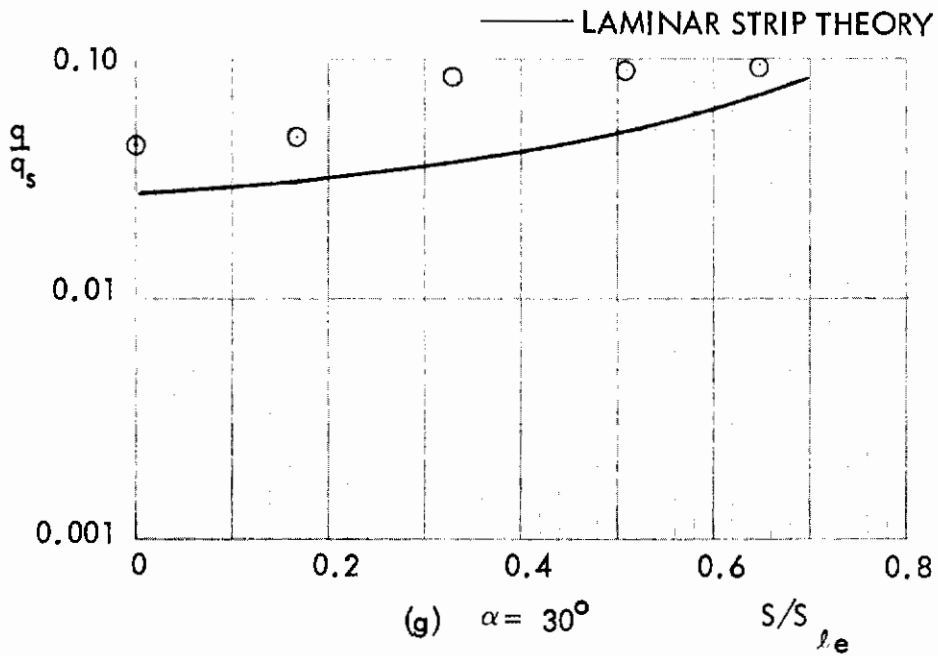
FIGURE 198 (U) CORRELATION OF TUNNEL F AFT LOWER SURFACE HEATING
DISTRIBUTIONS AT X/L = 0.96 (CONCLUDED)
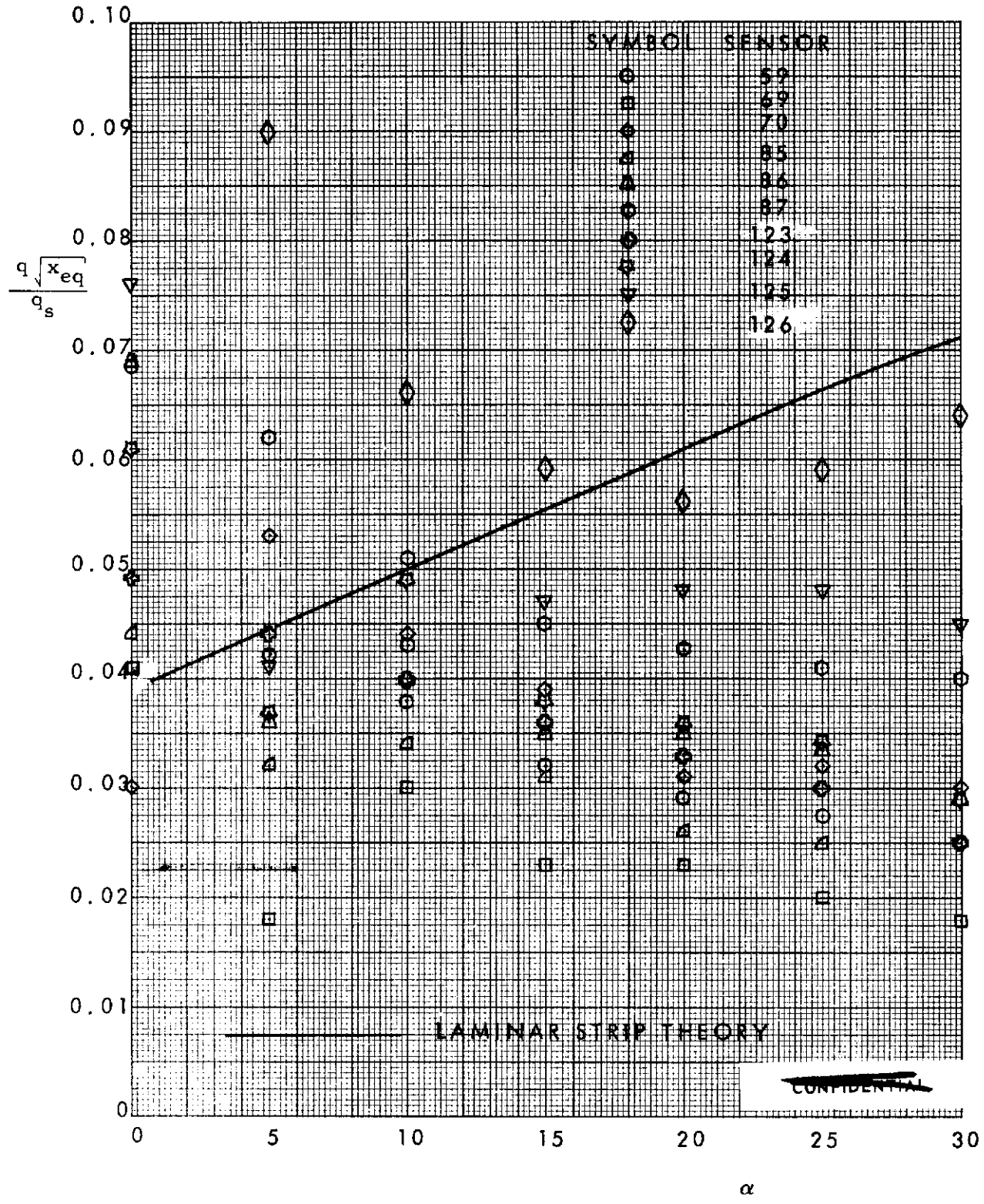
FIGURE 199 (U) CORRELATION OF TUNNEL C AFT LOWER COMPRESSION SURFACE HEATING DATA
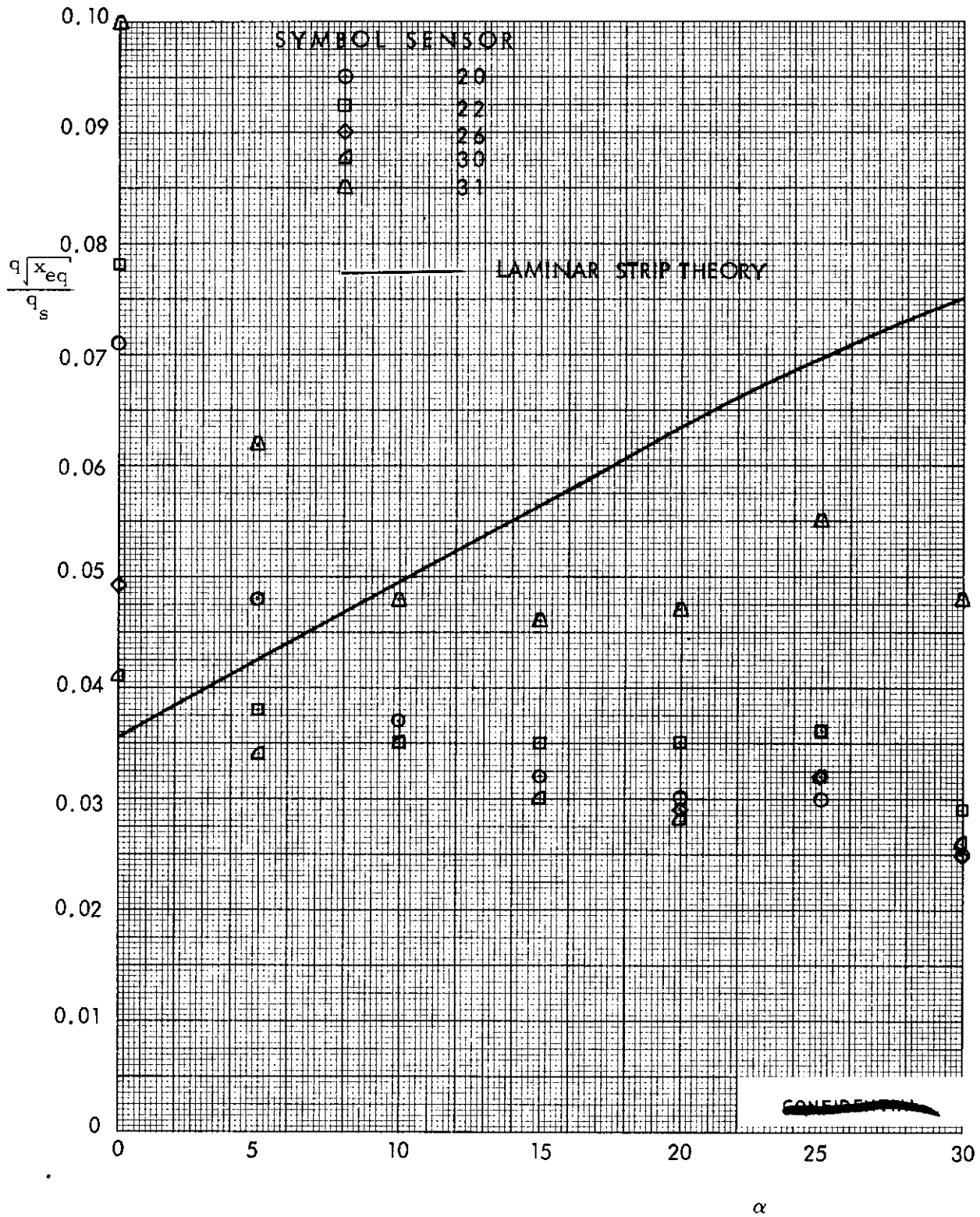
FIGURE 200 (U) CORRELATION OF TUNNEL F AFT LOWER COMPRESSION SURFACE HEATING DATA

FIGURE 201   (U) TUNNEL C UPPER SURFACE CENTERLINE HEATING RATES, β=0

292
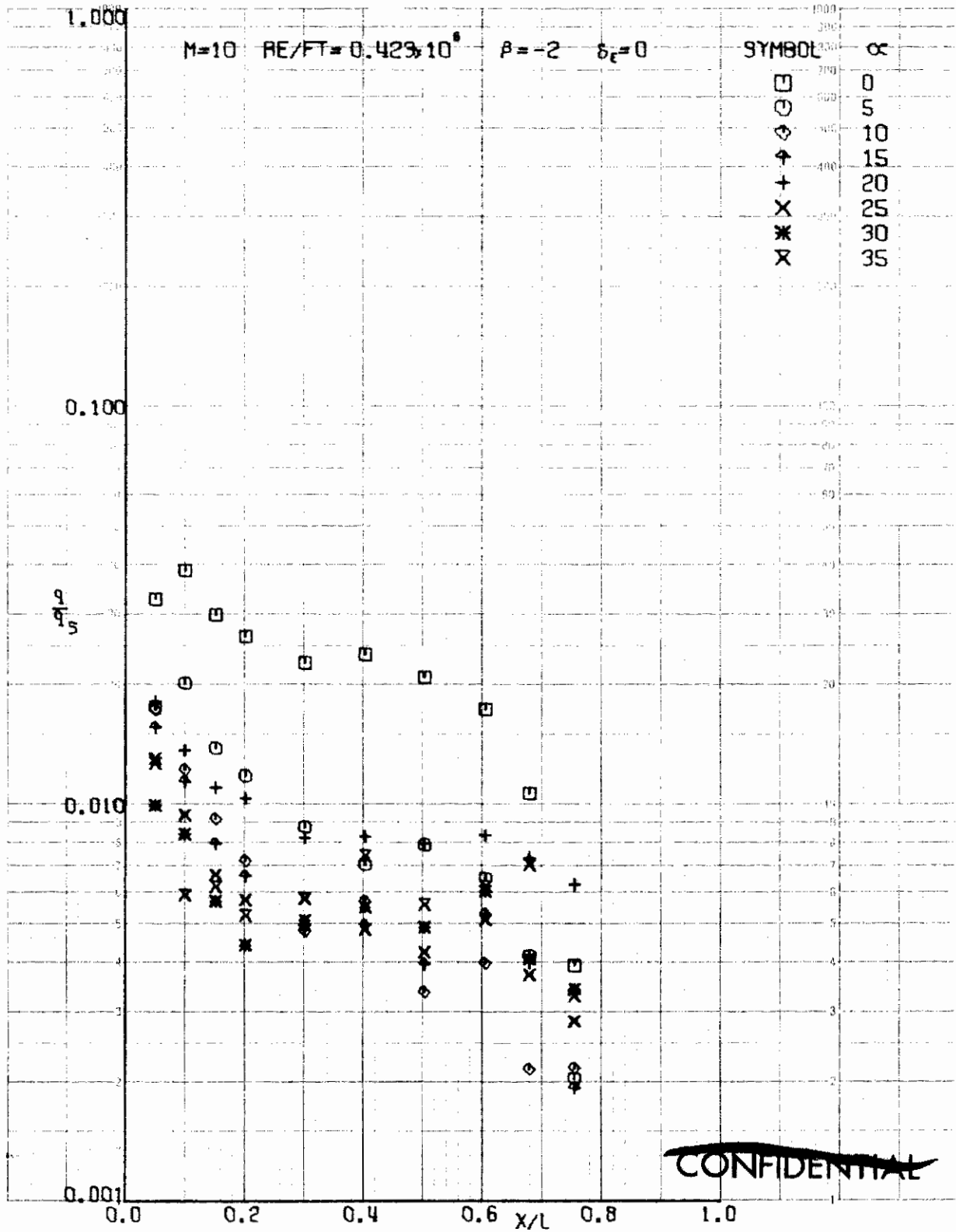
FIGURE 202 (U) TUNNEL C UPPER SURFACE CENTERLINE HEATING RATES, β=-2

293
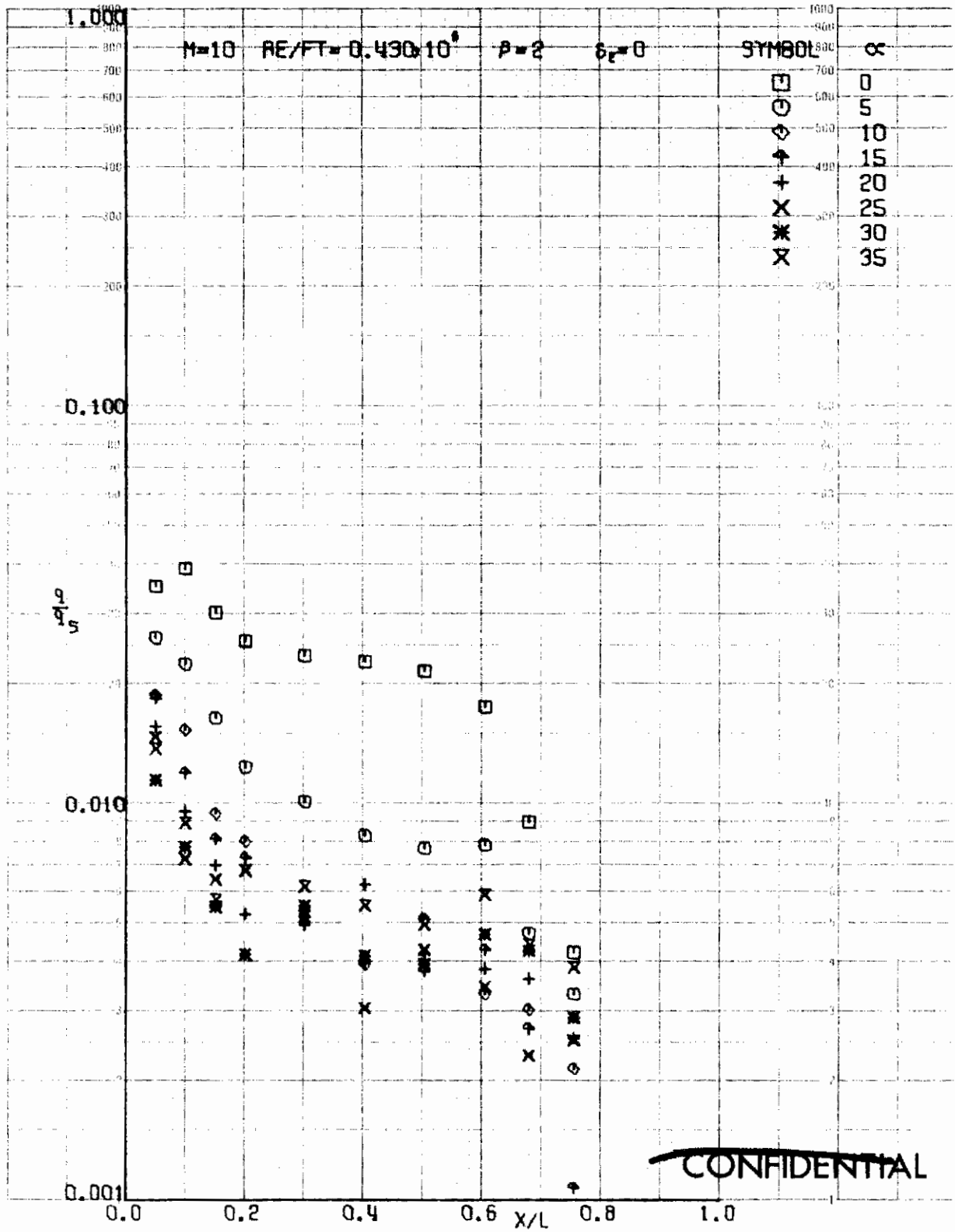
FIGURE 203   (U) TUNNEL C UPPER SURFACE CENTERLINE HEATING RATES, $\beta=2$
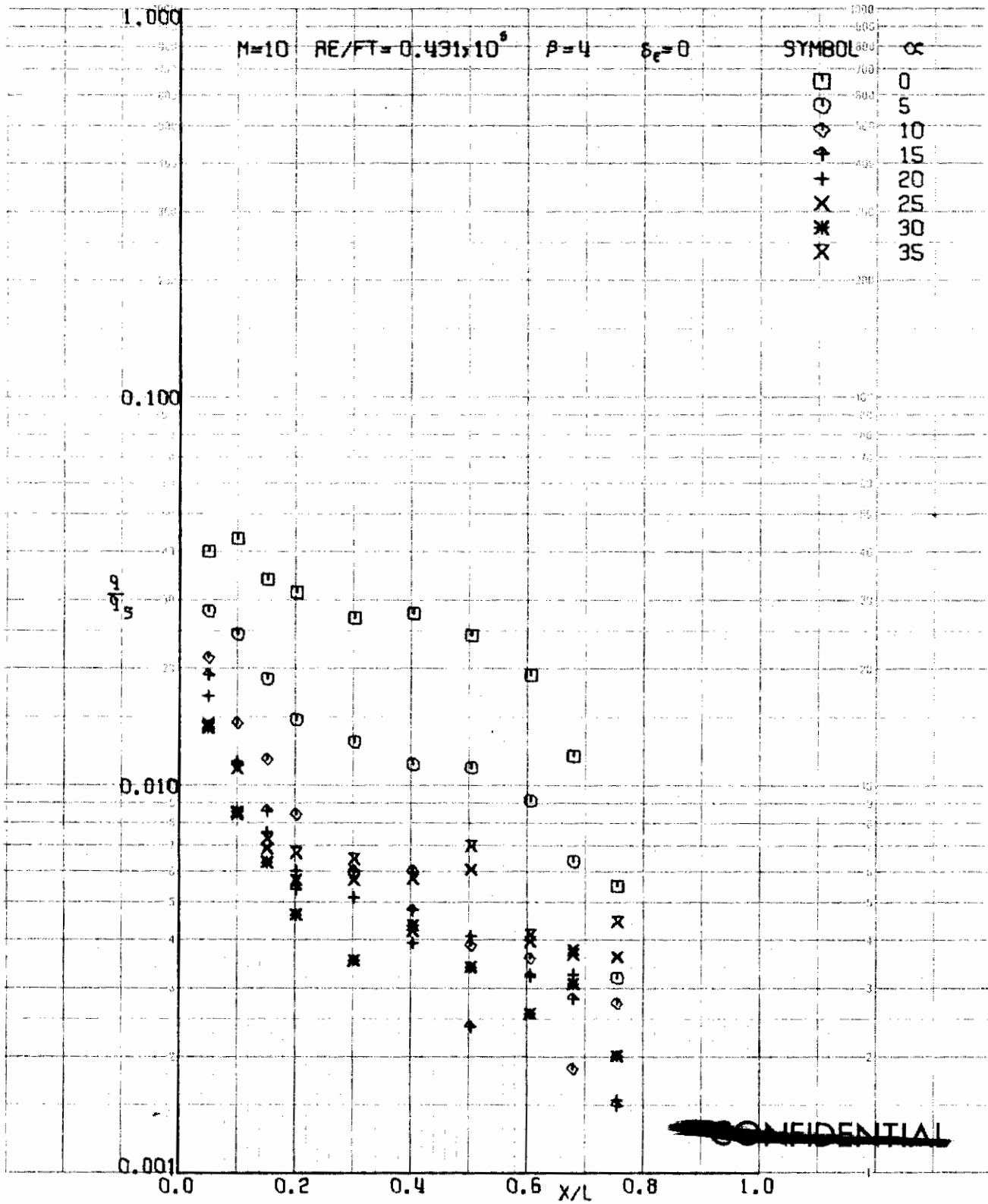
FIGURE 204 (U) TUNNEL C UPPER SURFACE CENTERLINE HEATING RATES, β=4

295
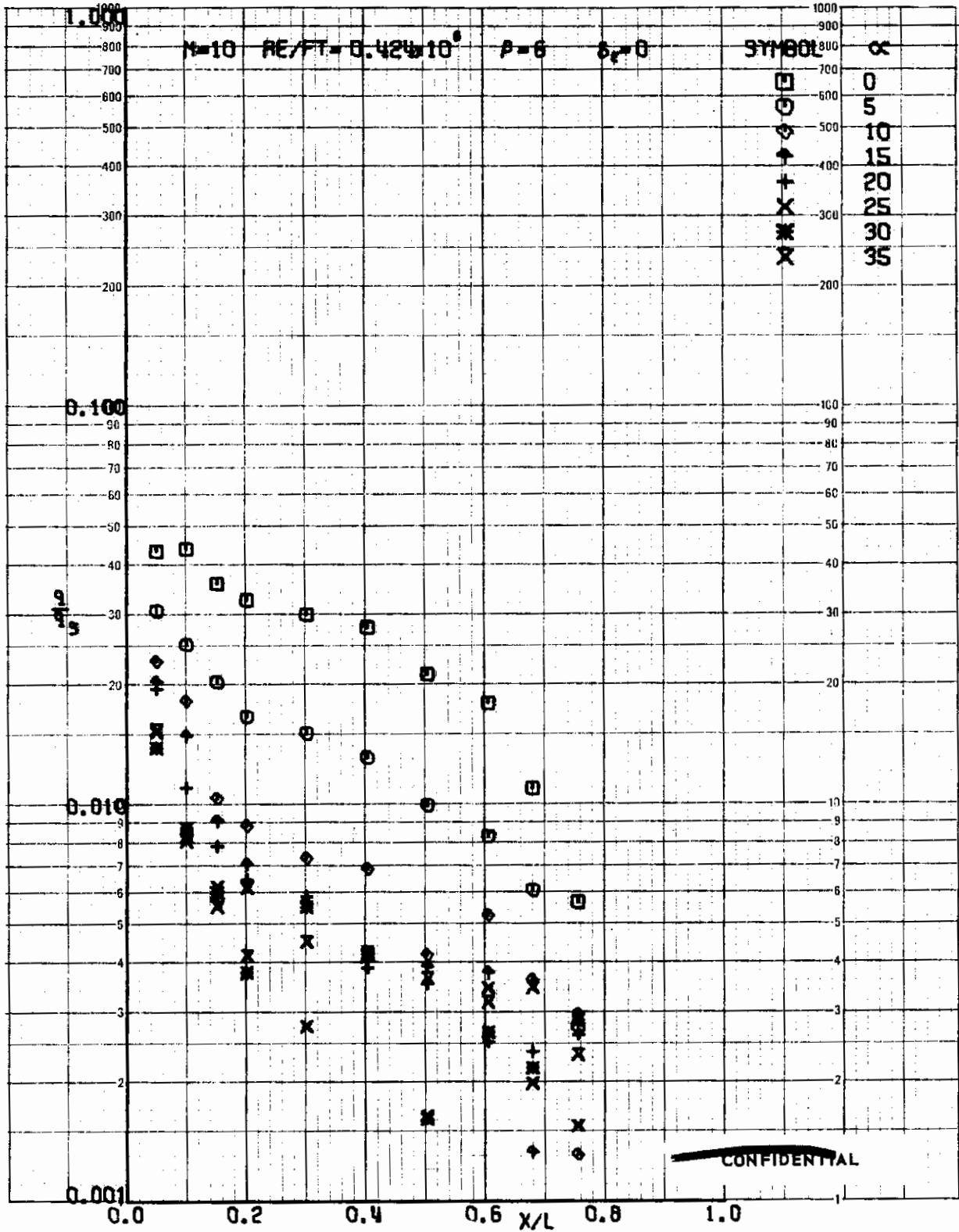
FIGURE 205 (U) TUNNEL C UPPER SURFACE CENTERLINE HEATING RATES, $\beta=6$
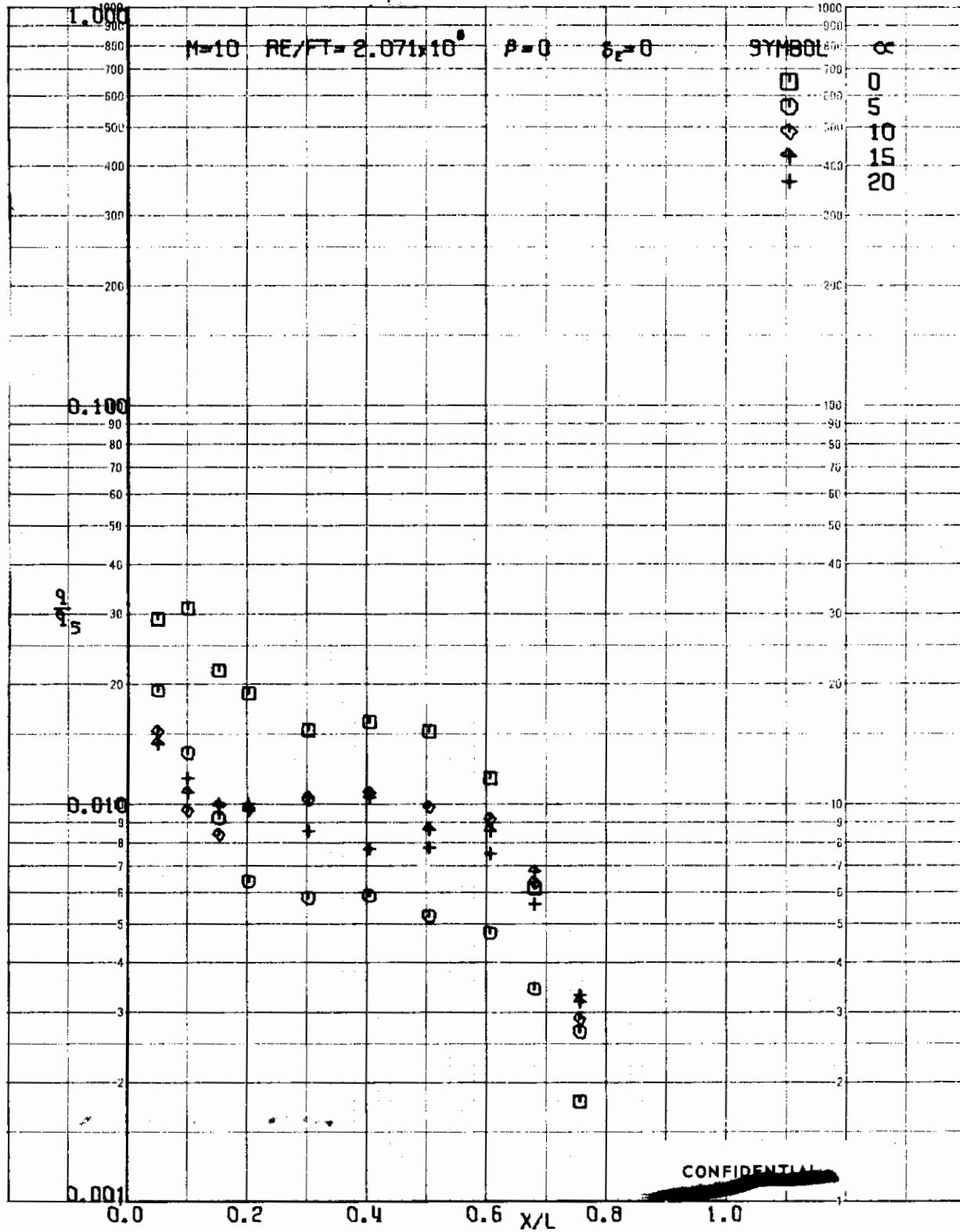
FIGURE 206 (U) TUNNEL C UPPER SURFACE CENTERLINE HEATING RATES, β=0
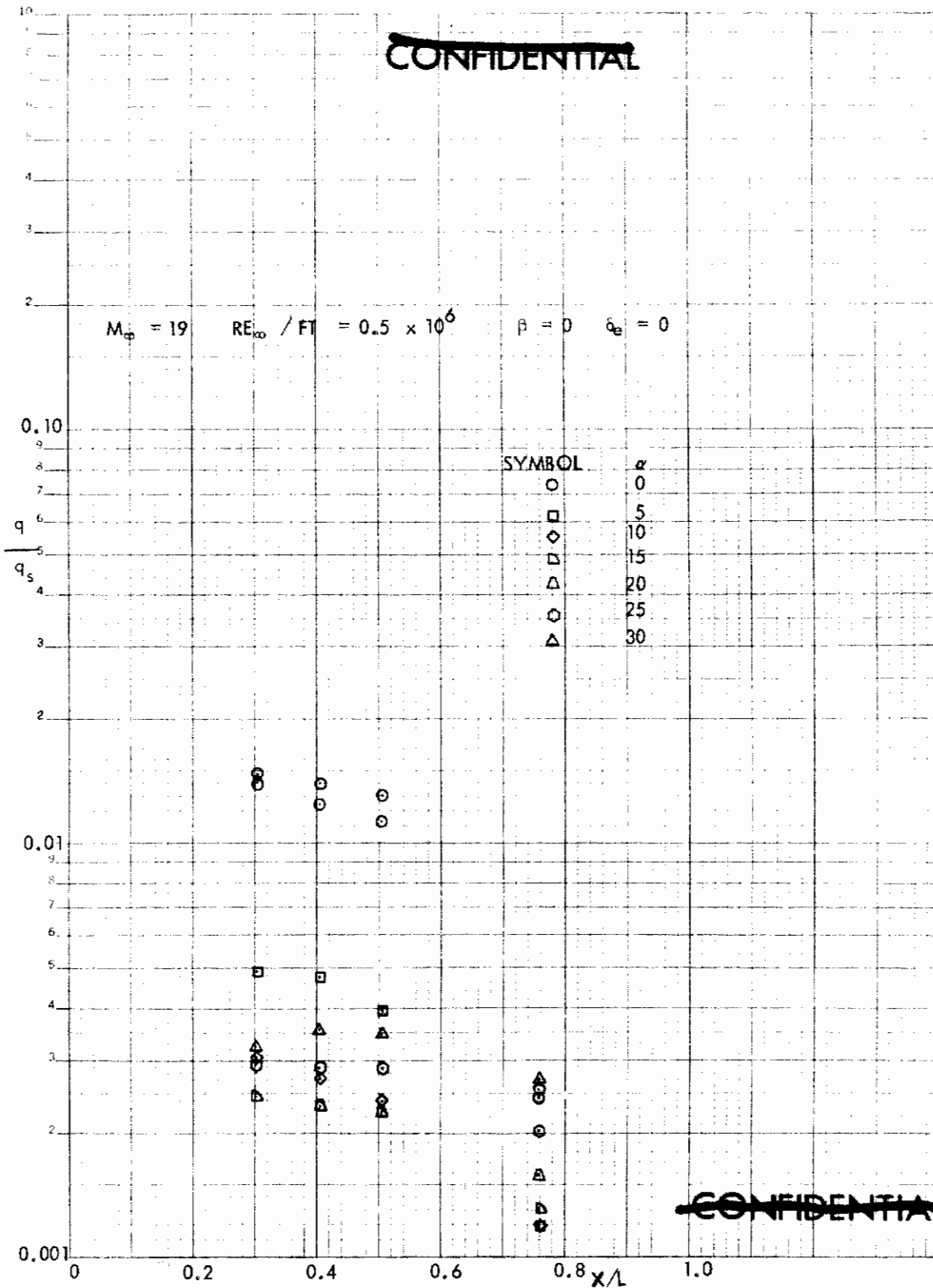
FIGURE 207 (U) TUNNEL F UPPER SURFACE CENTERLINE HEATING RATES, $\beta=0$

298

$M_\infty = 19$ $RE_\infty / FT = 0.5 \times 10^6$ $\beta = -2$ $\delta_e = 0$

SYMBOL	α
○	10
□	15
△	20
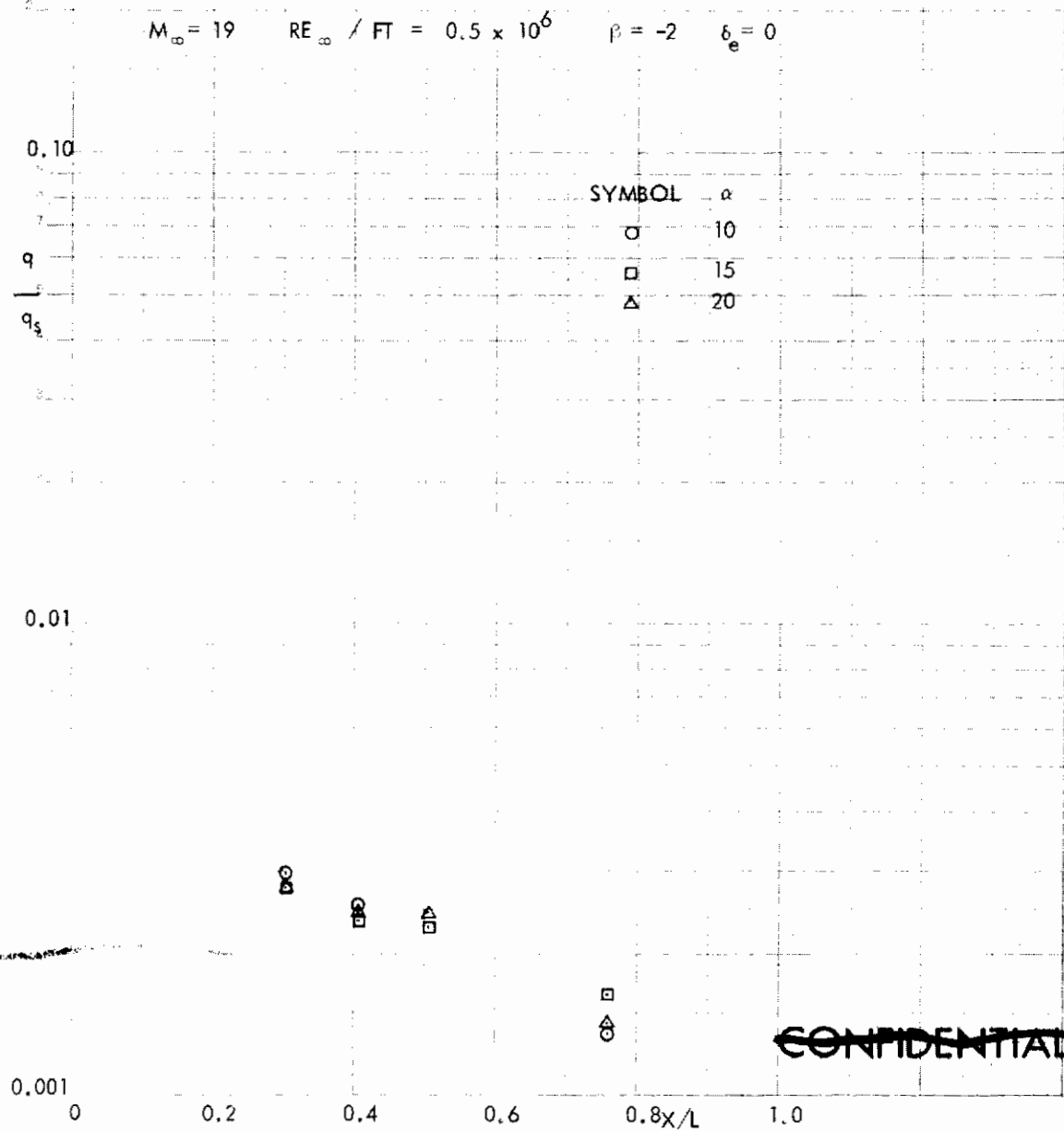
FIGURE 208   (U) TUNNEL F UPPER SURFACE CENTERLINE HEATING RATES, $\beta = -2$

$M_\infty = 19$ $RE_\infty / FT = 0.5 \times 10^6$ $\beta = 2$ $\delta_e = 0$

SYMBOL	α
○	10
□	15
△	20

$\dfrac{q}{q_s}$

X/L
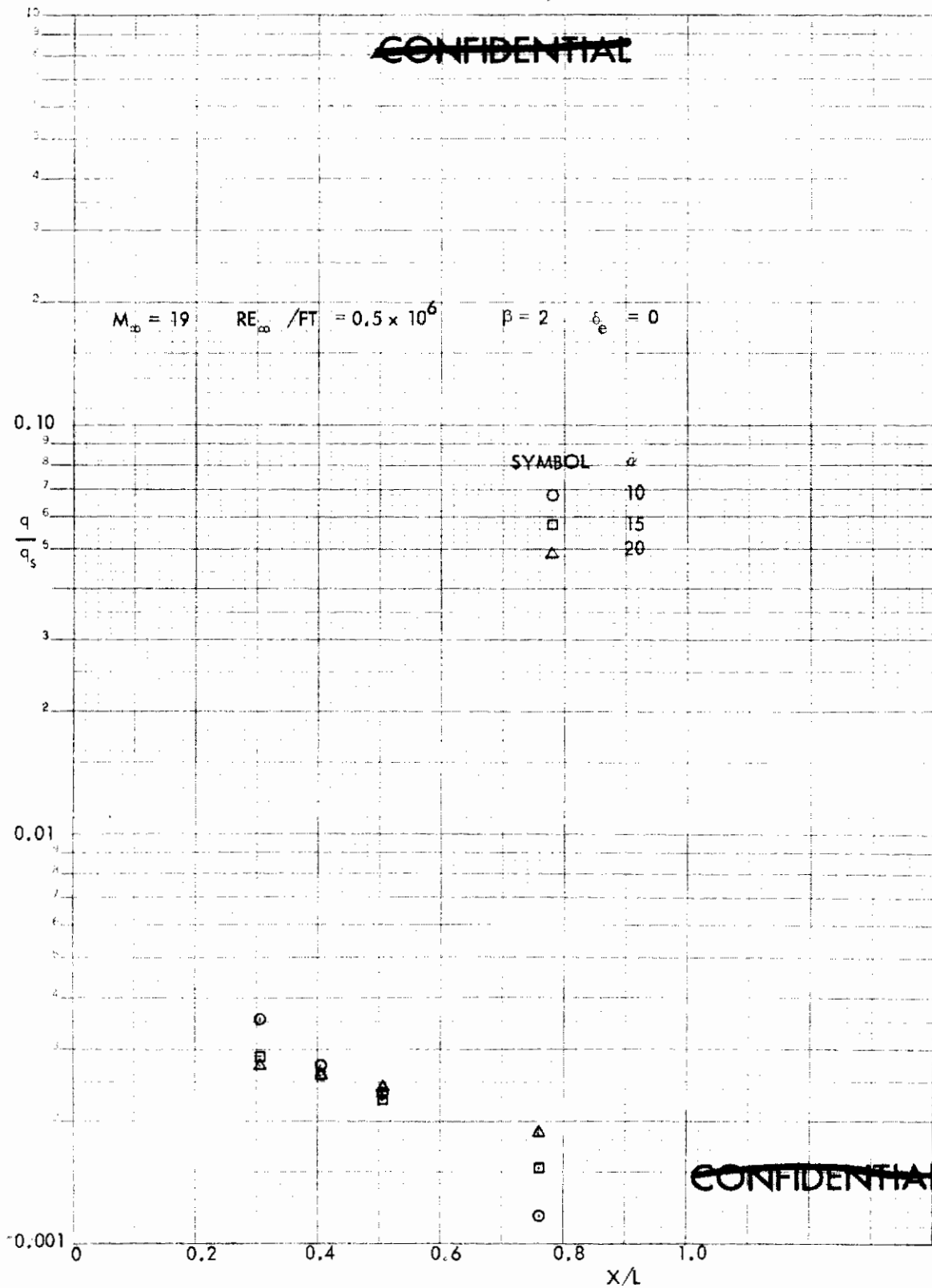
FIGURE 209   (U) TUNNEL F UPPER SURFACE CENTERLINE HEATING RATES, $\beta=2$
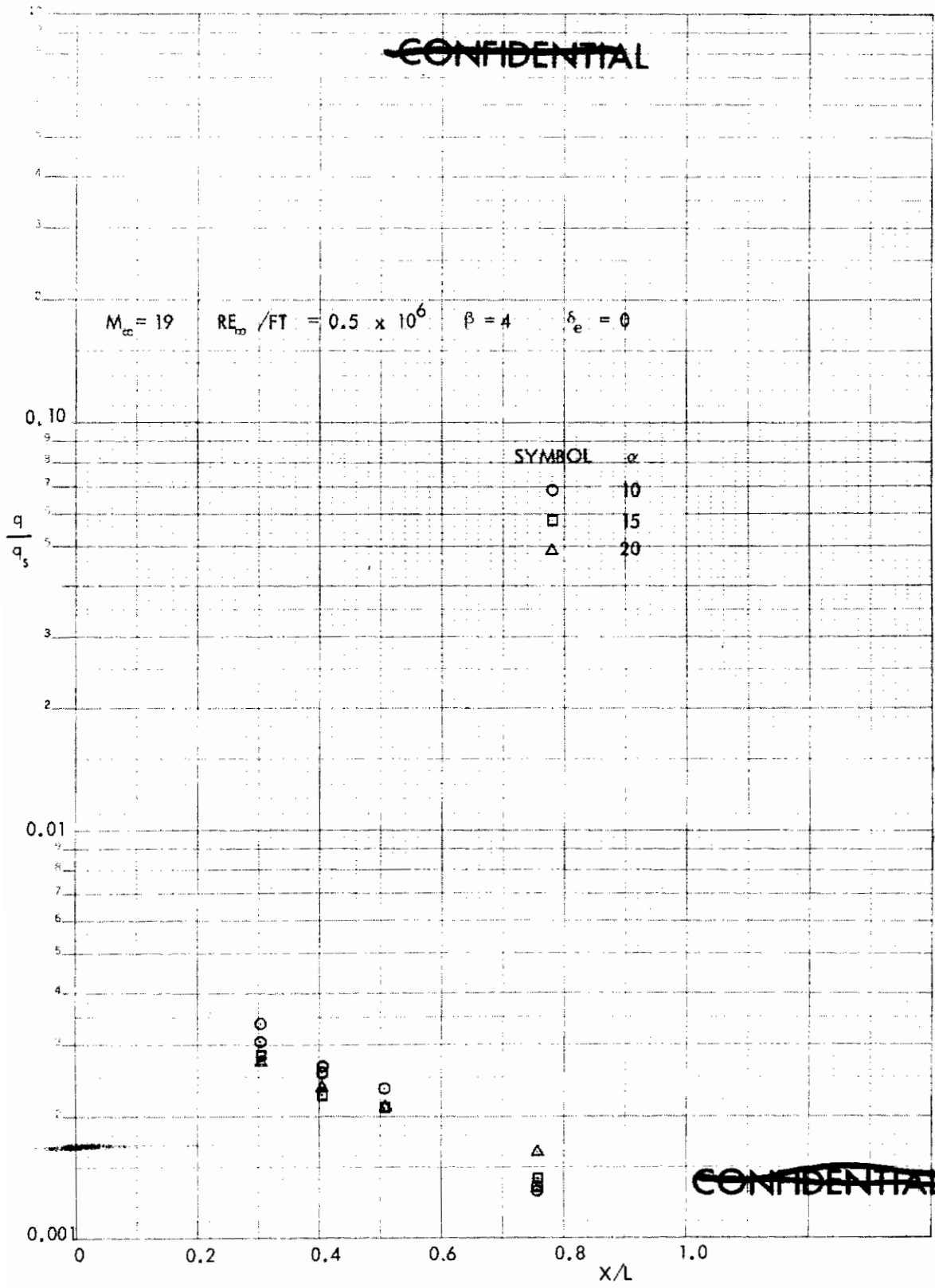
FIGURE 210 (U) TUNNEL F UPPER SURFACE CENTERLINE HEATING RATES, β=4
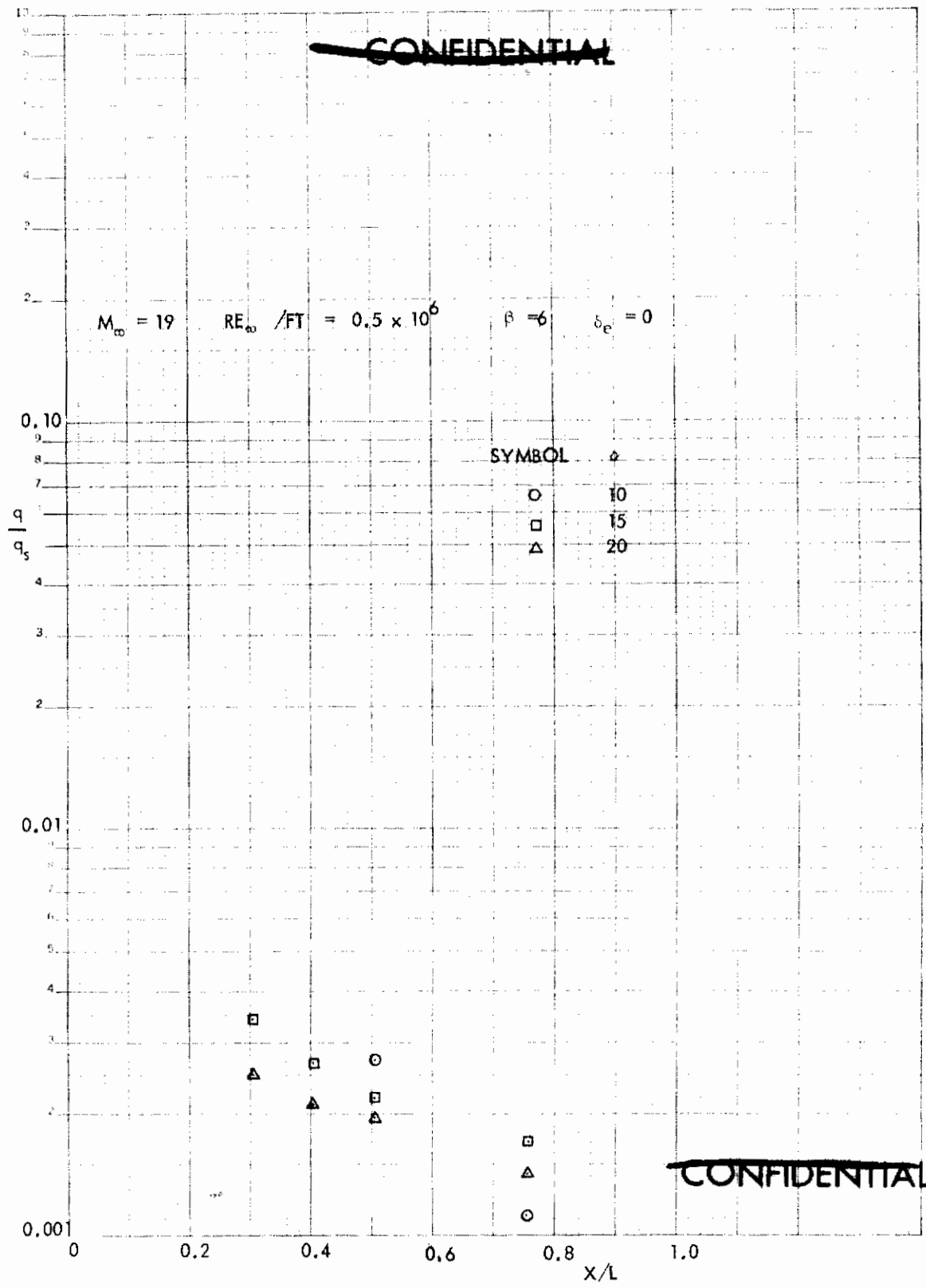
FIGURE 211 (U) TUNNEL F UPPER SURFACE CENTERLINE HEATING RATES, β=6

302
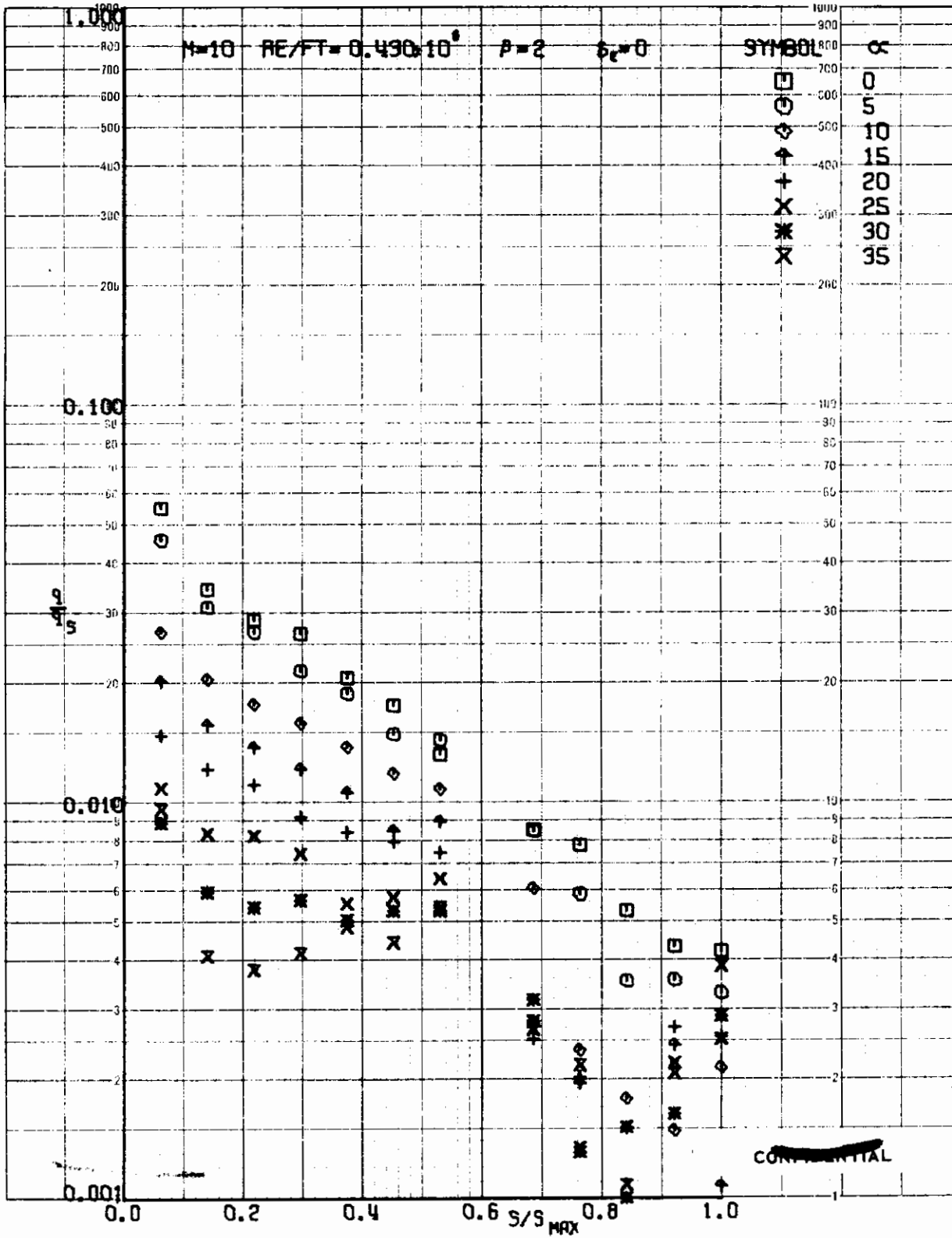
FIGURE 212   (U) TUNNEL C UPPER SURFACE SPANWISE HEATING RATES AT X/L = 0.30,
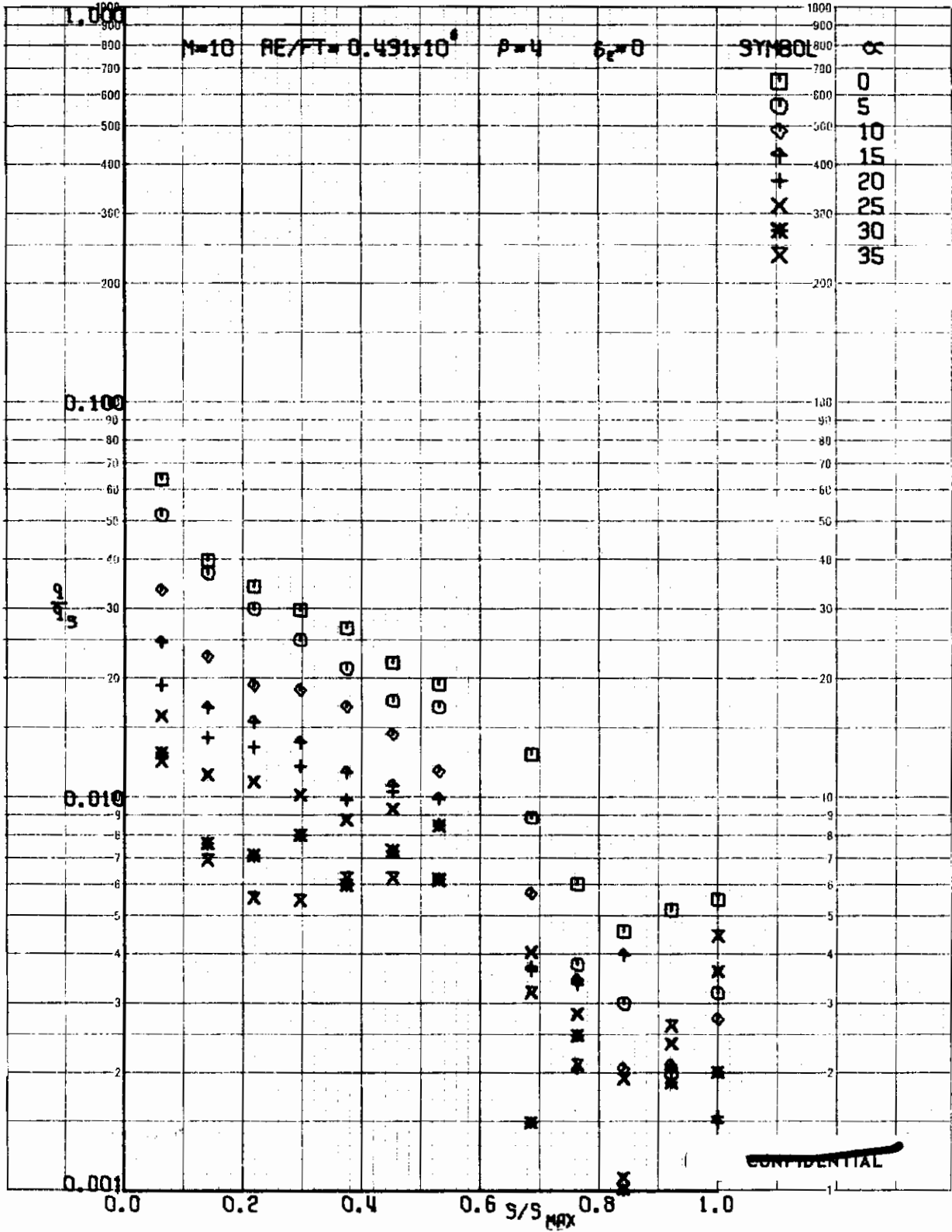   β=0

303
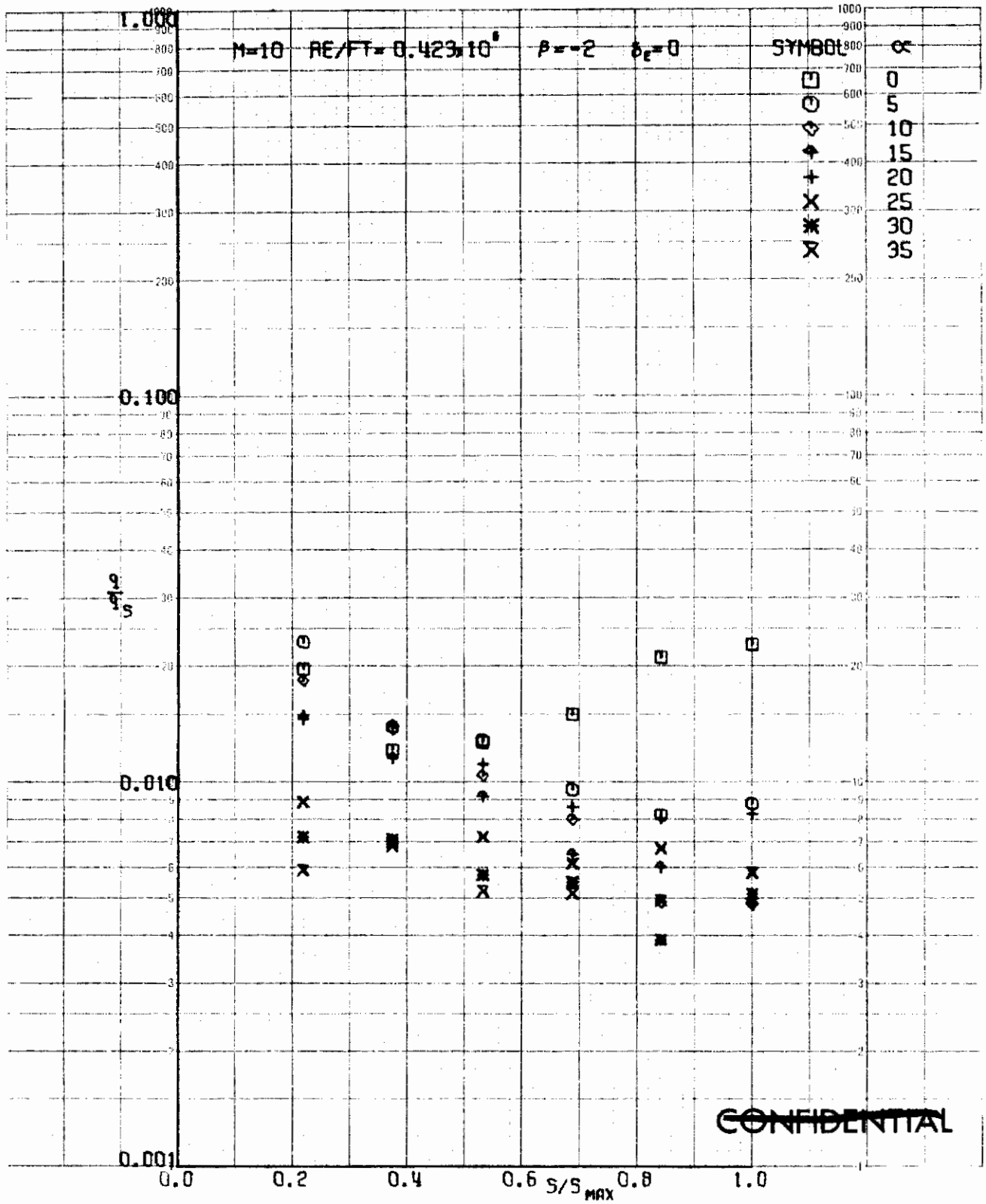
FIGURE 213   (U) TUNNEL C UPPER SURFACE SPANWISE HEATING RATES AT X/L = 0.30,
             β=-2
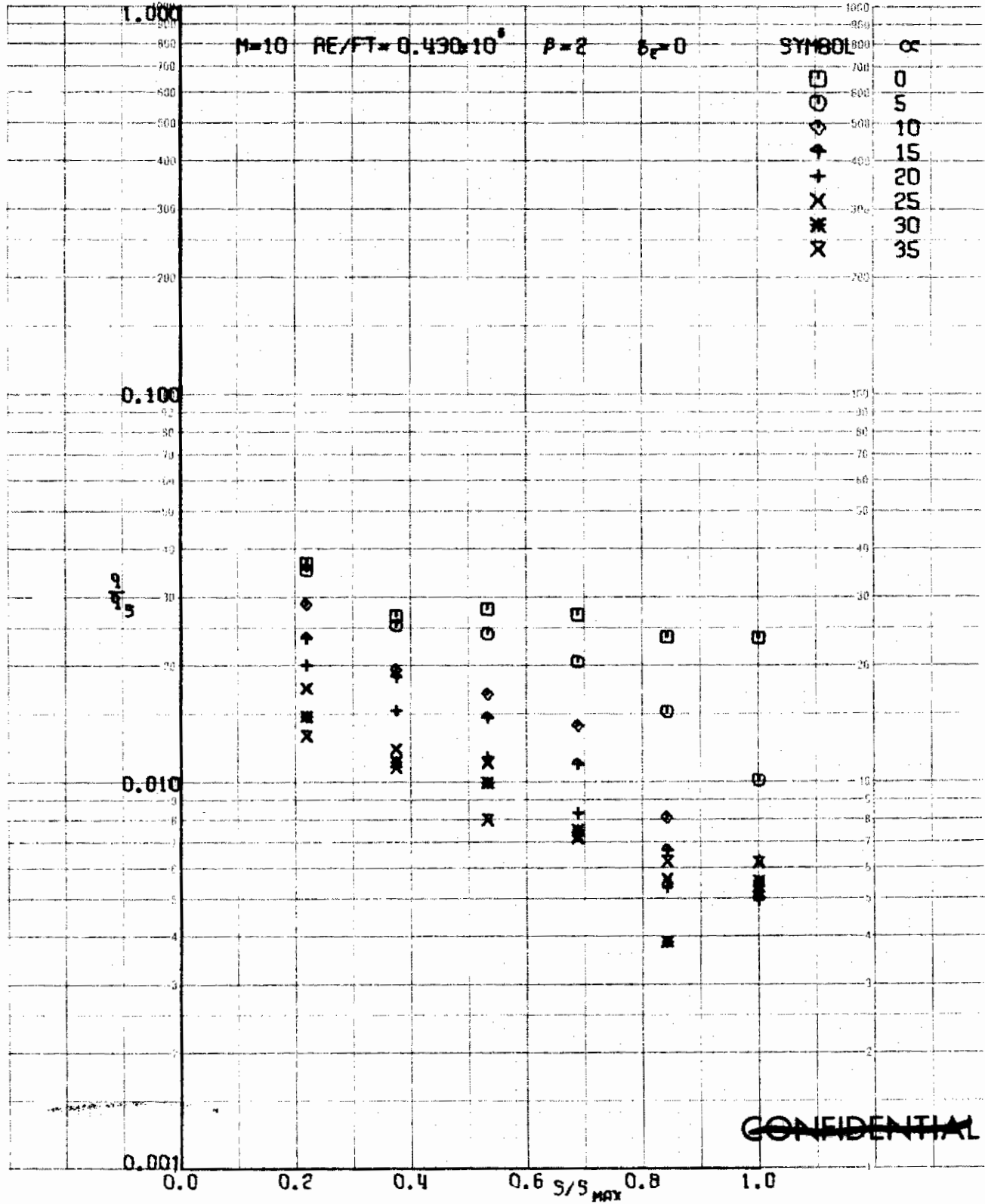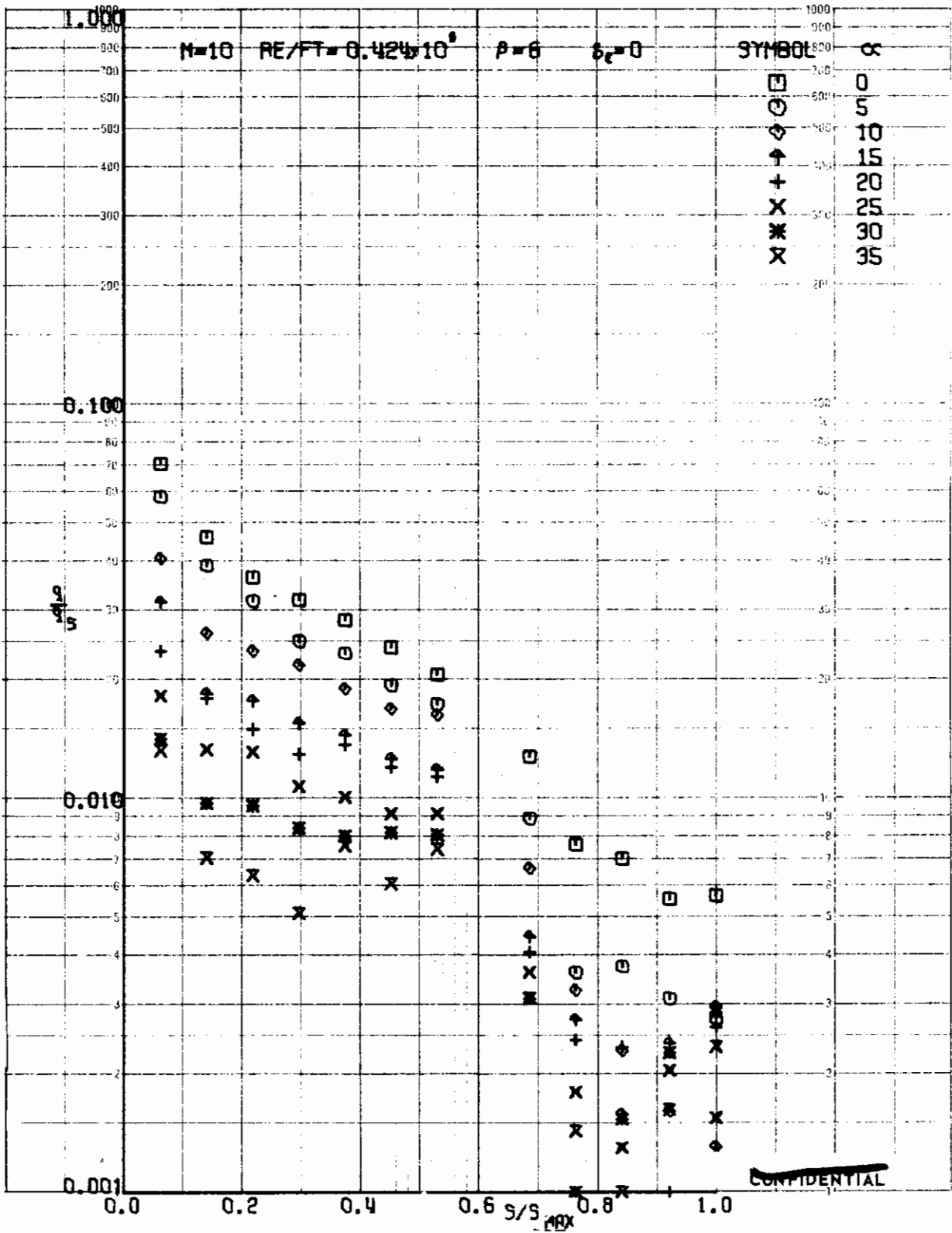
FIGURE 214   (U) TUNNEL C UPPER SURFACE SPANWISE HEATING RATES AT X/L = 0.30,
β=2
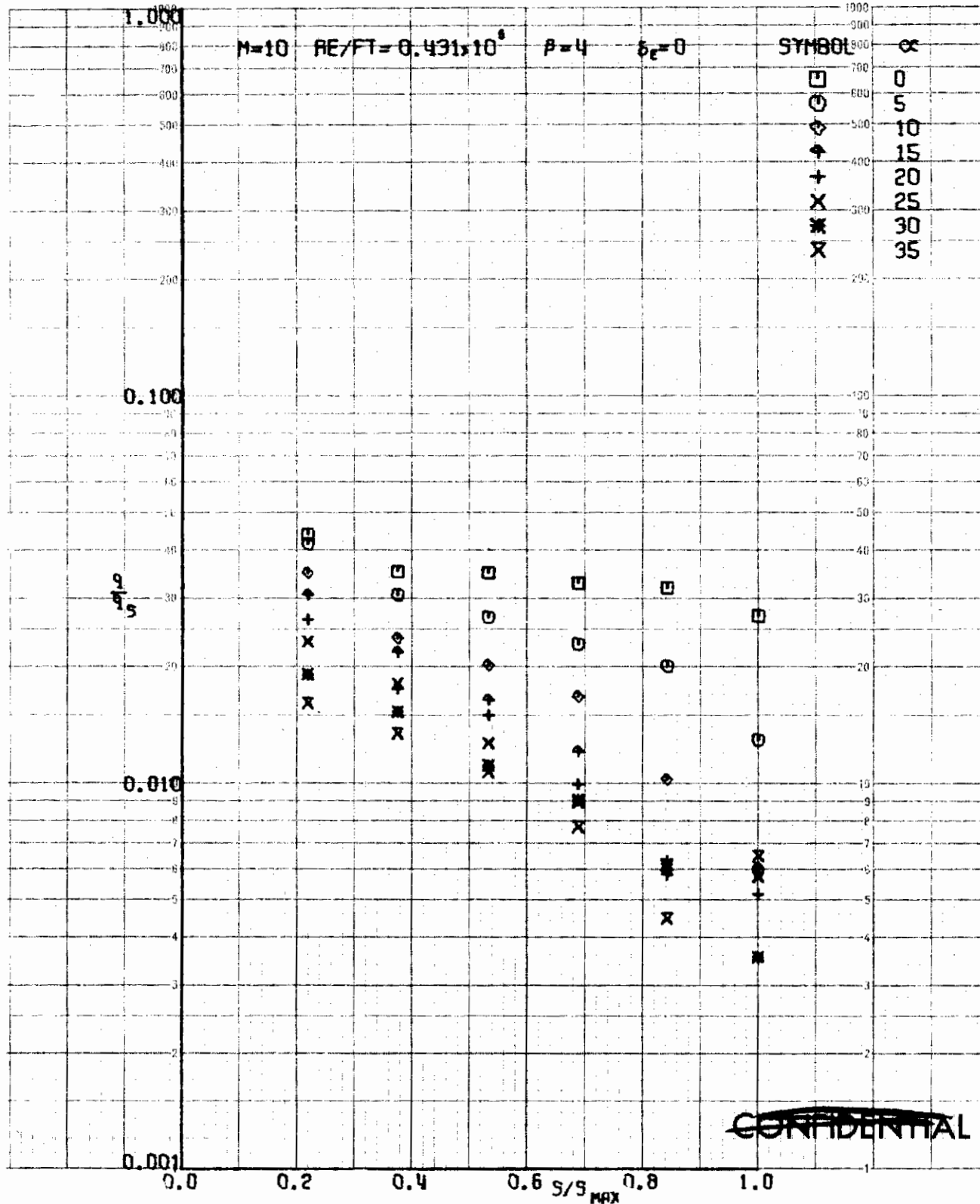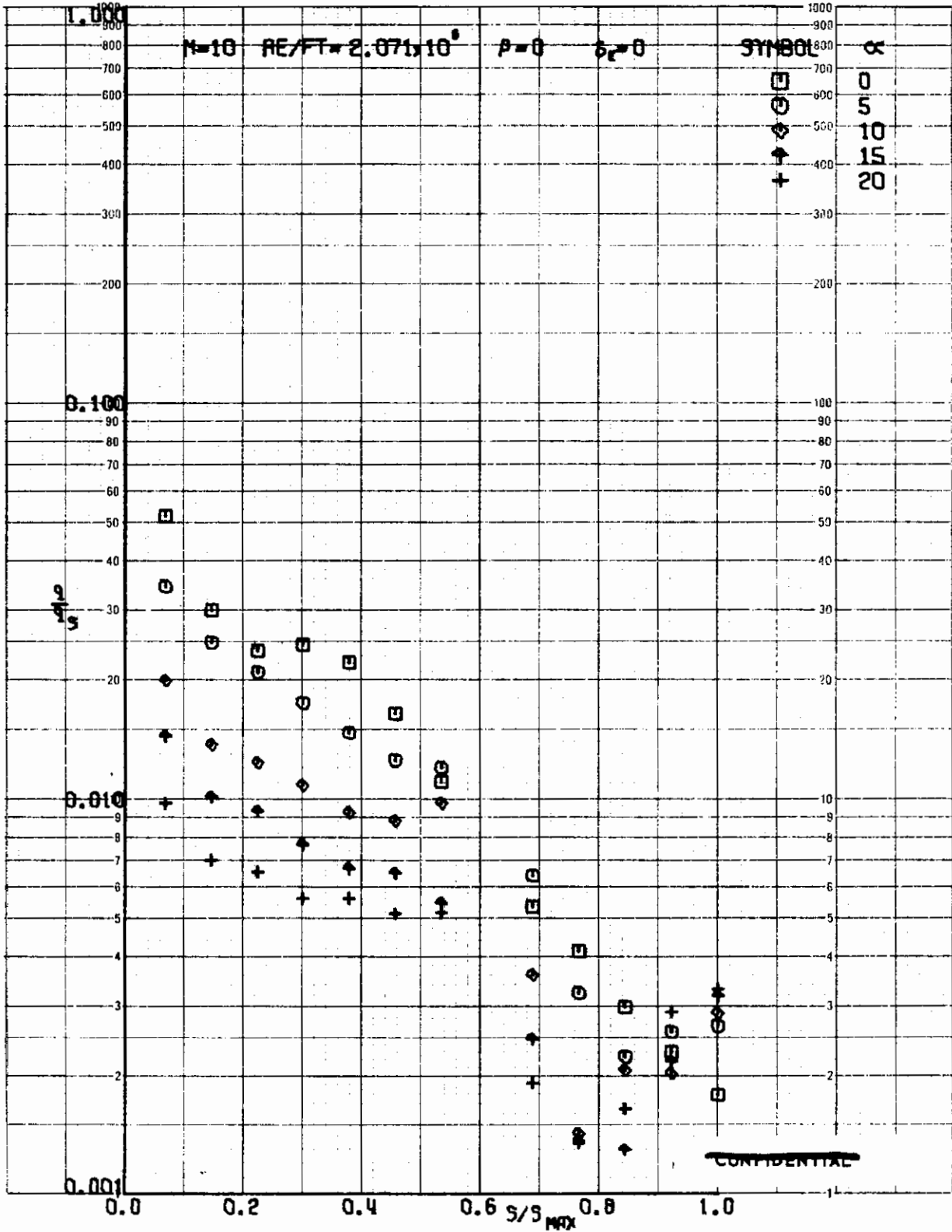
FIGURE 215   (U) TUNNEL C UPPER SURFACE SPANWISE HEATING RATES AT X/L = 0.30,
β=4
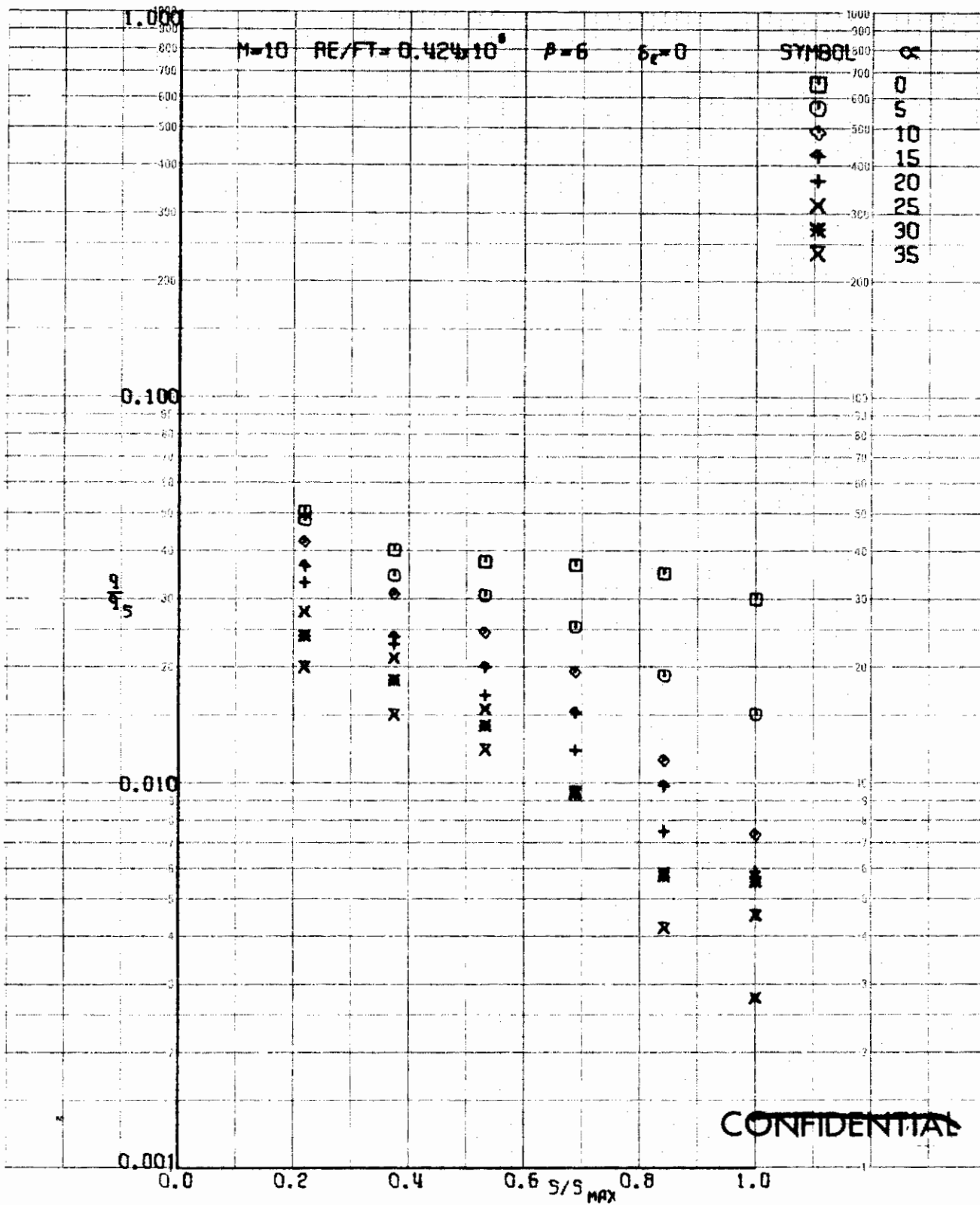
FIGURE 216 (U) TUNNEL C UPPER SURFACE SPANWISE HEATING RATES AT X/L = 0.30,
β=6
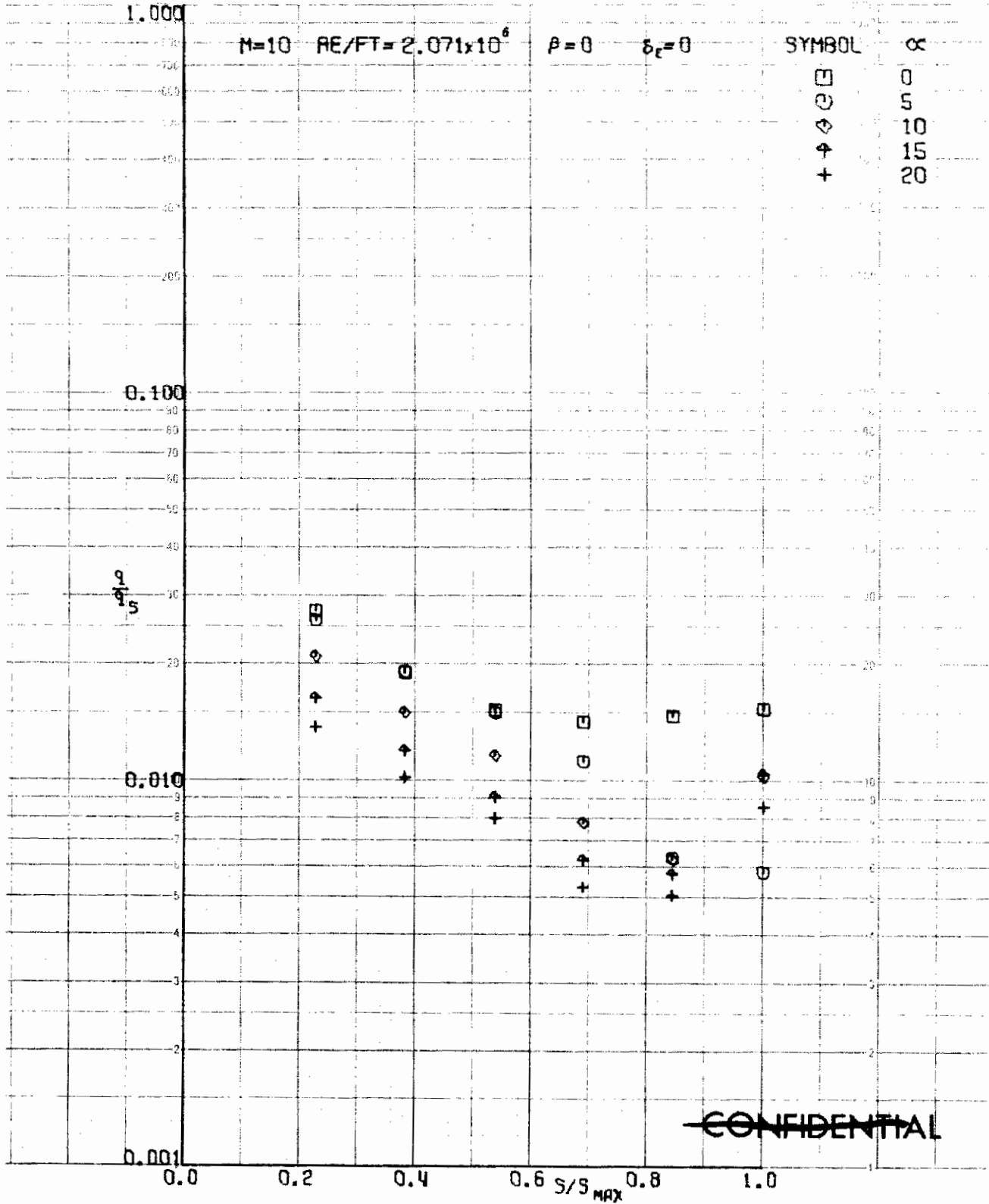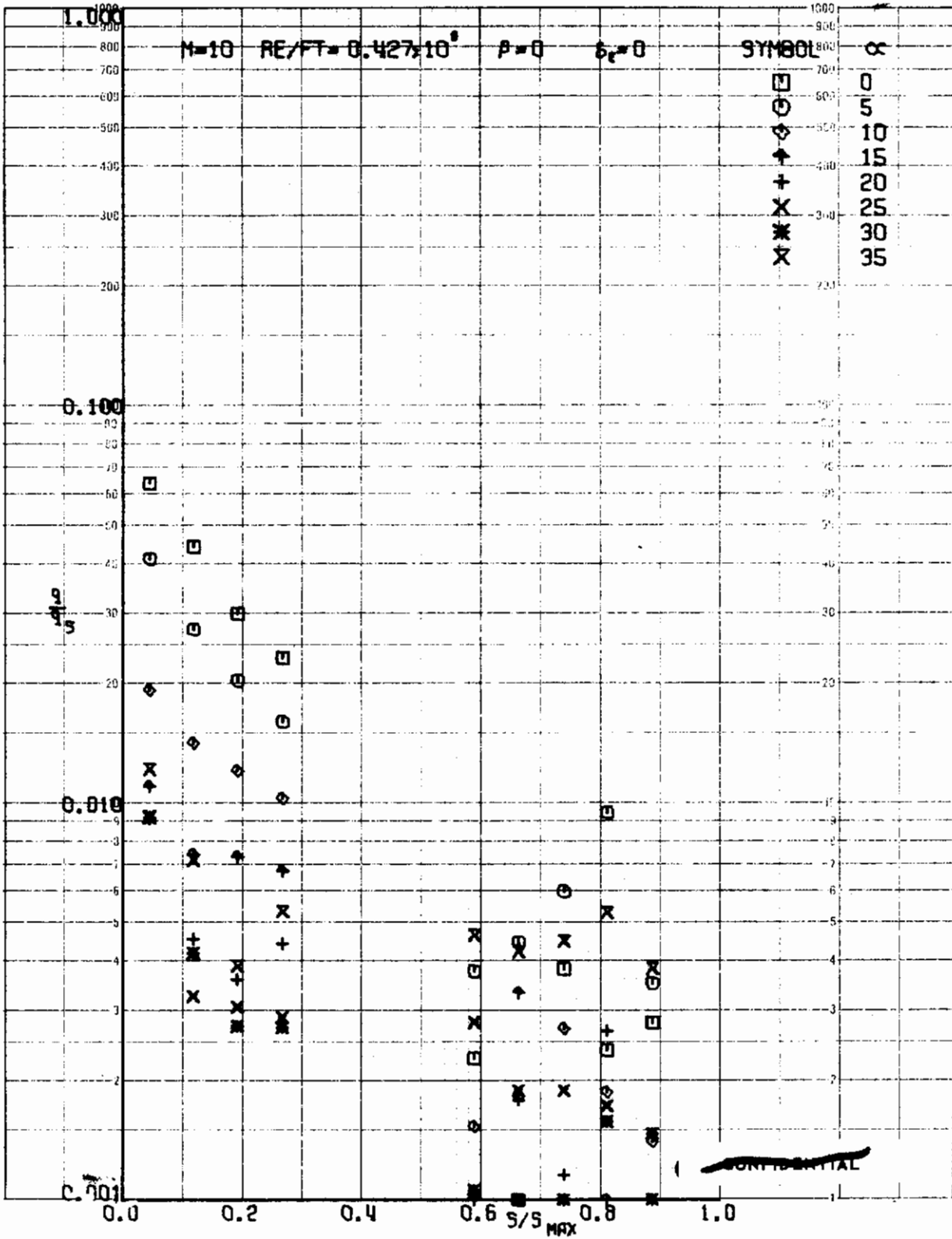
FIGURE 217 (U) TUNNEL C UPPER SURFACE SPANWISE HEATING RATES AT X/L = 0.30,
β=0

FIGURE 218 (U) TUNNEL F UPPER SURFACE SPANWISE HEATING RATES AT X/L = 0.30,
β=0

$M_\infty = 19$ $RE_\infty/FT = 0.5 \times 10^6$ $\beta = -2$ $\delta_e = 0$

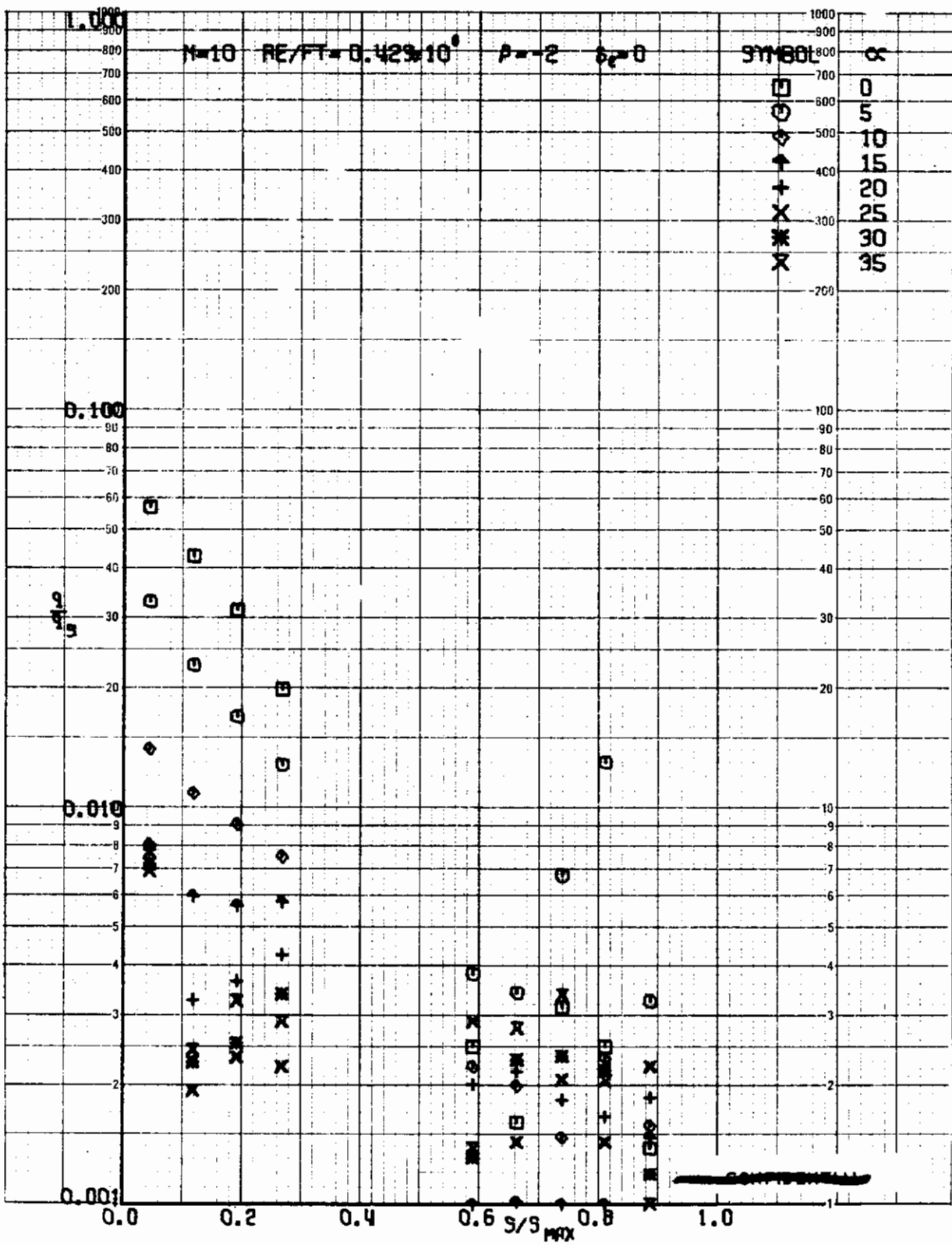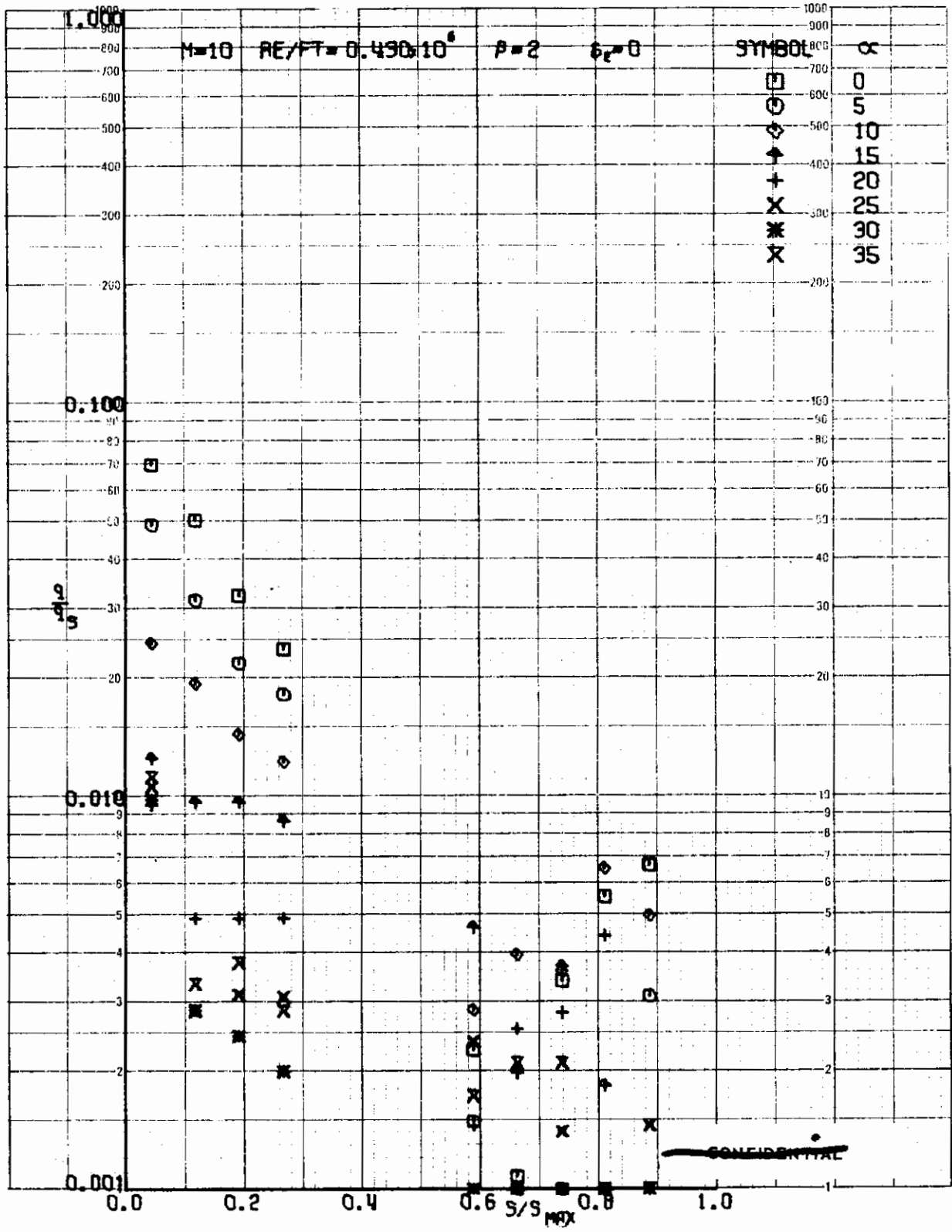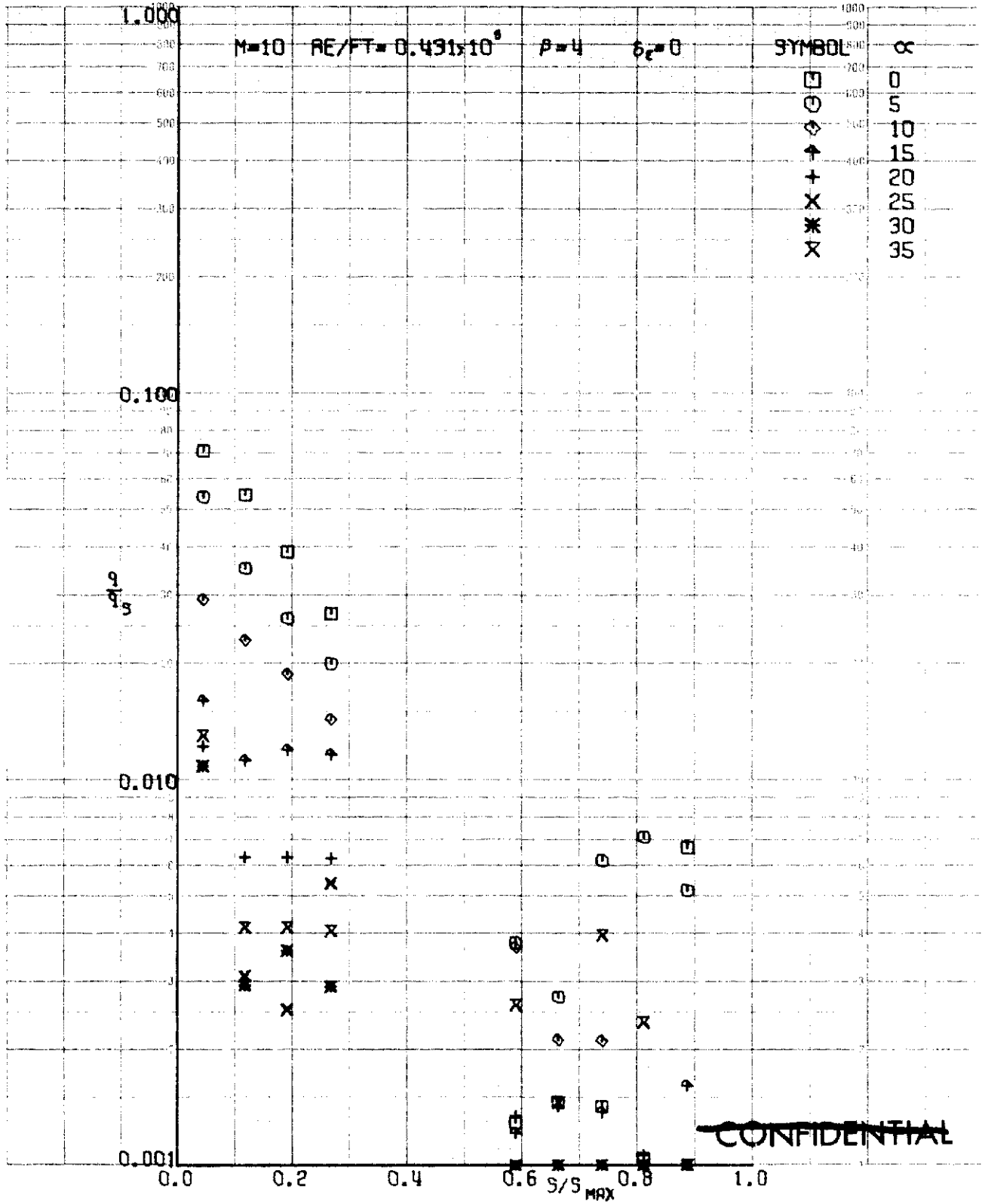| SYMBOL	α
⊙	10
⊟	15
△	20

FIGURE 219 (U) TUNNEL F UPPER SURFACE SPANWISE HEATING RATES AT X/L = 0.30,
$\beta = -2$

310

FIGURE 220 (U) TUNNEL F UPPER SURFACE SPANWISE HEATING RATES AT X/L = 0.30, β=2

$M_\infty = 19$ $RE_\infty / FT = 0.5 \times 10^6$ $\beta = 4$ $\delta_e = 0$

SYMBOL	α
○	10
□	15
△	20

$\dfrac{q}{q_s}$

S/S_{max}

FIGURE 221   (U) TUNNEL F UPPER SURFACE SPANWISE HEATING RATES AT X/L = 0.30,
$\beta = 4$

312

FIGURE 222 (U) TUNNEL F UPPER SURFACE SPANWISE HEATING RATES AT X/L = 0.30,
β=6

313
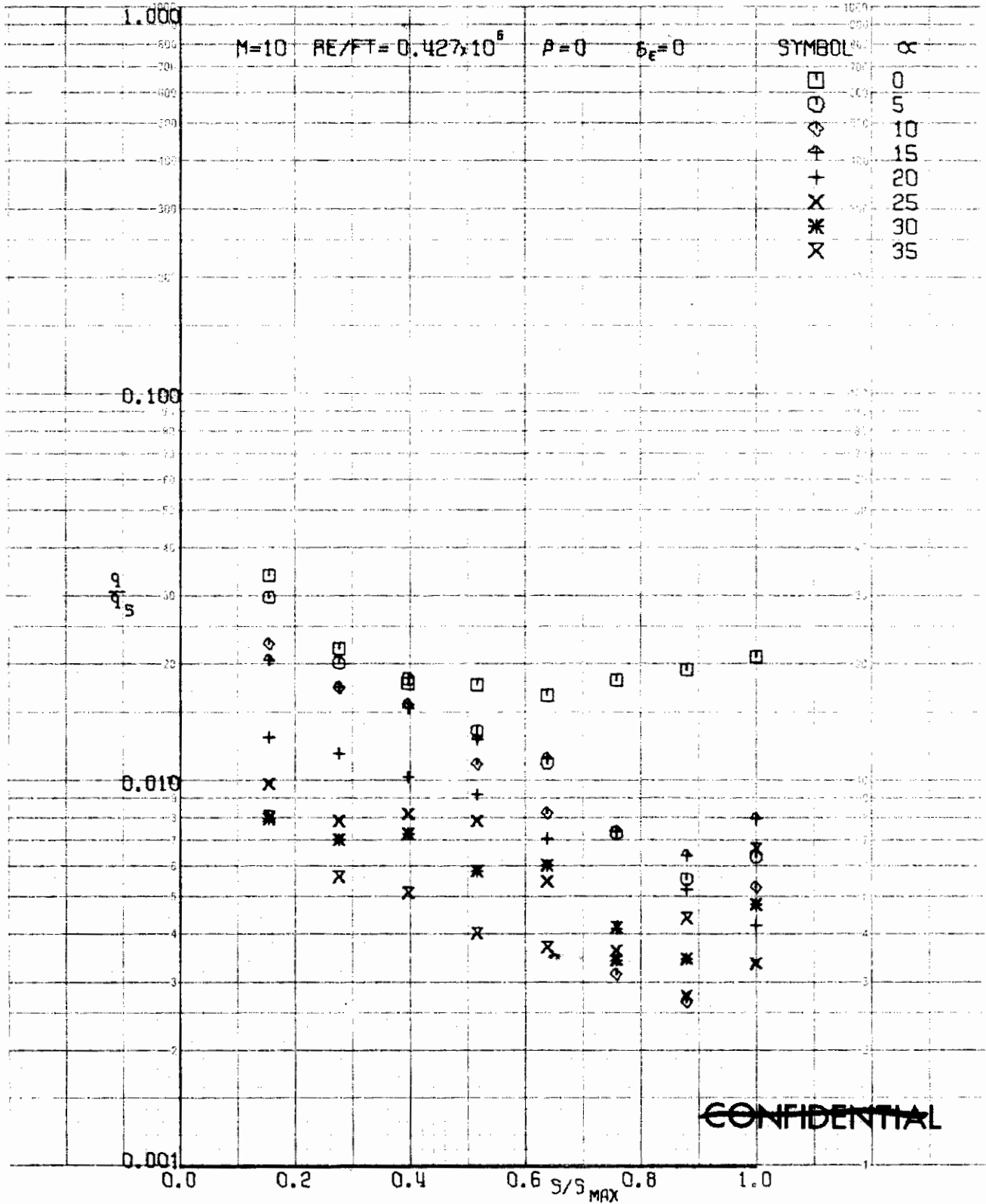
FIGURE 223 (U) TUNNEL C UPPER SURFACE SPANWISE HEATING RATES AT X/L = 0.40, β=0
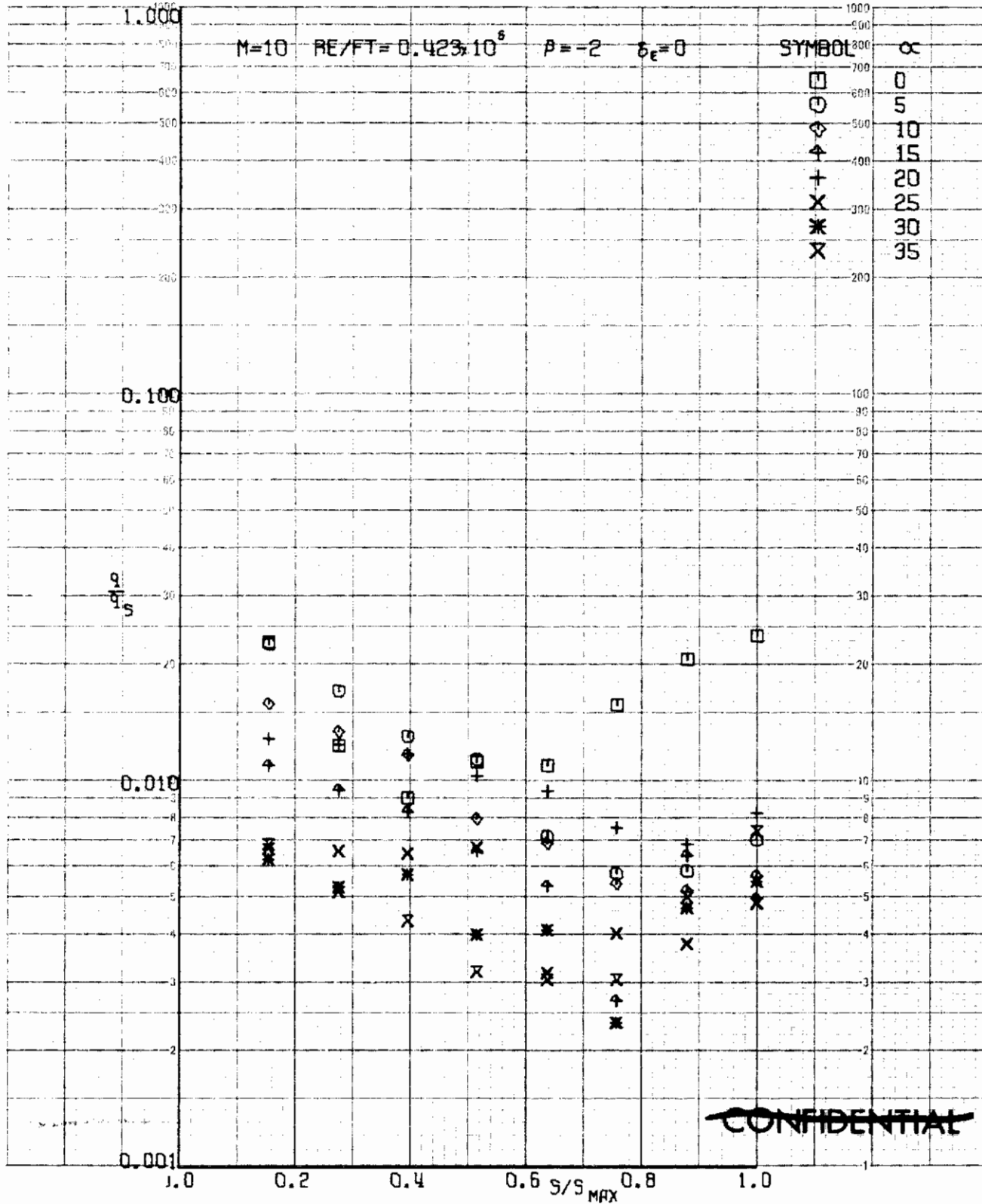
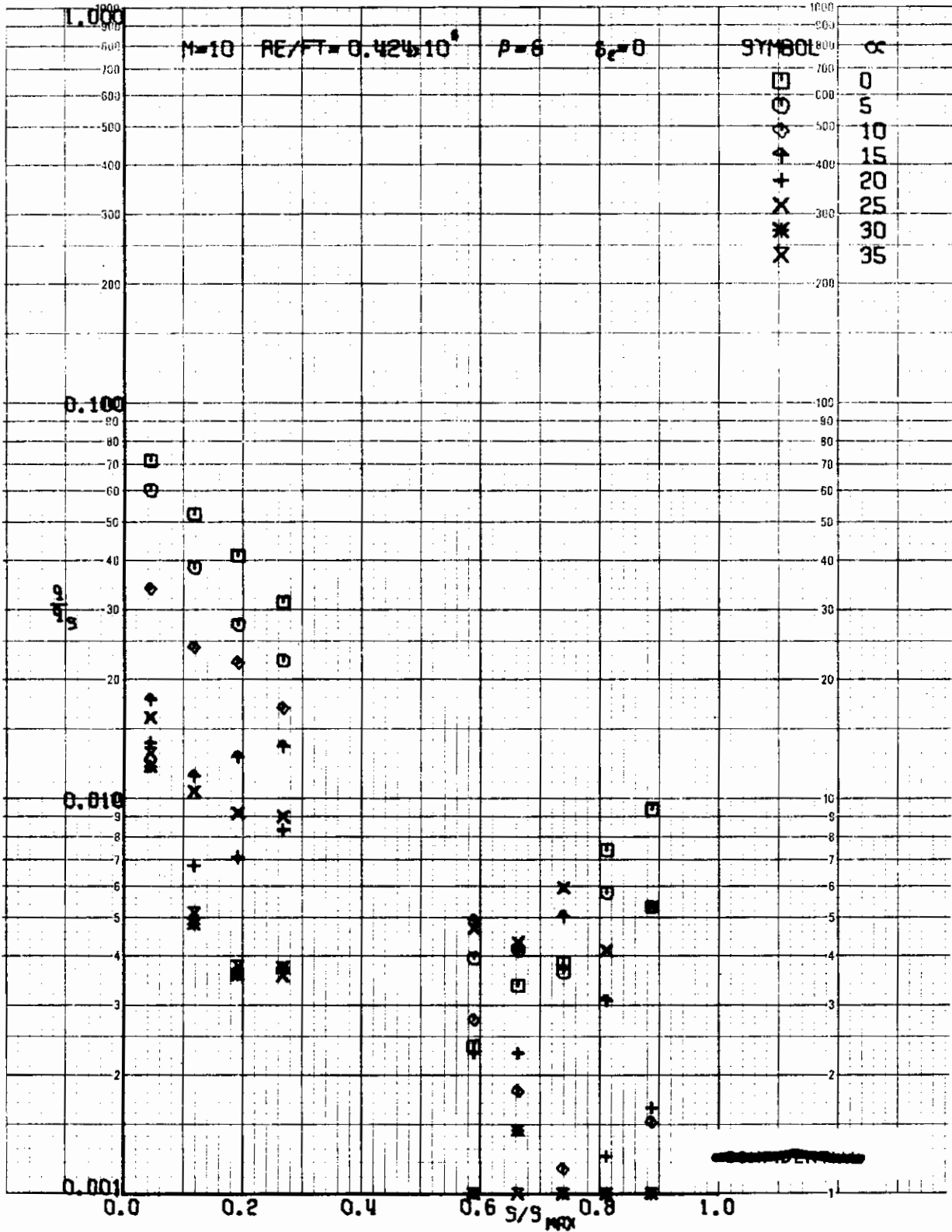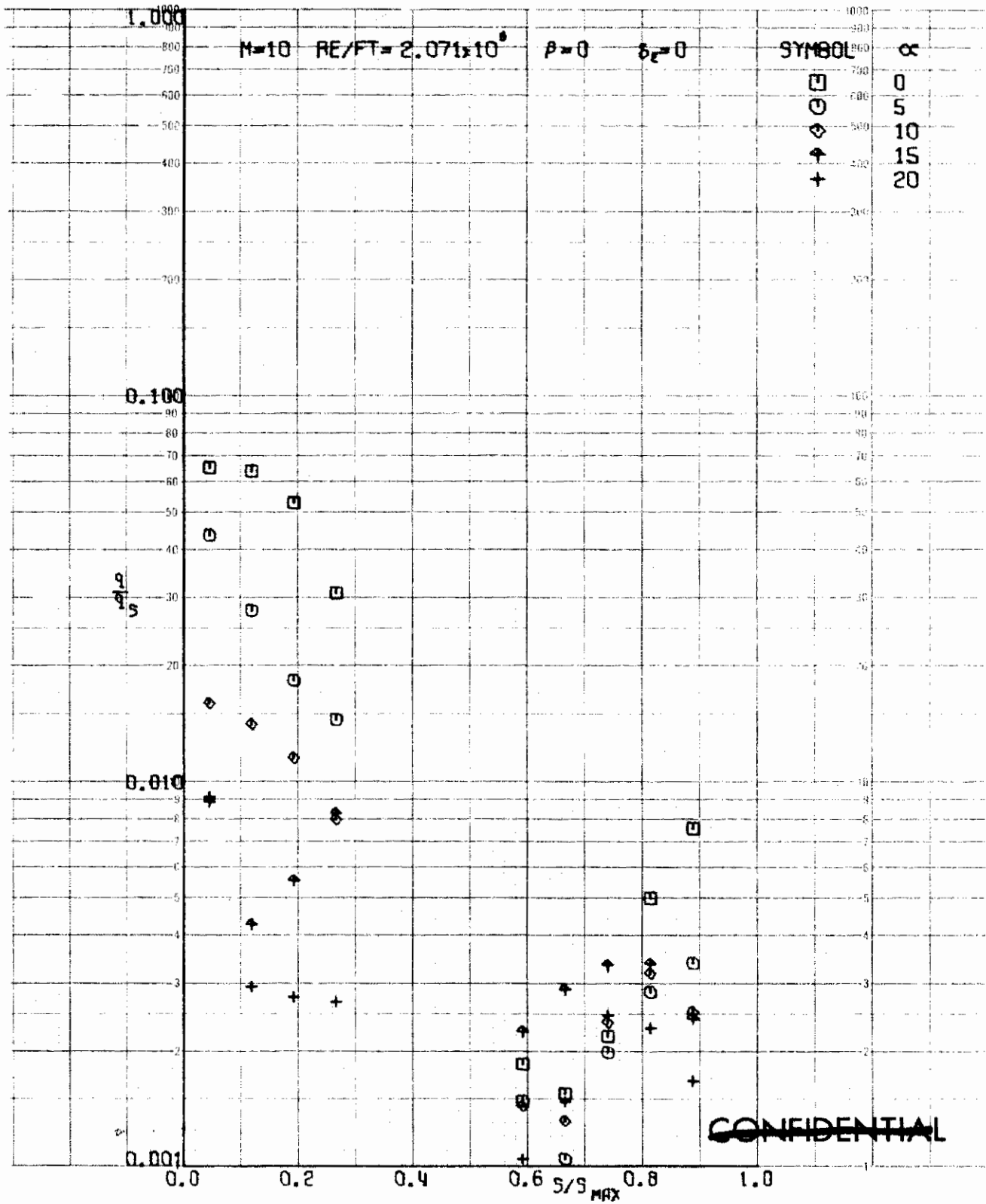FIGURE 224   (U) TUNNEL C UPPER SURFACE SPANWISE HEATING RATES AT X/L = 0.40,
β=-2
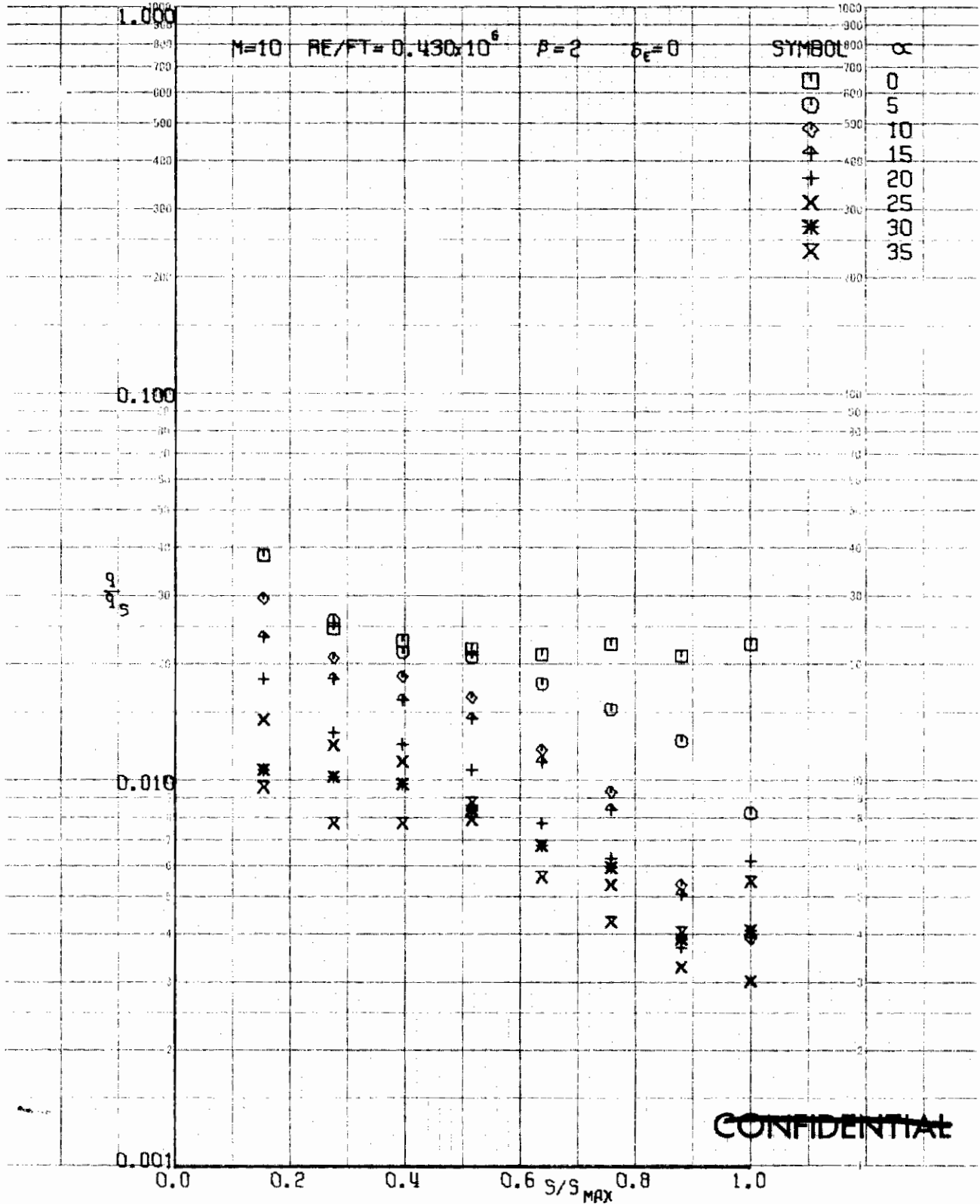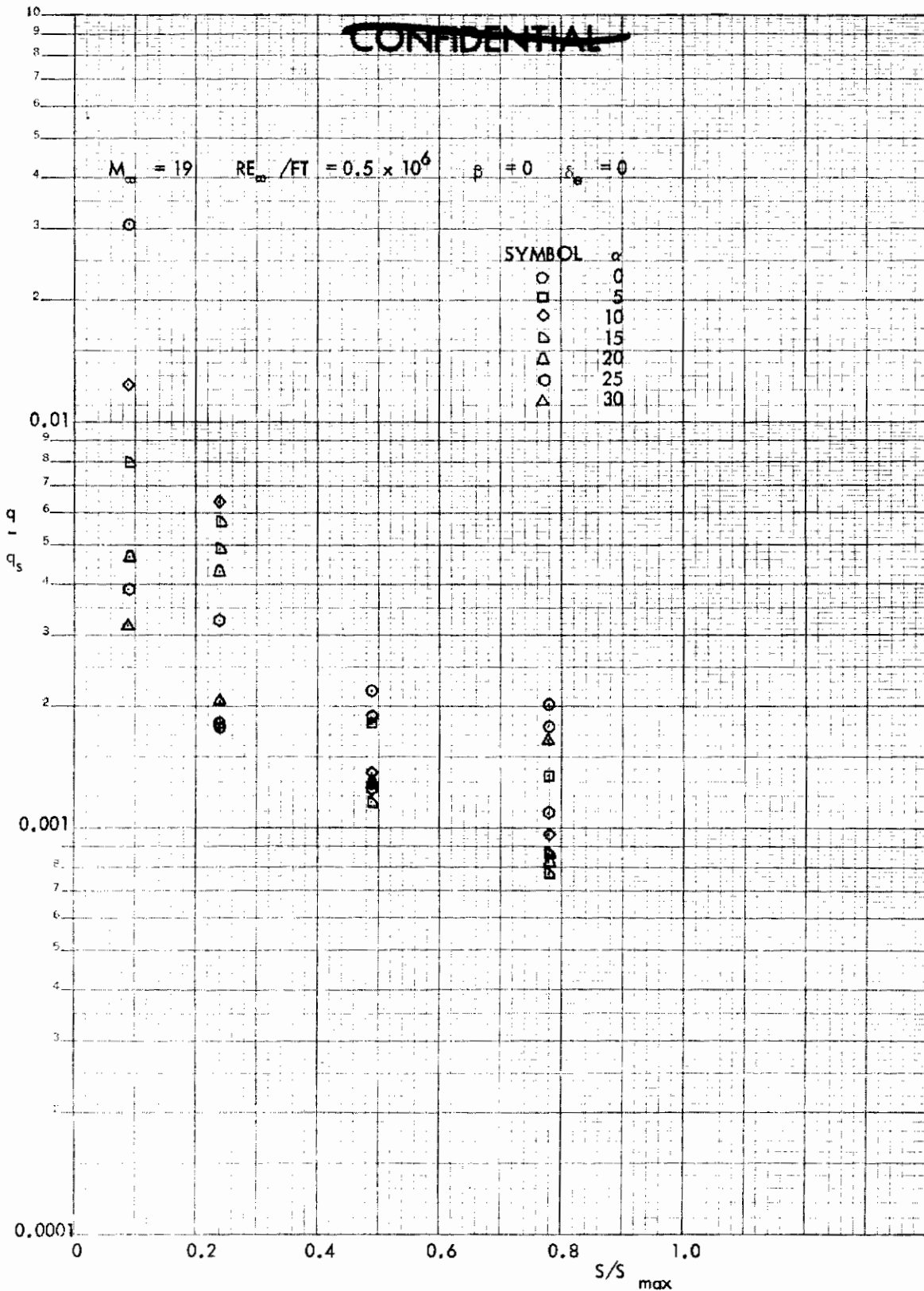
FIGURE 225   (U) TUNNEL C UPPER SURFACE SPANWISE HEATING RATES AT X/L = 0.40,
β=2
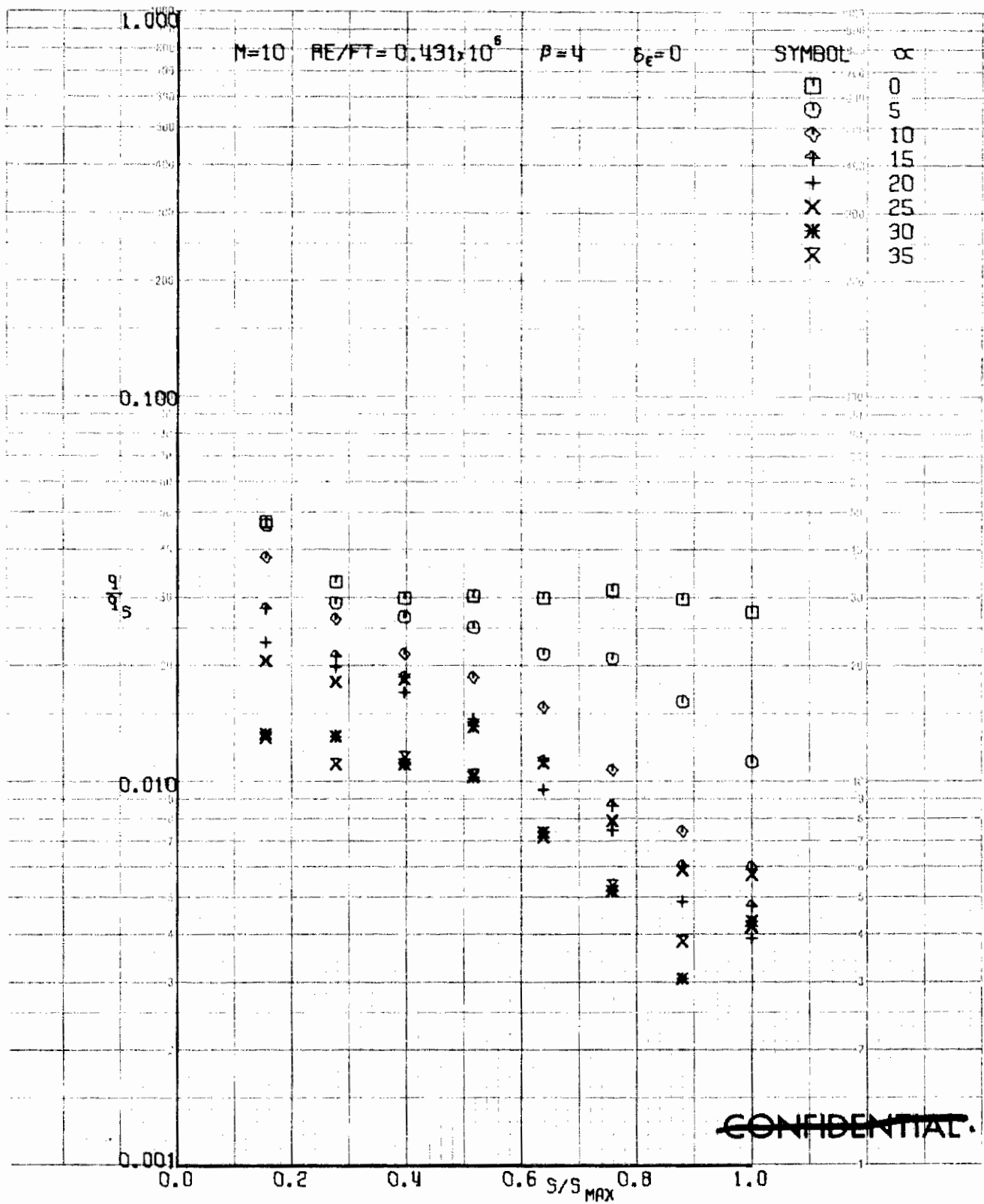
FIGURE 226 (U) TUNNEL C UPPER SURFACE SPANWISE HEATING RATES AT X/L = 0.40, β=4
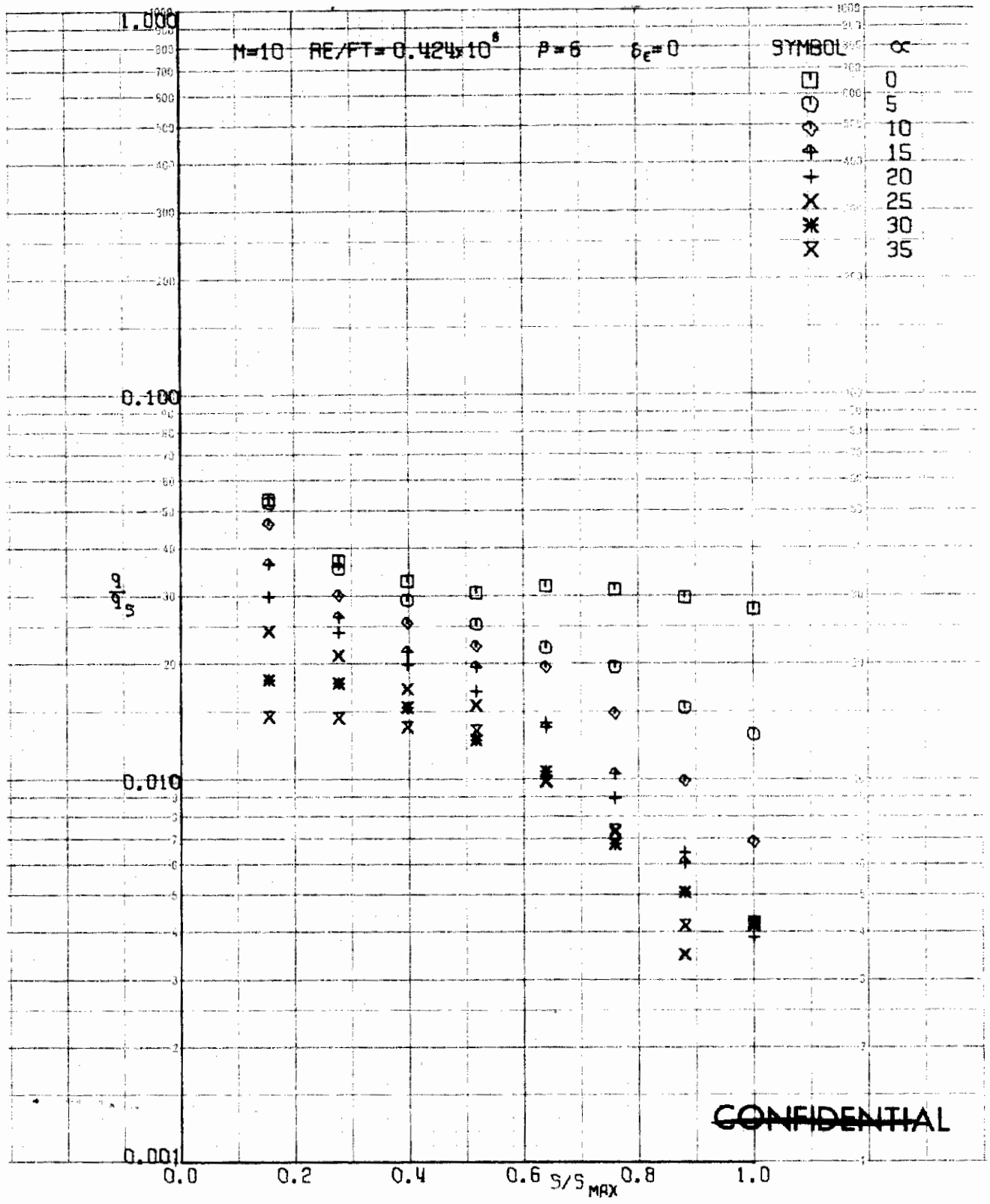
FIGURE 227 (U) TUNNEL C UPPER SURFACE SPANWISE HEATING RATES AT X/L = 0.40, β=6
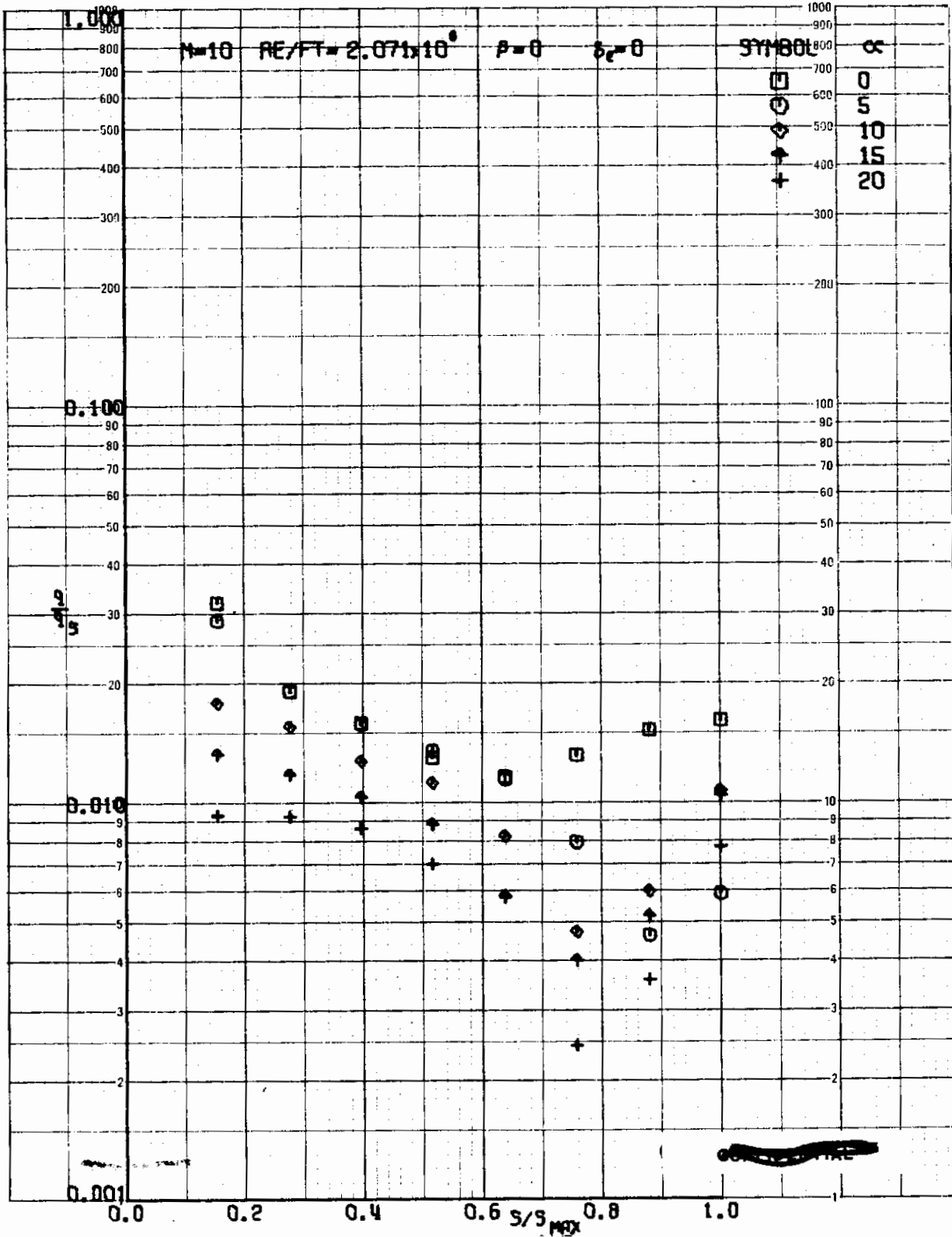
FIGURE 228   (U) TUNNEL C UPPER SURFACE SPANWISE HEATING RATES AT X/L = 0.40, β=0
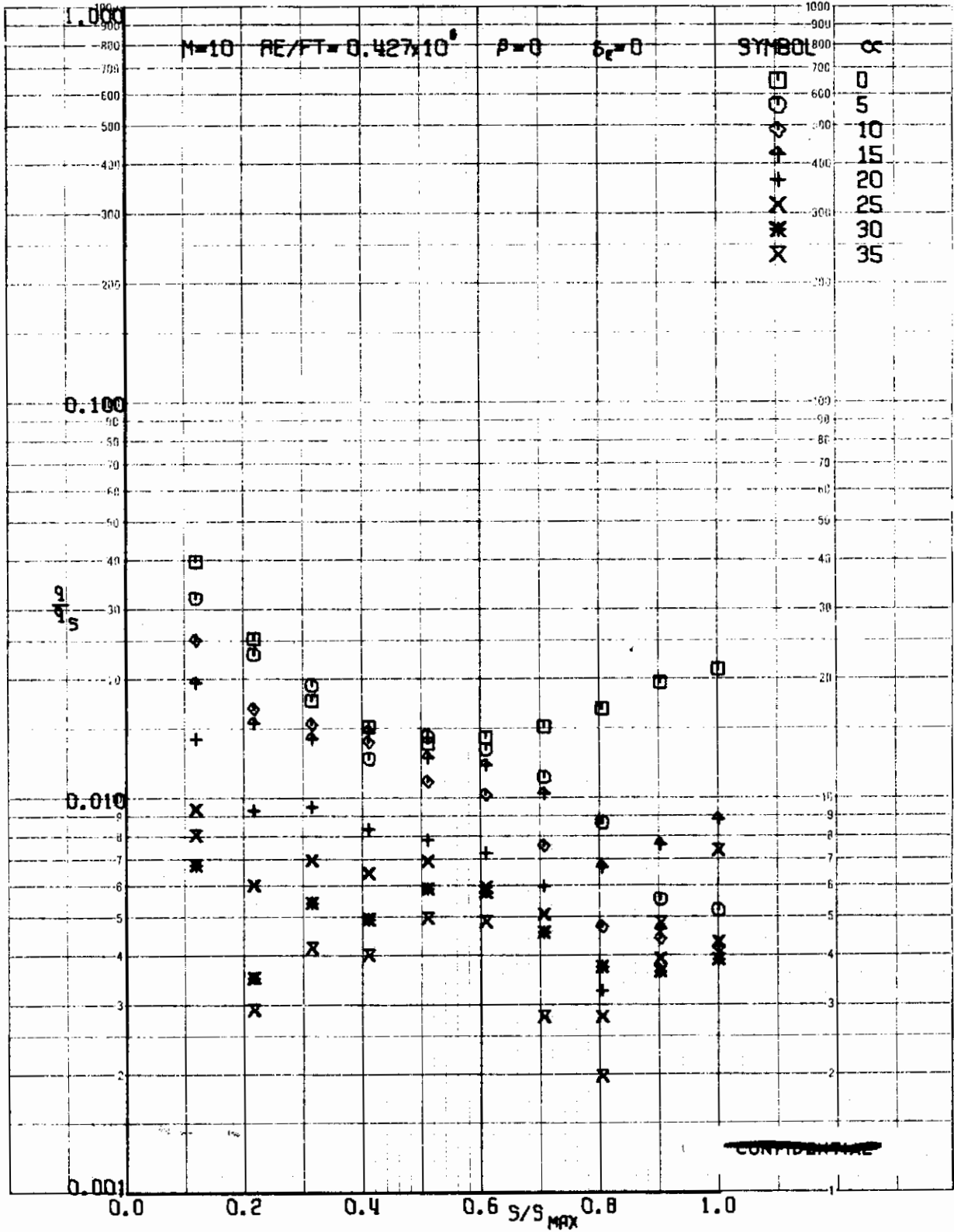
FIGURE 229 (U) TUNNEL C UPPER SURFACE SPANWISE HEATING RATES AT X/L = 0.50,
β=0
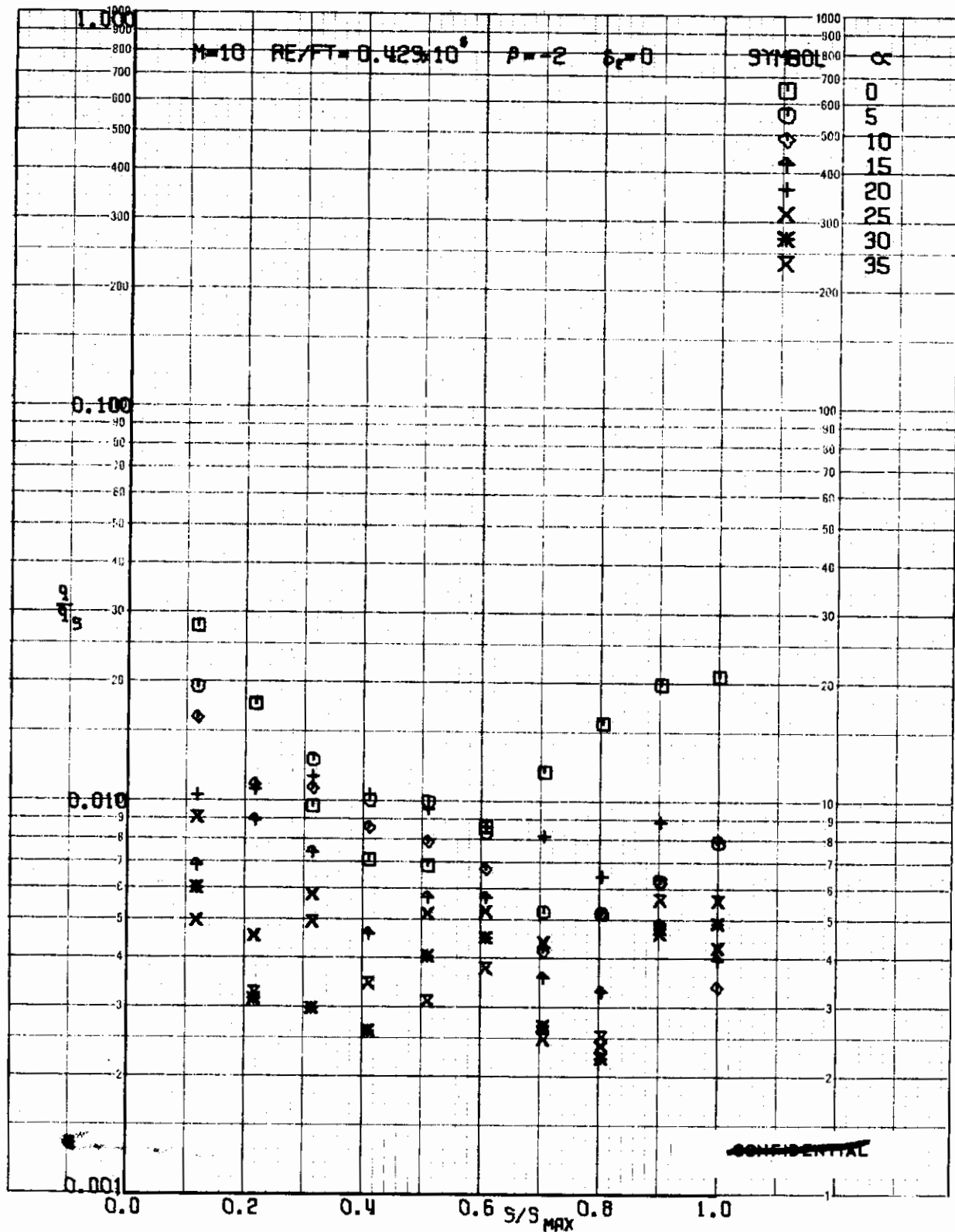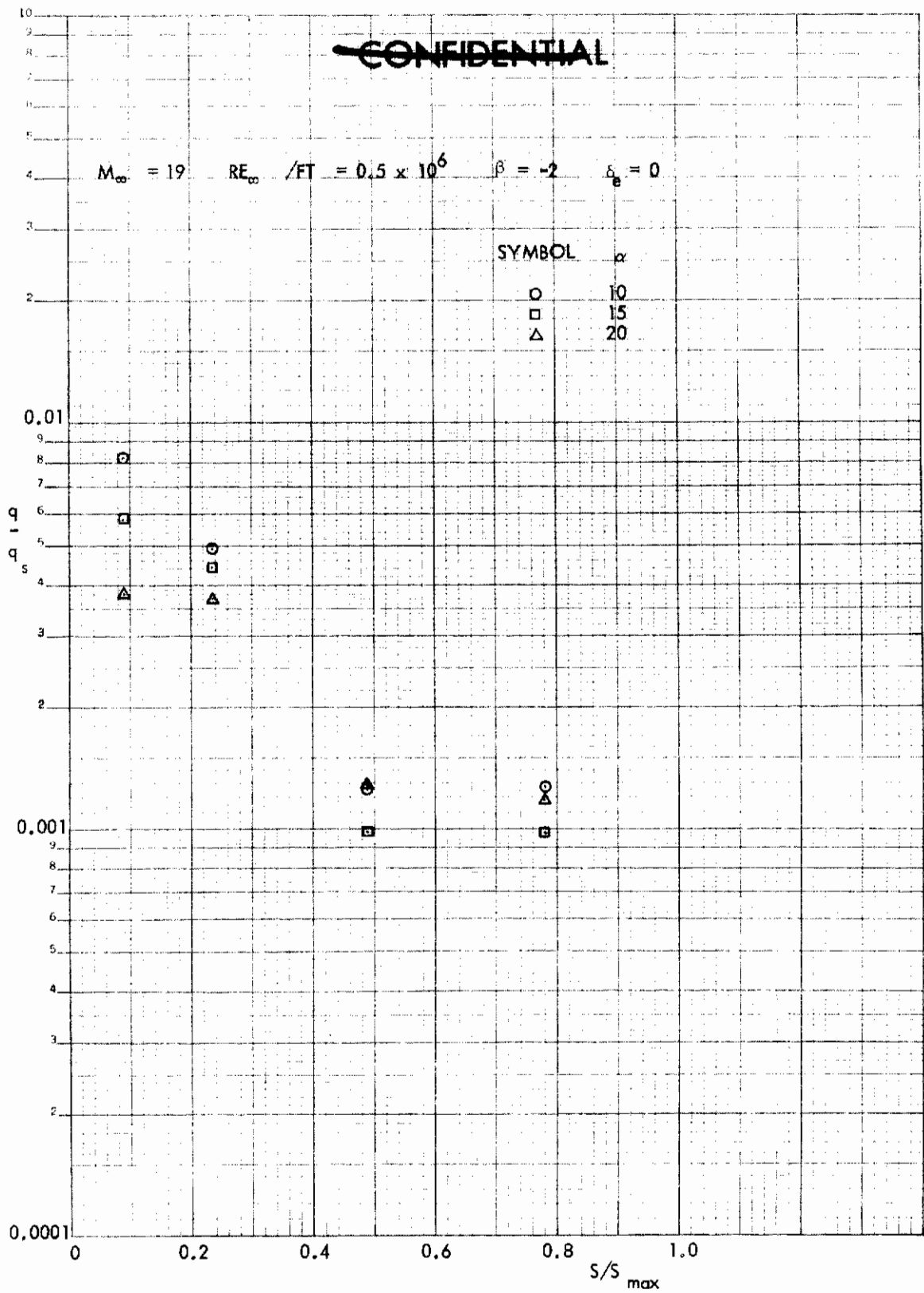
FIGURE 230 (U) TUNNEL C UPPER SURFACE SPANWISE HEATING RATES AT X/L = 0.50, β=-2
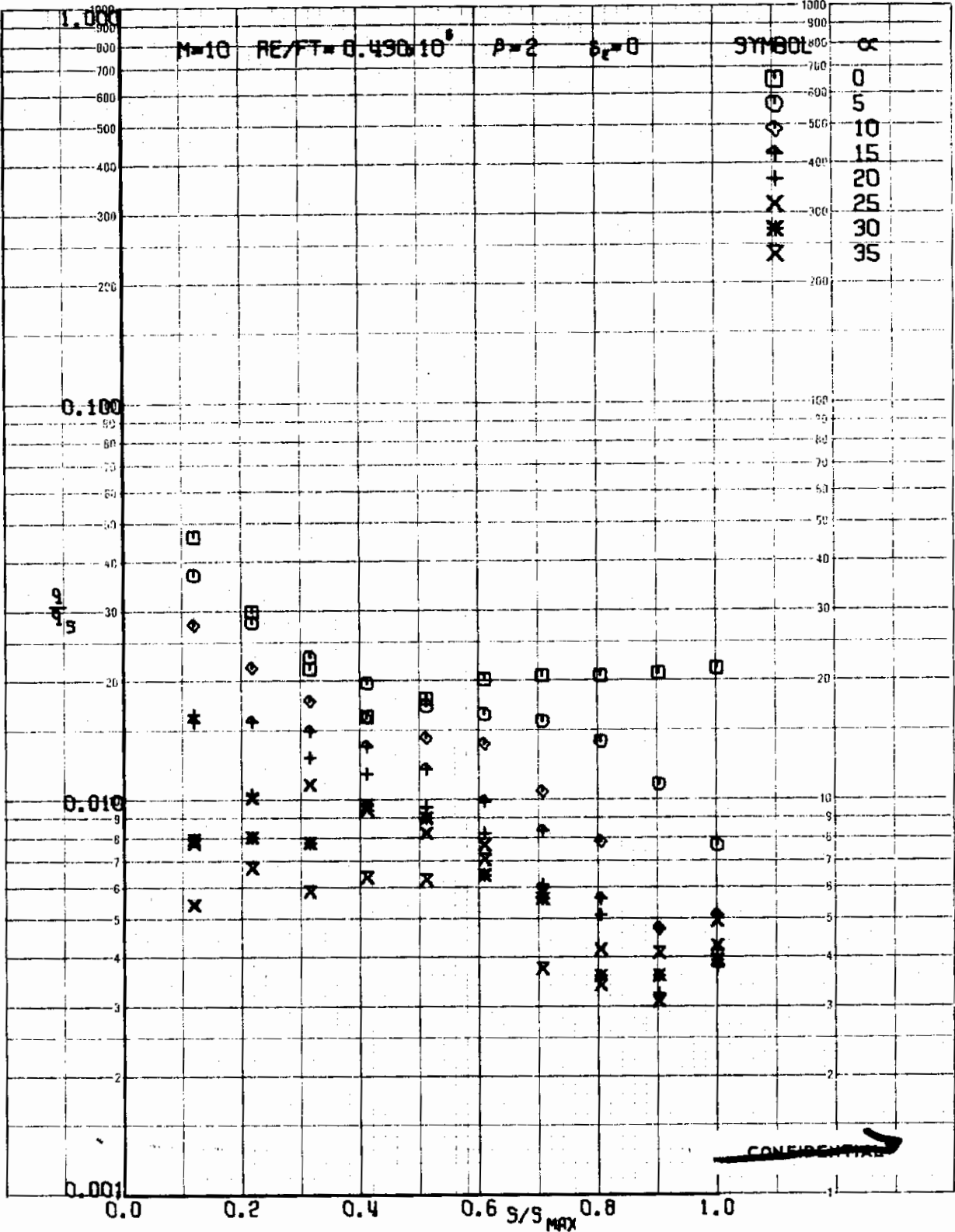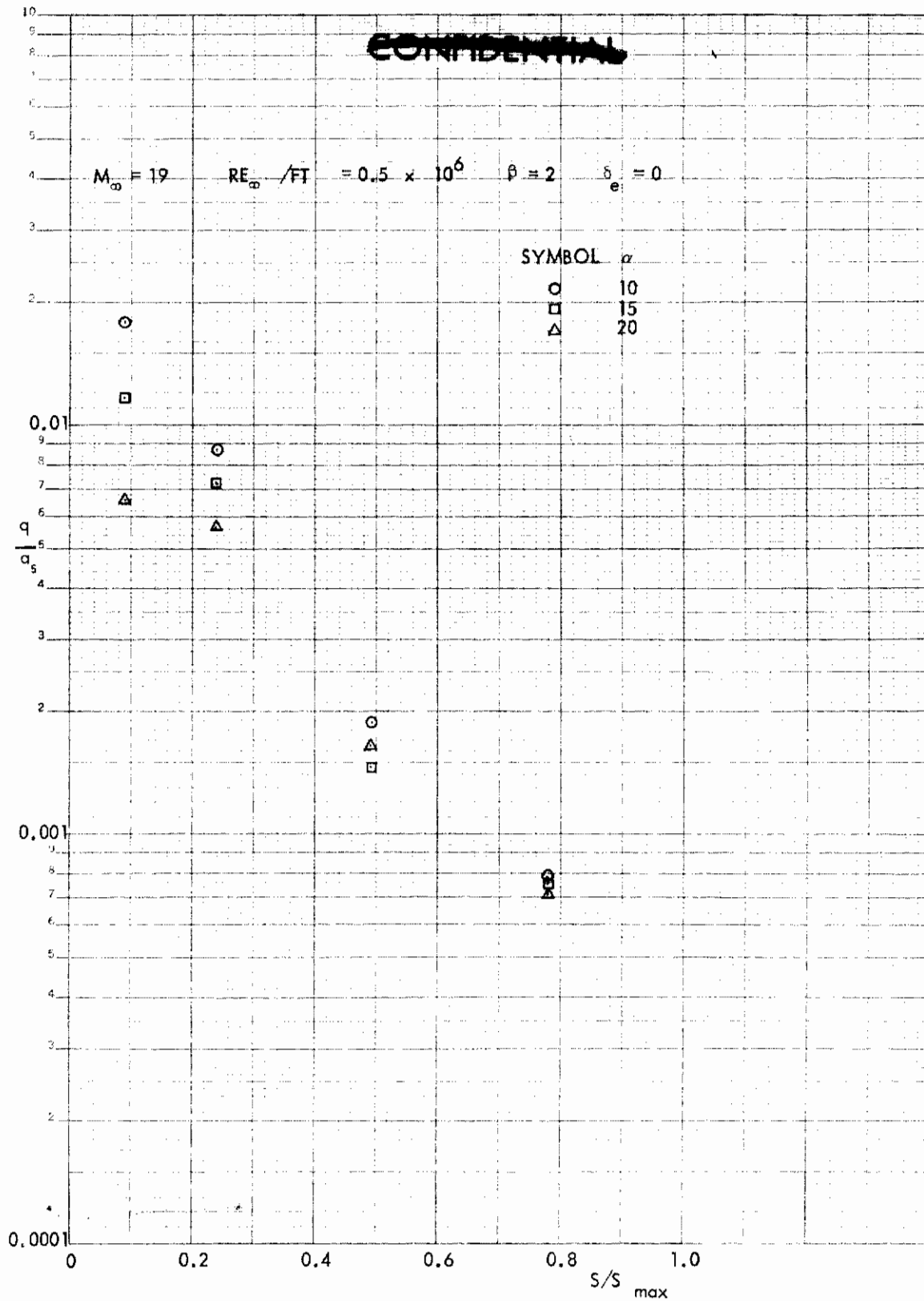
FIGURE 231   (U) TUNNEL C UPPER SURFACE SPANWISE HEATING RATES AT X/L = 0.50,
β=2
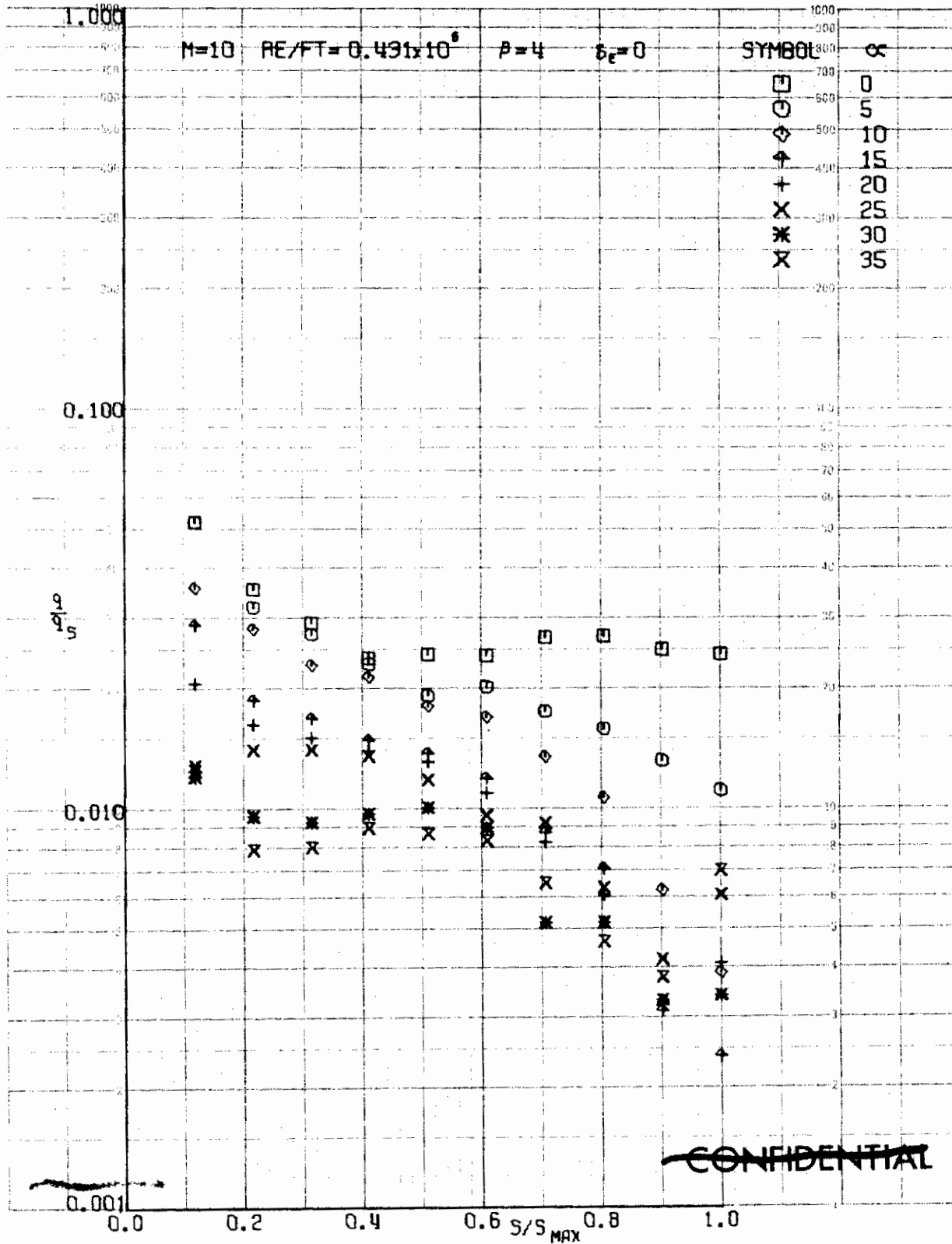
FIGURE 232   (U) TUNNEL C UPPER SURFACE SPANWISE HEATING RATES AT X/L = 0.50,
β=4
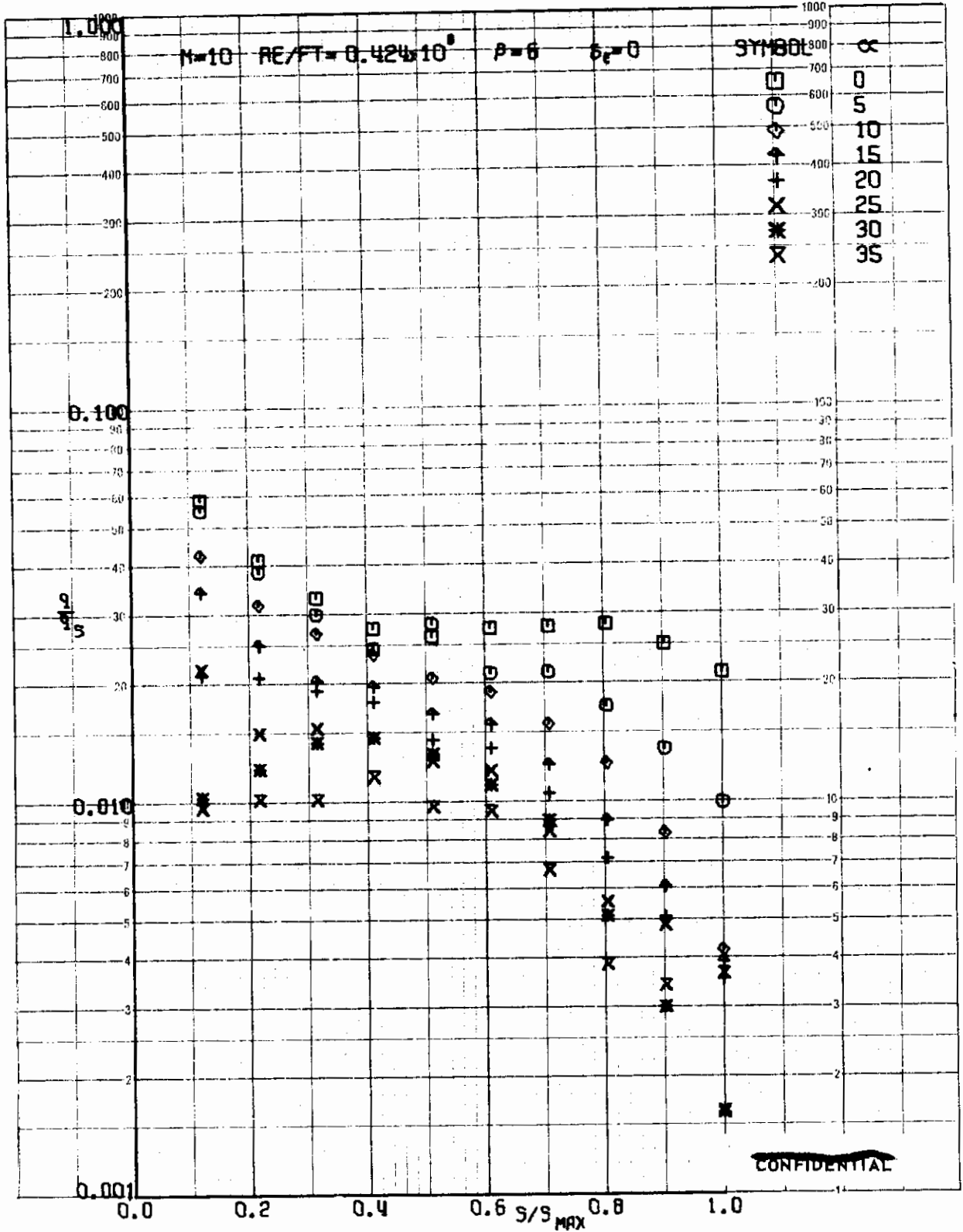
FIGURE 233 (U) TUNNEL C UPPER SURFACE SPANWISE HEATING RATES AT X/L = 0.50, β=6

324
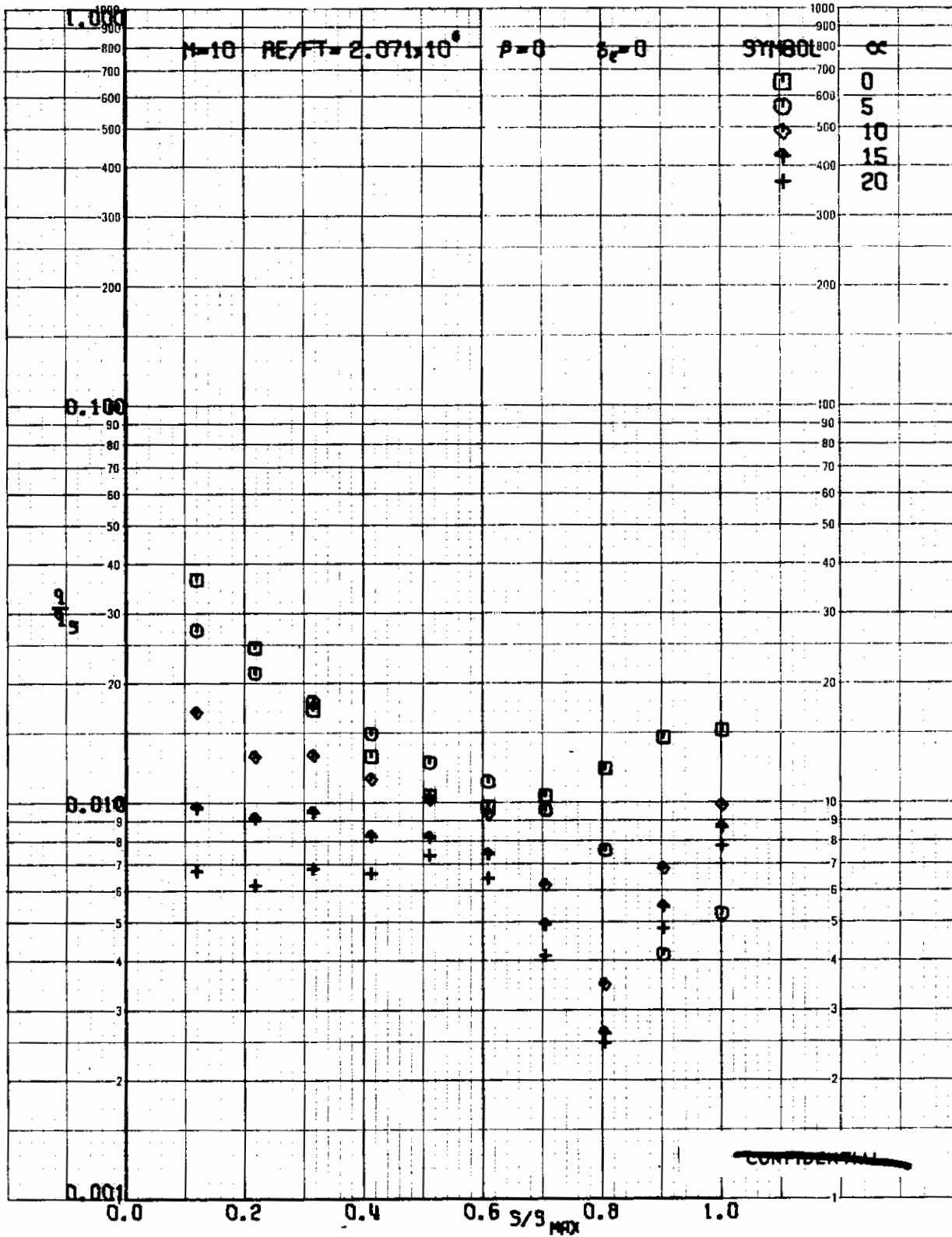
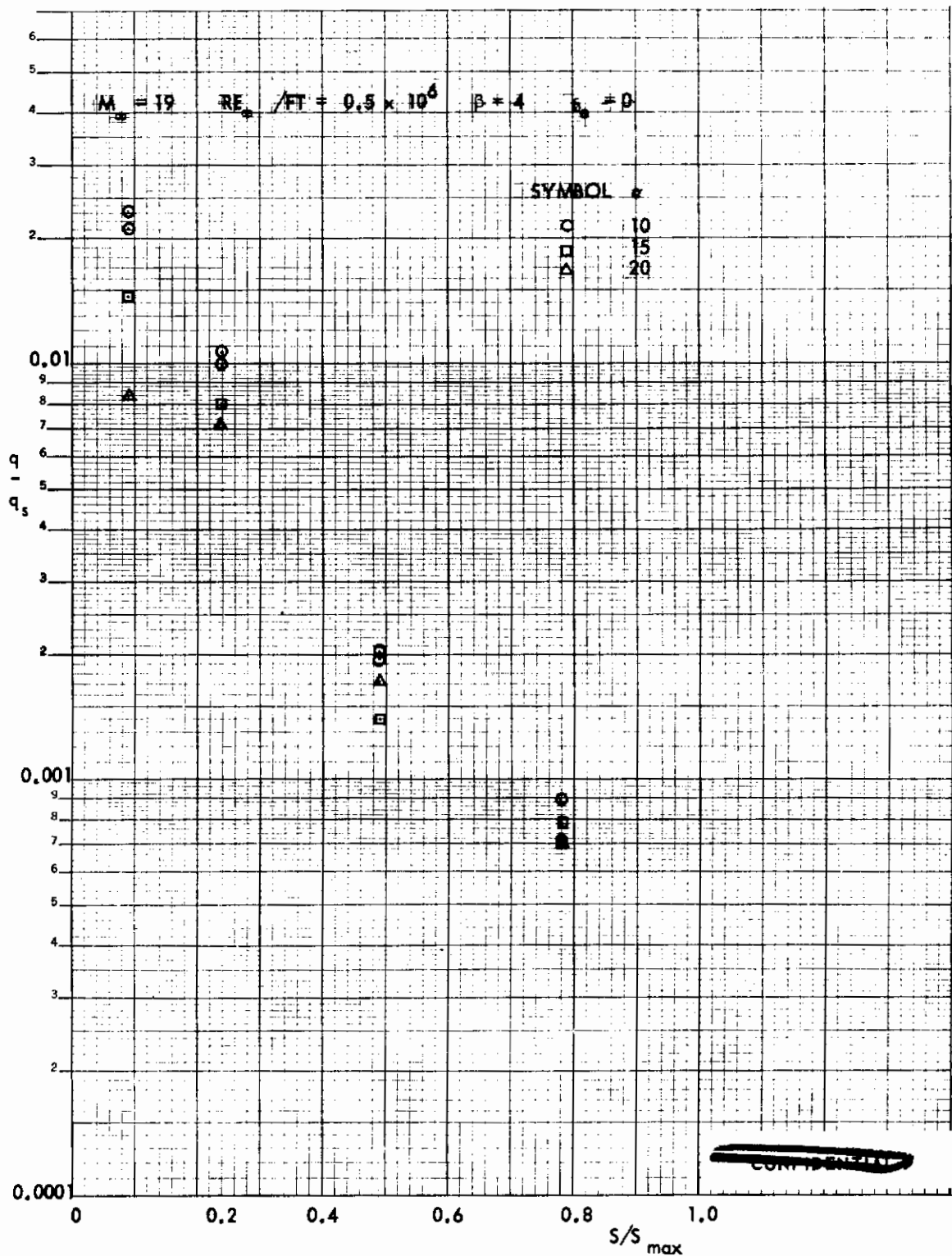FIGURE 234 (U) TUNNEL C UPPER SURFACE SPANWISE HEATING RATES AT X/L = 0.50,
β=0
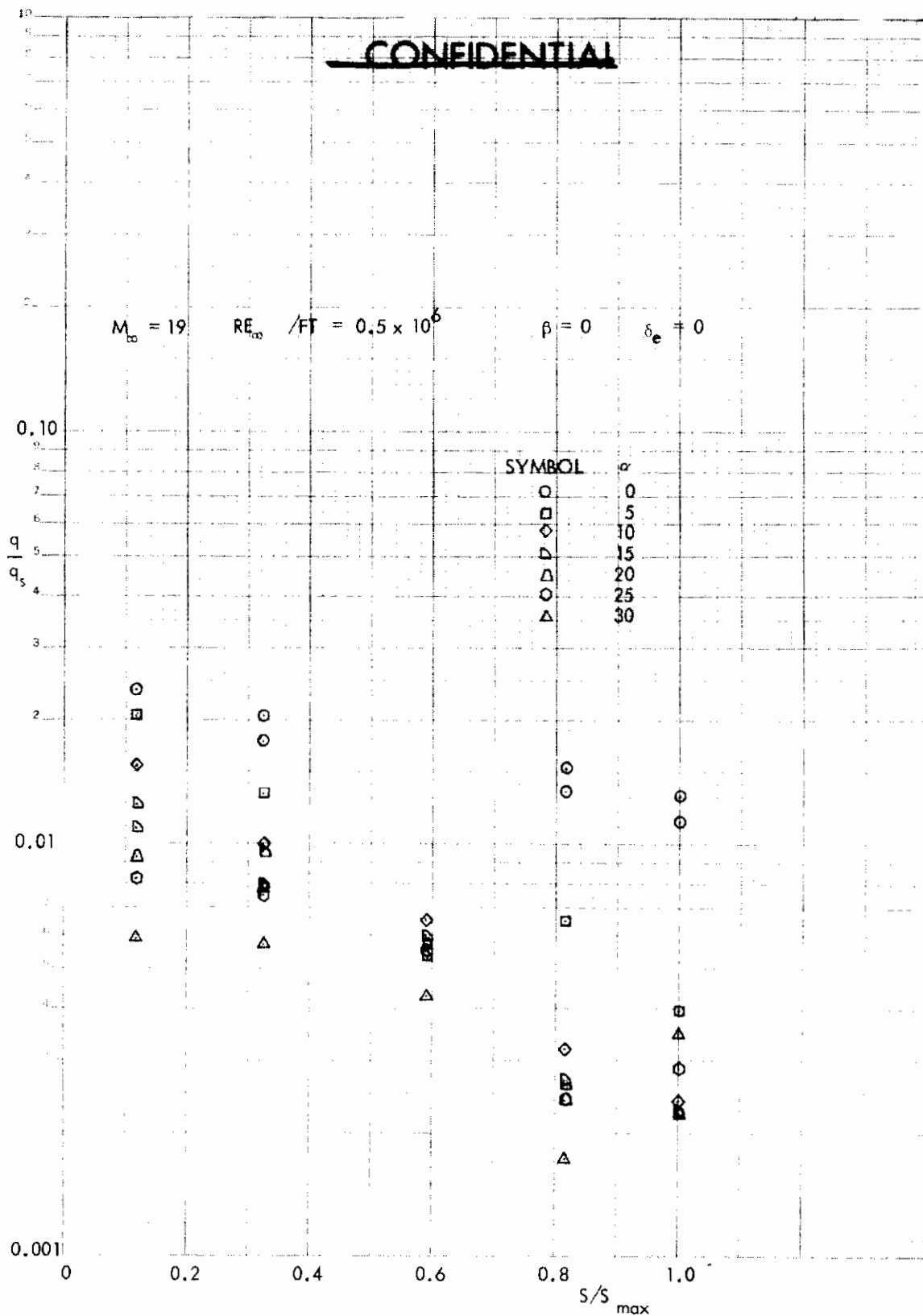
FIGURE 235 (U) TUNNEL F UPPER SURFACE SPANWISE HEATING RATES AT X/L = 0.50, β=0
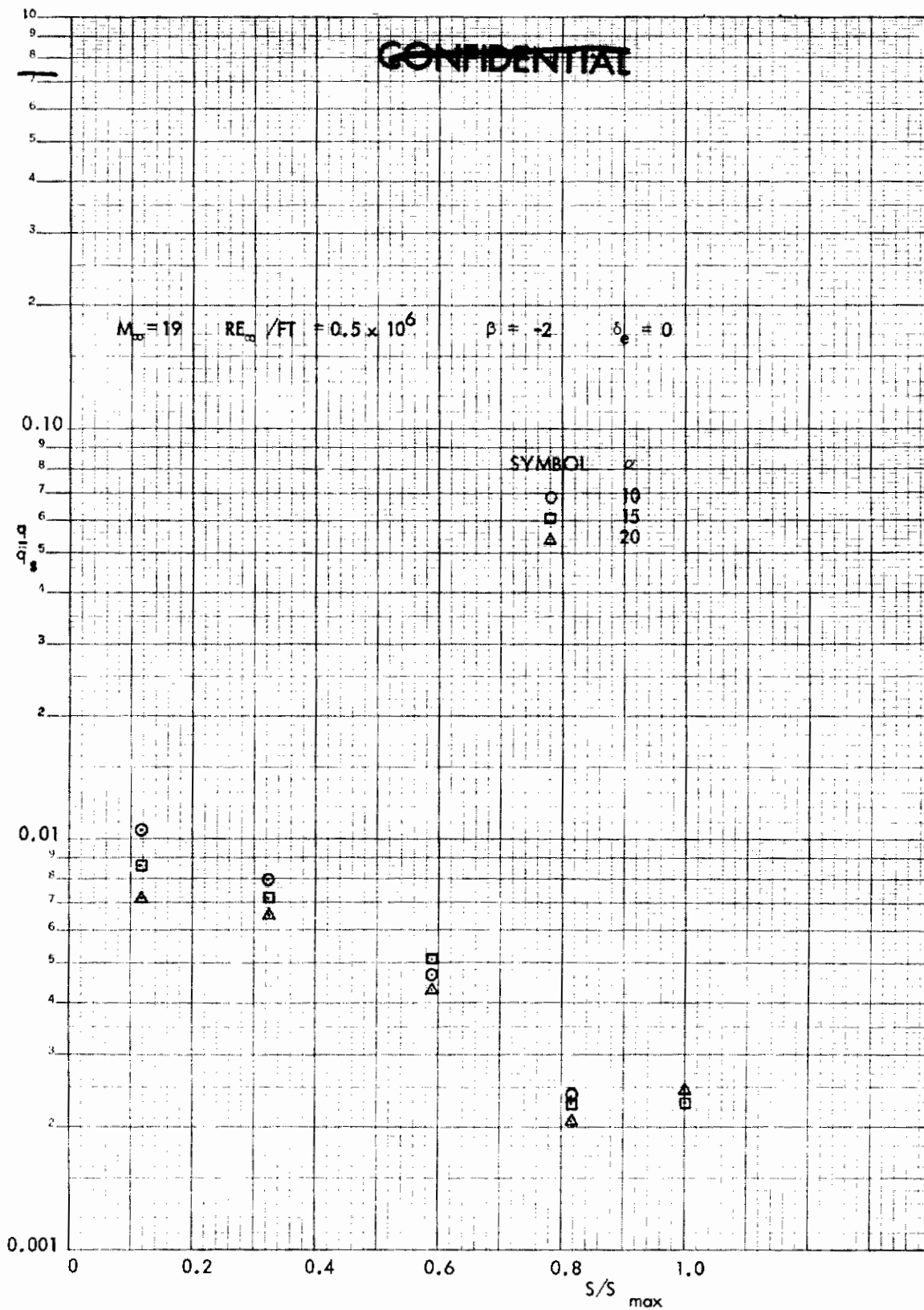
FIGURE 236 (U) TUNNEL F UPPER SURFACE SPANWISE HEATING RATES AT X/L = 0.50, β=-2
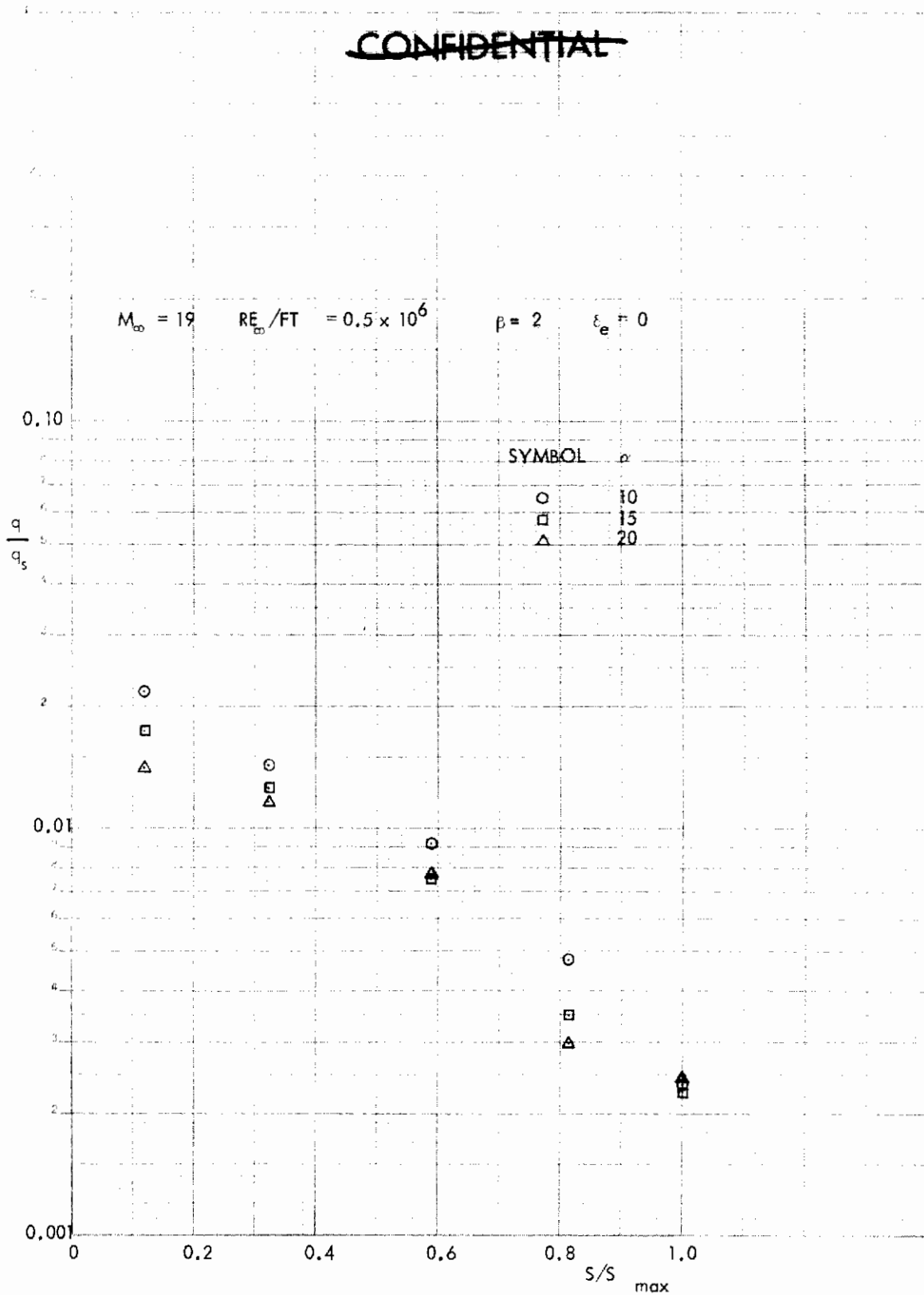
FIGURE 237 (U) TUNNEL F UPPER SURFACE SPANWISE HEATING RATES AT X/L = 0.50,
β=2
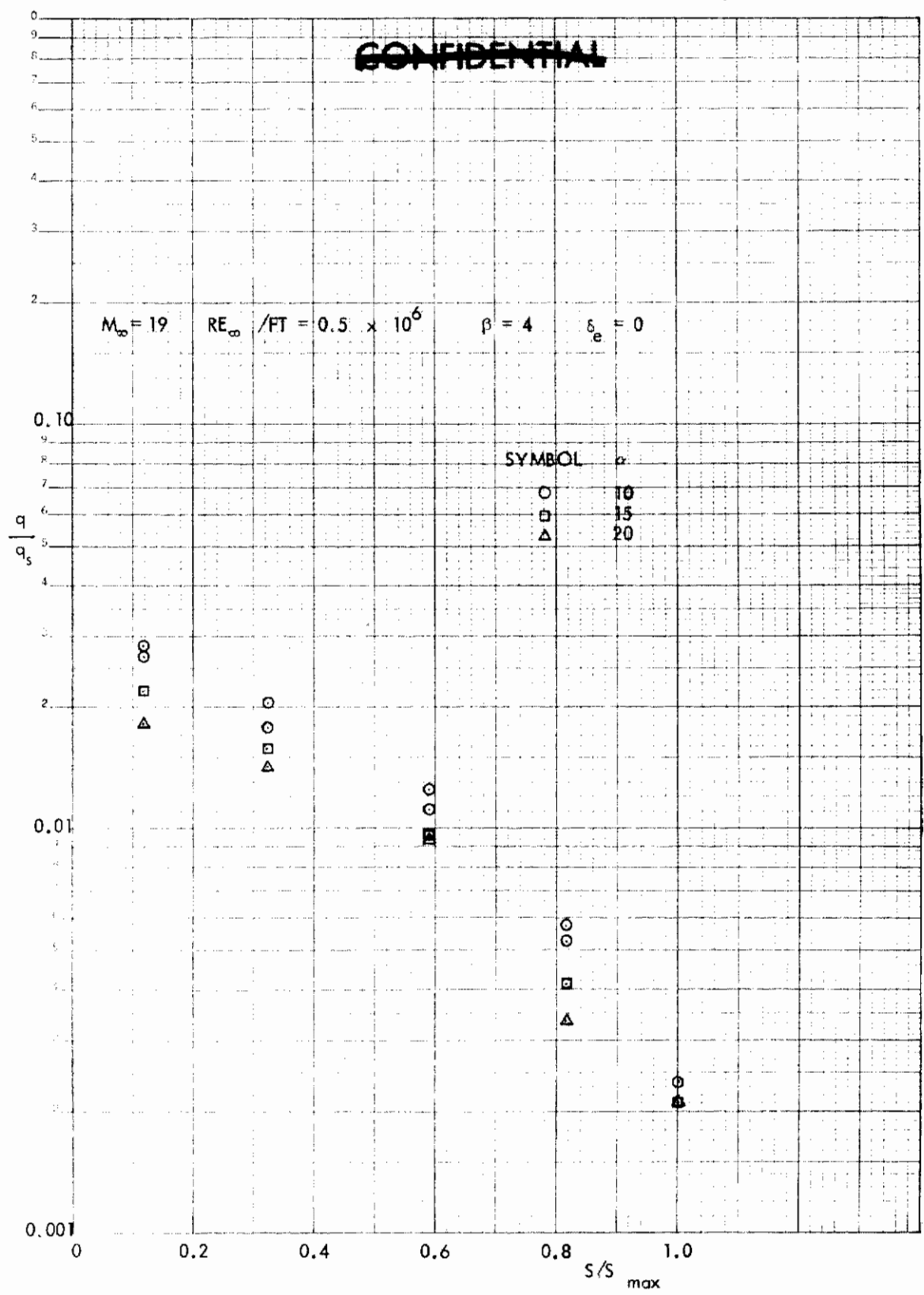
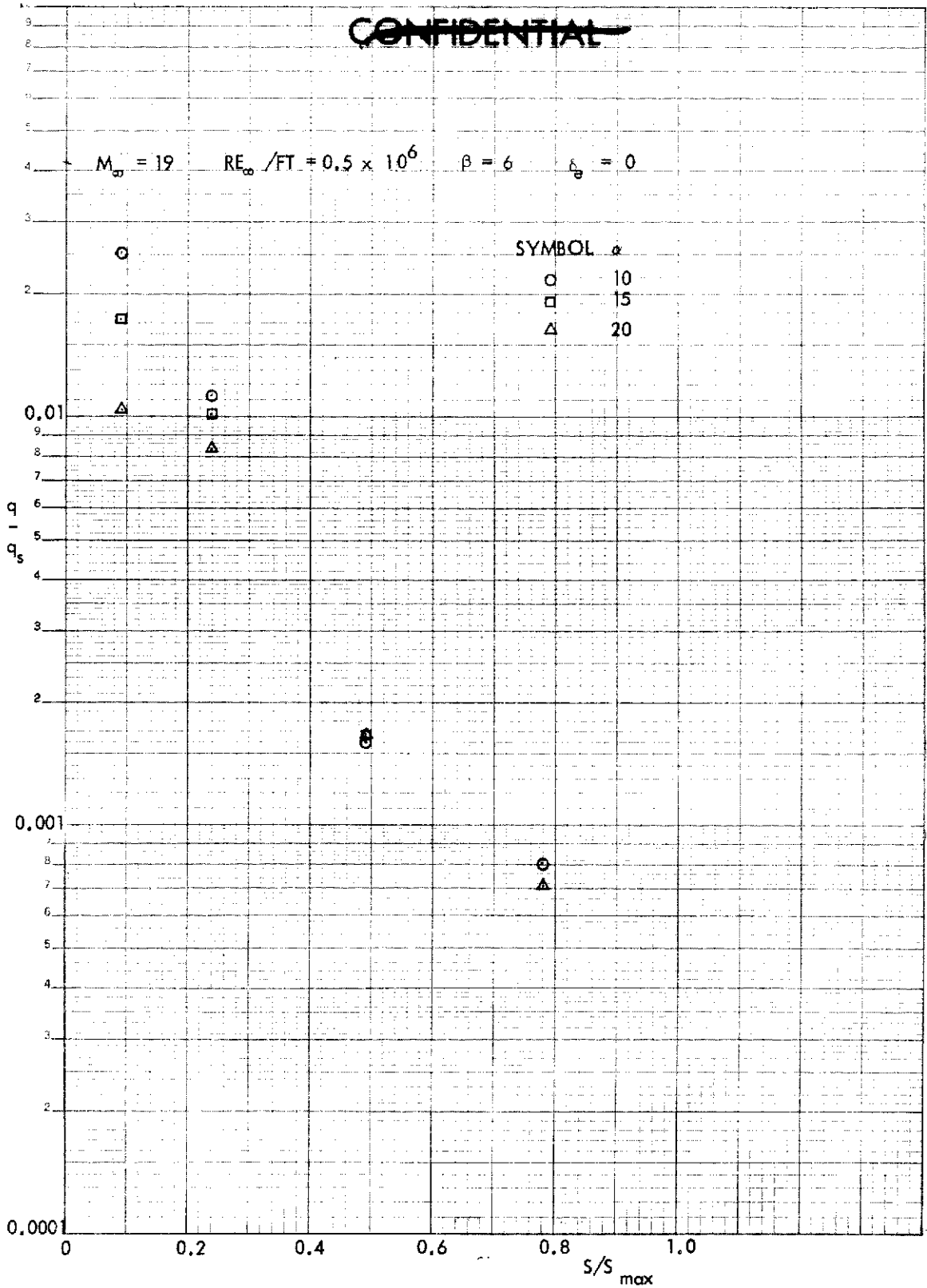FIGURE 238 (U) TUNNEL F UPPER SURFACE SPANWISE HEATING RATES AT X/L = 0.50,
β=4

$M_\infty = 19$ $RE_\infty/FT = 0.5 \times 10^6$ $\beta = 6$ $\delta_e = 0$

SYMBOL	α
○	10
□	15
△	20
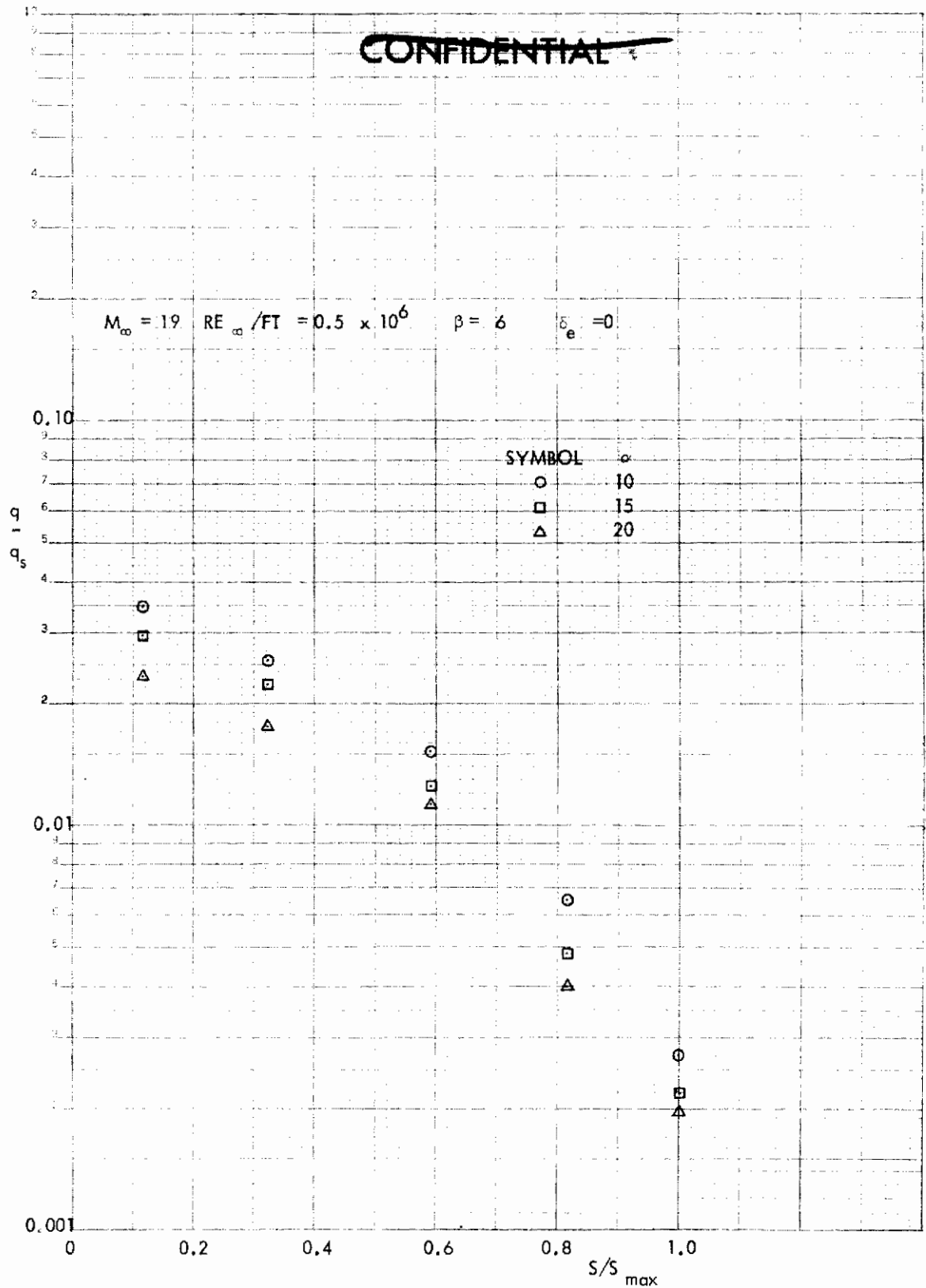
FIGURE 239   (U) TUNNEL F UPPER SURFACE SPANWISE HEATING RATES AT X/L = 0.50, β=6
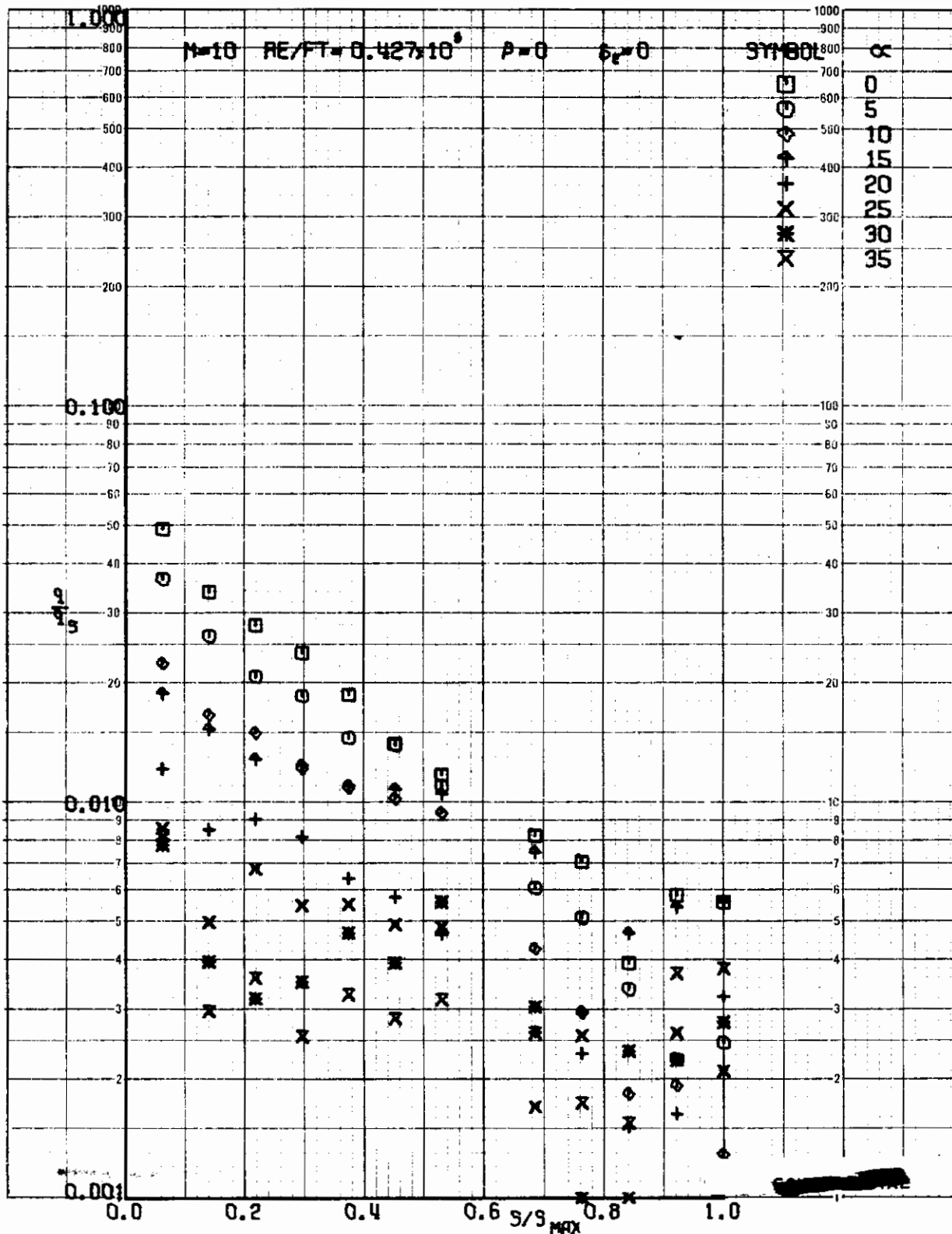
FIGURE 240 (U) TUNNEL C UPPER SURFACE SPANWISE HEATING RATES AT X/L = 0.75, β=0
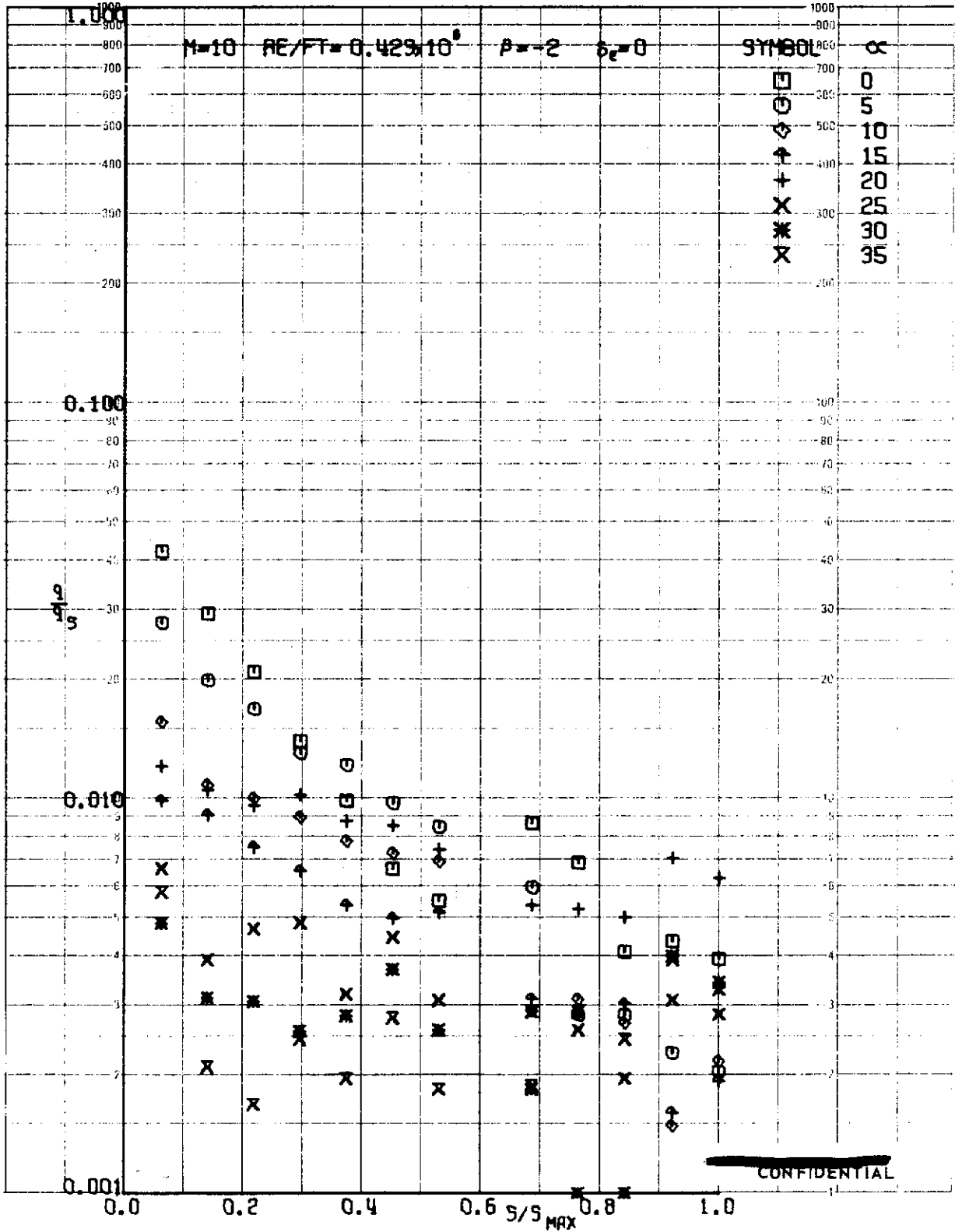
FIGURE 241 (U) TUNNEL C UPPER SURFACE SPANWISE HEATING RATES AT X/L = 0.75, β=-2

FIGURE 242   (U) TUNNEL C UPPER SURFACE SPANWISE HEATING RATES AT X/L = 0.75,
β=2

FIGURE 243   (U) TUNNEL C UPPER SURFACE SPANWISE HEATING RATES AT X/L = 0.75, β=4

FIGURE 244 (U) TUNNEL C UPPER SURFACE SPANWISE HEATING RATES AT X/L = 0.75, β=6

FIGURE 245 (U) TUNNEL C UPPER SURFACE SPANWISE HEATING RATES AT X/L = 0.75, β=0

FIGURE 246 (U) TUNNEL C UPPER SURFACE SPANWISE HEATING RATES AT X/L = 0.96, $\beta=0$

FIGURE 247 (U) TUNNEL C UPPER SURFACE SPANWISE HEATING RATES AT X/L = 0.96,
β=-2

FIGURE 248 (U) TUNNEL C UPPER SURFACE SPANWISE HEATING RATES AT X/L = 0.96,
β=2

FIGURE 249 (U) TUNNEL C UPPER SURFACE SPANWISE HEATING RATES AT X/L = 0.96, β=4

FIGURE 250 (U) TUNNEL C UPPER SURFACE SPANWISE HEATING RATES AT X/L = 0.96, β=6

341

FIGURE 251 (U) TUNNEL C UPPER SURFACE SPANWISE HEATING RATES AT X/L = 0.96, β=0

FIGURE 252 (U) TUNNEL F UPPER SURFACE SPANWISE HEATING RATES AT X/L = 0.96,
β=0

FIGURE 253 (U) TUNNEL F UPPER SURFACE SPANWISE HEATING RATES AT X/L = 0.96, β=-2

$M_\infty = 19$ $RE_\infty /FT = 0.5 \times 10^6$ $\beta = 2$ $\delta_e = 0$

SYMBOL α
⊙   10
⊡   15
△   20

FIGURE 254 (U) TUNNEL F UPPER SURFACE SPANWISE HEATING RATES AT X/L = 0.96,
          β=2

FIGURE 255 (U) TUNNEL F UPPER SURFACE SPANWISE HEATING RATES AT X/L = 0.96, β=4

FIGURE 256 (U) TUNNEL F UPPER SURFACE SPANWISE HEATING RATES AT X/L = 0.96, β=6
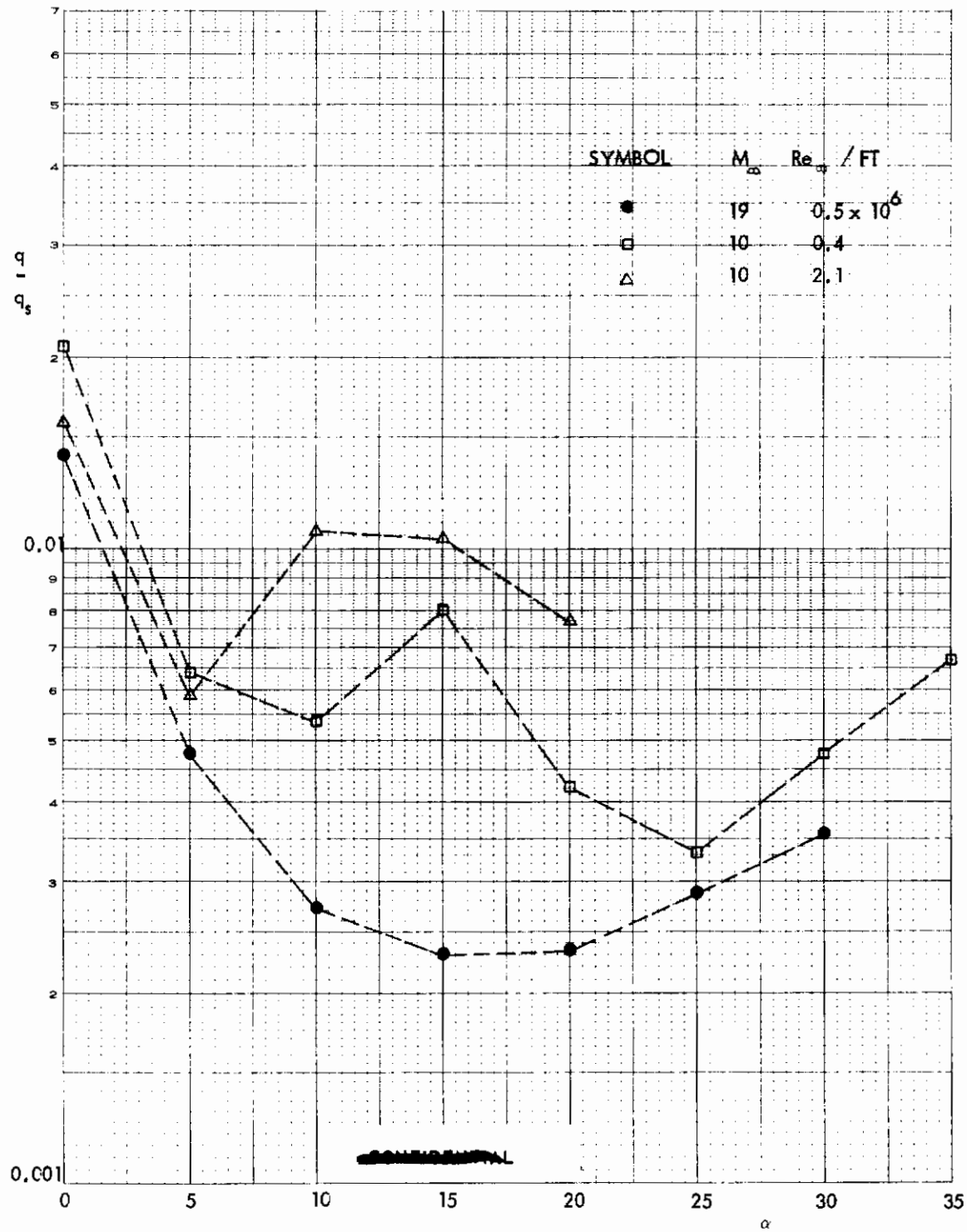
FIGURE 257 (U) COMPARISON OF TUNNEL C AND F UPPER CENTERLINE HEATING RATES
AT X/L = 0.40
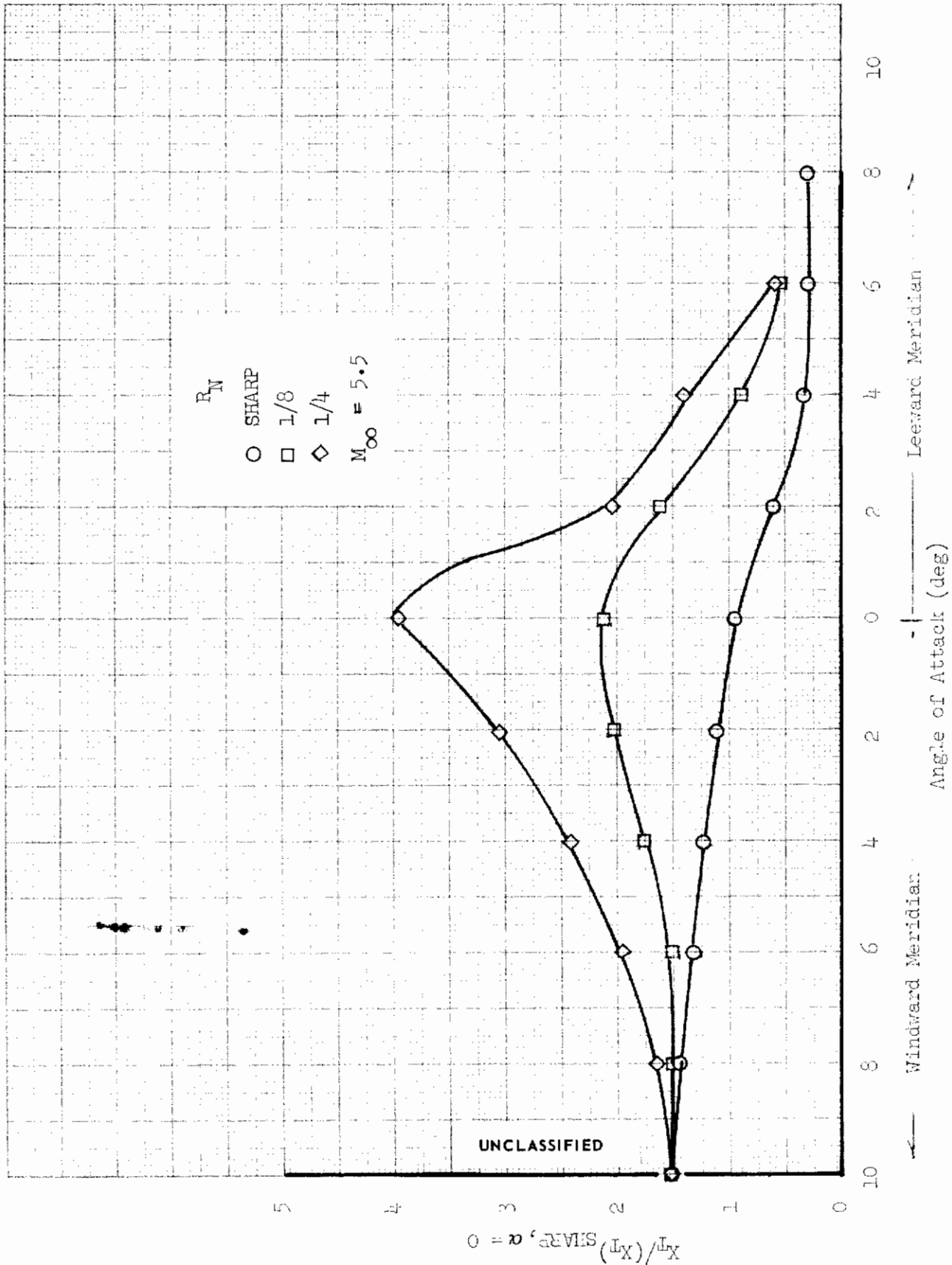
FIGURE 258 (U) EFFECT OF ANGLE OF ATTACK ON CONE BOUNDARY LAYER TRANSITION
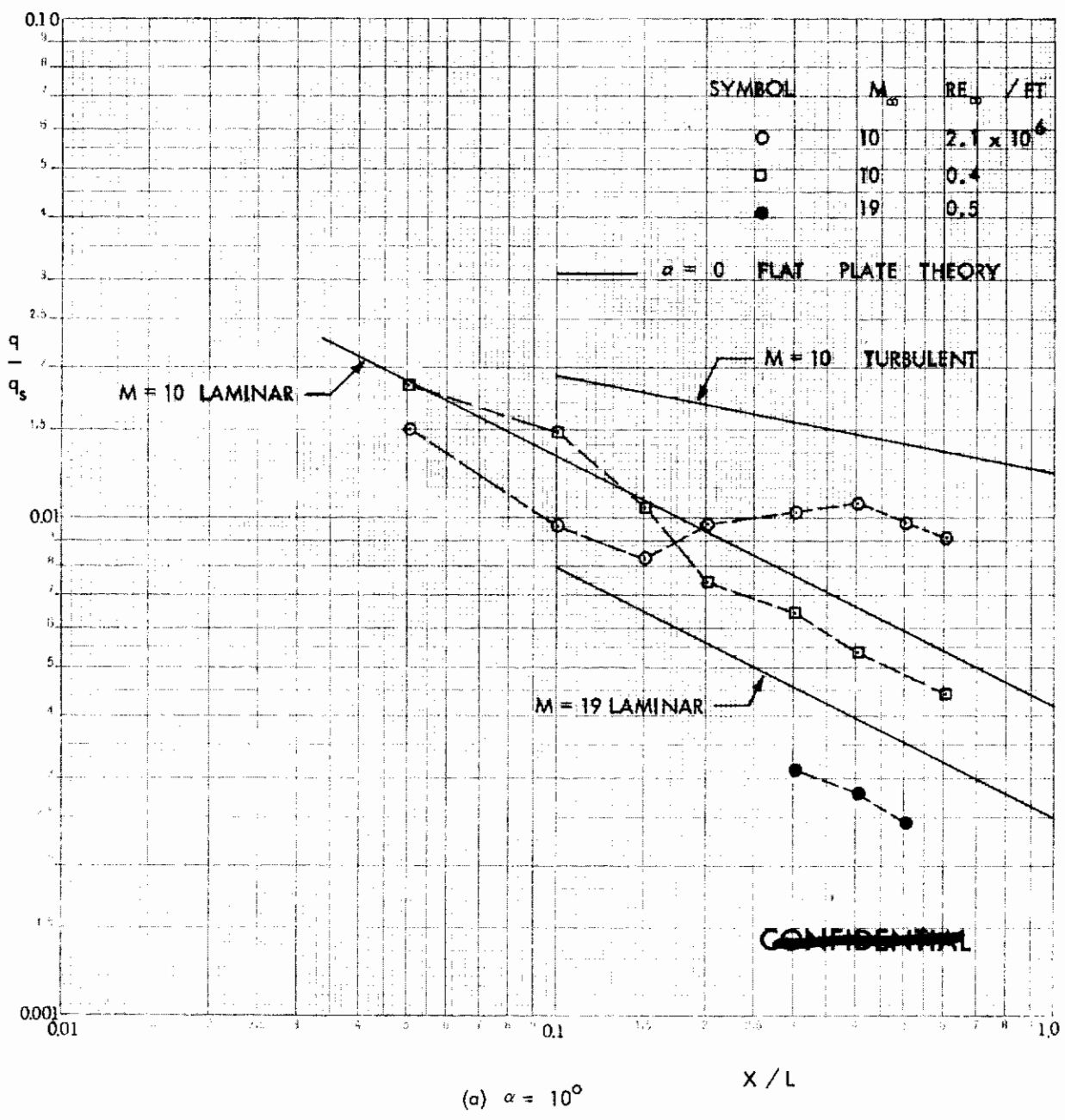
FIGURE 259 (U) COMPARISON OF UPPER SURFACE CENTERLINE HEATING DISTRIBUTIONS
FROM TUNNELS C AND F

SYMBOL	M_∞	RE_∞ /FT
⊖	10	2.1×10^6
⊡	10	0.4
■	19	0.5

$\alpha = 0$ FLAT PLATE THEORY

M = 10 TURBULENT

M = 10 LAMINAR

M = 19 LAMINAR
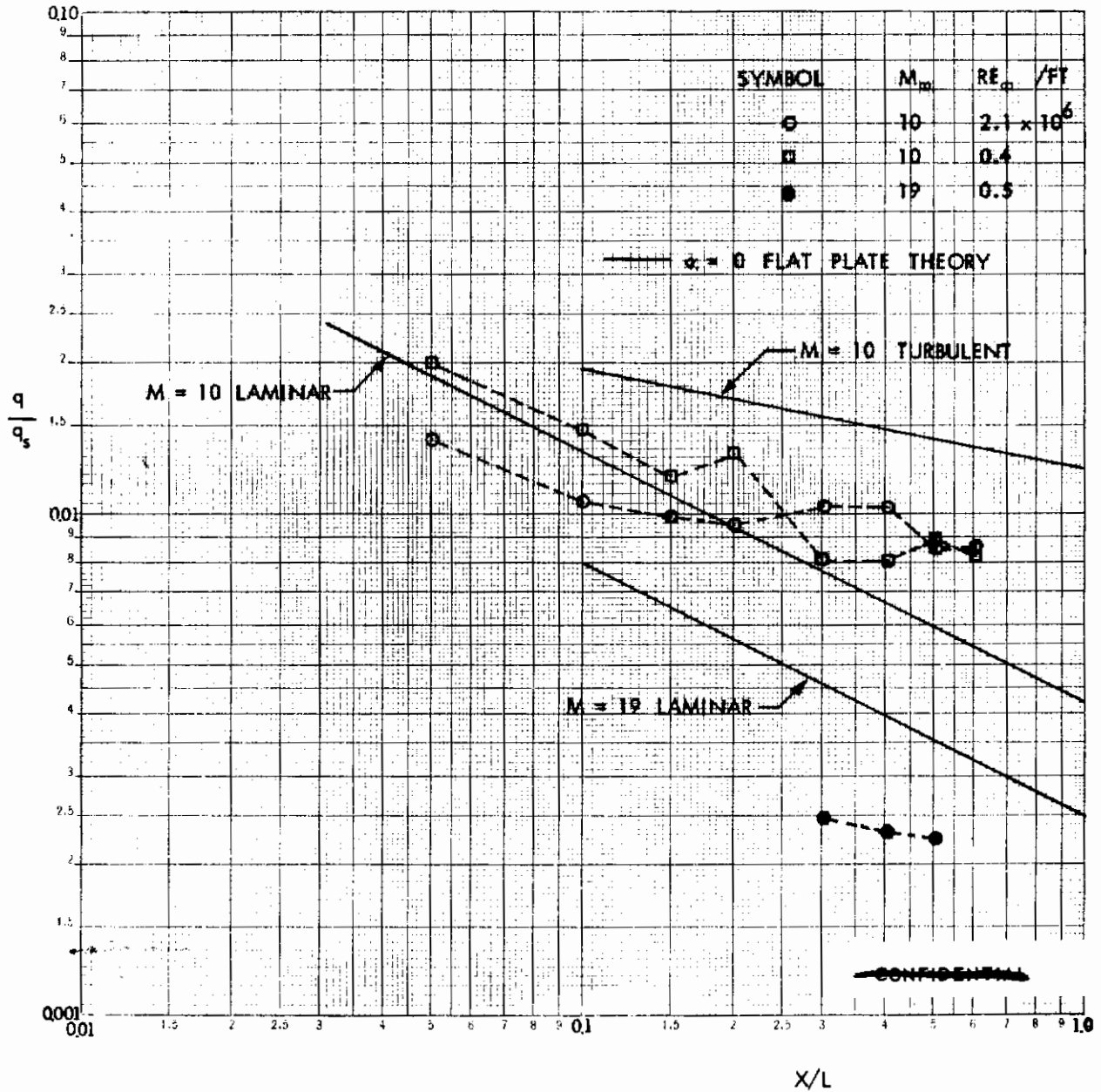
(b) $\alpha = 15°$

FIGURE 259 (U) (CONTINUED) COMPARISON OF UPPER SURFACE CENTERLINE HEATING
DISTRIBUTIONS FROM TUNNELS C AND F

351
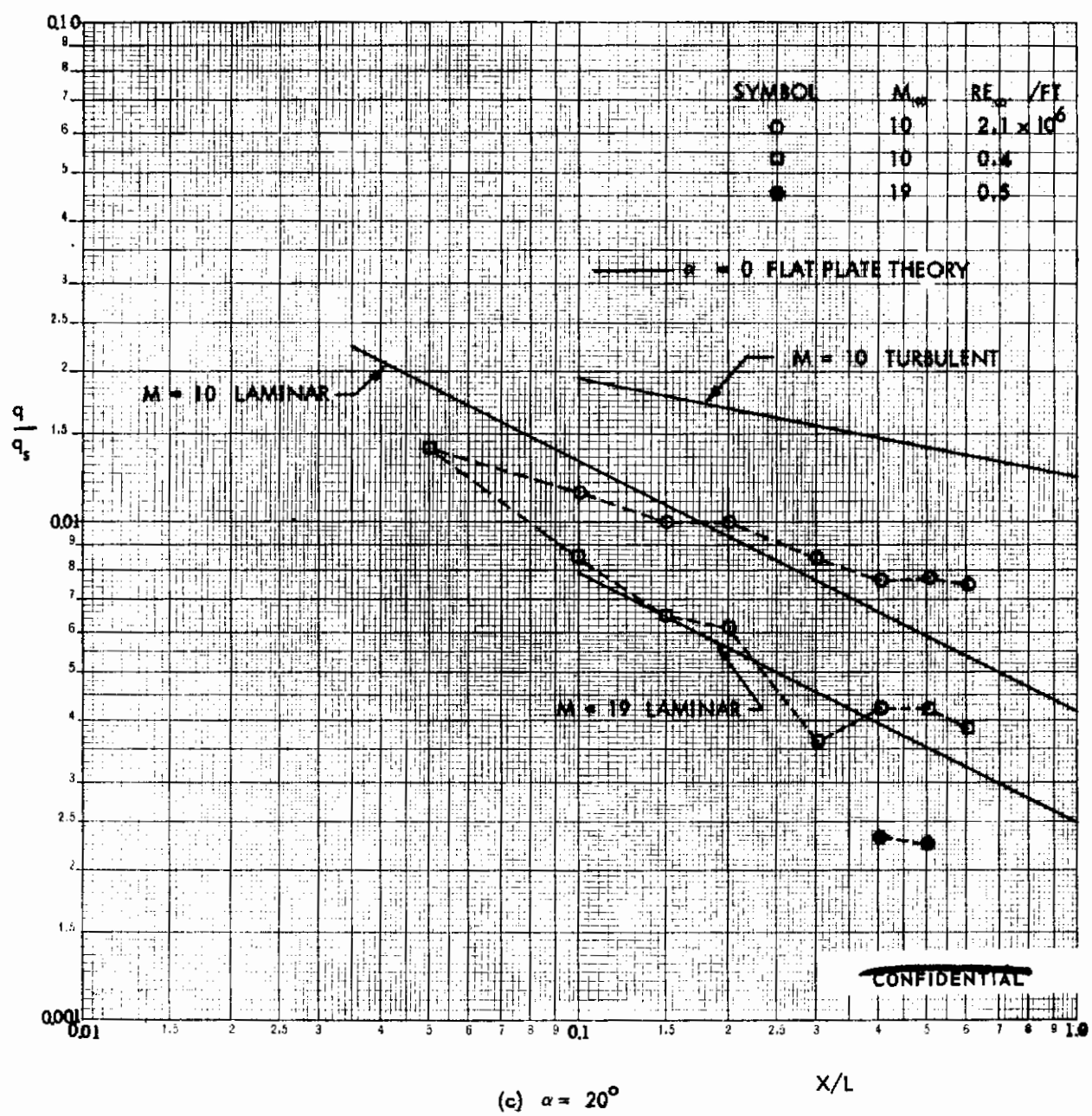
FIGURE 259 (U) (CONCLUDED) COMPARISON OF UPPER SURFACE CENTERLINE HEATING
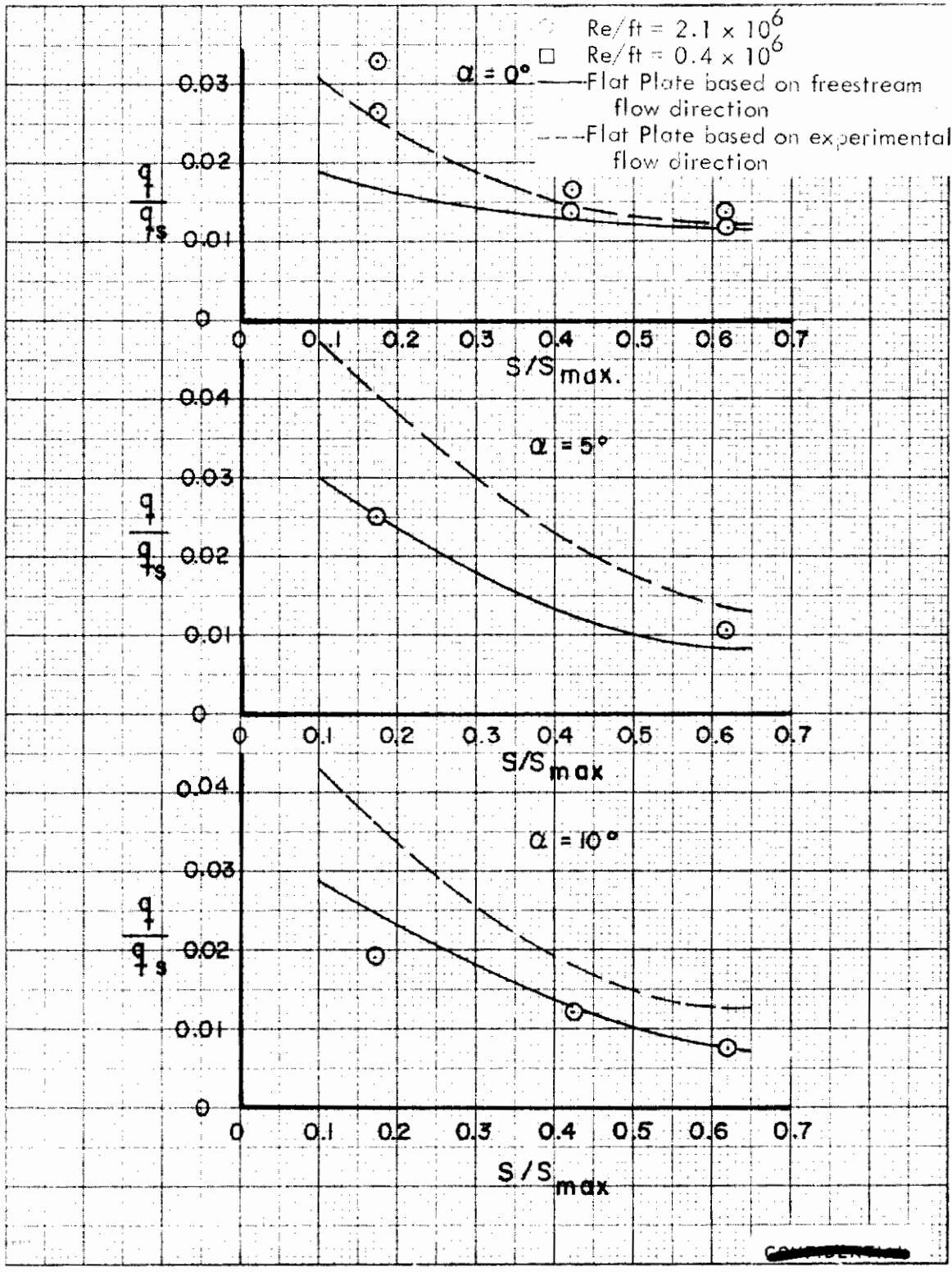DISTRIBUTIONS FROM TUNNELS C AND F
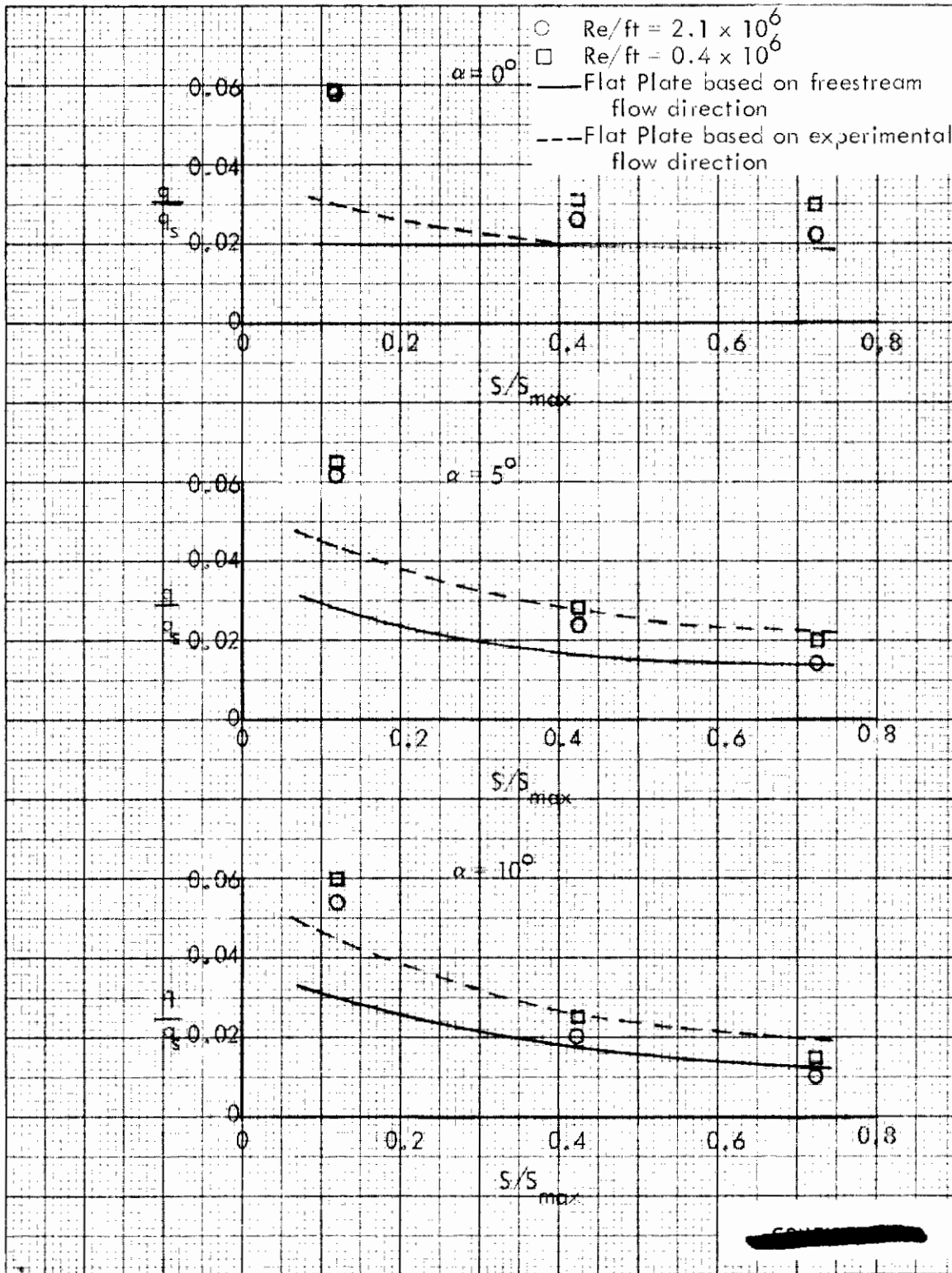
FIGURE 260   (U) CORRELATION OF TUNNEL C UPPER SURFACE SPANWISE HEATING
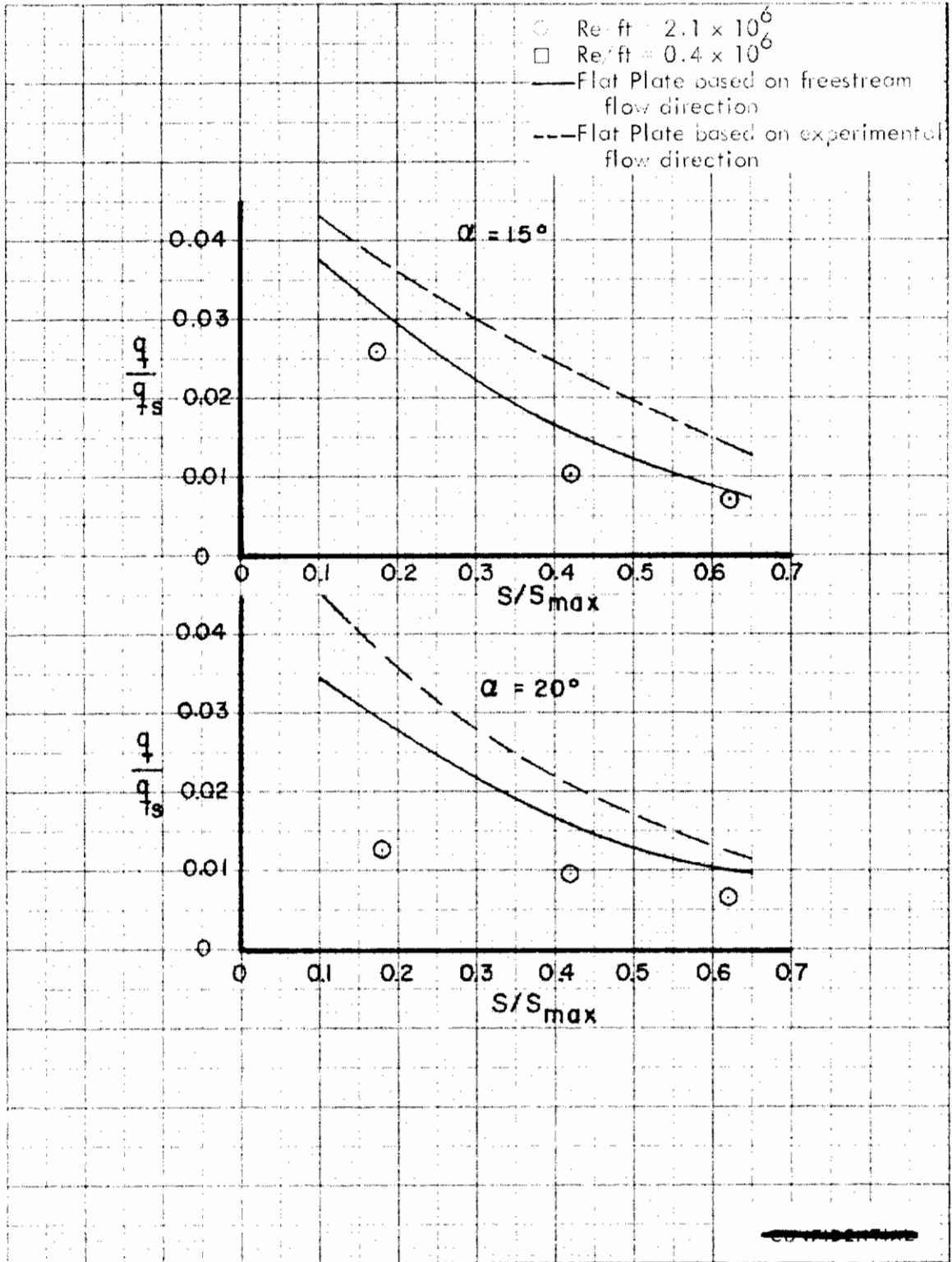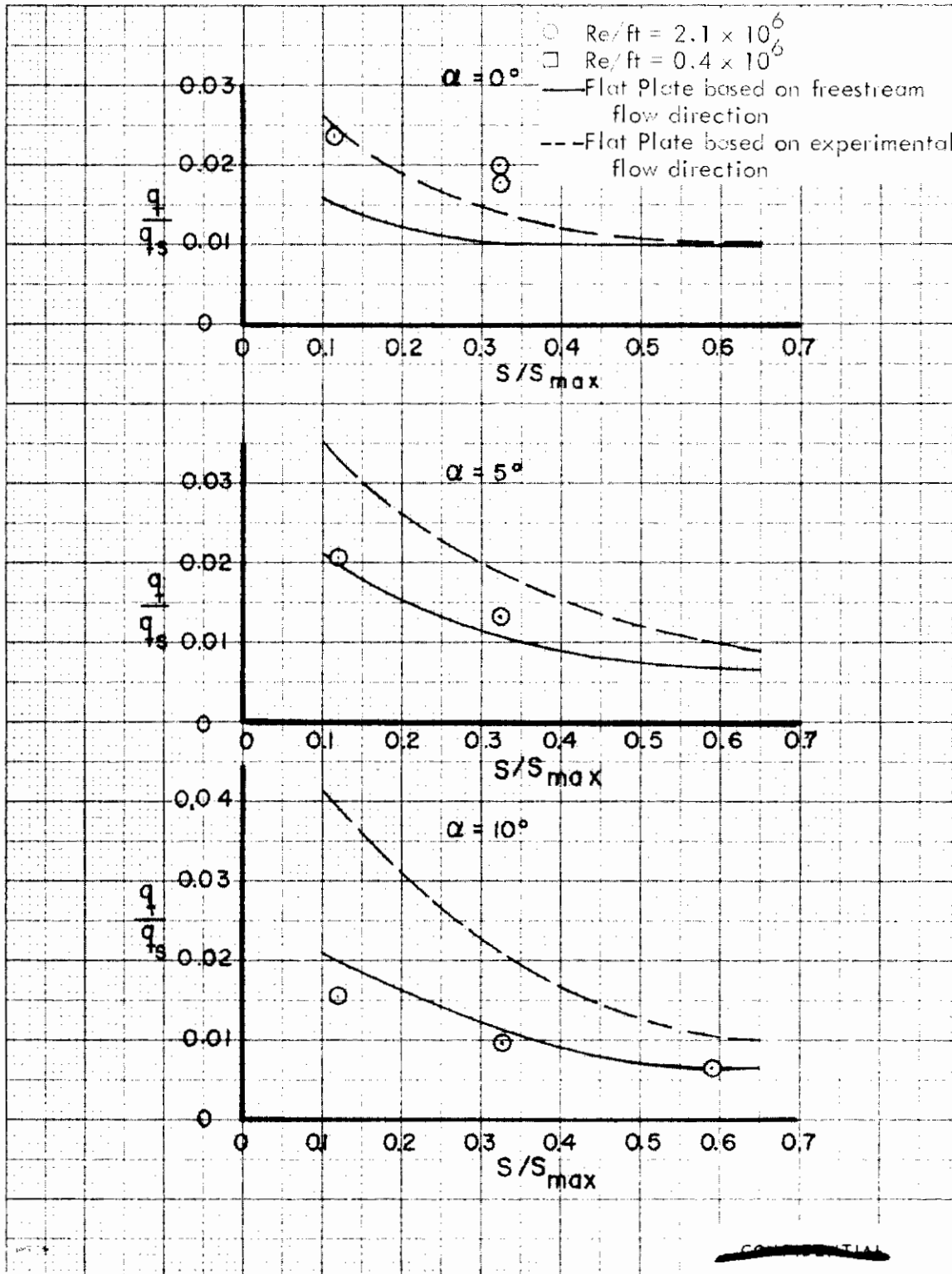RATES AT X/L = 0.15, β=0
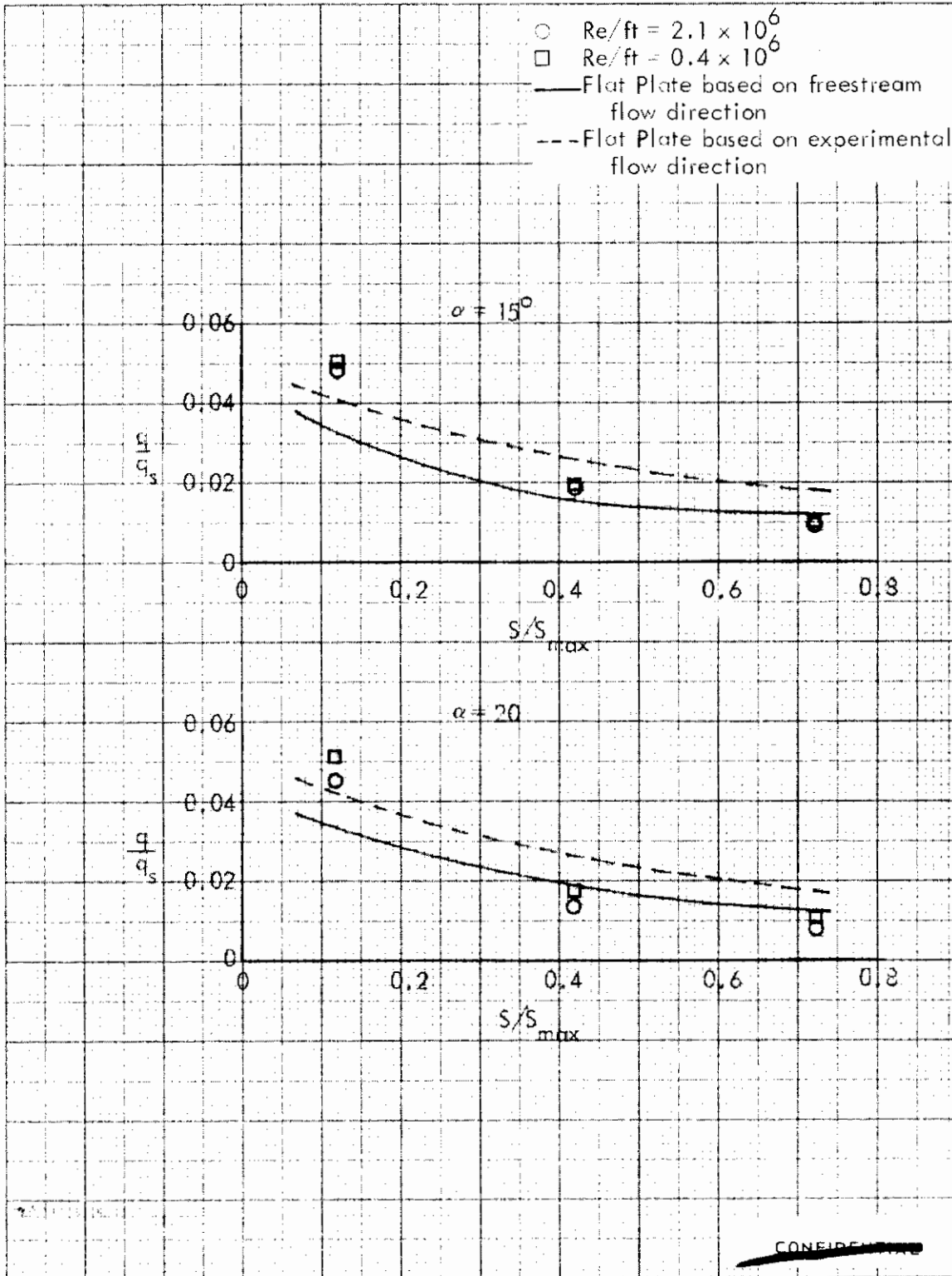
FIGURE 260 (U) CORRELATION OF TUNNEL C UPPER SURFACE SPANWISE HEATING
RATES AT X/L = 0.15, β=0 (CONCLUDED)

354
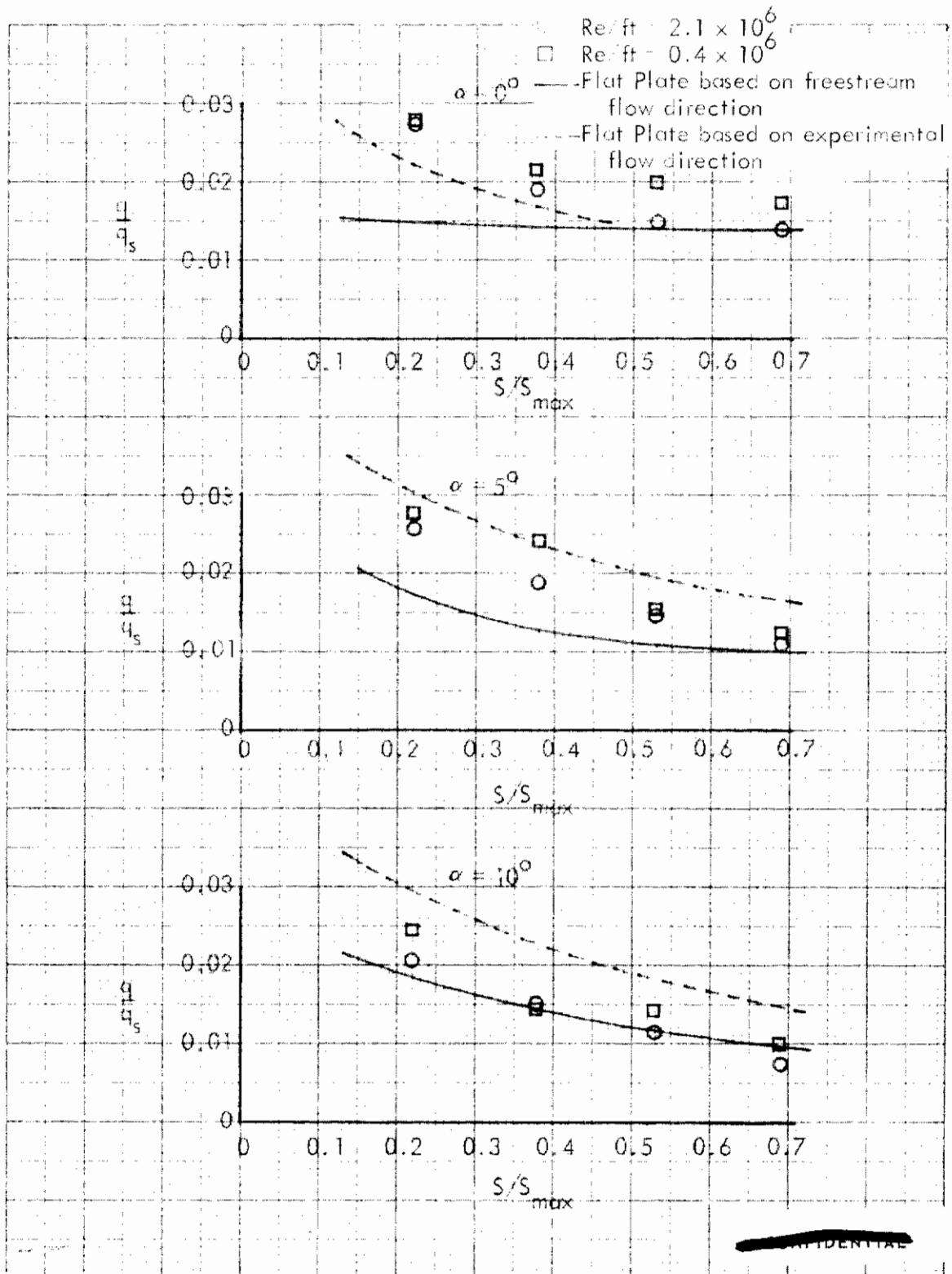
FIGURE 261   (U) CORRELATION OF TUNNEL C UPPER SURFACE SPANWISE HEATING
RATES AT X/L = 0.30, β=0

FIGURE 261 (U) CORRELATION OF TUNNEL C UPPER SURFACE SPANWISE HEATING
RATES AT X/L = 0.30, β=0 (CONCLUDED)

FIGURE 262 (U) CORRELATION OF TUNNEL C UPPER SURFACE SPANWISE HEATING
RATES AT X/L = 0.50, β=0
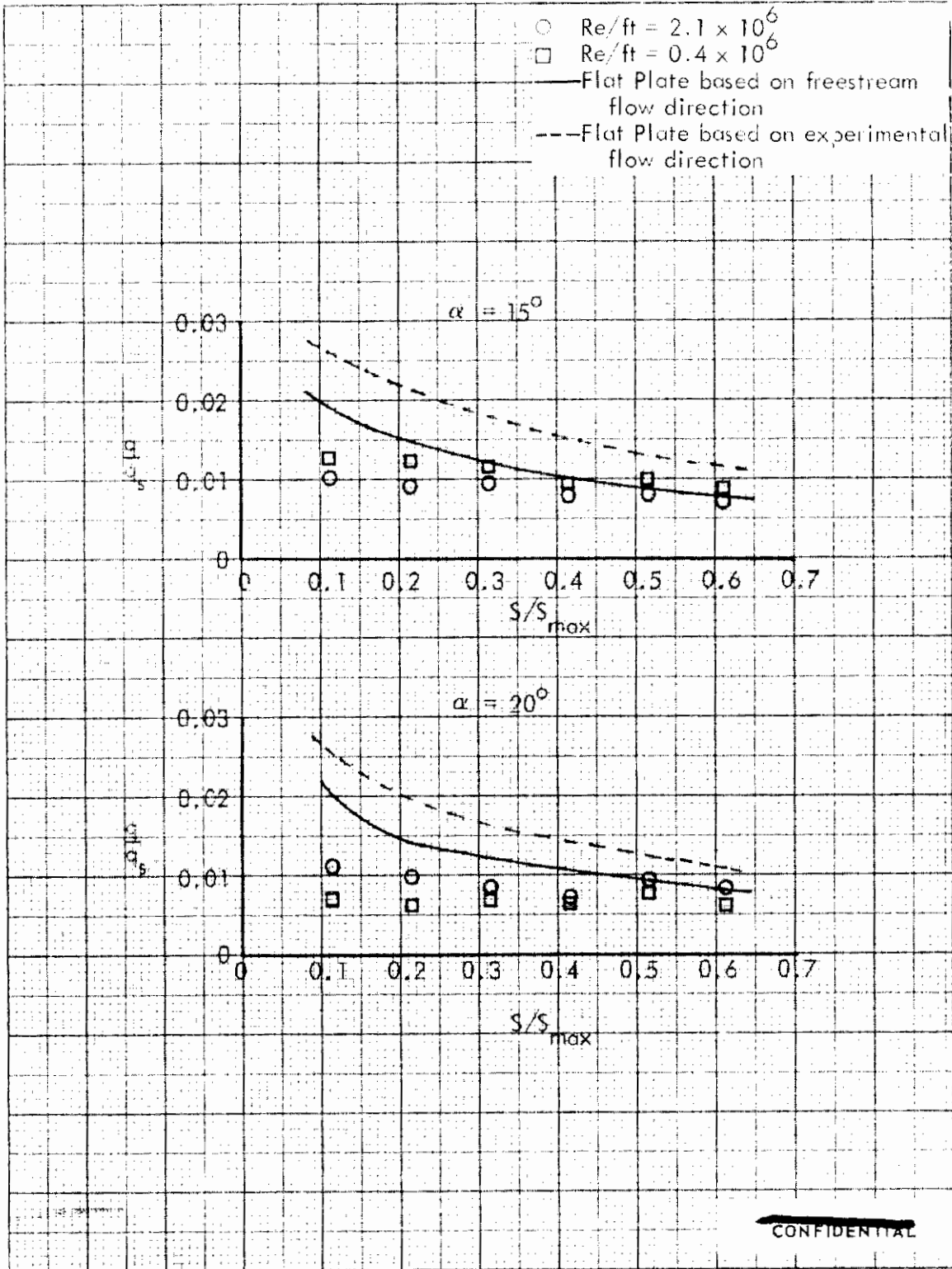
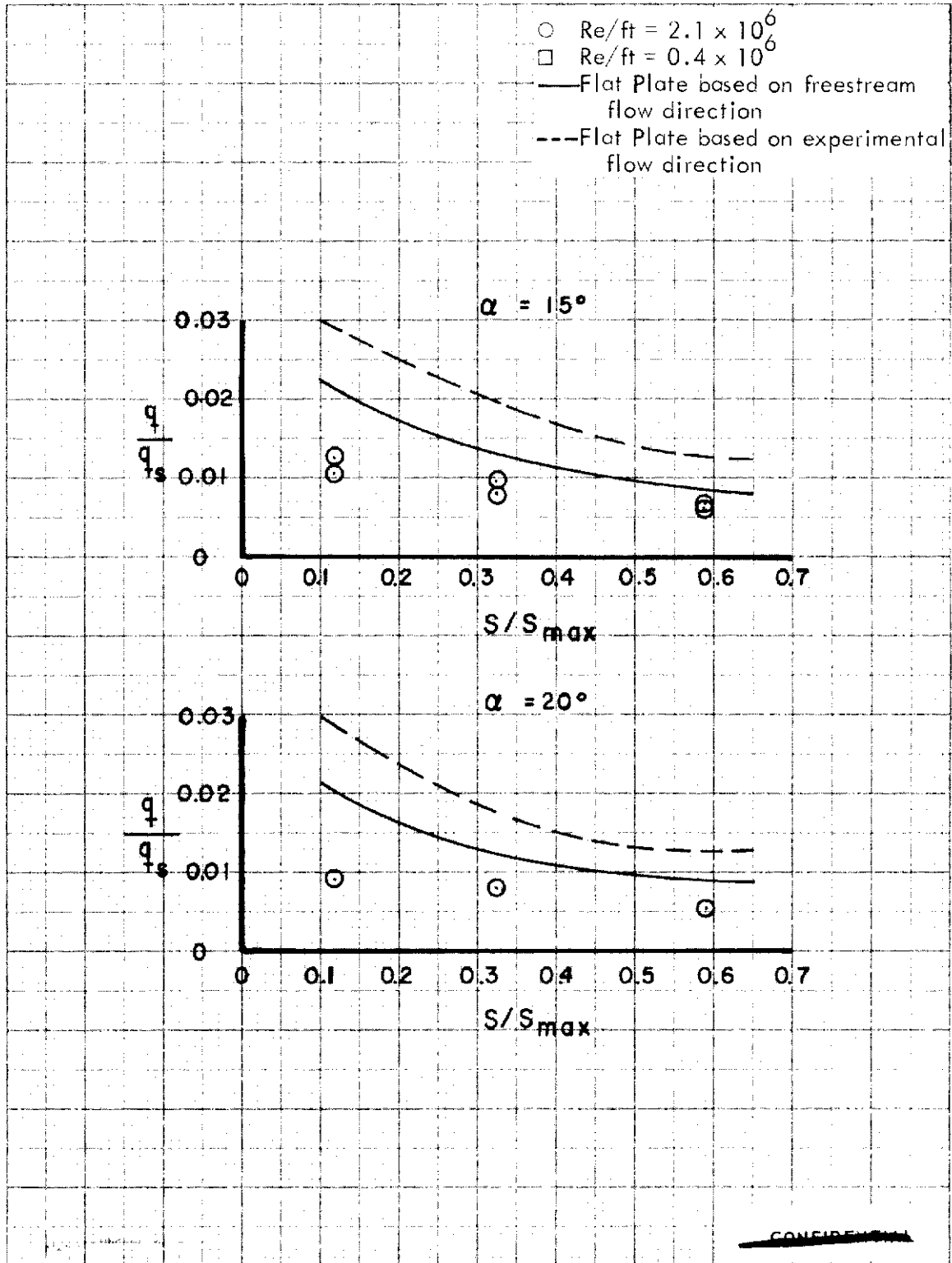FIGURE 262 (U) CORRELATION OF TUNNEL C UPPER SURFACE SPANWISE HEATING
RATES AT X/L = 0.50, β=0 (CONCLUDED)

FIGURE 263 (U) CORRELATION OF TUNNEL F UPPER SURFACE SPANWISE HEATING RATES AT X/L = 0.30, β=0

FIGURE 263 (U) CORRELATION OF TUNNEL F UPPER SURFACE SPANWISE HEATING
RATES AT X/L = 0.30, β=0 (CONCLUDED)

FIGURE 264 (U) CORRELATION OF TUNNEL F UPPER SURFACE SPANWISE HEATING
RATES AT X/L = 0.50, β=0

361

FIGURE 264   (U) CORRELATION OF TUNNEL F UPPER SURFACE SPANWISE HEATING
RATES AT X/L = 0.30, $\beta=0$ (CONCLUDED)
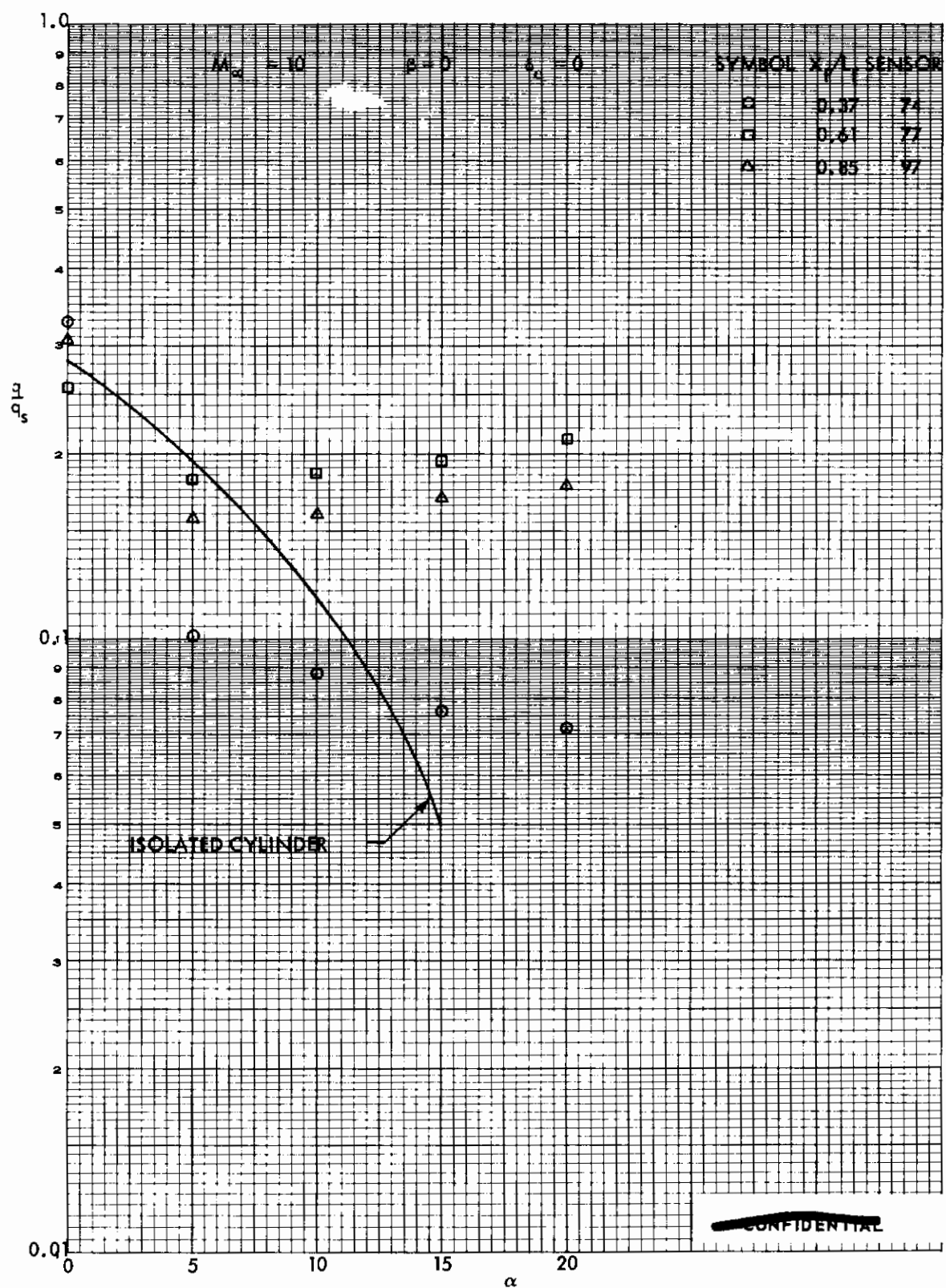
FIGURE 265   (C) ESTIMATED FIN STAGNATION LINE HEATING RATES
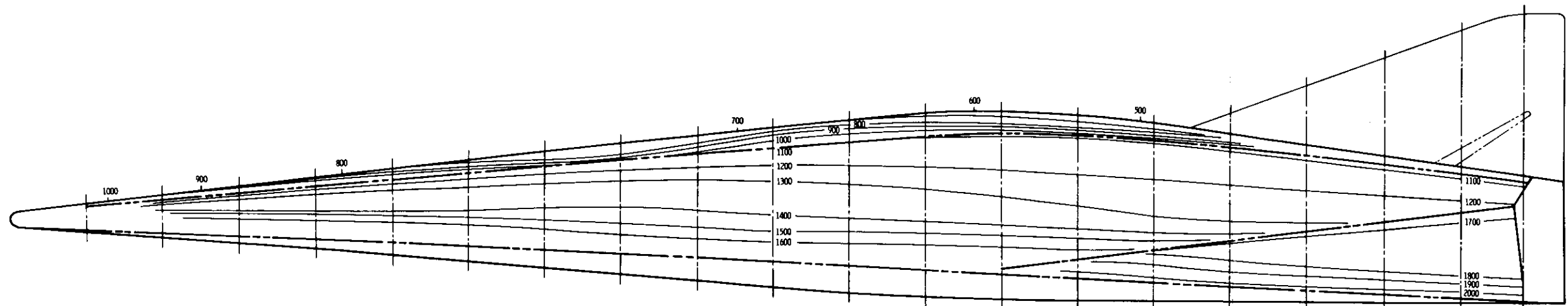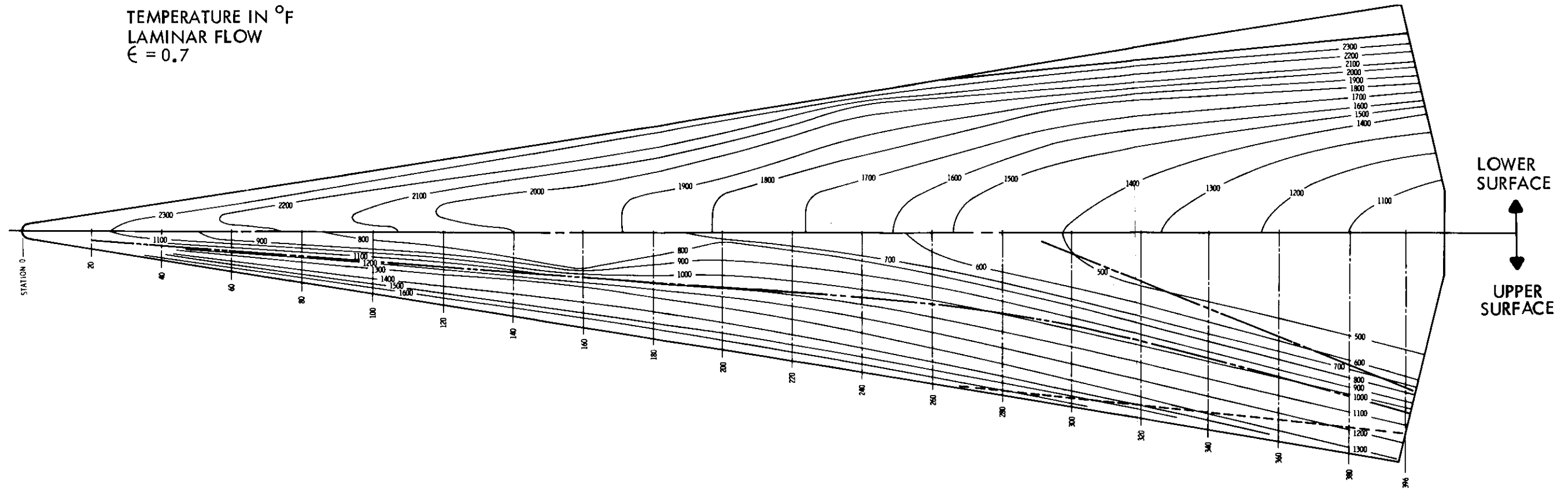
TEMPERATURE IN °F
LAMINAR FLOW
$\epsilon = 0.7$

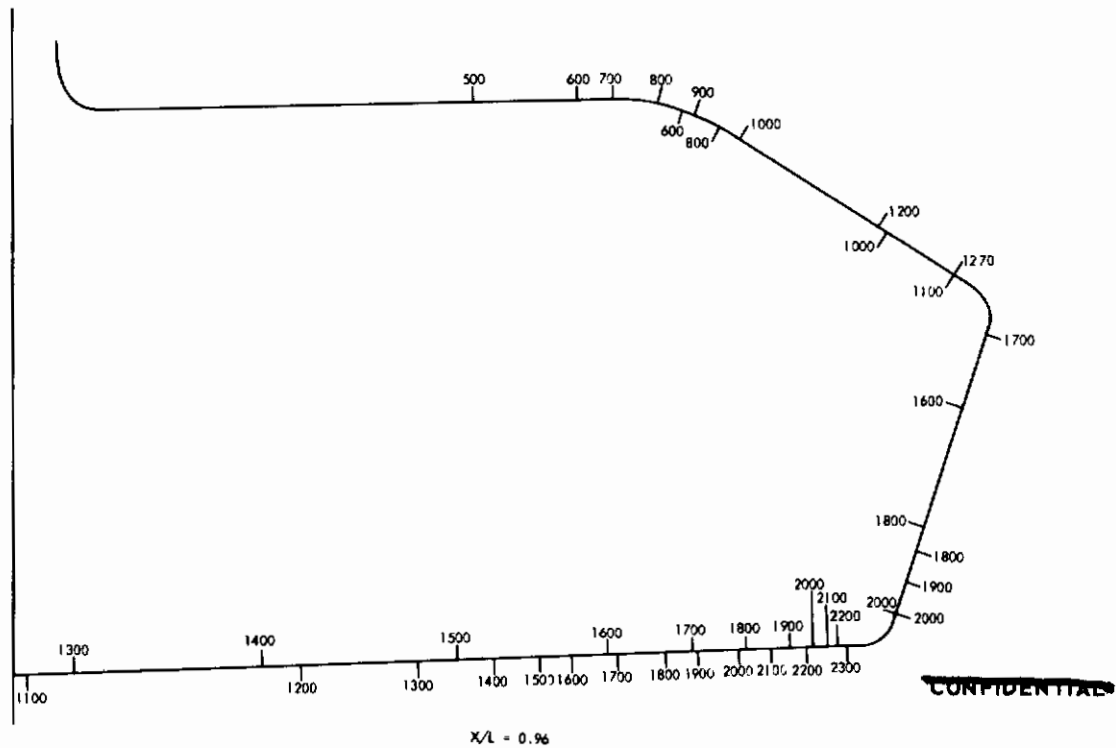FIGURE 266 (U) REVISED DESIGN POINT RADIATION
EQUILIBRIUM TEMPERATURES

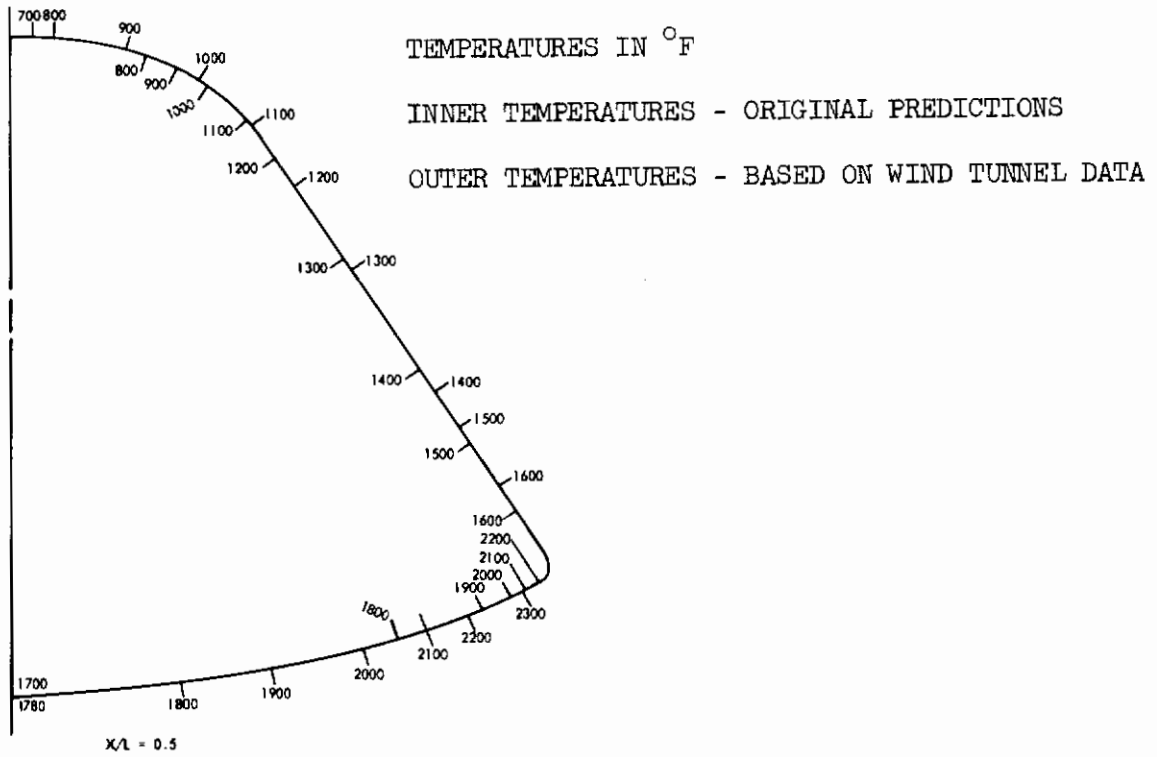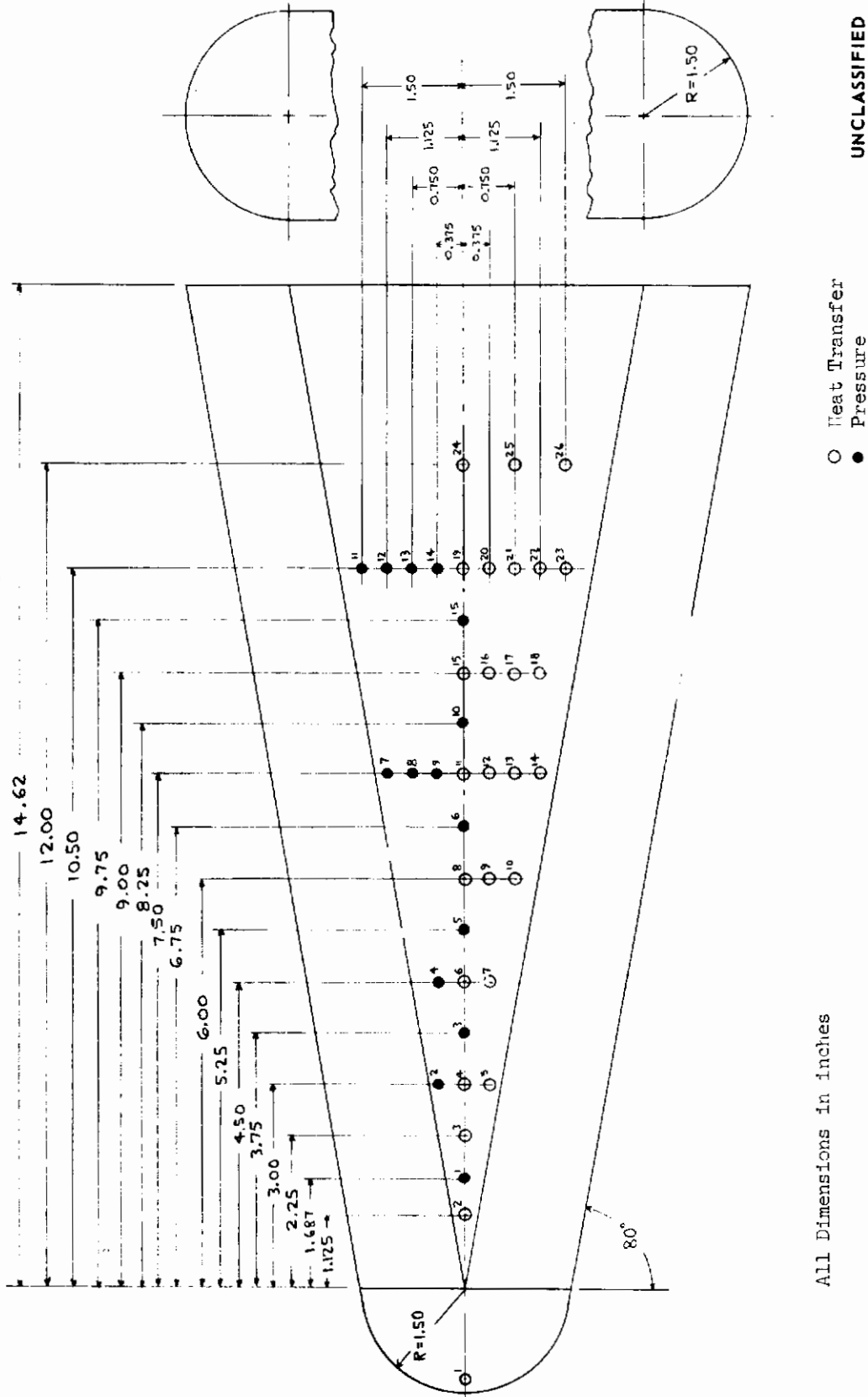365   (REVERSE SIDE IS BLANK)

TEMPERATURES IN °F

INNER TEMPERATURES - ORIGINAL PREDICTIONS

OUTER TEMPERATURES - BASED ON WIND TUNNEL DATA

X/L = 0.5

X/L = 0.96

FIGURE 267   (U) COMPARISON OF PREDICTED AND REVISED DESIGN POINT
             RADIATION EQUILIBRIUM TEMPERATURES AT 50 AND 96
             PERCENT CHORD

367

FIGURE 268   (U) HEAT TRANSFER AND PRESSURE SENSOR LAYOUT FOR 80° DELTA WING

All Dimensions in inches

○ Heat Transfer
● Pressure

UNCLASSIFIED

FIGURE 269 (U) CENTERLINE PRESSURE DISTRIBUTION AT $\alpha = 0°$

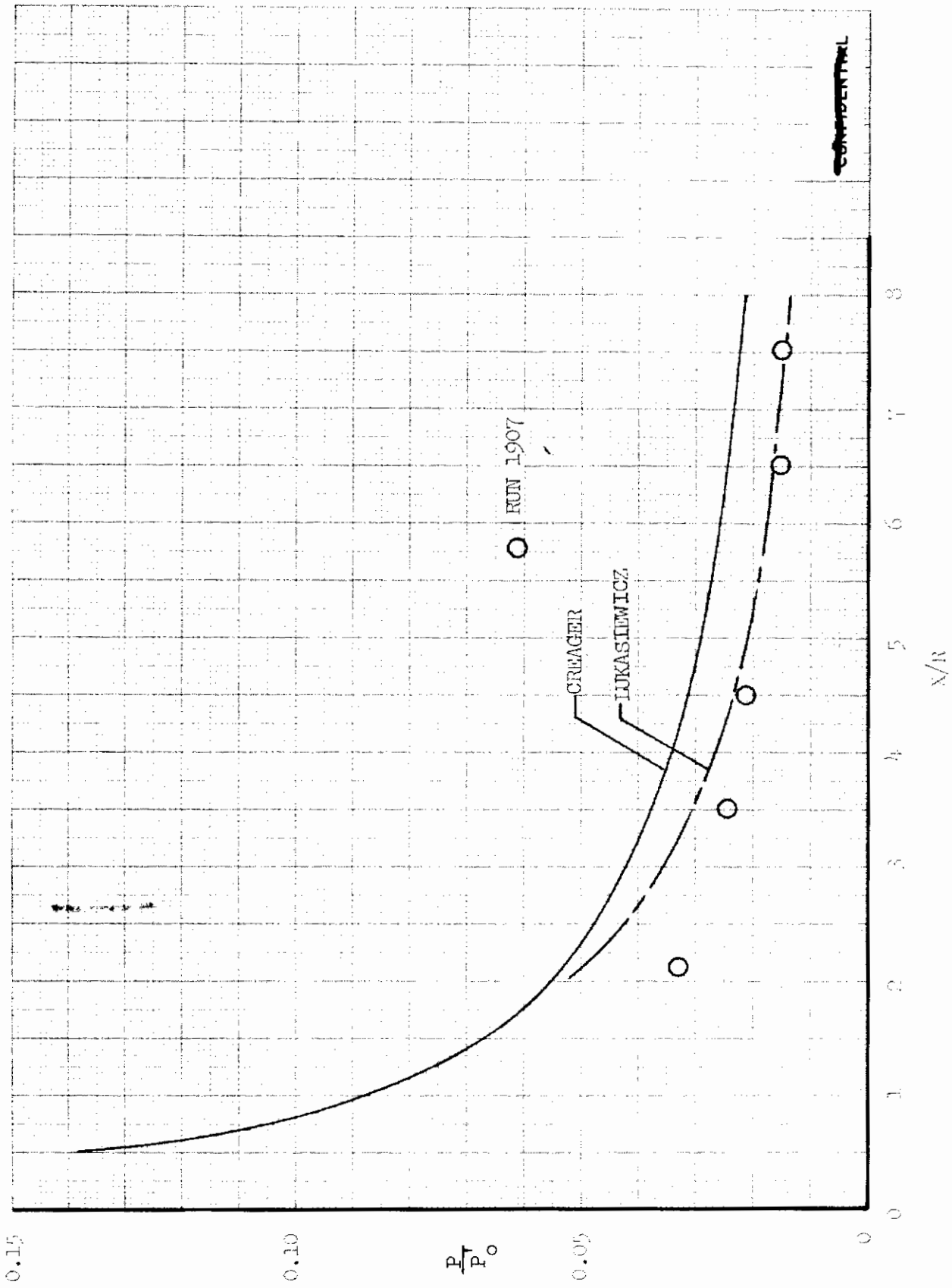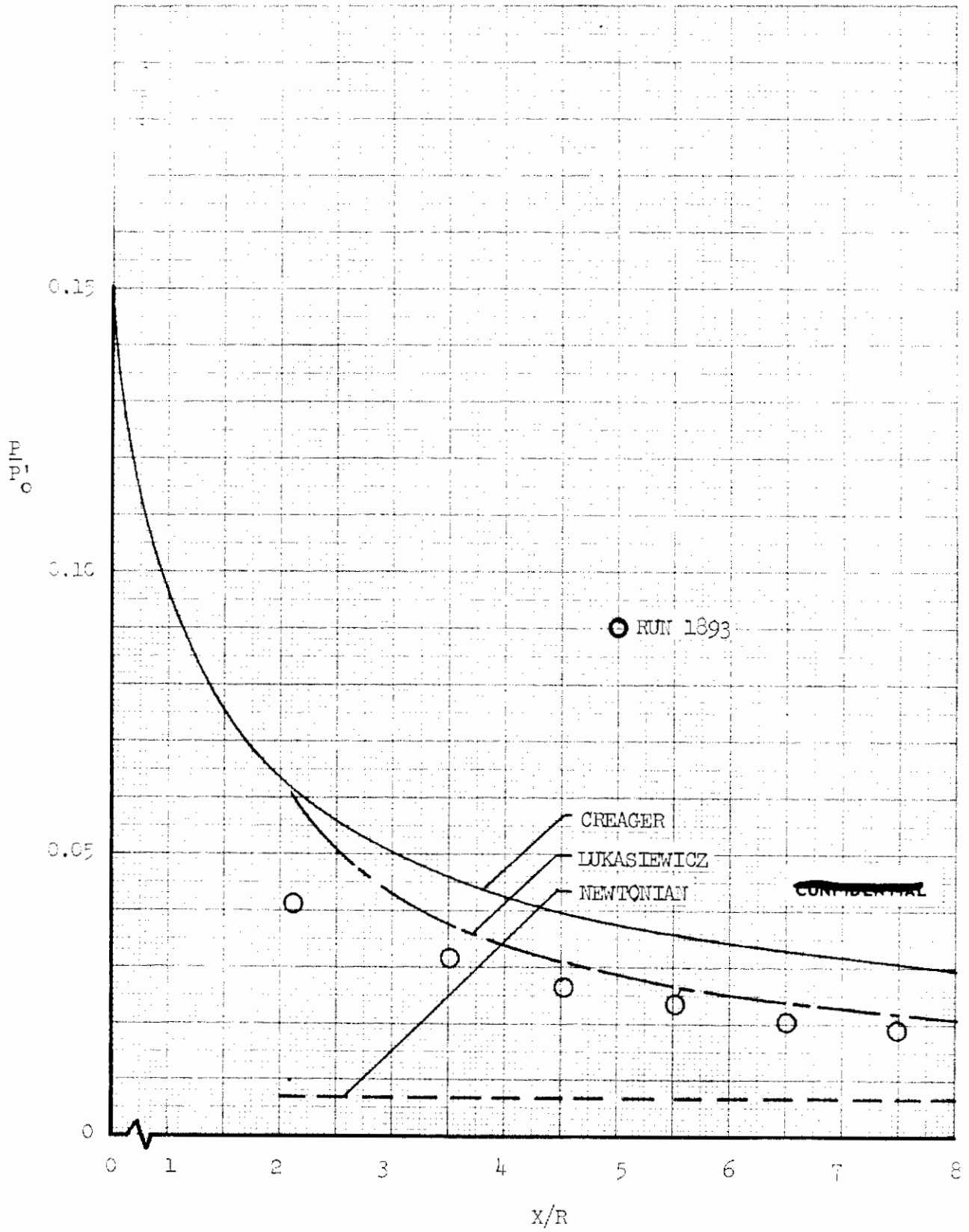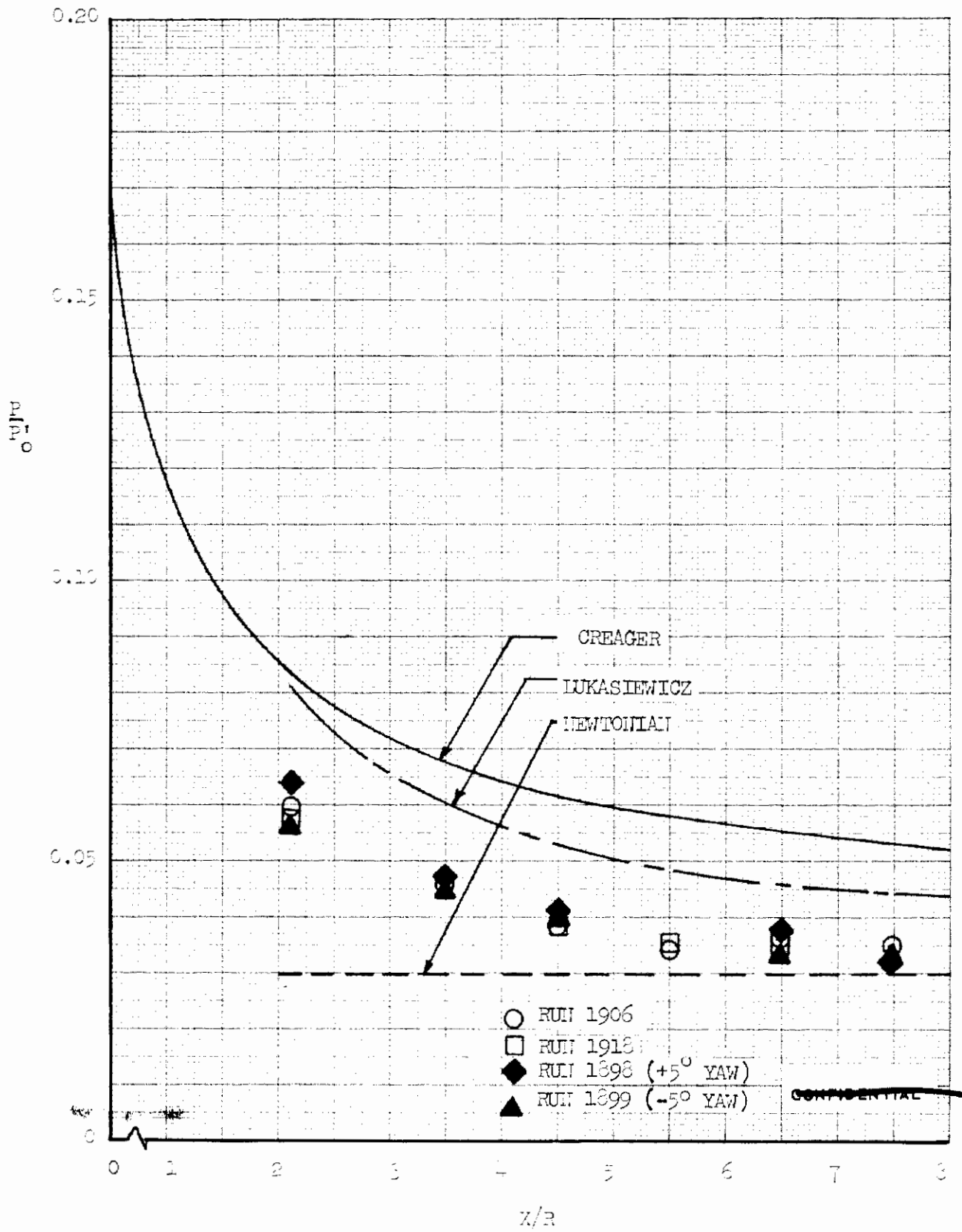FIGURE 270 (U) CENTERLINE PRESSURE DISTRIBUTION AT $\alpha = 5^{\circ}$

FIGURE 271 (U) CENTERLINE PRESSURE DISTRIBUTION AT $\alpha = 10^\circ$
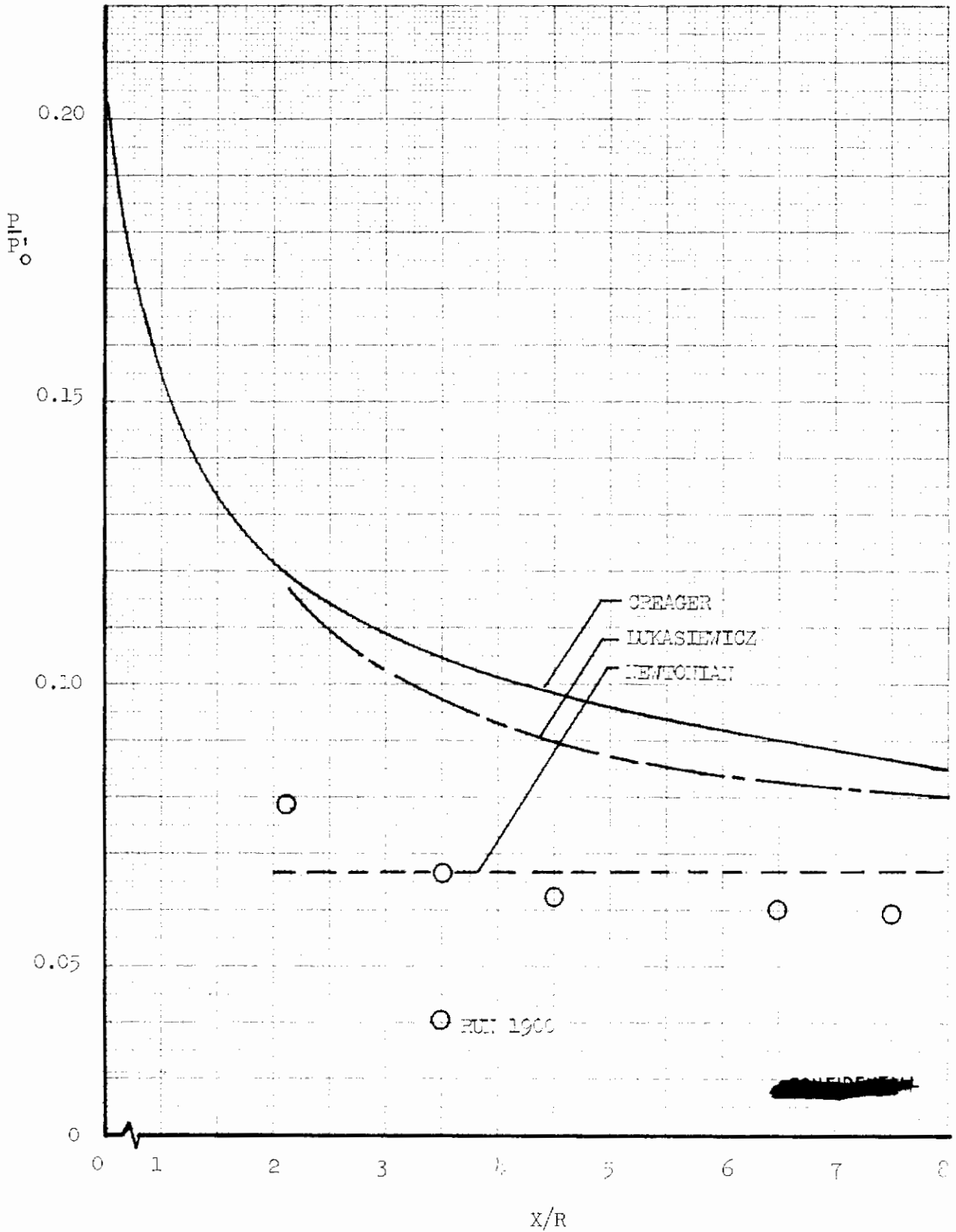
FIGURE 272 (U) CENTERLINE PRESSURE DISTRIBUTION AT $\alpha = 15^\circ$

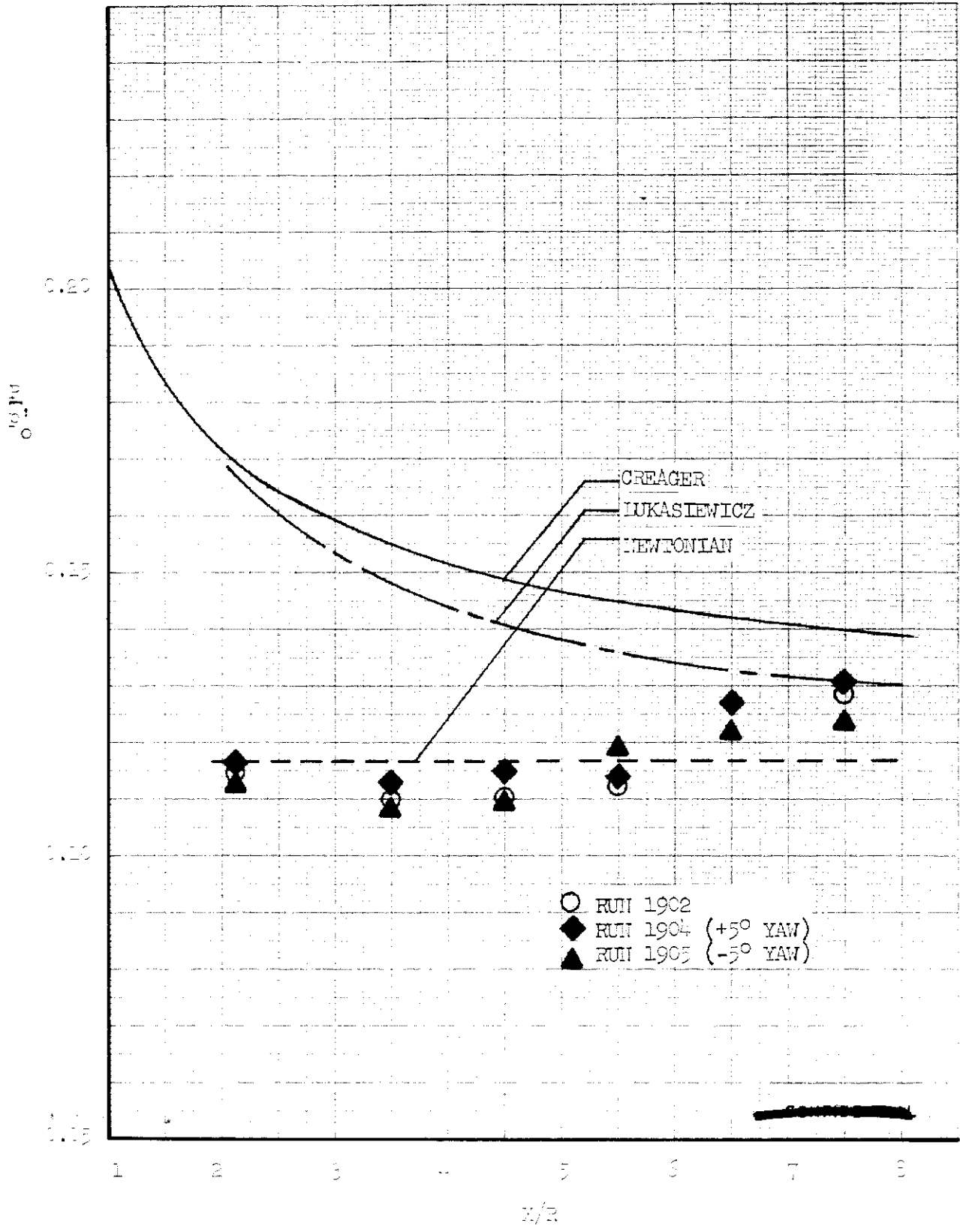FIGURE 273 (U) CENTERLINE PRESSURE DISTRIBUTION AT $\alpha = 20^{\circ}$

FIGURE 274 (U) CENTERLINE PRESSURE DISTRIBUTION AT $\alpha = 25^0$

FIGURE 275 (U) SPANWISE PRESSURE DISTRIBUTION AT STATION 12

375

FIGURE 276   (U) CORRELATION OF LEEWARD SURFACE CENTERLINE PRESSURES
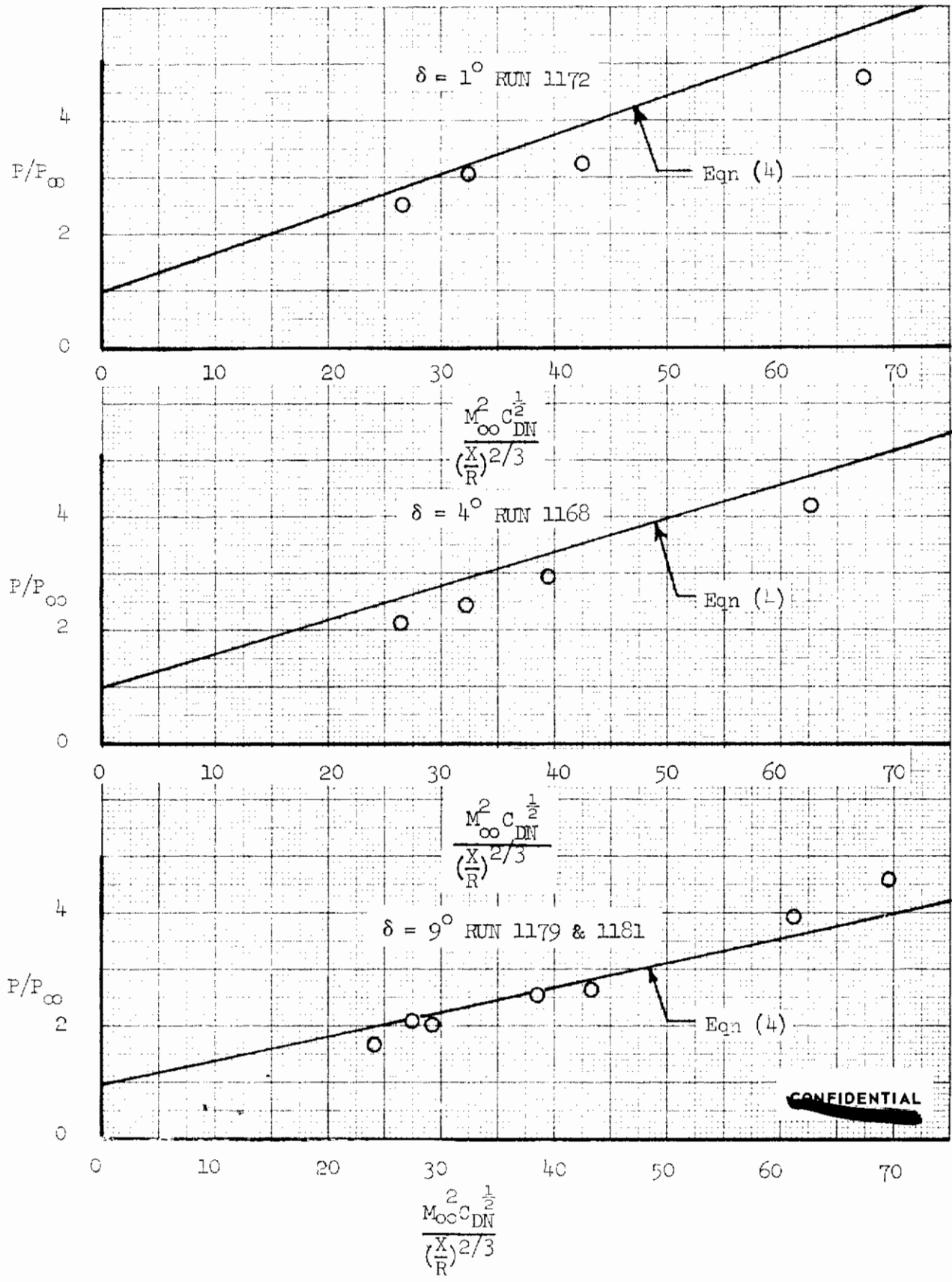
FIGURE 277 (U) UPPER SURFACE CENTERLINE PRESSURES ON AFFDL HIGH L/D
CONFIGURATION, SENSORS 31, 32, 33 and 34 (AEDC-TR-65-220)

377
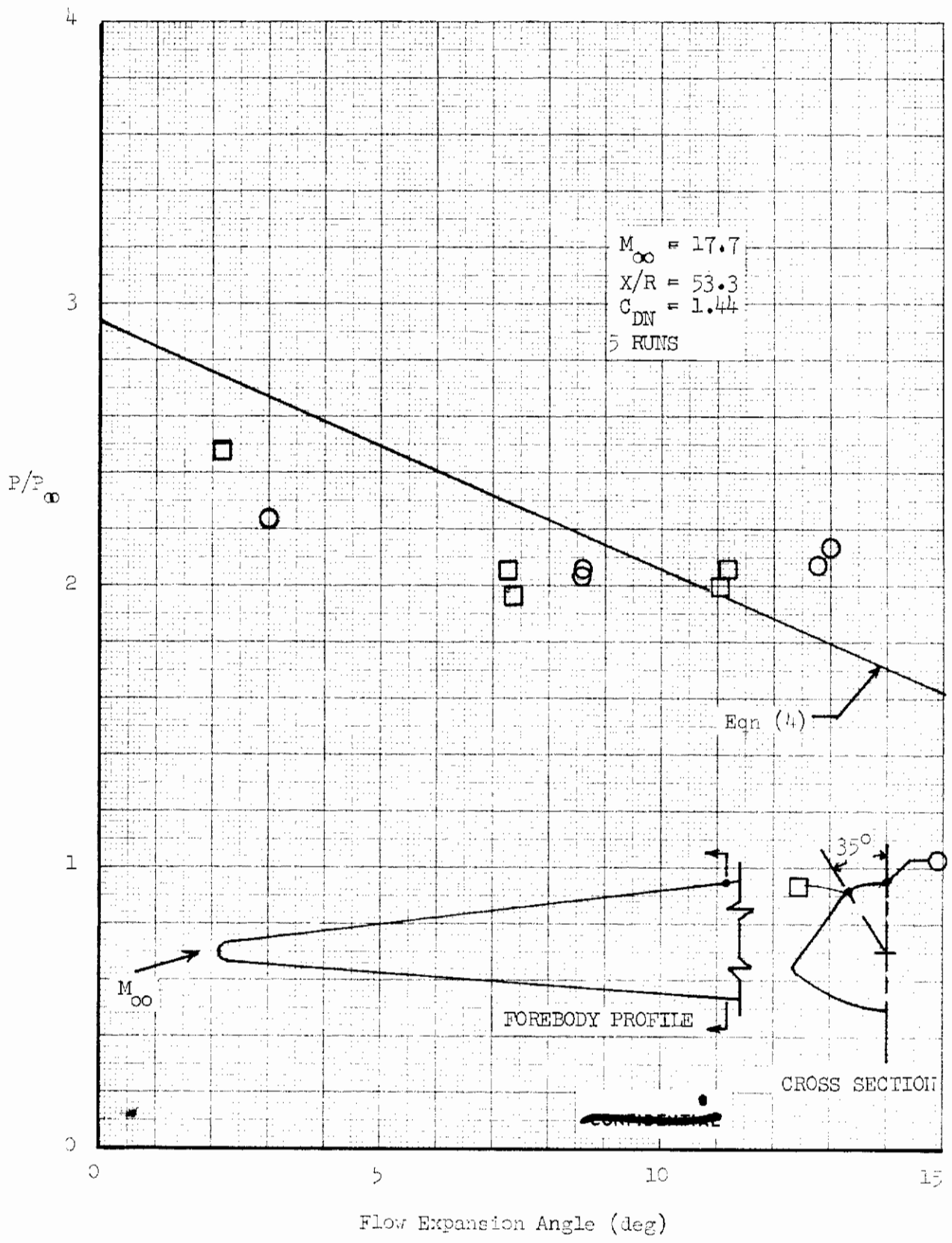
FIGURE 278   (U) UPPER FOREBODY PRESSURES ON F-5A MOD-1 HIGH L/D
CONFIGURATION

$$\frac{P}{P_\infty} = 1 + (0.110 - 0.005\delta)\frac{M_\infty^2 c_{DN}^{\frac{1}{2}}}{\left(\frac{X}{R}\right)^{2/3}}$$

■ $\alpha = 0°$ FROM FIG. 22 OF NASA TR-R-153

○ $\alpha = -5°$ FROM FIG. 27b OF NASA TR-R-153

◆ $\alpha = -10°$ FROM FIG. 27c OF NASA TR-R-153

UNCLASSIFIED
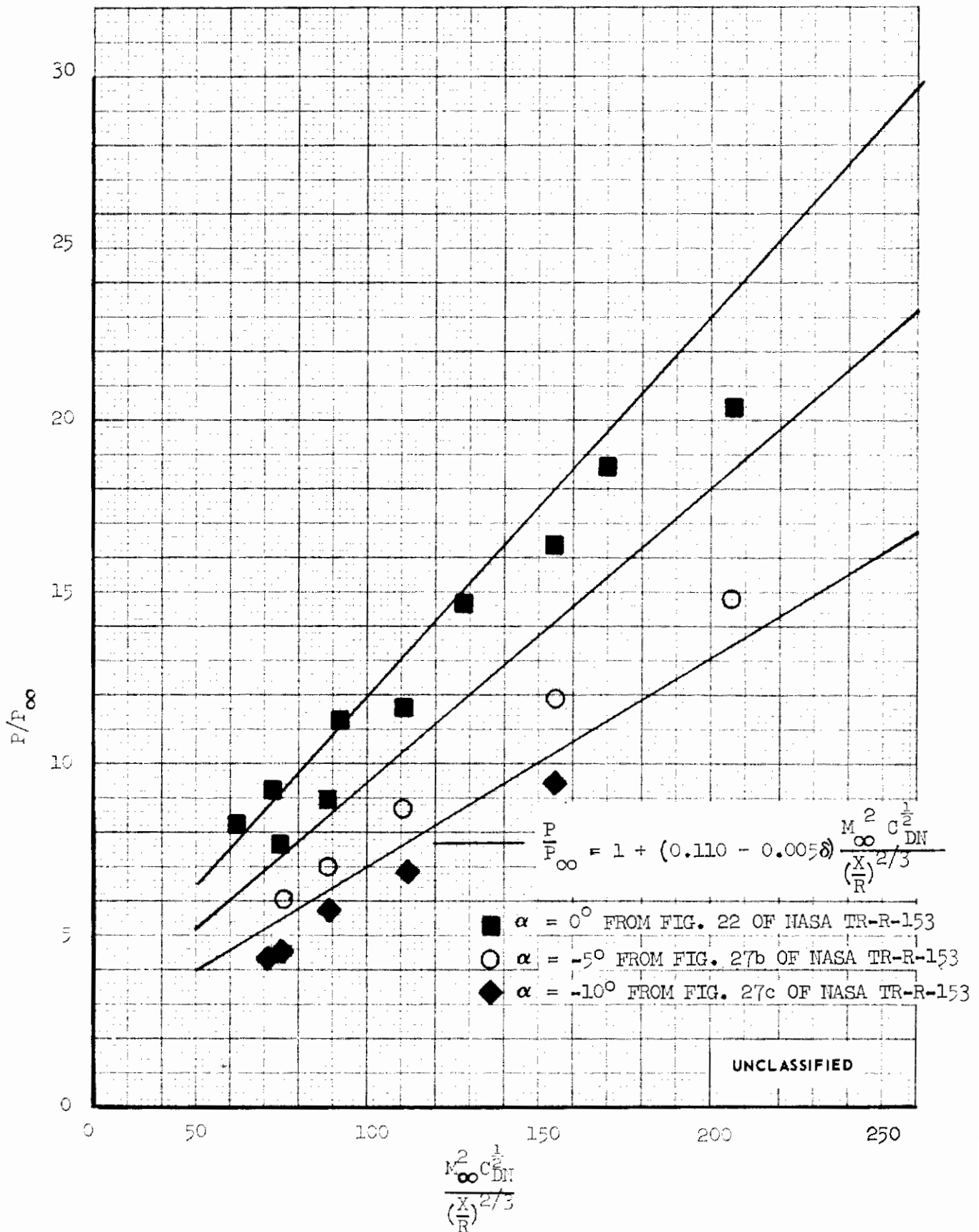
FIGURE 279 (U) CORRELATION OF LEEWARD SURFACE CENTERLINE PRESSURES AT
MACH 18 IN HELIUM

379
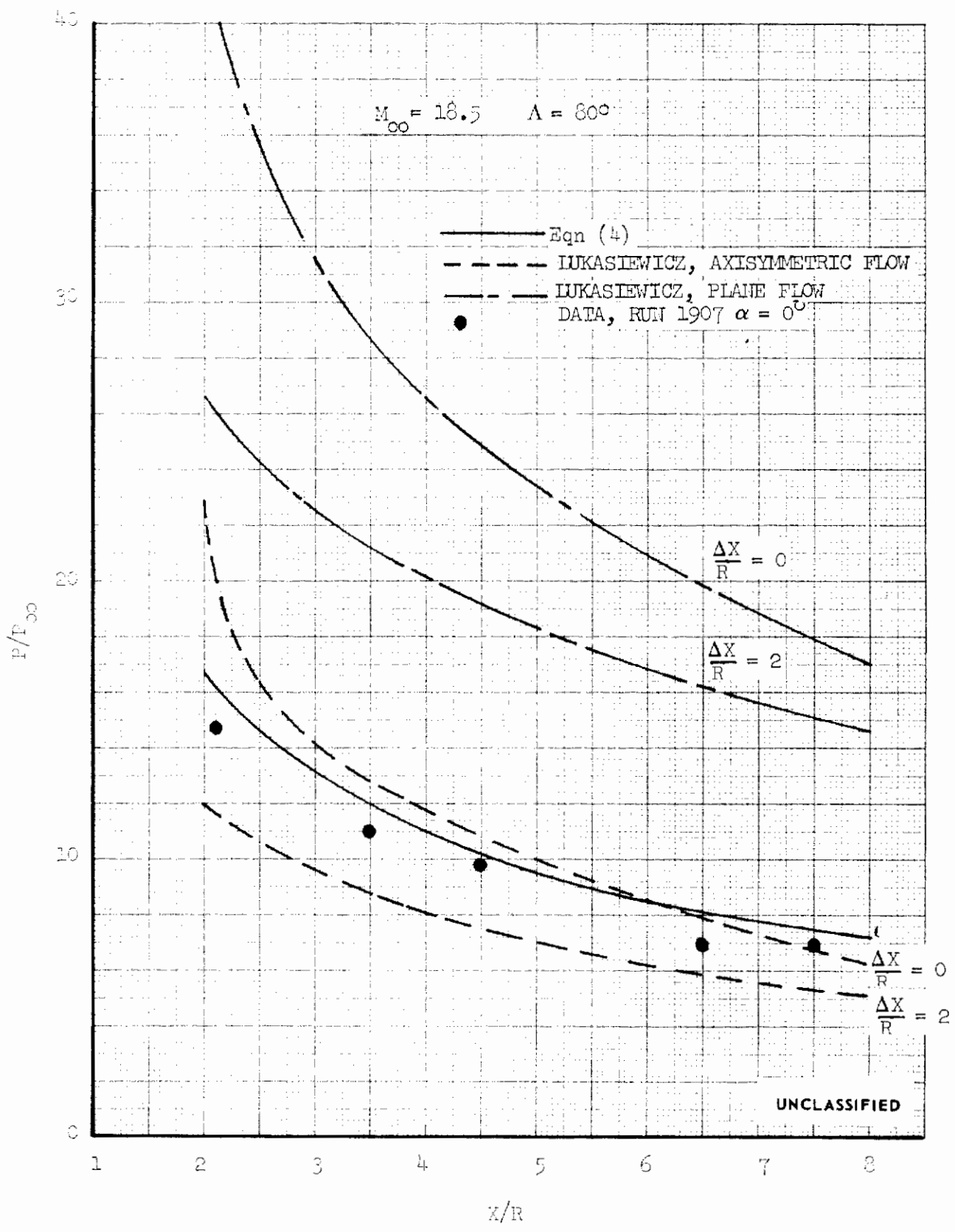
FIGURE 280   (U) CENTERLINE PRESSURE DISTRIBUTION AT $\alpha = 0$
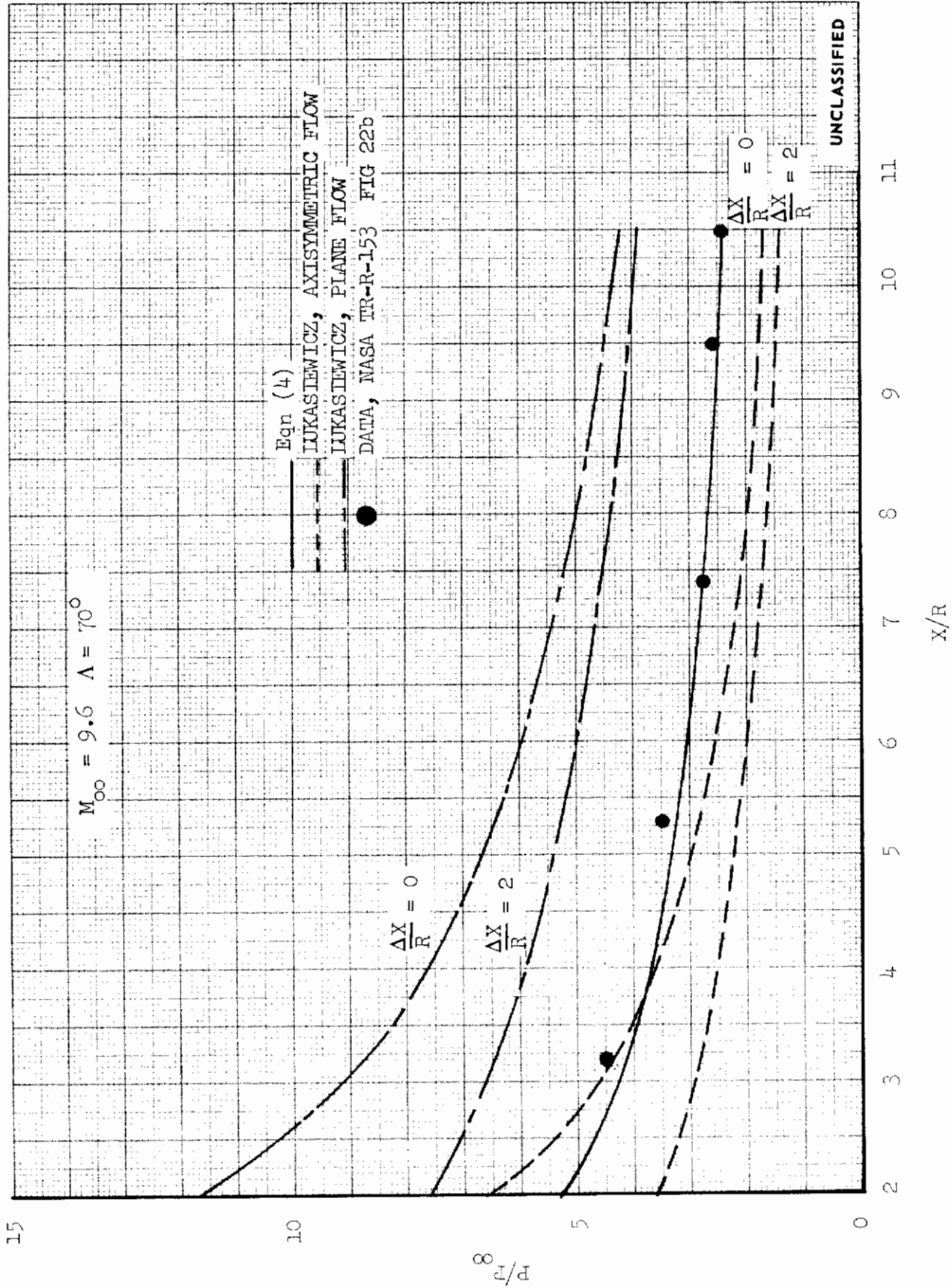
FIGURE 281 (U) CENTERLINE PRESSURE DISTRIBUTION AT $\alpha = 0°$
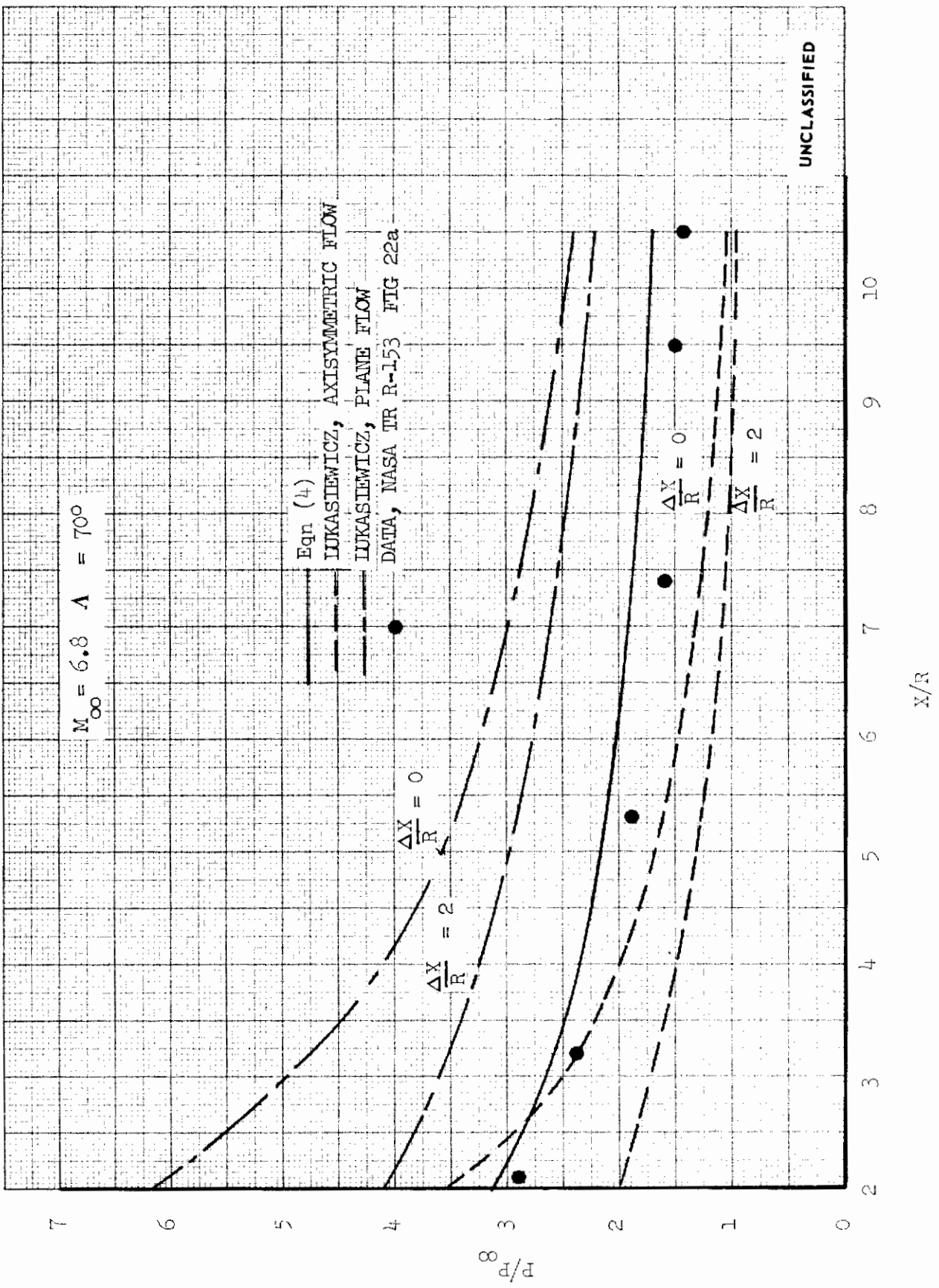
FIGURE 282 (U) CENTERLINE PRESSURE DISTRIBUTION AT $\alpha = 0^\circ$

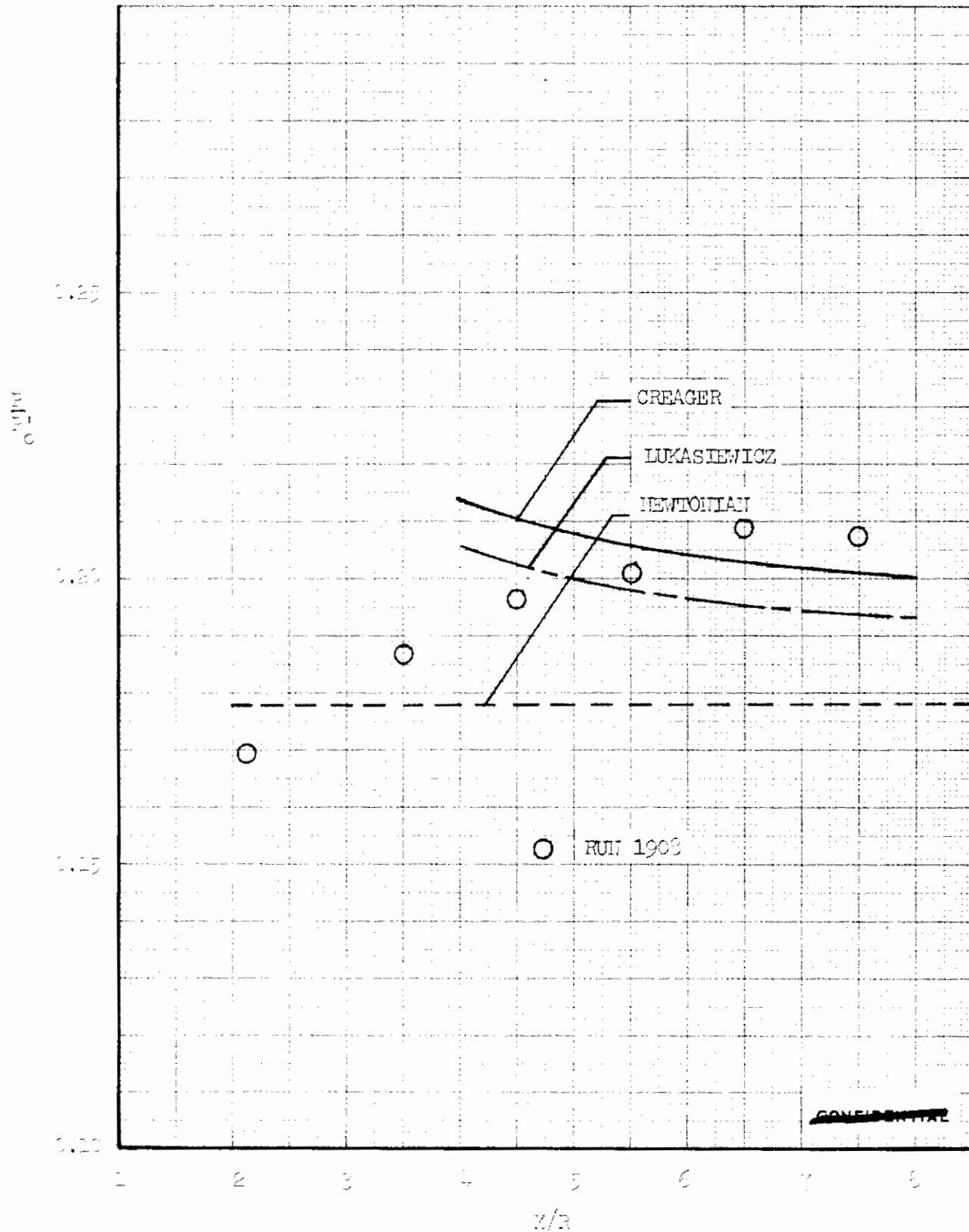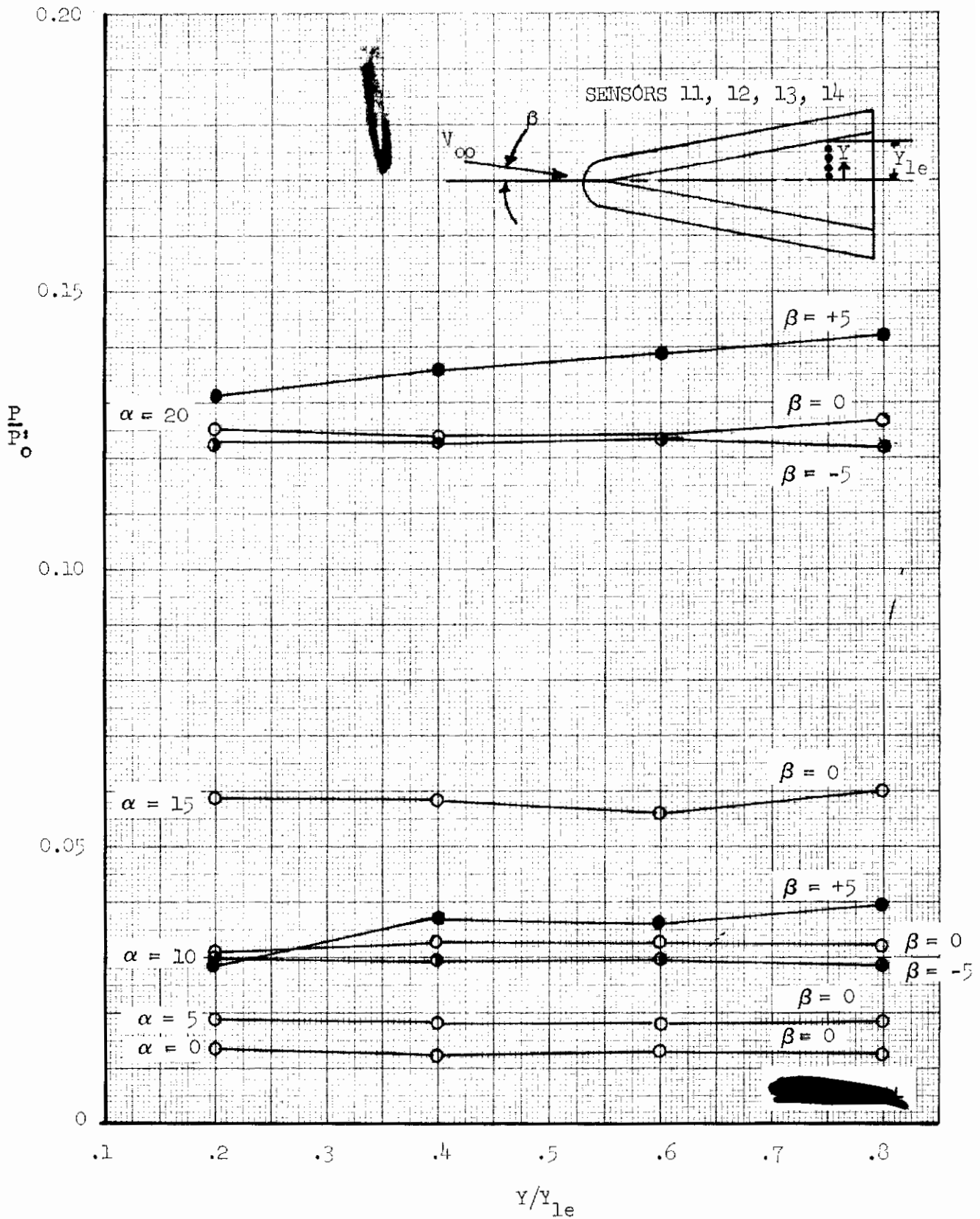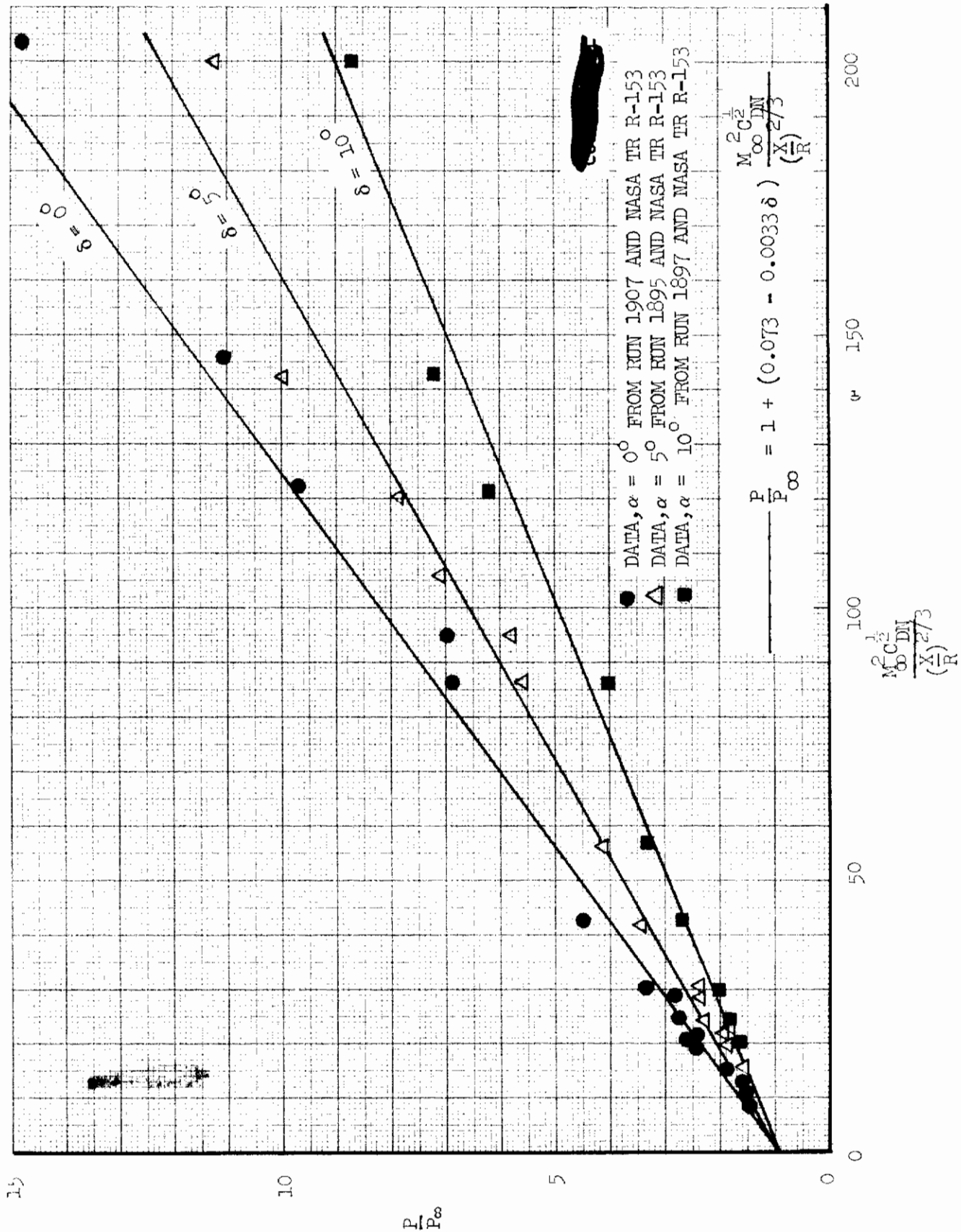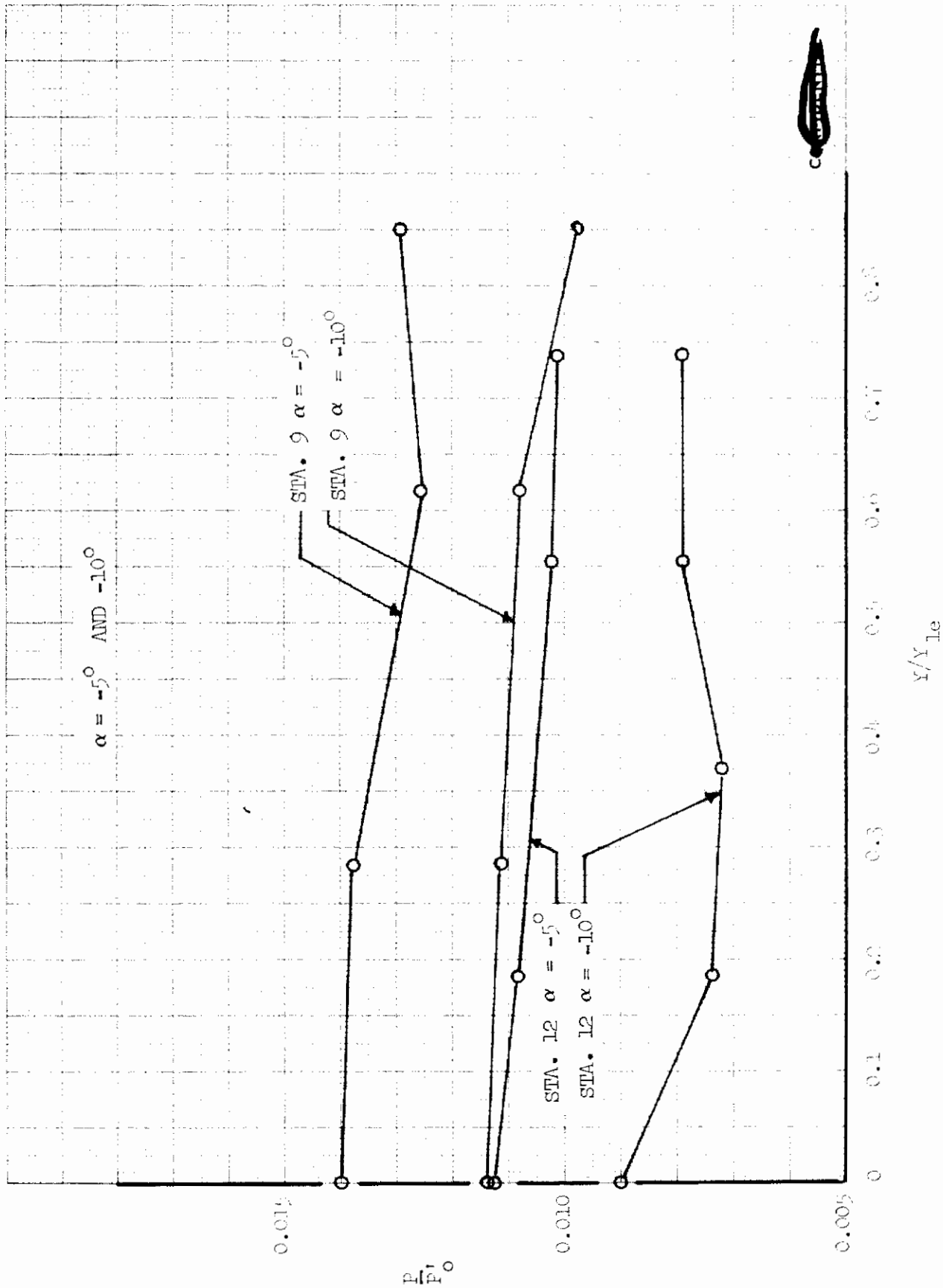FIGURE 283 (U) SPANWISE PRESSURE DISTRIBUTIONS AT STATIONS 9 AND 12
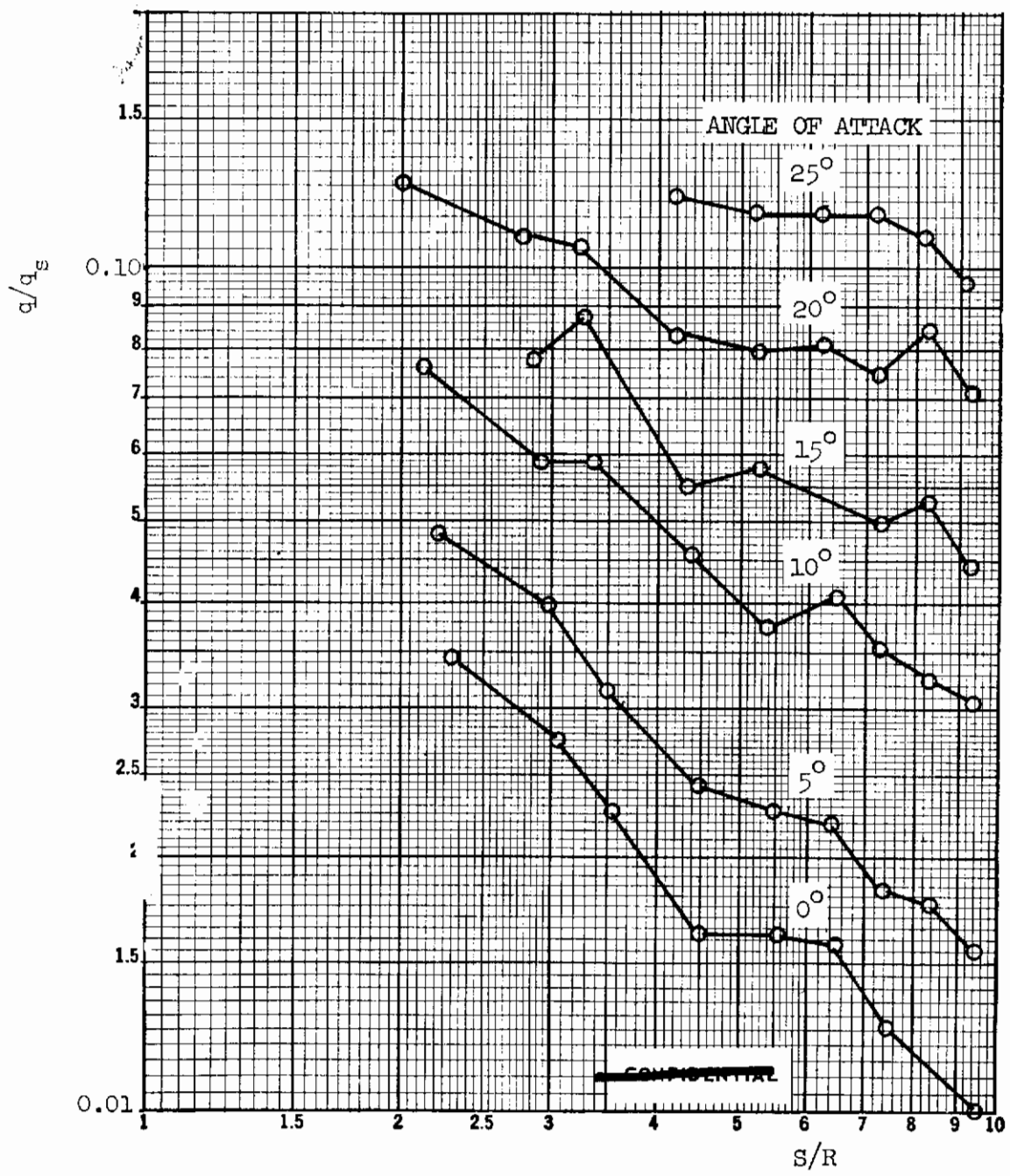
FIGURE 284 (U) CENTERLINE HEATING DISTRIBUTIONS ON 80 DEGREE SWEEP
DELTA WING

384
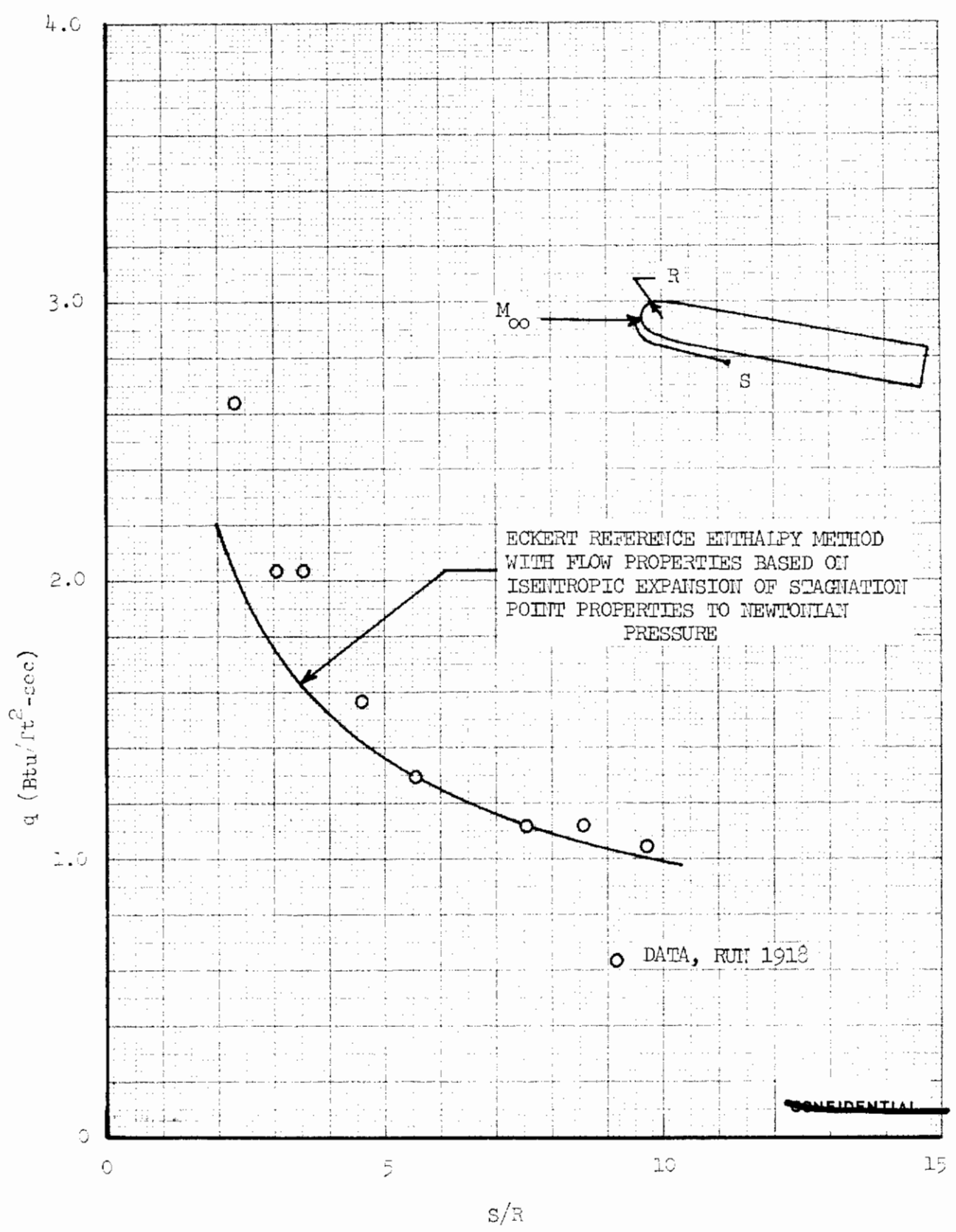
FIGURE 285 (U) CENTERLINE HEATING DISTRIBUTION AT $\alpha = 10^\circ$

385
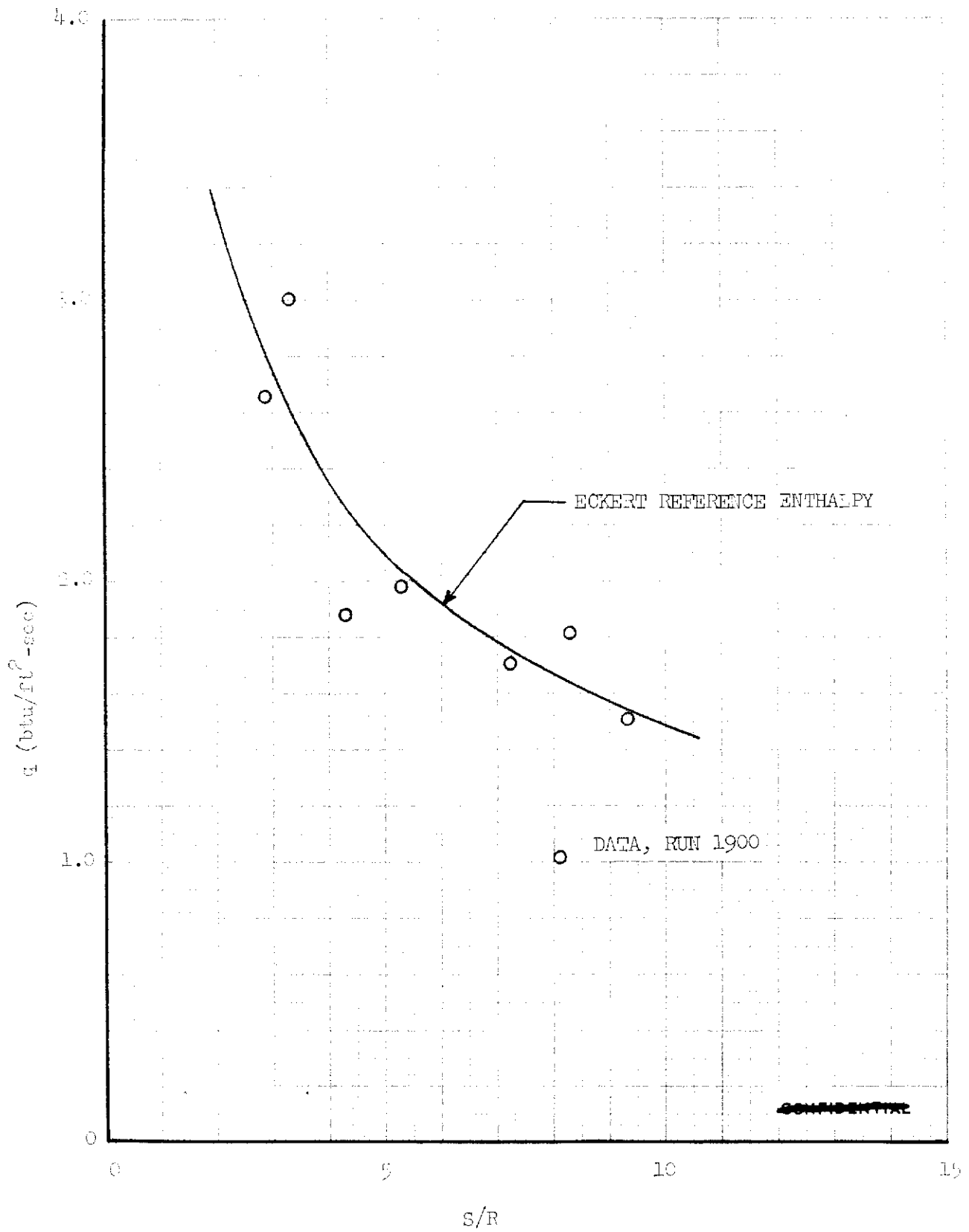
FIGURE 286 (U) CENTERLINE HEATING DISTRIBUTION AT $\alpha = 15^{\circ}$
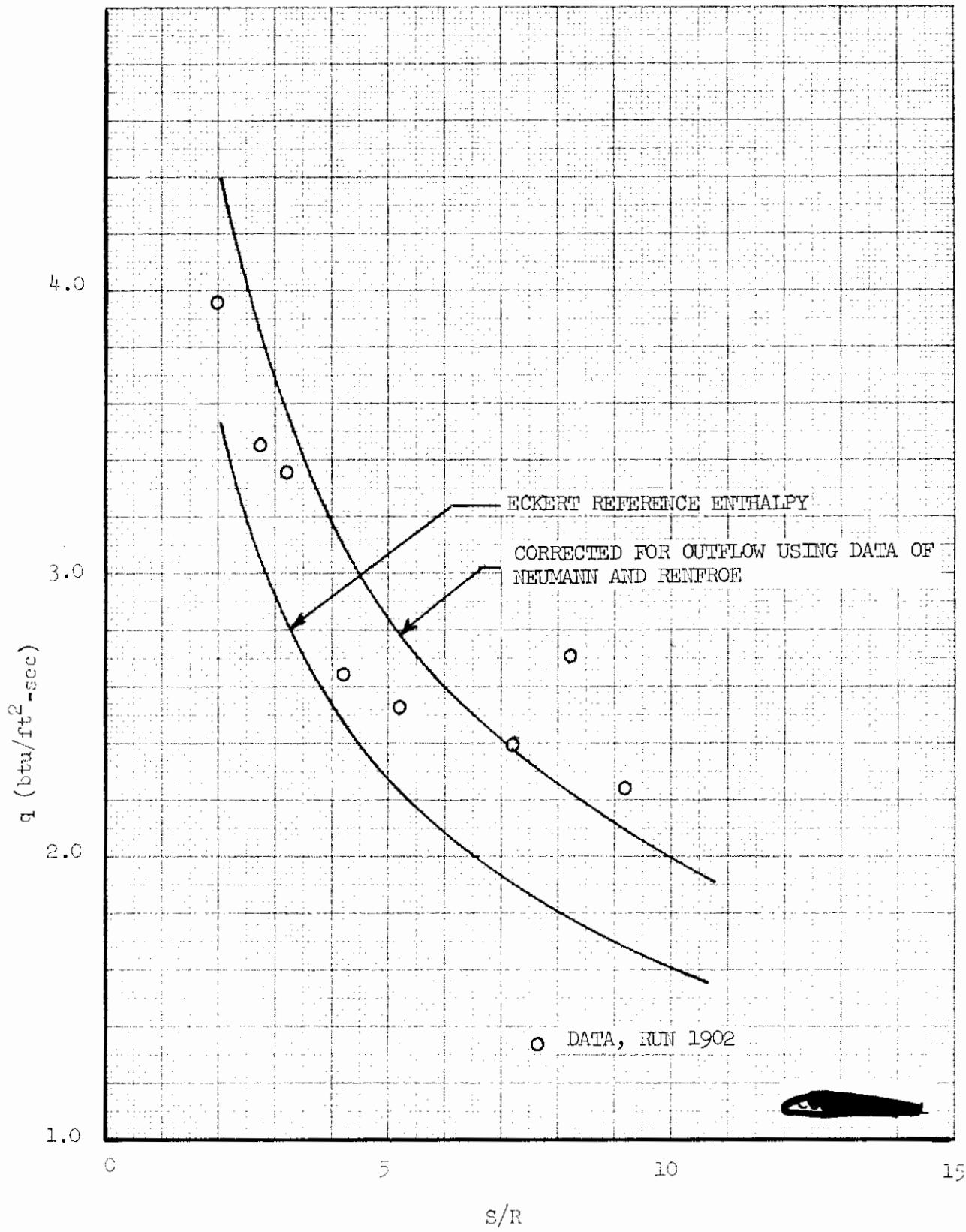
FIGURE 287 (U) CENTERLINE HEATING DISTRIBUTION AT $\alpha = 20^\circ$

387
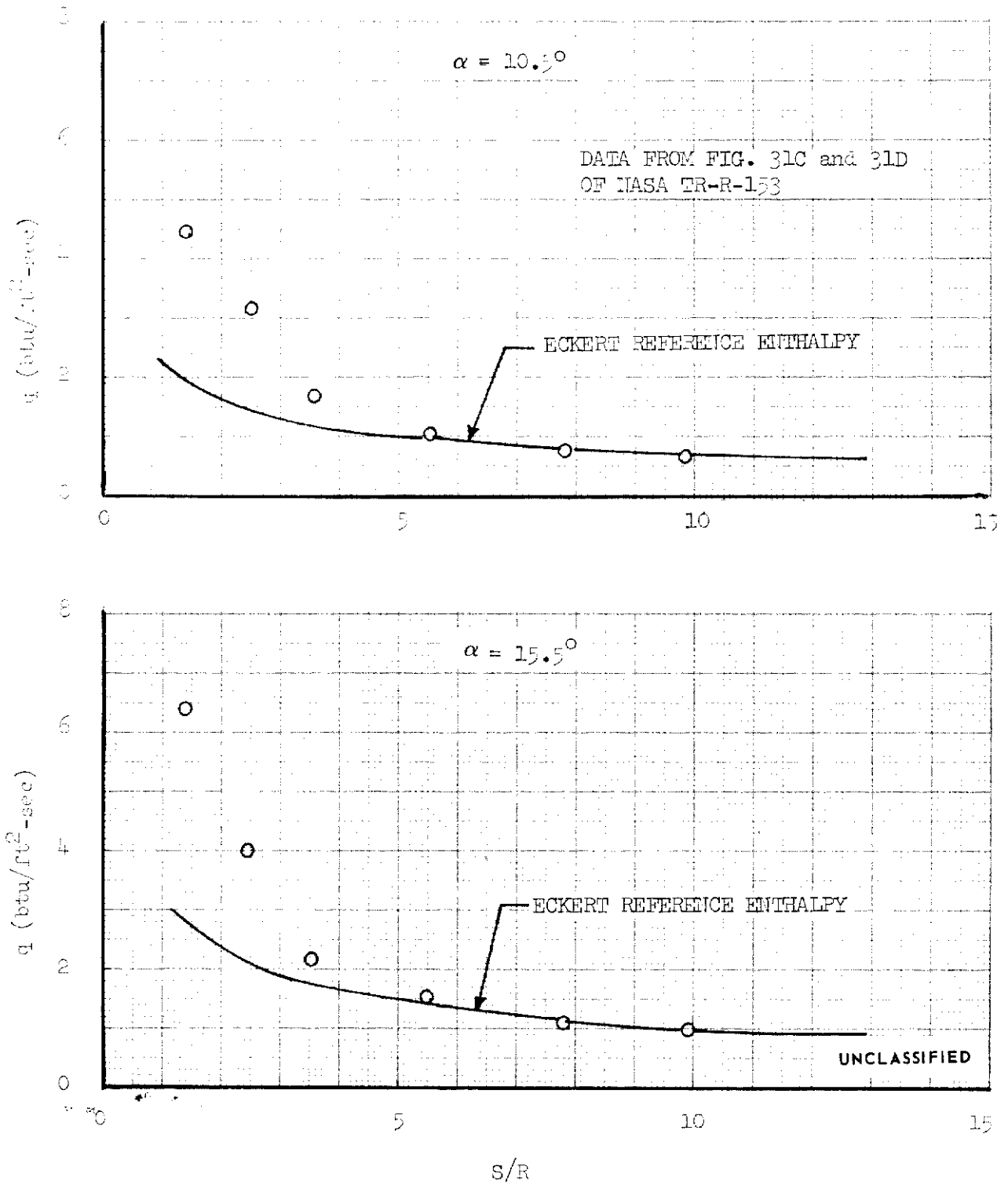
FIGURE 288   (U) CENTERLINE HEATING DISTRIBUTIONS ON A 70° SWEEP SLAB
DELTA WING $M_\infty = 9.6$ $Re_{\infty,D} = 8 \times 10^4$

388
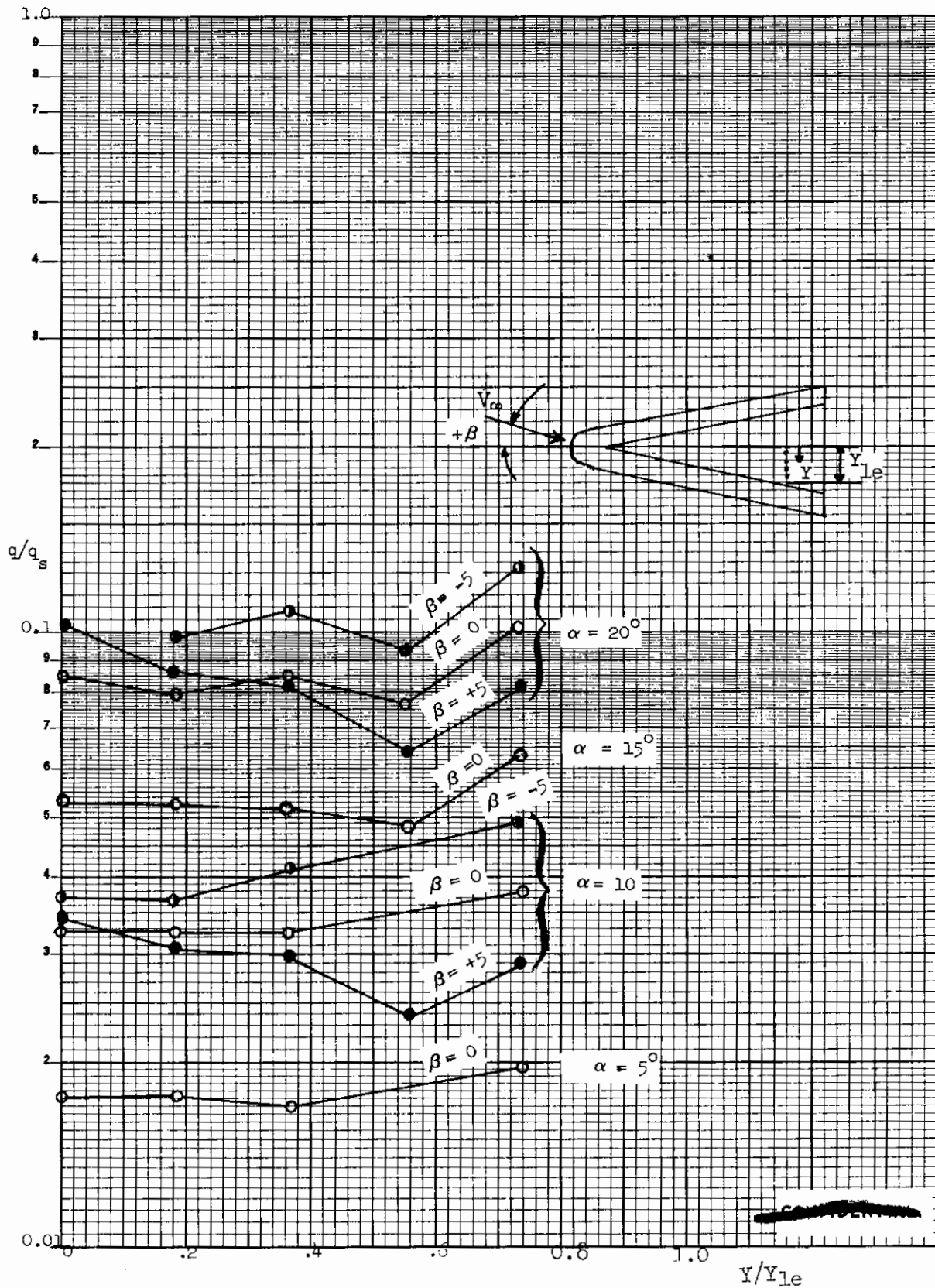
FIGURE 289 (U) SPANWISE HEATING DISTRIBUTION AT STATION 12
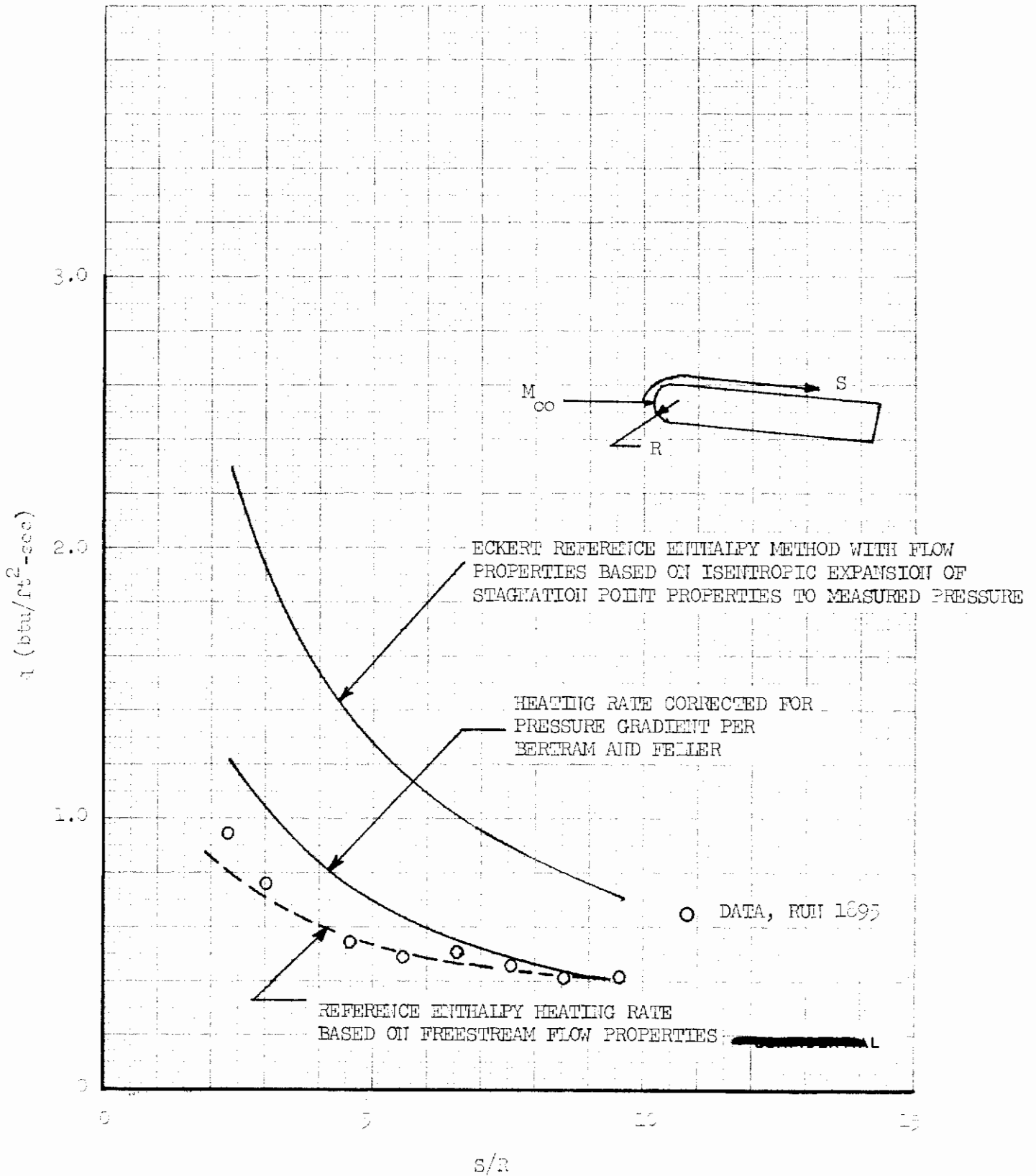
FIGURE 290   (U) CENTERLINE HEATING DISTRIBUTION AT $\alpha = -5^\circ$
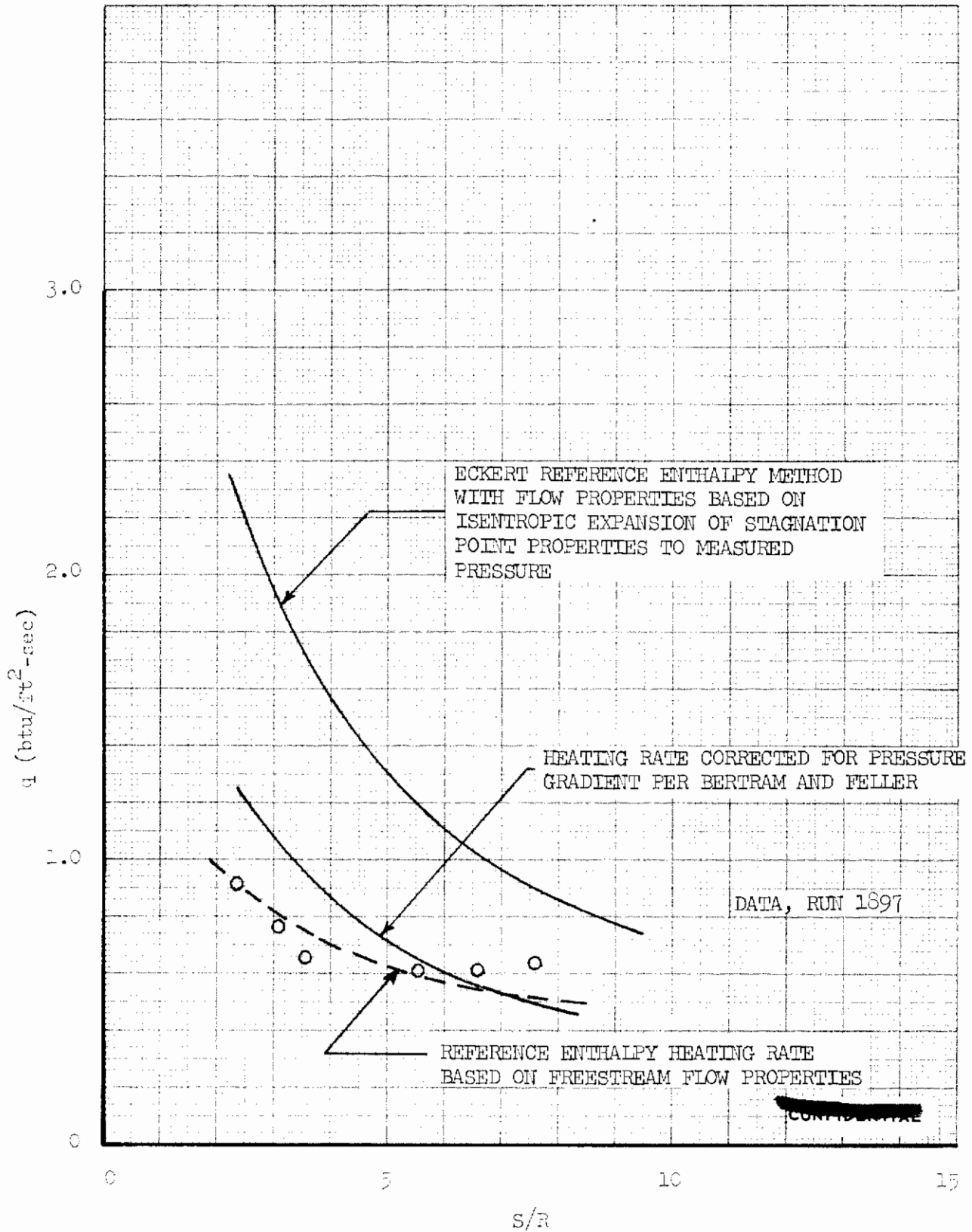
FIGURE 291 (U) CENTERLINE HEATING DISTRIBUTION AT $\alpha = -10^{O}$

391
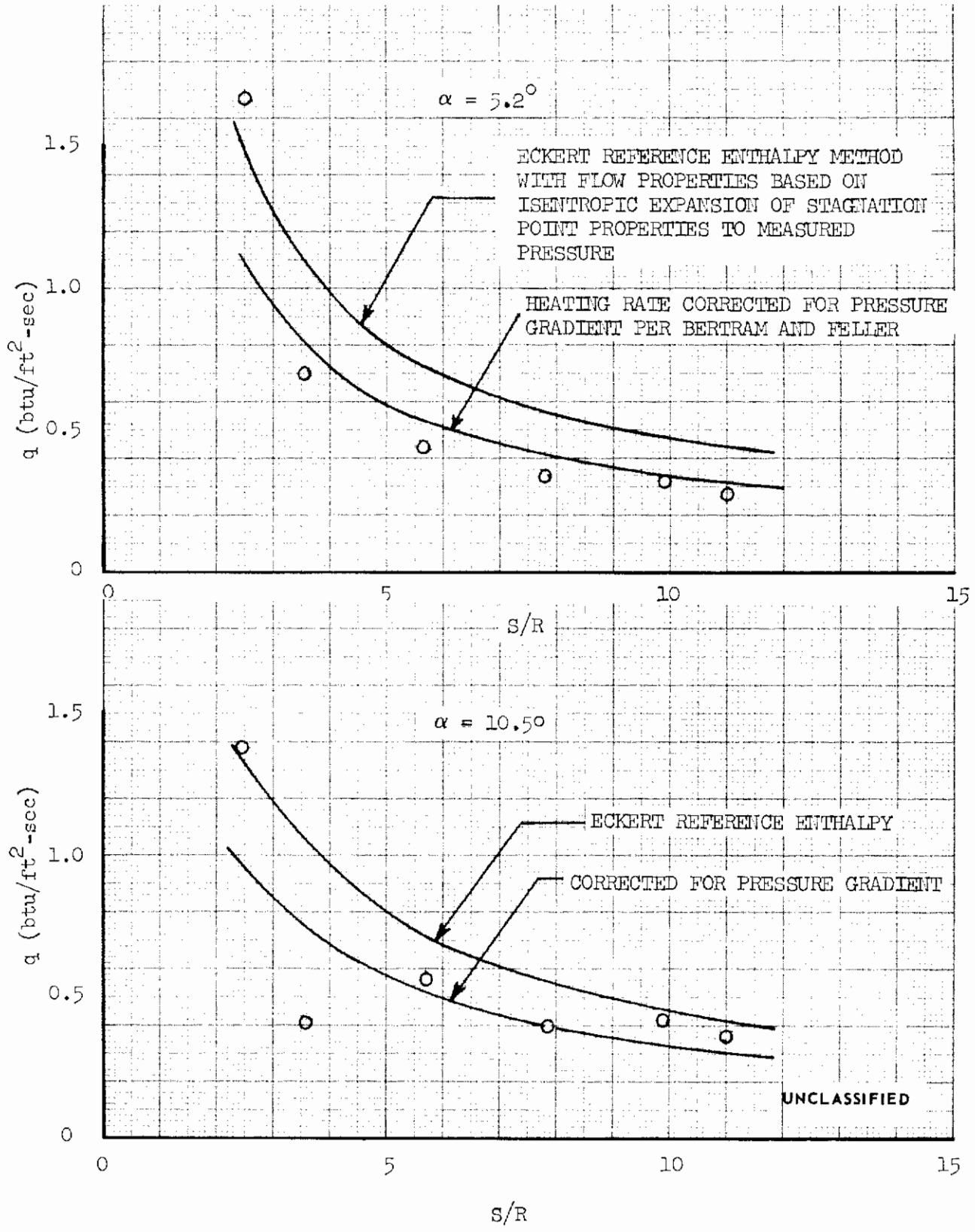
FIGURE 292 (U) LEEWARD SURFACE CENTERLINE HEATING ON A 70 DEGREE
SWEEP SLAB DELTA WING (FIGS. 31b and 31c OF NASA TR-R-153)

RUN 1229 $\alpha = 10^\circ$ (4° EXPANSION)

ECKERT REFERENCE ENTHALPY
ASSUMING ISENTROPIC EXPANSION
FROM STAGNATION POINT TO
PREDICTED SURFACE PRESSURE

CORRECTED FOR PRESSURE GRADIENT

RUN 1230 $\alpha = 15^\circ$ (9° EXPANSION)

ECKERT REFERENCE ENTHALPY

CORRECTED FOR PRESSURE GRADIENT

FIGURE 293   (U) UPPER SURFACE CENTERLINE HEATING ON AFFDL HIGH L/D
CONFIGURATION SENSORS 31, 32, 33 and 34 (AEDC-TR-65-220)

393
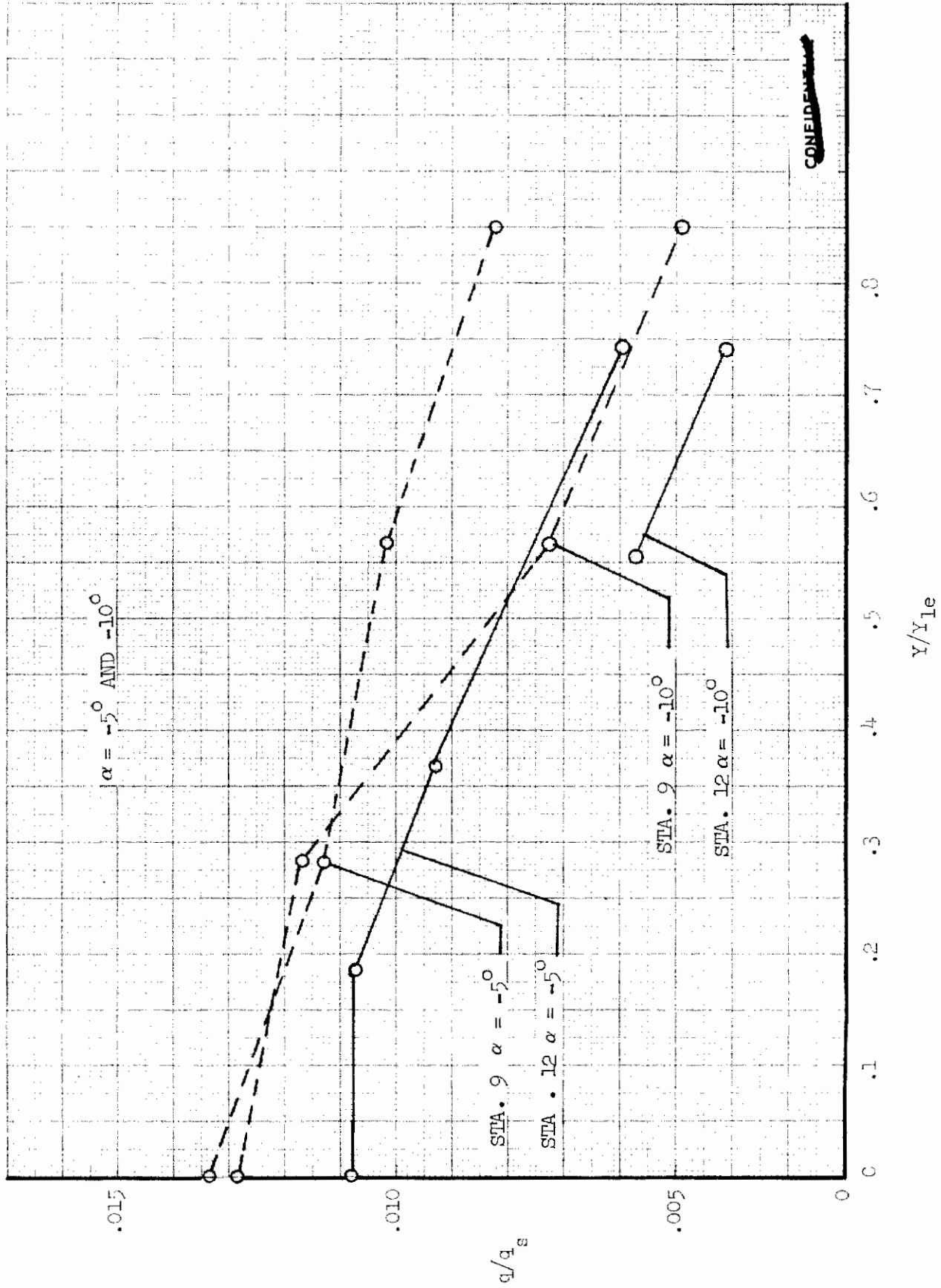
FIGURE 294 (U) SPANWISE HEATING DISTRIBUTION AT STATIONS 9 AND 12

Contrails

DOCUMENT CONTROL DATA - R&D

(Security classification of title, body of abstract and indexing annotation must be entered when the overall report is classified)

1. ORIGINATING ACTIVITY (Corporate author)	2a. REPORT SECURITY CLASSIFICATION
LOCKHEED AIRCRAFT CORP. BURBANK, CALIFORNIA	CONFIDENTIAL
	2b. GROUP 4

3. REPORT TITLE

PRELIMINARY DESIGN AND EXPERIMENTAL INVESTIGATION OF THE FDL-5A UNMANNED HIGH L/D SPACECRAFT (PART IV AEROTHERMODYNAMICS)

4. DESCRIPTIVE NOTES (Type of report and inclusive dates)

FINAL REPORT - VOLUME IV (July 1, 1966 through March 31, 1968)

5. AUTHOR(S) (Last name, first name, initial)

Guard, Fred L. and Schultz, Howard D.

6. REPORT DATE	7a. TOTAL NO. OF PAGES	7b. NO. OF REFS
March 1968	394	36

8a. CONTRACT OR GRANT NO.	9a. ORIGINATOR'S REPORT NUMBER(S)
AF 33(615)-5241	LR 21204 LAC/619518
b. PROJECT NO. 1366	
c.	9b. OTHER REPORT NO(S) (Any other numbers that may be assigned this report)
d.	AFFDL-TR-68-24 PART IV

10. AVAILABILITY/LIMITATION NOTICES

This report is subject to special export controls and each transmittal to foreign governments or foreign nationals may be made only with prior approval of the Air Force Flight Dynamics Laboratory (FDMS), Wright-Patterson Air Force Base, Ohio 45433.

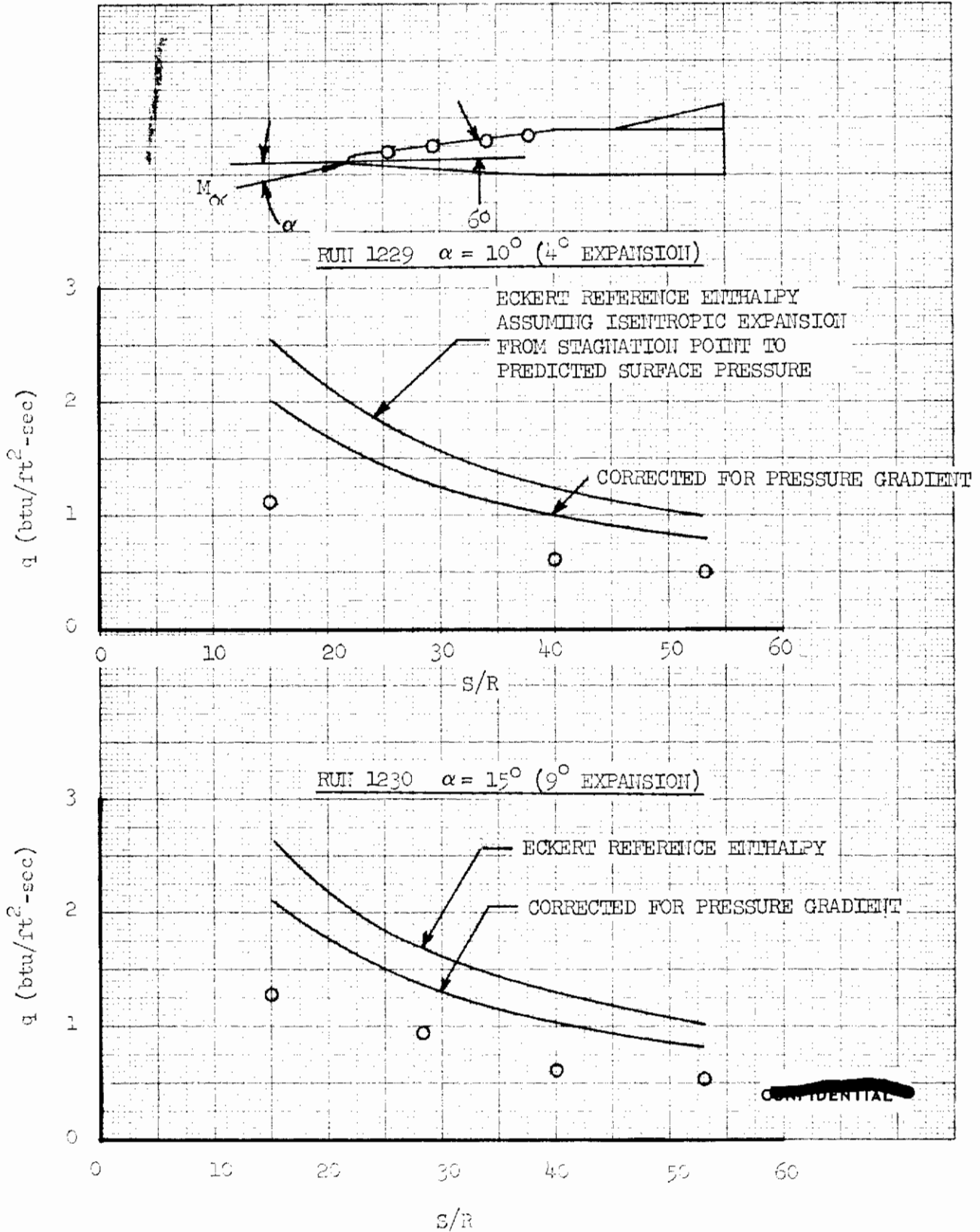| 11. SUPPLEMENTARY NOTES	12. SPONSORING MILITARY ACTIVITY
	Air Force Flight Dynamics Laboratory Air Force Systems Command Wright-Patterson Air Force Base, Ohio 45433

13. ABSTRACT

(U) Design and experimental analyses of unmanned entry research vehicles having high hypersonic L/D and high volume are described. Analytic parametric data are presented for two lifting body classes designated HLD-35 and FDL-5. Experimental aerodynamic and heat transfer data obtained from Arnold Engineering Development Wind Tunnels A, B, C, and F are compared with analytic data for the FDL-5 vehicle. Structure and subsystems are selected for performing unmanned hypersonic research with the vehicle.

DD FORM 1 JAN 64 **1473**   *0101-807-6800*

14. KEY WORDS	LINK A		LINK B		LINK C	
	ROLE	WT	ROLE	WT	ROLE	WT
* High L/D Entry Vehicles						
* Aerothermodynamic Wind Tunnel Test Program						
* FDL-5 Configuration						
* Pressure and Heat Transfer Test Data						

INSTRUCTIONS

1. ORIGINATING ACTIVITY: Enter the name and address of the contractor, subcontractor, grantee, Department of Defense activity or other organization (corporate author) issuing the report.

2a. REPORT SECURITY CLASSIFICATION: Enter the overall security classification of the report. Indicate whether "Restricted Data" is included. Marking is to be in accordance with appropriate security regulations.

2b. GROUP: Automatic downgrading is specified in DoD Directive 5200.10 and Armed Forces Industrial Manual. Enter the group number. Also, when applicable, show that optional markings have been used for Group 3 and Group 4 as authorized.

3. REPORT TITLE: Enter the complete report title in all capital letters. Titles in all cases should be unclassified. If a meaningful title cannot be selected without classification, show title classification in all capitals in parenthesis immediately following the title.

4. DESCRIPTIVE NOTES: If appropriate, enter the type of report, e.g., interim, progress, summary, annual, or final. Give the inclusive dates when a specific reporting period is covered.

5. AUTHOR(S): Enter the name(s) of author(s) as shown on or in the report. Enter last name, first name, middle initial. If military, show rank and branch of service. The name of the principal author is an absolute minimum requirement.

6. REPORT DATE: Enter the date of the report as day, month, year; or month, year. If more than one date appears on the report, use date of publication.

7a. TOTAL NUMBER OF PAGES: The total page count should follow normal pagination procedures, i.e., enter the number of pages containing information.

7b. NUMBER OF REFERENCES: Enter the total number of references cited in the report.

8a. CONTRACT OR GRANT NUMBER: If appropriate, enter the applicable number of the contract or grant under which the report was written.

8b, &c, & 8d. PROJECT NUMBER: Enter the appropriate military department identification, such as project number, subproject number, system numbers, task number, etc.

9a. ORIGINATOR'S REPORT NUMBER(S): Enter the official report number by which the document will be identified and controlled by the originating activity. This number must be unique to this report.

9b. OTHER REPORT NUMBER(S): If the report has been assigned any other report numbers (either by the originator or by the sponsor), also enter this number(s).

10. AVAILABILITY/LIMITATION NOTICES: Enter any limitations on further dissemination of the report, other than those imposed by security classification, using standard statements such as:

(1) "Qualified requesters may obtain copies of this report from DDC."

(2) "Foreign announcement and dissemination of this report by DDC is not authorized."

(3) "U. S. Government agencies may obtain copies of this report directly from DDC. Other qualified DDC users shall request through
_____ ."

(4) "U. S. military agencies may obtain copies of this report directly from DDC. Other qualified users shall request through
_____ ."

(5) "All distribution of this report is controlled. Qualified DDC users shall request through
_____ ."

If the report has been furnished to the Office of Technical Services, Department of Commerce, for sale to the public, indicate this fact and enter the price, if known.

11. SUPPLEMENTARY NOTES: Use for additional explanatory notes.

12. SPONSORING MILITARY ACTIVITY: Enter the name of the departmental project office or laboratory sponsoring (paying for) the research and development. Include address.

13. ABSTRACT: Enter an abstract giving a brief and factual summary of the document indicative of the report, even though it may also appear elsewhere in the body of the technical report. If additional space is required, a continuation sheet shall be attached.

It is highly desirable that the abstract of classified reports be unclassified. Each paragraph of the abstract shall end with an indication of the military security classification of the information in the paragraph, represented as (TS), (S), (C), or (U).

There is no limitation on the length of the abstract. However, the suggested length is from 150 to 225 words.

14. KEY WORDS: Key words are technically meaningful terms or short phrases that characterize a report and may be used as index entries for cataloging the report. Key words must be selected so that no security classification is required. Identifiers, such as equipment model designation, trade name, military project code name, geographic location, may be used as key words but will be followed by an indication of technical context. The assignment of links, roles, and weights is optional.